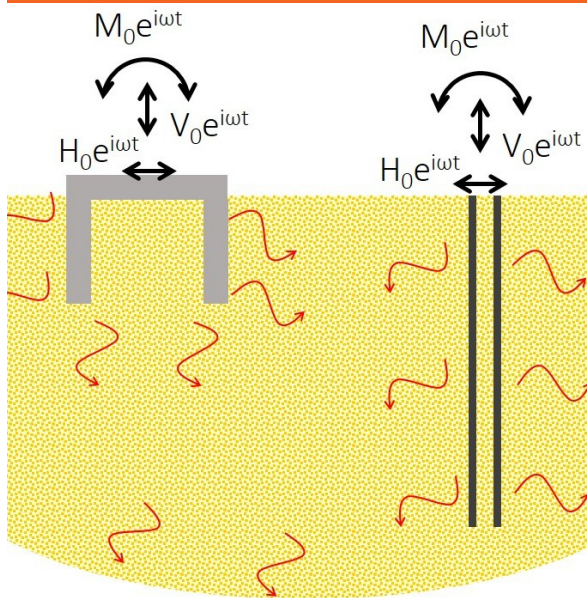


Numerical modelling of offshore foundations for jacket structures



Chiara Latini

PhD Thesis

Department of Civil Engineering
2018

DTU Civil Engineering Report 391

Numerical modelling of offshore foundations for jacket structures

Ph.D in Civil Engineering
Project Timeline: 01.08.2014-31.10.2017

Department of Civil Engineering
Technical University of Denmark

Supervisor:
Varvara Zania
Associate Professor
Department of Civil Engineering
Technical University of Denmark

Chiara Latini, s121315

Acknowledgements

I would like to thank my supervisor, Professor Varvara Zania, for giving me the opportunity to realize this Ph.D. project and for all the academic guidance, constant thorough supervising and moral support that she has offered me so kindly throughout the 3 years. This work has been supported by the Danish Council for Strategic Research through the project “Advancing BeYond Shallow waterS (ABYSS) - Optimal design of offshore wind turbine support structures”. The funding is sincerely acknowledged. During my PhD study I visited Department of Civil and Environmental Engineering at University of Perugia. The stay was very rewarding and special thanks should be directed to Professor Claudio Tamagnini for his tremendous assistance and helpfulness during my stay

In addition, I would like to express my gratitude to Gitte Lyng Grønbech for helping me in performing triaxial tests at DTU lab.

I am extremely grateful to my family for being by my side every time I needed it and supporting all my ideas. Thank to my friends for the support during the course of the project. Finally, I would like to thank Rasmus for his patience and moral support.

Preface

The present thesis “Numerical modelling of offshore foundations for jacket structures” has been prepared in connection with a Ph.D. study carried out in the period August 2014 to October 2017 at the Department of Civil Engineering, Technical University of Denmark. This thesis is divided into two parts. The first part introduces the research field, discusses the methodology, highlights the major findings and provides an overview of the work carried out within this project along with a discussion. The second part is a collection of papers which constitute the basis of the work and serves as scientific documentation. Tables, equations and figures are indicated with consecutive numbers in each individual chapter or appendix. Cited references are marked as e.g. Novak and Nogami (1977), with author specification and year of publication in the text.

Lyngby, 31st of October 2017

Chiara Latini

Abstract

Nowadays the offshore wind industry continues to push towards larger turbines with capacities greater than 8MW in deeper waters. The realization of such wind farms requires that the costs of the overall offshore wind turbine system are significantly reduced, in order to give the offshore wind industry an increasing edge in the competition with fossil–fuel–based energy sources. The cost–reduction target set can be achieved either by adopting new technologies or by optimizing design methods and existing technologies. One of the areas where cost reductions can be met is in the support structure. For an offshore wind turbine structure, the support structure design typically has some global requirements, e.g. frequency. The global constraints are influenced by both the soil properties and the foundation design. Hence, it is necessary to account for the possibilities of dynamic effects of the soil–foundation interaction in order to achieve reliable responses of the wind turbine structure.

The aim of this thesis is to evaluate the dynamic soil–foundation interaction of offshore wind turbines, focusing on different types of foundations (suction caissons and hollow steel piles), different load conditions (cyclic and dynamic) and soil conditions. Moreover, two approaches were followed in the soil modelling: small strain approach in which elastodynamic constitutive soil model is considered and large strain approach, where elasto–plastic constitutive soil model is taken into account.

The models adopted in this study can be classified as: a) simple analytical formulations and b) continuum finite element models (FEM). In the abovementioned models the soil is simplified as a homogeneous linear viscoelastic material. Existing analytical elastic solutions, which deal with the dynamic soil pile interaction, have been revisited and extended to account for different soil profiles and foundation geometries. Continuum finite element models have been developed for validation of the analytical procedures, and a parametric study has been established to investigate the application range of the simple analytical solutions (foundation length, diameter and bending stiffness, soil stiffness, and depth of soil layer/bedrock). The frequency dependent dynamic stiffness and damping coefficients of floating piles and suction caissons under various loading conditions have been estimated. The outcomes are presented in terms of non-dimensional graphs which show the frequency dependency of the dynamic stiffness and damping corresponding to the different degrees of freedom.

In addition, this research project was focused on modelling the cyclic behaviour of soil. The constitutive models based on perfect plasticity are not capable to reproduce the irreversible strains accumulated due to cyclic loads and to define the stress history of the material. Thus it is fundamental to deploy realistic constitutive models for realistic numerical analyses in order to describe properly highly nonlinear and anisotropic stress–strain behaviour of the soil. Particularly, the soil constitutive model of Manzari and Dafalias (SANISAND, 2004) has been modified in order to solve inefficient performance of the stress integration scheme for soil deposits in the low stress regime. The modified SANISAND (2004) has been implemented in Abaqus. Moreover, drained and undrained compression triaxial tests at DTU GEO–Lab were performed to calibrate the material constants of the constitutive model for Fontainebleau sand. The calibration is necessary for evaluating the model performance for Fontainebleau sand.

Finally a method for integrated design of offshore wind turbine jackets and foundations is proposed by adopting numerical structural optimization. The optimal design problem enables an automatic design process which minimizes the primary steel mass of the jacket and the foundations. Integrated design optimization of jacket and foundation has been performed for two different foundation types (piles and suction caissons), a range of different leg distances, and ten soil profiles.

Resumé

I de senere år har markedet for hav-vindmøller bevæget sig mod udviklingen af vindmølleparker, med højere kapacitet, og placering på større vanddybde. Dette giver større udfordringer til nye design, og for at sådanne vindmølleparker er konkurrencedygtige, i forhold til energi fra fossile brændstoffer, kræver det at omkostningerne bliver kraftigt reduceret. Målet om reducere omkostningerne kan opnås, enten gennem brug af nye teknologier, eller videreudvikling af eksisterende design og teknologi. Et af områderne, hvor omkostninger kan reduceres er på møllefundamentet, men når det drejer sig om havvindmøller, er der specifikke krav til fx frekvens. Disse krav varierer, afhængig af jordbundssammensætning, og fundamentets design, og for at opnå et pålideligt design, er det nødvendigt at tage højde for de dynamiske påvirkninger, som opstår i interaktionen mellem jordbund og fundamentet.

Formålet med denne afhandling er at evaluere dynamiske påvirkninger mellem jord og fundament, med fokus på forskellige fundamentstyper (sugebøtter og enkeltpæle), lastbetingelse (cyklisk og dynamisk) og jordbundsbetingelser. Ydermere er fremgangsmåder til modellering af jordbunden undersøgt separat for små og store tøjninger, med en henholdsvis tilhørende elasto-dynamisk og elasto-plastisk konstitutiv model.

Modeller anvendt i dette studie kan klassificeres som henholdsvis (a) simple analytiske metoder og (b) Finite Element Modeller (FEM) med sammenhængende elementer. Med de nævnte metoder simplificeres jordbunden som værende homogen og lineær viskoelastisk. Eksisterende analytiske metoder af dynamiske påvirkninger mellem jord og fundament er genovervejet, og udvidet til at inkludere forskellige jordprofiler samt fundament-geometrier. Finite Element Modeller er blevet udviklet til validering af de analytiske metoder, og for at fastlægge anvendelse af disse med hensyn til fundamentets længde, diameter og bøjningsstivhed samt jordbundens stivhed og dybde, blev et parameter-studie etableret. Dynamiske stivhed- og dæmpningskoefficienter for enkeltpæle samt sugebøtter er blevet estimeret under forskellige lastbetingelser. Resultaterne er præsenteret i dimensionsløse grafer og fremhæver frekvensafhængigheden på de forskellige frihedsgrader.

Dette forskningsprojekt har ydermere fokuseret på modellering af jordbundens egenskaber under cyklisk belastning, da konstitutive modeller baseret på ideel plasticitet ikke er i stand til at opfange de irreversible tøjninger akkumuleret som følge af cyklisk belastning eller karakteriserer jordbundens spændingshistorie. Anvendelse af realistiske konstitutive modeller i numeriske analyser er derfor fundamental for at kunne beskrive non-lineær stræk og anisotropiske spændings-tøjnings egenskaber i jorden. Specielt den konstitutive model af Manzari and Dafalias (SANISAND, 2004) er blevet modificeret for at kunne imødekomme bestemmelse af et system af spændingstilstande i jordforhold med lave spændinger. Den modificerede SANISAND (2004) model er blevet implementeret i Abaqus. En serie af drænet og udrænet triaxial forsøg er blevet udført i det geotekniske laboratorium på DTU for at kalibrere materiale-konstanter til Fontainebleau sand. Kalibrering er nødvendig for kunne opfange degradering af stivhed og permanent deformation akkumuleret under realistiske forhold. Slutteligt, gennem numerisk optimering foreslår dette studie en metode til integreret design af rig-konstruktion og fundering. Numerisk løsning af det optimale design muliggør en automatisk design-proces, som kan minimere den primære stål-masse til konstruktion af rig og fundering. Optimering af rig og fundering er bestemt gennem integreret design for to funderingstyper (sugebøtter og pæle) med en serie af forskellig afstande mellem konstruktionens ben samt ti forskellige jord profiler.

Contents

Acknowledgements	i
Preface	ii
Abstract	iii
Resumé	iv
List of Figures	ix
List of Tables	xv
Part I: Extended summary	xvi
1 Introduction	3
1.1 Offshore wind turbines	3
1.2 Loads on offshore wind turbines	4
1.3 Soil conditions	5
1.4 Support structure concepts	6
1.4.1 Monopods	6
1.4.2 Multipods	7
1.5 Scope of work	9
1.6 Thesis outline	10
2 State of the art	12
2.1 Introduction	12
2.2 Dynamic response of piles	12
2.3 Dynamic response of suction caissons	16
2.4 Elasto-plastic soil behaviour	16
2.4.1 Introduction	16
2.4.2 Monotonic and cyclic behaviour of sand	17
2.4.3 Advanced soil constitutive models: overview	17
2.4.4 SANISAND family of constitutive models	21
3 Dynamic response of piles	23
3.1 Lateral dynamic response of piles	23
3.1.1 Analytical approach	24
3.1.2 Numerical approach	29
3.1.3 Validation of the numerical model	33
3.1.4 Foundation modelling	39
3.1.5 Parametric study	41
3.2 Vertical dynamic response of piles	50
3.2.1 Analytical approach	50

3.2.2	Numerical approach	50
3.2.3	Validation of the numerical model	50
3.2.4	Parametric study	51
3.3	Conclusions	54
3.4	Recommendations for future work	55
4	Dynamic response of suction caissons	56
4.1	Lateral dynamic response of suction caissons	56
4.1.1	Analytical approach	56
4.1.2	Numerical approach	57
4.1.3	Validation of the numerical model	63
4.1.4	Parametric study	66
4.1.5	Suggested expressions	77
4.2	Vertical dynamic response of suction caissons	86
4.2.1	Analytical approach	86
4.2.2	Numerical approach	86
4.2.3	Validation of the numerical model	88
4.2.4	Parametric study	89
4.2.5	Suggested expressions	96
4.3	Conclusions	100
4.4	Recommendations for future work	101
5	The Modified SANISAND(2004) model	103
5.1	The modified SANISAND (2004) model in triaxial space	104
5.1.1	Elastic relations	104
5.1.2	Yield surface	104
5.1.3	Critical, bounding and dilatancy surface	107
5.1.4	Flow rule	107
5.2	The modified SANISAND(2004) in the low stress regime	108
5.3	Simulation of the response of shallow foundation using the modified SANISAND model	110
5.3.1	Numerical model	110
5.3.2	Verification	111
5.4	Calibration of Model Constants	113
5.4.1	Elasticity parameters	113
5.4.2	Critical state line parameters	114
5.4.3	Yield surface parameter	115
5.4.4	Dilatancy parameters	115
5.4.5	Kinematic hardening parameters	115
5.5	Model performance	116
5.6	Limitations of the modified SANISAND model	118
5.7	Conclusions	119
5.8	Recommendations for future work	119
6	Integrated optimal design	121
6.1	Introduction	121
6.2	Methodology	122
6.3	Results	123
6.4	Conclusions	125
6.5	Recommendations for future work	125
	Conclusion	126
	Bibliography	128

Part II: Publications	137
PAPER I: <i>Dynamic soil–pile interaction: an analytical solution for floating piles</i>	140
PAPER II: <i>Dynamic stiffness and damping of foundations for jacket structures</i>	172
PAPER III: <i>Dynamic lateral response of suction caissons</i>	181
PAPER IV: <i>Dynamic stiffness of horizontally vibrating suction caissons</i>	195
PAPER V: <i>Vertical dynamic impedance of suction caissons</i>	206
PAPER VI: <i>Vertical Dynamic Stiffness of Offshore Foundations</i>	241
PAPER VII: <i>Modelling of constitutive behaviour of sand in the low stress regime: an implementation of SANISAND</i>	248
PAPER VIII: <i>Integrated optimal design of jackets and foundations</i>	253
REPORT: <i>Triaxial Tests in Fontainebleau Sand</i>	286

List of Figures

1.1	Offshore wind turbine park, under construction (Energy efficiency and renewable energy).	3
1.2	a) Primary forces on offshore wind turbine and b) Typical range of forcing frequencies for an offshore wind turbine in agreement with DNV (2004).	4
1.3	Monopod support structures. a) gravity based; b) monopile; c) suction caisson.	7
1.4	Multipod support structures. a) gravity based; b) piles; c) suction caissons.	8
1.5	Overview of the research project.	11
2.1	Pile head impedances.	13
2.2	Illustration of monotonic behaviour of sand in e-p space: a) drained and b) undrained conditions.	17
2.3	Definition of cyclic liquefaction and cyclic mobility (Ibsen, 1994).	18
2.4	Kinematic hardening inside the Bounding surface (Tamagnini and Viggiani, 2002).	20
2.5	Radial mapping rule in Bounding surface models (Tamagnini and Viggiani (2002)).	21
3.1	Illustration of the two soil profiles investigated in this study.	23
3.2	Analytical model of soil–pile system	25
3.3	Finite element model of the foundation and the surrounding soil.	30
3.4	Comparison of the dynamic impedances obtained by the numerical model, Novak and Nogami (1977) and Mylonakis (2001) formulation for the case investigated.	34
3.5	Distribution of the soil and pile displacement along the depth at the three first eigenfrequencies of the soil layer.	35
3.6	Comparison of the dynamic impedances obtained by the numerical model and Novak and Nogami (1977) formulation for profile 1, considering different assumptions on displacements.	35
3.7	Comparison of the dynamic impedances obtained by the numerical model and Latini et al. (2015) formulation for profile 2.	37
3.8	Distribution of the soil and pile displacement along the depth at the three first eigenfrequencies of the soil layer for profile 2. Modified after <i>Paper I</i>	38
3.9	Distribution of the vertical displacements along the pile depth at three first eigenfrequency of the soil layer for profile 2. Modified after <i>Paper I</i>	38
3.10	Variation of the dynamic stiffness and damping coefficients with respect to the non–dimensional frequency. Effect of the foundation geometry on the real component a) and the imaginary component b) for profile 1.	39
3.11	Distribution of the soil and pile displacement along the depth at the two first eigenfrequencies of the soil layer.	40
3.12	Variation of the dynamic stiffness and damping coefficients with respect to the non–dimensional frequency. Effect of the foundation geometry on the real component and the imaginary component for profile 1. Modified after <i>Paper III</i>	41
3.13	Comparison of the static stiffness coefficients obtained by the numerical model, the analytical solution of Latini et al. (2015) a) and Syngros (2004) b).	42

3.14	Variation of the three dynamic stiffness coefficients with respect to the non-dimensional frequency. Effect of the slenderness ratio on the real component a) and the imaginary component b). Results are presented for $H_s/d=30$ and $E_p/E_s=60$. Modified after <i>Paper I</i>	43
3.15	Variation of the three dynamic stiffness coefficients with respect to the non-dimensional frequency. Effect of the slenderness ratio on the real component a) and the imaginary component b). Results are presented for $H_s/d=30$ and $E_p/E_s=500$. Modified after <i>Paper I</i>	44
3.16	Variation of the three dynamic stiffness coefficients with respect to the non-dimensional frequency. Effect of the relative thickness of the soil layer on the real component a) and the imaginary component b). Results are presented for $H_p/d=10$ and $E_p/E_s=60$. Modified after <i>Paper I</i>	45
3.17	Distribution of the bending moment along the depth for $H_s/d=15$ and 50 at the 1 st eigenfrequency of the soil layer. Modified after <i>Paper I</i>	46
3.18	Variation of the three dynamic stiffness coefficients with respect to the non-dimensional frequency. Effect of the soil stiffness on the real component a) and the imaginary component b). Results are presented for $H_s/d=30$ and $H_p/d=10$. Modified after <i>Paper I</i>	47
3.19	Distribution of the bending moment along the depth for $E_p/E_s=15, 60$ and 500 at the 3 rd eigenfrequency of the soil layer. Results are presented for $H_s/d=30$ and $H_p/d=10$. Modified after <i>Paper I</i>	48
3.20	Variation of the dynamic stiffness with respect to the relative thickness of the soil layer H_s/d for $E_p/E_s=60$ and $E_p/E_s=500$ at the 1 st eigenfrequency of the soil layer. Modified after <i>Paper I</i>	49
3.21	Variation of the vertical stiffness and damping coefficients with respect to the dimensionless frequency a) and distribution of the pile displacement along the depth at the 1 st vertical eigenfrequency of the soil layer b) for profile 1. Modified after <i>Paper V</i>	51
3.22	Variation of the vertical dynamic stiffness and damping coefficients with respect to the dimensionless frequency. Effect of the relative thickness of the soil layer on the real component a) and the imaginary component b) for $H_p/d = 10$. Modified after <i>Paper VI</i>	52
3.23	Variation of the vertical dynamic stiffness and damping coefficients with respect to the dimensionless frequency. Effect of the stiffness of the soil layer on the real component a) and the imaginary component b) for $H_p/d = 10$. Modified after <i>Paper VI</i>	53
3.24	Variation of the vertical dynamic stiffness and damping coefficients with respect to the non-dimensional frequency. Effect of the slenderness ratio on the real component a) and the imaginary component b) for $H_s/d = 15$	53
4.1	Illustration of the two soil profiles investigated for the analysis of suction caissons.	57
4.2	Foundation geometries investigated for the case of suction caissons embedded in profile 1 and 2. Modified after <i>Paper VI</i>	58
4.3	Variation of the dynamic stiffness and damping coefficients with respect to the non-dimensional frequency. Effect of the foundation geometry on the real component a) and the imaginary component b) for profile 1.	59
4.4	Displacement contour plot illustrating the presence of Rayleigh wave in the soil within the caisson. Modified after <i>Paper IV</i>	60
4.5	Distribution of the soil and suction caisson displacement along the depth at the three first eigenfrequency of the soil layer (profile 1).	60
4.6	Variation of the dynamic stiffness and damping coefficients with respect to the non-dimensional frequency. Effect of the foundation geometry on the real component a) and the imaginary component b) for profile 2.	61

4.7	Distribution of the soil and suction caisson displacement along the depth at the three first eigenfrequency of the soil layer (profile 2).	61
4.8	Variation of the dynamic lateral stiffness coefficients with respect to the non-dimensional frequency. Effect of the mesh discretization on the real component for profile 2.	63
4.9	Variation of the dynamic lateral stiffness coefficients with respect to the non-dimensional frequency for profile 1.	64
4.10	Variation of the dynamic lateral stiffness coefficients with respect to the non-dimensional frequency for profile 2.	65
4.11	Soil profiles considered for dynamic response of suction caissons. Modified after <i>paper III</i>	67
4.12	Static stiffness components of suction caissons. Mathematical expressions for the static stiffness components a). Comparison of the static stiffness components given by the numerical model and three analytical expressions b). Modified after <i>Paper III</i>	68
4.13	Comparison of the static stiffness components given by the numerical model, Gelagoti et al. (2015) and Shadlou and Bhattacharya (2016).	69
4.14	Variation of the dynamic stiffness and damping coefficients with respect to the non-dimensional frequency. Effect of slenderness ratio on the real component a) and the imaginary component b) for Profile 2. Modified after <i>Paper III</i>	70
4.15	Variation of the three dynamic stiffness and damping coefficients with respect to the non-dimensional frequency. Effect of the diameter of suction caisson on the real component a) and the imaginary component b) for profile 2. Modified after <i>Paper III</i>	72
4.16	Variation of the three dynamic stiffness and damping coefficients with respect to the non-dimensional frequency. Effect of the relative thickness of the soil layer on the real component a) and the imaginary component b) for profile 2. Modified after <i>Paper III</i>	73
4.17	Variation of the three viscous damping coefficients with respect to the non-dimensional frequency. Effect of the relative thickness of the soil layer.	73
4.18	Variation of the three dynamic stiffness coefficients with respect to the non-dimensional frequency. Effect of the stiffness of homogeneous soil layer (profile A) on the real component and the imaginary component for $H_p/d = 2$ a) and for $H_p/d = 0.25$ b). Modified after <i>Paper III</i>	74
4.19	Variation of the three dynamic stiffness and damping coefficients with respect to the non-dimensional frequency. Effect of slenderness ratio in the inhomogeneous soil layer (profile B) on the real component a) and the imaginary component b). Modified after <i>Paper III</i>	75
4.20	Variation of the three dynamic stiffness and damping coefficients with respect to the non-dimensional frequency. Effect of slenderness ratio in the inhomogeneous soil layer (profile C) on the real component a) and the imaginary component b). Modified after <i>Paper III</i>	76
4.21	Comparison between the simplified expression and the numerical outcomes with respect to the non-dimensional frequency. Effect of the skirt length on the real component a) and the imaginary component b).	81
4.22	Comparison between the simplified expression and the numerical outcomes with respect to the non-dimensional frequency. Effect of the relative thickness of the soil layer on the real component a) and the imaginary component b) for $H_p/d = 2$ and $H_p/d = 0.25$	82
4.23	Comparison between the simplified expression and the numerical outcomes with respect to the non-dimensional frequency. Effect of the stiffness of the soil layer (profile A) on the real component a) and the imaginary component b) for $H_p/d = 2$ and $H_p/d = 0.25$	83

4.24	Comparison between the simplified expression and the numerical outcomes with respect to the non-dimensional frequency. Effect of the stiffness of the soil layer (profile B) on the real component a) and the imaginary component b) for $H_p/d = 2$ and $H_p/d = 0.25$	84
4.25	Comparison between the simplified expression and the numerical outcomes with respect to the non-dimensional frequency. Effect of the stiffness of the soil layer (profile C) on the real component a) and the imaginary component b) for $H_p/d = 2$ and $H_p/d = 0.25$	85
4.26	Variation of the vertical dynamic stiffness and damping coefficients with respect to the non-dimensional frequency. Effect of the foundation geometry on the real component a) and the imaginary component b) for profile 1.	87
4.27	Variation of the vertical dynamic stiffness and damping coefficients with respect to the non-dimensional frequency. Effect of the foundation geometry on the real component a) and the imaginary component b) for profile 2. Modified after <i>Paper V</i>	87
4.28	Variation of the vertical stiffness a) and damping coefficients b) with respect to the non-dimensional frequency for profile 1.	88
4.29	Comparison of the vertical static stiffness component given by the numerical model and two analytical expressions.	88
4.30	Effect of the skirt length of the caisson on the real component a) and the imaginary component b) for cases 1–5. Distribution of the suction caisson displacement along the skirt at the 1 st vertical eigenfrequency c) and 2 nd vertical eigenfrequency d) of the soil layer. Modified after <i>Paper V</i>	90
4.31	Effect of Poisson's ratio on dimensionless coefficient η	91
4.32	Variation of the vertical dynamic stiffness with respect to the non-dimensional frequency. Effect of Poisson's ratio on the real component a) and the imaginary component b) for $H_p/d = 2$. Effect of the horizontal displacements on the real component for $\nu = 0.4$ c) and for $\nu = 0.495$ d). Modified after <i>Paper V</i>	92
4.33	Quilt-style contour plot of pressure in the soil medium for case 9 a) and 22 b) at the 1 st vertical resonance. Modified after <i>Paper V</i>	93
4.34	Variation of the vertical dynamic stiffness with respect to the dimensionless frequency. Effect of the stiffness of homogeneous soil layer (profile A) on the real component a) and the imaginary component b) for $H_p/d = 2$. Modified after <i>Paper V</i>	93
4.35	Variation of the vertical dynamic stiffness with respect to the dimensionless frequency. Effect of the stiffness of homogeneous soil layer (profile B) on the real component a) and the imaginary component b). Effect of the stiffness of homogeneous soil layer (profile C) on the real component c) and the imaginary component d). Modified after <i>Paper V</i>	94
4.36	Distribution of the suction caisson's vertical displacements along the depth for $H_p/d = 0.25$ at the 1 st resonance a) and $f = 1.8f_{1st}$ b) and for $H_p/d = 2$ at the 1 st resonance c) and $f = 1.8f_{1st}$ d), considering homogeneous (profile A) and inhomogeneous (profile B and C) soil layer. Modified after <i>Paper V</i>	95
4.37	Effect of the relative thickness of the soil layer on the real component a) and the imaginary component b) for cases 23–26.	96
4.38	Comparison between the simplified expression and the numerical outcomes with respect to the non-dimensional frequency. Effect of the skirt length of the caisson on the real component a) and the imaginary component b) for cases 1 and 5. Effect of Poisson's ratio on the real component c) and the imaginary component d) for $H_p/d = 2$. Effect of the shear wave velocity of the soil layer on the real component e) and the imaginary component f) for $H_p/d = 2$. Modified after <i>Paper V</i>	99

4.39	Comparison between the simplified expression and the numerical outcomes with respect to the non-dimensional frequency. Effect of the stiffness of homogeneous soil layer (profile B) on the real component a) and the imaginary component b) for $H_p/d = 2$ and 0.25. Effect of the stiffness of homogeneous soil layer (profile C) on the real component c) and the imaginary component d) for $H_p/d = 2$ and 0.25. Modified after <i>Paper V</i>	100
5.1	Critical state line (CSL) and state parameter.	104
5.2	SANISAND (2004) yield surface in p–q plane. Modified after <i>Paper VII</i>	105
5.3	The yield surface of the modified SANISAND (2004) model in q– p^* plane a) and in the multiaxial space b). Modified after <i>Paper VII</i>	106
5.4	Effect of b^* parameter on the hyperbolic yield surface in q–p plane. Modified after <i>Paper VII</i>	106
5.5	Effect of the back stress ratio α on the hyperbolic yield surface in q–p plane. Modified after <i>Paper VII</i>	107
5.6	Monotonic undrained compression triaxial test on Toyoura sand. Comparison between the performance of SANISAND (2004) (Dafalias and Manzari (2004)) and the modified SANISAND (2004) model. Modified after <i>Paper VII</i>	109
5.7	Monotonic undrained triaxial tests. Analysis of the efficiency of the algorithm, by varying the number of iterations N_{iter} . Modified after <i>Paper VII</i>	110
5.8	Monotonic undrained triaxial tests. Analysis of the accuracy of the algorithm, by varying the tolerance constant TOL. Modified after <i>Paper VII</i>	110
5.9	Finite element discretization of the shallow foundation problem.	111
5.10	Comparison between the modified SANISAND(2004) and hypoplastic model (Niemunis and Herle (1997), von Wolffersdorff (1996)) along with the bearing capacity estimated according to Terzaghi (1943). a) Load–deflection curves and b) Void ratio–depth.	112
5.11	Calibration of G_0 a) and Poisson' ratio ν b) constant using data of drained triaxial compression tests on Fontainebleau sand.	114
5.12	Calibration of critical state line constants using data of undrained and drained triaxial compression tests on Fontainebleau sand.	115
5.13	Calibration of constant n^d a) and n^b b) for Fontainebleau sand using drained compression triaxial tests.	116
5.14	Comparison of data and simulations for drained compression triaxial tests on isotropically consolidated samples of Fontainebleau sand ($p'_0 = 50 - 200kPa$) and initial void ratio $e_0 = 0.712$	117
5.15	Comparison of data and simulations for drained compression triaxial tests on isotropically consolidated samples of Fontainebleau sand ($p'_0 = 50 - 200kPa$) and initial void ratio $e_0 = 0.638$	117
5.16	Comparison of data and simulations for drained compression triaxial tests on isotropically consolidated samples of Fontainebleau sand ($p'_0 = 50 - 200kPa$) and initial void ratio $e_0 = 0.573$	117
5.17	Volumetric strain estimated from the data of drained compression triaxial test on isotropically consolidated samples of Fontainebleau sand ($p'_0 = 200kPa$) and initial void ratio $e_0 = 0.684$	118
5.18	Comparison of data and simulations for drained compression triaxial tests on isotropically consolidated samples of Fontainebleau sand ($p'_0 = 100kPa$).	118
5.19	Numerical modelling of cyclic load of piles.	120
6.1	A four-legged jacket substructure for large offshore wind turbines. Modified after <i>Paper VIII</i>	122

6.2	Variation of the jacket and foundation masses with respect to the leg distance in sand soil profile.	123
6.3	Effect of the soil type on the jacket and foundation masses in clay soil profile.	124
6.4	Variation of the frequency with respect to the leg distance and soil stiffness for pile foundation in sand a) and in clay soil profile b).	124

List of Tables

1.1	Pre-piled OWT foundations installed.	9
3.1	Parameters of the case of study for the analysis of pile foundation.	33
3.2	Static stiffness components of pile obtained from the numerical models and the analytical solutions of Novak and Nogami (1977), Mylonakis (2001) and Randolph (1981).	33
3.3	Parameters of the case of study for the analysis of pile foundation.	36
3.4	Static floating pile stiffness obtained from the numerical models and the analytical solutions.	36
3.5	Static end bearing pile stiffness obtained from the numerical models and the analytical solutions of Novak and Nogami (1977).	39
3.6	Static end bearing pile stiffness obtained from the analytical solutions of Novak and Nogami (1977) and the numerical models, where the expression of Randolph (1981) was used for the estimation of the Young modulus of the shell pile.	40
3.7	Cases selected in the parametric analysis for the static stiffness coefficients of floating piles.	42
3.8	Static end bearing pile stiffness obtained from the numerical models and the analytical solutions of Nogami and Novak (1976), Hu et al. (2004), Wu et al. (2013) and Zheng et al. (2014).	51
3.9	Dimensionless parameters and cases selected in the parametric analysis for floating piles.	52
4.1	Parameters of the case study for the analysis of suction caissons.	58
4.2	Mesh discretization for the mesh sensitivity analysis.	62
4.3	DOF's and the static lateral stiffness coefficients for the mesh sensitivity analysis.	62
4.4	Static suction caisson stiffness obtained from the numerical models and the analytical solution of Novak and Nogami (1977) for profile 1.	63
4.5	Static suction caisson stiffness obtained from the numerical models and the analytical solution of Latini et al. (2015) for profile 2.	65
4.6	Dimensionless parameters and cases selected in the parametric analysis for suction caisson.	66
4.7	Constants of the suggested expression for the dynamic horizontal stiffness and damping coefficient in the dimensionless frequency range $\alpha_0 \in [0; 3]$	78
4.8	Constants of the suggested expression for the dynamic coupling stiffness and damping coefficient in the dimensionless frequency range $\alpha_0 \in [0; 3]$	79
4.9	Constants of the suggested expression for the dynamic rocking stiffness and damping coefficient in the dimensionless frequency range $\alpha_0 \in [0; 3]$	80
4.10	Static stiffness of suction caisson embedded in profile 1 obtained from different foundation methodologies.	86
4.11	Static stiffness of suction caisson embedded in profile 2 obtained from different foundation methodologies.	87
4.12	Static stiffness of suction caisson embedded in profile 1 obtained from from the numerical model and the analytical solution of Nogami and Novak (1976).	88

4.13	Dimensionless parameters and cases selected in the parametric analysis for suction caisson.	89
4.14	Constants of the suggested expression for the dynamic vertical stiffness and damping coefficient in the dimensionless frequency range $\alpha_0 \in [0; 3/2\eta\pi]$	97
4.15	Constants of the suggested expression for the dynamic vertical stiffness and damping coefficient in the dimensionless frequency range $\alpha_0 \in [0; 4]$	98
5.1	Material constants of the modified SANISAND (2004) for Fontainebleau sand.	113
5.2	Critical state line parameters and typical range of values for sands.	114
5.3	Classification parameters for sand	116

Nomenclature

Latin upper case

A, B, C, D : integration constants

E_s : soil modulus of elasticity

E_p : Young modulus of pile

F_{in} : Fourier's coefficients

G : soil shear modulus

H_s : depth of soil layer

H_p : height of pile

I : moment of inertia of pile

K_r : pile flexibility factor

K_{Su} : dynamic stiffness coefficient—real part—force for unit displacement

K_{Mu} : dynamic stiffness coefficient—real part—moment for unit displacement

$K_{S\theta}$: dynamic stiffness coefficient—real part—force for unit rotation

$K_{M\theta}$: dynamic stiffness coefficient—real part—moment for unit rotation

K_{Su}^0 : static stiffness coefficient—force for unit displacement

K_{Mu}^0 : static stiffness coefficient—moment for unit displacement

$K_{S\theta}^0$: static stiffness coefficient—force for unit rotation

$K_{M\theta}^0$: static stiffness coefficient—moment for unit rotation

M : reaction moment at the pile head

S : horizontal reaction at the pile head

Q_s : soil shear resistance

V_s : soil shear wave velocity

Latin lower case

a_n : complex constant of the soil layer in horizontal direction

d : diameter of pile

f_{in} : dimensionless coefficients

$h_n = \pi/2H_s(2n - 1)$ $n=1,2,\dots$: parameter

\hat{h}_n : dimensionless parameter

m : mass of pile

r_0 : radius of pile

u : translational degree of freedom at the pile head

z : vertical coordinate with respect to RS

z_1 : vertical coordinate with respect to RS1

Greek

α_0 : dimensionless eigenfrequency of the soil layer

α_{hn} : horizontal resistance factor

ΔH_s : difference in soil depth

ζ_{Su} : damping coefficient—force for unit displacement

ζ_{Mu} : damping coefficient—force for unit rotation

$\zeta_{S\theta}$: damping coefficient—force for unit rotation

$\zeta_{M\theta}$: damping coefficient—moment for unit rotation

θ : rotation

λ : dimensionless eigenfrequency of free—standing pile

ν : Poisson's ratio of soil layer

ζ : hysteretic soil damping ratio

ρ : density of soil

ω : circular frequency of harmonic applied displacement

Chapter 1

Introduction

Carbon dioxide and other global warming emissions in the atmosphere, caused by human activity raise the planet's temperature and generate considerable and harmful impacts on people's health and the environment. Energy from wind turbines is sustainable and largely untapped alternative to fossil fuels, with the advantage of reduced carbon emissions. Compared with natural gas, which emits between 0.3 and 1 kilograms of carbon dioxide equivalent per kilowatt-hour (CO₂E/kWh) and coal, which emits between 0.6 and 1.6 kilograms of CO₂E/kWh, wind emits only 0.01 to 0.03 kilograms of CO₂E/kWh (Union of Concerned Scientists (2013)). In addition, the economic and supply risks associated with reliance on imported fuels will be drastically reduced by using wind energy.

1.1 Offshore wind turbines

In January 2008 the European Commission published a climate and energy package, where one of the targets was to increase the use of renewables to 20% of total energy production by the year 2020. Particularly, Denmark has proven to be a pioneer in wind power and a world leader in wind power technology. In Denmark, the first large-scale offshore wind farm was installed in 2002, and today, more than 40% of Denmark's energy supply comes from wind power. The plan of the danish government is to be 100% free of fossil fuel in 2050 and renewable energy will mostly be wind energy (Ministry of Foreign Affairs of Denmark (2017)). In the United Kingdom, political and industrial forces are investing on the development of offshore wind industry, with the target to reach 33GW of offshore wind energy by 2020 (The Crown Estate (2017)). Other countries supporting offshore wind energy comprise Belgium, Germany, Ireland, Netherlands and Sweden.

Nowadays, the majority of wind turbines are located onshore, since the installation and foundation



Figure 1.1: Offshore wind turbine park, under construction (Energy efficiency and renewable energy).

costs of offshore wind turbines are greater than those of onshore wind turbines. However, offshore wind farms are appealing, since on offshore sites the wind blows stronger and more constant (State of Green). In addition, existing built-up areas also limited suitable locations on land for the construction of wind energy plants. During the past decades, it was observed that efficiency of wind turbines has increased considerably as larger rotors and more powerful generators have been used. Today, offshore wind turbine generators (WTG) types are available with capacities up to 8MW. Further increases in the efficiency may be difficult to accomplish for the case of onshore wind turbines, since logistic problems during transportation of large wind turbine components might be experienced. These limitations do not exist for transporting offshore wind turbines, as ships and barges easily accommodate large structures.

Nonetheless, the development of offshore wind farms was restricted by the high cost of the support structure, which represents 20–25% of the total cost of an offshore wind farm. Therefore, the offshore wind market is developing towards wind farms with higher capacity generators and in deeper waters, in order to make the price on energy competitive. In order to achieve this, deep offshore industries will require advanced models and efficient and reliable numerical structural optimization techniques to automate the design process and significantly reduce the cost of new support structures.

1.2 Loads on offshore wind turbines

Foundations for offshore wind turbines are subjected to dynamic and cyclic loads such as wind, waves and earthquake. Particularly it is proven that lateral loads from wind and waves are the primary forces on an offshore wind turbine, see Figure 1.2a. Figure 1.2b shows a typical power spectra of the forces acting on an offshore wind turbine, where a peak wave frequency and a peak wind frequency are respectively 0.1 Hz and 0.01 Hz. The rotor frequency range, defined as 1P, and the blade passing frequency range from a three blade wind turbine, called 3P, are also shown in Figure 1.2b.

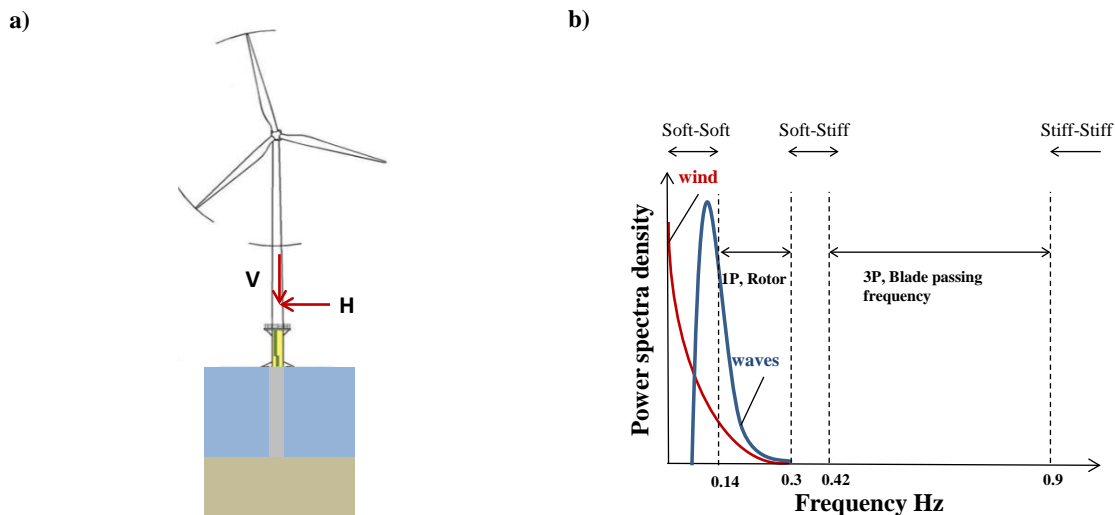


Figure 1.2: a) Primary forces on offshore wind turbine and b) Typical range of forcing frequencies for an offshore wind turbine in agreement with DNV (2004).

In the design of OWTs, it is fundamental to accurately assess the resonance frequencies of the wind turbine structure in order to ensure that the first resonance frequency of the wind turbines does not coincide with the excitation frequencies of the rotor system (DNV (2004)). This is

normally achieved through a design where the entire wind turbine structure has a eigenfrequency in between 1P and 3P (soft-stiff response).

Particularly, DNV guidelines (DNV (2004)) also specify that the global frequency of the system should be at least $\pm 10\%$ away from operational 1P and 2P/3P frequencies. Furthermore, it is worth mentioning that the overall damping of the structure reduces greatly fatigue damage, since the amplitude of vibrations at resonance is inversely proportional to the damping ratios (Devriendt et al. (2012)).

According to DNV (2004) four design limit states have to be taken into account in the design of a foundation supporting an offshore wind turbine:

1. Ultimate Limit State, ULS. The estimation of maximum loads on the foundation considering all possible design load cases is necessary to calculate the foundation capacity. This first step also provides the minimum dimensions (diameter and length) of the foundation. Such calculations requires data about site conditions (soil strength properties, wind and wave data) and turbine data. ULS failure can be of two types : a) where the soil fails and b) where the foundation collapses by forming a plastic hinge.
2. Serviceability Limit State, SLS. It is reached when the permanent rotation of turbine tower exceeds the allowable limits. Particularly, the loads adopted in the capacity analysis are required for the estimation of the maximum deflection and rotation; while accumulated average long-term deformation and rotation may be assessed by cyclic loads.
3. Fatigue Limit State, FLS. This would require predicting material collapse of the foundation as well as the effect on the foundation due to cyclic loadings.
4. Accident Limit State, ALS. This concerns total collapse of foundation from e.g. ship impact.

The governing design criteria are the Serviceability Limit State (SLS) and Fatigue Limit State (FLS) conditions for which the estimation of the foundation stiffness is fundamental. Indeed, the stiffness of the foundation defines the deformation of the substructure over the life time of the wind turbine, which cannot overcome 0.5° at the mudline level under operational and extreme loads according to DNV (2004). As mentioned previously, the Serviceability Limit State and Fatigue Limit State are influenced by cyclic loadings, since these loads might deteriorate the foundation and restructure the soil grains surrounding it. In the case of cohesive soils the degradation of the soil is initiated by the accumulation of pore pressure, which can cause a decrease in strength and stiffness of the soil and the formation of a gap between soil and foundation. For granular soils, it was observed that both the strength and stiffness will increase due to densification of surrounding soils. These changes in the structure of the soil grains surrounding the foundation may modify the stiffness of the soil–foundation system and induce accumulated rotation of the tower. Additionally, it has to be taken into account that the frequency of the system is altered due to the change in stiffness, which then can interfere with the excitation frequencies (Rasmussen et al. (2013)).

1.3 Soil conditions

The site conditions play a fundamental role for the choice of the foundation concept to put in use. In addition, more challenges are encountered when wind farms are installed in deeper water, since the site conditions may significantly vary. The coastal waters of Northern Europe are characterized by soil conditions ranging from soft clays to very dense sands and hard rock. The properties of the soil and its load bearing capacity are affected by the geological history, the size and the type of soil particles.

Furthermore, the design and the construction of the offshore wind turbine is strongly influenced by the site characterization performed by ground investigations. Geotechnical site investigations comprise surface investigations (topographic surveys), and sub-surface investigations, using seismic surveys, cone penetration testing (CPT), vibrocores and boreholes (LeBlanc (2009)). Number and

locations of the boreholes should be decided based on the interpretation of the geophysical and CPT data (Sturm (2017)). Additionally, it is recommended to perform laboratory tests (drained and undrained, monotonic and cyclic DSS, triaxial compression and triaxial extension tests) of all relevant soil layers within the CPT depth. It is important to mention that Andersen et al. (2013) provide a comprehensive list of required soil parameters for various foundation concepts.

1.4 Support structure concepts

As discussed previously, several aspects govern the actual selection of type of support structure for a wind turbine. The following factors are considered for the choice of the particular design foundation (Van Der Tempel (2006)):

- soil condition
- water depth
- size and type of wind turbine
- environmental conditions
- economics

The support structures of offshore wind turbines have to withstand large moments at the seabed, which are transferred to the surrounding soil by monopod or multipod structures. The main difference between monopod and multipod structures stands on foundation structure embedded into the soil; which is single in the case of monopod structures, while three or four for multipod structures. Foundations for offshore wind turbines can be gravity foundations, piles and suction caissons.

1.4.1 Monopods

In Figure 1.3 three monopod structures with different types of foundation are shown. The gravity foundation is normally a concrete based structure, where the loading is transferred by a large base to the seabed. Gravity foundations are competitive in shallow, protected waters particularly during the installation stage. In addition, this concept is cost-effective, since concrete is cheaper than steel and the maintenance costs are reduced, due to the durability of the concrete in the marine environment. It is good practise to install gravity foundations on sites where the upper soil layers have sufficient bearing capacity. Some of the wind farms where the gravitational solution has been deployed are Nysted and Middelgrunden (4C Offshore).

The wind farm industries have plenty of experience in using monopile foundations, because of their relative simple design and manufacture. This concept comprises two parts: a) the pile, which is drilled or driven into the seabed and b) the transition piece, which is grouted with the pile with an overlap of 8–10m. One of the main advantages of monopile foundations is that they can be installed in a wide range of soil profiles, from rather soft clays to softer rocks, where it is possible to drive the piles into the seabed. Nevertheless, monopile foundations are characterized by several issues. First of all, this type of substructures can experience failure at the level of the grouted connection between the foundation and the transition piece, connecting to turbine tower. The conventional method of installation is by pile driving. This procedure requires a considerable amount of impact energy to drive monopiles into the seabed.

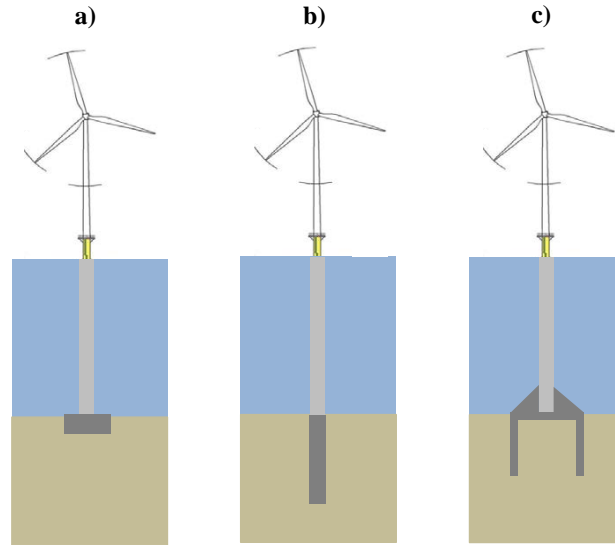


Figure 1.3: Monopod support structures. a) gravity based; b) monopile; c) suction caisson.

Furthermore, environmental consequences related to the noise disturbance of the installation procedure have to be taken into account. It is worth mentioning that the offshore projects at Horns Rev, North Hoyle and Kentish Flats are based on monopile foundations (4C Offshore). Additionally, Baltic II is the offshore wind farm where a monopile foundation is currently placed at the deepest water (37 m) as reported in Energinet (2015).

Besides gravity and monopile foundations, which have been widely deployed in the offshore wind market, a recently new foundation concept can be made by using suction caissons. Suction caissons are skirted shallow foundations (with a slenderness ratio H_p/d lower than 4, where H_p and d are the foundation height and diameter, respectively) that are first placed at the desired position and water trapped inside is pumped out. In the past, suction caissons have been deployed as anchors, which are commonly used in the oil and gas industry to secure floating platforms. According to Hously et al. (2005), suction caissons can be adopted as offshore wind turbine foundations embedded in suitable soil conditions and especially for deeper waters installation, of water depth of approximately up to 40m. Suction caissons have several advantages over monopiles, mainly reducing installation time, avoiding the noise associated to pile driving and being easier to remove during decommissioning. Moreover, suction caisson foundations are proven to be more cost-effective solution than monopile, since the amount of steel required for the fabrication is less. However, rather conservative design approaches have been considered so far due to the the lack of standardized design procedures for both the installation process and the load bearing behaviour. One of the main disadvantages is the low tensile force that this type of foundation can withstand. Furthermore, suction caissons are quite sensitive to the soil profile characteristics. Indeed, this type of foundations requires relatively homogeneous soil deposits without hard layers. Such foundations have been installed onshore in Frederikshavn, Denmark in 2005; while the following offshore projects, where suction caisson have been or will be used, are Borkum Riffgrund I, Borkum Riffgrund 2, Hornsea 1, Aberdeen Offshore Wind Farm, Hywind Scotland Pilot Park and Southwest Offshore Demonstration Wind Farm. It is estimated than by the end of 2010 more than 1000 permanent offshore suction caissons and anchors were installed (Sturm (2017)).

1.4.2 Multipods

Due to economic and technical limitations for larger offshore wind turbines at water depth greater than approximately 30m, the offshore wind market is moving towards alternative multipod foundations (i.e. tripods, tetrapods, jackets). Multipod structures are still based on gravity, piles and

suction caisson foundations, see Figure 1.4. Contrary to monopods, the moment resistance in multipods is given by a tension and compression forces.

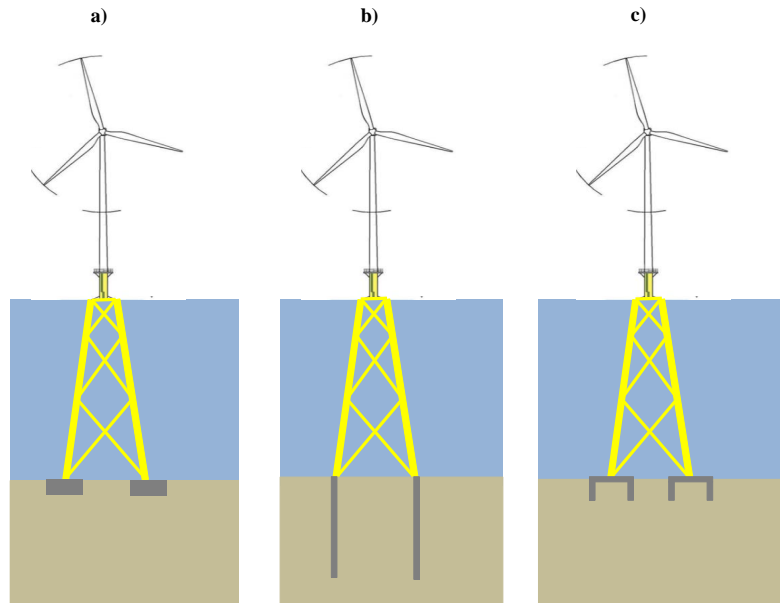


Figure 1.4: Multipod support structures. a) gravity based; b) piles; c) suction caissons.

As offshore wind turbines need to be installed in sites with water depth ranging from 20–50m (DNV (2004)), jacket structures are used. The cost of the material is relatively high compared to gravity-based solutions, causing jacket to be selected primarily when other, less costly alternative cannot be used. A jacket foundation consists of a three or four-legged steel lattice structure. The top of the three or four legs of the jacket is connected to the base of the turbine tower by a transition piece. Jacket structures can be installed on gravity based foundation, piles and suction caissons. The installation of jacket foundation may be approached in different ways:

Pre-installed piles Typically wind turbine jackets are constructed in two stages: first the piles are placed and then the jacket is installed. Tight installation tolerances for piles are required so that the jacket legs can fit into the piles. Hence a steel frame is used in the construction sites as a template to ensure the correct spacing and location of piles. Once the template is positioned on the seabed, the pile tip is placed in the template and driven into the seabed. The jacket is lifted from the installation vessel and lowered into the water and positioned so that the bases of the legs fit into the pile head. After the deployment of the jacket on location, the piles are connected to the jacket legs by grouting. It is worth highlighting that the pile installation and the jacket installation are two separate operations when pre-installed piles are used, consisting in total longer installation time. Additionally, the same installation methodology as for monopile is deployed in the case of pre-installed pile, which means the noise during pile driving is not avoided. Furthermore, the use of pre-installed piles influences the design of the jacket structure, since the jacket legs are required to be smaller in diameter than the pile foundations. Table 1.1 lists projects where pre-piled OWT foundations have been used.

Project	Description	Year
Alpha Ventus	6 units Quatropod jackets	2009
Ormonde	42 units Quatropod jackets	2010
Thornton	49 units Quatropod jackets	2011
Borkum West	41 units Tripods	2011
Baltic II	41 units Tripods jackets	2013-2014
Wikinger	70 units Quatropod jackets	2016
Beatrice	84 units Quatropod jackets	2017

Table 1.1: Pre-piled OWT foundations installed.

Post-installed piles In this method the pile installation is performed through the sleeves located on the jacket legs. To ensure the connection between the sleeves and piles, grouting is usually used. Pile swaging, which is a concept without grouting for the pile-jacket connection, may alternatively be adopted for a post-piled jacket. Mud-mats are required as a support foundation during the installation of piles. According to 4C Offshore the post-piling process has only been used at the Beatrice Demonstrator Offshore Wind farm.

Suction caissons When jackets are supported by suction caissons, the foundation can be welded to the bottom of the jacket avoiding a grouted or swaged connection. As described in Section 1.4.1 this type of foundation has the advantages of shorter installation time and negligible noise emission during the installation. Additionally, the fact that less steel is used in the fabrication, makes this type of foundation more cost-effective than piles.

1.5 Scope of work

As mentioned in the Introduction offshore wind industry is supporting the development of wind farms with higher capacity generators and in deeper waters, with the consequence of deploying deep offshore designs. On the other hand offshore installations are less accessible than onshore installations, which raise the operations and maintenance costs and possibly increase the downtime of the machines. Moreover, support structures for a specific site and water depth are adapted from other industries, particularly oil and gas.

In the years to come, the offshore wind market will require to develop cost-effective support structures, characterized by minimum offshore work and low-cost manufacturing. This is the aim of the ABYSS consortium (<http://www.abyss.dk> (2014)), which consists of eight partners uniquely combining expertise from offshore wind energy industry, foundation designers, design system developers and universities. The research project in “Numerical modelling of offshore foundations for jacket structures” is part of the ABYSS’s work plan.

The goal of this research project is to develop versatile practical tools that provide the soil-foundation dynamic impedances, which can be further applied to perform dynamic analyses of the support structure of a wind turbine. Particularly this study deals with the development of numerical and analytical design methods for jacket foundations of offshore wind turbine. The research is developed in order to model the behaviour of flexible hollow steel piles (slenderness ratio $H_p/d > 10$, where H_p and d are namely the length and the diameter of the foundation) and suction caissons (slenderness ratio $H_p/d < 5$) subjected to lateral and vertical, cyclic and dynamic loads and placed in saturated soil conditions and deep water conditions.

1.6 Thesis outline

The thesis contains six chapters and eight publications, the latter are listed at the end of the manuscript. Conclusions and directions for future work are given in each chapter based on the findings.

Chapter 3 contains the evaluation of the dynamic response of floating piles (piles embedded in soil layers of depth greater than the pile length) embedded in a homogeneous soil deposit and subjected to both horizontal and vertical loading. Considering linear elastic soil response, an already available continuum analytical solution for investigating the dynamic response of end bearing piles subjected to horizontal load is analysed and extended to flexible floating piles. The proposed analytical formulation is validated and compared with numerical models of end bearing and floating piles established in the finite element software Abaqus. Additionally, a parametric study is conducted focusing on the effect of slenderness ratio, the relative thickness and the stiffness of the soil layer on the dynamic impedances of the foundation. The analytical solution along with the parametric study is presented in *Paper I* and Latini et al. (2015) (*Paper II*).

Chapter 4 concerns the estimation of the dynamic impedances of suction caisson foundation subjected to vertical and horizontal loading. The dynamic stiffness components are evaluated by a 3D numerical model. The numerical methodology described in Chapter 3 is also applied for the case of suction caissons. Static stiffness coefficients are presented in a form of mathematical formulas obtained by fitting the numerical results. The dynamic impedances are determined for different combinations of the skirt length and various soil profiles. Note that both homogeneous and inhomogeneous soil deposits are examined in the numerical analyses. Moreover, the influence of the relative thickness of the soil layer on the vertical, lateral, coupling and rocking component of the dynamic impedances is studied. While the effect of the Poisson's ratio of the soil layer on the vertical dynamic stiffness and damping coefficient is analysed. Furthermore, mathematical expressions of the real and imaginary part of the dynamic impedances are derived pertaining foundations with various slenderness ratios and embedded in different soil profiles. The results from this chapter regarding the dynamic lateral response of suction caissons are presented in Latini and Zania (2017a) and Latini et al. (2016a), namely *Paper III* and *Paper IV* in the thesis. Whereas the outcomes investigating the vertical dynamic behaviour of suction caissons are described in *Paper V* and Latini et al. (2016b) (*Paper VI*).

Chapter 5 is about elasto-plastic constitutive models for cohesionless soil to describe properly highly nonlinear stress path dependent shear stiffness, the accumulation of pore pressure, permanent shear strains and volumetric strains under repeated number of cycles. Particularly, the soil constitutive model of Dafalias and Manzari (SANISAND, 2004) has been modified in order to solve inefficient performance of the stress integration scheme for soil deposits in the low stress regime. The modified SANISAND (2004) has been implemented in Abaqus. In addition, drained and undrained compression triaxial tests at DTU GEO-Lab were performed to calibrate the material constants of the constitutive model for Fontainebleau sand. The calibration is necessary for evaluating the model performance for Fontainebleau sand. The findings of this chapter are presented in Latini et al. (2017), named *Paper VII* in this manuscript. While details of drained and undrained triaxial tests performed at DTU GEO-Lab are given in Latini and Zania (2017b) (*Report*).

Chapter 6 deals with the use of numerical methods of structural design optimization to design piles and suction caissons for offshore wind turbine jacket foundations. Two different foundation types, a range of various leg distances and ten soil profiles were included in the integrated design optimization of jacket and foundation. The results presented in this chapter are shown in *Paper VIII*.

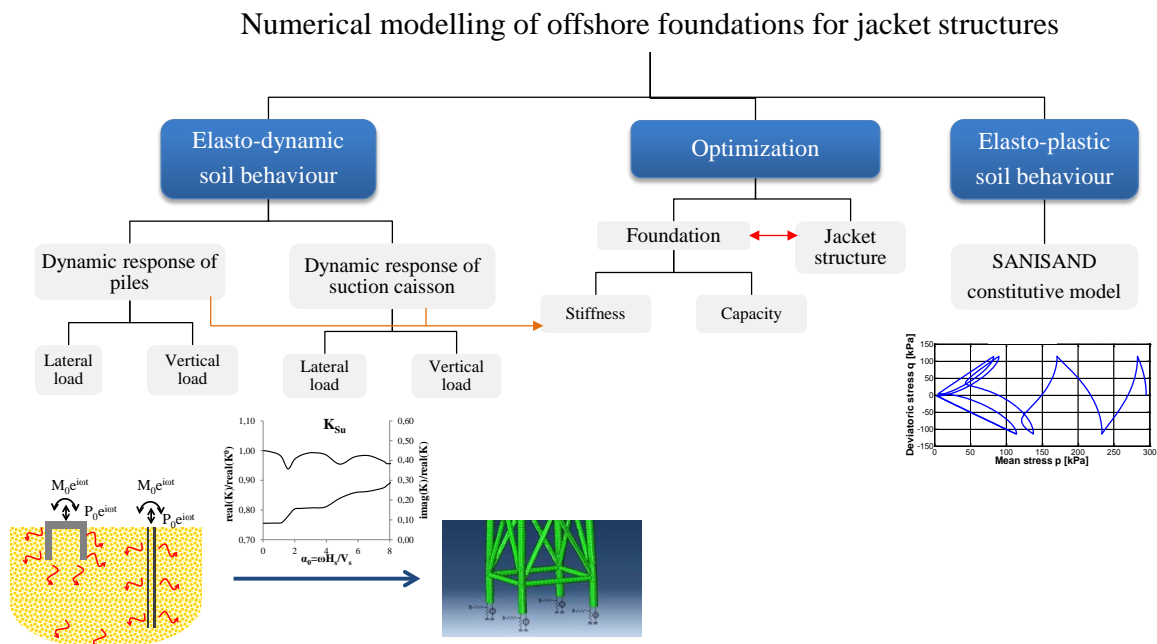


Figure 1.5: Overview of the research project.

Chapter 2

State of the art

The literature review here presented is based on Paper I, Latini and Zania (2017a) (Paper III), Paper VI and Latini et al. (2017) (Paper VII).

2.1 Introduction

The foundation has the function to transfer the loads acting on the superstructure to the soil layers. Special considerations must be included in the analysis of the foundation, when it deals with cyclic and dynamic loads such as is the case for wind and seismic loads. Therefore, the response of a structure subjected to these type of loadings depends mainly on the mechanical properties of the surrounding soil, the characteristics of the superstructure and the soil–foundation structure interaction. The present work intends to investigate the problem of soil–foundation interaction when the foundation is subjected to dynamic and cyclic loads. An extensive literature review was conducted on this problem first by considering linear elastic soil behaviour and dynamic loading conditions. Then an overview of the numerous soil constitutive models available in literature is briefly presented, which provides the basis for the choice of a soil model suitable for the simulation of foundations under cyclic lateral loading.

2.2 Dynamic response of piles

Pile foundations are deployed in geotechnical engineering projects in which the structure is subjected to dynamic loads due to environment factors, such as earthquake, wave, wind or human activities, such as passing traffic. In the abovementioned cases, the interaction between the foundation and the surrounding soil governs the structural response. Kramer (1996) showed that the eigenfrequency and the damping of any structure subjected to dynamic load are altered due to the soil–foundation interaction. Consequently, the dynamic stiffness and damping of the soil–foundation system should be taken into account when the natural vibration characteristics of the structure are determined. The Substructure Method is usually adopted to separately model the discrete superstructure and the continuum soil medium. The study of soil–structure interaction as shown in the Substructure Method can be divided into two phenomena: a) kinematic interaction which is due to inability of the foundation to match the free field motion and b) inertia interaction which represents the fact that the mass of the superstructure transmits the inertial force to the soil causing further deformation in the soil.

A simplified but rational approach to study these effects considers the structure as a single degree of freedom system, linked to foundation through the translational K_{Su} , rotational $K_{M\theta}$ and coupled $K_{S\theta}$ dynamic springs coefficients and dashpots of modulus ζ_{Su} , $\zeta_{M\theta}$ and $\zeta_{S\theta}$, which are called after the dynamic impedances of the soil foundation system. Hence, the impedance functions are defined as amplitudes of harmonic forces (or moments) that have to be applied to the foundation head in

order to generate a harmonic motion with a unit amplitude in the specified direction (Novak (1991)), see Figure 2.1. The complex stiffnesses \tilde{K} can be expressed in any of the following ways:

$$\tilde{K} = K_1 + iK_2 \quad (2.1)$$

$$\tilde{K} = K_{dyn} + i\omega C \quad (2.2)$$

$$\tilde{K} = K^0(k' + i\omega\zeta) \quad (2.3)$$

in which K_1 and K_2 are the real and imaginary parts of the complex stiffness, respectively and $i = \sqrt{-1}$; $K_{dyn} = K_1$ represents true stiffness, $C = K_2/w$ is the coefficient of equivalent viscous damping, i.e. energy dissipation due to hysteretic and radiation mechanisms. Whereas ω is circular frequency; K^0 is static stiffness and $k' = K_{dyn}/K^0$, $\zeta = C/k'$ are dimensionless stiffness and damping constants, respectively.

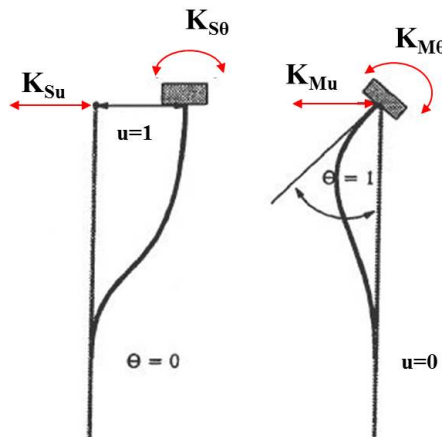


Figure 2.1: Pile head impedances.

In the literature the problem of the dynamic soil-pile interaction has been extensively investigated. The analytical and numerical studies in the literature can be broadly categorized as follows: a) Winkler type analytical solutions; b) analytical elastodynamic solutions and c) numerical finite element solution and discrete element models.

Winkler type analytical solutions

Winkler type analytical solutions (Novak (1974); Novak and Aboul-Ella (1978); Mylonakis (2001)) are the most deployed solutions in the literature, due to their simplicity and applicability. In such formulations the soil medium is represented as a system of independent, closely spaced elastic springs overlying rigid bedrock. For dynamic problems Novak (1974) recommended the use of Winkler foundation coefficients based on Baranov's equation (Baranov (1967)) for the in-plane and out-plane vibration of a disk. Winkler type analytical solutions are usually defined as plane strain cases, since zero strain is considered along the vertical direction. The assumption of zero shear deformations in the pile body can be considered valid, since these solutions are mostly used for slender piles ($H_p/d > 10$, where H_p and d are the foundation height and diameter, respectively). Winkler type model has the advantage of including the soil nonlinearity and inhomogeneity, even though the selection of a suitable Winkler modulus influences considerably the accuracy of these solutions.

It is worth mentioning that Mylonakis (2001) proposed an improved model, where the normal and shear stresses acting on the upper and lower faces of a horizontal soil element are incorporated in the analysis by integrating the governing equations over the thickness of the soil layer. Additionally, the plane strain model was also adopted to estimate the vertical dynamic impedance of floating piles (piles embedded in soil layers of depth H_s greater than the pile length H_p), as reported in the work of Novak (1977). The results showed that the stiffness of a floating pile increases when the pile

length increases; which is the opposite of what depicted for the stiffness of an end bearing pile. Furthermore, it was highlighted that the motion of the tip can be neglected for very long pile and when the pile's tip rests on rigid bedrock. These observations are in agreement with the outcomes shown in the work of Kuhlemeyer (1979b).

Analytical elastodynamic solutions

Analytical solutions for investigating the lateral dynamic behaviour of end bearing piles were proposed by Novak and Nogami (1977); Nogami and Novak (1977) and Nogami and Novak (1980). In these formulations a three-dimensional solution was provided by considering the soil as a continuum with hysteretic material damping. Differential equations of waves propagate through the elastic soil medium are firstly set in order to calculate the soil resistance. The horizontal dynamic response and the dynamic impedances of the pile foundation are determined by ensuring the continuity conditions between the pile and the soil. In such studies the vertical displacement was neglected; while Anoyatis et al. (2016) considered that vertical soil displacement is relatively small, by including two different compressibility factors in the estimation of the soil resistance. A benefit of this approach is that the sensitivity of the solution to Poisson's ratio, as ν approaches 0.5, vanished. Unlike the abovementioned studies, the formulation presented by Liu et al. (2016) suggested that the governing equations of the soil are solved directly, eliminating the need to introduce potential functions. The complex impedances determined by this solution perfectly correspond to those obtained by Novak and Nogami (1977). The main limitation of such studies lies in the assumption of elastic soil response; however it was proved that they are in good agreement with finite element results (Blaney (1976), Roesset and Angelides (1980)). Zheng et al. (2013) developed an analytical solution to investigate the horizontal dynamic response of large-diameter pipe pile. The governing equations of the outer and inner soil were decoupled by applying the potential functions. The effect of the inner soil on the vibration characteristics of the pile was found negligible in the low frequency range. Recall that concrete pipe piles were taken into account and the interval of frequency was considered up to 300Hz in this study.

For the case of the vertical dynamic response of end bearing pile, a three-dimensional continuum solution is proposed in the work of Nogami and Novak (1976), Hu et al. (2004) and Zheng et al. (2014). In the work of Nogami and Novak (1976) the motion of the soil layer is solved first and the wave modes of the layer are used in the analysis of the pile response. The pile response to a harmonic load is obtained in a closed form and deployed to define the stiffness and damping at the level of the pile head. Although analytical formulations exhibit the advantage of treating the soil layer in more realistic manner than the plane strain models, the radial component of the soil displacements is not included in the abovementioned formulations. A more accurate elastodynamic solution, where both vertical and radial displacements are included, was proposed by Wu et al. (2013). In this solution the displacements of the soil medium were studied by introducing the potential functions and the governing equations of the soil were solved applying Laplace transform. Whereas the method proposed by Zheng et al. (2014) does not incorporate potential functions in the solution of the governing equation of the soil layer. Liu et al. (2014) developed an elastodynamic formulation to analyze the vertical dynamic behaviour of a pipe pile installed in a saturated elastic layer, by adopting the dynamic consolidation theory of Biot (Biot (1956)). This study highlighted that the porosity of the soil layer marginally influences the dynamic response of the pile, since the oscillation amplitudes of the complex impedance reduces slightly by decreasing the permeability coefficient particularly in the high frequency range.

In addition to the aforementioned studies, analytical continuum formulations for investigating the dynamic response of floating piles are proposed by Nozoe et al. (1988), Haldar and Bose (1990) and Deng et al. (2014). The work of Nozoe et al. (1988) presented a theoretical analysis of both the vertical and lateral dynamic response of floating piles embedded in soil layer on rigid bedrock. In this solution Timoshenko's beam theory was used for modelling the pile foundation and the soil

medium was represented as a continuum, considering all the three components of soil displacements. On the contrary, Haldar and Bose (1990) formulated the general elastodynamic equations neglecting the vertical component of the displacement and the soil was assumed to be homogeneous elastic halfspace. It was found that the results reduce to a form attributed to Baranov's solution, when the pile length is made infinite. While the vertical dynamic behaviour of floating pile was analysed in the work of Deng et al. (2014), by introducing the fictitious soil–pile model. The outcomes were presented in terms of the velocity response in the frequency domain, derived by means of Laplace transform technique. It was found that the increase of the thickness of pile end soil layer $\Delta H = H_s - H_p$ can significantly influence the dynamic response at the pile head. Furthermore, the effect of the stiffness of pile end soil on the dynamic behaviour at pile head seemed more remarkable when the pile length decreases and the diameter increases. It is important to stress that a uniform distribution of soil displacements inside fictitious foundation is not valid for short piles.

Numerical methods

The soil-pile interaction problem can also be investigated by finite elements methods (FEM) (Blaney (1976), Kuhlemeyer (1979a), Roesset and Angelides (1980), Velez et al. (1983), Gazetas (1984), Gazetas and Dobry (1984), Syngros (2004)) and boundary element methods (BEM)(Kaynia and Kausel (1991), Mamoon et al. (1990), Maeso et al. (2005), Padron et al. (2007)). In finite element methods (Blaney (1976), Roesset and Angelides (1980), Velez et al. (1983), Gazetas (1984), Gazetas and Dobry (1984)) the soil was treated as an elastic continuum and the pile was assumed to be a series of regular beam segments, having rigid cross section; while Syngros (2004) used solid elements to allow for Poisson's effects and associated radial displacements in the pile to be captured. In addition Roesset and Angelides (1980) presented simple frequency–dependent expressions for dynamic pile stiffness coefficients based on finite element outcomes. Gazetas and Dobry (1984) proposed a simplified method, whose starting point is the estimation of the static pile deflection. The results were then validated with respect to finite element models. In this work different types of soil profiles were considered and the sensitivity of the solution to Poisson's ratio, as ν approaches to 0.5, was solved by adopting the expression of Lysmer and Kuhlemeyer (1969) for η . Velez et al. (1983) adopted the finite element formulation of Blaney (1976) and Roesset and Angelides (1980) to analyse the dynamic behaviour of piles embedded in a soil stratum. The outcomes showed that the drop of stiffness attained at the eigenfrequencies of the soil layer increases for lower values of the slenderness ratio. Additionally, it was found that no resonance practically occurred for floating piles in very deep soil. Velez et al. (1983) also suggested expressions for the static and dynamic active length of piles.

In the boundary element approach the soil and the pile are considered as separate substructures for which the coupling was enforced only at discrete locations. In the majority of the studies where boundary element methods is applied, the dynamic impedances of pile foundations were assessed by considering the soil as a homogeneous halfspace. While Padron et al. (2008) adopted BEM–FEM coupling model for predicting the lateral and vertical dynamic response of a single pile and pile groups embedded in viscoelastic homogeneous strata resting on a rigid bedrock. The study highlighted that the effect of rigid bedrock is not any more visible when the soil depth is greater than five times the pile length.

Maeso et al. (2005) proposed a 3D boundary element approach to investigate the vertical and lateral response of a single pile and pile groups embedded in a two phase poroelastic soil. The outcomes were in agreement with the solution of Rajapakse (1987), when the dissipation constant $b = \gamma_f \phi^2 / k$ is zero. Note that γ_f , ϕ and k represent the specific weight of fluid phase, porosity and permeability, respectively. It was found that for high values of b the real and imaginary part of the vertical impedance tend to those of a pile foundation embedded in an undrained elastic medium. While the drained elastic medium provides the lower limit towards which the two phase soil approaches when its permeability increases. On the contrary, the effect of the permeability of the soil medium becomes apparent for the real component of the lateral dynamic impedances. Indeed, the pattern of

the real component is below that of drained elastic soil, when the soil permeability is very high and in the higher frequency interval.

It is demonstrated that numerical methods provide reliable predictions with the limitation of being computationally intensive and time consuming.

Moreover, it is worth mentioning that very limited studies investigating numerically the response of floating piles are available in the literature (Kuhlemeyer (1979a)). Kuhlemeyer (1979a) estimated the dynamic impedances of floating piles in an elastic layer overlying a rigid half space by finite element analyses. Some deviation from Novak (1974) was observed and approximate polynomial expressions of the dynamic stiffness components were suggested for a practical range of E_p/E_s ratio.

2.3 Dynamic response of suction caissons

Regarding suction caisson foundations most of research studies deals with the analysis of the load capacity and the kinematic mechanism accompanying failure under the action of combined vertical, horizontal and moment loading (Randolph and House (2002), Aubeny and Murff (2003), Gourvenec (2008)). In addition, the response of suction caisson subjected to seismic loading was also examined (Kourkoulis et al. (2014)). However, the dynamic behaviour of suction caisson foundations has scarcely investigated, see Liingaard (2006), Varun and Gazetas (2009). In the work of Liingaard (2006) the dynamic stiffness coefficients were estimated, treating the soil as a linear viscoelastic medium and modelling the suction caisson using a coupled BE/FE model in homogeneous halfspace. Then the obtained outcomes were compared with analytical solutions for surface foundations. It was found that the dynamic impedances pattern determined by the analytical solution for surface foundations was in good agreement with the results of the BE/FE model for the case of surface footing, on the contrary it did not resemble the one obtained from the numerical model for $H_p/d > 0.25$. Furthermore, Liingaard (2006) pointed out the Poisson's ratio significantly influences the sliding and rocking component of the stiffness and investigated the effect of the skirt flexibility on the dynamic response of caisson foundations embedded in a homogeneous soil layer. It was found that the dynamic behaviour of suction caisson in the frequency domain is significantly dependent on the variation of the slenderness ratio ($H_p/d = 0.25 - 1$). While Varun and Gazetas (2009) developed an analytical formulation for the dynamic response of caisson foundations characterized by slenderness ratio 2–6 and embedded in linear elastic soil media, by using a simple Winkler spring model. In the work of Varun and Gazetas (2009) the analytical results were then validated with respect to finite element models and good agreement was achieved. Additionally, it was found that the sensitivity of the dynamic stiffness coefficients on the variation of Poisson's ratio was barely noticed, except for values very close to 0.5.

2.4 Elasto-plastic soil behaviour

2.4.1 Introduction

For long time simple elasto–plastic constitutive models, such as the Drucker–Prager and Mohr–Coulomb, have been adopted in geotechnical engineering to describe the mechanical response of soils. The soil stress state has been widely investigated in literature both experimentally and theoretically. During the 1960's Roscoe et al. (1958) and Schofield and Wroth (1968) introduced the concept of Critical State Soil Mechanics (CSSM) to properly understand soil behaviour by considering volume changes as well as changes in effective stresses. In the last decades, numerous advanced constitutive models in the framework of critical state theory were developed to reproduce in a realistic way the response of sand under static and dynamic loading, using a single set of parameters. In this section a review of the most characteristic aspects of the behaviour of sand is briefly described and an overview of constitutive models available in the literature is also presented.

2.4.2 Monotonic and cyclic behaviour of sand

It is general agreement that sand experiences shear-induced volume change until the critical state is reached, where shearing occurs at constant volume. During shearing, the soil can contract (positive volume change) or dilate (negative volume change); this fundamental difference in the behaviour depends on the initial state of the material in relation to the critical state. The critical state is defined by a surface formed in e - p - q space, which is projected as a line (CSL) in the e - p and q - p planes, where e , q and p are the void ratio, deviatoric stress and mean effective stress, respectively. Furthermore, it was proposed a unique critical state line (CSL) for each sand in an e - $\log p$ plot which is independent of type of loading, sample preparation method and initial density as explained in the work of Been et al. (1991). Figure 2.2 illustrates the monotonic behaviour of sand in e - p space for both drained and undrained conditions. If a state initially denser than critical (blue point), placed on the left hand side of CSL, is subjected to drained constant p triaxial compression, it first consolidates and then dilates until reaches the CSL where $e = e_c$ and critical failure occurs. Under undrained loading this state moves to the critical point as negative pore water pressure development due to initial dilative tendency increases the effective stress p . For state looser than critical (green point), located at the right side of CSL, experiences contractive behaviour, resulting in a reduction of void ratio under drained constant p loading and mean effective stress in a corresponding undrained loading.

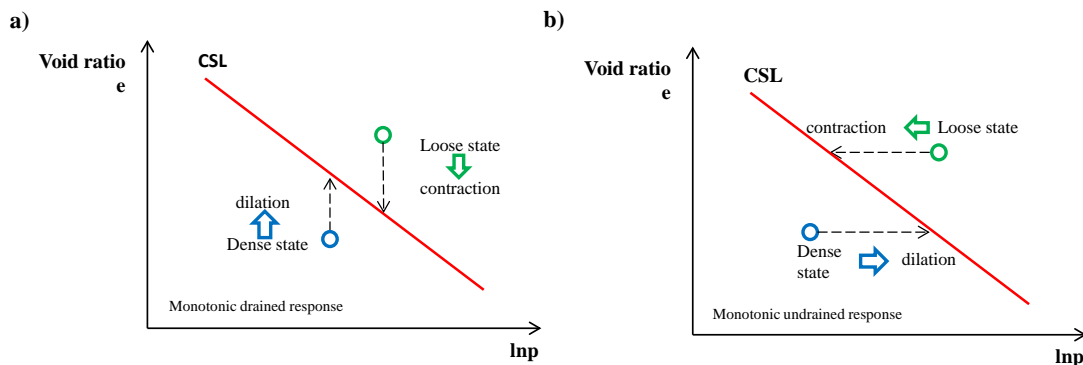


Figure 2.2: Illustration of monotonic behaviour of sand in e - p space: a) drained and b) undrained conditions.

Different behaviour is observed when sands undergo to cyclic loads. So far, it was shown that sands are characterized by a contractive response in drained conditions, since they attempt to reach the densest possible configuration, which is represented by the minimum void ratio (e_{min}). This contracting behaviour is known as cyclic hardening and it results in an increase in strength/stiffness. In undrained conditions sands experience accumulation of excess pore water pressure and this build-up reduces the effective stresses determining cyclic liquefaction or cyclic mobility, see Figure 2.3.

2.4.3 Advanced soil constitutive models: overview

The constitutive models based on perfect plasticity are capable to reproduce the nonlinearity and irreversible behaviour of the soil when subject to monotonic loadings. On the contrary they are not sufficient to describe the irreversible strains accumulated and the relaxation of effective stress due cyclic loads. In addition, it was observed a limited capacity to define the stress history of the material. Thus it is imperative to deploy realistic constitutive models for realistic numerical analysis in order to describe properly highly nonlinear and anisotropic stress-strain behaviour of soil.

In the last two decades several advanced constitutive models have been carried out to simulate the cyclic loading of granular cohesionless soils, which can be divided into the following categories according to their fundamental characteristics:

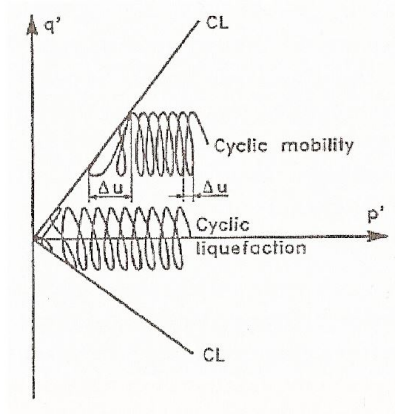


Figure 2.3: Definition of cyclic liquefaction and cyclic mobility (Ibsen, 1994).

- theory of plasticity with kinematic hardening, in which the yield surface can expand, contract and translate in stress space, along the prescribed stress path;
- theory of plasticity with rotational hardening, in which the yield surface can expand, contract and rotate in stress space, being oriented by the stress path direction;
- theory of plasticity with bounding surface;
- theory of hypoplasticity.

2.4.3.1 Theory of plasticity

The general structure of plasticity theory is widely discussed in several studies (Lubliner (1990), Simo and Hughes (1987), Jirásek and Bazant (2002)); while the theory of plasticity for geomechanics applications is explained in Vermeer and De Borst (1984) and Zienkiewicz et al. (1999).

The basic kinematic assumption is the decomposition of the rate of the strain tensor into an elastic component $\dot{\epsilon}^e$ and into a plastic component $\dot{\epsilon}^p$:

$$\dot{\epsilon} = \dot{\epsilon}^e + \dot{\epsilon}^p \quad (2.4)$$

The rate of elastic strain is associated to the increment of stress $\dot{\sigma}$ through the following relationship:

$$\dot{\sigma} = D^e(\sigma)\dot{\epsilon} = D^e(\sigma) | \dot{\epsilon} - \dot{\epsilon}^p | \quad (2.5)$$

where D^e is elastic tangent stiffness tensor, which is a 4th order tensor and depends normally on the current stress state. In the plasticity theory the current loading state of a material point is determined by the yield function f . The yield function is defined in terms of the stress state σ and the state parameters \mathbf{q} .

$$f = f(\sigma, \mathbf{q}) \leq 0 \quad (2.6)$$

The stress σ determines the position in the domain and the state parameters \mathbf{q} defines size, shape and position of the yield surface relative to an initial configuration where only elastic deformation has occurred. This leads to divide the stress space into two domains: an elastic domain where $f < 0$ and a plastic domain where $f = 0$. If the material point is in the elastic domain $f(\sigma, \mathbf{q}) < 0$, then elastic strains will occur.

A flow rule is introduced to describe the deformation taking place during plastic loading:

$$\dot{\epsilon}^p = \dot{\gamma} \frac{\partial g}{\partial \sigma}(\sigma, \mathbf{q}) \quad (2.7)$$

Where $g(\boldsymbol{\sigma}, \mathbf{q})$ is the plastic potential and $\dot{\gamma} \geq 0$ is the plastic multiplier. Concerning soil a non-associated flow rule ($g \neq f$) must be used (Crisfield (1991)) since the flow direction is generally not normal to the yield surface. The evolution of the state variables \mathbf{q} is defined through the hardening function:

$$\dot{\mathbf{q}} = \dot{\gamma} \mathbf{h}(\boldsymbol{\sigma}, \mathbf{q}) \quad (2.8)$$

where $\mathbf{h}(\boldsymbol{\sigma}, \mathbf{q})$ is a specific function. As mentioned before the plastic deformations can occur only when the material point is on the yield surface. This means that the plastic multiplier $\dot{\gamma}$ has to follow the so-called Kuhn–Tucker conditions:

$$\dot{\gamma} \geq 0, \quad f(\boldsymbol{\sigma}, \mathbf{q}) \leq 0, \quad \dot{\gamma} f(\boldsymbol{\sigma}, \mathbf{q}) = 0 \quad (2.9)$$

where $\dot{\gamma} f(\boldsymbol{\sigma}, \mathbf{q}) = 0$ is defined as consistency condition. Then the plastic multiplier can be calculated as follows:

$$\dot{\gamma} = \frac{1}{K_p} \left\langle \frac{\partial f}{\partial \boldsymbol{\sigma}} \cdot D^e \dot{\boldsymbol{\epsilon}} \right\rangle \quad (2.10)$$

in which $\langle x \rangle := \frac{x+|x|}{2}$ are Macaulay's parenthesis of x , and the plastic modulus K_p is defined as:

$$K_p := \frac{\partial f}{\partial \boldsymbol{\sigma}} \cdot D^e \frac{\partial g}{\partial \boldsymbol{\sigma}} + H_p > 0 \quad H_p := -\frac{\partial g}{\partial \mathbf{q}} \cdot \mathbf{h} \quad (2.11)$$

The scalar function H_p is called hardening modulus of the material and it represents hardening ($H_p > 0$), softening ($H_p < 0$) and perfect plasticity ($H_p = 0$).

The assumption of elastic domain, in which the response of the material is reversible, represents the main limitation of plasticity theory. Indeed, plastic deformations (irreversible deformations) occurred at those stress states that they are at the yielding surface. Experimental results generally indicate that the soil response can undergo to irreversible deformations and be path-dependent even for strongly preloaded states, and that plastic yielding is a rather gradual process (Tamagnini and Viggiani (2002)). Although these effects can be considered of little significance when the soil is subjected to monotonic loads; they must be taken into account for cyclic and dynamic loads. In response of the need for more accurate predictions of the performance of soils, several developed constitutive models based on the theory of plasticity with kinematic hardening, theory of plasticity with bounding surface or theory of hypoplasticity have appeared in the literature.

Theory of plasticity with kinematic hardening Several kinematic hardening models have been developed for geomaterials since the early '80, see i.e. Mroz, Norris and Zienkiewicz (Mroz et al. (1979), Mroz et al. (1981)), Wood and coworkers (Al-Tabbaa and Muir Wood (1989), Gajo and Muir Wood (1999)), Stallebrass and Taylor (1997).

The main reason for their development stems from the need to improve the description of cyclic behaviour of soils. Kinematic Hardening models have also been advocated to reproduce the observed nonlinearity at small strain levels and the effects of recent stress history on the stiffness decay with increasing strains as shown in the work of Stallebrass (1990) (Tamagnini (2011)). Kinematic hardening models are characterized by the following expression of the yield surface:

$$f(\boldsymbol{\sigma}, \boldsymbol{\alpha}, q_k) = \hat{f}(\hat{\boldsymbol{\sigma}}, q_k) = 0 \quad \hat{\boldsymbol{\sigma}} := \boldsymbol{\sigma} - \boldsymbol{\alpha} \quad (2.12)$$

where $\boldsymbol{\alpha}$ is the so-called back stress ratio and q_k represents scalar internal variables. As shown in Figure 2.4, the yield surface translates according to the variation of $\boldsymbol{\alpha}$ during the loading process.

On the other hand, the motion of the yield surface is limited by larger, outer surface, called Bounding surface of equation:

$$F(\boldsymbol{\sigma}, \bar{q}_k) = 0 \quad \{\bar{q}_k\} \subset \{q_k\} \quad (2.13)$$

The function of BS is to separate admissible states from impossible ones, and is generally similar in shape to the yield surface. Additionally, this formulation is characterized by the the fact that the

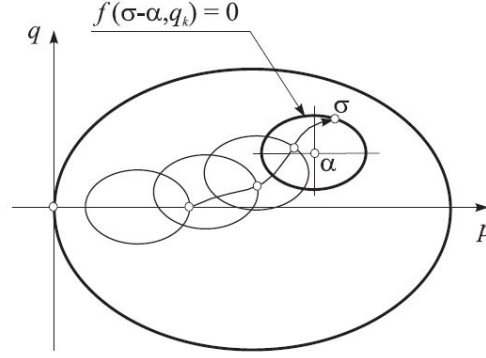


Figure 2.4: Kinematic hardening inside the Bounding surface (Tamagnini and Viggiani, 2002).

hardening modulus H_p is assigned as a monotonically decreasing function of the distance δ between the current state and the image state $\bar{\sigma}$ on the BS, defined as the point at which the unit normals to $f = 0$ and $F = 0$ have the same direction (Tamagnini and Viggiani (2002)):

$$H_p = \hat{H}(\bar{H}_p, \delta) \quad \frac{\partial \hat{H}}{\partial \delta} > 0 \quad \hat{H}(\bar{H}_p, 0) = \bar{H}_p \quad (2.14)$$

In Equation 2.14 $\delta := \|\bar{\sigma} - \sigma\|$ and \bar{H}_p is the plastic modulus at $\bar{\sigma}$.

Theory of plasticity with bounding surface The Bounding surface model is characterized by the presence of a surface in stress space, the bounding surface (BS), which separates admissible from impossible states. The abovementioned surface may vary in shape, orientation and size when plastic strains occur. Contrary to the yield surface in classical plasticity, stress states located inside BS can be associated to plastic deformations. Therefore, this formulation does not consider any elastic region. At each admissible stress state, the flow rule given in Equation 2.7 can be adopted, in which the plastic multiplier is given as:

$$\dot{\lambda} = \frac{1}{\tilde{K}_p} \left\langle \frac{\partial f}{\partial \sigma} \cdot D^e \dot{\epsilon} \right\rangle \quad (2.15)$$

where $\tilde{K}_p := \frac{\partial f}{\partial \sigma} \cdot D^e \frac{\partial g}{\partial \sigma} + \tilde{H}_p$, in which \tilde{H}_p is the plastic multiplier. In Bounding surface models a non-invertible mapping rule (radial mapping rule) is established, as shown Figure 2.5, which associates each stress state σ inside the BS to a corresponding image state $\bar{\sigma}$ on the BS. Once the image state is found, the loading direction is taken as the gradient of the BS at $\bar{\sigma}$, while the plastic modulus H_p is assumed to a monotonically decreasing function of distance $\delta := \|\bar{\sigma} - \sigma\|$ between the current state and the image state, and of plastic modulus \bar{H}_p at $\bar{\sigma}$ (Tamagnini and Viggiani (2002)):

$$\tilde{H}_p = \tilde{H}(\bar{H}_p, \delta) \quad \frac{\partial \tilde{H}}{\partial \delta} > 0 \quad \tilde{H}(\bar{H}_p, 0) = \bar{H}_p \quad (2.16)$$

Theory of hypoplasticity Hypoplasticity can be defined as a class of incrementally nonlinear constitutive models, developed specifically to predict the behaviour of soils. In hypoplasticity the notions of the yield surface and the plastic potential surface do not appear as in the case of elasto-plastic models. Additionally, the strain rate is not decomposed into elastic and plastic potential part. However, hypoplastic models are capable of representing the main features of the soil behaviour, such as the critical state, nonlinearity, irreversible strains accumulated, hysteretic behaviour and dependency on the stress history. The basic hypoplastic equation can be written as follows:

$$\bar{T} = L : D + N \|D\| \quad (2.17)$$

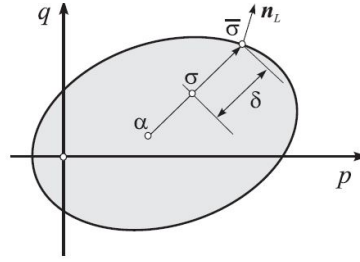


Figure 2.5: Radial mapping rule in Bounding surface models (Tamagnini and Viggiani (2002)).

where $\bar{\mathbf{T}}$ is the stress rate, \mathbf{D} is the Euler's stretching tensor and \mathbf{L} and \mathbf{N} are fourth and second order constitutive tensors, respectively. Equation 2.17 was modified by Gudehus (1996) in order to take into account the influence of the stress level (barotropy) and the influence of density (pyknotropy). The modified equation is given as:

$$\bar{\mathbf{T}} = f_s \mathbf{L} : \mathbf{D} + f_s f_d \mathbf{N} \|\mathbf{D}\| \quad (2.18)$$

where f_s and f_d are scalar factors, describing of barotropy and pyknotropy. The standard hypoplastic model for fine grained soils is the one developed by von Wolffersdorff (1996), which refined the hypoplastic formulation proposed by Gudehus (1996). The standard hypoplastic model requires the estimation of 8 parameters, which can be determined in standard laboratory tests as described in the work of Herle and Gudehus (1999). The main drawback of the hypoplastic models is an exaggerate *ratcheting* behaviour (accumulated plastic deformation) for load cycles. Therefore, Niemunis and Herle (1997) proposed an improved model by considering additional state variable "intergranular strain". The rate formulation of the model suggested by Niemunis and Herle (1997) can be written as:

$$\bar{\mathbf{T}} = \mathbf{M} : \mathbf{D} \quad (2.19)$$

where \mathbf{M} is the fourth-order tangent stiffness tensor of the material. In this formulation an internal strain-dependent variable δ was introduced in order to increase the stiffness response after a strain reversal. Indeed, the total strain can be thought of as the sum of a component related to the deformation of interface layers at intergranular contacts, quantified by the intergranular strain tensor δ ; and a component related to the rearrangement of the soil skeleton (Masin (2013)). This extension requires to establish 5 extra material constants, which can be estimated by means of resonance column tests in conjunction with high-resolution triaxial tests (Niemunis and Herle (1997)).

2.4.4 SANISAND family of constitutive models

SANISAND model is the name used for a family of Simple Anisotropic SAND constitutive models developed over the past few years. SANISAND Family of models is based on two concepts: two-surface plasticity formulation and the concept of the state parameter ψ , introduced by Been and Jefferies (1985), in the framework of Critical State Soil Mechanics (CSSM). With the introduction of the state parameter ψ it was possible to distinguish dense samples from loose ones and provide realistic prediction for stress-strain behaviour of sands. In addition, SANISAND constitutive models have the advantage to use a single set of model parameters for any initial void ratio or confining pressure. This family of sand models has been extensively investigated. In the work of Papadimitriou et al. (1999) a plastic multiplier was firstly related to evolving sand fabric in order to simulate both the densifying effect associated to the contractive phase of shearing and the opposite effect connected to dilation. While Manzari and Dafalias (1997) suggested a scalar multiplier of the dilatancy to describe accurately the cyclic mobility phase of shearing. An improved version of the SANISAND model was later presented in Dafalias and Manzari (2004). In this formulation the capability of the basic model under cyclic loading was

improved by considering the effect of the fabric change on dilatancy. In addition, the Lode's angle effect on the bounding surface was introduced determining more realistic response in non-triaxial conditions. Papadimitriou et al. (2001) and Papadimitriou and Bouckovalas (2002) proposed two new features in the two surface model of Manzari and Dafalias (1997): a) a Ramberg–Osgood type nonlinear hysteretic formulation of the elastic moduli to govern shear modulus degradation and the hysteretic damping increase for small to medium cyclic shear strains and b) a scalar multiplier of the plastic modulus, which controls soil behaviour from medium to large cyclic shear strains. In the study of Li and Dafalias (2002), Dafalias et al. (2004) and Loukidis and Salgado (2009) the effect of inherent anisotropy (due to depositional process) on sand stress–strain strength response was further studied. Additionally, it is important mentioning the SANISAND version suggested by Chiu and Ng (2003) for unsaturated sands. While a modified SANISAND model addressing the problem of sand liquefaction was proposed by Lashkari (2009). Taiebat and Dafalias (2008) introduced some modifications on the basic SANISAND model of Dafalias and Manzari (2004), in order to represent the particle crushing when sands are subjected to high confining pressures. Introducing a cap type of loading surface it was also possible to represent plastic strain due to the increase of stress under a constant stress ratio. Lately, Dafalias and Taiebat (2016) developed the so-called SANISAND–Z model, where they considered the possibility of vanishing yield surface. This new formulation is then characterized by simplified structure, since it consists of only one surface (bounding/failure surface).

Chapter 3

Dynamic response of piles

*The findings of this chapter are presented in Paper I, Latini et al. (2015) (Paper II). And those passages denoted by superscript * and *** have been quoted verbatim from Paper I and Paper V, respectively.*

The aim of this chapter is to evaluate the dynamic soil–structure interaction of pile for offshore wind turbines. The investigations include evaluation of the vertical and coupled sliding–rocking vibrations. The chapter is divided according to the type of loading applied on the foundation. The dynamic stiffness of the pile is expressed in terms of dimensionless frequency–dependent coefficients corresponding to different degrees of freedom. The dynamic stiffness coefficients for the pile foundation are evaluated both by adopting analytical formulations and by establishing a 3D numerical model in Abaqus software. The validation of the analytical solutions along with their limitations was also discussed. The analysis was carried out for different combinations of the slenderness ratio H_p / d , relative thickness H_s / d , Poisson’s ratio ν and stiffness of the soil layer V_s (E_p / E_s). The influence of the foundation geometry on the dynamic impedances was also addressed.

3.1 Lateral dynamic response of piles

Two layered soil profile characterized by high stiffness contrast is analysed. Then, 3D numerical models were established taken into consideration different depths of the surface soil layer with respect to the pile length, see Figure 3.1.

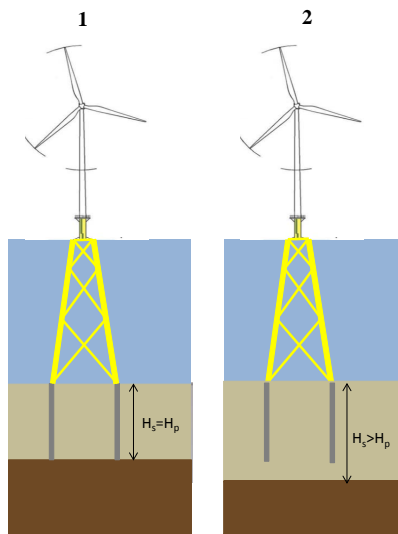


Figure 3.1: Illustration of the two soil profiles investigated in this study.

For many geotechnical engineering works the condition of piles embedded in a soil layer laying on a rigid bedrock is much more representative and encountered than the case of a foundation in an infinite half space. In this study the soil profile with depth equal to the pile length is defined as profile 1 (end bearing pile), while the one with increased depth as profile 2 (floating pile). Specifically, a floating pile is one for which there is no abrupt change in the properties of the soil material at the end of the pile; while in the case of an end bearing pile the foundation passes through a soil profile and the tip bears on soil layer much stiffer such as rock.

The dynamic response of end bearing piles has been widely investigated in the literature and thus, a numerical model was first established for profile 1 and then, for profile 2 in this work. The numerical results of profile 1 and profile 2 are compared respectively with the continuum analytical solution formulated for end bearing piles by Novak and Nogami (1977) and that for floating piles by Latini et al. (2015), which is herein described. Sensitivity of the dynamic impedances of piles on the slenderness ratio was showed in this study. Moreover, the overall dynamic response was analysed by varying the relative thickness and the stiffness of the soil layer.

3.1.1 Analytical approach

Profile 1 - End bearing piles The estimation of lateral dynamic stiffness and damping coefficients was performed by adopting the continuum analytical solution of Novak and Nogami (1977). In the formulation of Novak and Nogami (1977), the soil is modelled as a continuum with hysteretic material damping and the elastic soil reaction is considered in the far field, since deformations are small enough. The soil resistance is determined by solving the differential equations of wave propagation within the elastic soil medium. The horizontal dynamic response and the dynamic impedances of the pile foundation are obtained by applying the continuity conditions between the pile and the soil. This solution offered a good insight into the behaviour of the soil–pile system; even though vertical displacement is not taken into account in the estimation of the lateral dynamic impedances.

Profile 2 - Floating piles The literature review showed there is only a study (Nozoe et al. (1988)) investigating analytically the dynamic response of floating piles embedded in a soil layer overlying rigid bedrock. In this work an inconsistency on the horizontal displacements can be observed, since an abrupt variation of the displacement field was recorded at the interface between the pile and the soil layer. Hence, the aim of this study is to formulate an analytical solution for the dynamic response of floating piles focusing on the estimation of the dynamic stiffness and damping coefficients with respect to the frequency. The analytical solution was developed by appropriately modifying the elastodynamic formulation for end bearing piles proposed by Novak and Nogami (1977). The improvement of the model lies in a better prediction of soil response which ultimately yields more accurate results for pile impedances. The main assumptions of the solution are: 1) the soil layer is linear, elastic, free at the surface; 2) the pile is vertical, uniform, linearly elastic and of circular cross section; 3) the material damping is of the hysteretic type–frequency independent. Free pile tip and perfect contact between the foundation and the surrounding soil were taken into account in the proposed solution. Additionally, the vertical displacements associated with horizontal pile vibration are ignored in agreement with the work of Novak and Nogami (1977). This assumption can be considered rational when the pile deforms in bending without substantial shear deformations (Zania (2014)).

In this formulation to account for the fact that the depth of the viscoelastic layer undergoing harmonic motion was larger than the pile length as shown in Figure 3.2, two reference systems were introduced: 1) RS starting from the bottom of the rigid bedrock and 2) RS1 set from the pile tip.

In the new reference system (RS1) the horizontal motion of the pile when subjected to harmonic horizontal load $P(\omega, t) = Pe^{i\omega t}$ at the pile head is given in the form of:

$$u(z_1, t) = u(z_1)e^{(i\omega t)} \quad (3.1)$$

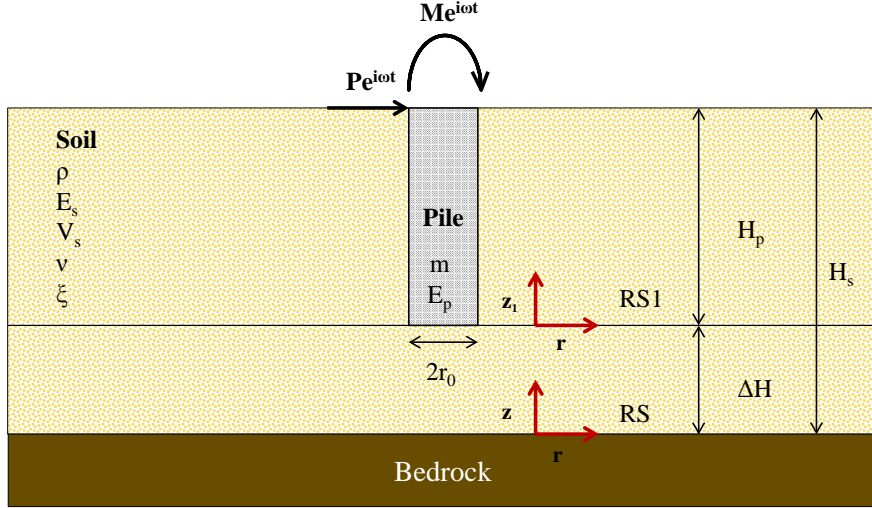


Figure 3.2: Analytical model of soil–pile system

where t is the time variable, ω is the cyclic excitation frequency, $i(=\sqrt{-1})$ is the imaginary number and z_1 is the vertical coordinate. The governing equation of the pile motion is written in agreement with the corresponding for beam on elastic foundation by Hetényi (1971).

$$E_p I \frac{\partial^4 (u e^{i\omega t})}{\partial z_1^4} + m \frac{\partial^2 (u e^{i\omega t})}{\partial t^2} = -p(z_1) e^{i\omega t} \quad (3.2)$$

in which $E_p I$, m and $p(z_1)$ are respectively the bending stiffness of the pile (with a moment of the inertia of $I = \pi d^4/64$ for a circular cross section), the mass of the pile per unit length and the amplitude of the soil resistance to the motion of the pile. Whereas, the dynamic resistance of the soil to the lateral pile motion $p(z_1, t) = p(z_1, \omega) e^{i\omega t}$ expressed in the local pile's coordinate system is

$$p(z_1, t) = \sum_{n=1}^{\infty} \alpha_{hn} U_n \sin(h_n(z_1 + \Delta H)) \quad (3.3)$$

where α_{hn} is the horizontal resistance factor, depending on the pile radius r_0 , shear modulus G of the soil layer and a number of dimensionless parameters such as the dimensionless frequency $\alpha_0 = H_s \omega / V_s$, pile slenderness H_p/d , material hysteretic damping ζ and Poisson's ratio ν ; U_n is the modal amplitude independent of z , $\sin(h_n(z_1 + \Delta H))$ was the n th mode shape of the soil layer, $\Delta H = H_s - H_p$ and $h_n = (\pi/2H_s)(2n - 1)$ where H_s was the thickness of the soil layer and n is the mode number. According to the work of Novak and Nogami (1977) the horizontal resistance factor which was defined as:

$$\alpha_{hn} = \pi r_0 G \left[(1 + i\zeta) h_n^2 - \left(\frac{\omega}{V_s} \right)^2 \right] T_n \quad (3.4)$$

where the expression of parameter T_n was given as following:

$$T_n = \frac{4K_1(q_n r_0)K_1(s_n r_0) + s_n r_0 K_1(q_n r_0)K_0(s_n r_0) + q_n r_0 K_0(q_n r_0)K_1(s_n r_0)}{q_n K_0(q_n r_0)K_1(s_n r_0) + s_n K_1(q_n r_0)K_0(s_n r_0) + q_n s_n r_0 K_0(q_n r_0)K_0(s_n r_0)} \quad (3.5)$$

where K_m is the modified Bessel function of second kind and order m . The variables q_n and s_n were functions of the dimensionless frequency α_0 and they are reported in Novak and Nogami (1977). Substituting Equation 3.3 into Equation 3.2 and eliminating the time variable t the following expression for the pile amplitude is shown in Equation 3.6:

$$E_p I \frac{d^4 u}{dz_1^4} - m \omega^2 u = - \sum_{n=1}^{\infty} \alpha_{hn} U_n \sin(h_n(z_1 + \Delta H)) \quad (3.6)$$

The solution to Equation 3.6 is given as a sum of the complete solution of the homogeneous equation u_h , and a particular solution of the non-homogeneous equation u_p . The particular solution u_p can be expressed as

$$u_p(z_1) = \sum_{n=1}^{\infty} a_n \sin(h_n(z_1 + \Delta H)) \quad (3.7)$$

where a_n is a complex constant. Substitution of Equation 3.7 into Equation 3.6 yields

$$E_p I \sum_{n=1}^{\infty} a_n h_n^4 \sin(h_n(z_1 + \Delta H)) - m\omega^2 \sum_{n=1}^{\infty} a_n \sin(h_n(z_1 + \Delta H)) = - \sum_{n=1}^{\infty} \alpha_{hn} U_n \sin(h_n(z_1 + \Delta H)) \quad (3.8)$$

Hence, the constant a_n is determined as

$$a_n = \frac{-\alpha_{hn} U_n}{E_p I h_n^4 - m\omega^2} \quad (3.9)$$

The solution of the homogeneous equation is written as

$$u_h(z_1) = A \sin(\lambda z_1) + B \cos(\lambda z_1) + C \sinh(\lambda z_1) + D \cosh(\lambda z_1) \quad (3.10)$$

where A , B , C and D are the integration constants obtained by the boundary conditions at the pile head ($z_1 = H_p$) and at the bottom of the soil layer ($z_1 = -\Delta H$). And

$$\lambda = \sqrt[4]{\frac{m\omega^2}{E_p I}} \quad (3.11)$$

Then the pile displacement is given as:

$$u(z_1) = A \sin(\lambda z_1) + B \cos(\lambda z_1) + C \sinh(\lambda z_1) + D \cosh(\lambda z_1) - \sum_{n=1}^{\infty} \frac{\alpha_{hn} U_n}{E_p I h_n^4 - m\omega^2} \sin(h_n(z_1 + \Delta H)) \quad (3.12)$$

The displacement of the soil layer at the pile is expressed as

$$U(z_1) = \sum_{n=1}^{\infty} U_n \sin(h_n(z_1 + \Delta H)) \quad (3.13)$$

The displacement compatibility between the pile and the soil layer is imposed. Then, the variable z_1 is written as $z_1 = z - \Delta H$ and expanding $\sin(\lambda(z - \Delta H))$, $\cos(\lambda(z - \Delta H))$, $\sinh(\lambda(z - \Delta H))$ and $\cosh(\lambda(z - \Delta H))$ into a Fourier sine series of argument $(h_n z)$ the following formula is obtained:

$$U_n = \frac{AF_{1n} + BF_{2n} + CF_{3n} + DF_{4n}}{1 + \left[\frac{\alpha_{hn}}{E_p I h_n^4 - m\omega^2} \right]} \quad (3.14)$$

where

$$\begin{cases} F_{1n} = \frac{2}{H_s} \int_0^{H_s} \sin(\lambda(z - \Delta H)) \sin(h_n z) dz \\ F_{2n} = \frac{2}{H_s} \int_0^{H_s} \cos(\lambda(z - \Delta H)) \sin(h_n z) dz \\ F_{3n} = \frac{2}{H_s} \int_0^{H_s} \sinh(\lambda(z - \Delta H)) \sin(h_n z) dz \\ F_{4n} = \frac{2}{H_s} \int_0^{H_s} \cosh(\lambda(z - \Delta H)) \sin(h_n z) dz \end{cases} \quad (3.15)$$

Substituting U_n into Equation 3.12, the amplitude of the pile motion is

$$u(z) = A \sin(\lambda(z - \Delta H)) + B \cos(\lambda(z - \Delta H)) + C \sinh(\lambda(z - \Delta H)) + D \cosh(\lambda(z - \Delta H)) - \sum_{n=1}^{\infty} \frac{\alpha_{hn} (AF_{1n} + BF_{2n} + CF_{3n} + DF_{4n})}{E_p I h_n^4 - m\omega^2 + \alpha_{hn}} \sin(h_n z) \quad (3.16)$$

Using the displacement of the pile presented in Equation 3.16, the amplitude of the angle of rotation θ , the bending moment M and the shear force S were obtained by the corresponding derivatives. The unknown coefficients A, B, C, D have been estimated by considering the boundary conditions and applying a unit horizontal translation and a unit rotation at the pile head as listed:

$$\begin{cases} u(H_s) = 1, & \theta(H_s) = 0 & \text{for } \tilde{K}_{Su}, \tilde{K}_{Mu} \\ u(H_s) = 0, & \theta(H_s) = 1 & \text{for } \tilde{K}_{S\theta}, \tilde{K}_{M\theta} \\ u(0) = 0, & \theta(0) = 0 \end{cases} \quad (3.17)$$

where $\tilde{K}_{Su}, \tilde{K}_{Mu}, \tilde{K}_{S\theta}$ and $\tilde{K}_{M\theta}$ are the complex valued impedances, which can be written in the following form:

$$\tilde{K}_{xx} = \text{Real}(\tilde{K}_{xx}) + i\text{Imag}(\tilde{K}_{xx}) = K_{xx}(\omega)(1 + 2i\zeta_{xx}) \quad (3.18)$$

The dynamic impedances $\tilde{K}_{Su}, \tilde{K}_{Mu}, \tilde{K}_{S\theta}$ and $\tilde{K}_{M\theta}$ at the level of the pile head are then calculated as reaction force (S) and moments (M) for unit displacement (u) and rotation (θ). Therefore, the general expressions for dynamic displacement, rotation, bending moment and shear force of floating pile are given as follows:

$$\begin{pmatrix} u \\ \theta \\ \frac{M}{EI} \\ \frac{F_{p1}}{b_{p1}} \end{pmatrix} = \begin{bmatrix} \sin(\lambda(z - \Delta H)) - Y \sum_{n=1}^{\infty} F_{1n} \sin(h_n z) & \cos(\lambda(z - \Delta H)) - Y \sum_{n=1}^{\infty} F_{2n} \sin(h_n z) & \sinh(\lambda(z - \Delta H)) - Y \sum_{n=1}^{\infty} F_{3n} \sin(h_n z) & \cosh(\lambda(z - \Delta H)) - Y \sum_{n=1}^{\infty} F_{4n} \sin(h_n z) \\ \lambda \cos(\lambda(z - \Delta H)) - Y \sum_{n=1}^{\infty} h_n F_{1n} \cos(h_n z) & -\lambda \sin(\lambda(z - \Delta H)) - Y \sum_{n=1}^{\infty} h_n F_{2n} \cos(h_n z) & \lambda \cosh(\lambda(z - \Delta H)) - Y \sum_{n=1}^{\infty} h_n F_{3n} \cos(h_n z) & \lambda \sinh(\lambda(z - \Delta H)) - Y \sum_{n=1}^{\infty} h_n F_{4n} \cos(h_n z) \\ -\lambda^2 \sin(\lambda(z - \Delta H)) + Y \sum_{n=1}^{\infty} h_n^2 F_{1n} \sin(h_n z) & -\lambda^2 \cos(\lambda(z - \Delta H)) + Y \sum_{n=1}^{\infty} h_n^2 F_{2n} \sin(h_n z) & \lambda^2 \sinh(\lambda(z - \Delta H)) + Y \sum_{n=1}^{\infty} h_n^2 F_{3n} \sin(h_n z) & \lambda^2 \cosh(\lambda(z - \Delta H)) + Y \sum_{n=1}^{\infty} h_n^2 F_{4n} \sin(h_n z) \\ -\lambda^3 \cos(\lambda(z - \Delta H)) + Y \sum_{n=1}^{\infty} h_n^3 F_{1n} \cos(h_n z) & \lambda^3 \sin(\lambda(z - \Delta H)) + Y \sum_{n=1}^{\infty} h_n^3 F_{2n} \cos(h_n z) & \lambda^3 \cosh(\lambda(z - \Delta H)) + Y \sum_{n=1}^{\infty} h_n^3 F_{3n} \cos(h_n z) & \lambda^3 \sinh(\lambda(z - \Delta H)) + Y \sum_{n=1}^{\infty} h_n^3 F_{4n} \cos(h_n z) \end{bmatrix} \begin{pmatrix} A \\ B \\ C \\ D \end{pmatrix} \quad (3.19)$$

where

$$Y = \frac{\alpha h n}{(E_p I h_n^4 - m \omega^2 + \alpha h n)}$$

3.1.2 Numerical approach

3.1.2.1 Methodology

3D finite element model in the commercial software Abaqus (Systèmes (2014)) is described and its main features are discussed. Note that the numerical methodology was presented in Latini and Zania (2017a), Latini et al. (2016a) and Latini et al. (2016b).

Assumptions The following assumptions are considered in the numerical models: 1) linear elastic isotropic behaviour of the pile; 2) linear viscoelastic isotropic behaviour of soil with hysteretic type damping and 3) perfect contact between the foundation and the soil during the analysis. The abovementioned hypotheses are consistent with those accounted in the analytical solutions.

Boundary conditions In dynamic analyses the soil layers are considered as infinite in the horizontal direction. This approach differs from that adopted in static analyses, where fixed boundary conditions can be applied at some distance from the region of interest. Whereas it was observed in dynamic analyses that outward propagating waves will be reflected back into the model by deploying such boundary conditions. In addition, fixed boundary conditions do not model appropriately the outward radiation of energy at the boundary of the model. In finite element programs there are several alternatives to solve the aforementioned issues. In this study infinite elements were deployed to adequately model the infinite medium boundary conditions. During dynamic analyses, infinite elements provide “quiet” boundaries at the finite element model boundaries based on the model of Lysmer and Kuhlemeyer (1969). It was considered that the dominant direction of the wave propagation is orthogonal to the boundary and the response adjacent to the boundary is of small enough amplitude so that the medium is linearly elastic (Systèmes (2014)).

Geometry Due to the symmetry of the problem only half of the foundation and the surrounding soil was considered. The reference model consists of:

- foundation (pile or suction caisson)
- finite soil domain (near-field soil domain surrounded the foundation)
- infinite soil domain (far-field soil domain)

As reported in Figure 3.3 the finite soil domain is characterized by a radius of $L_f = 180m$, while the radius of the infinite soil domain is defines as $L_{inf} = 180m$.

Analysis and frequency increment As shown in Equation 2.2 the stiffness of the soil–foundation system is a complex number, where the real component K_{dyn} and the imaginary component ωC can be divided into a spring and dashpot depending on the property of the imaginary part in the frequency domain. The value of K_{dyn} for $\omega \approx 0$ is defined as the static stiffness. The complex stiffness could be arranged as in Equation 2.3 in which the ratio between the imaginary part and real part $\omega C/K_{dyn} = 2\zeta$ denotes the hysteretic material damping. In this work the following notation is considered for the stiffness components of the soil–foundation system:

- K_{Su} - Lateral stiffness component.
- $K_{M\theta}$ - Rocking stiffness component.
- $K_{Mu} = K_{S\theta}$ - Coupling stiffness component.
- K_V - Vertical stiffness component.

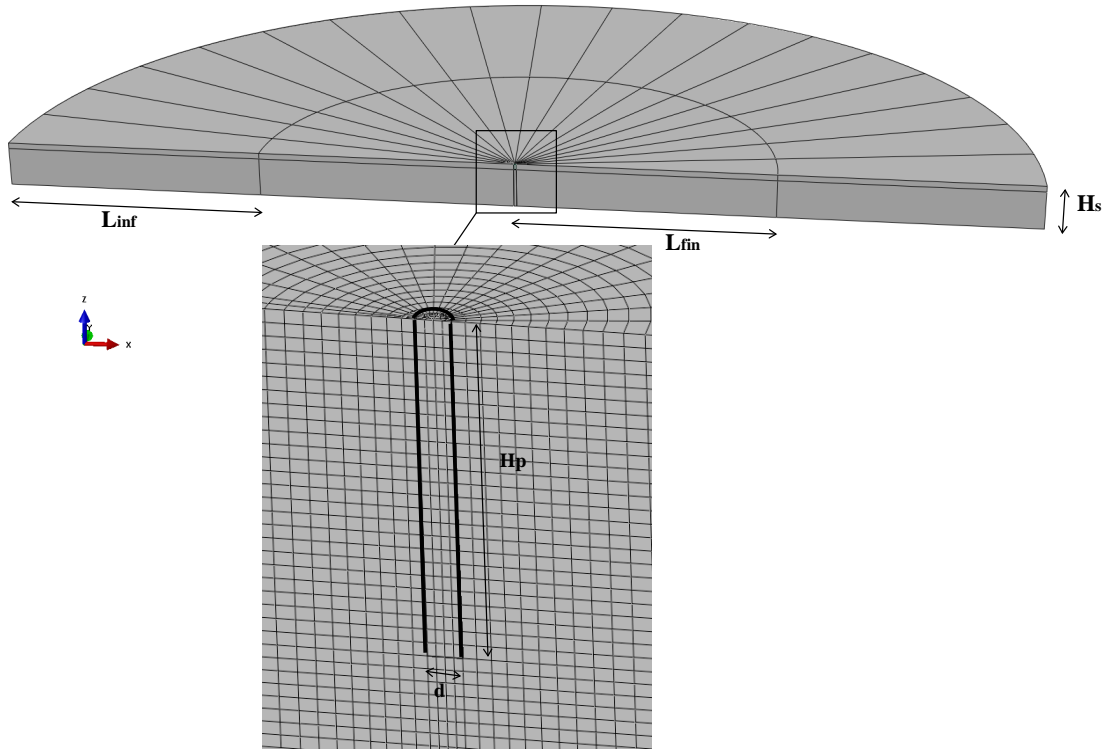


Figure 3.3: Finite element model of the foundation and the surrounding soil.

Displacements/rotations are related to force/moment as reported in Equation 3.20, where u is the horizontal displacement along x_1 , θ is the rotation around x_2 and w is the vertical displacement along x_3 . While S, M, N are respectively shear force along x_1 , bending moment around x_2 and axial force in the vertical direction x_3 .

$$\begin{bmatrix} K_{Su} & K_{S\theta} & 0 \\ K_{Mu} & K_{M\theta} & 0 \\ 0 & 0 & K_V \end{bmatrix} \begin{bmatrix} u \\ \theta \\ w \end{bmatrix} = \begin{bmatrix} S \\ M \\ N \end{bmatrix} \quad (3.20)$$

In the present work all dynamic impedances are reported as:

- Normalized dynamic stiffness: $real(K_{dyn})/real(K^0)$
- Normalized imaginary part (indication of damping): $2\zeta = imag(K_{dyn})/real(K_{dyn})$

where $real(K^0)$ represents the static stiffness.

In order to determine the aforementioned dynamic stiffness components the type of analysis conducted is the so-called ‘‘Steady-State Dynamic Analysis’’, provided by Abaqus software. This procedure allows to perform steady state linearised response of the model subject to harmonic excitation, i.e. a displacement or a force applied on the model for a user-defined range of frequency. For a given frequency interval, the stress/displacements fields are calculated at each node of the entire model. To obtain K_{Su} and K_{Mu} at the pile head a unit displacement $U1 = 1$ is applied, keeping the other displacements and rotations fixed to zero $U2 = U3 = UR1 = UR2 = UR3 = 0$. $K_{M\theta}$ is achieved by setting a unit rotation $UR2 = 1$ at the pile head, while the displacements and rotations in the other directions are considered equal to zero $U1 = U2 = U3 = UR1 = UR3 = 0$. In this work the torsional component of the soil-pile system is not investigated. In addition, the

range of frequency studied includes the 2nd eigenfrequency of the soil layer $\alpha_0 = 3/2\eta\pi$, where $\eta = \sqrt{(2(1-\nu)/(1-2\nu))} = 2.08$. Recall that α_0 is a dimensionless frequency corresponding to the eigenfrequency of the soil layer, since it is given as the product of the wave number and the thickness of the soil layer:

$$\alpha_0 = \frac{\omega H_s}{V_s} \quad (3.21)$$

where ω (rad/sec), H_s (m) and V_s (m/s) are respectively the frequency, the thickness and the shear wave velocity of the soil layer.

Type of elements For each component of the model, the element definition assigned in the finite element models is herein explained:

Finite soil domain The near field soil domain ($L_{fin} = 180m$) was discretized by 3D solid continuum hexahedral elements (C3D8). Such elements are continuum finite elements with 8 integration points and linear shape function, which means that a linear approximation of displacement field over the domain of the element is used.

Infinite soil domain The far field soil response ($L_{inf} = 180m$) was modelled using infinite elements (CIN3D8) to avoid spurious reflections. Such elements are continuum, infinite elements with 8 integration points and linear shape function.

The infinite elements which represent “quiet” boundaries have to be placed so that only one infinite element face is in contact with the exterior face of the finite elements defining the region of interest. Moreover, the infinite elements are characterized by the same material properties of the finite soil domain they surround.

Foundation Depending on each modelling solution the type of elements considered are: a) solid continuum elements (C3D8) for the solid pile and b) shell elements with linear interpolation (S4) for the shell pile.

The motivation of having two modelling approaches also stemmed to investigate the influence of the inner soil on the dynamic impedances of the soil–pile system. Note that in the finite element analysis it was decided to adopt fully integration than reduced integration, in order to ensure the accuracy of the numerical results. Reduced integration elements have the advantage of reducing the running time of the analysis, but they may suffer of hourglassing problem, which consists of an uncontrolled distortion of the mesh.

Connectivity It is required that the pile and the soil are bounded together in order to guarantee the continuity of field displacement between each parts during the analysis. Depending on the pile modelling solution the typology of connectivity are described:

Solid pile The soil and pile parts are connected together by a “Tie constraint” between the inner lateral soil surface and the external lateral pile surface. Such constraint bounds the slave nodes (soil part) from separating to the master surface (foundation surface).

Additionally, a “Rigid Body constraint” constraint was assigned on the top surface of the pile. All points of the surface are rigidly linked to the reference point placed at the centre of the pile. This implies that they are obliged to follow the displacement of the reference point, on which the unit displacement/rotation has been applied.

Shell pile The inner soil, shell pile and the outer soil are connected by “Tie constraint” in order to guarantee the perfect connection between soil and foundation during the analysis. As seen for the solid pile a “Rigid Body constraint” is defined between the nodes on the pile’s circumference and the reference point (RP) defined at the center of the pile.

Boundary conditions The FE models are characterized by the following boundary conditions:

- $U_1 = U_2 = U_3 = 0$ at the bottom of the soil domain;
- Symmetry condition in direction x_2 for the lateral vertical surface of the soil domain and the pile foundation, and the reference point;
- Unit displacement/rotation on the reference point depending on the stiffness component to determine.

Mesh size Particular care was placed in the selection of the maximum element size to capture the stress wave accurately. A mesh size given by 10 – 20 elements per wavelength is assumed a good approximation. The wavelength is calculated using Equation 3.22:

$$H_{i,max} = \frac{\lambda_{max}}{6 \simeq 8} = \frac{V_s T}{6 \simeq 8} = \frac{V_s}{(6 \simeq 8) f_{max}} \quad (3.22)$$

where H_{max} is the maximum dimension of each finite element, λ_{max} is the maximum shear wave length in the soil stratum. λ_{max} is related to the shear wave velocity V_s and to the maximum frequency of the harmonic vibration f_{max} . According to each part of the numerical model, the mesh size arrangement is given as follows:

Finite soil domain Regarding the radial direction the size of each finite element increases from the symmetry line of the model to the outer part with dimensions $0.40m - 2.00m$. In the vertical direction the subdivision of elements is set $0.40m$ and 20 elements are deployed in the hoop direction.

Infinite soil domain It is characterized by one element along the radial direction and the mesh has 20 elements on the circular edge.

Foundation In the vertical direction the size of the mesh is $0.40m$ for the solid equivalent pile, shell pile and suction caisson. In addition, the subdivision of elements in the longitudinal direction is of $0.25m$ for the solid equivalent pile.

3.1.3 Validation of the numerical model

Profile 1 The numerical results of the pile foundation embedded in profile 1 were compared and validated with the continuum analytical solutions of Novak and Nogami (1977) and Mylonakis (2001). The validation of the analytical solution was performed by considering a small diameter ($d = 2r_0 = 1m$) pile of height $H_p = 10m$ embedded in a homogeneous soil layer and constant profile of shear wave velocity ($V_s = 68.2m/s$), hysteretic material damping ($\beta = 5\%$) and Poisson's ratio ($\nu = 0.40$). Details of the case of study adopted are presented in Table 3.1.

Table 3.1: Parameters of the case of study for the analysis of pile foundation.

Pile foundation		
Young modulus	E_p	$2.5 \cdot 10^7 kPa$
Diameter	d	$1.00m$
Density	ρ_p	$2.40tn/m^3$
Soil		
Young modulus	E_s	$2.5 \cdot 10^4 kPa$
Shear modulus	G	$8928kPa$
Shear ware velocity	V_s	$68.2m/s$
Soil layer thickness	H_s	$10.00m$
Density	ρ_s	$1.92tn/m^3$
Hysteretic damping	β	0.05
Poisson's ratio	ν	0.40

In Table 3.2 the normalized static stiffness terms for all the components are reported and compared with those obtained according to Novak and Nogami (1977), Mylonakis (2001) and Randolph (1981). Note that the static stiffness coefficients of the numerical model were calculated at low frequencies. A discrepancy less than 5% between the numerical model and the analytical solution of Novak and Nogami (1977) is recorded for all components. It is evident that the expressions proposed by Mylonakis (2001) underestimated the static stiffness coefficients, with the horizontal component showing the highest difference (16%). While the discrepancy between the static stiffness coefficients obtained from the numerical model and those calculated according to Randolph (1981) is approximately of 9.6%, 16% and 11% for the horizontal, coupling and rocking component, respectively.

Table 3.2: Static stiffness components of pile obtained from the numerical models and the analytical solutions of Novak and Nogami (1977), Mylonakis (2001) and Randolph (1981).

<i>Model</i>	$K_{Su}/(E_s \cdot d)$	$K_{S\theta}/(E_s \cdot d^2)$	$K_{M\theta}/(E_s \cdot d^3)$
Novak and Nogami (1977)	5.02	-8.07	29.62
Mylonakis (2001)	4.18	-7.46	26.91
Randolph (1981)	4.38	-6.63	27.43
Numerical Model	4.87	-7.96	30.87

In Figure 3.4 the real (K_{Su} , $K_{S\theta}$, and $K_{M\theta}$) and the imaginary ($2\zeta_{Su}$, $2\zeta_{S\theta}$, and $2\zeta_{M\theta}$) parts of the dynamic impedances are presented. Due to the unavailability of data, the comparison of the numerical results with respect to those obtained by the formulation of Mylonakis (2001) was performed only for the horizontal dynamic impedance. The outcomes exhibited a drop of stiffness after the 1st horizontal eigenfrequencies ($\alpha_0 = \pi/2$) for the horizontal, coupling and rocking stiffness component. Additionally, the numerical outcomes exhibit an extra drop in stiffness recorded at the

1st vertical resonance ($\alpha_0 = 1/2\pi\eta$), which is less prominent for the case of the cross coupling and rocking components. This might be motivated by the fact that the vertical displacements are neglected in the analytical solutions. While the reduction in stiffness attained at the 2nd eigenfrequency of the soil layer ($\alpha_0 = 3\pi/2$) become more apparent for the horizontal and coupling coefficients. Generally, an increasing pattern of the coupling and rocking component of the stiffness was noticed after the 2nd resonance; even though the variation of the rocking stiffness component is barely noticeable for frequencies higher than the 1st resonance.

The imaginary part of the dynamic coefficient of the dynamic impedances gives an indication of the damping generated due to the soil–pile interaction. Particularly, radiation damping was developed after the 1st eigenfrequency of the soil layer for all the components. Indeed, the linear increasing values of the coefficients with frequency confirmed that viscous type damping was generated for this frequency range.

Finally, good agreement between the outcomes of the numerical model and those obtained by the analytical formulation of Novak and Nogami (1977) was achieved in the frequency interval examined. However a slight scatter was observed between the results proposed respectively by Novak and Nogami (1977) and Mylonakis (2001) for the horizontal component of the stiffness, with the latter exhibiting stiffer behaviour.

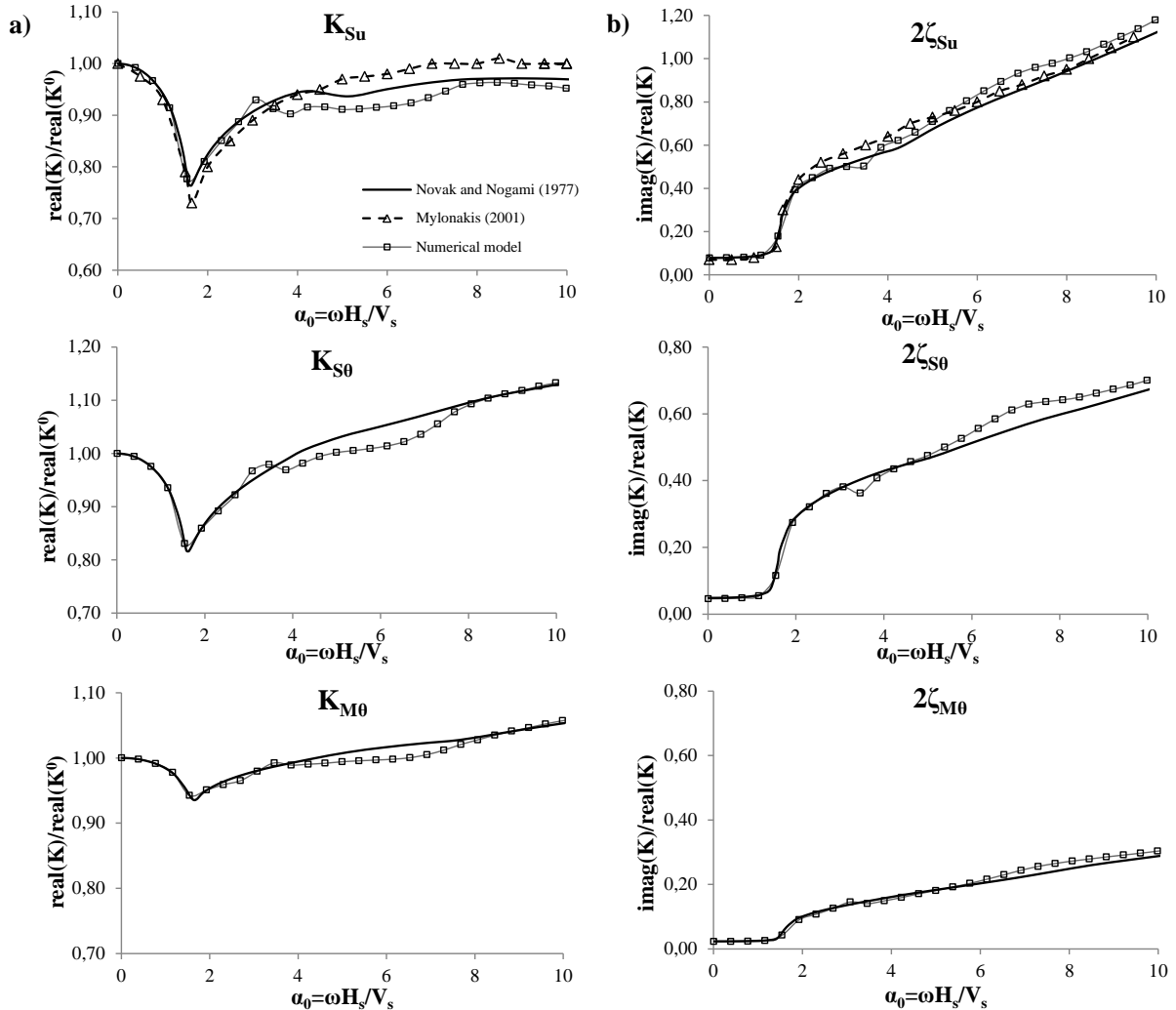


Figure 3.4: Comparison of the dynamic impedances obtained by the numerical model, Novak and Nogami (1977) and Mylonakis (2001) formulation for the case investigated.

In Figure 3.5 the modal displacement of the pile at the three first eigenfrequencies of the soil layer is illustrated along the depth. The results are referred to end bearing pile with properties listed in Table 3.3. It is evident that the numerical results are practically identical with those obtained from the analytical solution of Novak and Nogami (1977). Additionally, it was noticed that all the pile length mobilizes the soil displacements.

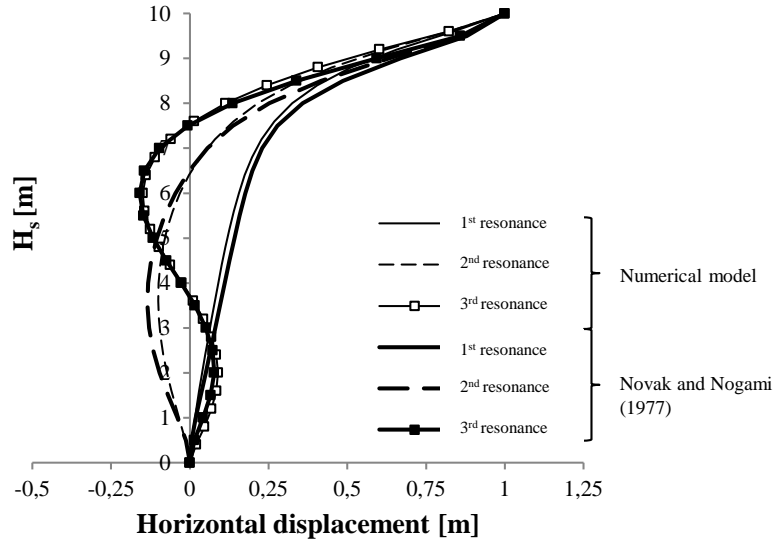


Figure 3.5: Distribution of the soil and pile displacement along the depth at the three first eigenfrequencies of the soil layer.

Discussion on the effect of vertical displacements One of the assumption of the analytical solution of Novak and Nogami (1977) is that the vertical displacements are negligibly small, which is not the case in the numerical model established. It is of interest to see the influence of the vertical displacements on the static and dynamic response of piles. Therefore, a numerical simulation was performed where vertical displacements are disregarded and, the results are compared with those of the numerical model originally established. Note that the case of study referred to a pile foundation embedded in profile 1 ($H_s = H_p = 10m$) with material properties given in Table 3.3. Additionally, the two numerical models are characterized by the same mesh discretization and dimensions of the soil domain.

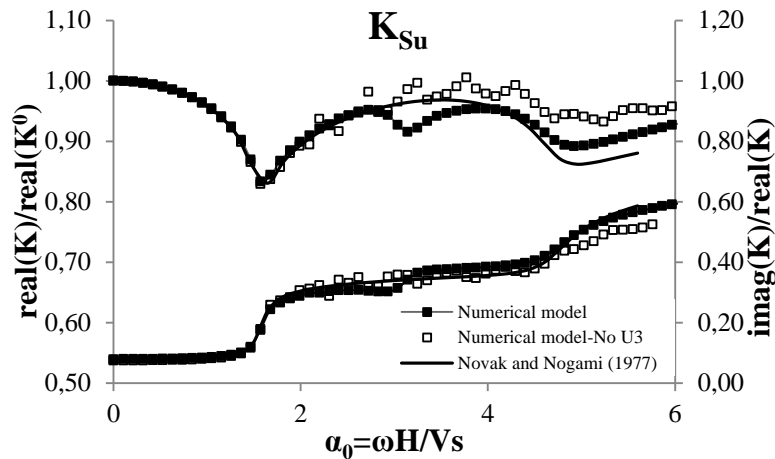


Figure 3.6: Comparison of the dynamic impedances obtained by the numerical model and Novak and Nogami (1977) formulation for profile 1, considering different assumptions on displacements.

Firstly, it was found that the horizontal static stiffness component determined by the numerical model is smaller (17%) than the one referred to the numerical model, where no vertical displacements are taken into account. In Figure 3.6 the dynamic horizontal stiffness and damping coefficients are depicted in the frequency range analysed. It appears that the numerical analysis of the pile foundation in which the vertical displacements are neglected provided stiffer response after the 1st vertical resonance with respect to the numerical model characterized by no assumption on the displacements. Furthermore, it was observed that the dynamic stiffness does not exhibit a smooth pattern approximately after the 1st horizontal resonance when the vertical displacements are disregarded. While the imaginary part of the lateral dynamic impedance seems not to be influenced by the vertical component of displacements. A possible explanation might be the wave reflection occurred in the model with blocked vertical displacements and this can be a direct consequence of the constraint applied on the mesh. It is important to highlight that this issue did not take place in the numerical model for which any assumptions on the displacements were not considered. However it can be stated that the results of the numerical model where the vertical displacements are restrained fairly resembled those of the analytical formulation for frequencies up to the 1st vertical eigenfrequency of the soil layer.

Profile 2 The validation of the proposed analytical solution was performed by considering a small diameter ($d = 2r_0 = 1m$) pile of height $H_p = 10m$ embedded in a homogeneous soil layer with thickness $H_s = 30m$ and constant profile of shear wave velocity ($V_s = 250m/s$), hysteretic material damping ($\beta = 5\%$) and Poisson's ratio ($\nu = 0.35$) over a wide frequency range including at least the 3rd eigenfrequency of the soil layer ($\alpha_0 = 5/2\pi$). Details of the case of study are also listed in Table 3.3.

Table 3.3: Parameters of the case of study for the analysis of pile foundation.

Pile foundation		
Young modulus	E_p	$2.138 \cdot 10^8 kPa$
Diameter	d	$1.00m$
Density	ρ_p	$7.86tn/m^3$
Thickness	$t = r_0/50$	$0.01m$
Soil		
Young modulus	E_s	$286875kPa$
Shear modulus	G	$106250kPa$
Shear wave velocity	V_s	$250m/s$
Density	ρ_s	$1.7tn/m^3$
Hysteretic damping	β	0.05
Poisson's ratio	ν	0.35

Table 3.4: Static floating pile stiffness obtained from the numerical models and the analytical solutions.

<i>Model</i>	$K_{Su}/(E_s \cdot d)$	$K_{S\theta}/(E_s \cdot d^2)$	$K_{M\theta}/(E_s \cdot d^3)$
Latini et al. (2015)	2.78	-1.98	3.62
Syngros (2004)	2.58	-1.61	3.18
Randolph (1981)	2.93	-1.97	3.63
Numerical Model	2.60	-1.75	3.85

The static stiffness coefficients of the numerical model were determined at low frequencies and

listed in Table 3.4, along with the corresponding values given by the suggested analytical solution, the simplified expressions of Syngros (2004) for piles embedded in homogeneous halfspace, and the analytical solution of Randolph (1981) for end bearing piles. It was found a variation in percentage of 7.0%, 13.2% and 5.8% between the outcomes of the numerical model and those of the proposed analytical formulation for the horizontal, coupling and rocking terms, respectively; while the discrepancy between the results from the numerical model and the simplified expressions of Syngros (2004), was 0.8%, 8.3% and 17.3%. Furthermore, the rocking term calculated by using the analytical solution of Randolph (1981) differs less than 6% with respect to the numerical outcomes, whereas the lateral and coupling components of the dynamic impedances are overestimated approximately of 13%.

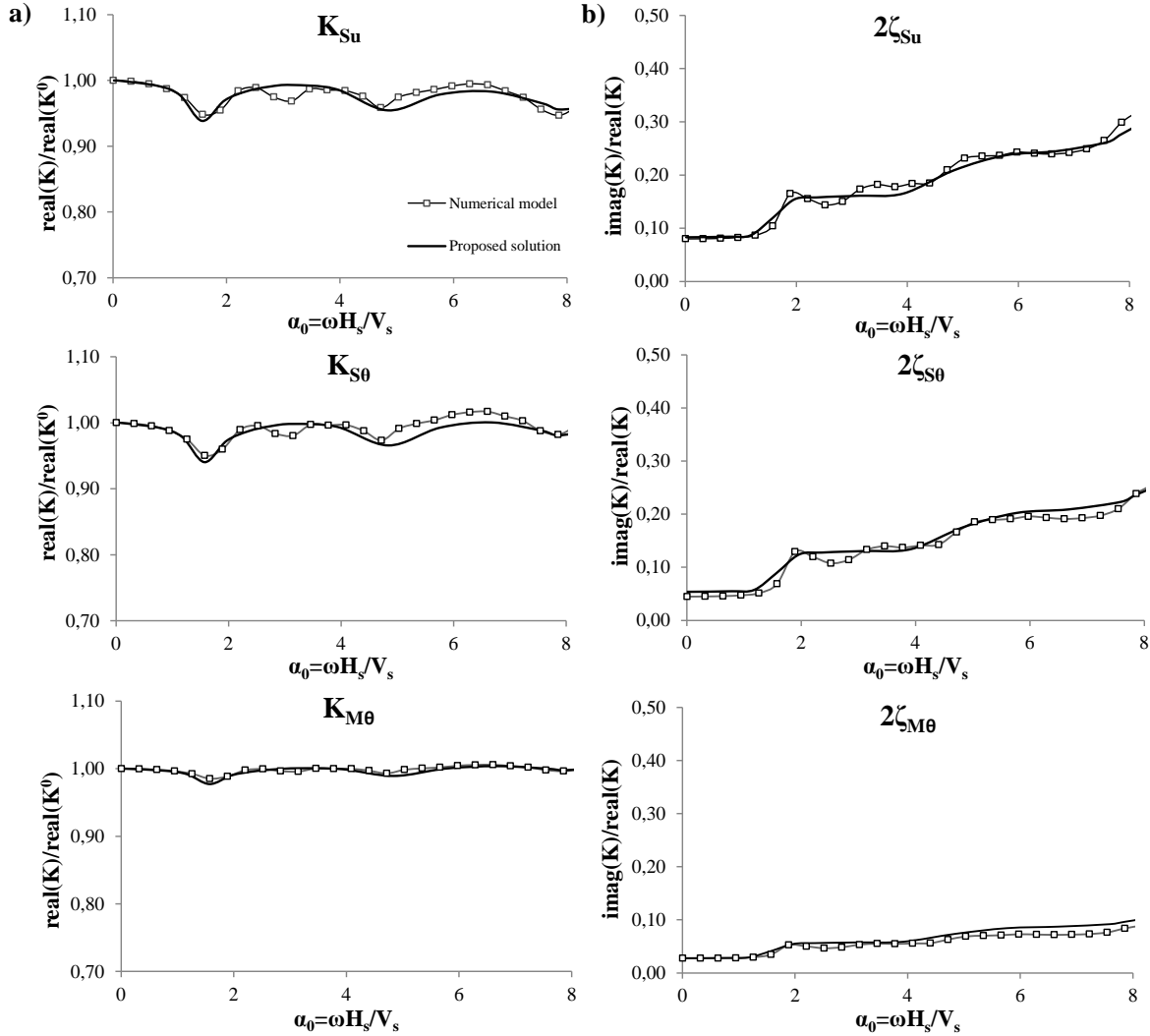


Figure 3.7: Comparison of the dynamic impedances obtained by the numerical model and Latini et al. (2015) formulation for profile 2.

In Figure 3.7 the real (K_{Su} , K_{S0} , and K_{M0}) and the imaginary ($2\zeta_{Su}$, $2\zeta_{S0}$, and $2\zeta_{M0}$) coefficients of the dynamic impedances are illustrated. The numerical model is characterized by a reduction of stiffness at the 1st and 2nd eigenfrequency of the soil layer ($\alpha_0 = 1/2\pi$, $\alpha_0 = 3/2\pi$, accordingly). In addition, an extra drop in stiffness attained around the 1st vertical resonance $\alpha_0 = 1/2\pi\eta$, where $\eta = \sqrt{2(1-\nu)/(1-2\nu)}$ was observed and it was less prominent for the case of the cross coupling and rocking terms. This can be explained by the fact that the analytical formulation disregards the vertical displacement in the dynamic analysis of the soil–pile system. The analytical results presented slightly scattered results with respect to the numerical model after the 2nd horizontal eigenfrequency of the soil layer.

The imaginary part of the dynamic component of the dynamic impedances provides an insight of the generated damping, due to the soil–pile interaction. The radiation damping was developed after the 1st eigenfrequency of the soil layer for all the components. Indeed, it is possible to observe that the imaginary part is characterized by a step–linear pattern and this proved that viscous type damping was generated in the frequency range examined.

In addition, it is important to highlight that reduction in stiffness at the 1st vertical resonance of the soil stratum showed by the numerical model was previously observed in the outcomes of the 3D BEM-FEM coupling model proposed by Padron et al. (2008). Figure 3.8 illustrates the deformed shape of the pile with respect to the depth at the three first eigenfrequencies of the soil layer. Very good agreement was achieved comparing the results obtained from the proposed model and the numerical outcomes. It is also worth showing the influence of the vertical displacements on the dynamic impedances of floating piles.

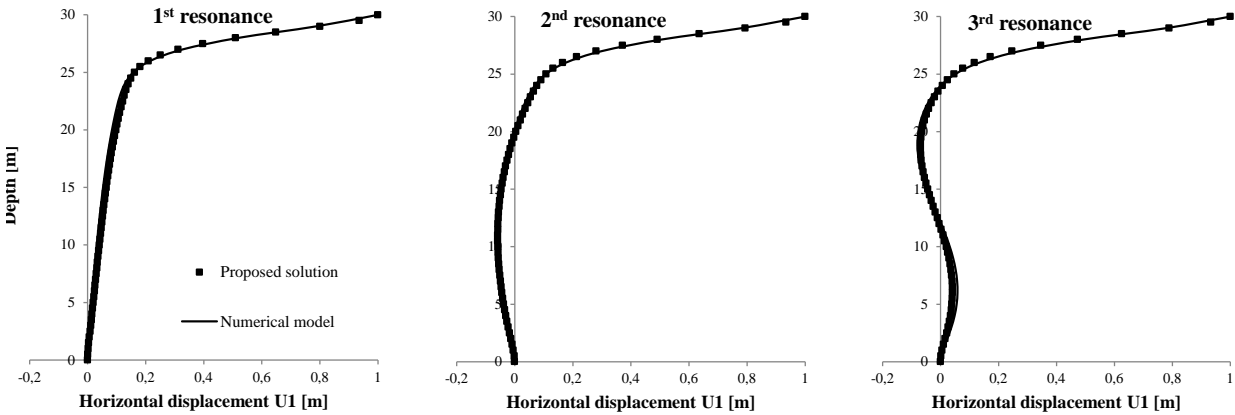


Figure 3.8: Distribution of the soil and pile displacement along the depth at the three first eigenfrequencies of the soil layer for profile 2. Modified after *Paper I*.

In Figure 3.9 the vertical displacement of the pile is presented with respect to the depth at the three first eigenfrequencies of the soil medium. Recall that the abovementioned results were derived from the numerical models, since the analytical solution neglects vertical deformations.

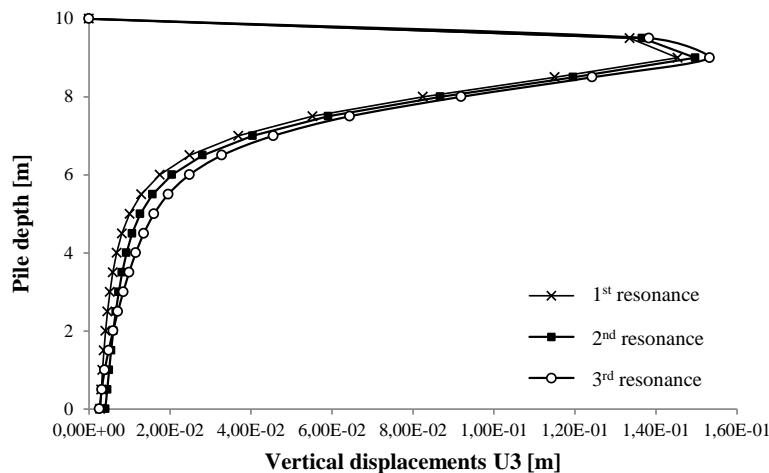


Figure 3.9: Distribution of the vertical displacements along the pile depth at three first eigenfrequency of the soil layer for profile 2. Modified after *Paper I*.

It is clear that the vertical displacements along the depth of the soil layer increase considerably for higher frequencies than the 1st eigenfrequency of the soil medium. It is of interest to note that the vertical displacements at the pile tip recorded at the 3rd eigenfrequency of the soil layer increases

of 40% (at $z = 4.5m$) with respect to those at the 1st eigefrequency. This further explains the fact that the difference between the dynamic impedances obtained by the numerical analysis and the suggested analytical solution became more prominent for frequencies higher than the 2nd resonance.

3.1.4 Foundation modelling

The effect of the foundation geometry on the soil–end bearing pile interaction has been herein assessed. Additionally, this study investigates the applicability of the analytical solution of Novak and Nogami (1977), in which the pile cross section is assumed solid, to piles characterized by hollow cross section. Hence, two different pile foundation modelling approaches are examined: 1) shell pile, where the foundation is modelled by shell; 2) equivalent solid pile for which equivalent material properties are applied to match the bending stiffness.

Zheng et al. (2013) studied the influence of the soil within the pipe pile on the lateral dynamic behaviour of the soil–foundation system, highlighting that the real and imaginary part are affected by the inner soil only in the higher frequency interval. The influence of the foundation modelling on the dynamic response of piles embedded in profile 1 ($H_s = H_p = 10m$) was performed considering the parameters listed in Table 3.3 and the results are presented only for the translational component of the dynamic impedances. Firstly, the static horizontal stiffness coefficients determined by the different numerical models were compared along with the analytical value, see Table 3.5.

Table 3.5: Static end bearing pile stiffness obtained from the numerical models and the analytical solutions of Novak and Nogami (1977).

Reference	Novak and Nogami (1977)	Equivalent solid pile	Shell pile
$K_{Su}/(E_s d)$	2.61	2.71	2.18

It was found that the lateral static stiffness coefficient of the equivalent solid pile differs approximately of 4% with respect to the analytical one; while the discrepancy increases considerably (16%) when the results of the shell pile are compared to the numerical outcomes of the foundation characterized by solid cross section, with the latter showing stiffer behaviour. In Figure 3.10 the real (K_{Su}) and the imaginary ($2\zeta_{Su}$) part of the translational dynamic impedances are shown. It is evident that the dynamic response of the solid pile is softer than the one of the shell foundation and this is also confirmed by the deformed shape of the two foundations plotted with respect to the depth at the two first eigenfrequencies of the soil layer, see Figure 3.11.

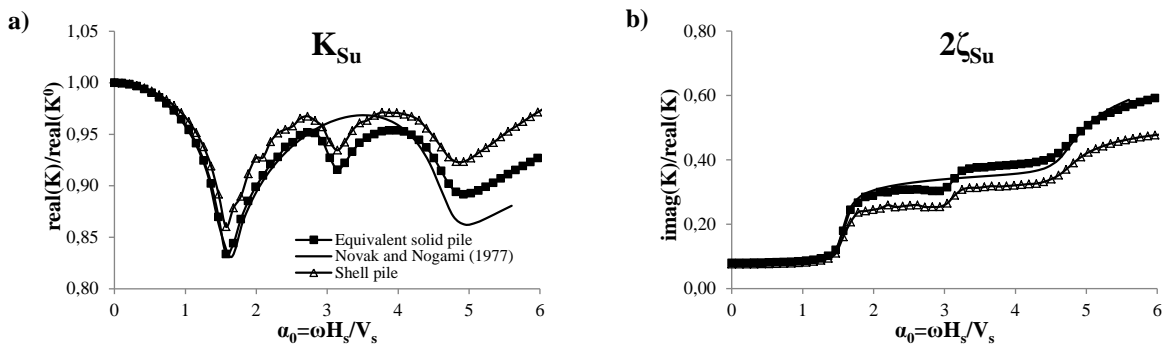


Figure 3.10: Variation of the dynamic stiffness and damping coefficients with respect to the non–dimensional frequency. Effect of the foundation geometry on the real component a) and the imaginary component b) for profile 1.

A good agreement between the analytical solution and the numerical outcomes of the solid equivalent pile was achieved up to approximately $\alpha_0 = 4$, while the difference increases by nearly 5% for frequencies higher than the 2nd eigenfrequency of the soil layer. This might be attributed to the different behaviour of the inner soil with respect to the surrounding soil. Nevertheless it was found that the deformed shape of the inner soil matches the one of the shell pile at the 2nd horizontal resonance. It might also be that the solid equivalent pile develops more shear deformation than the shell pile and this can be corroborated by the fact that slightly higher vertical displacements were generated along the foundation with solid cross section.

In light of this difference, it was chosen to establish the Young modulus of the shell pile, matching the one of the solid foundation, by adopting the expression suggested by Randolph (1981):

$$K_{Su,solid}^0 \simeq 6.29426G^*r_0 \left(\frac{E_{p,eq}}{G^*} \right)^{(1/7)} \quad (3.23)$$

$$K_{Su,shell}^0 \simeq 6.29426G^*r_0 \left(\frac{E_p}{G^*} \right)^{(1/7)} \quad (3.24)$$

where $E_{p,eq}$ is the Young modulus of the equivalent solid pile, E_p is the Young modulus of the shell pile, r_0 is the pile radius, G^* is the modified shear modulus of the soil layer given in Randolph (1981), $K_{Su,solid}^0$ and $K_{Su,shell}^0$ are the lateral static stiffness coefficients of the solid equivalent pile and shell pile obtained by the numerical models, respectively. Hence, the Young modulus E_p which provides the same static stiffness of the shell pile by assuming a solid cross section can be determined by solving Equation 3.24 with respect to E_p .

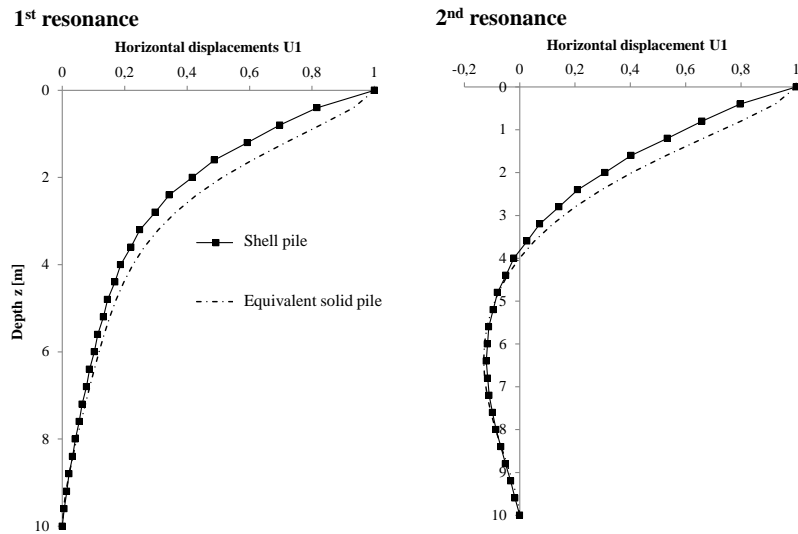


Figure 3.11: Distribution of the soil and pile displacement along the depth at the two first eigenfrequencies of the soil layer.

Table 3.6: Static end bearing pile stiffness obtained from the analytical solutions of Novak and Nogami (1977) and the numerical models, where the expression of Randolph (1981) was used for the estimation of the Young modulus of the shell pile.

Reference	Novak and Nogami (1977)	Equivalent solid pile	Shell pile
$K_{Su}/(E_s d)$	2.24	1.96	2.18

In the first place the horizontal static stiffness coefficient is obtained from the different foundation modellings as shown in Table 3.6. Results highlighted that the shell pile differs of 10%

with respect to the numerical outcomes of the foundation having solid cross section with the shell pile showing stiffer behaviour. This discrepancy might be due to the fact that the expression of Randolph (1981) is an approximate closed-form solution, based on the results of finite element simulations.

While the difference is approximately of 12% between the static stiffness calculated according to Novak and Nogami (1977) and the one of the equivalent solid pile.

In Figure 3.12 the real (K_{Su}) and the imaginary ($2\zeta_{Su}$) part of the translational dynamic impedances are shown. It is apparent that the results of the shell pile and the equivalent solid pile model matched perfectly in the frequency range investigated. Whereas there is a more marked discrepancy (3%) between the numerical results and the analytical ones after the 2nd resonance ($\alpha_0 = 3/2\pi$).

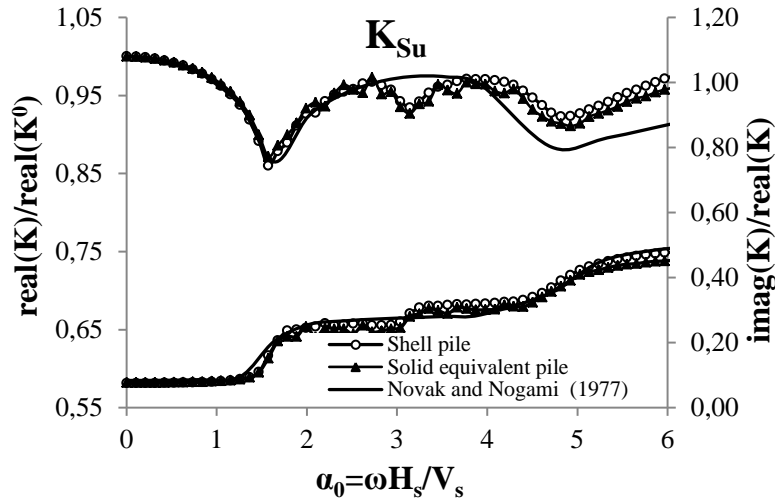


Figure 3.12: Variation of the dynamic stiffness and damping coefficients with respect to the non-dimensional frequency. Effect of the foundation geometry on the real component and the imaginary component for profile 1. Modified after *Paper III*.

3.1.5 Parametric study

The literature review showed that the dynamic response of end bearing pile foundations have been extensively investigated. The main focus of these works (Poulos and Davis (1980), Randolph (1981)) was to illustrate the role of key non-dimensional parameters such as the stiffness ratio E_p/E_s , the slenderness ratio H_p/d and the pile flexibility factor K_r on the response of end bearing piles. It must be highlighted that the effect of the dimensionless parameter H_s/d , defined as the relative thickness of the soil layer, was studied only for the case of surface footings in the work of Gazetas (1983)*. Regarding the case of floating piles few studies examined the effect of these major dimensionless parameters on the dynamic stiffness and damping of the soil-pile system.

Hence, the dynamic soil-floating pile interaction was investigated, showing the applicability of the suggested analytical formulation along with an analysis of the influence of the abovementioned dimensionless parameters. The rationale behind their selection was to investigate pile foundations with different slenderness ratio (H_p/d) embedded in different site conditions (E_p/E_s , H_s/d)*. It is important to note that the influence of the diameter on the dynamic stiffness coefficients of floating piles was not examined, since previous studies (Zania (2014), Latini and Zania (2017a)) pointed out that the dynamic impedances are scarcely affected by the variation of the diameter for both end bearing piles and suction caissons.

Static stiffness In this study the static stiffness coefficients obtained by the numerical models are compared with those determined by using the proposed analytical solution, see Figure 3.13a. In

addition the numerical results are also compared with respect to the static stiffness values calculated according to the expressions suggested by Syngros (2004) as illustrated in Figure 3.13b. It is evident that the static stiffness coefficients obtained by the proposed analytical solution differ less than 5% with respect to the numerical ones. While the scatter between the results of Syngros (2004) and the numerical model is still acceptable (less than 3%) for the horizontal and rocking component. On the other hand the discrepancy regarding the coupling component attained around 10%.

Table 3.7: Cases selected in the parametric analysis for the static stiffness coefficients of floating piles.

Case Nr.	H_s [m]	H_p [m]	d [m]	H_p/d	H_s/d	V_s [m/s]	E_p/E_s
1	30	10	1	10	30	250	60
2	20	10	1	10	20	250	60
3	15	10	1	10	15	250	60
4	30	10	1	10	30	400	23
5	30	10	1	10	30	500	15
6	20	10	1	10	20	100	367
7	15	10	1	10	15	100	367
8	20	10	1	10	20	500	15
9	15	10	1	10	15	500	15

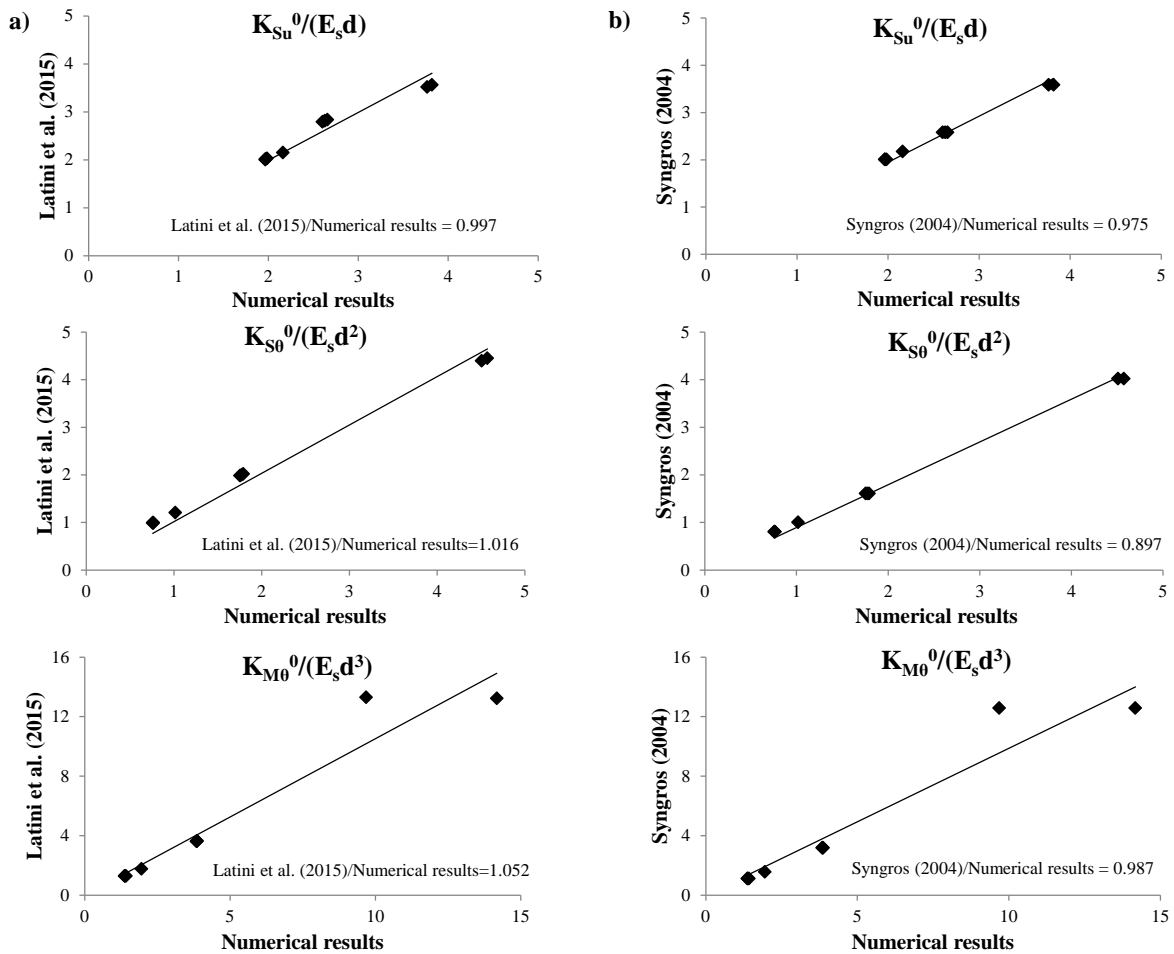


Figure 3.13: Comparison of the static stiffness coefficients obtained by the numerical model, the analytical solution of Latini et al. (2015) a) and Syngros (2004) b).

Effect of the slenderness ratio In Figure 3.14 and 3.15 the real (K_{Su} , $K_{S\theta}$, and $K_{M\theta}$) and the imaginary ($2\zeta_{Su}$, $2\zeta_{S\theta}$, and $2\zeta_{M\theta}$) parts of the dynamic impedances are shown by varying the slenderness ratio for different soil profiles $E_p/E_s=60$ and 500, respectively. It is clear that the variation of the slenderness ratio H_p/d does not influence the dynamic impedances of floating piles in the frequency range examined.

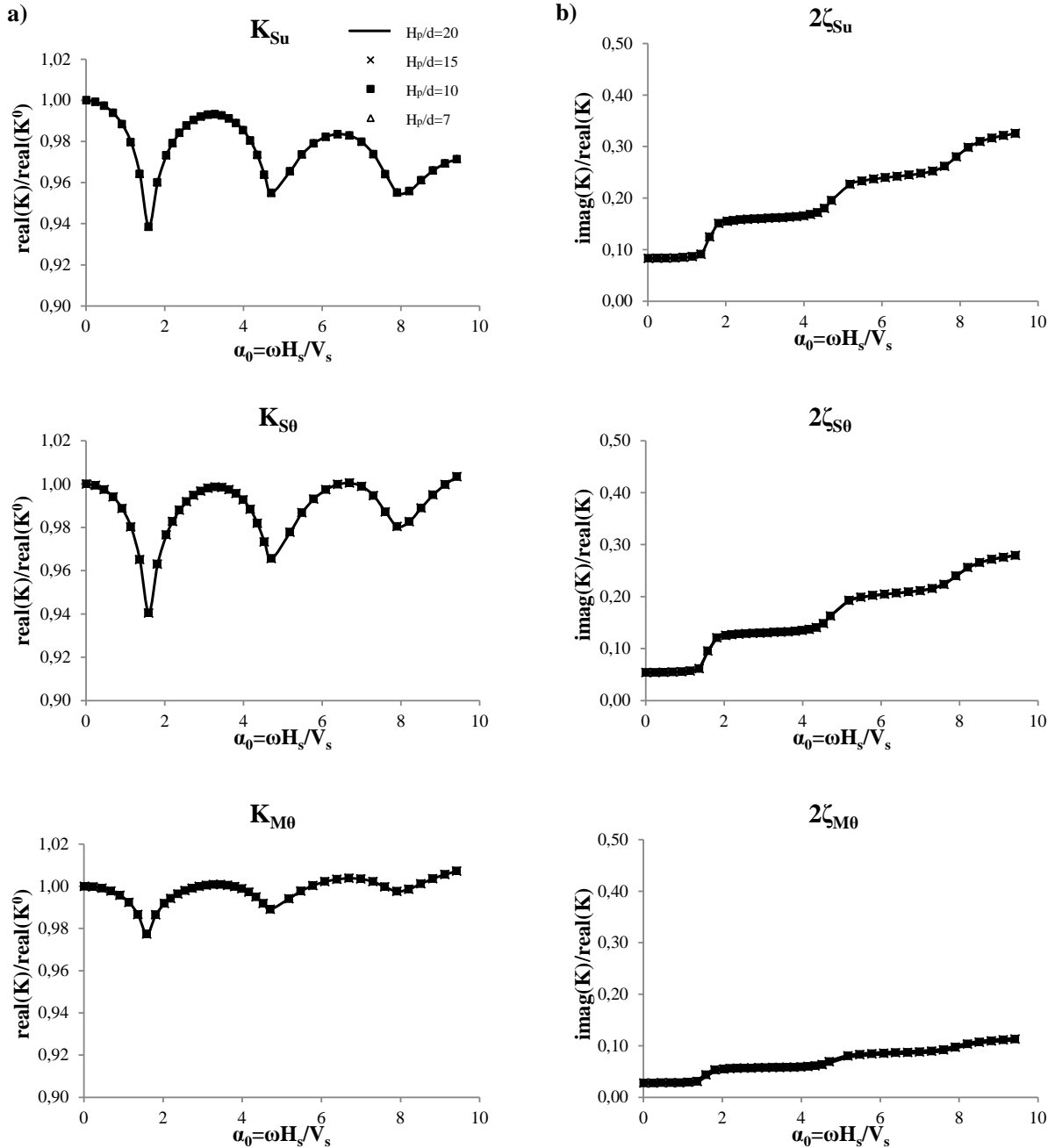


Figure 3.14: Variation of the three dynamic stiffness coefficients with respect to the non-dimensional frequency. Effect of the slenderness ratio on the real component a) and the imaginary component b). Results are presented for $H_s/d=30$ and $E_p/E_s=60$. Modified after *Paper I*.

This was demonstrated for both soft ($E_p/E_s=500$) and medium stiff ($E_p/E_s=60$) soil profile. The findings also highlighted that the design of floating piles is not influenced by the active length L_a . Recall that the definition of “active length” L_a given in the literature (Velez et al. (1983), Randolph (1981), Kuhlemeyer (1979a)) for end bearing piles, implies that the size $H_p - L_a$ has no

effect on the dynamic stiffness coefficients at the top of the pile when foundation has length greater than L_a . Indeed, the dynamic behaviour does not show any difference for piles with length greater or smaller than L_a . It is important to mention that the bending moment distribution was adopted for the estimation of the dynamic active length. Additionally, the dynamic active length matches the one proposed by Velez et al. (1983), which is approximately $L_a/d=8.5$ and 11 for floating piles embedded in a homogeneous soil profile with $E_p/E_s=60$ and 500, respectively.

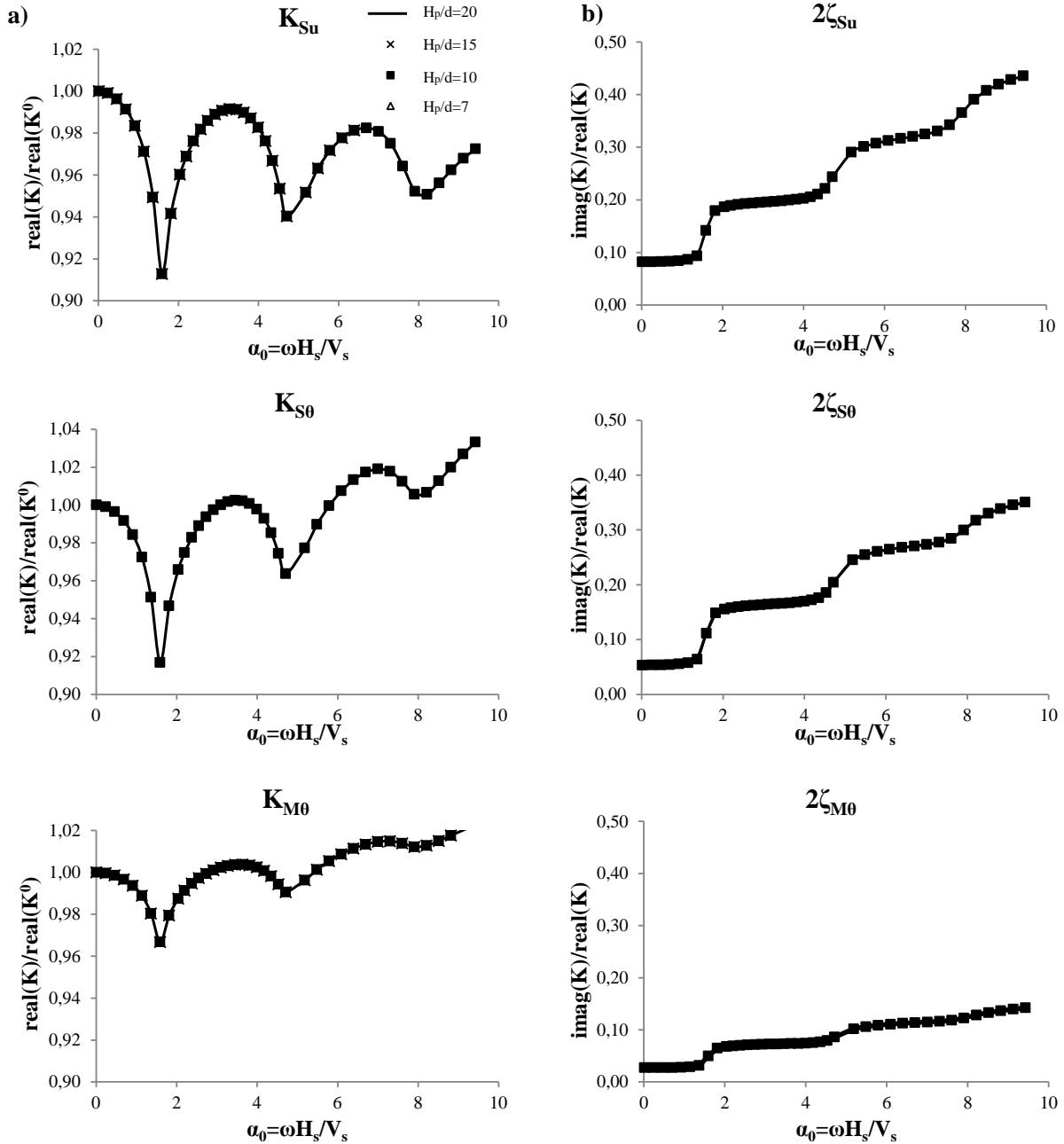


Figure 3.15: Variation of the three dynamic stiffness coefficients with respect to the non-dimensional frequency. Effect of the slenderness ratio on the real component a) and the imaginary component b). Results are presented for $H_s/d=30$ and $E_p/E_s=500$. Modified after *Paper I*.

Effect of the relative thickness of the soil layer Figure 3.16 presents the real (K_{Su} , K_{S0} , and K_{M0}) and the imaginary ($2\zeta_{Su}$, $2\zeta_{S0}$, and $2\zeta_{M0}$) terms of the dynamic impedances varying the

dimensionless parameter H_s/d . This was investigated by keeping all dimensionless parameters constant and changing only the thickness of the soil layer, while referring to the same slenderness ratio. The results highlighted that the relative thickness of the soil layer H_s/d has a significant influence on the dynamic stiffness components in the frequency range investigated. Firstly the reduction of stiffness recorded at the 1st resonance ($\alpha_0 = \pi/2$) for all the coefficients appeared to be less marked as the relative thickness of the soil layer H_s/d increased.

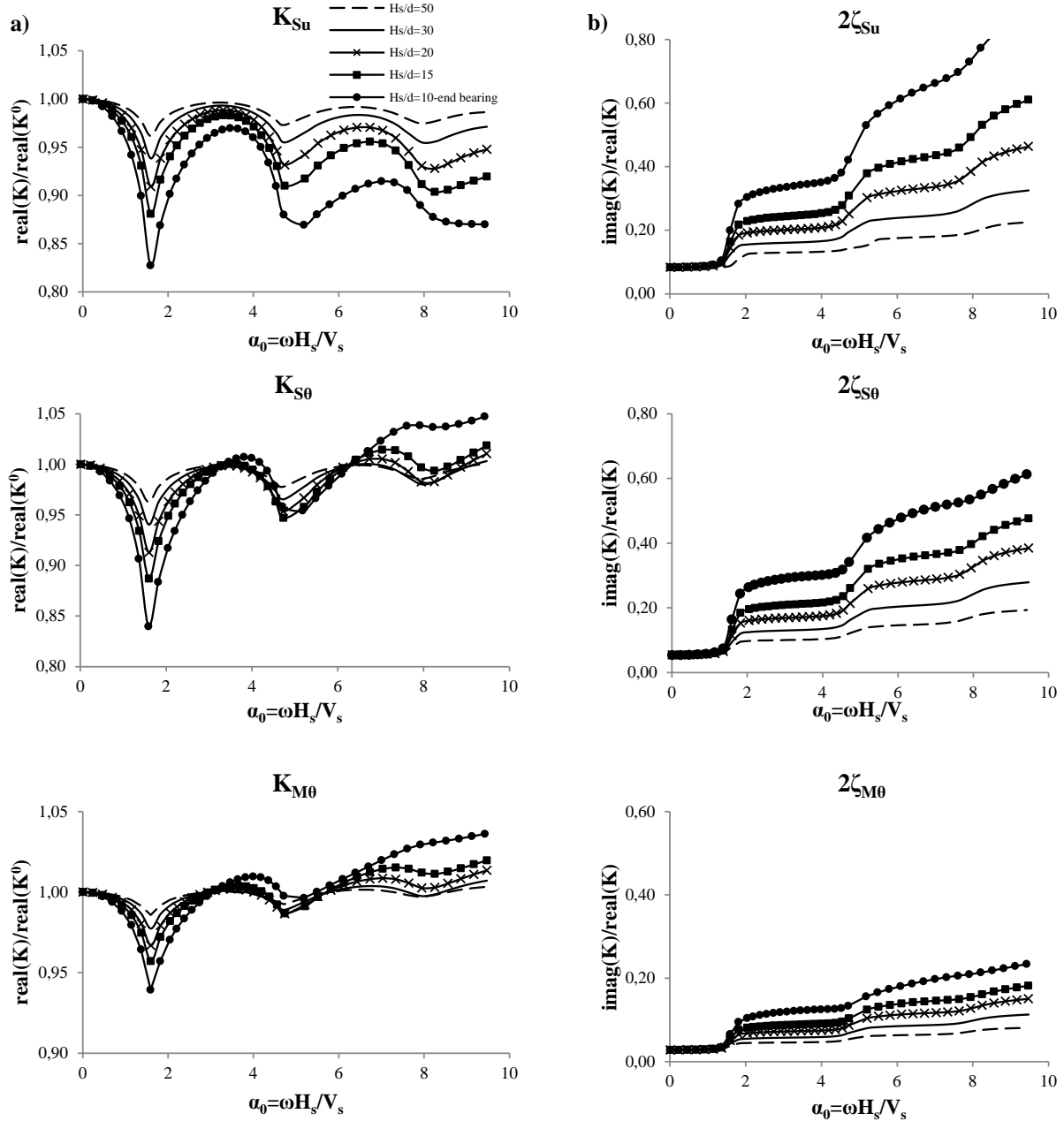


Figure 3.16: Variation of the three dynamic stiffness coefficients with respect to the non-dimensional frequency. Effect of the relative thickness of the soil layer on the real component a) and the imaginary component b). Results are presented for $H_p/d=10$ and $E_p/E_s=60$. Modified after *Paper I*.

Nevertheless, the comparison of the dynamic impedances of floating pile and end bearing pile ($H_s = H_p$) showed that the highest decrease in stiffness at the 1st eigenfrequency of the soil layer was attained for the case of the end bearing foundation. These results proved to be consistent with the work of Nozoe et al. (1988) and Padron et al. (2008). In addition, this trend is still noticeable for the horizontal stiffness component of the floating pile at the 2nd and 3rd resonance. In light of

the findings it can be stated that the longer the path the propagating waves travel, the more the stress waves are attenuated with the distance and therefore the mismatch decay between the dynamic impedances is smaller*. On the contrary the coupling and rocking components exhibited an increase of stiffness for lower values of H_s/d at the anti-resonance frequencies ($\alpha_0 \approx 3$ and 7). A possible explanation might be that the resonance in rotation of the free-standing pile ($\lambda_0 = 3.141$) is achieved closely to the anti-resonance, enhancing the stiffness for lower values of H_s/d . In addition, the small decrease in stiffness recorded at the anti-resonance frequencies can be also attributed to the less concurrent energy dissipation as illustrated hereafter.

In regards with the imaginary component, a step-linear increasing pattern was depicted after the 1st resonance and it is characterized by smaller slope as the relative thickness of the soil layer increases. The increase of the imaginary part observed for smaller values of soil profile depth is justified by the concurrent decrease of the dynamic component of the stiffness coefficients. On the other hand, it was obtained that the increase of the viscous damping coefficients in the frequency range examined is associated to the increase of H_s/d , indicating that more energy is dissipated as the propagating waves travel at longer distance. These outcomes are consistent with previous studies showing increase of the imaginary component of the dynamic impedances for suction caisson foundations, when H_s/d decreases (Latini and Zania (2017a)). Furthermore, it was noticed that the slope of the radiation damping recorded at each eigefrequency of the soil layer changed slightly for the rocking term.

Figure 3.17 illustrates the bending moment distribution for floating piles with $H_s/d=50$ and $H_s/d=15$ and then, the dynamic active lengths were also estimated. It appears that the dynamic active length ($L_a \approx 8.5\text{m}$) assumed the same values, when the relative thickness of the soil medium is the only parameter varies. The findings are in agreement with the active lengths suggested by Velez et al. (1983) and they pointed out that the dynamic active length of floating piles does not depend on the non-dimensional parameter H_s/d .

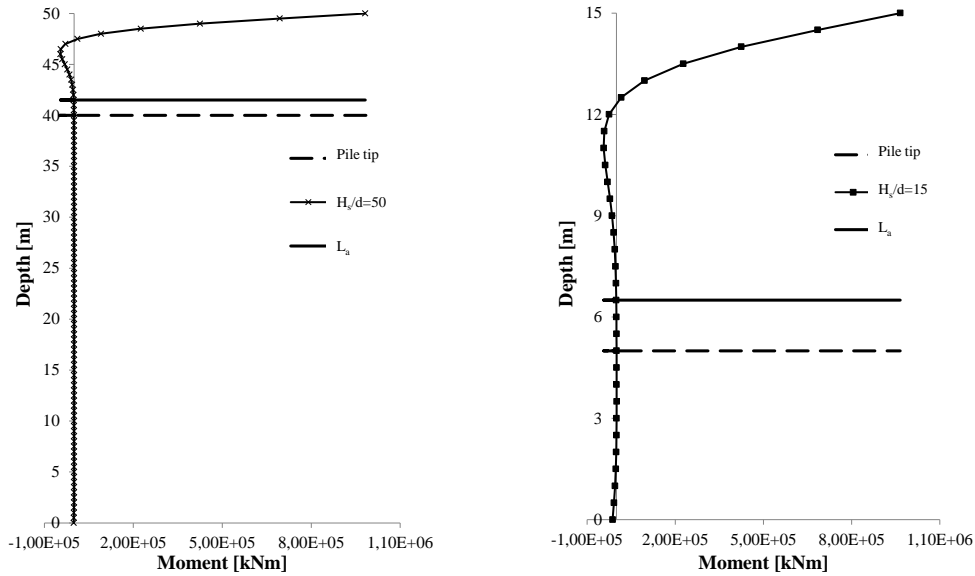


Figure 3.17: Distribution of the bending moment along the depth for $H_s/d=15$ and 50 at the 1st eigenfrequency of the soil layer. Modified after *Paper I*.

Effect of the stiffness of the soil layer Figure 3.18 shows the real (K_{Su} , $K_{S\theta}$, and $K_{M\theta}$) and the imaginary ($2\zeta_{Su}$, $2\zeta_{S\theta}$, and $2\zeta_{M\theta}$) terms of the dynamic impedances varying the shear wave velocity of the soil medium for floating pile with slenderness ratio $H_p/d=10$. In an attempt to examine a broad spectrum of soil conditions, different pile–soil stiffness ratios which resemble soft, medium and stiff soil profiles were selected. The findings highlighted that the dynamic impedances slightly decrease by decreasing of the shear wave velocity of the soil layer ($V_s > 250m/s$) for the frequency interval of interest.

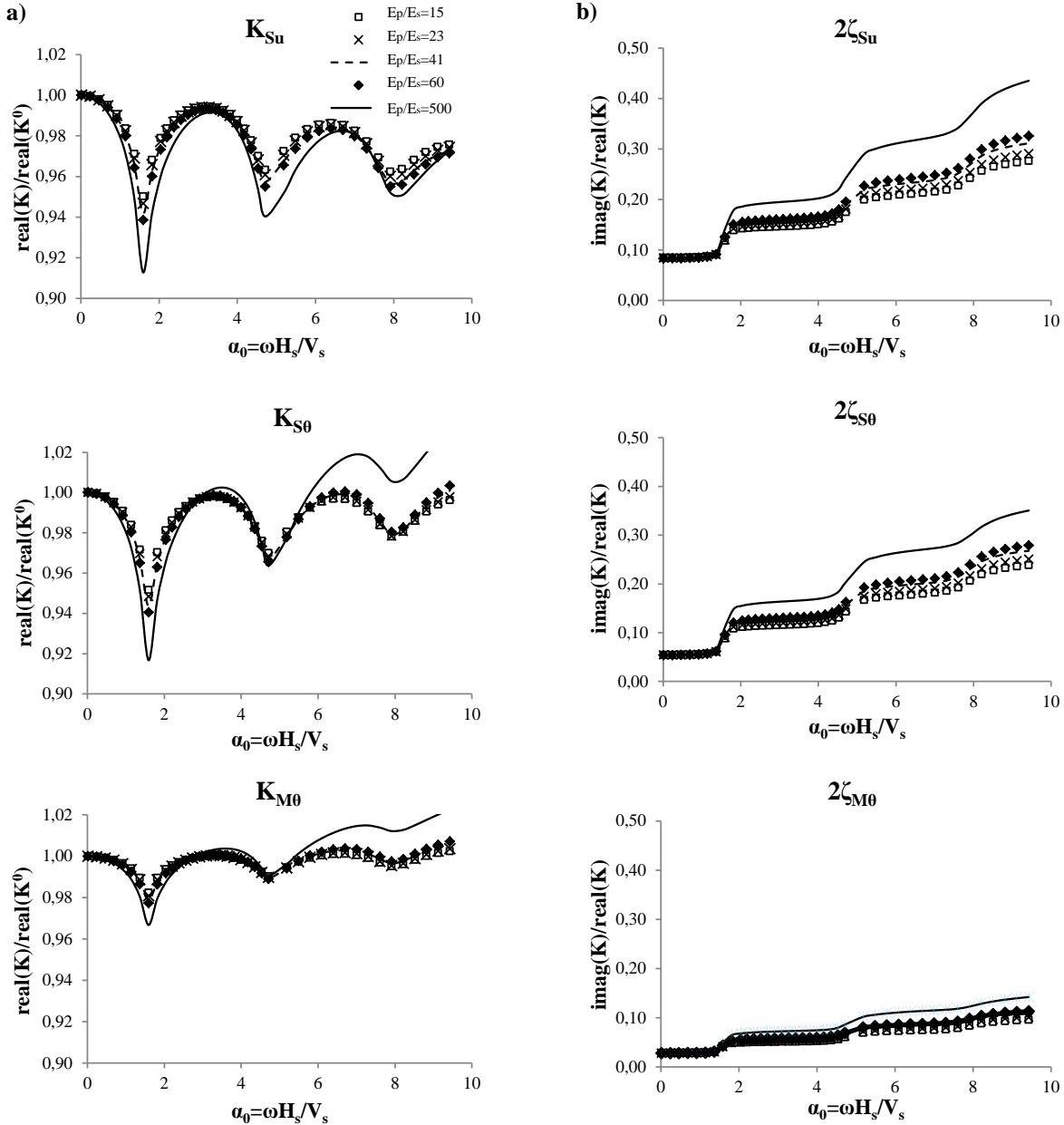


Figure 3.18: Variation of the three dynamic stiffness coefficients with respect to the non–dimensional frequency. Effect of the soil stiffness on the real component a) and the imaginary component b). Results are presented for $H_s/d=30$ and $H_p/d=10$. Modified after *Paper I*.

The highest gradient towards the 1st resonance was observed for all the components of the dynamic stiffness of pile embedded in soft soil deposit; this trend was still visible for the results of the horizontal component attained at the 2nd and 3^d resonance of the soil layer. Additionally, it was observed that the difference in the reduction of stiffness for all the coefficients at the 1st

eigenfrequency of the soil layer is approximately of 1% when the soil profile varies from medium stiff to stiff. The effect of stiffness ratio E_p/E_s reduces for the coupling and rocking stiffness component, with the latter attaining nearly the static value in the case of medium stiff and stiff soil deposits and for frequency higher than the 1st resonance.

On the contrary, an increase of the coupling and rocking coefficients was clearly found for frequencies greater than $\alpha_0 \approx 5$ for soft soil profiles. This can be explained by the fact that higher rotation is observed at the pile tip after the 2nd resonance of the soil layer is reached, which is further enhanced when the foundation is embedded in a soft deposit. Indeed at high frequency ($\alpha_0 > 5$), the moment reaction at the pile tip slightly increases for lower values of the shear wave velocity of the soil layer, as depicted in Figure 3.19.

In regards with the imaginary components, the radiation damping does not vary appreciably for $E_p/E_s < 60$ over the frequency interval investigated. However, the effect of the stiffness ratio becomes more visible with decreasing the shear wave velocity of the soil medium ($E_p/E_s=500$). Generally, it seemed that the dynamic response was to some extent influenced by the variation of the soil stiffness in the frequency range examined, as indicated in Chapter 4 for suction caisson foundations.

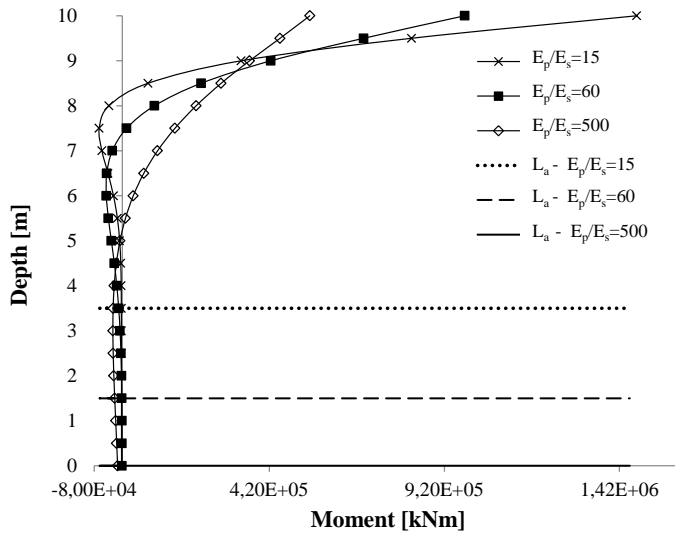


Figure 3.19: Distribution of the bending moment along the depth for $E_p/E_s=15, 60$ and 500 at the 3rd eigenfrequency of the soil layer. Results are presented for $H_s/d=30$ and $H_p/d=10$. Modified after *Paper I*.

Discussion The effect of the relative thickness of the soil layer on the dynamic response of the pile can easily be described by comparing the dynamic stiffness coefficients at the 1st resonance with respect to the relative thickness of the soil layer H_s/d for different soil profiles ($E_p/E_s=60$ and 500), see Figure 3.20. It can be stated that the trend of all three dynamic stiffness coefficients for $H_s/d < 50$ is substantially affected by the relative thickness of the soil layer. On the other hand no significant difference (less than 3%) between the static and the dynamic stiffness at the 1st resonance was recorded for floating piles embedded in a soil layer with $H_s/d > 50$. It can be concluded that the dynamic component is negligible, since the variation of the stiffness components with frequency seemed less evident after the 1st resonance. It is worth underlining that the effect of the relative thickness of the soil layer depends slightly on the stiffness of the soil medium. Indeed, the foundation embedded in soft soil profiles experiences more prominent variation of dynamic stiffness components with H_s/d . This means that the dynamic component of the stiffness for floating piles in

deep soil profiles ($H_s/d > 50$) may be disregarded when structure-foundation interaction analyses are performed. Then the expressions of the static stiffness coefficients available in the literature can be applied for the design of the pile foundation. In addition, it is worth emphasizing that preliminary design calculations can be conducted by adopting the parametric graph illustrated in Figure 3.20, which provides an indication of the dynamic effects on the soil–floating pile system.

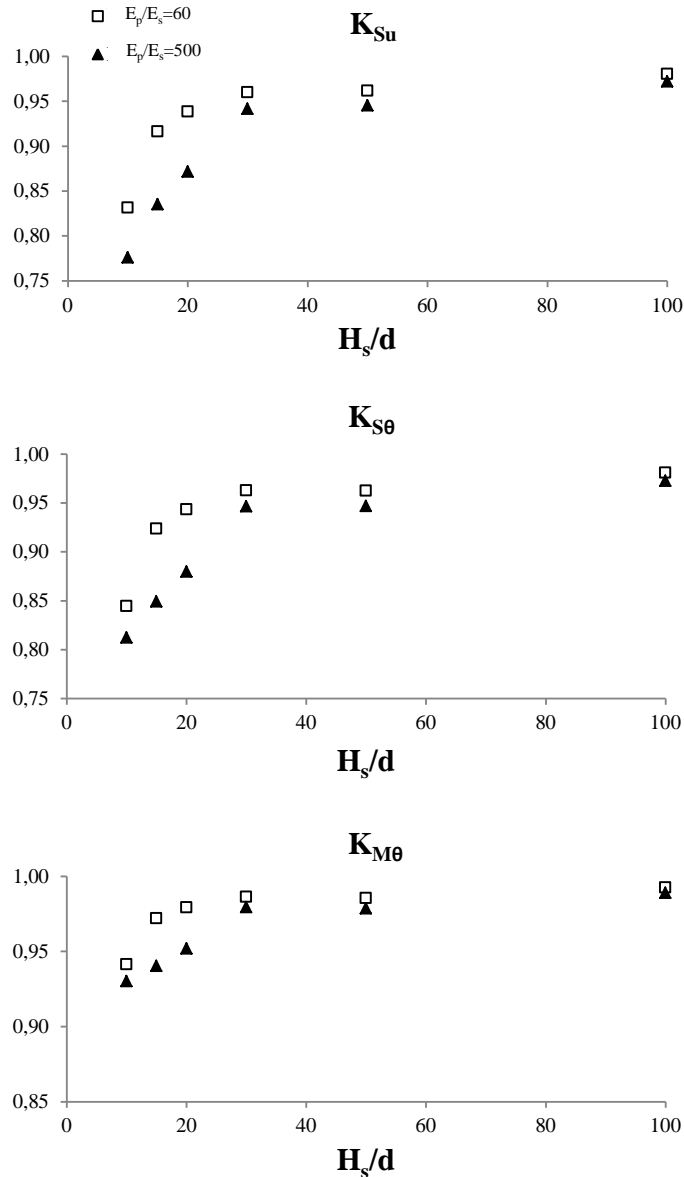


Figure 3.20: Variation of the dynamic stiffness with respect to the relative thickness of the soil layer H_s/d for $E_p/E_s=60$ and $E_p/E_s=500$ at the 1st eigenfrequency of the soil layer. Modified after *Paper I*.

It can be clearly seen that the dynamic active length can be only related to the stiffness ratio (E_p/E_s) as presented already for end bearing piles, since the dynamic active length is independent of the slenderness ratio and the relative thickness of the soil layer. Figure 3.19 shows the dynamic active length for three different soil profiles ($E_p/E_s=15$, 60 and 500). The results highlighted that the dynamic active length decreases for lower values of E_p/E_s and it is equal to the total pile length in the case of soft soil deposit ($E_p/E_s=500$). Furthermore, the values of the dynamic active length obtained for all the results presented in this study are in agreement with those calculated according to the formulation of Velez et al. (1983)*.

3.2 Vertical dynamic response of piles

In analogy with Section 3.1 the dynamic response of piles subjected to vertical loading is herein investigated. The vertical dynamic impedance of a pile foundation embedded in profile 1 obtained by the numerical models was validated against analytical continuum solutions. The validated numerical methodology was then applied to carry out a parametric study in order to analyse the influence of the slenderness ratio on the soil–foundation system along with site effects.

3.2.1 Analytical approach

The literature review showed that there are several analytical formulations for predicting the vertical dynamic response of end bearing piles. The analytical solutions of Nogami and Novak (1976), Wu et al. (2013) and Zheng et al. (2014) were adopted to estimate the vertical dynamic impedance and hence, validated the numerical outcomes. Discussion on the validity and applicability of the abovementioned solutions was also provided. In consideration of these remarks the analytical solution of Nogami and Novak (1976) was taken into account as the reference formulation for the estimation of the dynamic vertical stiffness and damping coefficients of end bearing piles embedded in homogeneous soil layer.

3.2.2 Numerical approach

3.2.2.1 Methodology

Analysis and frequency increment In regards of K_V , a unit vertical displacement $U3 = 1$ is assigned at the pile head, whereas the remaining displacements and rotations are denoted as zero $U1 = U2 = UR1 = UR2 = UR3 = 0$. In addition, the range of frequency investigated include the 3rd vertical eigenfrequency of the soil layer.

Type of elements The element definition assigned for each component of the numerical model is applied as explained in Section 3.1.2.1.

Connectivity Different connectivity scenarios between the soil and the pile surfaces are adopted as described in Section 3.1.2.1.

Boundary conditions The numerical analyses were performed applying boundary conditions, which are the same used in Section 3.1.2.1.

Mesh size The maximum element size was decided in order to capture the stress wave accurately and the mesh size arrangement is given as presented in Section 3.1.2.1.

3.2.3 Validation of the numerical model

Profile 1 The numerical results for the end bearing pile case were compared respectively with the different analytical solutions formulated by Nogami and Novak (1976), Wu et al. (2013) and Zheng et al. (2014). The reference case analysed only for the validation of the numerical model consists of a solid concrete pile with diameter $d = 1m$ and length $H_p = 10m$, embedded in a soil layer with constant shear wave velocity $V_s = 68m/s$, hysteretic material damping $\beta = 1.0\%$ and Poisson's ratio $\nu = 0.40$.

Table 3.8 presents the static stiffness coefficient of the numerical model calculated at low frequencies, along with the corresponding analytical values. It was recorded a discrepancy of less than 1% over the analytical solution of Nogami and Novak (1976), Hu et al. (2004) and Zheng et al. (2014); while the analytical solution of Wu et al. (2013) differs of 5.2% with respect to the numerical model.

Reference	Nogami and Novak (1976)	Hu et al. (2004)	Wu et al. (2013)	Zheng et al. (2014)	Numerical model
$K_V/(E_s d)$	74.3	74.1	70.1	73.4	73.9

Table 3.8: Static end bearing pile stiffness obtained from the numerical models and the analytical solutions of Nogami and Novak (1976), Hu et al. (2004), Wu et al. (2013) and Zheng et al. (2014).

In Figure 3.21a the real (K_V) and the imaginary ($2\zeta_V$) term of the dynamic vertical impedance are illustrated with respect to the dimensionless frequency α_0 . Both the analytical formulations and the numerical model are characterized by a reduction in stiffness at the 1st resonance of the soil layer ($\alpha_0 = 1/2\eta\pi$). However, an additional cut-off frequency around $\alpha_0 = 2$ was observed in the analytical formulation suggested by Wu et al. (2013) and Zheng et al. (2014). Zheng et al. (2014) commented that this extra drop of stiffness was assumed to represent the 1st horizontal resonance, since the radial displacements were included in the solution. The numerical results proved that this cannot be a possible explanation, since any limitations on the soil displacements were not considered in the finite element models and still this second decrease in stiffness was not observed***. Nonetheless, the pattern of the abovementioned analytical formulations solutions approximated very well the numerical results for frequencies higher than the 1st resonance. The imaginary part of the dynamic component of the vertical impedance displayed that radiation damping was generated for frequencies higher than the 1st eigenfrequency of the soil layer. Moreover, viscous type radiation damping was produced for $\alpha_0 > 1/2\eta\pi$, since all the analytical solutions converge to the same linear pattern. Figure 3.21b presents the deformed shape of the pile plotted as a function of the depth at the 1st vertical resonance of the soil layer and the numerical outcomes are in agreement with the one obtained by the analytical formulation of Nogami and Novak (1976).

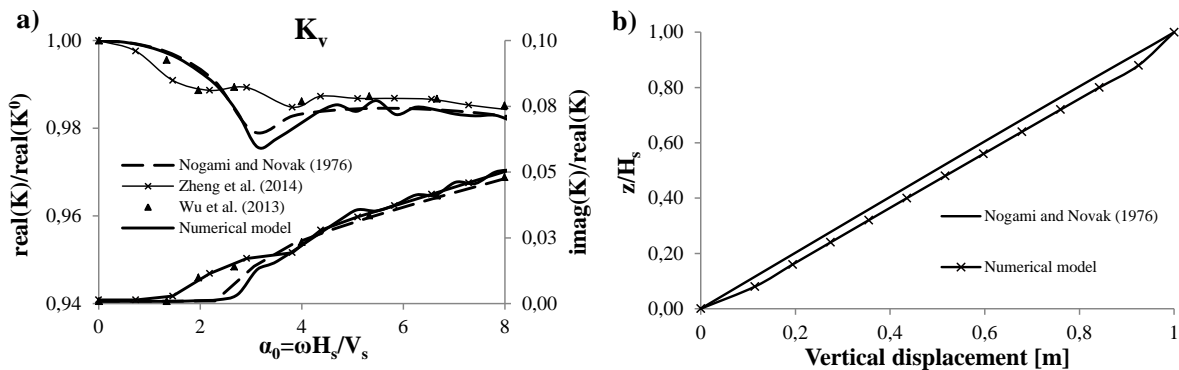


Figure 3.21: Variation of the vertical stiffness and damping coefficients with respect to the dimensionless frequency a) and distribution of the pile displacement along the depth at the 1st vertical eigenfrequency of the soil layer b) for profile 1. Modified after *Paper V*.

3.2.4 Parametric study

The vertical dynamic response of floating piles (profile 2) is analysed by adopting finite element analysis described in the previous section. In the current study the effects of the pile diameter, the depth and stiffness of the soil layer on the soil–floating pile response are investigated. This makes it possible to discuss the role of some well-established dimensionless parameters such as the slenderness ratio H_p/d , the stiffness ratio E_p/E_s and the relative thickness of the soil layer H_s/d on the dynamic behaviour of the foundation. The cases selected in this study including also the

dimensionless parameters are listed in Table 3.9, while the rationale for their selection was to examine piles with different slenderness ratio ($H_p/d = 7, 10$ and 12) embedded in a homogenous soil layer with various constant profiles of shear wave velocity ($V_s = 250, 400$ and 500m/s), thickness ($t = r_0/50$), hysteretic material damping ($\beta = 5.0\%$) and Poisson's ratio ($\nu = 0.35$).

Table 3.9: Dimensionless parameters and cases selected in the parametric analysis for floating piles.

Case Nr.	H_s [m]	H_p [m]	d [m]	H_p/d	H_s/d	V_s [m/s]	E_p/E_s
1	30	10	1	10	30	250	60
2	20	10	1	10	20	250	60
3	15	10	1	10	15	250	60
4	30	10	1	10	30	400	23
5	30	10	1	10	30	500	15
6	30	25	2	12	15	250	60
7	30	20	2	10	15	250	60
8	30	14	2	7	15	250	60

Effect of the relative thickness of the soil layer In Figure 3.22 the real (K_V) and the imaginary ($2\zeta_V$) components of the vertical stiffness are shown for different heights of the soil layer (case 1, 2 and 3). The drop of stiffness at the 1st eigenfrequency of the soil layer ($\alpha_0 = 1/2\eta\pi$) became more marked in the case of floating piles with $H_s/d = 15$.

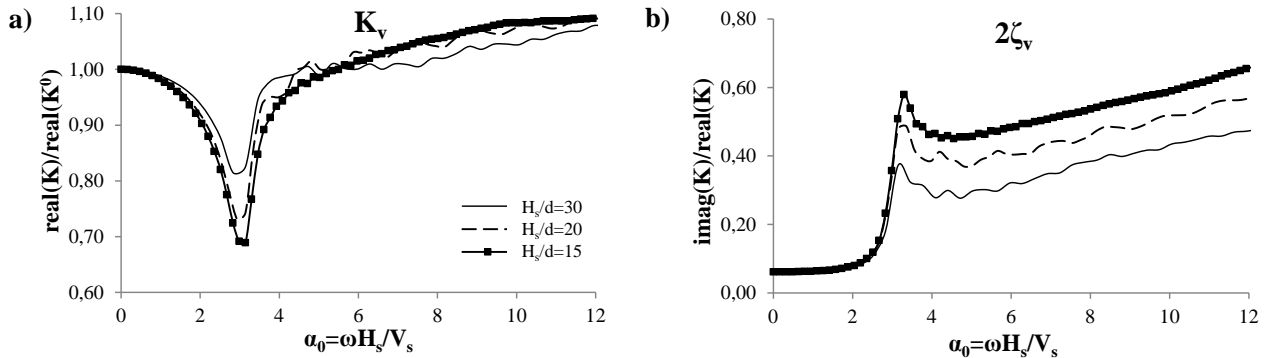


Figure 3.22: Variation of the vertical dynamic stiffness and damping coefficients with respect to the dimensionless frequency. Effect of the relative thickness of the soil layer on the real component a) and the imaginary component b) for $H_p/d = 10$. Modified after *Paper VI*.

This is motivated by the fact that the longer the path the propagating waves travel, the more the amplitude of the stress waves is reduced with the distance and hence, the decrease of the dynamic stiffness is less noticeable. Additionally, it was noticed a constant linear increase in the dynamic stiffness trend for frequency greater than the 1st eigenfrequency of the soil medium. In the frequency interval $\alpha_0 = 6 - 12$ it was observed that the vertical dynamic stiffness assumed higher values than the corresponding static component. The radiation damping (viscous type) is produced for frequencies higher than the 1st resonance. The three cases investigated were characterized by identical slope, on the other hand the offset recorded approximately at the 1st resonance of the soil medium reduces with H_s/d . The fact that the variation of the imaginary component of the dynamic vertical impedance increases for smaller values of soil profile thickness is related to the concurrent decrease of the dynamic component of the stiffness coefficient. On the contrary, the viscous damping coefficients in the frequency interval examined decreases by decreasing H_s/d , indicating that less energy is dissipated in shallow soil deposits. Finally, it can be stated that the variation of the

relative thickness of the soil layer can significantly influence the dynamic response at the pile head in accordance with the results shown by Deng et al. (2014).

Effect of the stiffness of the soil layer In Figure 3.23 the real (K_V) and the imaginary ($2\zeta_V$) parts of the dynamic vertical impedance are presented for different values of the shear wave velocity of the soil layer ($V_s = 250, 400$ and 500m/s —case 1, 4 and 5, respectively). The same values for the height of the foundation and the soil layer are considered for the cases examined. Slightly scattered results are achieved by varying the shear wave velocity of the soil layer. The reduction of stiffness attained at the 1st eigenfrequency of the soil layer is to some extent less prominent for stiff soil deposits ($V_s = 500\text{m/s}$). In the intermediate frequency range ($\alpha_0 = 1/2\eta\pi - 7$) the vertical dynamic response seems to be marginally affected by the increase of the shear wave velocity of the soil layer. For very stiff soil profiles, the real component of the stiffness can be considered frequency-independent after 1st resonance. These findings are in agreement with the work of Nogami and Novak (1976) for the case of end bearing piles.

The analysis highlighted that increasing the shear wave velocity of the soil layer or decreasing E_p/E_s the damping decreases. Furthermore, a linear pattern was observed for the imaginary part of the dynamic impedance after the 1st eigenfrequency, indicating that viscous-type damping is developed.

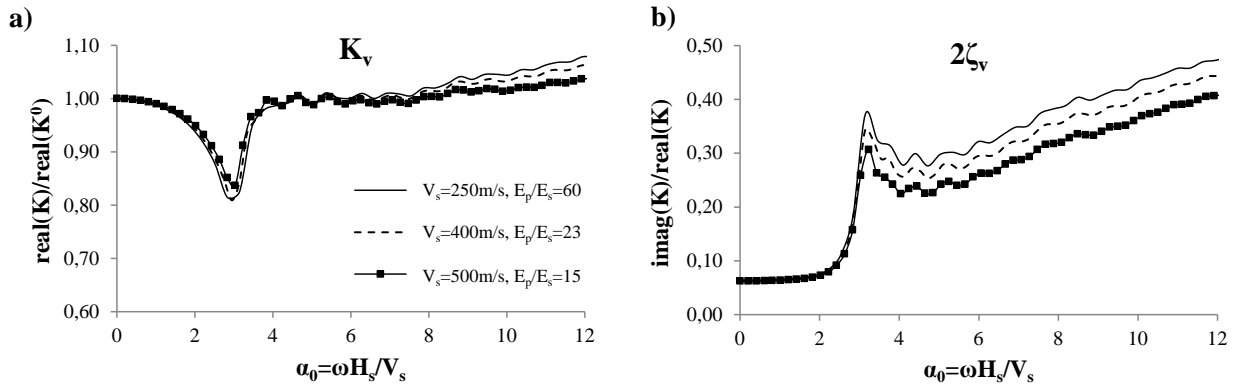


Figure 3.23: Variation of the vertical dynamic stiffness and damping coefficients with respect to the dimensionless frequency. Effect of the stiffness of the soil layer on the real component a) and the imaginary component b) for $H_p/d = 10$. Modified after *Paper VI*.

Effect of the slenderness ratio In Figure 3.24 the real (K_V) and the imaginary ($2\zeta_V$) parts of the vertical dynamic impedance are displayed, varying the slenderness ratio H_p/d (cases 6–8).

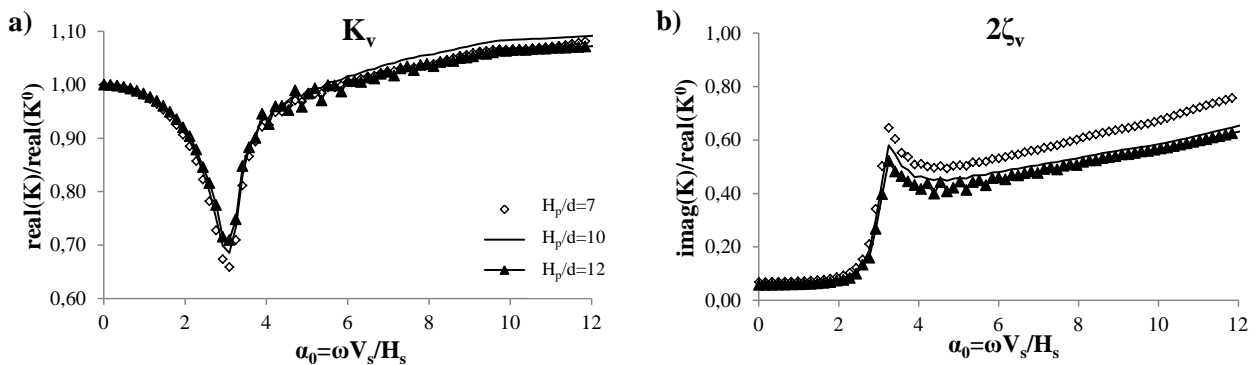


Figure 3.24: Variation of the vertical dynamic stiffness and damping coefficients with respect to the non-dimensional frequency. Effect of the slenderness ratio on the real component a) and the imaginary component b) for $H_s/d = 15$.

The parametric study is conducted keeping the same depth and shear wave velocity of the soil layer for all the numerical models established. The reduction in stiffness at the 1st eigenfrequency of the soil layer ($\alpha_0 = 1/2\eta\pi$) became more marked by decreasing the slenderness ratio. The dynamic impedance is moderately sensitive to the variation of H_p/d and it is characterized with some extent by slightly linear increasing pattern for frequencies higher than the 1st resonance. Indeed, no drop of stiffness at the 2nd eigenfrequency of the soil medium is recorded. This might be attributed to the fact that response of the system is controlled to large extent by the dissipative soil medium as observed in Nogami and Novak (1976) for end bearing piles.

In regards of the imaginary part, the radiation damping generated after the 1st resonance is characterized by a linear trend, whose slope slightly increases when the slenderness ratio reduces.

3.3 Conclusions

In this study the dynamic response of piles embedded in linear elastic soil layer with hysteretic damping is investigated by adopting both analytical and numerical methodologies. A parametric study was presented to analyse the vibration characteristics of floating piles and illustrate the effects of major parameters on the stiffness and damping properties. The main dimensionless parameters examined were the slenderness ratio, the relative thickness and the stiffness of the soil layer. The following conclusions can be summarized regarding the type of load applied on the foundation.

Lateral dynamic response of piles The lateral dynamic response of end bearing pile was investigated by establishing a 3D numerical model, which was then validated against the analytical results of Novak and Nogami (1977) and Mylonakis (2001). Additionally, a continuum analytical solution for the estimation of the eigenfrequency and damping of floating piles was proposed. The analytical formulation was validated against finite element numerical models for floating piles.

It must be highlighted that these results are applicable to flexible floating piles, while the given solution cannot reproduce correctly the dynamic response of short and rigid foundations, since vertical displacements are not taken into consideration. In light of the findings it can be stated that the slenderness ratio is not influential dimensionless parameter, indicating that the dynamic active length is not an appropriate design criterion for floating piles.

On the other hand the variation of the thickness of the soil layer was shown to strongly affect the dynamic response of floating piles. The variation of the dynamic stiffness with frequency becomes more evident when the thickness of the soil layer is only marginally larger than the length of the pile, while the generated damping due to soil-pile interaction decreases with the decrease of the thickness of the soil layer. Nevertheless, it was found that the dynamic stiffness coefficients for a floating pile can be neglected in case of foundations embedded in deep soil deposit ($H_s/d > 50$).

While the non-dimensional parameter E_p/E_s influences slightly the stiffness and its effect was found more prominent for soft soil profiles. Moreover, the analytical outcomes showed that the dynamic active length depends only on the stiffness ratio in agreement with previous studies for end bearing piles. The results indicated that the expression of dynamic active length by Velez et al. (1983) can be adopted also in the case of floating piles.

The findings of the current study highlighted that the proposed analytical formulation can be applied in the frame of the substructure approach, to perform complete dynamic soil–structure interaction analyses of structures on such kind of foundations. In addition, the suggested analytical solution can be applied to estimate the static stiffness coefficients of the pile foundation with minimal computational effort. Nevertheless, it must be stated that this formulation is applicable to soil profiles with constant stiffness along the depth, nonlinear soil behaviour is not taken into account, and the sliding and the separation along the soil–pile interface is not included.

Vertical dynamic response of piles A 3D numerical model for the estimation of the vertical dynamic impedance of end bearing and floating piles was established and the numerical modelling

procedure was validated against existing analytical solutions for end bearing. The validation highlighted that the analytical solution of Novak and Nogami (1977) is consistent with the numerical outcomes; on the contrary the formulation of Wu et al. (2013) and Zheng et al. (2014) differed significantly for frequencies smaller than the 1st vertical resonance of the soil layer. The parametric study conducted showed that the dynamic response of floating piles is slightly affected by increasing E_p/E_s , particularly after the 2nd vertical resonance of the soil layer. On the contrary a decrease of the relative thickness of the soil layer on the vertical dynamic impedance determines a more significant reduction of stiffness at the 1st resonance. Moreover, it was found that the influence of the slenderness ratio on the vertical dynamic behaviour of floating piles can be considered negligible when the foundation is embedded in medium–stiff soil profile. The proposed numerical methodology is limited by the assumptions of linearity in the soil layer and foundation materials, and the perfect contact at the soil–foundation interface.

3.4 Recommendations for future work

- Elaborate an analytical formulation for estimating the vertical dynamic impedance of floating piles, possibly including the radial displacements of the soil medium;
- Investigate the response of pile groups and the pile–soil–pile interaction, subjected to vertical and horizontal dynamic loading;

Chapter 4

Dynamic response of suction caissons

*The findings of this chapter are presented in Latini and Zania (2017a) (Paper III), Latini et al. (2016a) (Paper IV), Paper V and Latini et al. (2016b) (Paper VI). And those passages denoted by superscript ** and *** have been quoted verbatim from Paper III and Paper V, respectively.*

This chapter focuses on the evaluation of the dynamic soil–foundation interaction of suction caissons for offshore wind turbines. Hence, a 3D numerical model in Abaqus software was established in order to determine the dynamic stiffness and damping coefficients of the suction caisson foundation subjected to vertical and lateral loading. The numerical model was then compared against analytical solutions for pile foundations.

Groups of crucial dimensionless parameters related to the soil profile and the foundation geometry are identified and their effects on the response of suction caissons are studied**. Static stiffness coefficients are presented in a form of mathematical expressions obtained by fitting the numerical data, representing foundations with different slenderness ratios and embedded in different soil deposits. Furthermore this work suggests mathematical formulas for the dynamic impedances of suction caissons in the frequency domain.

4.1 Lateral dynamic response of suction caissons

In this section the dynamic response of suction caissons subjected to lateral loading is studied. The section is organized as follows. Firstly the analytical approach adopted to predict the dynamic behaviour of suction caissons is described and afterwards the numerical methodology is provided. Different depths of the soil layer (H_s) with respect to the skirt of the suction caisson (H_p) were taken into account in the analyses. Two soil layered profile with high stiffness contrast was defined as illustrated in Figure 4.1. In analogy to the chapter regarding pile foundations, the soil profile with depth equal to the caisson skirt is defined as profile 1 (end bearing suction caisson), while the one with increased depth as profile 2 (floating suction caisson).

4.1.1 Analytical approach

Due to the absence in the literature of analytical solutions on the dynamic response of suction caissons embedded in a soil layer on rigid bedrock, the analytical solution of Nogami and Novak (1977) was selected for the dynamic analysis of suction caissons embedded in profile 1. While the analytical formulation of Latini et al. (2015) was adopted in the validation of the dynamic impedances of suction caisson embedded in profile 2. Note that these analytical solutions were established for slender solid piles, therefore some limitations on their applicability for the case of suction caissons are also discussed. It is worth underling that an equivalent cross section, which matches the bending stiffness of the hollow section of the suction caisson, was considered in the analytical formulations. Moreover, the analytical formulation does not indeed account for the

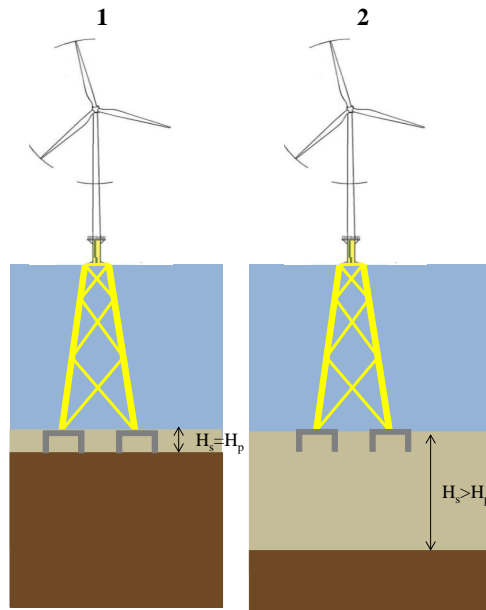


Figure 4.1: Illustration of the two soil profiles investigated for the analysis of suction caissons.

presence of the foundation lid (top plate). However, its effect on the dynamic impedances was proved to be marginally as discussed in Section 4.1.2.2.

4.1.2 Numerical approach

4.1.2.1 Methodology

The assumptions, the type of analysis procedure and the boundary conditions of the finite element models presented in Section 3.1.2.1 are kept for the investigation of the dynamic behaviour of suction caisson foundations.

Geometry The numerical model consists of:

- suction caisson foundation
- finite soil domain (near-field soil domain surrounded the foundation)
- infinite soil domain (far-field soil domain)

Type of elements The element definition assigned to the finite soil and infinite soil domain correspond to that discussed in Section 3.1.2.1. The suction caisson foundation consists of its shell and the lid. Therefore, shell elements (S4) were used for the shell part and for the top plate (lid).

Connectivity As explained in Section 3.1.2.1 the foundation and the soil need to be bounded together in order to guarantee the continuity of field displacement between each parts during the analysis. Thus, a “Tie constraint” was assigned to the caisson shell and the soil domain. Additionally, the caisson lid was tied to the top surface of the inner soil part and a “Rigid Body constraint” was defined between the nodes of the caisson lid and the reference point (RP) defined at the center of the cap.

Mesh size In the numerical analyses the soil medium was discretized as in Section 3.1.2.1; while the mesh dimension along the skirt length was 0.5m. Note that the subdivision of elements in the vertical direction was set equal to 0.125m, when the skirt length reduced to 1.25m. In regards with the caisson lid, at least 20 elements on the foundation's circumference were considered.

4.1.2.2 Modelling aspects

In this section different foundation modelling approaches were established to investigate the dynamic impedances of suction caisson for both profile 1 and profile 2. A mesh sensitivity analysis for soil domain was also performed.

Foundation modelling To study the effect of the foundation geometry on the dynamic impedances, three different caisson foundation modelling approaches are shown, see Figure 4.2: 1) equivalent solid pile for which equivalent material properties are applied to match the bending stiffness; 2) shell pile, where the foundation is modelled by its shell and 3) caisson.

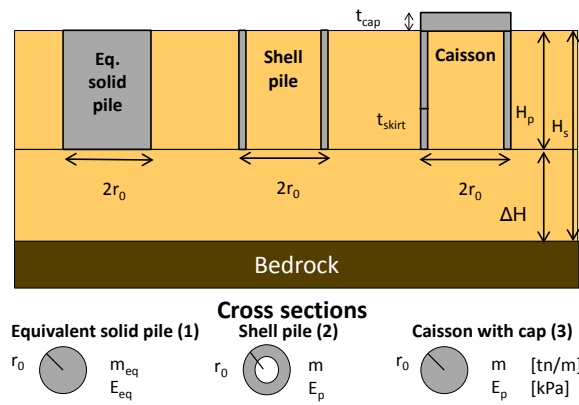


Figure 4.2: Foundation geometries investigated for the case of suction caissons embedded in profile 1 and 2. Modified after *Paper VI*.

In Table 4.1 the parameters considered for the analysis of suction caisson embedded in profile 1 and 2 are listed. Recall that profile 2 differs from profile 1 only in the value of the thickness of the soil medium, which was assumed equal to 30m for profile 2.

Table 4.1: Parameters of the case study for the analysis of suction caissons.

Suction caisson		
Young modulus	E_p	$2.138 \cdot 10^8 kPa$
Diameter	d	$5.00m$
Density	ρ_p	$7.86tn/m^3$
Thickness of the skirt	$t_{skirt} = d/50$	$0.1m$
Thickness of the cap	$t_{cap} = 5t_{skirt}$	$0.5m$
Soil		
Young modulus	E_s	$286875kPa$
Shear modulus	G	$106250kPa$
Shear wave velocity	V_s	$250m/s$
Soil layer height	H_p	$10.00m$
Density	ρ_s	$1.7tn/m^3$
Hysteretic damping	β	0.05
Poisson's ratio	ν	0.35

The discussion of the static stiffness coefficients for different foundation modellings is given in Section 4.1.4.1 along with the analytical values considering both profile 1 and profile 2. In Figure 4.3 the real (K_{Su} , $K_{S\theta}$ and $K_{M\theta}$) and the imaginary ($2\zeta_{Su}$, $2\zeta_{S\theta}$ and $2\zeta_{M\theta}$) terms of the dynamic impedances for different foundation geometry of profile 1 are presented. All the stiffness components are characterized by a drop of stiffness at the 1st eigenfrequency of the soil layer ($\alpha_0 = 1/2\pi$). While the pattern changes its slope around the 1st vertical resonance $\alpha_0 = 1/2\eta\pi$ and this is mostly observed for the horizontal and rocking coefficient. On the other hand an increase of stiffness at the same normalized frequency was noticed for the cross coupling component. In the intermediate frequency range ($\alpha_0 = 1/2\eta\pi - 6$) the results showed a linearly decrease of the dynamic stiffness consistent for all the components. Simultaneously, the caisson and the shell pile model are characterized by an exponential increase at the higher frequency interval $\alpha_0 = 6.5 - 7$. This can be due to the presence of a surface wave (Rayleigh wave). Indeed, the displacement contour plot at $\alpha_0 = 6.5$ (Figure 4.4) shows that the soil within the foundation and surrounding it experiences a surface wave with wave length almost equal to the diameter of the caisson and displays the occurrence of the Rayleigh wave through the s-pattern on the soil surface propagating radially from the caisson**.

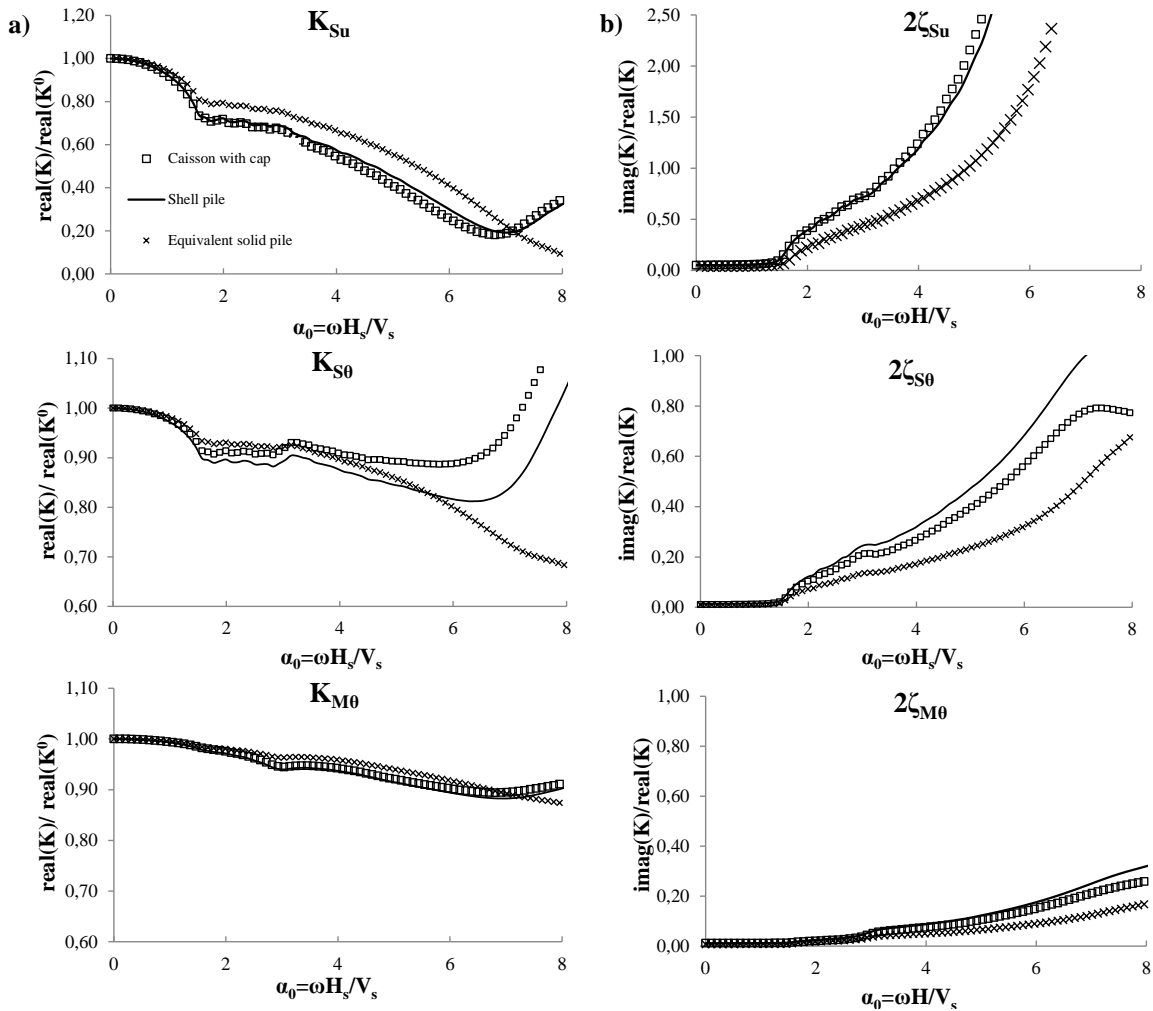


Figure 4.3: Variation of the dynamic stiffness and damping coefficients with respect to the non-dimensional frequency. Effect of the foundation geometry on the real component a) and the imaginary component b) for profile 1.

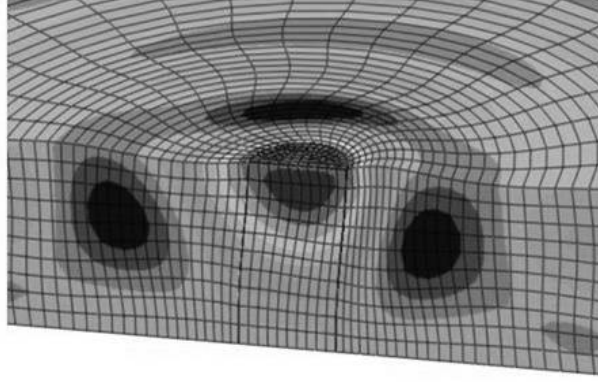


Figure 4.4: Displacement contour plot illustrating the presence of Rayleigh wave in the soil within the caisson. Modified after *Paper IV*.

In regards with the imaginary parts, the radiation damping is characterized by a linear trend in the intermediate interval ($\alpha_0 = 2 - 4$). In addition, it is important to mention that the slope of imaginary components slightly varies after each eigenfrequency of the soil layer. It can be stated that the equivalent solid pile exhibited stiffer behaviour when it is subjected to dynamic lateral loading than the shell pile and the suction caisson. This observation is supported by the lateral deformed shape of the foundation (Figure 4.5), which presented less fluctuations in the case of the equivalent solid pile.

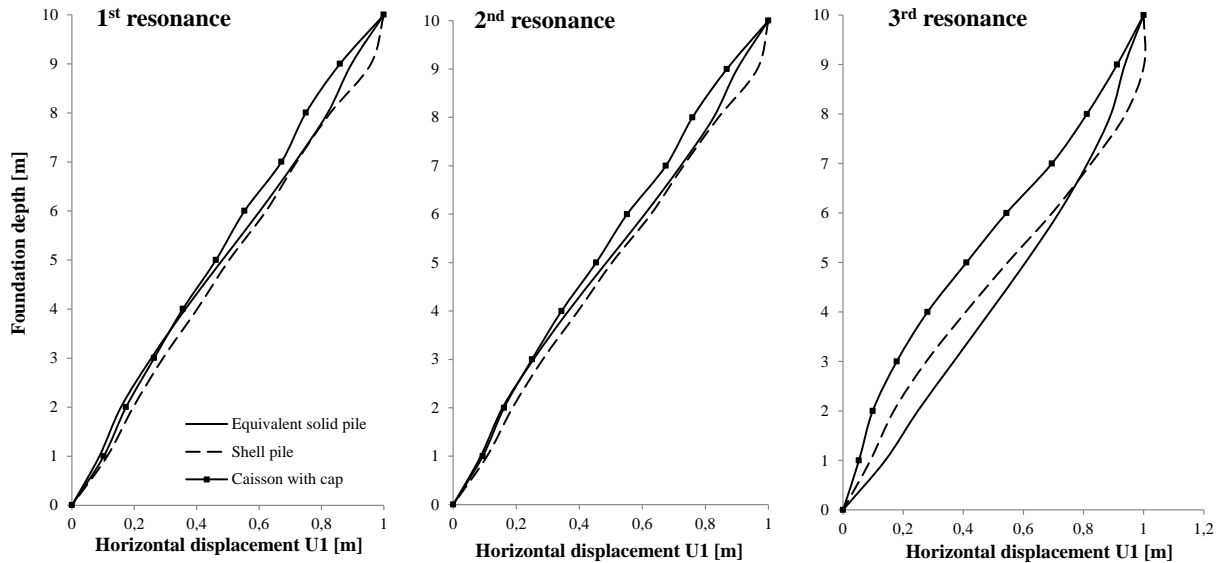


Figure 4.5: Distribution of the soil and suction caisson displacement along the depth at the three first eigenfrequency of the soil layer (profile 1).

Figure 4.6 shows the real (K_{Su} , $K_{S\theta}$ and $K_{M\theta}$) and the imaginary ($2\zeta_{Su}$, $2\zeta_{S\theta}$ and $2\zeta_{M\theta}$) parts of the dynamic impedances for different foundation geometries embedded in profile 2. A common trend for all the stiffness components is the observed reduction in stiffness at the 1st horizontal eigenfrequency of the soil layer. An increase of stiffness for frequencies higher than the 2nd horizontal resonance is recorded for the cross component, while the rocking coefficient is characterized by a constant trend up to $\alpha_0 = 7$ and then, it marginally increases. However, it might be concluded that the geometry of the foundation influenced slightly the horizontal dynamic response for frequencies higher than $\alpha_0 = 6$. The numerical models displayed similar results concerning the radiation damping associated to the components of the stiffness.

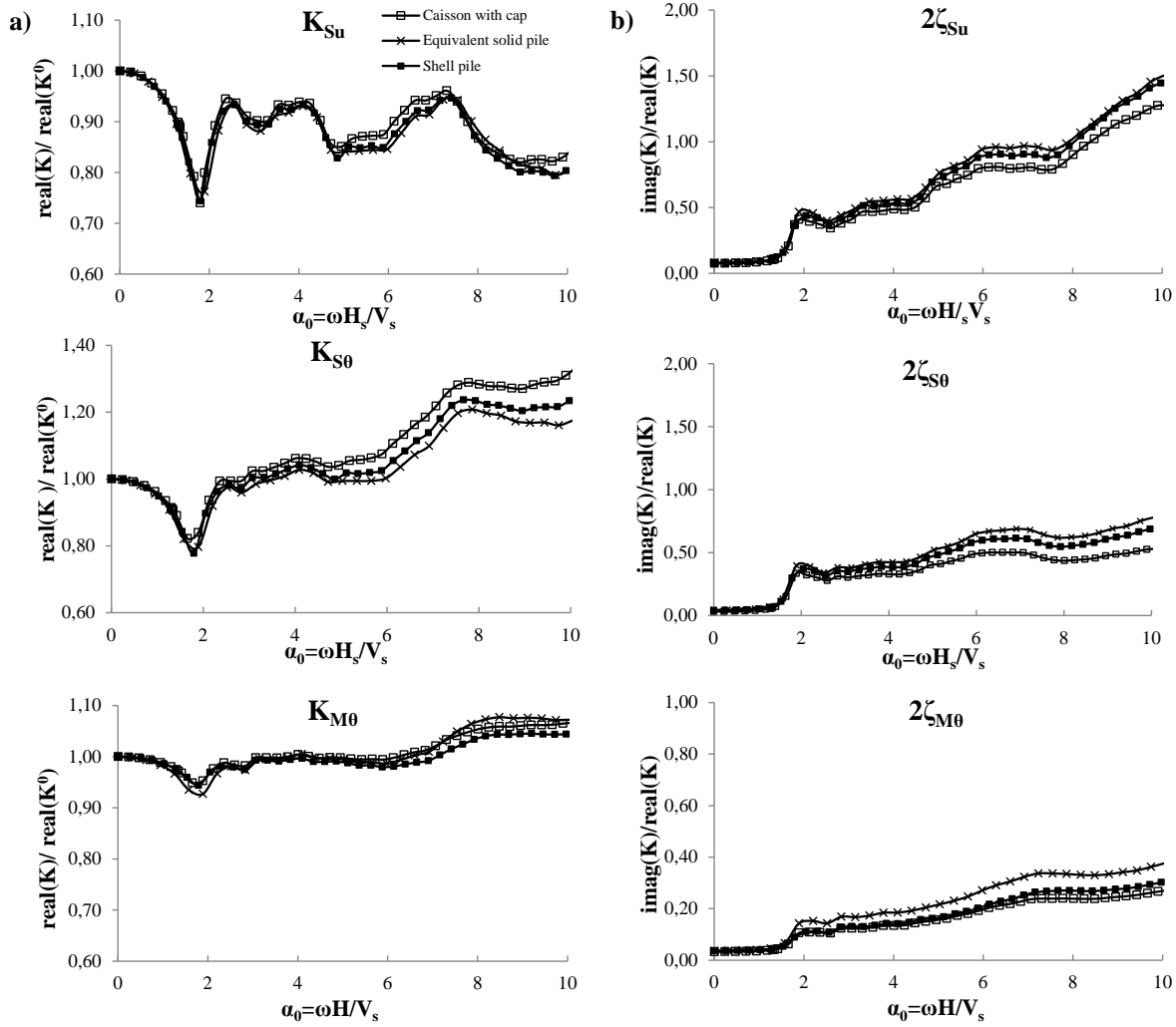


Figure 4.6: Variation of the dynamic stiffness and damping coefficients with respect to the non-dimensional frequency. Effect of the foundation geometry on the real component a) and the imaginary component b) for profile 2.

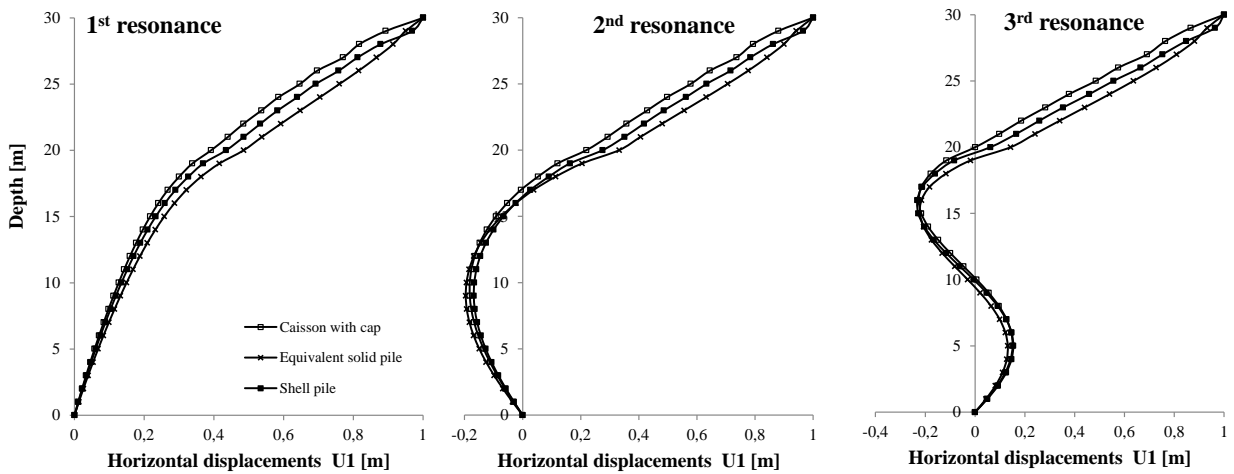


Figure 4.7: Distribution of the soil and suction caisson displacement along the depth at the three first eigenfrequency of the soil layer (profile 2).

Furthermore, the dynamic response of the soil–caisson system for the translation and rocking coefficient was found not dependent on the presence of the cap, since the dynamic behaviour of the shell pile and the caisson match almost perfectly. On the contrary an appreciable effect was observed on the coupling stiffness term after the 1st vertical resonance for both stiffness and damping coefficients. Finally, it can be stated that the numerical results in Figure 4.3 and 4.6 showed two different effects of the soil type profile (profile 1 and 2) on the dynamic response of the foundation, namely that the dynamic response of the soil–caisson system embedded in profile 1 is governed by the foundation rather than the soil; while the opposite is observed for profile 2. This can also be observed on the horizontal displacements of the three modelling foundations embedded in profile 2, see Figure 4.7. Indeed, it is evident that the deformed shape of the soil–foundation system resembled appreciably the one of the soil layer alone, showing a marginal influence of the foundation.

Investigation of mesh size accuracy In this section a mesh sensitivity study was performed to examine the effect of the mesh discretization of the soil domain on the dynamic stiffness coefficients. Particularly, the soil medium was discretized by considering four different mesh refinement. The reference case for the analysis consists of a suction caisson with diameter $d = 4m$, skirt length $H_p = 10m$ embedded in a homogeneous soil layer of depth $H_s = 30m$ with constant profile of shear wave velocities ($V_s = 250m/s$), hysteretic material damping ($\beta = 0.05$) and Poisson’s ratio ($\nu = 0.35$). Discretization features of each model are listed in Table 4.2:

Table 4.2: Mesh discretization for the mesh sensitivity analysis.

Mesh type	Radial discretization [m]	Vertical discretization along skirt length [m]	Vertical discretization below the caisson tip [m]
Extra coarse mesh	1.50–12.00	2.00	2.00
Coarse mesh	1.00–8.00	1.50	1.50
Actual/Medium mesh	0.40–4.00	0.50	1.00
Fine mesh	0.20–2.00	0.25	0.50–1.00

Note that all the numerical models in the mesh sensitivity analysis were characterized by 20 elements in the hoop direction of suction caisson foundation and soil domain. As specified in Section 3.1.2.1, the subdivision of elements of the infinite soil domain consisted of one element in the horizontal direction. Additionally the outcomes herein presented are referred only to the horizontal component of the dynamic impedances. First the horizontal static stiffness obtained at low frequencies is presented in Table 4.3.

Table 4.3: DOF’s and the static lateral stiffness coefficients for the mesh sensitivity analysis.

Mesh type	Degrees of freedom (DOF)	$K_{Su}/(E_s d)$
Extra coarse mesh	79758	1.144
Coarse mesh	153018	1.130
Actual/Medium mesh	587928	1.096
Fine mesh	2010948	1.090

It can be seen that the difference between the static stiffness of the foundation for extra coarse mesh and medium mesh refinement is around 4%, while this discrepancy reduced up to 0.5% when K_{Su}^0 for the medium and fine mesh refinement are compared. Furthermore it is evident that the more the mesh of the soil domain is refined, the more the static stiffness decreases.

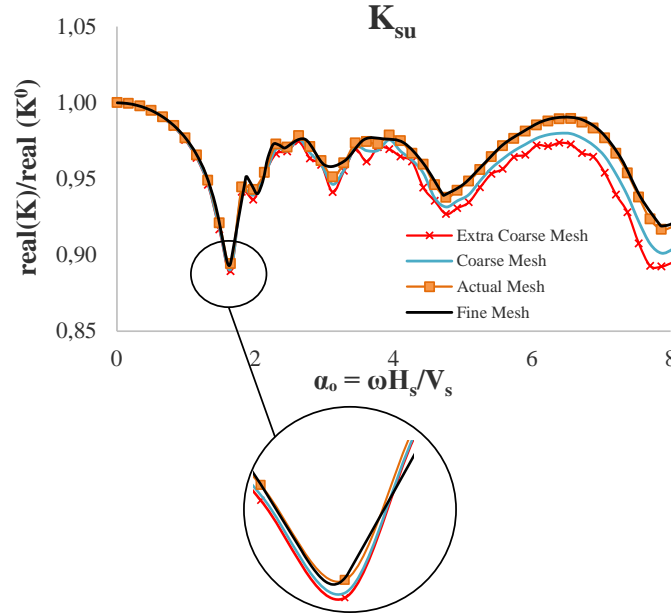


Figure 4.8: Variation of the dynamic lateral stiffness coefficients with respect to the non-dimensional frequency. Effect of the mesh discretization on the real component for profile 2.

In Figure 4.8 the real component K_{Su} of the translation dynamic stiffness is shown for the case examined. It is possible to observe that the first reduction in stiffness for the model characterized by medium and fine mesh discretization is attained at $\alpha_0 = 1.64$, while as for the model with fine mesh discretization is recorded at $\alpha_0 = 1.62$, which is closer to the theoretical value $\alpha_0 = 1.57$. Results of these two models are essentially identical for frequencies higher than the 1st horizontal eigenfrequency of the soil layer. Whereas significant discrepancy was noticed for the models with coarse and extra coarse mesh in the high frequency range. Thus, it might be concluded that the mesh size does influence with some extent the static response, while the dynamic behaviour is affected significantly in the high frequency interval. As a result, medium mesh for the discretization of the soil medium was chosen to be applied in all the numerical models established for the parametric study.

4.1.3 Validation of the numerical model

Profile 1 Details of the case of study selected for the validation of the numerical model are given in Table 4.1. To begin with the static stiffness coefficients the different modelling approaches are calculated and presented in Table 4.4 for the soil profile 1, along with the corresponding ones determined by the analytical solution.

Table 4.4: Static suction caisson stiffness obtained from the numerical models and the analytical solution of Novak and Nogami (1977) for profile 1.

<i>Model</i>	$K_{Su}/(E_s \cdot d)$	$K_{S\theta}/(E_s \cdot d^2)$	$K_{M\theta}/(E_s \cdot d^3)$
Novak and Nogami (1977)	6.17	-4.80	5.99
Caisson	3.25	-1.71	3.35
Shell pile	3.49	-1.97	3.69
Equivalent solid pile	4.96	-3.32	4.83

Slightly scattered results were achieved by comparing the static stiffness components of the caisson model with those of the shell pile, while the discrepancy becomes more noticeable with the

equivalent solid pile regarding all the components. Further, it is observed that the results obtained from the numerical models are overestimated by the analytical solution, particularly regarding the translational and the cross coupling terms. Comparing the numerical results of the static stiffness coefficients with those calculated according to Novak and Nogami (1977), a discrepancy of 24.4%, 44.3% and 24.1% was observed for the horizontal, coupling and rocking component, respectively. Figure 4.9 shows the real (K_{Su} , $K_{S\theta}$ and $K_{M\theta}$) and the imaginary ($2\zeta_{Su}$, $2\zeta_{S\theta}$ and $2\zeta_{M\theta}$) parts of the dynamic impedances for different foundation geometries embedded in profile 1 along with the results of the analytical solution. It is evident that the analytical formulation overestimated the dynamic stiffness and underestimated the damping for all the components, even though a relatively good agreement was achieved with respect to the equivalent solid pile. This suggests that the inner soil affects the dynamic behaviour of the caisson, by allowing wave propagation of smaller wave lengths**.

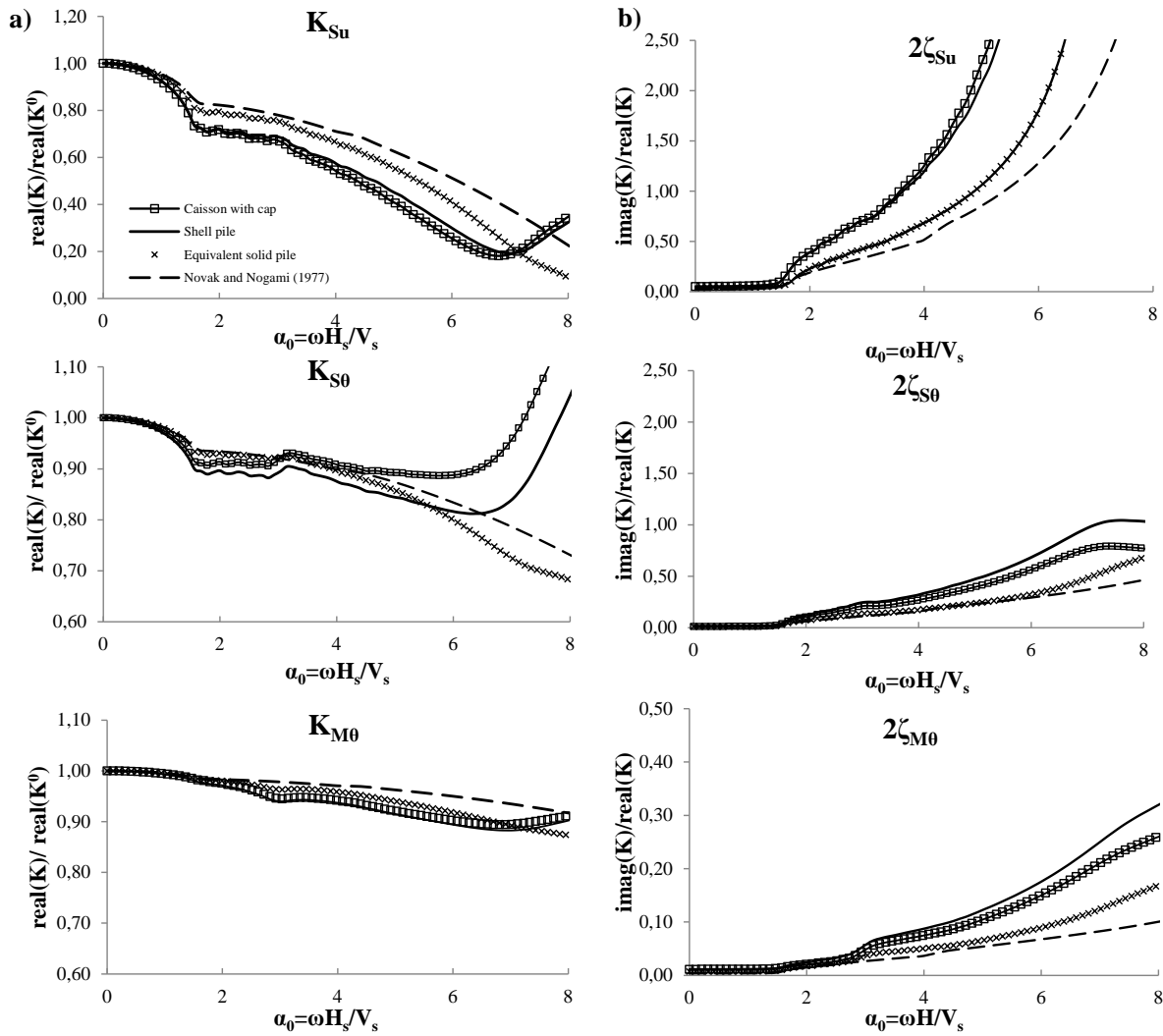


Figure 4.9: Variation of the dynamic lateral stiffness coefficients with respect to the non-dimensional frequency for profile 1.

Profile 2 Regarding the second soil profile, the static stiffness coefficients were estimated and the results are summarized in Table 4.5. Note that the static stiffness coefficients of the shell pile is not reported in the table, since they match with those of the caisson.

Table 4.5: Static suction caisson stiffness obtained from the numerical models and the analytical solution of Latini et al. (2015) for profile 2.

<i>Model</i>	$K_{Su}/(E_s \cdot d)$	$K_{S\theta}/(E_s \cdot d^2)$	$K_{M\theta}/(E_s \cdot d^3)$
Latini et al. (2015)	2.99	-2.13	3.73
Equivalent solid pile	2.67	-1.78	3.32
Caisson	2.25	-1.29	2.68

The static stiffness coefficients of the equivalent solid pile are quite higher than those of the caisson model, showing a difference less than 28%. The analytical solution suggests similar values to those acquired from the numerical models. A discrepancy between the analytical solution and the numerical results for the equivalent pile model was recorded of 10.8%, 16.4% and 11.0% for the horizontal, coupling and rocking component respectively. When the static stiffness coefficients of suction caisson were compared to those calculated by the analytical solution, the discrepancy was around 30–40% for all the components.

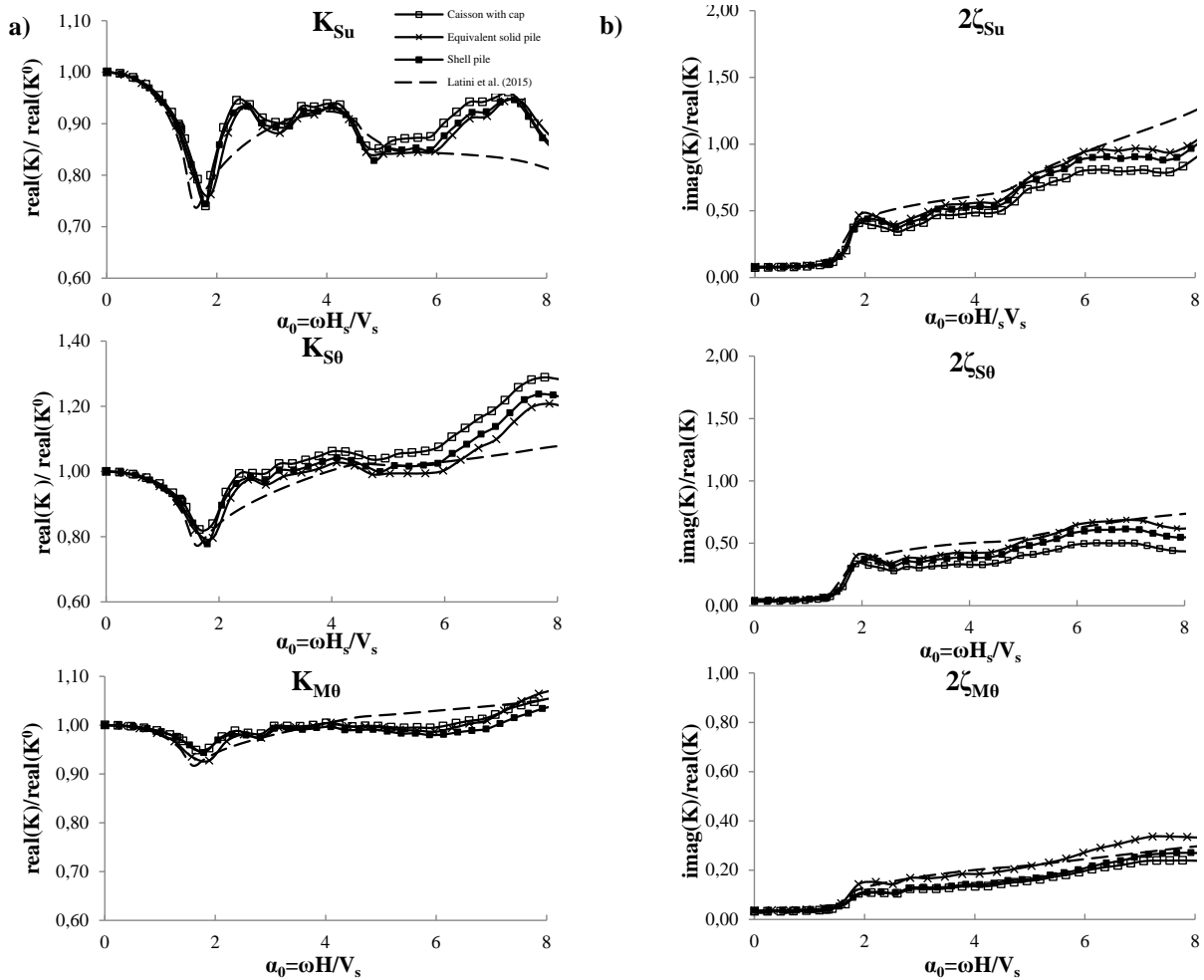


Figure 4.10: Variation of the dynamic lateral stiffness coefficients with respect to the non–dimensional frequency for profile 2.

It becomes apparent that the analytical solution of Latini et al. (2015) cannot be applied for the estimation of the static stiffness coefficients of suction caissons. Therefore, mathematical formulas obtained by fitting the numerical outcomes were established for the estimation of the static stiffness coefficients of suction caissons, see Section 4.1.4.1.

In Figure 4.10 the real (K_{Su} , $K_{S\theta}$, and $K_{M\theta}$) and the imaginary ($2\zeta_{Su}$, $2\zeta_{S\theta}$, and $2\zeta_{M\theta}$) parts of the dynamic impedances are presented for the numerical models and the analytical solution of Latini et al. (2015). It can be stated that the analytical solution shows fairly good agreement with the numerical results up to $\alpha_0 = \pi/2$. Nevertheless, the effect of the vertical displacements at the foundation tip on the dynamic response of suction caissons cannot be neglected.

4.1.4 Parametric study

This section has been quoted verbatim from the following source: Paper III.

The role of key dimensionless parameters such as the stiffness ratio E_p/E_s , the slenderness ratio H_p/d and the pile flexibility factor K_r on the response of end bearing piles has been illustrated previously (Poulos and Davis (1980) and Randolph (1981)). Moreover, studies on the dynamic response of floating piles (Nozoe et al. (1988), Chapter 3) highlighted the influence of the thickness of the soil layer on the dynamic impedances of this type of foundations.

Table 4.6: Dimensionless parameters and cases selected in the parametric analysis for suction caisson.

Case Nr.	H_s	H_p	d	H_p/d	H_s/d	Soil Profile		E_p/E_s	K_r		
						Type	n			V_H	V_0/V_H
	[m]	[m]	[m]								
1	30	10	5	2	6	A	1	250	1	60	1.80e-1
2	30	7.5	5	1.5	6	A	1	250	1	60	5.68e-1
3	30	5	5	1	6	A	1	250	1	60	2.88
4	30	2.5	5	0.5	6	A	1	250	1	60	46.08
5	30	1.25	5	0.25	6	A	1	250	1	60	737.3
6	30	1	4	0.25	7.5	A	1	250	1	60	737.3
7	15	0.5	2	0.25	7.5	A	1	250	1	60	737.3
8	30	8	4	2	7.5	A	1	250	1	60	1.80e-1
9	15	4	2	2	7.5	A	1	250	1	60	1.80e-1
10	30	0.5	2	0.25	15	A	1	250	1	60	737.3
11	30	4	2	2	15	A	1	250	1	60	1.80e-1
12	30	10	5	2	6	A	1	300	1	41	1.28e-1
13	30	10	5	2	6	A	1	400	1	23	7.20e-2
14	30	10	5	2	6	A	1	500	1	15	4.71e-2
15	30	1.25	5	0.25	6	A	1	300	1	41	515.6
16	30	1.25	5	0.25	6	A	1	400	1	23	295.1
17	30	1.25	5	0.25	6	A	1	500	1	15	193.0
18	30	7.5	5	1.5	6	A	1	500	1	15	1.49e-1
19	30	5	5	1	6	A	1	500	1	15	7.54e-1
20	30	2.5	5	0.5	6	A	1	500	1	15	12.1
21	30	10	5	2	6	B	0.25	500	0.01	15	4.71e-2
22	30	5	5	1	6	B	0.25	500	0.01	15	7.54e-1
23	30	1.25	5	0.25	6	B	0.25	500	0.01	15	193.0
24	30	10	5	2	6	C	0.5	500	0.1	15	4.71e-2
25	30	5	5	1	6	C	0.5	500	0.1	15	7.54e-1
26	30	1.25	5	0.25	6	C	0.5	500	0.1	15	193.0
27	30	10	2	5	15	A	1	250	1	60	4.60e-3
28	30	20	4	5	7.5	A	1	250	1	60	4.60e-3
29	15	10	2	5	7.5	A	1	250	1	60	4.60e-3

The dependency of dynamic stiffness coefficients on the dimensionless parameter H_s/d , defined

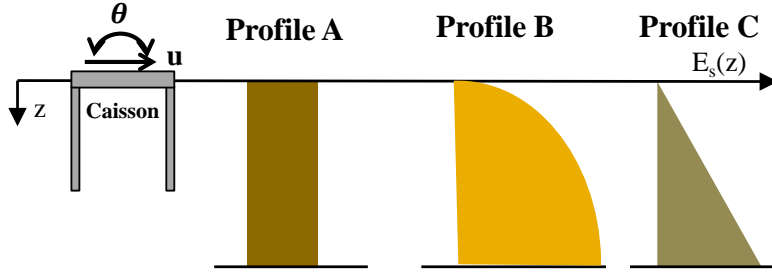


Figure 4.11: Soil profiles considered for dynamic response of suction caissons. Modified after *paper III*.

as the relative thickness of the soil layer, was pointed out only for the case of surface footings in the work of Gazetas (1983). Since these studies have been investigating piles with slenderness ratio more than 10 or surface footings, the relevance of these findings to suction caissons and the effects of the abovementioned dimensionless parameters to the dynamic soil suction caisson interaction is hereafter investigated. The cases selected in the current analysis and the dimensionless parameters are listed in Table 4.6, while the rationale behind their selection was to investigate foundations with different skirt length and diameter to study the dynamic response of suction caissons for different slenderness ratios (H_p/d) and site conditions (E_p/E_s , H_s/d).

Three soil profiles were considered, each with a different distribution of $E_s(z)$ with depth as reported in Figure 4.11. In the numerical analysis the shear wave velocity of the soil layer was assumed to increase with depth according to the following expression (Rovithis et al. (2011)):

$$V_s = V_H \left[b + (1 - b) \frac{z}{H_s} \right]^n \quad (4.1)$$

where b is given as a function of the shear wave velocity at the surface (V_0) and base (V_H) of the inhomogeneous soil layer ($b = (V_0/V_H)^{1/n}$), n is a dimensionless inhomogeneity factor ($n = 0 - 1$) and z represents the depth measured from the ground surface.

Profile A has constant shear wave velocity ($V_s = 250, 300, 400, 500$ m/s – cases 1–20), which is typical for overconsolidated clay deposits. The parameter n was set equal to 0.25 for profile B, representing uniform medium-dense sand deposits, see cases 21–23. In profile C, $E_s(z)$ is proportional to depth and $n = 0.5$ was taken into account in order to investigate normally consolidated clay strata (cases 24–26). Shear wave velocity ratio V_0/V_H (at the surface and the base of the inhomogeneous layer) was considered equal to 0.01 and 0.1 respectively for the soil models B and C to account for strong gradient in shear wave velocity. And the reference base shear wave velocity was 500 m/s in order to model a continuously inhomogeneous viscoelastic soil medium of thickness H_s over rigid bedrock. The hysteretic material damping ($\beta = 5\%$) and Poisson's ratio ($\nu = 0.35$) were identical for all the examined cases. These three models may adequately represent the dynamic characteristics of a fairly wide range of real soil profiles.

4.1.4.1 Static stiffness of suction caissons

The static stiffness components of suction caisson foundations were herein estimated, taking into consideration the effect of the slenderness ratio. Several approximate closed–form solutions for the static stiffness coefficients of piles (Gazetas (1984), Poulos and Davis (1980), Randolph (1981)) are available in the literature. In case of large slenderness ratio ($H_p/d > 10$), Randolph suggested a set of stiffness formulas highlighting the dependency on the stiffness ratio (E_p/G^*), where $G^* = G(1 + \frac{3}{4}\nu)$ in order to predict accurately the behaviour of flexible foundations. It is worth mentioning that the deformation mode changes for smaller slenderness ratio–like in the case of suction caissons– and consequently the static stiffness will be influenced by H_p/d . In order to

account for this aspect, Carter and Kulhawy (1988) formulated the static stiffness coefficients based on the slenderness ratio for rigid shafts. There are also other approaches to the problem. Gelagoti et al. (2015) modified the previously proposed formulas for embedded foundations (Gazetas (1983)) by considering that the point of load application is at the top of the foundation. Whereas Wolf and Deeks (2004) developed expressions for the stiffness of surface foundations.

Appropriately modified formulas were established based on the closed-form expressions given by Randolph (1981) for flexible piles by including also the contribution of the slenderness ratio, in order to provide closer approximations of the static stiffness coefficients of suction caissons. Figure 4.12a shows the results of the numerical analysis along with the exponential functions. A better curve fitting was achieved for foundations with $H_p/d > 0.5$. Additionally, the comparison between the numerical results of the static stiffness components for the suction caisson case and previously published expressions (Wolf and Deeks (2004), Gelagoti et al. (2015), Shadlou and Bhattacharya (2016)) was also presented.

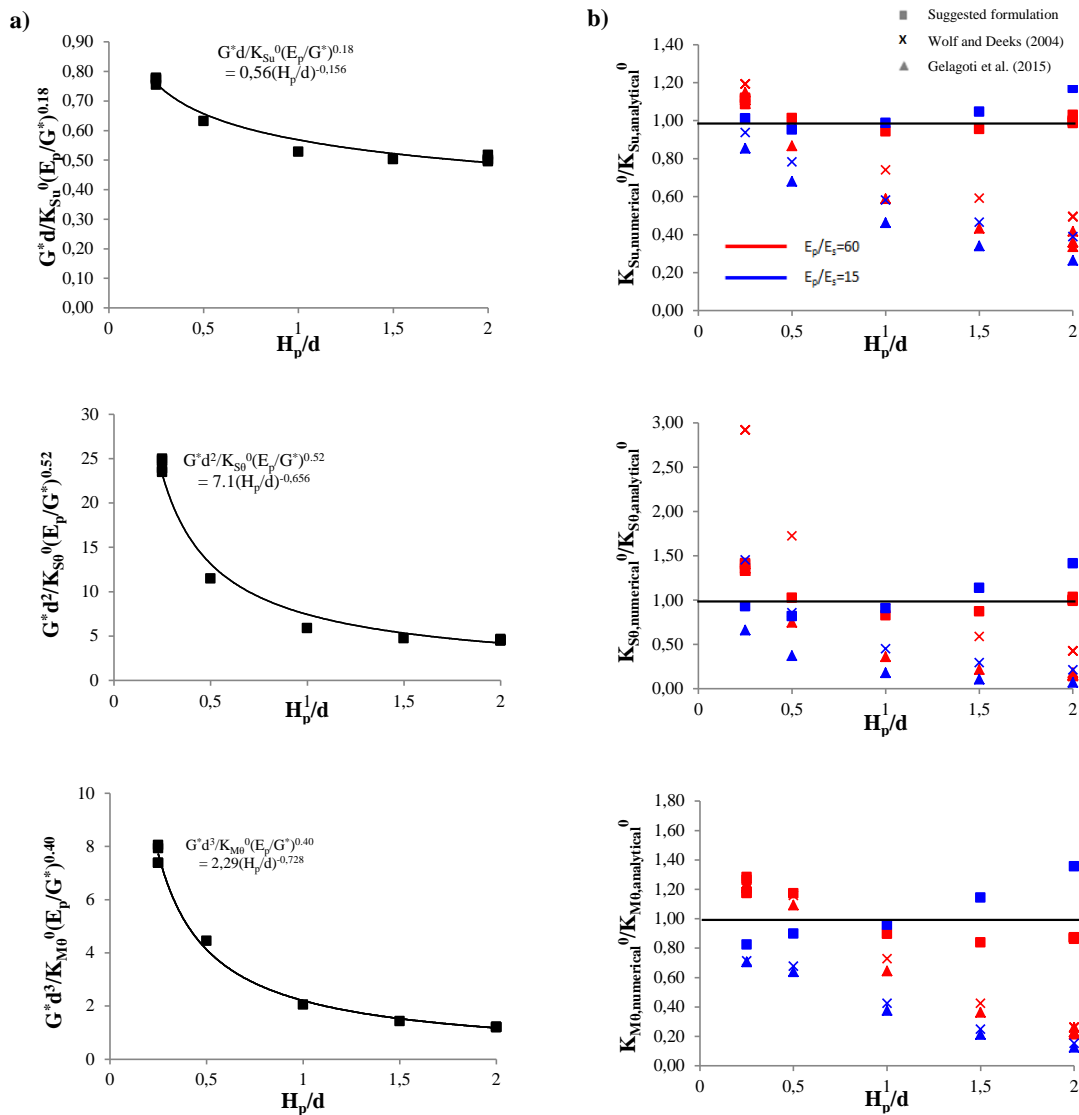


Figure 4.12: Static stiffness components of suction caissons. Mathematical expressions for the static stiffness components a). Comparison of the static stiffness components given by the numerical model and three analytical expressions b). Modified after *Paper III*.

The static stiffness coefficients calculated by the mathematical formulas were divided by the corresponding numerical ones and they are presented with respect to the slenderness ratio in Figure

4.12b. It seemed that the expressions suggested by Wolf and Deeks (2004) slightly overestimate all the static components up to $H_p/d = 0.5$ for $E_p/E_s = 60$, while the opposite is noticed for the expressions of Gelagoti et al. (2015) for the horizontal and coupling terms**. Moreover, the calculated stiffness coefficients using the formulas proposed by Shadlou and Bhattacharya (2016) which were developed for higher H_p/d values are largely the same of the ones obtained by Gelagoti et al. (2015) as shown in Figure 4.13. The deviation of the previous studies (Wolf and Deeks (2004), Gelagoti et al. (2015), Shadlou and Bhattacharya (2016)) becomes more apparent for higher H_p/d values. Therefore, the static stiffness components of suction caissons can be estimated by these simple mathematical equations determined by fitting the numerical data:

$$K_{Su}^0 = 1.785G^*d \left(\frac{H_p}{d}\right)^{0.156} \left(\frac{E_p}{G^*}\right)^{0.18} \quad (4.2)$$

$$K_{S\theta}^0 = 0.141G^*d^2 \left(\frac{H_p}{d}\right)^{0.656} \left(\frac{E_p}{G^*}\right)^{0.52} \quad (4.3)$$

$$K_{Mu}^0 = K_{S\theta}^0 \quad (4.4)$$

$$K_{M\theta}^0 = 0.437G^*d^3 \left(\frac{H_p}{d}\right)^{0.728} \left(\frac{E_p}{G^*}\right)^{0.40} \quad (4.5)$$

The new suggested expressions reduce substantially the scatter and provide a better approximation of static stiffness components of suction caissons.

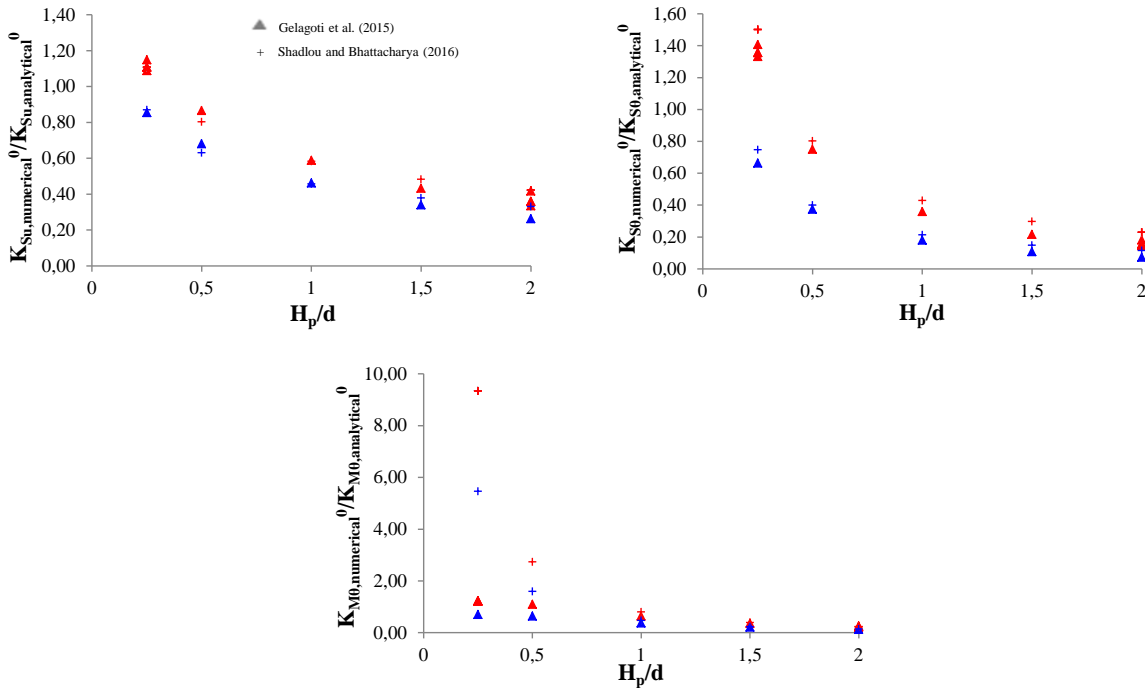


Figure 4.13: Comparison of the static stiffness components given by the numerical model, Gelagoti et al. (2015) and Shadlou and Bhattacharya (2016).

Effect of the slenderness ratio In Figure 4.14 the real (K_{Su} , $K_{S\theta}$, and $K_{M\theta}$) and the imaginary ($2\zeta_{Su}$, $2\zeta_{S\theta}$, and $2\zeta_{M\theta}$) terms of the dynamic impedances are presented for different values of the slenderness ratio H_p/d (cases 1–5). This parametric study was conducted keeping the same height and shear wave velocity of the soil layer as in the reference case. Recall that all examined cases resemble rigid foundation behaviour in agreement with the flexibility criterion introduced by Poulos and Davis (1980). Looking at the overall dynamic response, it can be stated that the slenderness ratio affected the pattern of the stiffness variation with frequency after the 1st vertical

eigenfrequency of the soil medium. It seemed that the drop of stiffness recorded at the 1st horizontal eigenfrequency ($\alpha_0 = \pi/2$) of the soil layer became more evident as the slenderness ratio increases.

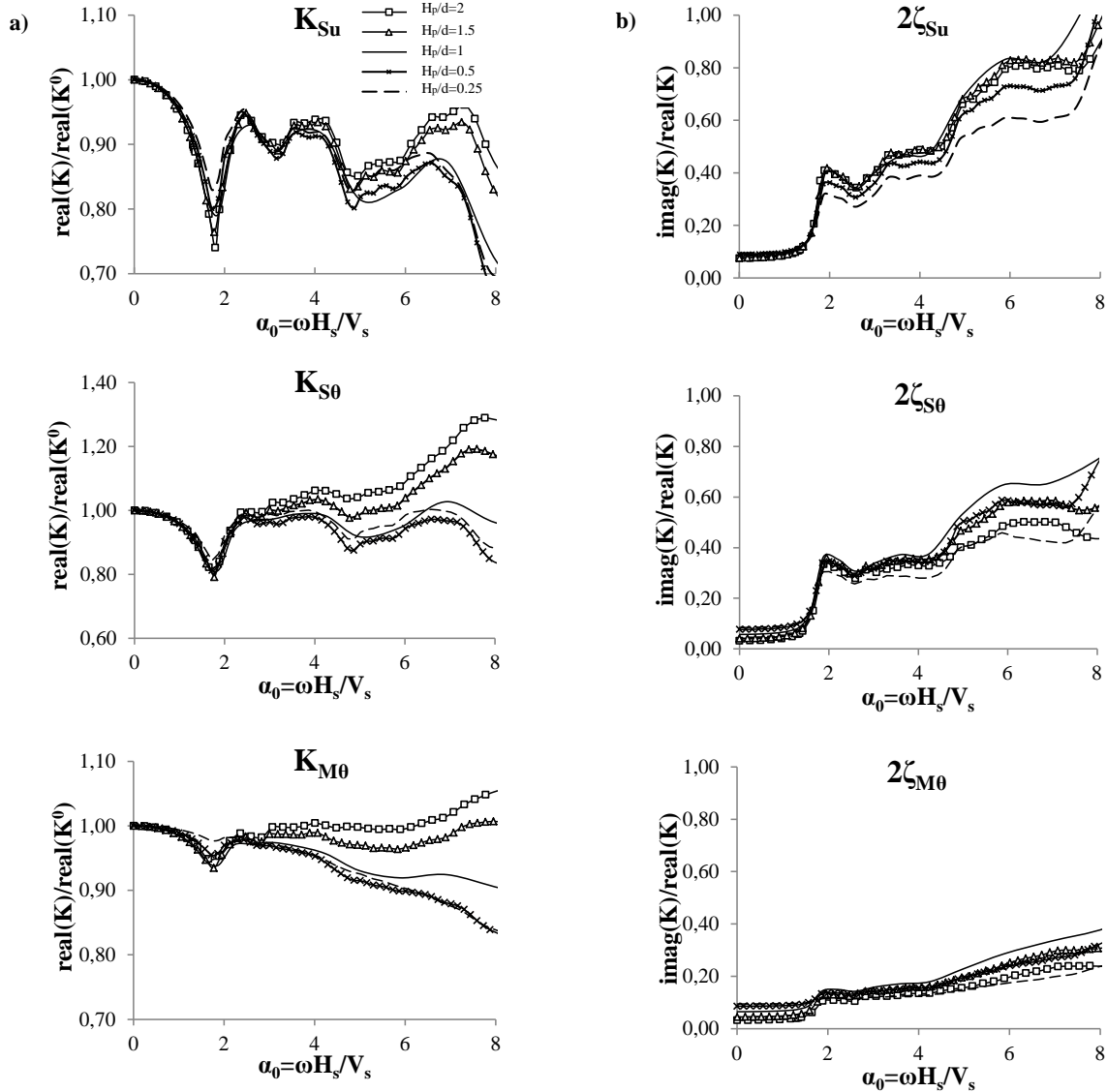


Figure 4.14: Variation of the dynamic stiffness and damping coefficients with respect to the non-dimensional frequency. Effect of slenderness ratio on the real component a) and the imaginary component b) for Profile 2. Modified after *Paper III*.

The dynamic stiffness components of suction caissons decrease for lower values of slenderness ratio at higher frequency interval, as previously observed for the case of suction caisson in homogeneous halfspace (Liingaard (2006)). With reference to the higher frequency range (larger than $\alpha_0 > 3$) it was observed that the dynamic stiffness of suction caisson with $H_p/d > 1$ increases attaining values even higher than the static ones especially for the coupling and rocking coefficients. This can be attributed to the effect of the coupling between the horizontal and the rotational degrees of freedom, which becomes more prominent with increasing slenderness ratio ($H_p/d > 1$), since the response is mainly governed by the rotation. Results of the displacement vectors in the higher frequency range showed a kind of a scoop–slide mechanism, which resembled the failure mechanism of suction caissons embedded in clay as observed in the work of Randolph and House (2002)**. On the other hand, it was found that the lateral response of the suction caissons with $H_p/d < 1$ is emphasized by the fact that horizontal vibrations induced by the foundation-soil interaction mainly

propagate to the surrounding soil at shallow depths. Indeed, the contribution of the vertical displacement to the displacement resultant can be disregarded along the whole foundation skirt. The outcomes do not show a distinctive trend of the variation of the imaginary components with respect to the skirt length; whereas the lowest damping ratios of all the examined cases is consistently obtained for suction caisson with $H_p/d = 0.25$. The pattern of the damping variation with respect to the normalised frequency is not influenced by the slenderness ratio and its slope increases after each eigenfrequency of the soil medium. There is indication that the increase of H_p/d would result to higher damping ratio, especially for the horizontal component and frequency range lower than the 2^{nd} eigenfrequency of the soil layer**.

Effect of the relative thickness of the soil layer In order to address the effect of the thickness of the soil layer, first it is prudent to figure out the adequate corresponding non-dimensional parameter**. Therefore dynamic analyses of suction caissons were conducted by keeping all dimensionless parameters constant and changing only the soil depth and the diameter, whereas taking into consideration the same slenderness ratio and relative thickness of the soil layer (H_s/d). Figure 4.15 presents the results of the real (K_{Su} , $K_{S\theta}$, and $K_{M\theta}$) and the imaginary ($2\zeta_{Su}$, $2\zeta_{S\theta}$, and $2\zeta_{M\zeta}$) parts of the dynamic impedances (cases 6–9, in Table 4.6). It was found that the dynamic response of suction was barely influenced by the variation of the diameter and thus, the relative thickness of the soil layer H_s/d can be considered an adequate dimensionless parameter in the estimation of the dynamic response of suction caissons. In addition, this observation stands for both the minimum and maximum slenderness ratio in this study.

Figure 4.16 illustrates the effect of H_s/d ratio on the frequency variation of the dynamic stiffness and damping coefficients (cases 7, 9–11, in Table 4.6). The pattern of the dynamic impedances seemed to be affected by the variation of the non-dimensional parameter H_s/d in the frequency interval examined. Firstly the reduction in stiffness attained at the 1^{st} resonance, when referring to same slenderness ratio H_p/d , became less evident as the relative thickness of the layer H_s/d increased. This can be attributed by the fact that the longer the path the propagating waves travel, the more the stress waves are attenuated with the distance and therefore the decay of the dynamic impedances is less appreciable**. The decrease of the dynamic impedances with the smaller H_s/d has been previously observed for the dynamic response of surface footing (Gazetas (1983))**. The variation of the rocking coefficient with frequency appears to be marginally dependent on the relative thickness of the soil medium, while the translational and coupling components are more sensitive to the dimensionless parameter H_s/d . This might be explained by the fact that the coupling between the horizontal and the rotational degrees of freedom is enhanced by the non-dimensional parameter H_s/d , since higher rotation at the pile tip was recorded for frequencies greater than the 1^{st} vertical resonance as the relative thickness of the soil layer decreases.

Simultaneously, the imaginary components are characterized by a step-linear increasing pattern at higher frequencies and the slope increases when the relative thickness of the soil layer decreases. This increase of the variation of the imaginary parts recorded for smaller values of soil profile thickness is attributed to the concurrent decrease of the dynamic component of the stiffness terms. On the contrary, the viscous damping coefficients in the frequency interval examined decreases by decreasing H_s/d , in agreement with the fact that less energy is dissipated as the propagating waves travel at shorter distance, see Figure 4.17. In conclusion the numerical findings highlighted that the relative thickness of the soil layer H_s/d is a fundamental non-dimensional parameter for understanding the dynamic behaviour of floating foundations.

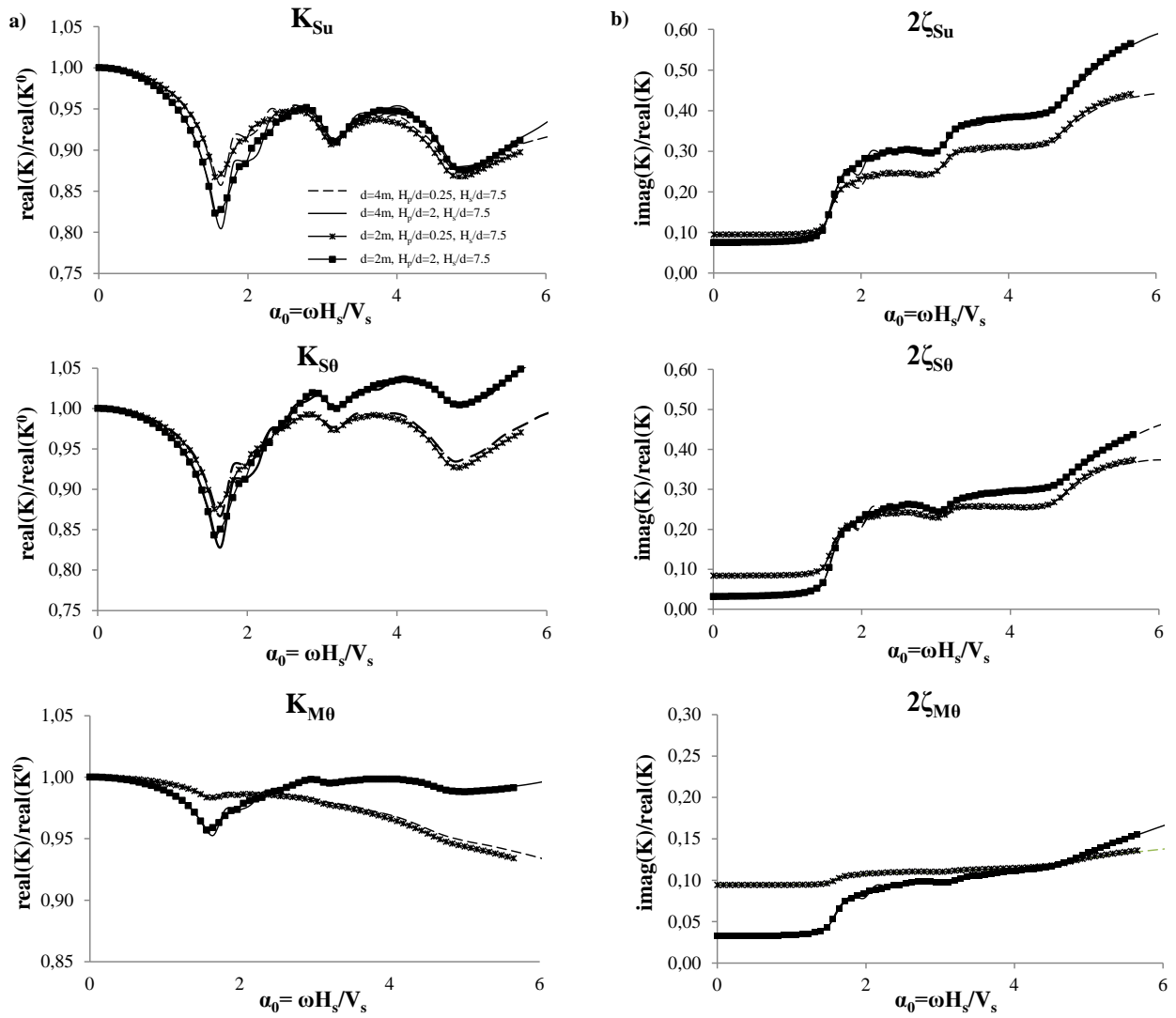


Figure 4.15: Variation of the three dynamic stiffness and damping coefficients with respect to the non-dimensional frequency. Effect of the diameter of suction caisson on the real component a) and the imaginary component b) for profile 2. Modified after *Paper III*.

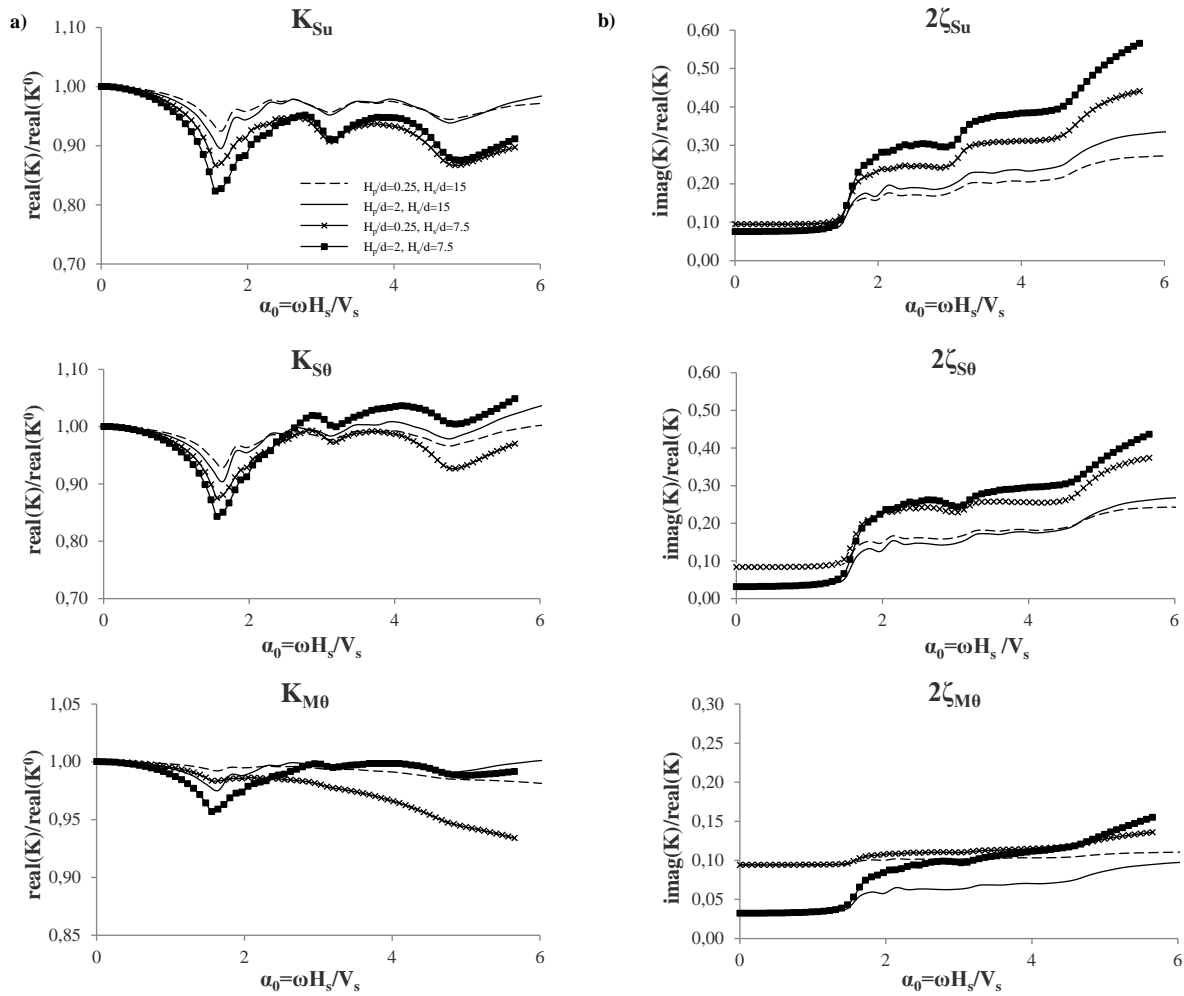


Figure 4.16: Variation of the three dynamic stiffness and damping coefficients with respect to the non–dimensional frequency. Effect of the relative thickness of the soil layer on the real component a) and the imaginary component b) for profile 2. Modified after *Paper III*.

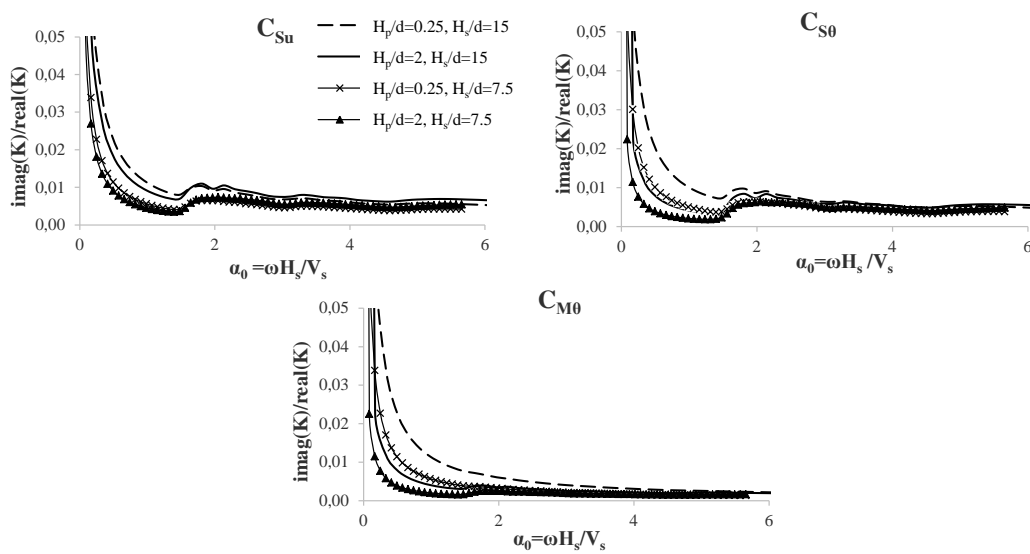


Figure 4.17: Variation of the three viscous damping coefficients with respect to the non–dimensional frequency. Effect of the relative thickness of the soil layer.

4.1.4.2 Effect of the stiffness of the soil layer

In Figure 4.18 the real (K_{Su} , $K_{S\theta}$, and $K_{M\theta}$) and the imaginary ($2\zeta_{Su}$, $2\zeta_{S\theta}$, and $2\zeta_{M\theta}$) part of the dynamic impedances are shown varying the stiffness of the homogeneous soil layer (profile A) respectively for $H_p/d = 2$ (cases 1, 12–14) and $H_p/d = 0.25$ (cases 5, 15–17). In regards to $H_p/d = 2$ the dynamic impedances are marginally affected by the increase of the stiffness of the soil medium. Additionally, the rocking coefficient seemed fairly frequency-independent particularly when the factor K_r decreased and for frequencies higher than the 1st eigenfrequency of the soil layer. The damping ratios slightly increase for decreased soil stiffness. The influence of the shear wave velocity for profile A was also analysed for small slenderness ratio ($H_p/d = 0.25$). The results for $H_p/d = 0.25$ indicated that at small skirt lengths the dynamic response of the caisson is insensitive to the soil stiffness at homogeneous soil layers**. This can be explained by the fact that the horizontal vibrations propagate through the surrounding soil at slightly larger depth than the foundation tip.

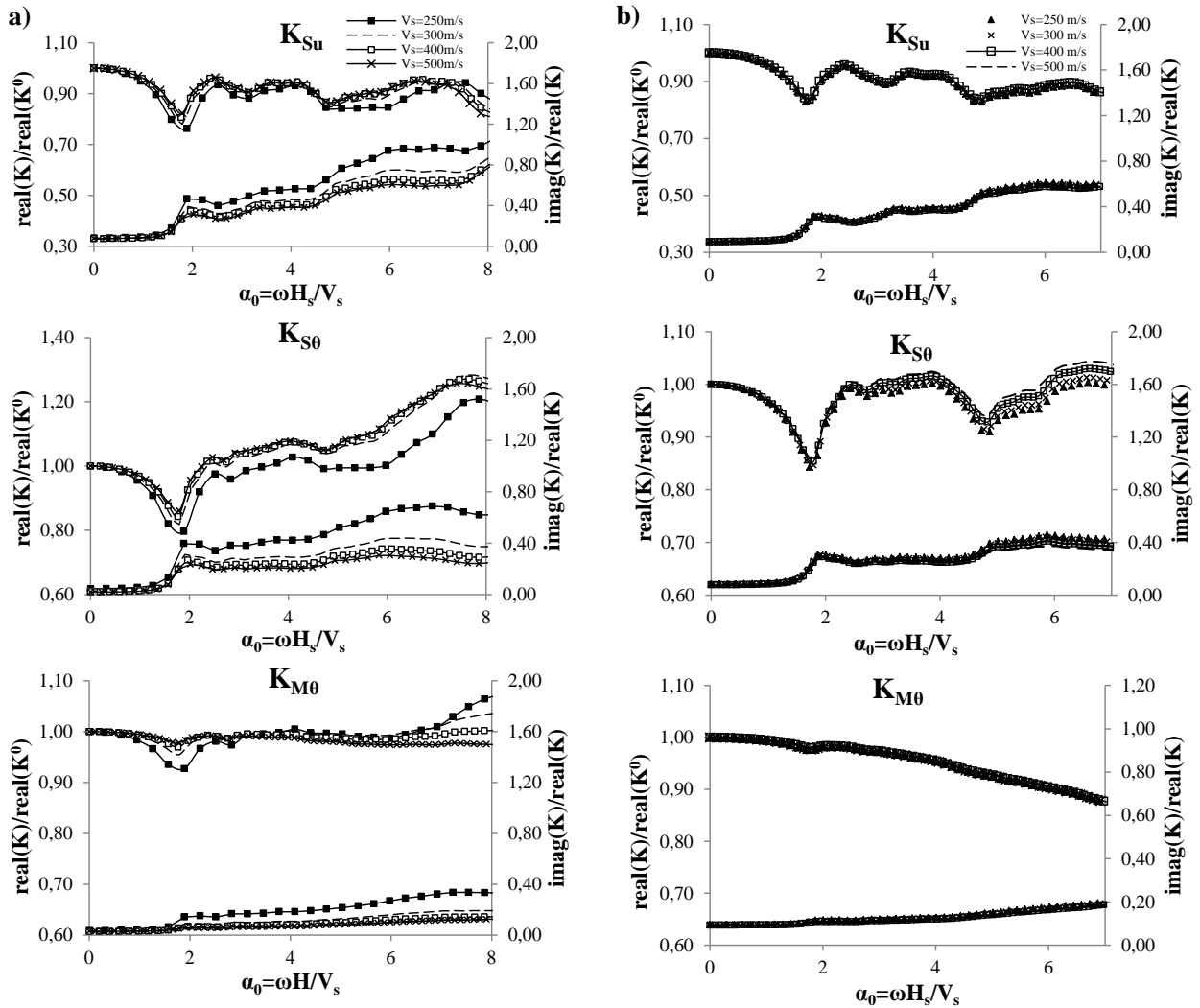


Figure 4.18: Variation of the three dynamic stiffness coefficients with respect to the non-dimensional frequency. Effect of the stiffness of homogeneous soil layer (profile A) on the real component and the imaginary component for $H_p/d = 2$ a) and for $H_p/d = 0.25$ b). Modified after *Paper III*.

Figure 4.19 and 4.20 show the effect of the stiffness variation with depth respectively for profiles

B and C. The findings are illustrated with respect to the frequency normalised by the fundamental resonant frequency of the homogeneous soil layer, f_{1st} (4.17 Hz). The drop of stiffness at $f = 0.92f_{1st}$ (profile B) and $0.76f_{1st}$ (profile C) was depicted for all the stiffness coefficients. Note that the 1st resonance of inhomogeneous soil profiles is slightly shifted back from the 1st eigenfrequency of the homogeneous layer. Additionally, it is in agreement with that calculated according to analytical solutions (Rovithis et al. (2011)). After the 1st resonance a decreasing trend was observed for the lateral stiffness coefficient, whereas the slope decreased for higher value of the slenderness ratio H_p/d both for profiles B and C, with profile C attaining larger slope decrease. When it comes to the coupling and rocking stiffness term, a fairly constant pattern particularly was observed for larger slenderness ratios and for profile B. On the other hand, the same stiffness coefficients of the caisson with shorter skirt length exhibited a monotonous decreasing pattern after the 1st resonance in the case of profile C.

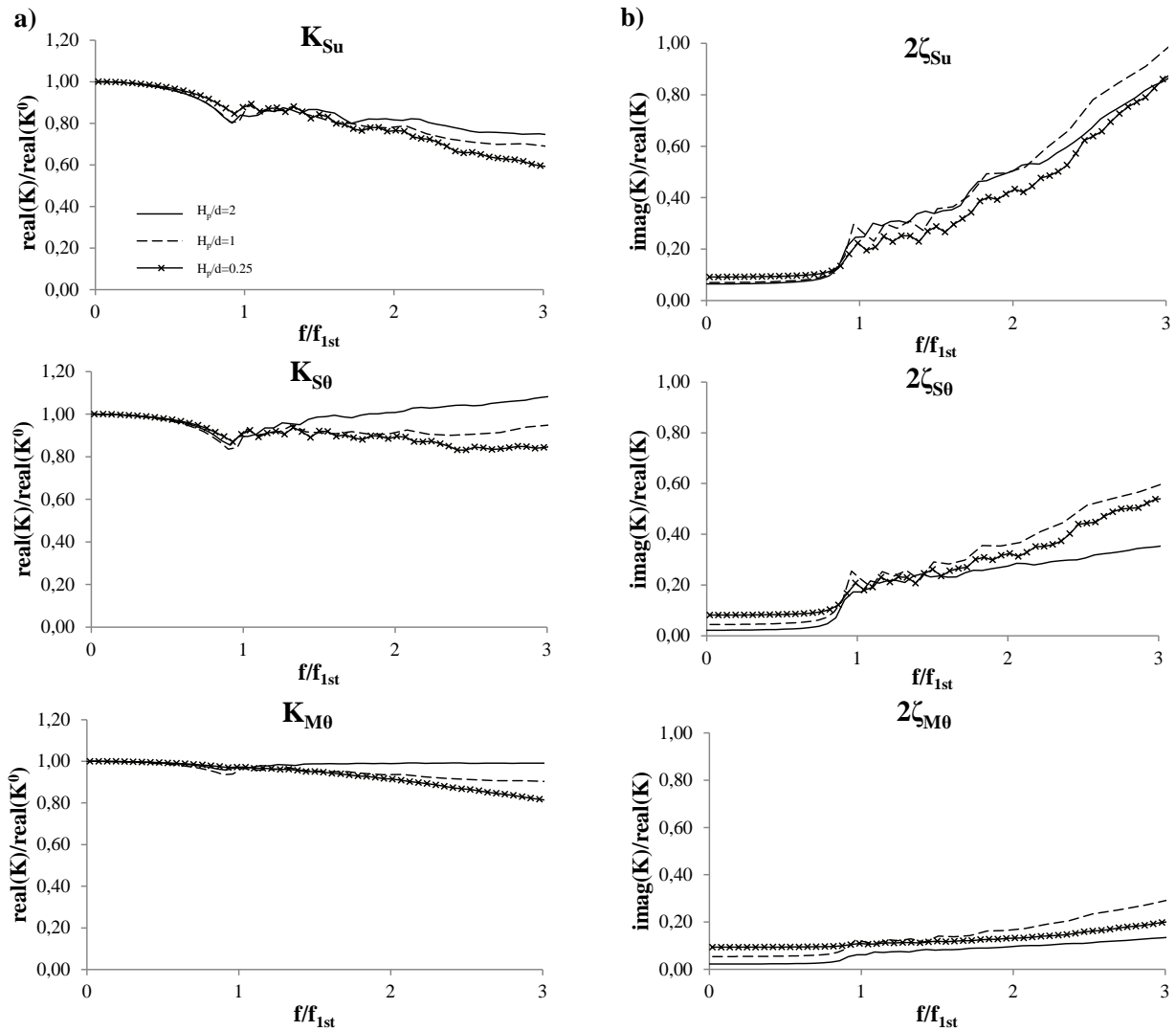


Figure 4.19: Variation of the three dynamic stiffness and damping coefficients with respect to the non-dimensional frequency. Effect of slenderness ratio in the inhomogeneous soil layer (profile B) on the real component a) and the imaginary component b). Modified after *Paper III*.

The imaginary part of the dynamic impedances gives an insight of the generated damping due to soil-caisson interaction. The damping ratio for both profiles at the lower frequency range increased for decreasing slenderness ratio. Looking at the results of profile C it was observed an exponential rather than a linear trend for frequencies higher than the 1st resonance and particularly

for $H_p/d = 0.25$. The sensitivity of the dynamic impedances on the variation of E_s in the high frequency range has been previously observed for end bearing piles (Gazetas (1984))**. Furthermore, Figure 4.20 highlights that the stronger the variation of E_s with respect to depth the higher is the reduction in dynamic stiffness after the 1st eigenfrequency of the soil medium. Moreover, this pattern is further emphasized by decreasing the slenderness ratio. Therefore, it can be concluded that the type of variation of soil modulus with depth influenced significantly the dynamic behaviour of suction caissons, especially at high frequencies.

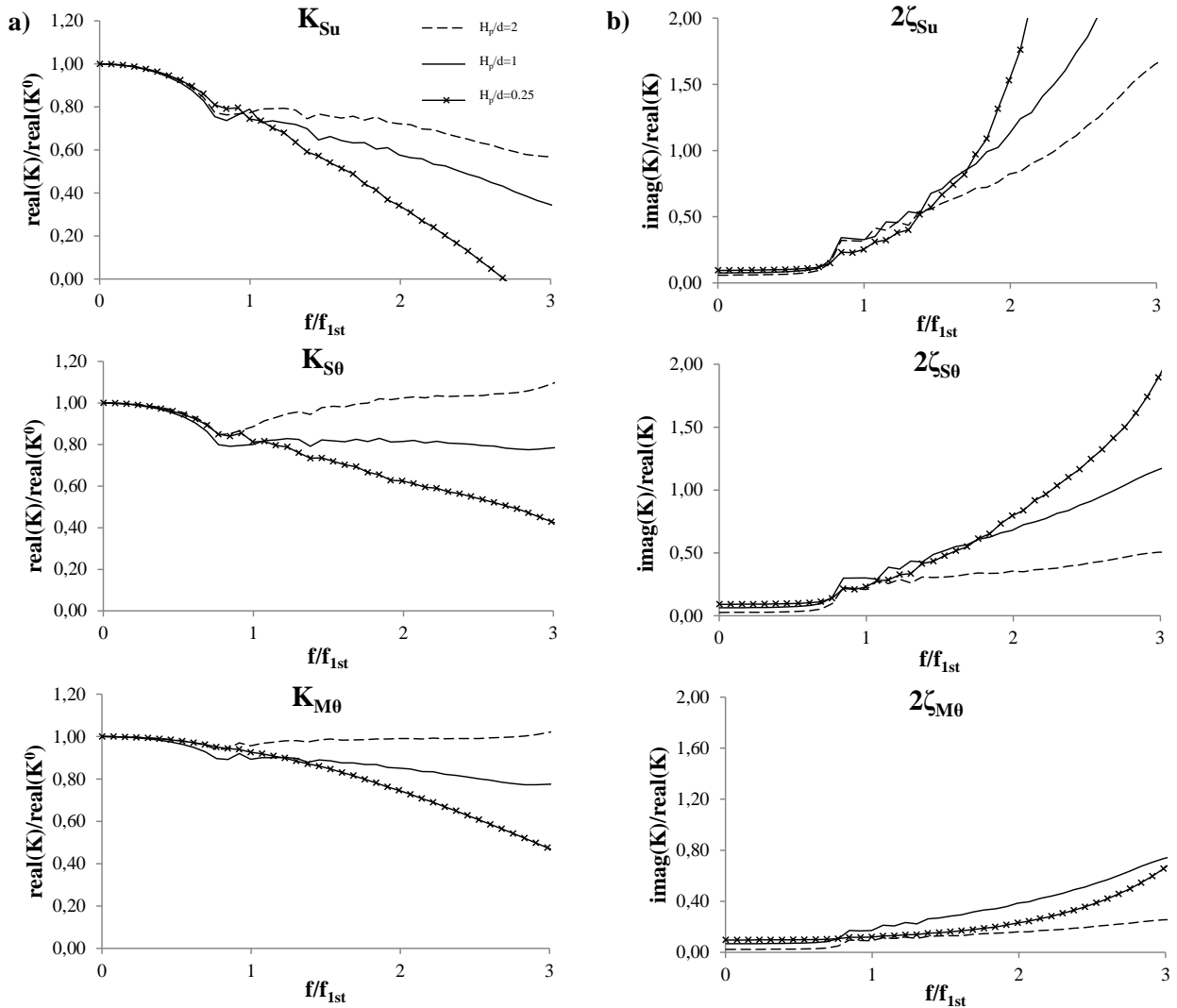


Figure 4.20: Variation of the three dynamic stiffness and damping coefficients with respect to the non-dimensional frequency. Effect of slenderness ratio in the inhomogeneous soil layer (profile C) on the real component a) and the imaginary component b). Modified after *Paper III*.

4.1.5 Suggested expressions

In this paragraph simplified mathematical expressions of the real and imaginary part of the dynamic impedances are developed in order to provide closer approximations of the numerical results:

$$K(\alpha_0) = 1 - \frac{c_{1,r}\alpha_0^2}{1 + c_{2,r}(\alpha_0 - c_{4,r}\alpha_{1st})^2} + c_{3,r}(\alpha_0 - c_{5,r}\alpha_{1st})^2 \quad (4.6)$$

$$2\zeta(\alpha_0) = c_{0,i} + \frac{c_{1,i}\alpha_0^2}{[1 + c_{1,i}(\alpha_0 - c_{4,i}\alpha_{1st})]^2} + \frac{c_{2,i}(\alpha_0 - c_{4,i}\alpha_{1st})^2}{[1 + c_{3,i}(\alpha_0 - c_{5,i}\alpha_{1st})]} \quad (4.7)$$

where $c_{j,r}$ and $c_{j,i}$ with $j = 0, \dots, 5$ are the coefficients for the real and imaginary component, respectively. Note that the dimensionless frequency α_0 in the abovementioned formulas is calculated by adopting the base shear wave velocity ($500m/s$) for the case of inhomogeneous soil profiles. In the proposed study the calibration of the coefficients was based on the selection of numerical cases that demonstrate characteristic behaviour and they were representative for the parametric study^{***}. The coefficients $c_{j,r}$ and $c_{j,i}$ were derived for a frequency range, pertaining to wind/wave loading, see Table 4.7, 4.8 and 4.9. In offshore applications the frequency range of interested can be narrowed up to the 1st horizontal resonance of the soil (Damgaard et al. (2014), Bhattacharya et al. (2013)). Table 4.7, 4.8 and 4.9 illustrate the percentage of the average relative error (ϵ_{mean}) and the maximum relative error (ϵ_{max}) of the suggested expressions with respect to the numerical outcomes in the frequency intervals considered, which gives an indication of the accuracy of the present functions. In Figure 4.21 the comparison between the proposed expression and the numerical results of the real and imaginary component of the dynamic impedances for different cases is presented in the frequency range $[0; 1/2\pi]$. It was observed good agreement between the real component of the dynamic lateral impedances (Figure 4.21a), achieved by the proposed function, and the numerical results for suction caissons with slenderness ratio $H_p/d = 2$ and $H_p/d = 0.25$, respectively. Indeed, an average discrepancy of less than 4% for suction caisson with $H_p/d = 2$ and less than 2% for $H_p/d = 0.25$ was recorded between the abovementioned solutions; whereas a maximum difference of 5.8% and 3.3% was found. With reference to the imaginary part (Figure 4.21b) the suggested expression provided relatively scattered results with respect to the numerical outcomes (average relative error less than 7.5%) for suction caisson with slenderness ratio of $H_p/d = 2$ and 0.25. Even though it was found that the maximum error of the imaginary component is generally smaller than 25%, a maximum error of 29% in the coupling component of the dynamic impedances was attained for suction caisson with slenderness ratio of $H_p/d = 0.25$.

Figure 4.22a and 4.22b show that the real and imaginary component of the lateral dynamic impedances calculated by the suggested expression resembles the ones obtained by the numerical model for suction caissons embedded in a soil layer with relative thickness $H_s/d = 30 - 15$. An average difference of less than 2% was observed for the real part of all dynamic stiffness coefficients; whereas the radiation damping exhibited values which differed less than 10% with respect to the numerical ones.

In the case of stiff soil layer ($V_s = 250m/s$) the real part of the coupling and rocking stiffness coefficient determined by the proposed formula approximates slightly better the numerical outcomes than for the case of medium stiff soil profile as illustrated in Figure 4.23a. This was demonstrated by the fact that the average and the maximum relative error reached small values (1.57% and 0.31%, respectively), while the opposite holds for the horizontal coefficient. Additionally, an increase of the average and the maximum relative error was recorded for the imaginary component of the dynamic impedances of the suction caisson embedded in stiff soil profile.

Table 4.7: Constants of the suggested expression for the dynamic horizontal stiffness and damping coefficient in the dimensionless frequency range $\alpha_0 \in [0; 3]$.

Case Nr.	Real component (K_{Su})					Imaginary component ($2\zeta_{Su}$)									
	$c_{1,r}$	$c_{2,r}$	$c_{3,r}$	$c_{4,r}$	$c_{5,r}$	ϵ_{max} (%)	ϵ_{mean} (%)	$c_{0,i}$	$c_{1,i}$	$c_{2,i}$	$c_{3,i}$	$c_{4,i}$	$c_{5,i}$	ϵ_{max} (%)	ϵ_{mean} (%)
1	0.086	8.5	0	1.065	0	4.2	3.2	0.048	0.0350	0.50	10	0.75	1.15	25.0	7.4
						$\alpha_0 = 1.18$								$\alpha_0 = 2.59$	
5	0.065	9.5	0	1.060	0	3.1	1.8	0.062	0.0250	0.70	14	0.83	1.08	13.3	6.1
						$\alpha_0 = 2.00$								$\alpha_0 = 2.72$	
9	0.041	17	0	1.000	0	3.6	0.8	0.080	0.0075	0.20	11	0.75	1.10	17.7	5.3
						$\alpha_0 = 3.12$								$\alpha_0 = 1.97$	
10	0.030	15	0	1.000	0	4.2	1.7	0.070	0.0100	0.20	10	0.70	1.10	21.5	1.9
						$\alpha_0 = 3.12$								$\alpha_0 = 1.97$	
14	0.070	12	0	1.060	0	4.4	3.3	0.050	0.0200	0.60	12	0.80	1.10	16.9	7.4
						$\alpha_0 = 1.10$								$\alpha_0 = 1.24$	
21	0.084	18	-0.024	0.87	0	7.3	1.3	0.050	0.0100	0.15	1.2	0.41	1.10	25.2	12.4
						$\alpha_0 = 3.00$								$\alpha_0 = 1.43$	
23	0.045	18	-0.030	0.89	0	13.6	3.0	0.080	0.0100	0.10	1.6	0.40	1.10	84.0	13.4
						$\alpha_0 = 2.77$								$\alpha_0 = 1.68$	
24	0.130	6.1	-0.023	0.71	0	9.7	2.2	0.055	0.0100	0.09	0.1	0.20	1.00	27.7	22.7
						$\alpha_0 = 2.04$								$\alpha_0 = 1.33$	
26	0.080	7	-0.070	0.60	0	8.1	2.4	0.080	0.0090	0.11	0.02	0.10	3.00	38.4	12.3
						$\alpha_0 = 2.17$								$\alpha_0 = 1.08$	

Table 4.8: Constants of the suggested expression for the dynamic coupling stiffness and damping coefficient in the dimensionless frequency range $\alpha_0 \in [0; 3]$.

Case	Real component ($K_{S\theta}$)					Imaginary component ($2\zeta_{S\theta}$)									
	$c_{1,r}$	$c_{2,r}$	$c_{3,r}$	$c_{4,r}$	$c_{5,r}$	ϵ_{max} (%)	ϵ_{mean} (%)	$c_{0,i}$	$c_{1,i}$	$c_{2,i}$	$c_{3,i}$	$c_{4,i}$	$c_{5,i}$	ϵ_{max} (%)	ϵ_{mean} (%)
1	0.060	9	0	1.07	0	5.8	3.6	0.015	0.025	0.50	12	0.75	1.15	14.5	4.1
5	0.052	10	0	1.06	0	$\alpha_0 = 1.18$ 3.3	1.34	0.062	0.025	0.7	14	0.83	1.08	$\alpha_0 = 1.65$ 19.5	4.5
9	0.016	10	0.004	1.00	0	$\alpha_0 = 2.29$ 2.29	0.55	0.025	0.0060	0.10	20	0.90	1.10	$\alpha_0 = 1.72$ 38.0	9.7
10	0.075	7	0.011	0.97	0	$\alpha_0 = 3.00$ 2.38	1.02	0.016	0.0180	0.25	6	0.70	1.14	$\alpha_0 = 3.00$ 19.4	9.3
14	0.061	8	0.010	1.05	0	$\alpha_0 = 0.99$ 3.50	1.57	0.001	0.0180	0.50	12	0.80	1.10	$\alpha_0 = 1.40$ 19.9	7.4
21	0.070	14	0	0.89	0	$\alpha_0 = 1.12$ 2.50	0.97	0.010	0.005	0.09	1.2	0.30	1.05	$\alpha_0 = 3.00$ 49.6	14.8
23	0.052	18	-0.014	0.89	0	$\alpha_0 = 1.00$ 4.50	1.04	0.070	0.010	0.09	1.6	0.41	0.99	$\alpha_0 = 1.28$ 19.2	7.9
24	0.089	14	-0.005	0.78	0	$\alpha_0 = 3.00$ 7.90	1.52	0.030	0.004	0.09	1.1	0.20	1.10	$\alpha_0 = 1.55$ 48.8	12.2
26	0.076	18	-0.040	0.78	0	$\alpha_0 = 2.90$ 5.20	1.71	0.080	0.003	0.10	0.03	0.15	3.00	$\alpha_0 = 1.33$ 21.7	9.0
						$\alpha_0 = 2.17$								$\alpha_0 = 1.08$	

Table 4.9: Constants of the suggested expression for the dynamic rocking stiffness and damping coefficient in the dimensionless frequency range $\alpha_0 \in [0; 3]$.

Case Nr.	Real component ($K_M\theta$)					Imaginary component ($2\zeta_M\theta$)									
	$c_{1,r}$	$c_{2,r}$	$c_{3,r}$	$c_{4,r}$	$c_{5,r}$	ϵ_{max} (%)	ϵ_{mean} (%)	$c_{0,i}$	$c_{1,i}$	$c_{2,i}$	$c_{3,i}$	$c_{4,i}$	$c_{5,i}$	ϵ_{max} (%)	ϵ_{mean} (%)
1	0.020	9	0	1.06	0	1.06	0.6	0.025	0.010	0.14	12	0.85	1.15	11.2	3.6
						$\alpha_0 = 1.18$								$\alpha_0 = 3.00$	
5	0.010	10	0	1.06	0	2.30	0.40	0.086	0.085	0.08	35	0.83	0.90	29.0	6.7
						$\alpha_0 = 3.00$								$\alpha_0 = 3.00$	
9	0.010	13	0	1.00	0	0.75	0.17	0.030	0.0050	0.07	30	0.75	1.10	23.2	4.7
						$\alpha_0 = 1.85$								$\alpha_0 = 3.00$	
10	0.018	9	0	0.98	0	0.61	0.22	0.026	0.0075	0.10	12	0.75	1.10	7.8	5.6
						$\alpha_0 = 1.07$								$\alpha_0 = 0.33$	
14	0.010	9	0	1.06	0	0.71	0.31	0.025	0.005	0.14	35	0.92	1.07	18.5	7.0
						$\alpha_0 = 1.91$								$\alpha_0 = 3.00$	
21	0.018	17	-0.0015	0.87	0	0.71	0.34	0.018	0.010	0.14	30	0.80	0.98	21.7	9.3
						$\alpha_0 = 3.00$								$\alpha_0 = 3.00$	
23	0.008	20	-0.0080	0.87	0	0.66	0.20	0.086	0.008	0.08	35	0.83	0.98	27.4	5.6
						$\alpha_0 = 2.80$								$\alpha_0 = 3.00$	
24	0.015	20	-0.0050	0.80	0	3.06	2.39	0.018	0.008	0.09	30	1.00	0.90	65.7	17.4
						$\alpha_0 = 2.40$								$\alpha_0 = 2.20$	
26	0.015	20	-0.0070	0.60	0	2.14	0.42	0.090	0.008	0.09	15	1.00	0.90	22.8	8.5
						$\alpha_0 = 2.17$								$\alpha_0 = 3.00$	

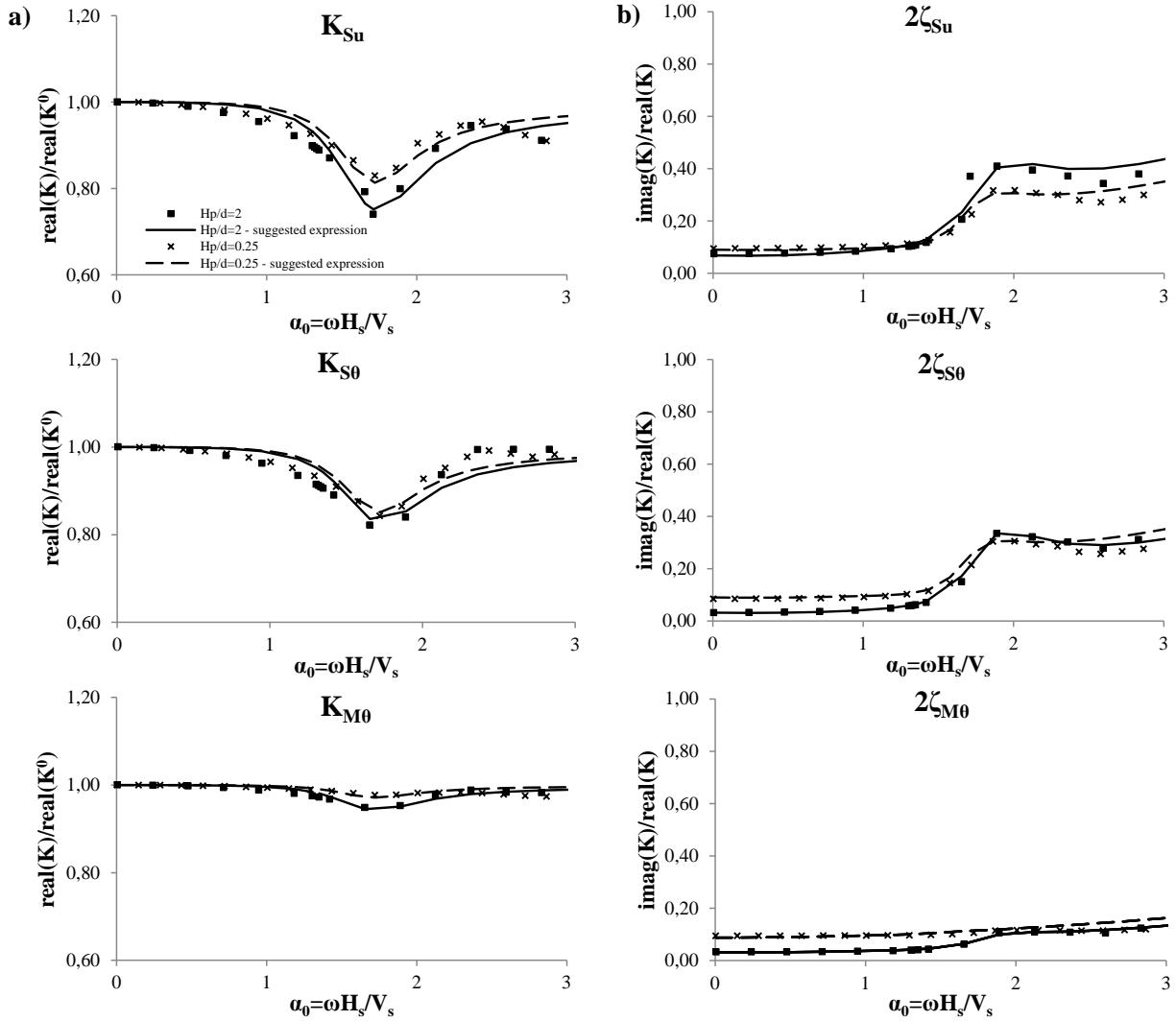


Figure 4.21: Comparison between the simplified expression and the numerical outcomes with respect to the non-dimensional frequency. Effect of the skirt length on the real component a) and the imaginary component b).

The dynamic impedances of suction caissons embedded in inhomogeneous soil profile B and C estimated by Equation 4.6 and 4.7 is presented in Figure 4.24 and 4.25. The real part of the dynamic impedance for both profile B and C does not overcome precisely the numerical results more than 3%. On the other hand, the inhomogeneity of the soil layer determined a more significant effect on the imaginary component, since the average relative error reached up to 15% for profile B; whereas the discrepancy is appreciably less than 25% in the case of suction caisson embedded in profile C. The maximum relative error calculated for the imaginary part is considerably high, even if it is attained for few values in the frequency range ($\alpha_0 = 1 - 1.7$) where the numerical results are characterized by a peak, which cannot be captured by the suggested expression. In light of these results, it is clearly outlined that the average discrepancy between the real component calculated by the proposed expression and those of the numerical model is less than 4%, while the maximum relative error does not overcome 6% for all the components (case 1,5,9,10 and 14). Furthermore the average relative error referred to the imaginary component assumed values lower than 10% for all the coefficients. Finally, it can be concluded that the proposed expressions provide a fairly good approximation of dynamic stiffness of suction caissons for the frequency interval examined.

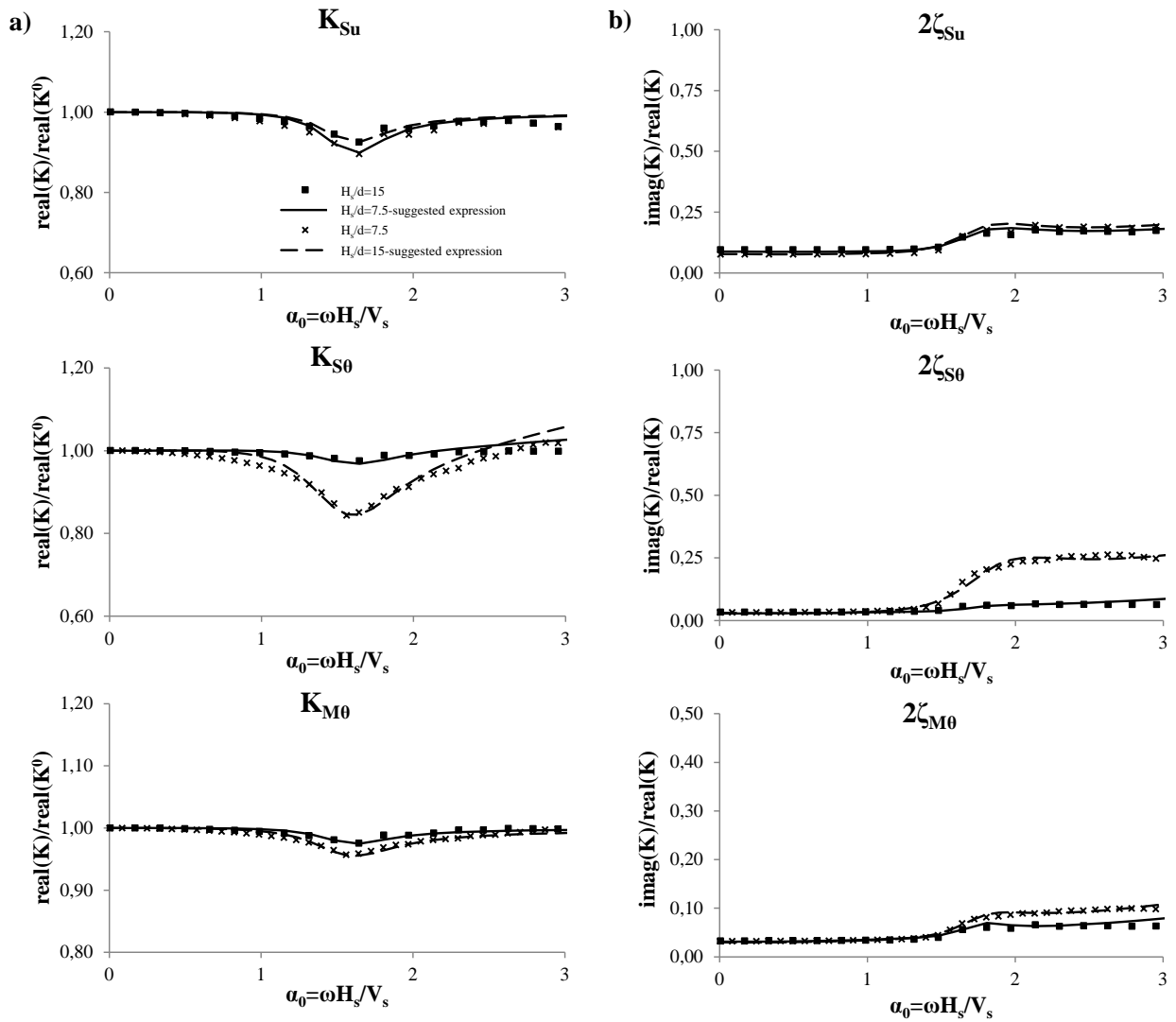


Figure 4.22: Comparison between the simplified expression and the numerical outcomes with respect to the non-dimensional frequency. Effect of the relative thickness of the soil layer on the real component a) and the imaginary component b) for $H_p/d = 2$ and $H_p/d = 0.25$.

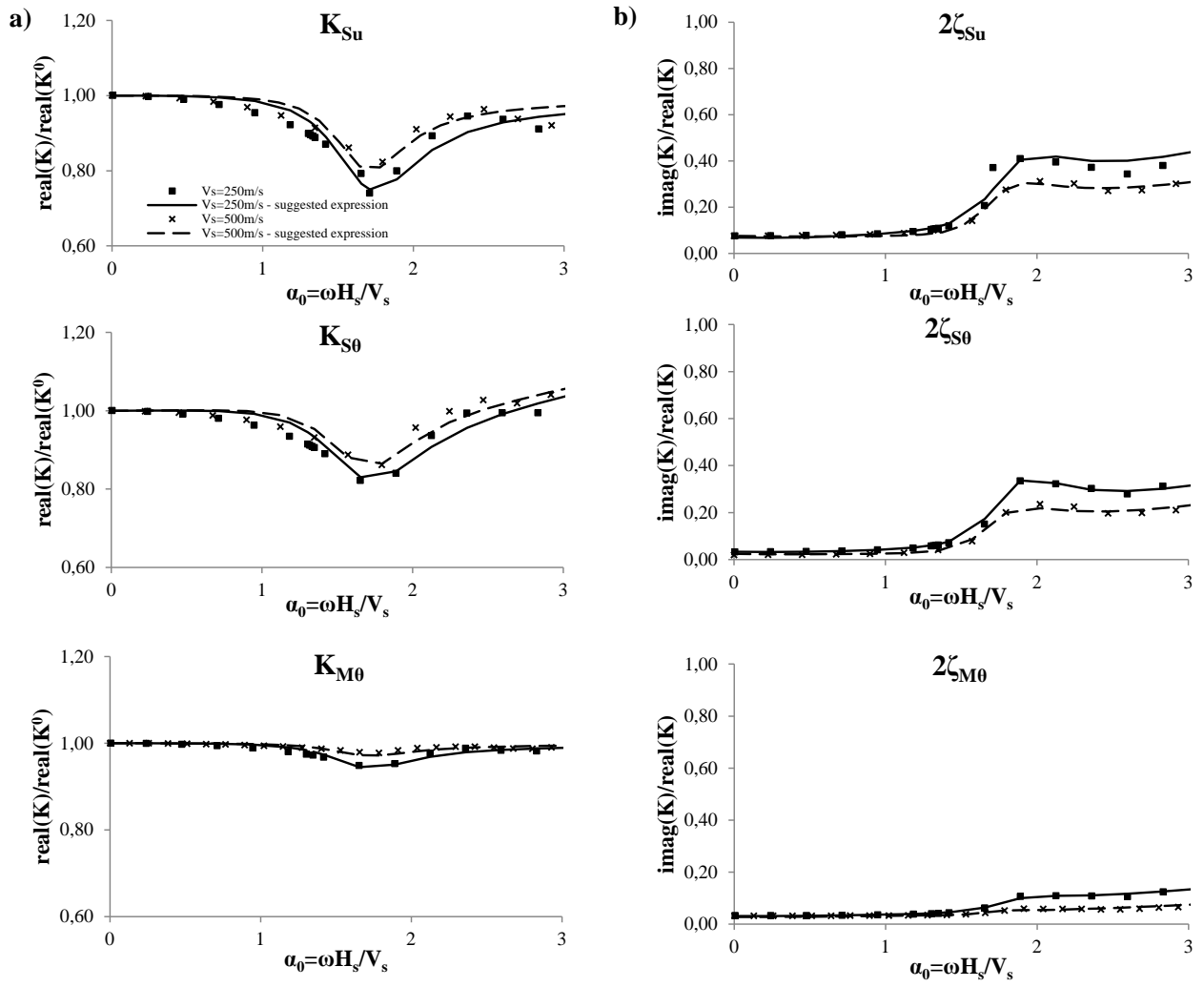


Figure 4.23: Comparison between the simplified expression and the numerical outcomes with respect to the non-dimensional frequency. Effect of the stiffness of the soil layer (profile A) on the real component a) and the imaginary component b) for $H_p/d = 2$ and $H_p/d = 0.25$.

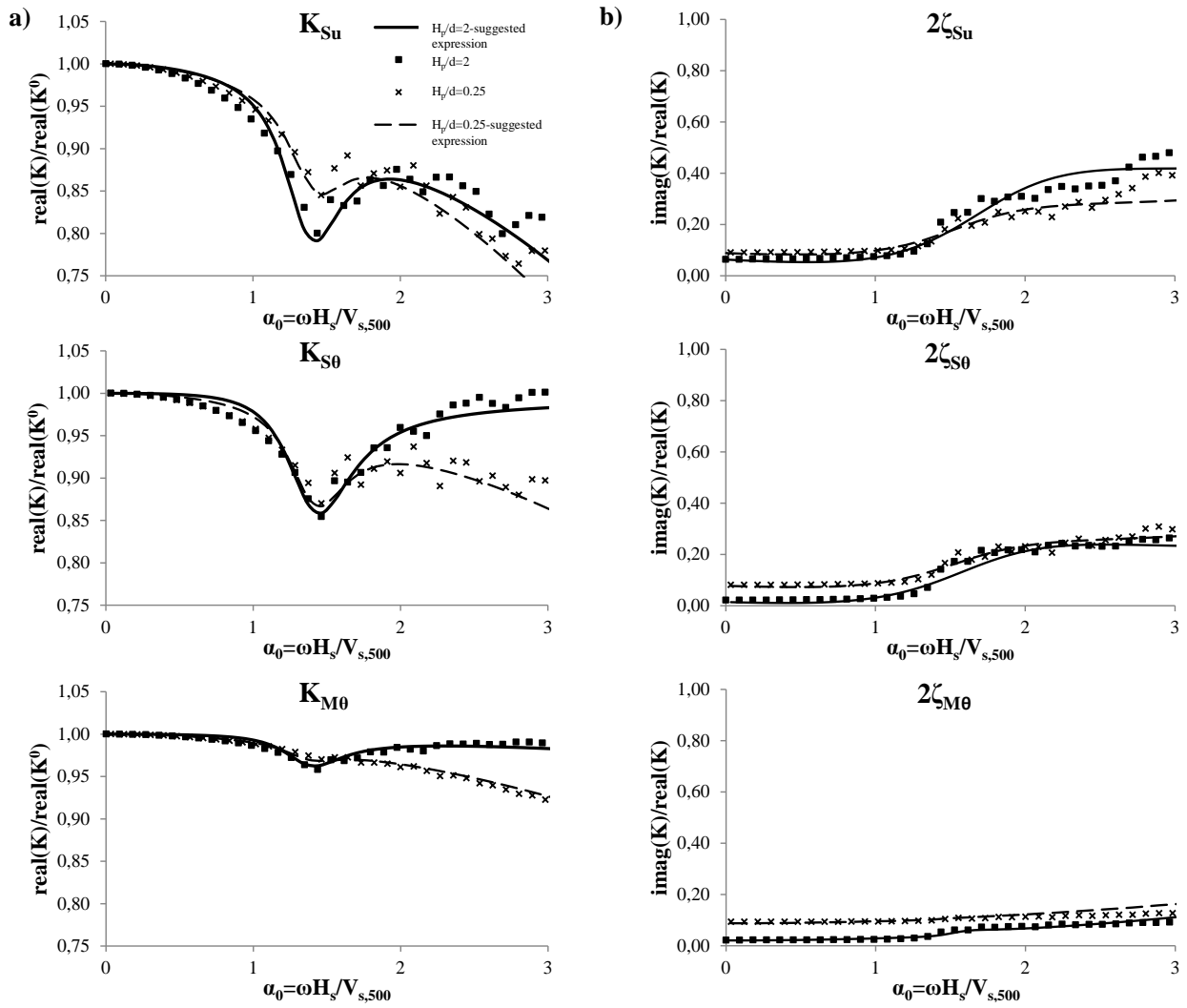


Figure 4.24: Comparison between the simplified expression and the numerical outcomes with respect to the non-dimensional frequency. Effect of the stiffness of the soil layer (profile B) on the real component a) and the imaginary component b) for $H_p/d = 2$ and $H_p/d = 0.25$.

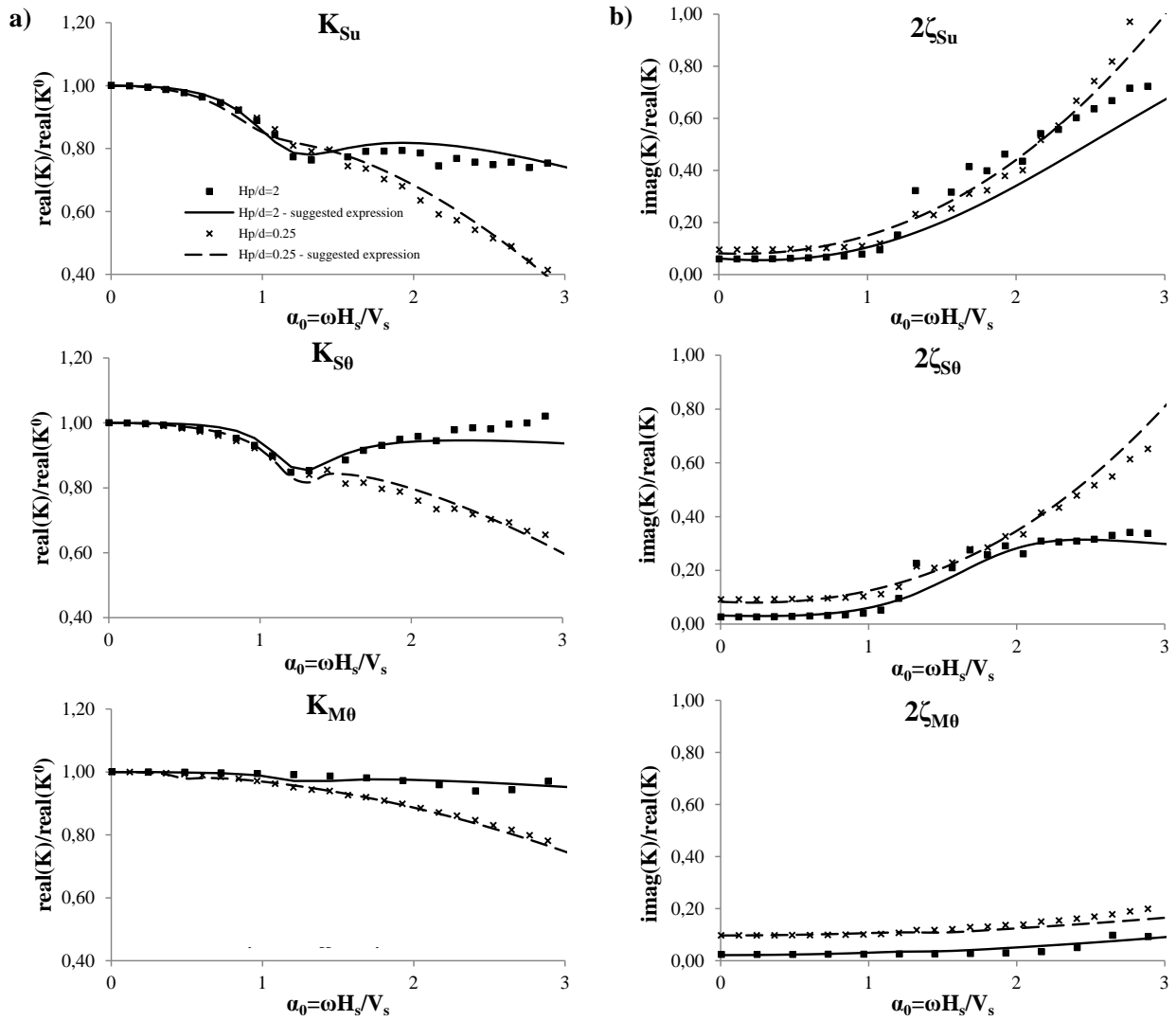


Figure 4.25: Comparison between the simplified expression and the numerical outcomes with respect to the non-dimensional frequency. Effect of the stiffness of the soil layer (profile C) on the real component a) and the imaginary component b) for $H_p/d = 2$ and $H_p/d = 0.25$.

4.2 Vertical dynamic response of suction caissons

This section focuses on the dynamic response of suction caissons subjected to vertical loading. The type of profiles (profile 1 and 2) shown in Figure 4.1 are considered for the estimation of the vertical dynamic stiffness and damping coefficients of suction caissons.

4.2.1 Analytical approach

Due to the absence in the literature of analytical solutions on the dynamic response of suction caissons embedded in a soil layer on rigid bedrock, the analytical solution of Nogami and Novak (1976) discussed in Section 3.2.1 is adopted for the dynamic analysis of suction caissons in profile 1. It is worth mentioning that an equivalent cross section, which matches the axial stiffness of the hollow section of the suction caisson, was considered in the analytical formulation. Moreover, the analytical formulation does not indeed account for the presence of the foundation lid (top plate). However, its effect on the dynamic impedances was proved to be marginally as discussed in Section 4.2.2.1. In regards with profile 2 only the static stiffness coefficient was calculated analytically according to the formulation of Wolf and Deeks (2004) and Gelagoti et al. (2015).

4.2.2 Numerical approach

The numerical methodology described in Section 3.1.2.1 is taken into account for the estimation of the vertical dynamic stiffness and damping coefficients of suction caissons. The effect of different foundation modelling on the vertical dynamic impedance is also assessed.

4.2.2.1 Modelling aspects

Foundation modelling Previous studies have examined the influence of the inner soil on the vertical dynamic response of piles (Zheng et al. (2014), Liu et al. (2014), Latini et al. (2016b)). Particularly, the works of Zheng et al. (2014) and Liu et al. (2014) showed that the interaction between the pile and the inner soil when dynamic loading is applied, determined a significantly increase of the oscillation amplitudes at resonance frequencies in the high frequency interval. While Latini et al. (2016b) showed that the influence of the inner soil on the vertical dynamic response becomes more apparent for frequencies higher than $\alpha_0 = 8$. Hence, the effect of the soil within the foundation is also analysed for suction caissons by implementing the three modelling approaches (Figure 4.2).

Firstly the vertical static stiffness of suction caisson embedded in profile 1 is calculated at the low frequencies and the results are listed in Table 4.10.

Table 4.10: Static stiffness of suction caisson embedded in profile 1 obtained from different foundation methodologies.

Reference	Caisson	Shell pile	Equivalent solid pile
$K_V/(E_s d)$	13.83	15.04	14.02

Similar values of the vertical static stiffness coefficient were obtained for the equivalent solid pile and the suction caisson; whereas the discrepancy with respect to the results of the shell pile is less than 8%. Figure 4.26 displays the real (K_V) and the imaginary ($2\zeta_V$) part of the vertical dynamic stiffness for different foundation modellings embedded in profile 1. The numerical results of the suction caisson and the shell pile matched up to approximately $\alpha_0 = 6$; while the equivalent solid pile clearly exhibited more rigid behaviour than the shell pile and the suction caisson for frequency higher than the 1st vertical resonance.

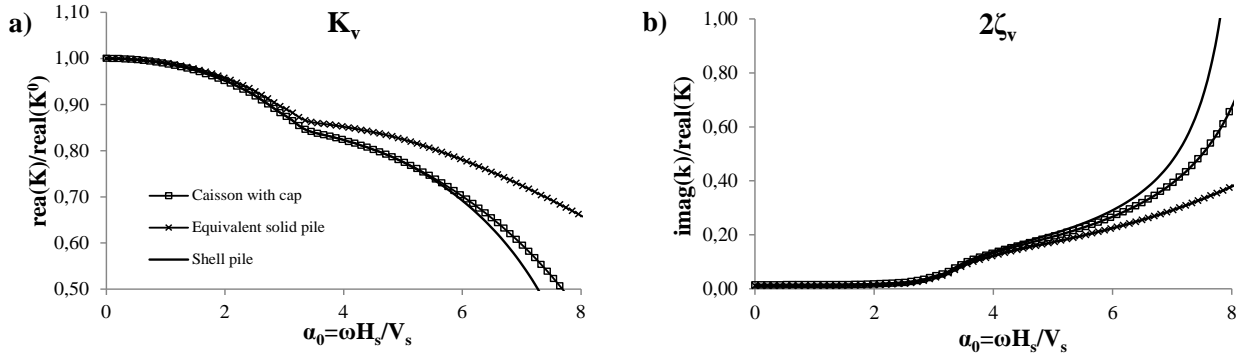


Figure 4.26: Variation of the vertical dynamic stiffness and damping coefficients with respect to the non-dimensional frequency. Effect of the foundation geometry on the real component a) and the imaginary component b) for profile 1.

In regards with profile 2 the vertical static stiffness for the three foundation modellings is listed in Table 4.11. It is evident that the suction caisson and the equivalent solid pile practically attained the same value of the static stiffness, while a discrepancy of less than 1% was estimated with respect to the shell pile. Concerning the dynamic response (Figure 4.27), the numerical outcomes of three modellings approaches match almost perfectly up to $\alpha_0 = 8$. It appears that the presence of the inner soil influenced to some extent the vertical dynamic response of the foundation in the high frequency range. This effect visible in the high frequency interval might also be due to the fact that hysteretic type damping is applied to the soil within the skirts of the caisson with cap and shell pile model.

Table 4.11: Static stiffness of suction caisson embedded in profile 2 obtained from different foundation methodologies.

Reference	Caisson	Shell pile	Equivalent solid pile
$K_V / (E_s d)$	1.57	1.58	1.57

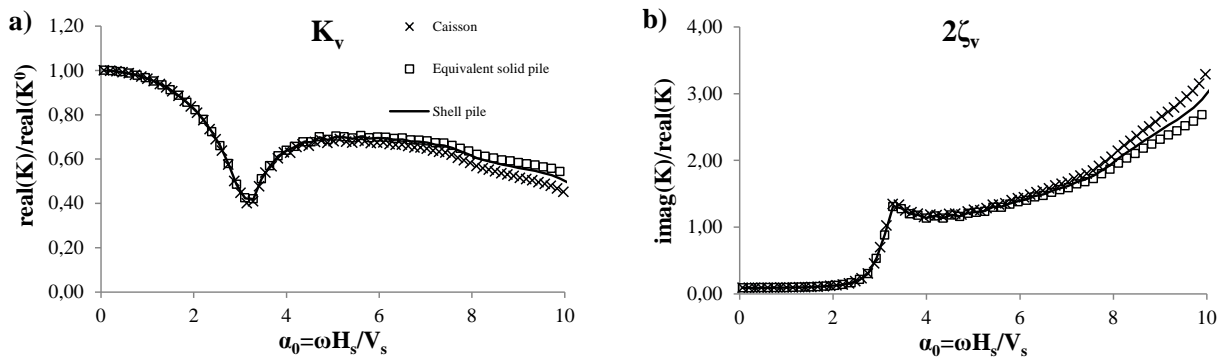


Figure 4.27: Variation of the vertical dynamic stiffness and damping coefficients with respect to the non-dimensional frequency. Effect of the foundation geometry on the real component a) and the imaginary component b) for profile 2. Modified after *Paper V*.

4.2.3 Validation of the numerical model

Profile 1 The static stiffness coefficient of the numerical model was determined at low frequencies and presented in Table 4.12, along with the corresponding analytical value.

Reference	Nogami and Novak (1976)	Equivalent solid pile
$K_V/(E_s d)$	13.92	14.02

Table 4.12: Static stiffness of suction caisson embedded in profile 1 obtained from the numerical model and the analytical solution of Nogami and Novak (1976).

Figure 4.28 illustrates the real (K_V) and the imaginary ($2\zeta_V$) part of the dynamic vertical impedance with respect to the non-dimensional frequency α_0 . It was found that the numerical results matched almost perfectly with the one proposed by the analytical solution regarding the static and dynamic term.

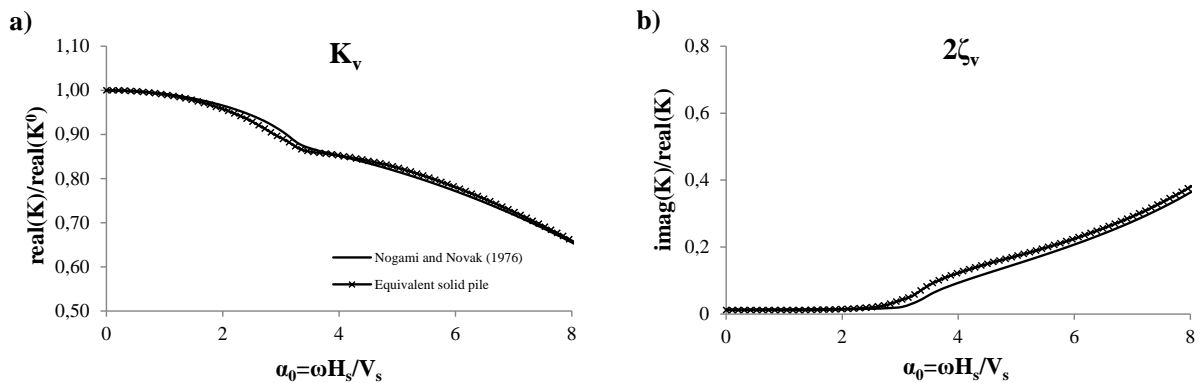


Figure 4.28: Variation of the vertical stiffness a) and damping coefficients b) with respect to the non-dimensional frequency for profile 1.

Profile 2 In this study the numerical outcomes of the static impedance were initially compared respectively with Wolf and Deeks (2004) and Gelagoti et al. (2015), see Figure 4.29. As mentioned in Section 4.1.4.1, both the analytical expressions of Wolf and Deeks (2004) and Gelagoti et al. (2015) are referred to shallow foundations embedded in a halfspace. Moreover, the formula suggested by Wolf and Deeks (2004) was derived by deploying the cone model and it can be applied to foundations with slenderness ratio less than 1.

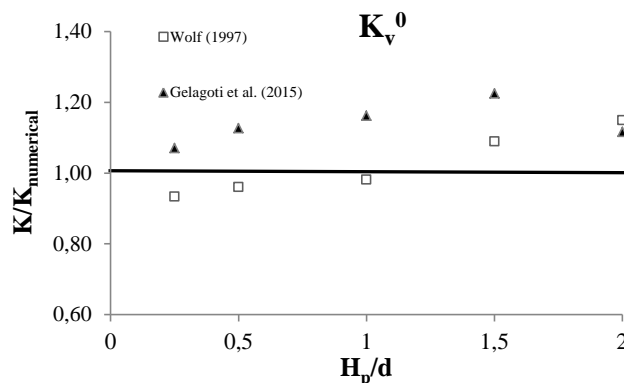


Figure 4.29: Comparison of the vertical static stiffness component given by the numerical model and two analytical expressions.

While the range of applicability of the expression proposed by Gelagoti et al. (2015) is up to $H_p/d = 1.5$. The comparison highlighted that the numerical results and the expressions given by Wolf and Deeks (2004) were in good agreement as far as the foundation has slenderness equal to 1. Particularly, the numerical outcomes were slightly overestimated by the formula given by Gelagoti et al. (2015).

4.2.4 Parametric study

The dynamic response of suction caissons is influenced by several parameters. Hereafter, the role of the slenderness ratio (H_p/d) and the soil profile (ν , E_p/E_s , H_s/d) on the dynamic response of the suction caisson in the frequency domain was analysed; all the cases investigated are shown in Table 4.13. Three soil profiles were considered in order to address the effect of soil inhomogeneity, each with a different distribution of $E_s(z)$ with depth as performed for the lateral dynamic response of suction caissons. The hysteretic material damping ($\beta = 5\%$) and Poisson's ratio ($\nu = 0.35$) were identical for all the examined cases.

Table 4.13: Dimensionless parameters and cases selected in the parametric analysis for suction caisson.

Case Nr.	H_s	H_p	d	ν	H_p/d	H_s/d	Soil Profile				E_p/E_s
							Type	n	V_H	V_0/V_H	
	[m]	[m]	[m]								
1	30	10	5	0.35	2	6	A	1	250	1	30
2	30	7.5	5	0.35	1.5	6	A	1	250	1	30
3	30	5	5	0.35	1	6	A	1	250	1	30
4	30	2.5	5	0.35	0.5	6	A	1	250	1	30
5	30	1.25	5	0.35	0.25	6	A	1	250	1	30
6	30	10	5	0.10	2	6	A	1	250	1	37
7	30	10	5	0.20	2	6	A	1	250	1	34
8	30	10	5	0.40	2	6	A	1	250	1	29
9	30	10	5	0.495	2	6	A	1	250	1	27
10	30	10	5	0.35	2	6	A	1	300	1	21
11	30	10	5	0.35	2	6	A	1	400	1	12
12	30	10	5	0.35	2	6	A	1	500	1	8
13	30	10	5	0.35	2	6	B	0.25	500	0.01	8
14	30	5	5	0.35	1	6	B	0.25	500	0.01	8
15	30	1.25	5	0.35	0.25	6	B	0.25	500	0.01	8
16	30	10	5	0.35	2	6	C	0.5	500	0.1	8
17	30	5	5	0.35	1	6	C	0.5	500	0.1	8
18	30	1.25	5	0.35	0.25	6	C	0.5	500	0.1	8
19	30	10	5	0.40	2	6	A	1	250	1	29
				No U1							
20	30	10	5	0.495	2	6	A	1	250	1	27
				No U1							
21	30	10	5	0.40	2	6	A	1	250	1	29
				No U1,U2							
22	30	10	5	0.495	2	6	A	1	250	1	27
				No U1,U2							
23	30	0.50	2	0.35	0.25	15	A	1	250	1	30
24	30	4	2	0.35	2	15	A	1	250	1	30
25	30	1.00	4	0.35	0.25	7.5	A	1	250	1	30
26	30	8	4	0.35	2	7.5	A	1	250	1	30

Effect of the slenderness ratio Figures 4.30a and 4.30b show the real (K_V) and the imaginary ($2\zeta_V$) term of the vertical dynamic impedance, highlighting the influence of the skirt length (cases 1–5). The drop of stiffness attained at the 1st vertical resonance of the soil layer is less marked by decreasing the slenderness ratio H_p/d in agreement with the study of Liingaard (2006). A linearly decreasing pattern of the dynamic stiffness was noticed for frequencies higher than $\alpha_0 = 4$; while the pattern of the radiation damping was characterized by an increased slope for higher values of the slenderness ratio.

Figures 4.30c and 4.30d illustrate the vertical displacement of the foundation as a function of the depth at the 1st and 2nd eigenfrequency of the soil stratum. It is evident that the dynamic behaviour of suction caissons is governed by the foundation rather than the soil and the response becomes stiffer by decreasing the slenderness ratio. This observation is confirmed by the vertical deformed shape of the foundation, which exhibited steeper slope with the decrease of caisson height (skirt length).

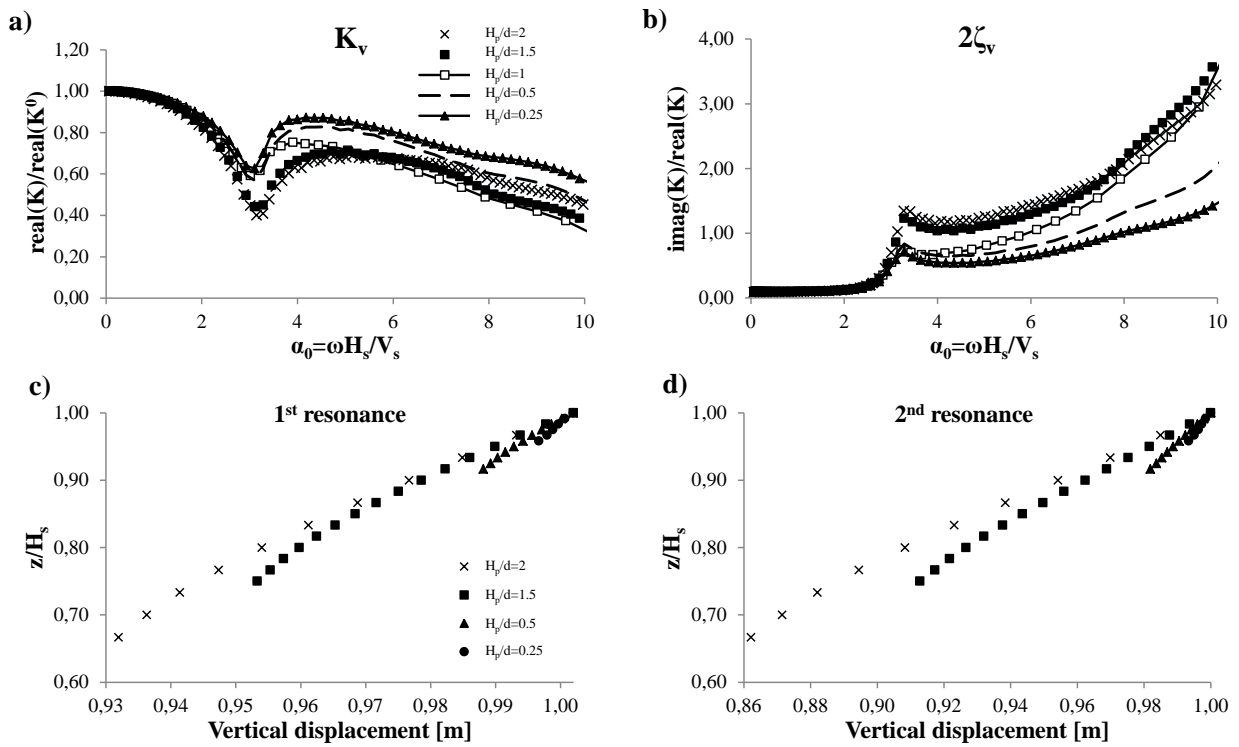


Figure 4.30: Effect of the skirt length of the caisson on the real component a) and the imaginary component b) for cases 1–5. Distribution of the suction caisson displacement along the skirt at the 1st vertical eigenfrequency c) and 2nd vertical eigenfrequency d) of the soil layer. Modified after *Paper V*.

Sensitivity to Poisson's ratio In the literature there are several studies (Mylonakis (2001), Anoyatis et al. (2016)) that examined the high sensitivity of elastodynamic analytical solutions for piles to Poisson's ratio since, as ν approaches 0.5, the dilatational wave velocity tends to infinity and the η parameter as well. This parameter correlates the shear wave velocity V_s to dilation wave velocity V_l , as reported in Equation (4.8).

$$\eta = \frac{V_l}{V_s} = \sqrt{\frac{2(1-\nu)}{1-2\nu}} \quad (4.8)$$

Different expressions of η parameter are available in the literature according to the assumptions on displacements considered. For vertical vibrations neglecting the horizontal stresses σ_r and σ_θ yields:

$$\eta = \sqrt{2(1 + \nu)} \quad (4.9)$$

Lysmer and Kuhlemeyer (1969) proposed an alternative formulation of η :

$$\eta = \frac{3.4}{\pi(1 - \nu)} \quad (4.10)$$

In axisymmetric vibrations where the tangential displacements are zero, we have:

$$\eta = \sqrt{\frac{2}{1 - \nu}} \quad (4.11)$$

In Figure 4.31 the effect of Poisson's ratio on the different formulations of the dimensionless coefficient η is shown.

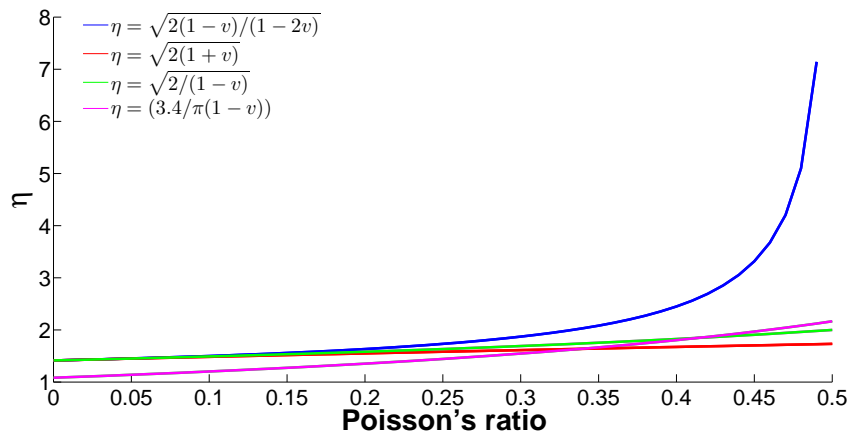


Figure 4.31: Effect of Poisson's ratio on dimensionless coefficient η

Figure 4.32a and 4.32b show the real (K_V) and the imaginary ($2\zeta_V$) term of the vertical dynamic impedance, varying the Poisson's ratio ν . It was noticed that ν influenced appreciably the frequency value, where the 1st vertical eigenfrequency was attained, because of the dependency of η on Poisson's ratio. In addition, the results showed that the value of the 1st vertical resonance obtained from the numerical models resembled the one calculated by adopting Equation 4.8 when Poisson's ratio is less than 0.40. By increasing Poisson's ratio ν up to 0.35, the decrease in stiffness attained at the 1st vertical resonance seemed marginally influenced by ν , since less than 15% of difference was recorded over the frequency interval examined. Moreover, a change in the stiffness's slope, recorded at the 3rd horizontal resonance ($\alpha_0 = 7.85$), became slightly more prominent for $\nu = 0.1$ and $\nu = 0.2$. This can be explained by the fact that the stiffer the soil is, the more the stress waves are attenuated and therefore the decay of the vertical dynamic impedance is less appreciable^{***}. With reference to the imaginary component, the radiation damping was developed for frequencies higher than the 1st vertical eigenfrequency of the soil deposit, which is shifted backwards as Poisson's ratio decreases. Furthermore, the trend of the radiation damping became steeper for frequencies greater than $\alpha_0 = 7.85$, when $\nu = 0.1 - 0.2$. Thus it may be stated that Poisson's ratio with values less than 0.4 influenced barely the vertical dynamic stiffness in agreement to previous works (Nogami and Novak (1976)).

When Poisson's ratio approaches 0.5, the soil behaves as a nearly incompressible material and the numerically calculated impedances showed fluctuations around the 1st vertical resonance^{***}. In order to explain these fluctuations two additional numerical models for suction caisson with $H_p/d = 2$ were established, by including an assumption on the soil layer's displacements. The first numerical model is characterized by no horizontal displacements (U1), while in the latter zero displacements on both horizontal directions (U1 and U2) were taken into consideration.

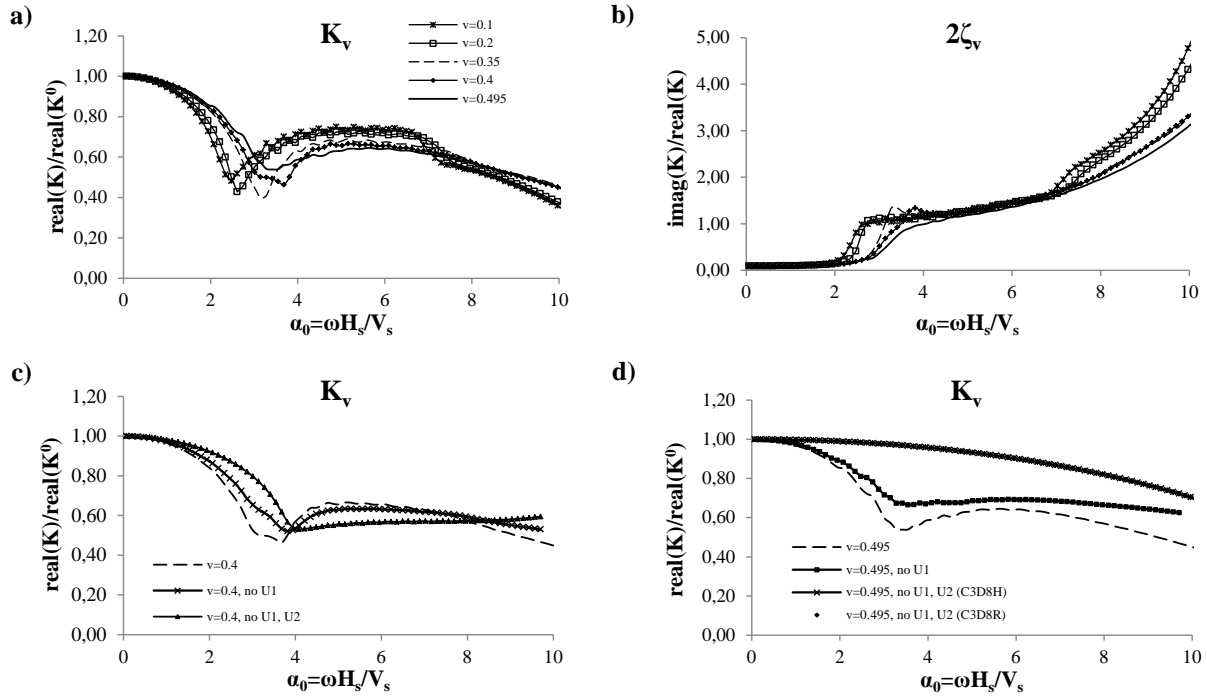


Figure 4.32: Variation of the vertical dynamic stiffness with respect to the non-dimensional frequency. Effect of Poisson's ratio on the real component a) and the imaginary component b) for $H_p/d = 2$. Effect of the horizontal displacements on the real component for $\nu = 0.4$ c) and for $\nu = 0.495$ d). Modified after *Paper V*.

In Figure 4.32c and 4.32d the effect of the horizontal displacements (U1 and U2) on the vertical dynamic stiffness is illustrated for suction caisson with $\nu = 0.4$ and $\nu = 0.495$, respectively. Particularly, it is of interest to note that the fluctuation of the vertical dynamic stiffness attained for suction caisson with $\nu = 0.4$ at $\alpha_0 = 3.0$ is primarily enhanced by the horizontal displacements (U1). Indeed, the elements at the edge of the foundation tip move horizontally and vertically, as a result of the bending response due to the axial force***. As the Poisson's ratio approached 0.5, the drop of stiffness at the 1st vertical eigenfrequency of the soil stratum decreased by neglecting the horizontal displacements (U1), while it is slightly visible when both horizontal displacements were restrained. A possible explanation is that volumetric locking occurred. It has been previously reported in the literature as a well-known problem that three-dimensional standard linear eight-node displacement element (C3D8) suffers of severe locking for nearly or fully incompressible material (Doll et al. (2000))***. In Figure 4.33b the checkerboard pattern of pressure values proved the occurrence of volumetric locking, since the pressure changes significantly from one integration point to the next.

On the contrary, this trend is not observed when the displacements are not restrained (Figure 4.33a). The issue of volumetric locking can be overcome by adopting hybrid formulation, where hybrid elements are used (C3D8H) or by applying selectively reduced-integration (C3D8R) (Systèmes (2014))***. It is of interest to note that the findings herein presented for the incompressible soil layer ($\nu = 0.495$) were achieved both using hybrid elements and elements with reduced integration formulation. Nevertheless, spurious pressure stresses were generated at the integration points, indicating an overly stiff behaviour when reduced-integration (C3D8R) is considered.

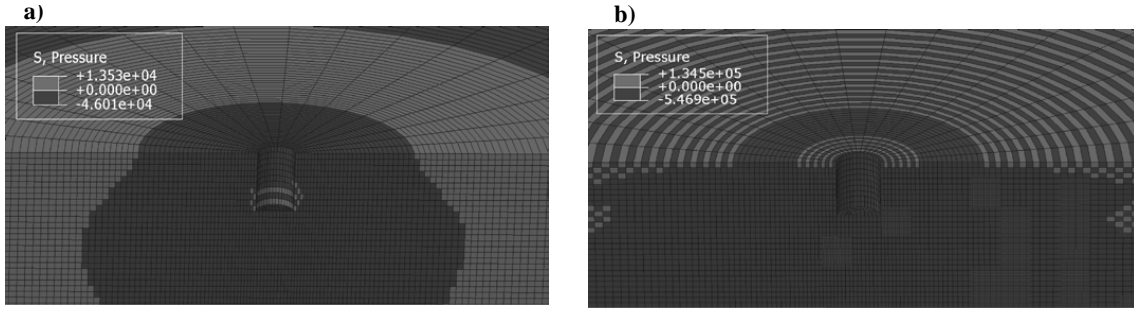


Figure 4.33: Quilt–style contour plot of pressure in the soil medium for case 9 a) and 22 b) at the 1st vertical resonance. Modified after *Paper V*.

Effect of the stiffness of the soil layer In Figure 4.34 the real (K_V) and the imaginary ($2\zeta_V$) term of the vertical dynamic impedance are illustrated, varying the stiffness of the homogeneous soil layer (profile A) for $H_p/d = 2$ (cases 3, 10–12). It was noticed a similar pattern of the dynamic stiffness when the shear wave velocity of the soil layer increases or E_p/E_s decreases; even though the influence of V_s on the vertical dynamic behaviour is to some extent visible. The reduction of stiffness attained at the 1st vertical resonance can be considered less marked for stiff soil deposits ($V_s = 500\text{m/s}$). In the intermediate frequency range ($\alpha_0 = 4 - 7$) an almost constant pattern of the dynamic vertical stiffness was recorded with respect to frequency. Particularly, when the soil is very stiff, the real component of the stiffness seemed even independent of the frequency after 1st vertical resonance***. These results are in agreement with the study of Nogami and Novak (1976) for the dynamic response of end bearing piles.

In relation to the imaginary part, the damping ratio exhibited higher values by decreasing the stiffness of the soil stratum for frequencies smaller than the 1st eigenfrequency. Moreover, the radiation damping produced after $\alpha_0 = 4$ was characterized by a linear pattern, which became less steep when the shear wave velocity of the soil layer increased. Looking at the overall vertical dynamic response of suction caissons, it is possible to see that the influence of the stiffness of the soil deposit on the vertical impedance is generally not appreciable, but it became more prominent in the high frequency interval as shown by Liingaard (2006).

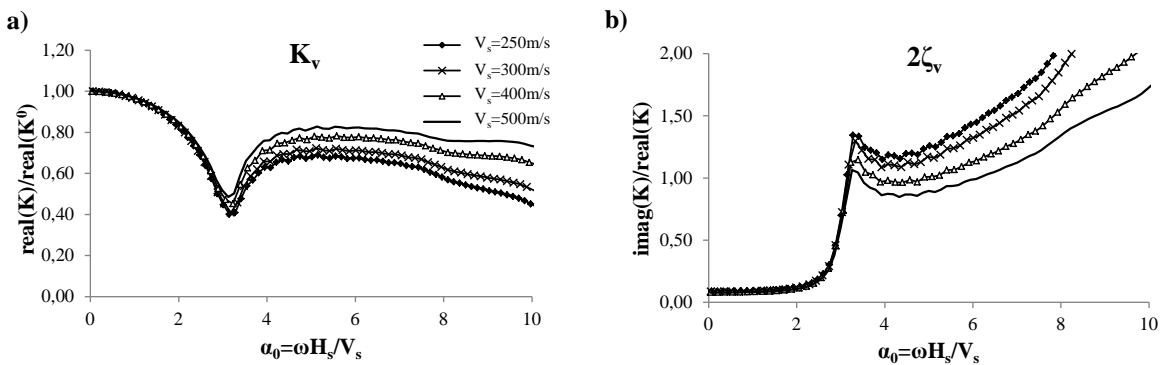


Figure 4.34: Variation of the vertical dynamic stiffness with respect to the dimensionless frequency. Effect of the stiffness of homogeneous soil layer (profile A) on the real component a) and the imaginary component b) for $H_p/d = 2$. Modified after *Paper V*.

The effect of the stiffness variation with depth is presented in Figure 4.35 for profiles B and C. The findings are displayed with respect to the frequency normalized by the 1st vertical eigenfrequency of the homogeneous soil layer of shear wave velocity $V_s = 500\text{m/s}$, f_{1st} . It is worth mentioning that the drop of stiffness is slightly shifted backward from the 1st vertical resonance of the homogeneous layer as expected ($f/f_{1st} = 0.81$ – profile B and 0.70 – profile C). Additionally, it

seemed that this decrease of stiffness is largely influenced by the variation of the slenderness ratio rather than the type of soil deposit. A small discrepancy (less than 6% at the 1st resonance) was recorded between the vertical stiffness components obtained for profile B and C at the 1st vertical eigenfrequency for a given value of H_p/d . This is supported by the displacements results at the 1st eigenfrequency of the soil layer for both $H_p/d = 0.25$ and 2. Figure 4.36a and 4.36c illustrate that similar vertical displacements were found for the suction caisson foundation embedded in profile B and profile C.

Additionally, it is of interest to note that the vertical deformed shape of suction caissons installed in profile B and C reasonably resembled the one of the same foundation embedded in homogeneous soil deposit with shear wave velocity $V_s = 250\text{m/s}$ (profile A) at the 1st eigenfrequency. In light of these results it can be stated that the vertical dynamic impedance is not significantly dependent on the variation of stiffness with depth for frequencies lower than 1st vertical eigenfrequency. After the 1st vertical resonance is achieved, the influence of the stiffness variation with depth on the real part became more evident. Indeed, the stiffness component of the vertical dynamic impedance experienced a decreasing pattern, with profile C presenting larger slope increase. Moreover, a similar pattern of the real term with frequency was observed for suction caissons with low slenderness ratio ($H_p/d = 0.25 - 1$), showing a softer response than the foundation with $H_p/d = 2$. The fact that the higher is the slenderness ratio the stiffer is the response of the foundation, diverges from the results achieved for the case of suction caissons embedded in a homogeneous soil layer***. The results displayed that the foundation behaviour is controlled by the soil stiffness at the bottom of the suction caisson, which attained higher values as the skirt length increased. Thus, it is likely that the suction caisson with smallest slenderness ratio ($H_p/d = 0.25$) and embedded in soil profile C underwent significant variation of vertical displacements along the depth.

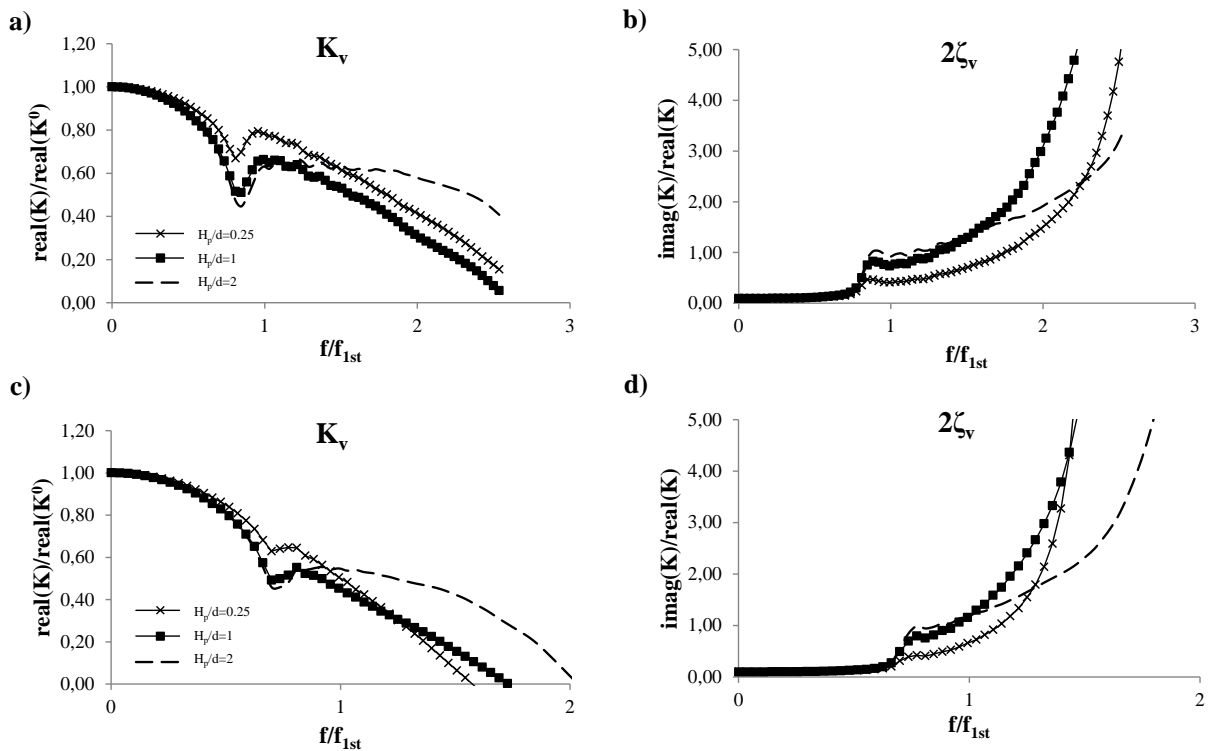


Figure 4.35: Variation of the vertical dynamic stiffness with respect to the dimensionless frequency. Effect of the stiffness of homogeneous soil layer (profile B) on the real component a) and the imaginary component b). Effect of the stiffness of homogeneous soil layer (profile C) on the real component c) and the imaginary component d). Modified after *Paper V*.

The outcomes shown in Figure 4.36b seemed to confirm this trend, while suction caissons in

profile A and C experienced similar vertical displacements along the depth, since the soil modulus at the foundation tip assumed comparable values.

When it comes to the imaginary component, it is of interest to note that the pattern of the damping ratio is consistent with the outcomes of the stiffness coefficient of the dynamic vertical impedance. It was observed that the type of variation of soil modulus with depth influenced considerably the damping for frequencies higher than the 1st vertical resonance. Indeed, suction caissons with $H_p/d = 0.25$ and 1 exhibited an exponential trend approaching $f/f_{1st} = 2$, which becomes more prominent for foundations embedded in profile C. In relation to suction caisson with $H_p/d = 2$, the exponential pattern of the real component of stiffness increases less rapidly, for frequencies higher than $f/f_{1st} = 2$.

In conclusion, it can be stated that the type of soil profile became the governing parameter for the estimation of the vertical dynamic impedance, when the soil stiffness varies significantly along the depth and for frequencies greater than the 1st vertical resonance***.

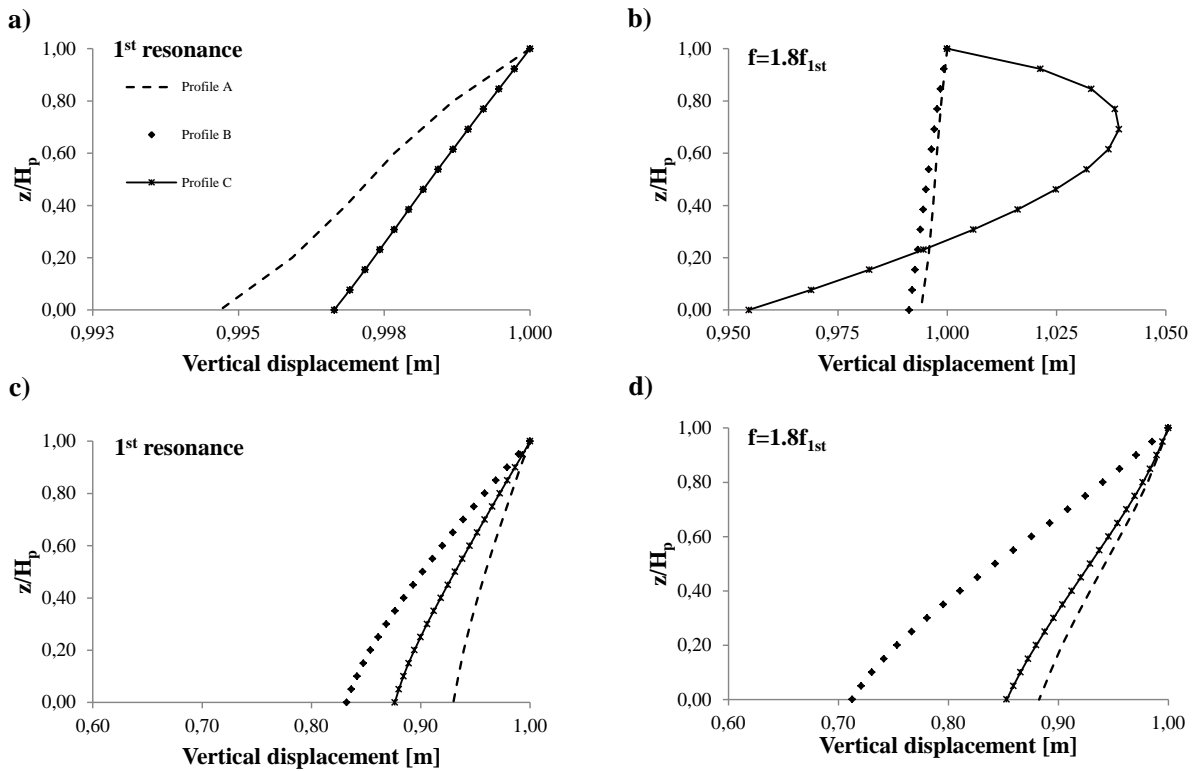


Figure 4.36: Distribution of the suction caisson’s vertical displacements along the depth for $H_p/d = 0.25$ at the 1st resonance a) and $f = 1.8f_{1st}$ b) and for $H_p/d = 2$ at the 1st resonance c) and $f = 1.8f_{1st}$ d), considering homogeneous (profile A) and inhomogeneous (profile B and C) soil layer. Modified after *Paper V*.

Effect of the relative thickness of the soil layer The effect of the relative thickness of the soil layer (H_s/d) on the vertical dynamic impedance is depicted in Figure 4.37 (case 23–26, in Table 4.13). The results showed that the vertical dynamic impedance is strongly dependent on the variation of the dimensionless parameter H_s/d in the frequency interval examined. Firstly the reduction in stiffness manifests at the 1st resonance, when referring to the same slenderness ratio H_p/d , became more apparent as the relative thickness of the soil medium decreased. This can be explained by the fact that the stress attenuation is more prominent as the propagating waves travel longer paths. The decrease of the dynamic impedances associated to smaller H_s/d was also observed for the dynamic response of suction caissons subjected to lateral loading. After the 1st resonance, the vertical stiffness coefficient exhibited a decreasing pattern and the drop of stiffness attained at

the 2nd eigenfrequency of the soil layer became more appreciable for higher values of the slenderness ratio. Regarding the imaginary component, a step–linear increasing trend was observed at higher frequency. Its slope assumed higher values when the relative thickness of the soil layer decreased. This increase of the variation of the radiation damping recorded for smaller values of H_s/d is related to the concurrent decrease of the dynamic component of the vertical stiffness coefficient. On the contrary, it was found that the viscous damping coefficient in the frequency interval examined decreased by decreasing H_s/d , in accordance with the fact that less energy is discharged as the path of the propagating waves reduces.

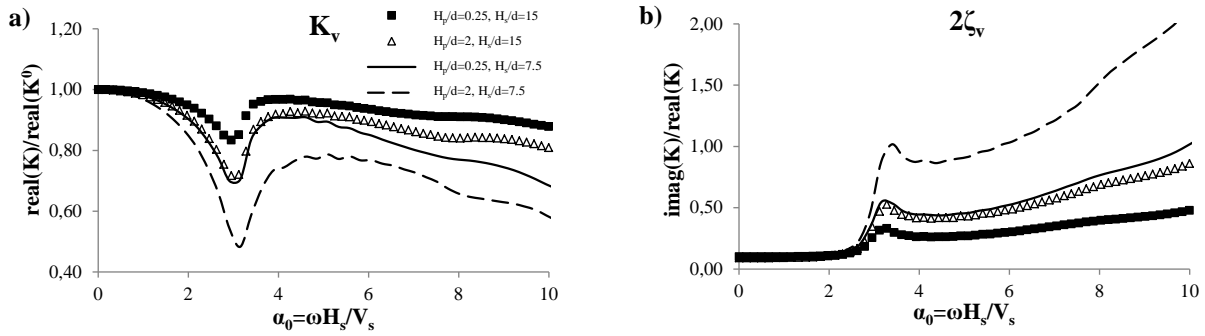


Figure 4.37: Effect of the relative thickness of the soil layer on the real component a) and the imaginary component b) for cases 23–26.

4.2.5 Suggested expressions

In analogy with Section 4.1.5 new simplified expressions were introduced to represent soil–suction caisson interaction in vertical dynamic response. Thus, Equations 4.6 and 4.7 can be applied to express the real and imaginary part of the vertical dynamic impedance.

In the proposed study the calibration of the coefficients was based on the selection of numerical cases that demonstrate characteristic behaviour and they were representative for the parametric study^{***}. The coefficients $c_{j,r}$ and $c_{j,i}$ were established for two different frequency intervals, one referring to earthquake loading ($0 \leq \alpha_0 \leq 3/2\eta\pi$) and one to wind/wave loading, see respectively Table 4.14 and 4.15. In offshore applications the frequency interval of interested can be reduced up to the 1st vertical eigenfrequency of the soil (Damgaard et al. (2014), Bhattacharya et al. (2013)), and this allowed decreasing the number of coefficients $c_{j,r}$ applied in the proposed expressions for the estimation of the real part of the vertical dynamic impedance. In addition, the accuracy of the suggested expressions was shown by listing the percentage of the average relative error (ϵ_{mean}) and the maximum relative error (ϵ_{max}) of the proposed formulas with respect to the numerical outcomes in the frequency ranges investigated, as outlined in Table 4.14 and Table 4.15.

Figure 4.38 shows the comparison between the proposed expressions and the numerical outcomes of the real and imaginary part of the vertical dynamic impedance for different cases in the frequency range $[0; 3/2\eta\pi]$. It can be observed that the real component of the dynamic vertical impedance (Figure 4.38a) of the proposed formula is in good agreement with respect to the numerical outcomes for suction caissons with slenderness ratio $H_p/d = 2$ and $H_p/d = 0.25$, respectively. This is confirmed by the fact that an average difference of 6% for suction caisson with $H_p/d = 2$ and 5.1% for $H_p/d = 0.25$ was recorded between the abovementioned solutions; whereas a maximum discrepancy of 11.8% and 9.30% was achieved and only at $\alpha_0 \cong 3.5$. When it comes to the damping coefficient (Figure 4.38b) the proposed expression exhibited relatively scattered results with respect to the numerical outcomes ($\epsilon_{mean} = 10\%$) for suction caisson with slenderness ratio of $H_p/d = 2$, while the discrepancy doubled ($\epsilon_{mean} = 20.5\%$) when the slenderness ratio reduced to $H_p/d = 0.25$. In addition, it was found that the maximum error of the real and the imaginary part is approximately two times the average error.

Table 4.14: Constants of the suggested expression for the dynamic vertical stiffness and damping coefficient in the dimensionless frequency range $\alpha_0 \in [0; 3/2\eta\pi]$.

Case Nr.	Real component (K_V)					Imaginary component ($2\zeta_V$)									
	$c_{1,r}$	$c_{2,r}$	$c_{3,r}$	$c_{4,r}$	$c_{5,r}$	ϵ_{max} (%)	ϵ_{mean} (%)	$c_{0,i}$	$c_{1,i}$	$c_{2,i}$	$c_{3,i}$	$c_{4,i}$	$c_{5,i}$	ϵ_{max} (%)	ϵ_{mean} (%)
3	0.065	1.57	-0.0068	0.890	0.50	11.8	6.0	-0.040	0.035	1.7	7	0.735	0.942	25.0	9.9
5	0.042	3.0	-0.0068	0.890	0.64	9.3	5.1	-0.020	0.020	1.3	9	0.75	0.942	38.1	20.5
6	0.092	1.50	-0.0072	0.945	0.68	9.6	2.2	-0.047	0.048	1.3	5	0.76	1.03	24.6	7.5
9	0.045	0.83	-0.0085	0.935	0.50	6.9	1.9	-0.091	0.040	1.10	4	0.840	1.02	24.7	4.8
12	0.058	2.45	-0.0045	0.890	0.67	8.7	3.2	-0.038	0.026	1.7	8	0.745	0.95	26.9	11.3
13	0.062	3.00	-0.013	0.79	0	8.9	2.4	0.080	0.030	0.20	1.7	0.42	0.94	82.0	29.0
15	0.040	11	-0.012	0.79	0	9.8	3.0	0.10	0.030	0.07	4.0	0.420	0.89	77.9	28.9
16	0.080	6.2	-0.027	0.68	0	11.7	4.3	0.058	0.019	0.15	0.3	0.25	0.95	65.9	15.6
18	0.035	5	-0.040	0.68	0	8.6	1.5	0.070	0.019	0.10	0.16	0.39	1.10	28.3	9.4

$\alpha_0 = 2.4$

Table 4.15: Constants of the suggested expression for the dynamic vertical stiffness and damping coefficient in the dimensionless frequency range $\alpha_0 \in [0; 4]$.

Case Nr.	Real component (K_V)					Imaginary component ($2\zeta_V$)									
	$c_{1,r}$	$c_{2,r}$	$c_{3,r}$	$c_{4,r}$	$c_{5,r}$	ϵ_{max} (%)	ϵ_{mean} (%)	$c_{0,i}$	$c_{1,i}$	$c_{2,i}$	$c_{3,i}$	$c_{4,i}$	$c_{5,i}$	ϵ_{max} (%)	ϵ_{mean} (%)
3	0.065	1.57	0	0.890	0.0	7.6	3.9	-0.035	0.035	1.5	6.7	0.735	0.942	17.0	8.7
						$\alpha_0 = 2.9$								$\alpha_0 = 1.7$	
5	0.042	3.0	0	0.890	0.0	8.1	2.8	-0.010	0.019	1.2	7.8	0.76	0.93	37.0	12.3
						$\alpha_0 = 2.2$								$\alpha_0 = 2.6$	
6	0.092	1.50	0.0	0.945	0.0	7.6	2.2	-0.047	0.048	1.3	5	0.76	1.03	24.6	10.3
						$\alpha_0 = 2.9$								$\alpha_0 = 1.5$	
9	0.045	0.83	0.0	0.95	0.0	6.1	2.8	-0.091	0.040	1.10	4	0.840	1.02	24.7	9.3
						$\alpha_0 = 1.9$								$\alpha_0 = 3.3$	
12	0.058	2.45	0.0	0.890	0.0	8.7	3.4	-0.031	0.026	1.6	7.8	0.745	0.95	22.9	9.8
						$\alpha_0 = 2.1$								$\alpha_0 = 2.6$	

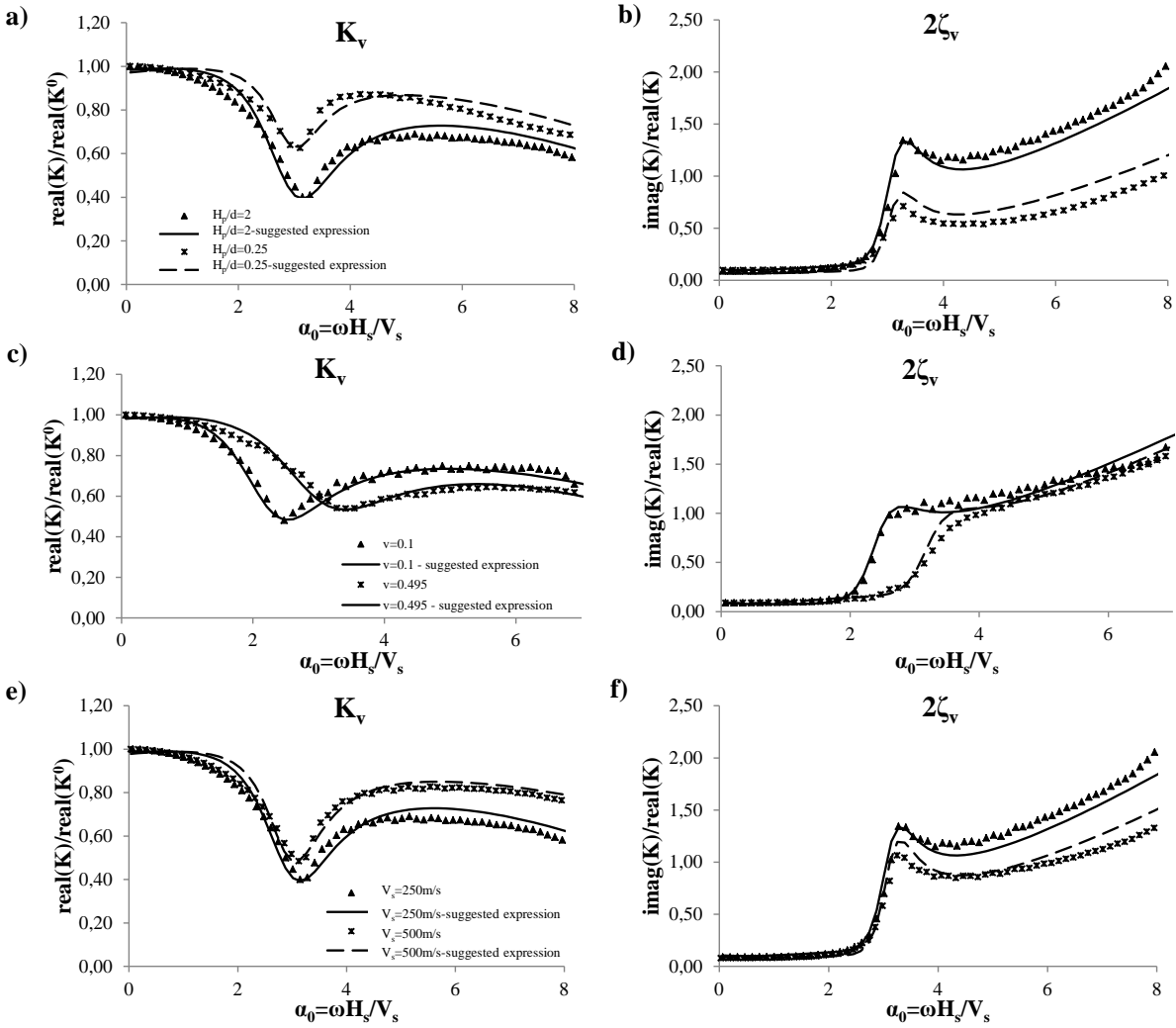


Figure 4.38: Comparison between the simplified expression and the numerical outcomes with respect to the non-dimensional frequency. Effect of the skirt length of the caisson on the real component a) and the imaginary component b) for cases 1 and 5. Effect of Poisson's ratio on the real component c) and the imaginary component d) for $H_p/d = 2$. Effect of the shear wave velocity of the soil layer on the real component e) and the imaginary component f) for $H_p/d = 2$. Modified after *Paper V*.

Figure 4.38c and 4.38d illustrate that the real and imaginary component of the vertical dynamic stiffness given by the proposed formulas resembled the ones obtained by the numerical model for suction caissons installed in a soil deposit with Poisson's ratio $\nu = 0.1$ and $\nu = 0.495$. A discrepancy of less than 3% was recorded for the real term of the vertical dynamic stiffness; while the radiation damping attained values, which differed less than 8% with respect to the numerical ones. With reference to stiff soil layer ($V_s = 500\text{m/s}$) the real part determined by the suggested expression approximated better the numerical outcomes than for the case of medium stiff soil profile as shown in Figure 4.38e. This was demonstrated by the fact that ϵ_{mean} and ϵ_{max} exhibited small values (3.2% and 8.7%, respectively). On the other hand, an increase of the average and the maximum relative error was observed for the imaginary part. Figure 4.39 displays the vertical dynamic impedance of suction caissons embedded in inhomogeneous soil profile B and C estimated by Equation 4.6 and 4.7. The real component of the vertical dynamic impedance for both profile B and C does not overcome the numerical results more than 5%. On the contrary, the inhomogeneity of the soil layer had stronger influence on the imaginary part, since the average relative error reached up to 30% for profile B and 15% for profile C.

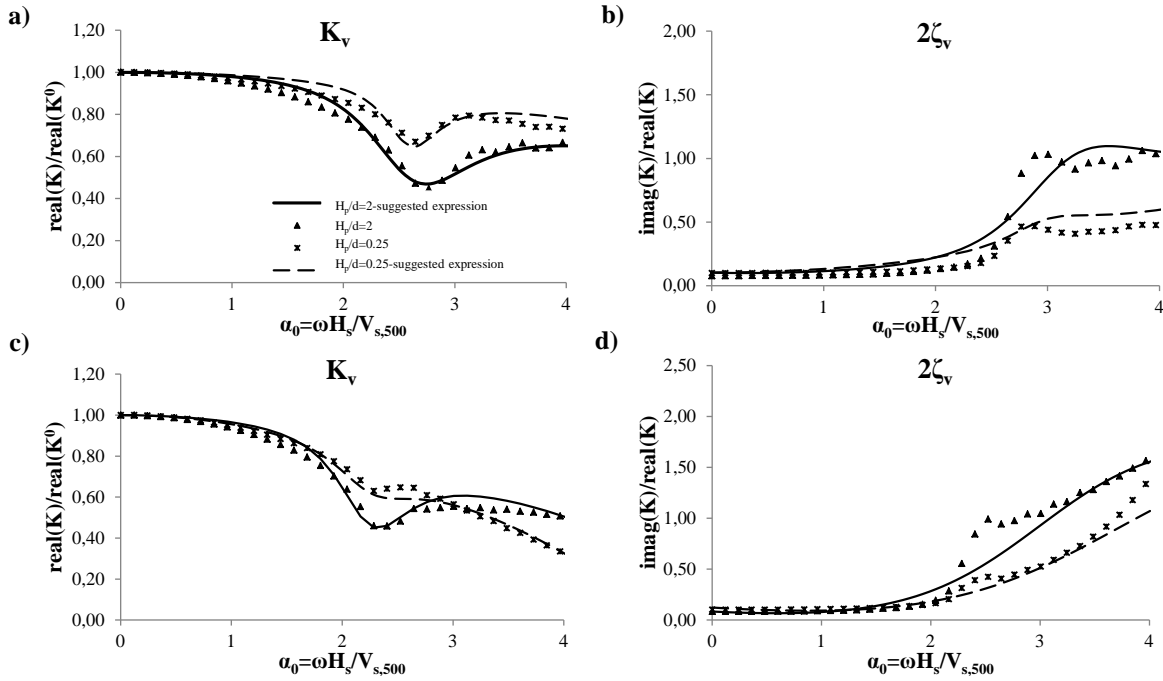


Figure 4.39: Comparison between the simplified expression and the numerical outcomes with respect to the non-dimensional frequency. Effect of the stiffness of homogeneous soil layer (profile B) on the real component a) and the imaginary component b) for $H_p/d = 2$ and 0.25. Effect of the stiffness of homogeneous soil layer (profile C) on the real component c) and the imaginary component d) for $H_p/d = 2$ and 0.25. Modified after *Paper V*.

The maximum relative error recorded for the imaginary part is significantly high, even if it is attained for few values in the frequency range ($\alpha_0 \cong 2 - 3$) where the numerical outcomes are characterized by a peak, which cannot be represented by the suggested expression. Looking at Table 4.15, it can be observed that the average difference between the real part calculated by the proposed formula considering a smaller frequency interval and those of the numerical model is less than 4%, while ϵ_{max} does not overcome 9%. The average relative error referred to the imaginary part assumed values lower than 13% for cases 3,5,6,9,12. Finally, it can be concluded that the suggested expressions provide a fairly good approximation of dynamic vertical stiffness of suction caissons for both the frequency ranges considered***.

4.3 Conclusions

In this study numerical analyses were performed to examine the vertical and lateral dynamic response of suction caissons embedded in elastic soil layer with hysteretic material damping. The numerical modelling procedure was validated against existing analytical solutions for end bearing and floating foundations. A parametric study was presented to analyse the vibration characteristics of suction caissons and illustrate the effects of major parameters on the stiffness and damping properties. The main dimensionless parameters investigated were the slenderness ratio, the relative thickness and the stiffness of the soil layer. According to the type of loading applied, the following observations can be drawn:

Lateral dynamic response of suction caissons The numerical results provided the basis for the formulation of simple mathematical expressions for the static stiffness components of suction caissons. The proposed expressions accommodate a more accurate estimation of the stiffness components compared to previous analytical expressions.

In light of the findings the skirt length can be considered quite substantial parameter to determine the dynamic stiffness coefficients of the suction caissons. It was found that the dynamic behaviour of suction caissons decreased by decreasing the skirt length for frequencies higher than the 1st eigenfrequency of the soil layer. Additionally, the results showed that the reduction in the dynamic stiffness due to the decrease of the soil stiffness with depth was more prominent when the skirt length decreased.

Moreover, it was noticed that the stiffness ratio E_p/E_s for homogeneous profiles slightly influenced the dynamic response of suction caissons in the frequency range examined. On the contrary, the type of variation of soil modulus with depth in inhomogeneous profiles exhibited a significant effect on the dynamic impedances of suction caissons. Particularly, the dynamic stiffness and damping of the suction caisson varied significantly in the frequency range considered, when the soil profile with linearly increasing stiffness with depth was taken into account. This indicates that steep variations of stiffness with depth may lead to small dynamic stiffness and high damping ratios at high frequencies. Furthermore, this work illustrated that the dynamic response of suction caissons is profoundly influenced by the non-dimensional parameter H_s/d and valuable insight on the physics of the problem is obtained by including the relative thickness of the soil layer.

Vertical dynamic response of suction caissons The findings showed that the vertical dynamic behaviour of the soil–caisson system depends significantly on the variation of the skirt length. Particularly, a more marked reduction of the stiffness term and increase of the damping term was obtained when the skirt length decreases. While the vertical response of suction caissons was found to be marginally sensitive to Poisson’s ratio with values less than 0.40 in the frequency range investigated. At higher values of Poisson’s ratio the vertical eigenfrequency increases compared to the theoretical one and the horizontal displacements were proved to influence the vertical dynamic stiffness. In addition, it can be stated that the numerical results can be assumed unreliable, when nearly incompressible soil medium ($\nu = 0.495$) and the horizontal displacements are taken into account in the analysis.

The effect of the stiffness ratio E_p/E_s was found to affect the vertical dynamic response primarily at the higher frequency interval. On the contrary, it was depicted that the type of variation of soil modulus with depth had a significant influence on the vertical dynamic impedance of suction caissons for frequencies greater than the 1st vertical resonance.

In this study simply mathematical formulas were developed for the estimation of the vertical and lateral dynamic impedances. In regards with the vertical behaviour of suction caissons, two sets of coefficients for the real and imaginary component of the vertical dynamic impedances were provided for two different frequency intervals, which make it possible to simplify considerably the mathematical expressions in the case of the offshore wind applications where the frequency range of interest is narrower than in earthquake loading. While the calibration of the lateral dynamic coefficients was performed including only the frequency interval suitable for the design of offshore wind turbines. A good agreement was achieved between the numerical results and the suggested expressions for the frequency ranges examined.

The study showed that the applied numerical methodology can be used in structural analyses for predicting the dynamic response of jackets. However, it is empathized that the suggested model is based on the assumptions of linearity in the soil layer and foundation materials, and the perfect contact at the soil–foundation interface. In addition, some of the aspects that influence the flexibility of the suction caisson as the flexibility of the lid and the thickness of the skirt are not investigated in this study.

4.4 Recommendations for future work

- Elaborate an analytical formulation for estimating the lateral dynamic impedance of floating suction caissons including the vertical displacement of the soil medium;

- Elaborate an analytical formulation for estimating the vertical dynamic impedance of suction caisson, possibly including the radial displacement of the soil medium;
- Investigate the effect of the flexibility of the lid and the thickness of the skirt on the dynamic response of suction caisson foundations;
- Investigate the response of suction caisson groups and the caisson–soil–caisson interaction, subjected to vertical and horizontal dynamic loading.

Chapter 5

The Modified SANISAND(2004) model

The findings of this chapter are presented in Latini et al. (2017) (Paper VII).

In this study the soil mechanics convention is considered, where compression is assumed positive and effective stresses are taken into account. To represent vector and tensor quantities, the following standard notation is adopted. For any two vectors, $\mathbf{u}, \mathbf{v} \in R^3$, the dot product is defined as: $\mathbf{u} \cdot \mathbf{v} = u_i v_i$ and the dyadic product as $[\mathbf{u} \otimes \mathbf{v}]_{ij} = u_i v_j$. For any two second-order tensors $\mathbf{X}, \mathbf{Y} \in L$, $\mathbf{X} \cdot \mathbf{Y} = X_{ij} Y_{ij}$ and $[\mathbf{X} \otimes \mathbf{Y}]_{ijkl} = X_{ij} Y_{kl}$.

Considering small deformations and rotations, the total strain rate can be divided into elastic ($\dot{\epsilon}^e$) and plastic term ($\dot{\epsilon}^p$):

$$\dot{\epsilon} = \dot{\epsilon}^e + \dot{\epsilon}^p \quad (5.1)$$

where ϵ is the strain tensor.

The concept of critical state is applied to all versions of SANISAND models, for which a soil sample deforms continuously in shear experiencing zero volumetric change. In this context, the variation of e_c and p is specified by the expression suggested by Li and Wang (1998), providing the location of the critical state line:

$$e_c = e_0 - \lambda_c \left(\frac{p_c}{p_{atm}} \right)^\xi \quad (5.2)$$

where e_0 , λ_c and ξ are model parameters and p_{atm} is a reference pressure which is usually assumed equal to the value of the atmospheric pressure. While e_c and p_c refer to the critical void ratio and confining pressure respectively. The critical state line cannot always be expressed by a linear relationship especially at stresses higher than 1000 kPa. However, the range of interest in general engineering applications is lower than 500 kPa; thus it is possible to treat the critical state line in linear form.

The distance to the critical state line is given by the state parameter $\psi = e - e_c$ as defined in the work of Been and Jefferies (1985). A typical material response is showed in Figure 5.1. Point a represents a state initially denser than critical ($\psi < 0$) and it is subjected to drained constant p triaxial compression. Firstly it will consolidate, moving to point a'_d and then dilate until critical failure occurs (a'_c and $e = e_c$). When undrained loading is applied, point a will shift to point a''_d due to positive pore water pressure development, which reduces the effective stress p , and then will move to the critical point a''_c , showing dilatancy tendency.

Whereas point b represents a state looser than critical ($\psi > 0$). Under drained constant p loading the material consolidates and b moves to the corresponding critical point b'_c and fails, in general without dilation and softening. In a corresponding undrained loading the state moves from point b to point b''_c where it fails, and in fact most often it passes first b'_c and reaches b''_d before it turns to point b''_c where it fails (Manzari and Dafalias (1997)). In light of the abovementioned observations, the state parameter has been incorporated in the family of simple anisotropic sand constitutive

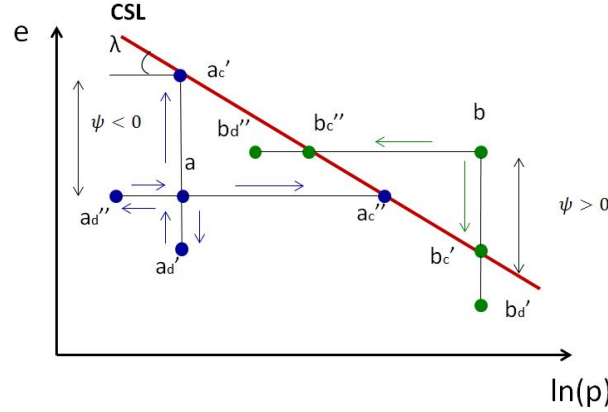


Figure 5.1: Critical state line (CSL) and state parameter.

models and it is adopted in the current model.

5.1 The modified SANISAND (2004) model in triaxial space

5.1.1 Elastic relations

For the elastic part of the model, the isotropic hypo-elasticity assumption is considered, giving

$$d\epsilon_q^e = \frac{ds}{2G} \quad d\epsilon_v^e = \frac{dp}{K} \quad (5.3)$$

where G and K are the elastic shear and bulk moduli respectively. The elastic shear modulus G is a function of p and current void ratio e according to the equation proposed by Richart et al. (1970), while K can be determined by introducing the Poisson's ratio ν as follows:

$$K = \frac{2(1+\nu)}{3(1-2\nu)}G \quad G = G_0 p_{atm} \frac{(2.97 - e)^2}{(1 + e)} \left(\frac{p}{p_{atm}} \right)^{1/2} \quad (5.4)$$

G_0 is a model parameter and p_{atm} is a reference pressure which is usually assumed equal to the value of the standard atmospheric pressure. Thus, the hypoelastic constitutive matrix is given as:

$$\mathbf{D}^e = K \mathbf{1} \otimes \mathbf{1} + 2G \left(\mathbf{I} - \frac{1}{3} \mathbf{1} \otimes \mathbf{1} \right) \quad (5.5)$$

The symbol $\mathbf{1}$ and \mathbf{I} are used for the second-order and fourth-order identity tensors.

5.1.2 Yield surface

In SANISAND (2004) constitutive model (Dafalias and Manzari (2004)) suggested the following expression for the yield surface:

$$f = \{(\mathbf{s} - p\boldsymbol{\alpha}) \cdot (\mathbf{s} - p\boldsymbol{\alpha})\}^{1/2} - \sqrt{2/3}mp \quad (5.6)$$

where \mathbf{s} is the deviatoric stress tensor and p is the pressure. While the stress-ratio quantity $\boldsymbol{\alpha}$ is called the back-stress ratio and it is the rotational hardening variable of the yield surface, which represents the slope in p - q space of the bisector of the yield surface. The coefficient m is the tangent of half the opening angle of the yield surface at the origin. The open conical yield surface defined in the SANISAND (2004) is characterized by a singular point, which is the apex, see Figure 5.2. In order to avoid the gradient discontinuity at the apex, a hyperbolic yield surface was introduced. Therefore, the yield surface was regularized by adopting the trigonometric rounding technique of Zienkiewicz and Pande (1977). This procedure was also used in the work of Gens et al.

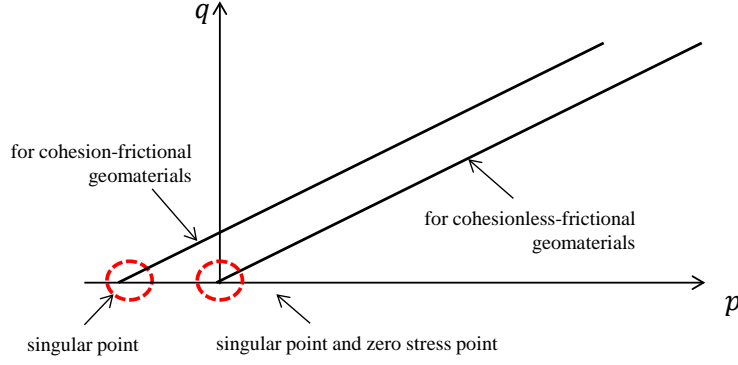


Figure 5.2: SANISAND (2004) yield surface in p - q plane. Modified after *Paper VII*.

(1990) and Sloan and Booker (1986). The main features of this yield surface are: 1) continuous and differentiable at all stress states and 2) approximate SANISAND (2004) yield function as closely as required by adjusting one parameter. The modified model still maintains an open conical yield surface, which can rotate around the cone apex at the origin of the stress space, and three additional open wedge-type surfaces with apex at the origin of stress space: the critical state surface (CSS), the bounding surface (BS) and the dilatancy surface (DS). In the present formulation the cohesion c was first introduced as $p_t = c \cot \phi$ and then, the hydrostatic pressure p^* is given as:

$$p^* = p + p_t \quad (5.7)$$

where ϕ is the friction angle. The distance between the vertex of the original yield surface and the hyperbolic yield surface is defined by the constant parameter b , which is a fraction of p_t :

$$b = \eta p_t \quad (5.8)$$

where $\eta \in (0, 1]$. Therefore, the yield function can be written as follows:

$$f^* = \{(\mathbf{s} - p^* \boldsymbol{\alpha}) \cdot (\mathbf{s} - p^* \boldsymbol{\alpha}) + (mb)^2\}^{1/2} - \sqrt{2/3} m p^* \quad (5.9)$$

In the triaxial stress plane the equation of the yield surface is proposed in terms of the triaxial stress quantities $p = (\sigma_1 + 2\sigma_3)/3$ and $q = (\sigma_1 - \sigma_3)$, where σ_1 and σ_3 are respectively the maximum and the minimum principle stress. Considering $\mathbf{s}^* = \mathbf{s} - p^* \boldsymbol{\alpha}$ the yield surface can be written as:

$$\hat{f} = \{\mathbf{s}^* \cdot \mathbf{s}^* + (mb)^2\}^{1/2} - \sqrt{2/3} m p^* \quad (5.10)$$

The yield surface in Equation 5.10 can be simplified assuming axisymmetric conditions:

$$s_1^* \neq s_2^* = s_3^*, \quad s_{ij}^* = 0 \quad \text{if } i \neq j \quad (5.11)$$

From the definition of the 1st and 2nd deviatoric invariants respectively J_1 and J_2 , the following expressions are obtained:

$$J_1 = \mathbf{s}^* \cdot \mathbf{s}^* = s_1^{*2} + s_2^{*2} + s_3^{*2} = s_1^{*2} + 2s_2^{*2} \quad (5.12)$$

$$J_2 = s_1^* + s_2^* + s_3^* = 0 \rightarrow s_2^* = -\frac{1}{2}s_1^* \quad (5.13)$$

Substituting Equation 5.13 in Equation 5.12 $\mathbf{s}^* \cdot \mathbf{s}^*$ can be expressed as

$$\mathbf{s}^* \cdot \mathbf{s}^* = \frac{3}{2}s_1^{*2} \quad (5.14)$$

Therefore the deviatoric stress s_1^* can be formulated in terms of q and p^* :

$$\begin{aligned} s_1^{*2} &= s_1 - p^* \hat{\alpha}_1 = \sigma_1 - \frac{1}{3}(\sigma_1 + 2\sigma_2) - p^* \left\{ \alpha_1 - \frac{1}{3}(\alpha_1 + 2\alpha_2) \right\} = \\ &= \frac{2}{3}(\sigma_1 - \sigma_2) - p^* \left\{ \frac{2}{3}(\alpha_1 - \alpha_2) \right\} = \frac{2}{3}(q - p^* q_\alpha) \end{aligned} \quad (5.15)$$

And the yield surface is given as:

$$\hat{f} = \{(q - p^* q_\alpha)^2 + m^2 b^{*2}\}^{1/2} - m p^* = 0 \quad (5.16)$$

where $b^* = \sqrt{\frac{3}{2}}b$. In Figure 5.3a and 5.3b the yield surface of the modified SANISAND (2004) model is illustrated in triaxial stress plane and in the multiaxial space, respectively along with the CSS (α^c), the BS (α^b) and the DS (α^d).

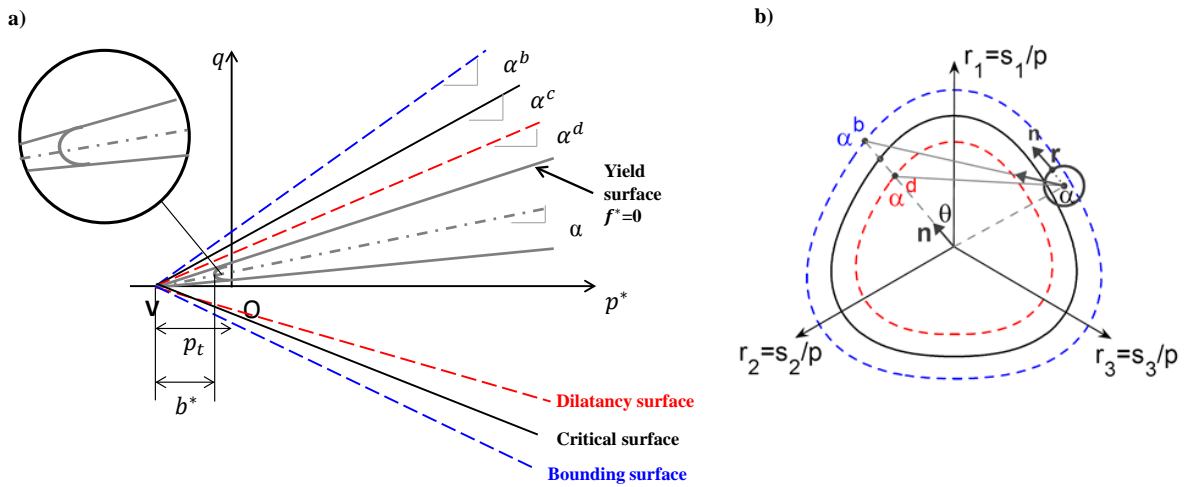


Figure 5.3: The yield surface of the modified SANISAND (2004) model in $q-p^*$ plane a) and in the multiaxial space b). Modified after *Paper VII*.

Several meridional sections of the hyperbolic yield surface are plotted in Figure 5.4, varying the parameter b^* and setting the hardening variable α equal to zero. Recall that the hyperbolic yield surface closely represents the original yield surface for $b^* \leq 0.25p_t$. While the effect of the back stress ratio is investigated by considering $b = p_t$, see Figure 5.5.

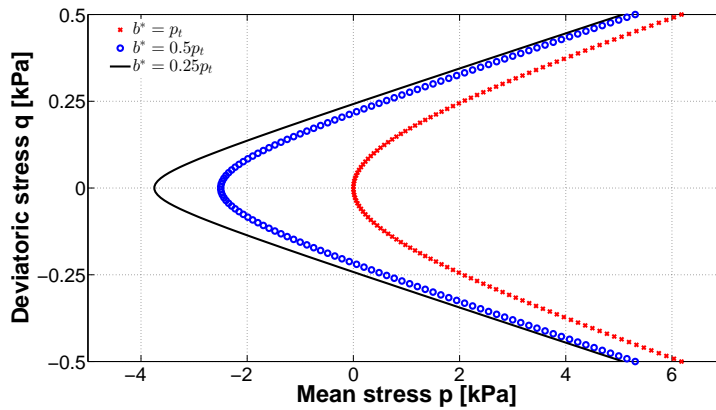


Figure 5.4: Effect of b^* parameter on the hyperbolic yield surface in $q-p$ plane. Modified after *Paper VII*.

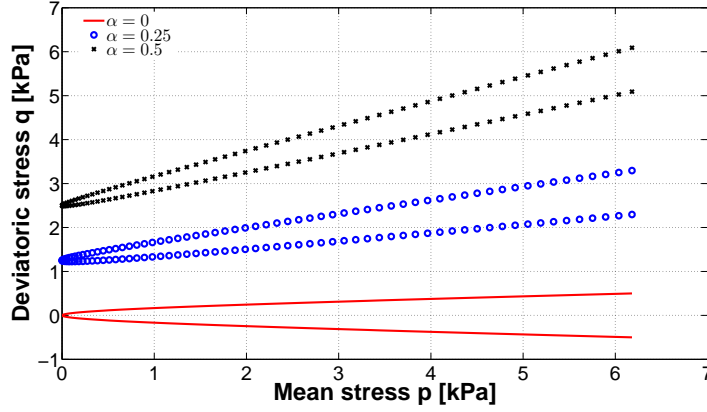


Figure 5.5: Effect of the back stress ratio α on the hyperbolic yield surface in q - p plane. Modified after *Paper VII*.

5.1.3 Critical, bounding and dilatancy surface

The critical state, bounding and dilatancy surfaces depend on the back stress ratio α . According to Dafalias and Manzari (2004), the stress ratios of the DS and BS, respectively α_{θ}^d and α_{θ}^b , are function of the state parameter ψ and α^c .

$$\alpha_{\theta}^b = \sqrt{\frac{2}{3}} [g(\theta, c) \alpha^c \exp(-n^b \psi) - m] \mathbf{n} \quad (5.17)$$

$$\alpha_{\theta}^d = \sqrt{\frac{2}{3}} [g(\theta, c) \alpha^c \exp(n^d \psi) - m] \mathbf{n} \quad (5.18)$$

For states looser than critical we have $\alpha^b < \alpha^c < \alpha^d$, with reverse ordering for states denser than critical. Note that in the original formulation the dependency of CSS, BS and DS in the q - p space on the Lode angle θ is given by the expression suggested by Argyris et al. (1974). Nevertheless, the implementation of the modified SANISAND (2004) takes into account the expression suggested by Van Eekelen (1980), which is more accurate for high values of the critical state friction angle (Lin and Bažant (1986)).

5.1.4 Flow rule

The plastic flow direction is defined as:

$$\dot{\epsilon}^p = \dot{\gamma} \mathbf{R} \quad (5.19)$$

where $\dot{\gamma} \geq 0$ and it represent the plastic multiplier. \mathbf{R} is the plastic potential, which is expressed as follows:

$$\mathbf{R} = \frac{\partial g}{\partial \sigma} = \mathbf{n} + \frac{1}{3} D \mathbf{I} \quad (5.20)$$

$$D = x D_{DM} = \begin{cases} D = D_{DM}, & x = 1, & \text{if } p > p_t \\ D = x D_{DM}, & & \text{if } p \in [0; p_t] \\ D = 0, & & \text{if } p < 0 \end{cases}$$

Where $x = p/p_t$ and D_{DM} is the dilatancy coefficient defined by Dafalias and Manzari (2004). This implies that D depends on the variation of the plastic volumetric strain, which was assumed zero for negative values of the mean pressure. The linear interpolation of the dilatancy coefficient in the interval $[0, p_t]$ was taken into account in order to have zero change in volume at the critical state and have a plastic potential function which varies in the proximity of the apex of the hyperbole. In addition, these assumptions may be considered valid, since the area subjected to regularization is

small $[-p_t, p_t]$. The loading index L is obtained by applying the consistency condition $f^* = 0$ and yields to:

$$L = \frac{1}{K_p} \left(\frac{\partial f}{\partial \boldsymbol{\sigma}} \cdot \dot{\boldsymbol{\sigma}} \right) = \frac{1}{K_p} \left(\frac{\partial f}{\partial \mathbf{s}} \cdot \dot{\mathbf{s}} + \frac{\partial f}{\partial p^*} \cdot \dot{p}^* \right) \quad (5.21)$$

$$K_p = - \left(\frac{\partial f}{\partial \boldsymbol{\alpha}} \cdot \boldsymbol{\alpha} \right) \quad (5.22)$$

The partial derivatives of the yield surface with respect to the stress and the internal variables can be determined as follows:

$$\begin{aligned} \frac{\partial f}{\partial \boldsymbol{\sigma}} &= \frac{\partial f}{\partial \mathbf{s}} \frac{\partial \mathbf{s}}{\partial \boldsymbol{\sigma}} + \frac{\partial f}{\partial p^*} \frac{\partial p^*}{\partial p} \frac{\partial p}{\partial \boldsymbol{\sigma}} = \\ &= \frac{1}{A} \{ (\mathbf{s} - p^* \boldsymbol{\alpha}) - \frac{1}{3} [\boldsymbol{\alpha} \cdot (\mathbf{s} - p^* \boldsymbol{\alpha})] \mathbf{1} \} - \frac{1}{3} \sqrt{\frac{2}{3}} m \mathbf{1} \end{aligned} \quad (5.23)$$

$$\frac{\partial f}{\partial \boldsymbol{\alpha}} = -\frac{1}{A} p^* (\mathbf{s} - p^* \boldsymbol{\alpha}) \quad (5.24)$$

where

$$\frac{\partial f}{\partial \mathbf{s}} = \frac{1}{A} \{ (\mathbf{s} - p^* \boldsymbol{\alpha}) \} \quad (5.25)$$

$$\frac{\partial \mathbf{s}}{\partial \boldsymbol{\sigma}} = \mathbf{I} - \frac{1}{3} \mathbf{1} \otimes \mathbf{1} \quad (5.26)$$

$$\frac{\partial f}{\partial \mathbf{p}} = \frac{1}{A} \{ (\mathbf{s} - p^* \boldsymbol{\alpha}) \cdot (-\boldsymbol{\alpha}) \} - \sqrt{\frac{2}{3}} m \quad (5.27)$$

$$\frac{\partial p}{\partial \boldsymbol{\sigma}} = \frac{1}{3} \mathbf{1} \quad (5.28)$$

with $A = \sqrt{(\mathbf{s} - p^* \boldsymbol{\alpha}) \cdot (\mathbf{s} - p^* \boldsymbol{\alpha}) + \frac{2}{3} m^2 b^2}$.

5.2 The modified SANISAND(2004) in the low stress regime

The implementation of the modified SANISAND (2004) model in finite element code was performed by modifying the subroutine freely available on the open-source database of constitutive models soilmodels.info (Gudehus et al. (2008)). The modified SANISAND (2004) was implemented in the code by deploying an explicit, adaptive stress-point algorithm with error control, based on Runge-Kutta-Fehlberg scheme of third order (RKF-32) to integrate the constitutive equations at the Gauss point level.

In this section the performance of the stress integration scheme of the modified SANISAND (2004) model is compared with respect to that of the original constitutive soil model for the case of low stress regime, see Figure 5.6. The simulations of undrained triaxial tests for loose sandy sample ($e_0=0.996$) were carried out by deploying IncrementalDriver (Niemunis (2008)). In addition, the analyses were conducted setting $p_t = 5kPa$ and initial hydrostatic pressure $p_0 = 30kPa$. Note that the material constants considered are those referred to Toyoura sand, which are listed in the work of Dafalias and Manzari (2004).

The outcomes in Figure 5.6 highlighted that in the new formulation the stress integration does not fail as in the original formulation, when it deals with sandy soil deposits subjected to low initial confining pressure.

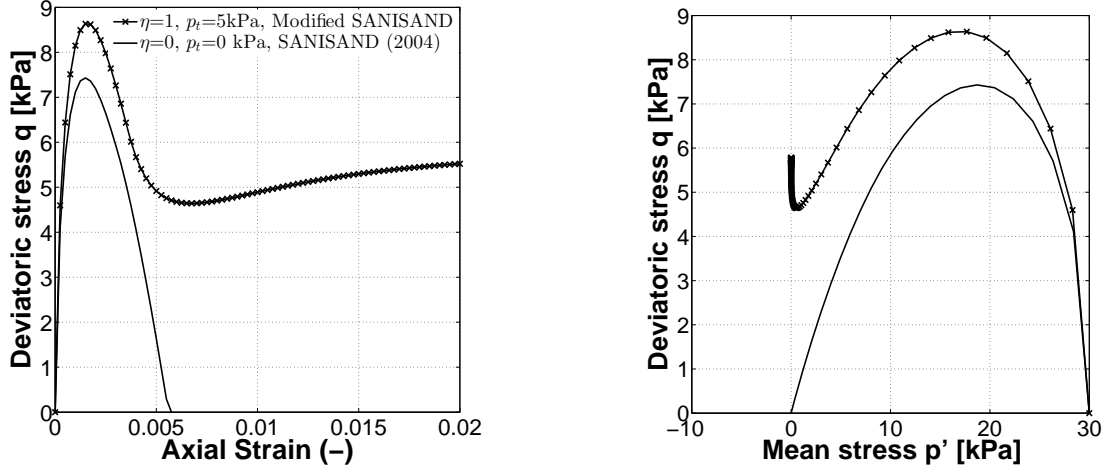


Figure 5.6: Monotonic undrained compression triaxial test on Toyoura sand. Comparison between the performance of SANISAND (2004) (Dafalias and Manzari (2004)) and the modified SANISAND (2004) model. Modified after *Paper VII*.

Then, the efficiency and the accuracy of the algorithm were evaluated with respect to the integration error, by varying respectively the number of increments N_{incr} and the tolerance parameter TOL . N_{incr} represents the number of times that the consistency equation was solved during the numerical integration. The integration error is defined as:

$$ERR_{\sigma} = \sqrt{(\sigma_1 - \sigma_1^*)^2 + 2(\sigma_2 - \sigma_2^*)^2} \quad (5.29)$$

$$ERR_{\alpha} = \sqrt{(\alpha_1 - \alpha_1^*)^2 + 2(\alpha_2 - \alpha_2^*)^2} \quad (5.30)$$

where σ_1, σ_2 and α_1, α_2 are the components of the stress tensor and the hardening variable. The quantities σ_1^*, σ_2^* and α_1^*, α_2^* are the numerical solutions obtained by deploying RKF23 algorithm considering a tolerance of $TOL = 10^{-6}$ and setting the number of iterations $N_{incr} = 1000$. The algorithm was first tested by decreasing the number of increments of the strain step applied ($N_{incr} = 500, 100$ and 50). First, it was observed that the outcomes of the simulations overlapped the results obtained by setting $N_{incr} = 1000$ for a given error tolerance of the explicit, adaptive stress–point algorithm ($TOL = 10^{-5}$), as shown in Figure 5.7. A relative error with respect the exact solutions of σ and α , obtained numerically by deploying the RKF23 for error tolerance of $TOL = 10^{-6}$, was calculated for each simulation. Results showed that a relative error of $ERR(\sigma, \alpha) = 10^{-6}$ was achieved assuming $N_{incr} = 500$. While the accuracy of the algorithm was estimated for the following tolerance values: $TOL = 10^{-5}, 10^{-4}$ and 10^{-3} , as illustrated in Figure 5.8. It was noticed that the accuracy of the solution decreased by increasing the tolerance constant TOL . Furthermore, it was possible to obtain a relative error $ERR(\sigma, \alpha) \leq 10^{-4}$, by setting the error tolerance not larger than 10^{-4} .

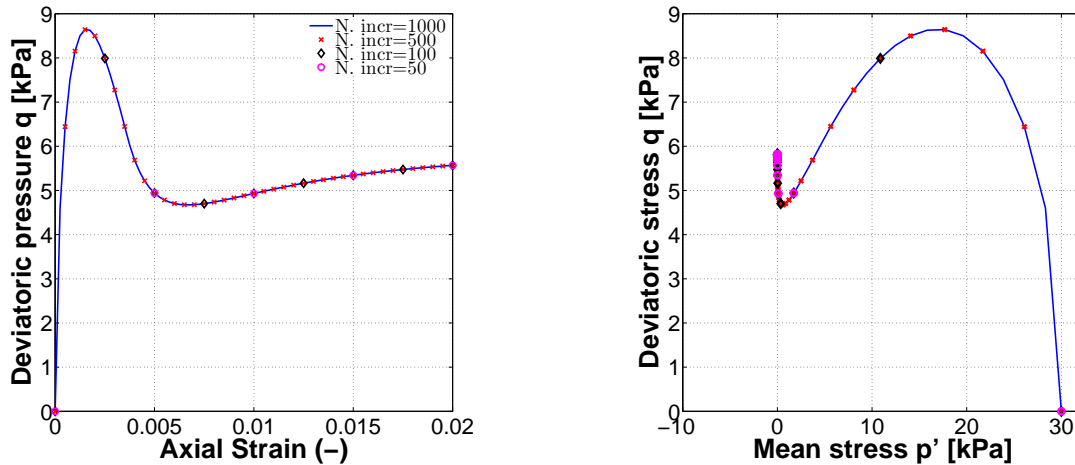


Figure 5.7: Monotonic undrained triaxial tests. Analysis of the efficiency of the algorithm, by varying the number of iterations N_{iter} . Modified after *Paper VII*.

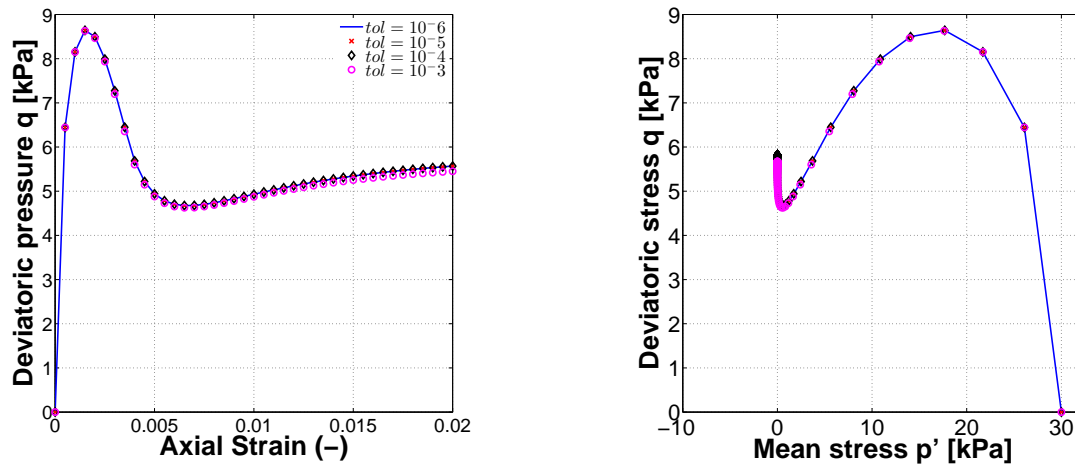


Figure 5.8: Monotonic undrained triaxial tests. Analysis of the accuracy of the algorithm, by varying the tolerance constant TOL. Modified after *Paper VII*.

5.3 Simulation of the response of shallow foundation using the modified SANISAND model

In this section the performance of the modified SANISAND (2004) was tested to simulate the response of a shallow footing embedded in sandy soil and subjected to vertical load.

5.3.1 Numerical model

A 2D model in Abaqus was constructed to obtain a load–deflection curve for a given shallow foundation embedded in a sandy soil and loaded vertically at its centre. A strip footing of width 5m was considered in the analysis. However, the model was simplified by taking into account only the body of sand and the nodes corresponding to the foundation were grouped by a rigid link. In addition, the differential settlements under the shallow footing were considered negligible due to the rigidity of the foundation. Furthermore, two boundary conditions were taken into account in the model. The nodes at the base of the model are fixed against displacement; while the nodes at the far bounds cannot undergo lateral displacements. The depth and width of the sand layer are 25m and 200m, respectively.

The model was discretized by 4–node bilinear elements (CPE4). A mesh size of at least 648 elements was used and it is shown in Figure 5.9. It is noted that the mesh is finer in the vicinity of the foundation since that zone is the zone of stress concentration. The analysis was performed using static approach with both load and displacement control. Note the results of these analyses match. The sand behaviour was simulated by adopting both the modified SANISAND (2004) and the hypoplastic model with intergranular strains (Niemunis and Herle (1997), von Wolffersdorff (1996)). The initial conditions for the modified SANISAND (2004) model request the definition, in addition of the geostatic stress field, of the void ratio and the internal variables distribution with depth (e_0, α, z). Hence, a preliminary simulation was carried out under 1D conditions in order to determine these data. First the initial stress state was set to a small initial isotropic value ($p'_0 = 1kPa$), the void ratio e_0 to 0.810 and the internal variables to zero. Then the final geostatic equilibrium conditions were reached by applying the soil weight ($\gamma = 17kN/m^3$) in small steps. The final converged state at the end of the preliminary simulation was assumed as the geostatic state for the analysis of the footing.

Note that the material constants for SANISAND (2004) and hypoplastic model are those referred to Toyoura sand ($e_0 = 0.810$), which are listed in the work of Dafalias and Manzari (2004) and Herle and Gudehus (1999), respectively.

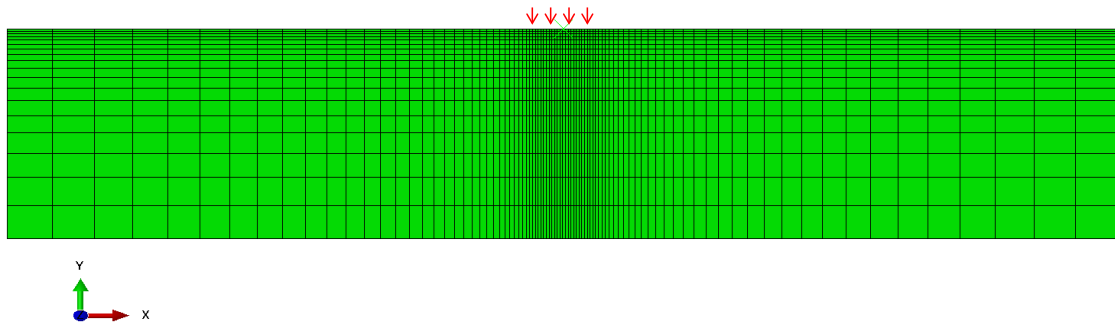


Figure 5.9: Finite element discretization of the shallow foundation problem.

5.3.2 Verification

In Figure 5.10 the load–deflection curve obtained from the numerical simulations with the modified SANISAND (2004) and the hypoplastic model, is compared against the bearing capacity calculated according to Terzaghi (1943) for a loose sandy soil deposit with an initial angle of friction of 28° – 30° .

The finite element prediction using the modified SANISAND (2004) model was automatically terminated approximately at the maximum load of 234kPa, due to the difficulty in convergence of the numerical algorithm. Additionally, severe distortion of some elements in the vicinity of the corner of the foundation was observed. While the finite element prediction adopting hypoplastic model continued until a much more advanced stage, where the maximum load of 793kPa was recorded. However, good agreement was achieved between the numerical results of the modified SANISAND and hypoplastic constitutive model up to 10cm of foundation settlement. Furthermore, it was found that the numerical simulation with the hypoplastic model does not reach the failure load and additionally, the maximum load (793kPa) recorded in the numerical simulation was quite smaller than Terzaghi’s bearing capacity (857kPa). This discrepancy can be attributed to the fact that Terzaghi’s equation assumes that the soil is a rigid–perfectly plastic material; while both the hypoplastic and the modified SANISAND (2004) model consider that the soil is an elastoplastic material with hardening. Therefore, the soil will compact under external applied loads, resulting in

a reduction of void ratio as shown in Figure 5.10b. It can be stated that the hypoplastic model produces more realistic predictions, since the contractant response of the soil upon load increment is captured.

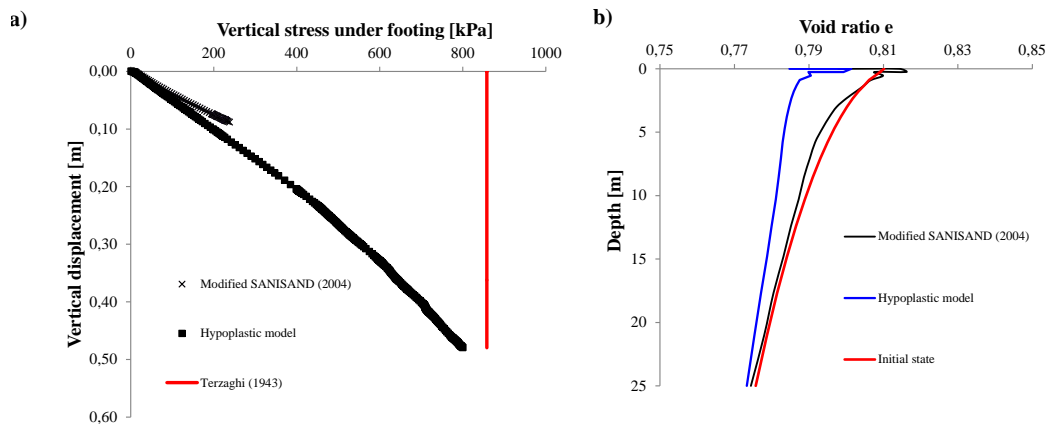


Figure 5.10: Comparison between the modified SANISAND(2004) and hypoplastic model (Niemunis and Herle (1997), von Wolffersdorff (1996)) along with the bearing capacity estimated according to Terzaghi (1943). a) Load–deflection curves and b) Void ratio–depth.

5.4 Calibration of Model Constants

The proposed modified model requires calibration of 16 parameters for Fontainebleau sand shown in Table 5.1 divided in different groups according to the particular role they play. The calibration of the parameters was carried out from the data of standard types of laboratory tests performed at DTU GEO–Lab, see Latini and Zania (2017b). Particularly drained and undrained triaxial compression tests at different values of initial void ratio and confining pressure were performed to determine different features of hardening/softening and dilatancy/contractancy of the model as it was presented in previous versions of SANISAND model (Dafalias and Manzari (2004), Taiebat and Dafalias (2008)). The calibration procedure of the modified SANISAND (2004) model and simulation of some available laboratory experiments are presented in this section.

Parameter	Physical meaning	Value
G_0	Constant of elastic shear modulus	293.5kPa
ν	Poisson's ratio	0.30
α^c	Critical back stress ratio in triaxial compression	1.35
c	Ratio of extension to compression quantities	0.70
λ	Slope of the critical state line in $e - p$ plane	0.0309
e_0	Intercept of the critical state line in $e - p$ plane	0.934
ξ	Exponent of the critical state line in $e - p$ plane	0.60
m	Tangent of half the opening angle of the yielding surface	0.01
h_0	Constant of hardening modulus H	3.41
c_h	Constant of hardening modulus H	1.25
n^b	Material constant needed to calculate the stress image on the boundary surface	0.59
A_0	Dilatancy constants	1.06
n^d	Material constant needed to calculate the stress image on the dilatancy surface	1.01
c_z	1 st constant of fabric dilatancy tensor – control of the pace evolution of z	600
z_{max}	2 nd constant of fabric dilatancy tensor – maximum value that z can attain	4

Table 5.1: Material constants of the modified SANISAND (2004) for Fontainebleau sand.

5.4.1 Elasticity parameters

The constant of elastic shear modulus G_0 was calibrated by fitting Equation 5.31 to the initial stage of the stress–strain curves of triaxial drained tests ($\epsilon_q - q$ curves). The range of deviatoric strains considered was up to 0.02%.

$$G = G_0 p_{atm} \frac{(2.97 - e)^2}{1 + e} \left(\frac{p}{p_{atm}} \right)^{1/2} \quad (5.31)$$

The elastic shear modulus G_0 is 20% less of G_{max} assuming a mean effective confining pressure of 50kPa for the range of deviatoric strain deformations considered (Kramer (1996)). Poisson's ratio ν was obtained by the ratio between volumetric and axial strains in the loading–unloading phase, see Figure 5.11b. The value of Poisson's ratio suggested is in agreement with the one adopted in the work of Miriano (2011) for Toyoura sand, Tricarico (2015) for Leighton Buzzard sand and additionally it is within the range presented by Papadimitriou et al. (2001) and Papadimitriou and Bouckovalas (2002).

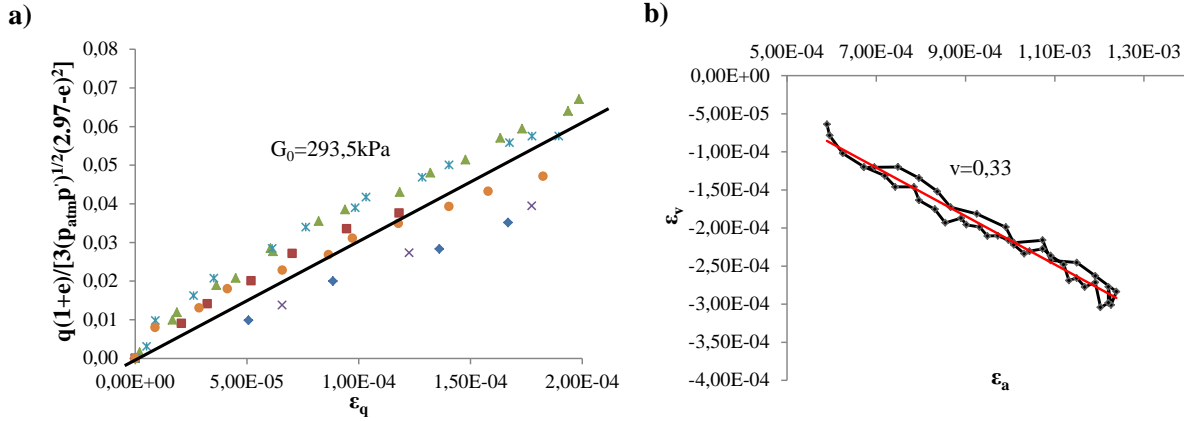


Figure 5.11: Calibration of G_0 a) and Poisson' ratio ν b) constant using data of drained triaxial compression tests on Fontainebleau sand.

5.4.2 Critical state line parameters

The critical state parameters in SANISAND model are the critical back–stress ratio in triaxial compression α_c^c and extension α_e^c , critical void ratio e_0 , slope of the critical state line λ_c and the exponent of the critical state line ξ in $e - p$ plane. They are introduced to define the location of the critical state line. The calibration can be performed using monotonic tests that approach the critical state. For the case of sandy soil Papadimitriou et al. (2001) and Papadimitriou and Bouckovalas (2002) suggested a range of values for the constants defying the critical state line as reported in Table 5.2. These values can be considered in the calibration procedure, since the expression of the critical state line in the work of Papadimitriou and Bouckovalas (2002) coincides with that of SANISAND(2004) and the modified SANISAND model.

Parameter	Physical meaning	Value
α_c^c	Critical back stress ratio in triaxial compression	1.20-1.37
α_e^c	Critical back stress ratio in triaxial extension	0.86-1.00
c	Ratio of extension to compression quantities	0.717-0.730
λ	Slope of the critical state line in $e - p$ plane	0.01-0.03
e_0	Intercept of the critical state line in $e - p$ plane	0.72-0.90

Table 5.2: Critical state line parameters and typical range of values for sands.

This observation is corroborated by the fact that the calibrated values for the above mentioned constants reported in the work of Dafalias et al. (2004) and Tricarico (2015) are within the corresponding interval suggested by Papadimitriou et al. (2001) and Papadimitriou and Bouckovalas (2002). The critical back–stress ratio in compression α_c^c is defined as $\alpha_c^c = (q/p)_{critical}$. The ratio $(q/p)_{critical}$ is the slope obtained by plotting the results of triaxial compression tests at the critical state in $p-q$ space and fitting a best–fit line through the data points as shown in Figure 5.12a. The critical back–stress ratio in extension α_e^c was determined assuming $(\alpha_e^c)/(\alpha_c^c) = 0.70$. It was proven that Van Eekelen function (Van Eekelen (1980)), which shows the dependency of α^c on θ , is convex for $\alpha_c^c = 1.35$ and $\alpha_e^c/\alpha_c^c = 0.70$. In addition, the proposed value of α_c^c and α_e^c is within the interval given by Papadimitriou et al. (2001) and Papadimitriou and Bouckovalas (2002).

The constants e_0 , λ and ξ can be calibrated by plotting triaxial test data in $e - p/p_{atm}$ space and fit them to a line having expression as Equation 5.32. This means that once the best fitted line is drawn, e_0 and λ are the intercept with the e -axis and the slope of the best fitted line, see Figure 5.12b.

$$e_c = e_0 - \lambda \left(\frac{p_c}{p_{atm}} \right)^\xi \quad (5.32)$$

The critical state line parameters for Fontainebleau sand are slightly different with those obtained by Goorani and Hamidi (2015). It is important mentioning that in the work of Goorani and Hamidi (2015) the estimation of the critical state line constants was performed by adopting only data of drained compression triaxial tests.

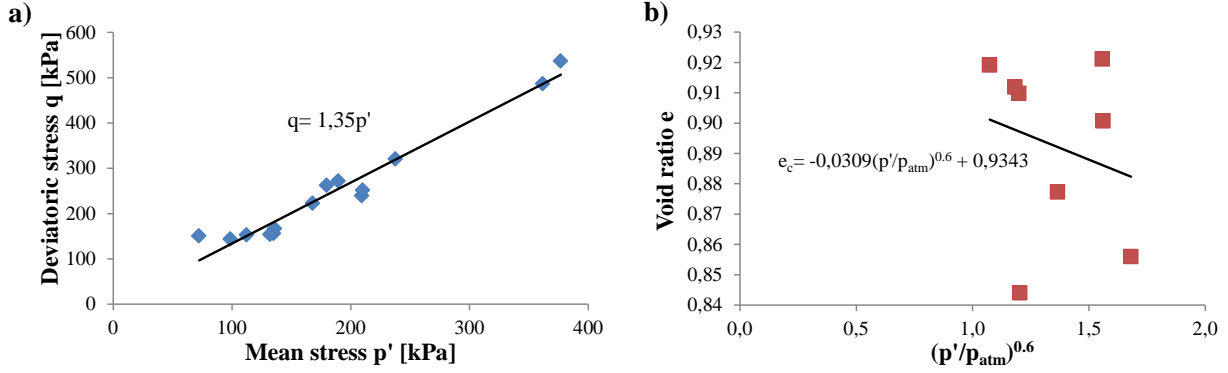


Figure 5.12: Calibration of critical state line constants using data of undrained and drained triaxial compression tests on Fontainebleau sand.

5.4.3 Yield surface parameter

m is defined as the tangent of half the opening angle of the yield surface and it is usually set equal to about $1/100\alpha_c^c$, which is approximately 0.01 for the case of Fontainebleau sand. It is worth mentioning that the same value has been obtained both for Toyoura sand and Leighton Buzzard sand, as reported in the work of Dafalias et al. (2004) and Tricarico (2015), respectively.

5.4.4 Dilatancy parameters

The dilatancy parameters are the material constant needed to calculate the stress image on the dilatancy surface n^d and the dilatancy material constant A_0 . The constant n^d is determined as:

$$n^d = \frac{1}{\psi^d} \ln\left(\frac{\alpha^d}{\alpha^c}\right) \quad (5.33)$$

where ψ^d and α^d are the values at phase transformation measured from undrained or drained test. In drained test the phase transformation corresponds to the peak of volumetric strain ϵ_v , while the peak of excess pore pressure $u - u_0$ in undrained tests. Note that the value of α^d must be negative for extension.

Therefore, the constant n^d can be determine by plotting the $\ln\left(\frac{\alpha^d}{\alpha^c}\right)$ with respect the corresponding ψ^d of different tests, see Figure 5.13a.

To determine A_0 the following relationship can be adopted by ignoring the small elastic deformations in a drained triaxial test:

$$\frac{\dot{\epsilon}_v}{\dot{\epsilon}_q} \cong \frac{\dot{\epsilon}_v^p}{\dot{\epsilon}_q^p} = A_0(\alpha^d - \alpha) \quad (5.34)$$

5.4.5 Kinematic hardening parameters

The kinematic hardening constants are the stress image on the boundary surface n^b , the 1st and 2nd positive material constant to define the hardening modulus, respectively h_0 and c_h . The constant n^b is determined as:

$$n^b = \frac{1}{\psi^b} \ln\left(\frac{\alpha^c}{\alpha^b}\right) \quad (5.35)$$

where ψ^b and α^b are the values at the peak stress ratio state from undrained or drained test. In Figure 5.13b the constant n_b is shown by plotting the $\ln\left(\frac{\alpha^c}{\alpha^b}\right)$ with respect the corresponding ψ^b of different tests, see Figure 5.13b.

The constants h_0 and c_h are related to the effect of distance from the bounding. The constant h_0 can be obtained by matching the model predictions to the flattening slope of the $q - \epsilon_a$ curve in a drained compression test. While c_h was obtained by trial and error procedure.

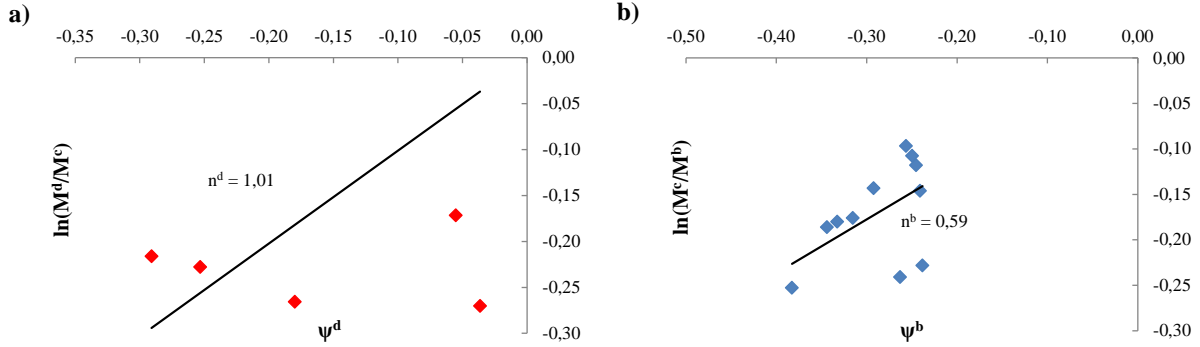


Figure 5.13: Calibration of constant n^d a) and n^b b) for Fontainebleau sand using drained compression triaxial tests.

5.5 Model performance

In this section the performance of the modified SANISAND model, adopting the material constants calibrated in Section 5.4, is validated against experimental data of triaxial drained compression tests performed at Navier Laboratory (Dupla et al. (2010)) and the University of Western Australia (Truong (2017)).

Fontainebleau sand

The Fontainebleau Sand is natural uniform silica sand from the region of Etampes south of Paris in France. The sand type used in the triaxial tests is a Fontainebleau sand. Fontainebleau sand is a well-sorted, clean sand with a particle size ranging from 0.063mm to 0.25mm , and a uniformly index of $U < 2$. Further classification parameters are given in Table 5.3 and they have been determined according to Bulletin (2001).

Relative grain density	d_s	2.655
Densest deposition	e_{min}	0.549
Loosest deposition	e_{max}	0.853

Table 5.3: Classification parameters for sand

Figures 5.14, 5.15 and 5.16 compare the data and simulations for drained triaxial compression (CID) tests on isotropically consolidated samples of Fontainebleau sand by using the data of Dupla et al. (2010). Particularly, the comparison in terms of deviatoric stress–axial strain is showed in Figure 5.14a, while Figure 5.14b does the same in terms of volumetric and axial strain response for the loose samples ($e_0 = 0.712$) with initial confining pressures in the range of 50 kPa to 200 kPa. Similarly comparison between data and simulations at medium dense ($e_0 = 0.638$) and dense ($e_0 = 0.573$) samples is presented in Figures 5.15 and 5.16 respectively.

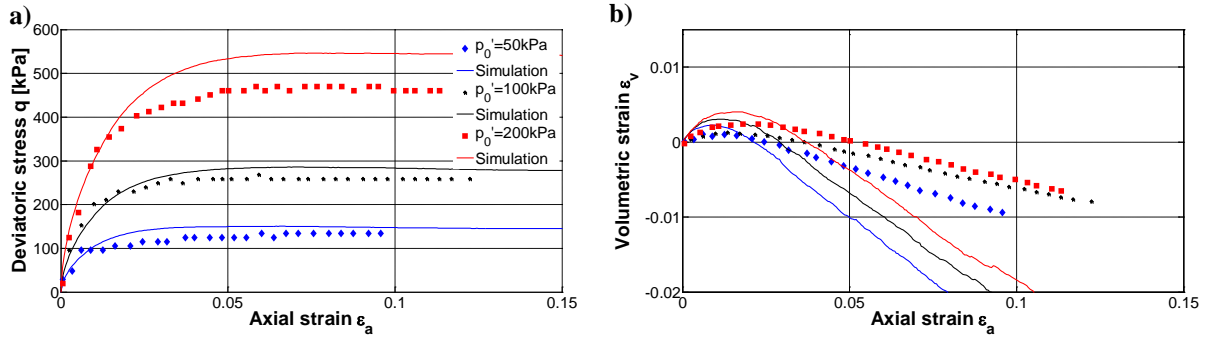


Figure 5.14: Comparison of data and simulations for drained compression triaxial tests on isotropically consolidated samples of Fontainebleau sand ($p'_0 = 50 - 200\text{kPa}$) and initial void ratio $e_0 = 0.712$.

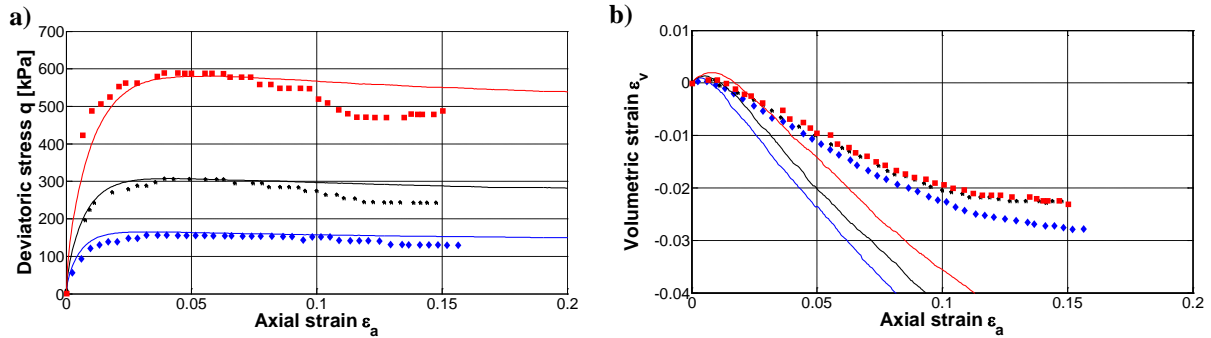


Figure 5.15: Comparison of data and simulations for drained compression triaxial tests on isotropically consolidated samples of Fontainebleau sand ($p'_0 = 50 - 200\text{kPa}$) and initial void ratio $e_0 = 0.638$.

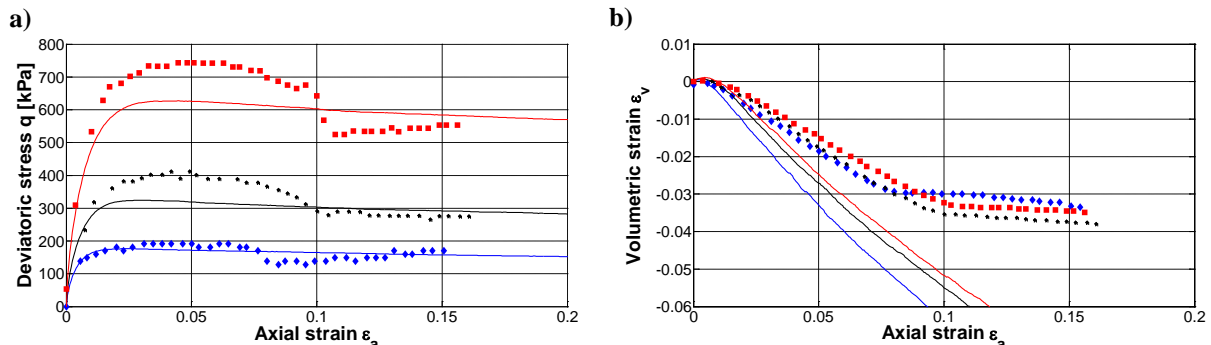


Figure 5.16: Comparison of data and simulations for drained compression triaxial tests on isotropically consolidated samples of Fontainebleau sand ($p'_0 = 50 - 200\text{kPa}$) and initial void ratio $e_0 = 0.573$.

Good agreement between the experimental data and the numerical simulations in terms of deviatoric stress–axial strain was achieved for loose and medium dense samples; while the discrepancy became more apparent for dense sand with high initial confining pressure ($p'_0 = 200\text{kPa}$). Furthermore, it is evident that the simulations underpredicted the volumetric strains. A possible explanation might be that in the data of Dupla et al. (2010) the volumetric strain was calculated by measuring the water volume in the triaxial cell. Whereas the material constants have been estimated calculating the volumetric strain from the data of water weight. Additionally, the triaxial tests performed at DTU showed that the volumetric strains obtained from the measurements of the water volume in the cell are smaller than those calculated by using the water weight as shown in Figure 5.17.

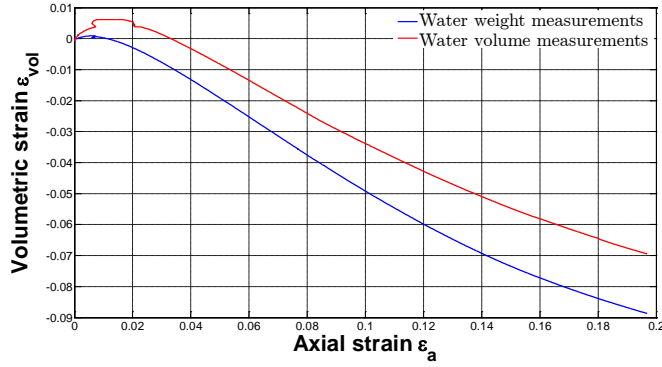


Figure 5.17: Volumetric strain estimated from the data of drained compression triaxial test on isotropically consolidated samples of Fontainebleau sand ($p'_0 = 200kPa$) and initial void ratio $e_0 = 0.684$.

However, both the data and the numerical outcomes showed highly dilatant sand behaviour in samples characterized by higher density and lower confining pressure; whereas for lower density values and higher confining pressures the contractant behaviour became more visible. Figure 5.18 compares the data and simulations for drained triaxial compression (CID) tests on isotropically consolidated samples of Fontainebleau sand by using the data reported in Truong (2017). It is apparent that the simulations approximate well the experimental results both in $q-\epsilon_a$ and $\epsilon_a - \epsilon_v$ plane.

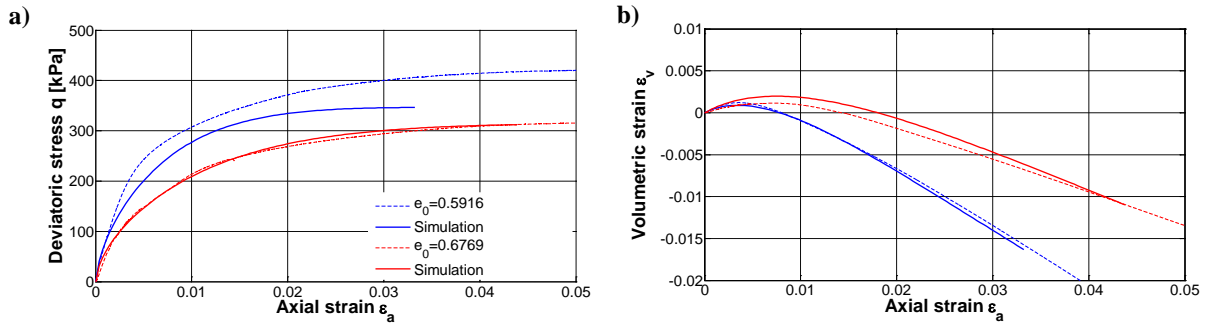


Figure 5.18: Comparison of data and simulations for drained compression triaxial tests on isotropically consolidated samples of Fontainebleau sand ($p'_0 = 100kPa$).

5.6 Limitations of the modified SANISAND model

- The proposed model as the original one does not allow for flow under loading proportional path. This limitation was solved in the work of Taiebat and Dafalias (2008) by introducing a yield surface with cap;
- Both SANISAND (2004) and the modified SANISAND (2004) are characterized by an inaccurate prediction of plastic and volume strains in drained cyclic tests. The abovementioned shortcoming can be overcome by expressing the hardening parameter, h_0 , as a function which decreases throughout the cycles. Practically, the hardening parameter can be implemented as a function of the fabric change, similarly to the dilatancy. This would provide better representation of the hardening of the sand and incremental shear strains.
- In both the proposed formulation and the original one, the elasticity of sand is assumed isotropic. Experimental observations (e.g., Kuwano and Jardine (2002)) have highlighted that

the elastic stiffness is typically anisotropic and evolves with deformation, see the work of Lashkari (2009).

5.7 Conclusions

A smooth hyperbolic approximation to SANISAND (2004) yield function is derived. The rounded hyperbolic surface is continuous and differentiable for all stress states, and it can approximate the original yield surface by adjusting one parameter. The present modification does not alter the features of the previous version of SANISAND (2004). Additionally, the modified SANISAND model was used to simulate the response of a shallow foundation subjected to a vertical load. The results showed that the model was able to reproduce the foundation settlement up to 10cm. This can be motivated by the difficulty in convergence of the numerical algorithm that involves a number of highly nonlinear rate equations. On the other hand, the performance of the hypoplastic model was proved to be quite satisfactory, since the analysis continued until a much more advanced stage and the contractant response of the soil upon load increment was captured. In light of these observations it is recommended to deploy the hypoplastic model for future numerical analyses of foundations in sand.

Furthermore, the material constants of the modified SANISAND model were calibrated for Fontainebleau sand by using drained and undrained compression triaxial tests performed at DTU GEO–Lab. The calibration of the material constants can be considered satisfactory, since deviatoric stress–axial strain and volumetric strains of the model were well compared with samples with different relative density and initial confining pressure, provided by two independent laboratories. Additionally, the outcomes highlighted that the modified SANISAND constitutive model is able to predict well shear strength and strain characteristics of Fontainebleau sand.

5.8 Recommendations for future work

- Perform further triaxial tests in Fontainebleau sand in order to have more precise estimation of the material constants;
- Perform dynamic cyclic numerical analysis of a 3D soil–pile system in finite element software Abaqus by applying the modified SANISAND constitutive model;
- Validate the computational results with respect to experimental data obtained after cyclic pile testing performed in the geotechnical centrifuge at DTU.

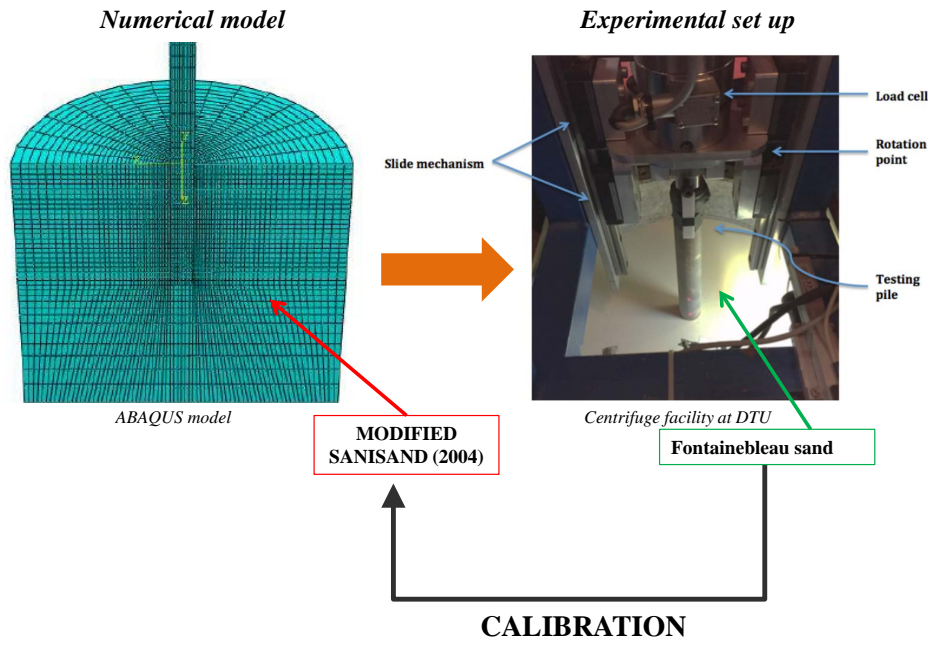


Figure 5.19: Numerical modelling of cyclic load of piles.

Chapter 6

Integrated optimal design of jackets and foundations

The findings of this chapter are presented in Paper VIII.

6.1 Introduction

This chapter is about the optimal design of jackets and their foundations, highlighting the influence of soil characteristics and design procedures. It is assumed that these interaction effects can be properly considered by adopting an integrated design approach. In the literature the optimization problem of wind turbine components has been broadly investigated and it has been showed that the cost of energy can be significantly reduced by an integrated optimal design approach (Ashuri (2012)). Optimal design of support structures for offshore wind turbines has been extensively addressed, by assuming fixed-base conditions at the foundation level. In the geotechnical engineering field there are very few studies concerning the optimization of foundations. It is worth mentioning the work of Pucker and Grabe (2011) and Seitz and Grabe (2016), which focus on the topology optimization of foundation. However the author does not have knowledge of studies where an integrated optimal design of the jacket and its foundation has been performed. The main advantage of this approach is that it provides a useful basis for the detailed design of the overall structure, since new foundation designs can be quickly determined in case of changing design conditions. This approach is required for a more complex model, since all the design constraints for both the foundation, the substructure, and the full support structure are included in one design procedure. The complexity of the problem would further increase if variable soil conditions are also accommodated.

The aim is to examine the design of offshore wind turbines, considering the interaction effects between soil properties, foundation design, and the support structure. In the structural optimization problem the target is to minimize the combined mass of foundation and jacket taking into consideration the requirements on fatigue, frequency, buckling and foundation capacities. The optimal design problem is solved considering different foundation types (piles and suction caissons) and both analytical and CPT-based design procedures for piles are included. In an attempt to examine a wide spectrum of soil conditions, different sets of soil profiles have been taken into account, from very soft to very stiff soil. Additionally both cohesive (clay) and cohesionless (sand) soil were represented in this study.

Due to the multidisciplinary nature of the problem, the work has been done in collaboration with Kasper Sandal, former Ph.d. student at DTU Wind Energy Department, in order to combine expertise in the design optimization and foundation design.

6.2 Methodology

The design procedures for pile foundations and suction caisson foundations are implemented into the existing framework for optimal conceptual design of jacket structures called JADOP (Jacket Design Optimization, see Figure 6.1). Note that the initial configuration of the jacket, the transition piece, tower and RNA are herein modelled according to DTU 10MW reference wind turbine (Bak et al. (2013), Borstel (2013)).

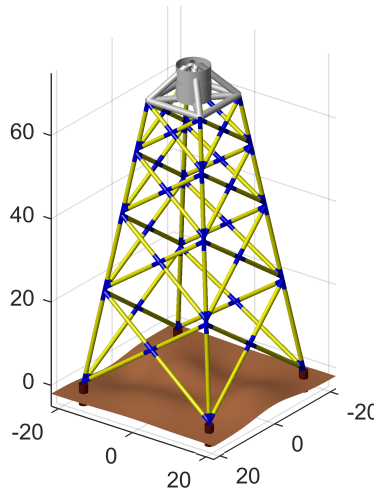


Figure 6.1: A four-legged jacket substructure for large offshore wind turbines. Modified after *Paper VIII*.

The mathematical implementation in JADOP has been carried out by Kasper Sandal (Sandal (2017)), while the foundation modelling and design constraints have been provided by the author of the thesis and they are shortly described hereafter for both piles and suction caissons, and a simple elasto-plastic formulation (model) has been adopted. Hence the stiffness and the ultimate capacity for the different load components have been defined. In order to estimate the global displacement of the system (jacket and foundation) it is fundamental to establish the stiffness of the foundation. The stiffness coefficients of the soil-pile system have been determined according to the expressions suggested by Randolph (1981), while the expressions proposed by Latini and Zania (2017a) have been adopted for the stiffness coefficients of suction caisson-soil system. The optimization of the pile foundation was accomplished calculating axial and lateral ultimate capacities according to the current state of practice for offshore foundations (API (2011)). Axial pile resistance is given by two separate contributions: shaft resistance acting along the pile length and end bearing resistance at the pile tip. Note that both plugged and unplugged capacities have been calculated and the final axial capacity is given by the minimum of the two. Particularly the shaft resistance is determined according to the α -method (API (2011)) and the β -method (API (2011)) for piles embedded in clay and sand profiles, respectively. The end bearing capacity of piles in sand can be assessed by multiplying the effective vertical stress in the soil with a dimensionless factor N_q , which incorporates the dependency of the soil internal friction angle on the stress level. While in clays the maximum bearing strength, usually set as $9s_u$, where s_u is the undrained shear strength of the soil, governs the end bearing response of piles. Additionally real CPT records were used and then the optimal design of piles was performed by adopting UWA CPT-based method (Lehane et al. (2005)) for the estimation of the shaft resistance and end bearing capacity of pile foundations in sand soils. In this way it was possible to evaluate the influence of the design method in the foundation optimization. Suction caisson is a novel form of foundation for offshore wind turbine installed on jacket structures. No standard design methods are currently well defined for this type of foundation and hence, the author decided to adopt state-of-art formulations in the framework of API provisions (API (2011)). The failure envelopes formulations of Gourvenec (2008) and Supachawarote et al. (2004) were adopted for the estimation of the bearing capacity of suction caissons embedded in clay and

subjected to combined vertical, horizontal and moment loading. The abovementioned studies have developed failure envelopes after fitting the ultimate capacity derived from numerical analyses where the soil was assumed to behave as a linear elastic-perfectly plastic material and the soil failure conditions were defined according to Tresca criterion. The difference of these solutions is the range of slenderness ratio. In order to cover all ranges of slenderness ratio both methods were implemented. While the closed-form expression proposed by Gottardi et al. (1999) for circular footing on dense sand was selected in this study, since mathematical formulations on the ultimate resistance of suction caissons in sands are not available in the literature. This is considered conservative, since the shaft resistance at the skirt of the caisson is disregarded. In regards with the tensile capacity, the uplift capacity was calculated as a reverse bearing capacity considering a minimum recommended factor of safety equal to 2.0 in agreement with API provisions (API (2011)).

6.3 Results

This study shows that several standard methods for foundation design can be automatically calculated by applying numerical optimization. Hereafter only representative results from the investigation of the optimization problem are presented. The reader is referred to *Paper VIII* for further results. It is important to highlight that numerical simulations can also be performed by taking into account integrated design of the jacket and the foundation. Generally the numerical results indicated that an integrated design approach is valuable in the conceptual design phase. Regarding the effect of the foundation design, a comparison between the traditional and the CPT-based method is shown in Figure 6.2. The consistency of the two methods was ensured, as after classification of the CPT record an uniform soil profile with consistent soil properties was considered for the traditional method.

It is evident that the design of the jacket structure is not affected by the foundation design; on the contrary the foundation mass shows high sensitivity to the applied design method and consistently the CPT based method provides the optimal design for piles in sand soils. Additionally, it was found that the jacket mass increases as the leg distance increases, on the other hand a large leg distance is desired for the foundation design. This trend is motivated by the fact that the axial forces are redistributed among the single foundations. In order to keep the total mass at minimum the critical leg distance is slightly larger from the one minimizing the jacket, see *Paper VIII*.

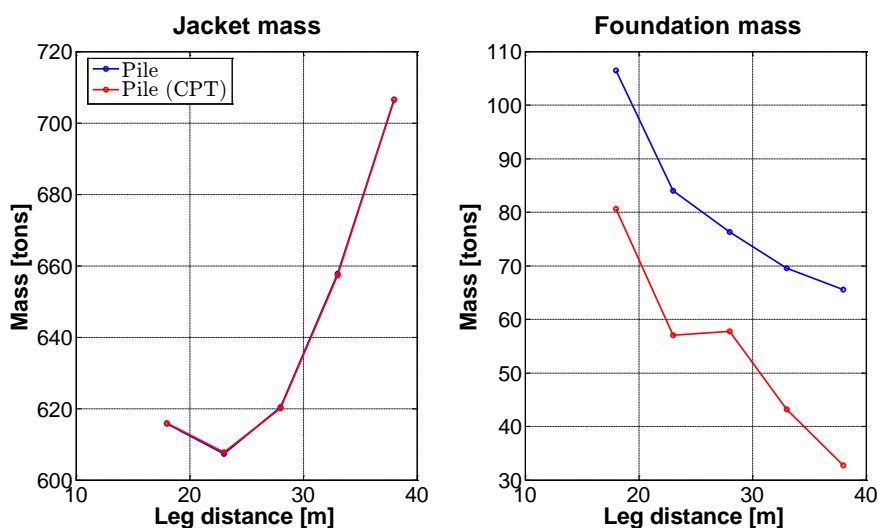


Figure 6.2: Variation of the jacket and foundation masses with respect to the leg distance in sand soil profile.

Figure 6.3 illustrates the variation of the jacket and foundation mass with respect to the soil stiffness, where A and E represent the stiffest and the softest soil profile, respectively. Note that the

outcomes are presented for clay deposits. The results highlighted that the jacket and the foundation mass increase when the stiffness and the strength of the soil deposit reduce. Whereas the design of the jacket is slightly influenced when suction caissons with large slenderness ratio are adopted. At soft soil deposits the optimized caisson diameter increases drastically ($d > 6\text{m}$), hence the observed increase in foundation mass. Moreover, it was found that the caisson with the larger slenderness ratio is preferable for medium stiff and stiff soil profiles, on the contrary long pile provides more economical design for soil type D and E.

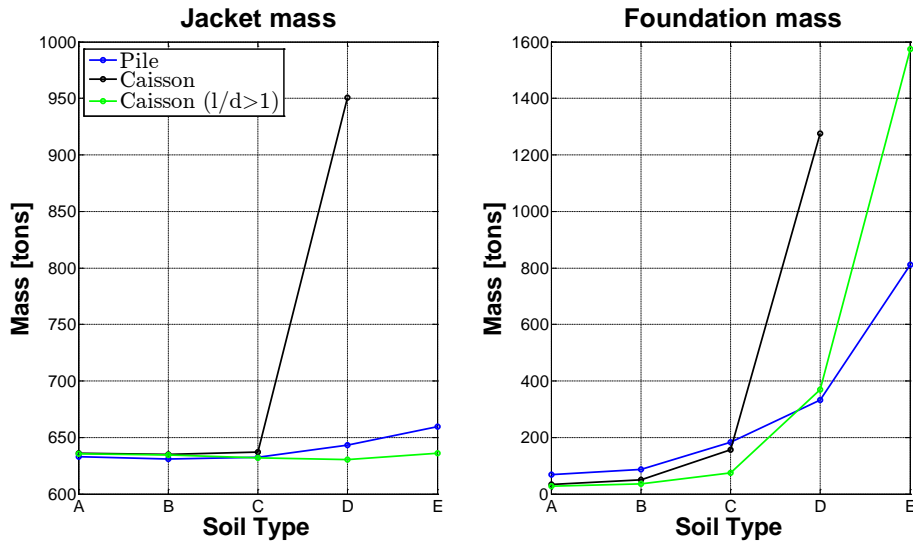


Figure 6.3: Effect of the soil type on the jacket and foundation masses in clay soil profile.

Furthermore, the influence of the optimization on the structural eigenfrequency was investigated. Figure 6.4 presents how the frequency varies with respect to the leg distance and soil stiffness for pile foundation in sand and in clay soil deposits. It is worth mentioning that the frequency range for the DTU 10MW reference wind turbine is between 0.16–0.30Hz. The outcomes showed that the frequency reduces when the leg distance decreases and in the case of soft soil conditions. The influence of the soil stiffness on the natural frequency of the overall structure achieved approximately 8% in the case of soft sand soils, while it is smaller in clay profiles because the foundation behaves stiffer and it is characterized by larger mass.

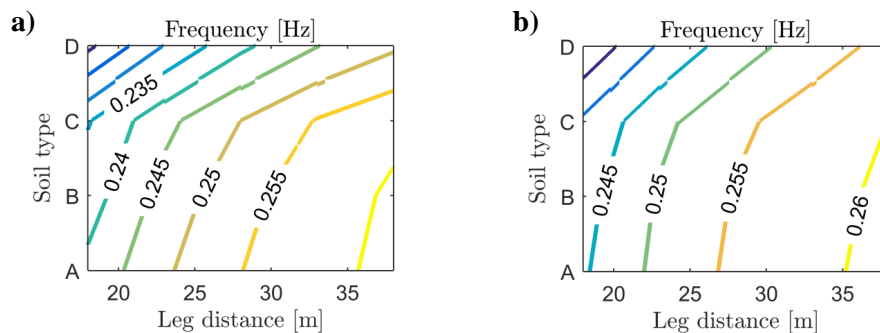


Figure 6.4: Variation of the frequency with respect to the leg distance and soil stiffness for pile foundation in sand a) and in clay soil profile b).

6.4 Conclusions

The results showed that the design of the jacket structure is not affected by the foundation design, with exception of very soft soil conditions. In addition it was found that leg distance plays an important role on the foundation design and therefore a long leg distance is desired. Moreover the CPT-based method provides a more economic pile design than the traditional design approach in sand sites. For clay deposits the optimal foundation design is given by piles embedded in soft soils, while in medium stiff and stiff soils suction caissons with slenderness ratio larger than 1 are recommended. Furthermore, it was noticed that the soil stiffness affects the natural frequency of the overall structure and this influence is more prominent in soft soil deposits.

It is emphasized that the findings are based on extreme static loads and the assumption of linearity in the soil deposit. Additionally, the mass function does not taken into account the lid and the stiffeners of the foundation and therefore, this prevents a reliable estimation of the mass, especially for suction caissons.

6.5 Recommendations for future work

- Include dynamic loads in the integrated optimal design of jackets and foundations;
- Model the behaviour of the soil by more advanced constitutive models, in order to represent the effect of cyclic loading and nonlinear response;
- Perform the optimization with cost function that includes the installation costs of the foundation.

Conclusions

- In this study the dynamic response of piles and suction caissons embedded in linear elastic soil layer with hysteretic damping is investigated by adopting both analytical and numerical methodologies. A parametric study was presented to analyse the vibration characteristics of floating piles and suction caissons; and illustrate the effects of major parameters on the stiffness and damping properties. The main dimensionless parameters examined were the slenderness ratio, the relative thickness and the stiffness of the soil layer. The following conclusions can be summarized regarding the type of foundation.

Piles The lateral dynamic response of end bearing pile was investigated by establishing a 3D numerical model, which was then validated against the analytical results of Novak and Nogami (1977) and Mylonakis (2001). Moreover, a continuum analytical solution for the estimation of the dynamic impedances of floating piles was proposed. The analytical formulation was validated against finite element numerical models for floating piles. The findings presented are applicable to flexible floating piles; while the given formulation cannot predict correctly the dynamic response of short and rigid piles, since vertical displacements are disregarded. The dynamic soil–pile interaction analysis of flexible floating piles showed that the slenderness ratio is not influential and consequently pointed out that the dynamic active length is not an appropriate design criterion for floating piles. On the contrary, the dynamic impedances were found to be profoundly influenced by the variation of the thickness of the soil layer; while the dimensionless parameter E_p/E_s had relatively small influence on the stiffness and this was demonstrated by slightly scattered results particularly for soft soil profiles. The proposed analytical solution can be applied in the frame of the substructure approach, to perform complete dynamic soil–structure interaction analyses of structures on such kind of foundations.

A 3D numerical model for the estimation of the vertical dynamic impedance of end bearing and floating piles was established and the numerical modelling procedure was validated against existing analytical solutions for end bearing. Particularly, it was found that the analytical solution of Novak and Nogami (1977) is in close agreement with the numerical outcomes. The parametric study conducted indicated that the dynamic response of floating piles is slightly influenced by increasing E_p/E_s , especially after the 2nd vertical resonance of the soil layer. On the other hand, a decrease of the relative thickness of the soil layer on the vertical dynamic impedance determined a more prominent reduction of stiffness at the 1st resonance. Furthermore, the results showed that the effect of the slenderness ratio on the vertical dynamic response of floating piles can be assumed negligible for foundations embedded in medium–stiff soil profile.

Suction caissons The numerical results contributed to establish simple mathematical expressions for the static stiffness coefficients of suction caissons. The suggested formulas provide a more accurate estimation of the stiffness components compared to previous analytical expressions.

Contrary to the case of floating piles, the skirt length was found quite substantial parameter

for predicting the lateral and vertical dynamic response of the suction caissons. With reference to the stiffness ratio E_p/E_s , it was observed that the dynamic impedances are mainly affected by E_p/E_s at the higher frequency interval. The outcomes are consistent with the trends observed on the dynamic response of floating piles. On the other hand, the type of variation of soil modulus with depth in inhomogeneous profiles strongly influenced the dynamic response of suction caissons. In addition, this work highlighted that the dynamic response of suction caissons was significantly dependent on the dimensionless parameter H_s/d and valuable insight on the physics of the problem is obtained by taking into account the relative thickness of the soil medium. Whereas the effect of Poisson's ratio with values less than 0.40 was demonstrated to be marginal on the vertical behaviour of suction caissons in the frequency interval examined. At higher values of Poisson's ratio, the vertical eigenfrequency increased compared to the theoretical one, while the vertical dynamic stiffness was also found dependent on the horizontal displacements. The numerical results at nearly incompressible soil medium ($\nu = 0.495$), when the horizontal displacements are constrained, can be considered unreliable. In this study simple mathematical functions were developed for the estimation of the vertical and lateral dynamic impedances. A good agreement was achieved between the numerical results and the proposed expressions for the frequency ranges examined. It is important to note that the suggested model is limited by the assumptions of linearity in the soil layer and foundation materials, and the perfect contact at the soil–foundation interface. Moreover, the dynamic response of suction caisson foundations is also influenced by the thickness of the skirt and the flexibility of the lid, whose effects are not being studied in this work.

- In addition, this research project was focused on modelling the cyclic behaviour of soil. Particularly, the soil constitutive model of Manzari and Dafalias (SANISAND, 2004) has been modified in order to solve inefficient performance of the stress integration scheme for soil deposits in the low stress regime. Moreover, drained and undrained compression triaxial tests at DTU GEO-Lab were performed to calibrate the material constants of the constitutive model for Fontainebleau sand. The calibration of the material constants can be considered satisfactory, since deviatoric stress–axial strain and volumetric strains of the model were well compared with samples with different relative density and initial confining pressure, provided by two independent laboratories.
- Finally this work suggests a method for integrated design of offshore wind turbine jackets and foundations by adopting numerical structural optimization. In the optimal design problem the design procedure is automated by minimizing the combined mass of foundation and jacket and accounting for the requirements on fatigue, frequency, buckling and foundation capacities. Two different foundation types (piles and suction caissons), a range of different leg distances, and ten soil profiles were included in the integrated design optimization of jacket and foundation. The outcomes highlighted that the jacket design is not significantly influenced by the foundation design, whereas the jacket mass and the leg distance were found quite substantial parameters to determine the foundation design. Additionally, the natural frequency of the overall structure is affected by the stiffness of the soil profile. Particularly, the influence of the soil conditions is more prominent for piles embedded in relatively soft soils. Furthermore the CPT-based method always provides the optimal design and it was found that the pile mass is slightly sensitive to the variation of the tip resistance.

Bibliography

4C Offshore. Jacket or lattice structures.

Al-Tabbaa, A. and Muir Wood, D. An experimentally based "bubble" model for clay. *Numerical models in geomechanics. NUMOG III*, pages 91–99, 1989.

Andersen, K.; Puech, A., and Jardine, R. Cyclic resistant geotechnical design and parameter selection for offshore engineering and other applications. In *Proceedings of the TC-209 Workshop, Design for Cyclic Loading: Piles and Other Foundations, Paris. Presses des Ponts*, pages 9–44, 2013.

Anoyatis, G.; Mylonakis, G., and Lemnitzer, A. Soil reaction to lateral harmonic pile motion. *Soil Dynamics and Earthquake Engineering*, 87:164–179, 2016.

API. Geotechnical and foundation design considerations. ANSI/API RP 2GEO 1st edition Petroleum and natural gas industries: Specific requirements for offshore structures, Part 4. Technical report, API, 2011.

Argyris, J.; Faust, G.; Szimmat, J.; Warnke, E., and Willam, K. Recent developments in the finite element analysis of prestressed concrete reactor vessels. *Nuclear Engineering and Design*, 28(1): 42–75, 1974.

Ashuri, T. *Beyond Classical Upscaling : Integrated Aeroservoelastic Design and Optimization of Large Offshore Wind Turbines*. PhD thesis, Technische Universiteit Delft, 2012.

Aubeny, C. and Murff, J. Simplified limit solutions for undrained capacity of suction anchors. In *Deepwater Mooring Systems: Concepts, Design, Analysis, and Materials*, pages 76–90. 2003.

Bak, C.; Zahle, F.; Bitsche, R.; Kim, T.; Yde, A.; Henriksen, L. C.; Natarajan, A., and Hansen, M. The DTU 10 MW reference wind turbine. Technical report, DTU Wind Energy, 2013.

Bank of International Settlements. Triennial central bank survey of foreign exchange and derivatives market activity in 2013. Technical report, sep 2013.

Baranov, V. On the calculation of excited vibrations of an embedded foundation. *Voprosy Dynamiki Prochnosti*, 14:195–209, 1967.

Been, K. and Jefferies, M. A state parameter for sands. *Géotechnique*, 35(2):99–112, 1985.

Been, K.; Jefferies, M., and Hachey, J. Critical state of sands. *Géotechnique*, 41(3):365–381, 1991.

Bhattacharya, S. Challenges in design of foundations for offshore wind turbines. *Engineering & Technology Reference*, 1(1), 2014.

Bhattacharya, S.; Nikitas, N.; Garnsey, J.; Alexander, N.; Cox, J.; Lombardi, D.; Muir Wood, D., and Nash, D. Observed dynamic soil–structure interaction in scale testing of offshore wind turbine foundations. *Soil Dynamics and Earthquake Engineering*, 54:47–60, 2013.

- Biot, M. Theory of propagation of elastic waves in a fluid-saturated porous solid. i. low-frequency range. *The Journal of the acoustical Society of america*, 28(2):168–178, 1956.
- Blaney, G. Dynamic stiffness of piles. In *Proc. 2nd Int. Conf. Numer. Meth. Geomech, Blacksburg, 1976*, pages 1001–1012, 1976.
- Borstel, T. Design report - reference jacket. Technical Report D4.3.1, DTU Wind Energy, 2013.
- Broms, B. Methods of calculation for laterally loaded piles. *Royal Swedish Geotechnical Institute – Reprints and Preliminary Reports*, (9), 1965.
- Bulletin. *Dansk geoteknisk forening (DGF)*, volume 15. ISBN 87–983058–7–5, 2001.
- Carter, J. and Kulhawy, F. Analysis and design of drilled shaft foundations socketed into rock. Technical report, Electric Power Research Inst., Palo Alto, CA (USA); Cornell Univ., Ithaca, NY (USA). Geotechnical Engineering Group, 1988.
- Chiu, C. and Ng, C. A state-dependent elasto-plastic model for saturated and unsaturated soils. *Géotechnique*, 53(9):809–830, 2003.
- Clausen, C.; Aas, P., and Karlsrud, K. Bearing capacity of driven piles in sand, the NGI approach. In *Proceedings of Proceedings of International Symposium. on Frontiers in Offshore Geotechnics, Perth*, pages 574–580, 2005.
- Crisfield, M. Basic plasticity. *Non-linear finite element analysis of solids and structures Vol, 1*: 152–200, 1991.
- Dafalias, Y. and Manzari, M. Simple plasticity sand model accounting for fabric change effects. *Journal of Engineering mechanics*, 130(6):622–634, 2004.
- Dafalias, Y. and Taiebat, M. Sanisand-z: zero elastic range sand plasticity model. *Géotechnique*, 66 (12):999–1013, 2016.
- Dafalias, Y.; Papadimitriou, A., and Li, X. Sand plasticity model accounting for inherent fabric anisotropy. *Journal of Engineering Mechanics*, 130(11):1319–1333, 2004.
- Damgaard, M.; Bayat, M.; Andersen, L., and Ibsen, L. Assessment of the dynamic behaviour of saturated soil subjected to cyclic loading from offshore monopile wind turbine foundations. *Computers and Geotechnics*, 61:116–126, 2014.
- Deng, G.; Zhang, J.; Wu, W.; Shi, X., and Meng, F. Estimation of impedance and transfer functions for end bearing and floating piles. *Journal of Applied Mathematics*, 11, 2014.
- Devriendt, C.; El-Kafafy, M.; De Sitter, G., and Guillaume, P. Estimating damping of an offshore wind turbine using an overspeed stop and ambient excitation. In *15th International Conference on Experimental Mechanics 2012*, volume 2897, 2012.
- DNV, O. S. D.-O. J101: Design of offshore wind turbine structures. *Det Norske Veritas*, 2004.
- Doll, S.; Schweizerhof, K.; Hauptmann, R., and Freischläger, C. On volumetric locking of low-order solid and solid-shell elements for finite elastoviscoplastic deformations and selective reduced integration. *Engineering Computations*, 17(7):874–902, 2000.
- Dupla, J.; Andria-Ntoanina, I., and Canou, J. Caractérisation mécanique du sable de fontainebleau a l'appareil triaxial sous cisaillement monotone. 2010.
- Energinet. Technical project description for offshore wind farms (200mw). Technical report, 2015.
- Energy efficiency and renewable energy. Offshore wind technologies market report.

- Eurocode, C. 8: Design of structures for earthquake resistance—part 1: General rules, seismic actions and rules for buildings (en 1998-1: 2004). *European Committee for Normalization, Brussels*, 2004.
- Gajo, A. and Muir Wood, D. A kinematic hardening constitutive model for sands: the multiaxial formulation. *International Journal for Numerical and Analytical Methods in Geomechanics*, 23(9): 925–965, 1999.
- Gazetas, G. Analysis of machine foundation vibrations: state of the art. *International Journal of Soil Dynamics and Earthquake Engineering*, 2(1):2–42, 1983.
- Gazetas, G. Seismic response of end-bearing single piles. *International Journal of Soil Dynamics and Earthquake Engineering*, 3(2):82–93, 1984.
- Gazetas, G. and Dobry, R. Horizontal response of piles in layered soils. *Journal of Geotechnical engineering*, 110(1):20–40, 1984.
- Gelagoti, F.; PPLekkakis, K. R., and Gazetas, G. Estimation of elastic and non-linear stiffness coefficients for suction caisson foundations. 2015.
- Gens, A.; Carol, I., and Alonso, E. A constitutive model for rock joints formulation and numerical implementation. *Computers and Geotechnics*, 9(1-2):3–20, 1990.
- Goorani, M. and Hamidi, A. A generalized plasticity constitutive model for sand-gravel mixtures. *International Journal of Civil Engineering*, 13(2):133–145, 2015.
- Gottardi, G.; Houlsby, G., and Butterfield, R. Plastic response of circular footings on sand under general planar loading. *Géotechnique*, 49(4):453–470, 1999.
- Gourvenec, S. Effect of embedment on the undrained capacity of shallow foundations under general loading. *Géotechnique*, 58(3):177–186, 2008.
- Gudehus, G. A comprehensive constitutive equation for granular materials. *Soils and foundations*, 36(1):1–12, 1996.
- Gudehus, G.; Amorosi, A.; Gens, A.; Herle, I.; Kolymbas, D.; Mašín, D.; DMuir Wood, N.-A.; Nova, R.; Pastor, M., et al. The soilmodels. info project. *International Journal for Numerical and Analytical Methods in Geomechanics*, 32(12):1571–1572, 2008.
- Haldar, S. and Bose, S. Dynamic soil stiffness in lateral vibrations of a floating pile. *Soil Dynamics and Earthquake Engineering*, 9(1):51–56, 1990.
- Herle, I. and Gudehus, G. Determination of parameters of a hypoplastic constitutive model from properties of grain assemblies. *Mechanics of Cohesive-frictional Materials*, 4(5):461–486, 1999.
- Hetényi, M. *Beams on elastic foundation: theory with applications in the fields of civil and mechanical engineering*. University of Michigan, 1971.
- Houlsby, G.; Kelly, R., and Byrne, B. The tensile capacity of suction caissons in sand under rapid loading. In *Proceedings of the international symposium on frontiers in offshore geomechanics, Perth*, pages 405–410, 2005.
- <http://www.abys.dk>. Optimal design of offshore wind turbine support structures, 2014.
- Hu, C.; Wang, K., and Xie, K. Time domain analysis of vertical dynamic response of a pile considering the effect of soil-pile interaction. *Chinese Journal Computational Mechanics*, 21(8): 392–399, 2004.

- Jamiolkowski, M.; Lo Presti, D., and Manassero, M. Evaluation of relative density and shear strength of sands from cpt and dmt. In *Soil behavior and soft ground construction*, pages 201–238. 2003.
- Jirásek, M. and Bazant, Z. *Inelastic analysis of structures*. John Wiley & Sons, 2002.
- Juang, C. and Wang, L. Reliability-based robust geotechnical design of spread foundations using multi-objective genetic algorithm. *Computers and Geotechnics*, 48:96 – 106, 2013.
- Kaynia, A. and Kausel, E. Dynamics of piles and pile groups in layered soil media. *Soil Dynamics and Earthquake Engineering*, 10(8):386–401, 1991.
- Kourkoulis, R.; Lekakakis, P.; Gelagoti, F., and Kaynia, A. Suction caisson foundations for offshore wind turbines subjected to wave and earthquake loading: effect of soil-foundation interface. *Géotechnique*, 64(3):171, 2014.
- Kramer, S. *Geotechnical Earthquake Engineering*. Prentice-Hall, Inc., 1996.
- Kuhlemeyer, R. Static and dynamic laterally loaded floating piles. *Journal of Geotechnical and Geoenvironmental Engineering*, 105(ASCE 14394), 1979a.
- Kuhlemeyer, R. Vertical vibration of piles. *Journal of Geotechnical and Geoenvironmental Engineering*, 105(ASCE 14393), 1979b.
- Kuwano, R. and Jardine, R. On the applicability of cross-anisotropic elasticity to granular materials at very small strains. *Géotechnique*, 52(10):727–749, 2002.
- Lashkari, A. A constitutive model for sand liquefaction under rotational shear. *Iranian Journal of Science and Technology*, 33(B1):31, 2009.
- Latini, C. and Zania, V. Dynamic lateral response of suction caissons. *Soil Dynamics and Earthquake Engineering*, 100:59–71, 2017a.
- Latini, C. and Zania, V. Triaxial tests in fontainebleau sand. 2017b.
- Latini, C.; Zania, V., and Johannesson, B. Dynamic stiffness and damping of foundations for jacket structures. In *Proceedings of 6th International Conference on Earthquake Geotechnical Engineering (6ICEGE 2015), Christchurch, New Zealand*, 2015.
- Latini, C.; Cisternino, M., and Zania, V. Dynamic stiffness of horizontally vibrating suction caissons. In *The 17th Nordic Geotechnical Conference*. International Society of Offshore and Polar Engineers, 2016a.
- Latini, C.; Cisternino, M., and Zania, V. Vertical dynamic stiffness of offshore foundations. In *The 26th International Ocean and Polar Engineering Conference*, 2016b.
- Latini, C.; Zania, V., and Tamagnini, C. Modelling of constitutive behavior of sand in the low stress regime: an implementation of sanisand. In *19th International Conference on Soil Mechanics and Geotechnical Engineering*, 2017.
- LeBlanc, C. Design of offshore wind turbine support structures. *Doctor of Philosophy, Technical University of Denmark*, 2009.
- Lehane, B.; Schneider, J., and Xu, X. The UWA-05 method for prediction of axial capacity of driven piles in sand. *Frontiers in Offshore Geotechnics: ISFOG*, pages 683–689, 2005.
- Li, X. and Dafalias, Y. Constitutive modeling of inherently anisotropic sand behavior. *Journal of Geotechnical and Geoenvironmental Engineering*, 128(10):868–880, 2002.

- Li, X. and Wang, Y. Linear representation of steady-state line for sand. *Journal of geotechnical and geoenvironmental engineering*, 124(12):1215–1217, 1998.
- Liingaard, M. *Dynamic behaviour of suction caissons*. PhD thesis, Department of Civil Engineering, Aalborg University, 2006.
- Lin, F. and Bažant, Z. Convexity of smooth yield surface of frictional material. *Journal of engineering mechanics*, 112(11):1259–1262, 1986.
- Liu, H.; Zheng, C.; Ding, X., and Qin, H. Vertical dynamic response of a pipe pile in saturated soil layer. *COMPUTERS and Geotechnics*, 61:57–66, 2014.
- Liu, H.; Zheng, C.; Ding, X.; Kouretzis, G., and Sloan, S. A revised solution for the horizontal vibration of an end-bearing pile in viscoelastic soil. *International Journal for Numerical and Analytical Methods in Geomechanics*, 40(13):1890–1900, 2016.
- Loukidis, D. and Salgado, R. Modeling sand response using two-surface plasticity. *Computers and Geotechnics*, 36(1):166–186, 2009.
- Lubliner, J. *The theory of plasticity*, 1990.
- Lunne, T.; Robertson, P., and Powell, J. Cone penetration testing. *Geotechnical Practice*, 1997.
- Lysmer, J. and Kuhlemeyer, R. Finite dynamic model for infinite media. *Journal of the Engineering Mechanics Division*, 95(4):859–878, 1969.
- Maeso, O.; Aznarez, J., and Garcia, F. Dynamic impedances of piles and groups of piles in saturated soils. *Computers & Structures*, 83(10):769–782, 2005.
- Mamoon, S.; Kaynia, A., and Banerjee, P. Frequency domain dynamic analysis of piles and pile groups. *Journal of Engineering Mechanics*, 116(10):2237–2257, 1990.
- Manzari, M. and Dafalias, Y. A critical state two-surface plasticity model for sands. *Géotechnique*, 47(2):255–272, 1997.
- Masin, D. Geo-slope, implementation of hypoplasticity. Technical report, 2013.
- Meyerhof, G. Compaction of sands and bearing capacity of piles. *Transactions of the American Society of Civil Engineers*, 126(1):1292–1322, 1961.
- Ministry of Foreign Affairs of Denmark. Independent from fossil fuel by 2050, 2017. URL <http://denmark.dk/en/green-living/strategies-and-policies/independent-from-fossil-fuels-by-2050>.
- Miriano, C. *Modellazione numerica della risposta sismica di strutture di sostegno flessibili*. PhD thesis, Department of Civil Engineering, University of Perugia, 2011.
- Mroz, Z.; Norris, V., and Zienkiewicz, O. Application of an anisotropic hardening model in the analysis of elasto-plastic deformation of soils. *Géotechnique*, 29(1):1–34, 1979.
- Mroz, Z.; Norris, V., and Zienkiewicz, O. An anisotropic, critical state model for soils subject to cyclic loading. *Géotechnique*, 31(4):451–469, 1981.
- Mylonakis, G. Winkler modulus for axially loaded piles. *Géotechnique*, 51(5):455–462, 2001.
- Niemunis, A. Incremental driver. *User's manual*. University of Karlsruhe, Germany, 2008.
- Niemunis, A. and Herle, I. Hypoplastic model for cohesionless soils with elastic strain range. *Mechanics of Cohesive-frictional Materials*, 2(4):279–299, 1997.

- Nogami, T. and Novak, M. Soil-pile interaction in vertical vibration. *Earthquake Engineering & Structural Dynamics*, 4(3):277–293, 1976.
- Nogami, T. and Novak, M. Resistance of soil to a horizontally vibrating pile. *Earthquake Engineering & Structural Dynamics*, 5(3):249–261, 1977.
- Nogami, T. and Novak, M. Coefficients of soil reaction to pile vibration. *Journal of Geotechnical and Geoenvironmental Engineering*, 106(ASCE 15433), 1980.
- Novak, M. Dynamic stiffness and damping of piles. *Canadian Geotechnical Journal*, 11(4):574–598, 1974.
- Novak, M. Vertical vibration of floating piles. *Journal of the Engineering Mechanics Division*, 103(1):153–168, 1977.
- Novak, M. Piles under dynamic loads. 1991.
- Novak, M. and Aboul-Ella, F. Impedance functions of piles in layered media. *Journal of the Engineering Mechanics Division*, 104(3):643–661, 1978.
- Novak, M. and Nogami, T. Soil-pile interaction in horizontal vibration. *Earthquake Engineering & Structural Dynamics*, 5(3):263–281, 1977.
- Nozoe, H.; Gyoten, Y.; Mizuhata, K., and Fukusumi, T. Estimation of impedance and transfer functions for end bearing and floating piles. *Proceeding of 9th CEE*, pages 563–568, 1988.
- Padron, L.; Aznarez, J., and Maeso, O. Bem–fem coupling model for the dynamic analysis of piles and pile groups. *Engineering Analysis with Boundary Elements*, 31(6):473–484, 2007.
- Padron, L.; Aznarez, J., and Maeso, O. Dynamic analysis of piled foundations in stratified soils by a bem-fem model. *Soil Dynamics and Earthquake Engineering*, 28(5):333–346, 2008.
- Papadimitriou, A. and Bouckovalas, G. Plasticity model for sand under small and large cyclic strains: a multiaxial formulation. *Soil Dynamics and Earthquake Engineering*, 22(3):191–204, 2002.
- Papadimitriou, A.; Bouckovalas, G., and Dafalias, Y. Use of elastoplasticity to simulate cyclic sand behavior. In *Proceedings of the Second International Conference on Earthquake Geotechnical Engineering. Lisbon*, volume 1, pages 125–30, 1999.
- Papadimitriou, A.; Bouckovalas, G., and Dafalias, Y. Plasticity model for sand under small and large cyclic strains. *Journal of Geotechnical and Geoenvironmental Engineering*, 127(11):973–983, 2001.
- Poulos, H. and Davis, E. *Pile foundation analysis and design*. Number Monograph. 1980.
- Pucker, T. and Grabe, J. Structural optimization in geotechnical engineering: Basics and application. *Acta Geotechnica*, 6:41–49, 2011.
- Rajapakse, R. and Shah, A. On the lateral harmonic motion of an elastic bar embedded in an elastic half-space. *International Journal of Solids and Structures*, 23(2):287–303, 1987. ISSN 18792146, 00207683. doi: 10.1016/0020-7683(87)90061-8.
- Randolph, M. The response of flexible piles to lateral loading. *Géotechnique*, 31(2):247–259, 1981.
- Randolph, M. and House, A. Analysis of suction caisson capacity in clay. In *Offshore technology conference*. Offshore Technology Conference, 2002.

- Rasmussen, K.; Hansen, M.; Kirk Wolf, T.; Ibsen, L., and Roesen, H. A literature study on the effects of cyclic lateral loading of monopiles in cohesionless soils. Technical report, Department of Civil Engineering, Aalborg University, 2013.
- Richart, F.; Hall, J., and Woods, R. Vibrations of soils and foundations. 1970.
- Robertson, P. Soil classification using the cone penetration test. *Canadian Geotechnical Journal*, 27(1):151–158, 1990.
- Roesset, J. and Angelides, D. Dynamic stiffness of piles. In *Numerical methods in offshore piling*, pages 75–81. Thomas Telford Publishing, 1980.
- Roscoe, K.; Schofield, A., and Wroth, C. On the yielding of soils. *Géotechnique*, 8(1):22–53, 1958.
- Rovithis, E.; Parashakis, H., and Mylonakis, G. 1d harmonic response of layered inhomogeneous soil: Analytical investigation. *Soil Dynamics and Earthquake Engineering*, 31(7):879–890, 2011.
- Sandal, K. *Design optimization of jacket structures for mass production*. PhD thesis, Department of Wind Energy, Denmark Technical University, 2017.
- Sandal, K. and Zania, V. Optimization of pile design for offshore wind turbine jacket foundations. In *12th EAWC PhD seminar on Wind Energy in Europe*, 2016.
- Schofield, A. and Wroth, C. *Critical State Soil Mechanics*. McGraw-Hill, 1968.
- Seitz, K. and Grabe, J. Three-dimensional topology optimization for geotechnical foundations in granular soil. *Computers and Geotechnics*, 80:41–48, 2016.
- Shadlou, M. and Bhattacharya, S. Dynamic stiffness of monopiles supporting offshore wind turbine generators. *Soil Dynamics and Earthquake Engineering*, 88:15–32, 2016.
- Shariatmadari, N.; Eslami, A., and Karimpour-Fard, M. Bearing capacity of driven piles in sands from spt-applied to 60 case histories. *Iranian Journal of Science and Technology*, 32(B2):125, 2008.
- Simo, J. and Hughes, T. General return mapping algorithms for rate-independent plasticity. *Constitutive laws for engineering materials: theory and applications*, 1:221–232, 1987.
- Sloan, S. and Booker, J. Removal of singularities in tresca and mohr–coulomb yield functions. *International Journal for Numerical Methods in Biomedical Engineering*, 2(2):173–179, 1986.
- Stallebrass, S. *Modelling the effect of recent stress history on the deformation of overconsolidated soils*. PhD thesis, City University London, 1990.
- Stallebrass, S. and Taylor, R. The development and evaluation of a constitutive model for the prediction of ground movements in overconsolidated clay. *Géotechnique*, 47:235–253, 1997.
- State of Green. Offshore wind farms.
- Sturm, H. Design aspects of suction caissons for offshore wind turbine foundations. In *Proceedings of the 19th International Conference on Soil Mechanics and Geotechnical Engineering*, 2017.
- Supachawarote, C.; Randolph, M., and Gourvenec, S. Inclined pull-out capacity of suction caissons. In *The Fourteenth International Offshore and Polar Engineering Conference*. International Society of Offshore and Polar Engineers, 2004.
- Syngros, K. *Seismic response of piles and pile-supported bridge piers evaluated through case histories*. PhD thesis, City University of New York, 2004.

- Systèmes, D. Abaqus analysis user's guide. *Dassault Systèmes Simulia Corp., Providence, RI, USA*, 2014.
- Taiebat, M. and Dafalias, Y. Sanisand: Simple anisotropic sand plasticity model. *International Journal for Numerical and Analytical Methods in Geomechanics*, 32(8):915–948, 2008.
- Tamagnini, C. Theory of plasticity. theoretical fundamentals and applications to soil mechanics. Technical report, Department of Civil Engineering, University of Perugia, 2011.
- Tamagnini, C. and Viggiani, G. Constitutive modelling for rate-independent soils: a review. *Revue française de génie civil*, 6(6):933–974, 2002.
- Terzaghi, K. *Theoretical soil mechanics*, volume 18. Wiley Online Library, 1943.
- The Crown Estate. Offshore wind electricity, 2017. URL <https://www.thecrownestate.co.uk/energy-minerals-and-infrastructure/offshore-wind-energy>.
- Tricarico, M. *Centrifuge Modelling of Flexible Retaining Walls in Saturated Sand under Seismic Actions*. PhD thesis, Università degli Studi di Napoli Federico II, 2015.
- Truong, P. *Experimental investigation on the behaviour of laterally loaded piles in soft clay, sand and residual soils*. PhD thesis, University of Western Australia, 2017.
- Union of Concerned Scientists. Benefits of renewable energy use, 2013. URL <http://www.ucsusa.org/clean-energy/renewable-energy/public-benefits-of-renewable-power>.
- Van Der Tempel, J. Design of support structures for offshore wind turbines. 2006.
- Van Eekelen, H. Isotropic yield surfaces in three dimensions for use in soil mechanics. *International Journal for Numerical and Analytical Methods in Geomechanics*, 4(1):89–101, 1980.
- Varun, A. and Gazetas, G. A simplified model for lateral response of large diameter caisson foundations—linear elastic formulation. *Soil Dynamics and Earthquake Engineering*, 29(2): 268–291, 2009.
- Velez, A.; Gazetas, G., and Krishnan, R. Lateral dynamic response of constrained-head piles. *Journal of Geotechnical Engineering*, 109(8):1063–1081, 1983.
- Vermeer, P. and De Borst, R. Non-associated plasticity for soils, concrete and rock. *HERON*, 29 (3), 1984, 1984.
- von Wolffersdorff, P. A hypoplastic relation for granular materials with a predefined limit state surface. *Mechanics of Cohesive-frictional Materials*, 1(3):251–271, 1996.
- Wolf, J. *Foundation vibration analysis using simple physical models*. Pearson Education, 1994.
- Wolf, J. and Deeks, A. Cones to model foundation vibrations: incompressible soil and axi-symmetric embedment of arbitrary shape. *Soil Dynamics and Earthquake Engineering*, 24(12):963–978, 2004.
- Wu, G.; Wang, K.; Zhang, Z., and Chin, J. Soil–pile interaction in the pile vertical vibration considering true three–dimensional wave effect of the soil. *International Journal for numerical and analytical methods in geomechanics*, 37:2860–2876, 2013.
- Zania, V. Natural vibration frequency and damping of slender structures founded on monopiles. *Soil dynamics and Earthquake engineering*, 59:8–20, 2014.
- Zheng, C.; Ding, X., and Fu, Q. Horizontal vibration of a large-diameter pipe pile in viscoelastic soil. 2013.

- Zheng, C.; Ding, X.; Li, P., and Qiang, F. Vertical impedance of an end-bearing pile in viscoelastic soil. *Journal for Numerical and Analytical Methods in Geomechanics*, 39(6):676–684, 2014.
- Zienkiewicz, O. and Pande, G. Some useful forms of isotropic yield surface for soil and rock mechanics. *Finite elements in geomechanics*, pages 179–190, 1977.
- Zienkiewicz, O.; Chan, A.; Pastor, M.; Schrefler, B., and Shiomi, T. *Computational geomechanics*. Wiley Chichester, 1999.

Part II

Publications

Paper I

Dynamic soil-pile interaction: an analytical solution for floating piles

C. LATINI AND V. ZANIA

Submitted for publication: -,2017

DYNAMIC SOIL-PILE INTERACTION: AN ANALYTICAL SOLUTION FOR FLOATING PILES

C. Latini

PhD Student

Civil Engineering Department, Technical University of Denmark

e-mail: chila@byg.dtu.dk

V. Zania

Associate Professor

Civil Engineering Department, Technical University of Denmark

ABSTRACT

An analytical solution is proposed for estimating the lateral dynamic stiffness and damping coefficients of floating piles (piles embedded in soil layers of depth greater than the pile length). At first, the soil resistance was defined, considering 3d wave propagation within linear elastic soil layer with hysteretic damping. Thereafter, the dynamic response of the pile was determined assuming soil pressure equal to the soil resistance and imposing displacement compatibility. The estimation of the natural vibration characteristics (eigenfrequency and damping) was performed disregarding the vertical displacement of the soil-foundation system. The analytical formulation in both, static and dynamic regime was first validated against a 3d finite element model. Results were presented in terms of dimensionless graphs which highlighted the frequency dependency of the dynamic stiffness and damping. A detailed discussion on the limitations of the solution along with the effect of major dimensionless parameters on the dynamic impedances of floating piles is presented. Design recommendations are provided based on the results of the analytical formulation for the dynamic response of floating piles.

Keywords: soil – structure – interaction, dynamic stiffness, damping, floating foundations, elastodynamic analytical solution, numerical modelling

INTRODUCTION

Pile foundations are often subjected to lateral dynamic loads due to environmental factors, such as earthquake, wave, wind or human activities, such as passing traffic. In these cases, the structural response is influenced by interaction between the foundation and the surrounding soil highlighting that the assumption of fixed-base conditions at the foundation level misrepresents the dynamic behaviour of the structure. This is a well-known problem of dynamic soil-structure-interaction, which has been analysed extensively in the literature; it has been demonstrated that the eigenfrequency and the damping of any structure subjected to dynamic load are altered due to its effects [1]. Therefore the dynamic stiffness and damping of the soil-foundation system should be included in the estimation of the natural vibration characteristics of the structure. In the literature, the problem of the dynamic soil-pile interaction has been widely investigated. Winkler type analytical solutions [2-4] are the most commonly used ones in the literature, due to their simplicity and applicability. In Winkler type models the supporting soil was substituted by a bed of independent elastic springs overlying rigid bedrock. The advantage of such formulations is that the soil nonlinearity and inhomogeneity can be included, even though their accuracy is strongly related to the selection of a suitable Winkler modulus. On the other hand, Winkler type models are not capable to capture the coupled vibration between the pile foundation and the soil due to the assumption of plane strain conditions, as pointed out in the work of Novak and Aboul-Ella [3]. An improved model incorporating in the analysis the normal and shear stresses acting on the upper and lower faces of a horizontal soil element by integrating the governing equations over the thickness of the soil layer was developed by Mylonakis [4]. Analytical elastodynamic continuum solutions [5-7] provide a three-dimensional formulation of the governing equations of wave propagation, by considering the soil as an elastic continuum with hysteretic material damping. The soil resistance is determined by solving the differential equations of wave propagation within the elastic soil medium. The horizontal dynamic response and the dynamic impedances of the pile foundation are obtained by applying the continuity conditions between the pile and the soil. In these studies the vertical displacement was considered negligible; while Anoyatis et al. [8] assumed that vertical displacement at the soil surface is small, by taking into account two different compressibility factors in the estimation of the soil resistance. This approach allowed also overcoming the sensitivity of the solution to Poisson's ratio (ν), as it approaches 0.5. Unlike the abovementioned studies, the formulation presented by Liu et al. [9] suggested that the governing equations of the soil are solved directly, eliminating the need to introduce potential functions. The complex

1
2
3 impedances calculated with this solution match those obtained by Novak and Nogami [5]. Analytical formulations
4 are limited to elastic soil response and they have been shown to compare well with finite element results [10-12].
5

6
7 As to other approaches to the problem, there are also finite elements methods (FEM) [10-15] and boundary element
8 methods [16-18]. In finite element methods [11, 13-15] the pile was modelled as series of regular beam segments,
9 having rigid cross section and the soil was treated as an elastic continuum; while the dynamic finite element
10 formulation of Latini and Zania [12] used shell elements to model end bearing steel hollow piles. In the boundary
11 element approach the soil and the pile are considered as separate substructures for which the coupling was enforced
12 only at discrete locations. Most of these works estimated the dynamic impedances of pile foundations embedded in
13 homogeneous halfspace, providing reliable predictions with the disadvantage of being computationally intensive and
14 time consuming [17,18].
15
16
17
18
19
20
21
22
23

24
25 Contrary to the dynamic response of end bearing piles, very limited studies investigating the response of floating
26 piles are available in the literature. The work of Nozoe et al. [19] presented a theoretical analysis of the dynamic
27 response of floating piles embedded in a soil layer on rigid bedrock. In this study the pile was modelled according to
28 Timoshenko's beam theory and the soil layer was considered as a continuum, taking into account all the three
29 components of soil displacements. While in the solution proposed by Haldar and Bose [20] the general elastodynamic
30 equations have been treated assuming that the vertical component of the displacement is negligible and the soil is
31 considered to be homogeneous elastic halfspace. Furthermore, the dynamic behaviour of floating piles with the
32 surrounding soil overlying rigid bedrock was investigated numerically in the study of Gazetas and Dobry [15].
33
34
35
36
37
38
39
40
41

42 The motivation of the current study is to provide a continuum analytical solution to predict the dynamic response of
43 floating piles embedded in a homogeneous soil layer on rigid bedrock in terms of stiffness and damping. Hence an
44 appropriately modified formulation based on the analytical solution of soil-pile vibration by Novak and Nogami [5]
45 was developed. The improvement of the model lies in a better prediction of soil response which ultimately yields
46 more accurate results for pile impedances. The analytical results of static and dynamic impedances were compared
47 to those of a 3d numerical model in Abaqus. Additionally a parametric study was conducted in order to clarify the
48 role of major dimensionless parameters (i.e. slenderness ratio H_p/d , relative thickness of the soil layer H_s/d , relative
49 stiffness E_p/E_s) and thus, illustrate the limitations of the present solution.
50
51
52
53
54
55
56
57
58
59
60

METHODOLOGY

The analytical solution for horizontally vibrating floating piles was first presented by the authors in Latini et al. [21], however the analysis is herein shown in more detail. The main assumptions of the solution were: 1) the pile is vertical, uniform, linearly elastic and of circular cross section; 2) the soil layer is linear, elastic, free at the surface; 3) the material damping is of the hysteretic type - frequency independent. It was considered that the pile was free at the tip and perfectly attached to the soil. In addition, the proposed method in agreement with the work of Nogami and Novak [5] formulated the harmonic wave propagation equations of the soil layer disregarding the vertical displacements associated with horizontal pile vibration. This consideration is assumed rational when the pile deforms in bending without substantial shear deformations [22].

In this formulation to account for the fact that the depth of the viscoelastic layer undergoing harmonic motion was larger than the pile length as shown in Figure 1, two reference systems were introduced: 1) RS starting from the bottom of the rigid bedrock and 2) RS1 set from the pile tip. In the new reference system (RS1) the horizontal motion of the pile when subjected to harmonic horizontal load $P(\omega, t) = Pe^{i\omega t}$ at the pile head is given in the form of:

$$u(z_1, t) = u(z_1) e^{i\omega t} \quad (1)$$

where t is time variable, ω is the cyclic excitation frequency, $i(=\sqrt{-1})$ is the imaginary number and z_1 is the vertical coordinate. The governing equation of the pile motion is written in agreement with the corresponding for beam on elastic foundation by Hetényi [23].

$$E_p I \frac{\partial^4}{\partial z_1^4} (ue^{i\omega t}) + m \frac{\partial^2}{\partial t^2} (ue^{i\omega t}) = -p(z_1)e^{i\omega t} \quad (2)$$

in which $E_p I$, m and $p(z_1)$ are respectively the bending stiffness of the pile (with a moment of the inertia of $I = \pi d^4/64$ for a circular cross section), the mass of the pile per unit length and the amplitude of the soil resistance to the motion of the pile. Whereas, the dynamic horizontal soil resistance of the soil to the lateral pile motion $p(z_1, t) = p(z_1, \omega)e^{i\omega t}$ expressed in the local pile's coordinate system is

$$p(z_1, t) = \sum_{n=1}^{\infty} \alpha_{hn} U_n \sin(h_n(z_1 + \Delta H)) \quad (3)$$

where α_{hn} is the horizontal resistance factor, depending on the pile radius r_0 , shear modulus G of the soil layer and a number of dimensionless parameters such as the dimensionless frequency $\alpha_0 = H_s \omega / V_s$, pile slenderness H_p / d

material hysteretic damping ζ and Poisson's ratio ν , U_n is the modal amplitude independent of z , $\sin(h_n(z_1 + \Delta H))$ is the n th mode shape of the soil layer, $\Delta H = H_s - H_p$ and $h_n = (\pi/2H_s)(2n - 1)$ where H_s is the thickness of the soil layer and n is the mode number. According to the work of Novak and Nogami [5] the horizontal resistance factor α_{hn} is defined as:

$$\alpha_{hn} = \pi r_0 G \left[(1 + i\zeta) h_n^2 - \left(\frac{\omega}{V_s} \right)^2 \right] T_n \quad (4)$$

where the expression of parameter T_n is given as follows:

$$T_n = \frac{4K_1(q_n r_0)K_1(s_n r_0) + s_n r_0 K_1(q_n r_0)K_0(s_n r_0) + q_n r_0 K_0(q_n r_0)K_1(s_n r_0)}{q_n K_0(q_n r_0)K_1(s_n r_0) + s_n K_1(q_n r_0)K_0(s_n r_0) + q_n s_n r_0 K_0(q_n r_0)K_0(s_n r_0)} \quad (5)$$

where K_m is the modified Bessel function of second kind and order m . The variables q_n and s_n are functions of the dimensionless frequency α_0 and they are reported in Nogami and Novak [5].

Substituting Eq. 3 into Eq. 2 and eliminating the time variable t the following expression for the pile amplitude is derived from Eq. 4:

$$E_p I \frac{d^4 u}{dz_1^4} - m\omega^2 u = - \sum_{n=1}^{\infty} \alpha_{hn} U_n \sin(h_n(z_1 + \Delta H)) \quad (6)$$

The solution to Eq. 6 is given as a sum of the complete solution of the homogeneous equation u_h , and a particular solution of the non-homogeneous equation u_p .

The particular solution u_p can be expressed as

$$u_p(z_1) = \sum_{n=1}^{\infty} a_n \sin(h_n(z_1 + \Delta H)) \quad (7)$$

where a_n is a complex constant. Substitution of Eq. 7 into Eq. 6 yields

$$E_p I \sum_{n=1}^{\infty} a_n h_n^4 \sin(h_n(z_1 + \Delta H)) - m\omega^2 \sum_{n=1}^{\infty} a_n \sin(h_n(z_1 + \Delta H)) = - \sum_{n=1}^{\infty} \alpha_{hn} U_n \sin(h_n(z_1 + \Delta H)) \quad (8)$$

Hence, the constant a_n is determined as

$$a_n = \frac{-\alpha_{hn} U_n}{E_p I h_n^4 - m\omega^2} \quad (9)$$

The solution of the homogeneous equation is written as

$$u_h(z_1) = A \sin(\lambda z_1) + B \cos(\lambda z_1) + C \sinh(\lambda z_1) + D \cosh(\lambda z_1) \quad (10)$$

where A, B, C and D are the integration constants obtained by the boundary conditions at the pile head ($z_1 = H_p$) and at the bottom of the soil layer ($z_1 = -\Delta H$). And

$$\lambda = \sqrt[4]{\frac{m\omega^2}{E_p I}} \quad (11)$$

Then the pile displacement is given as:

$$u(z_1) = A \sin(\lambda z_1) + B \cos(\lambda z_1) + C \sinh(\lambda z_1) + D \cosh(\lambda z_1) - \sum_{n=1}^{\infty} \frac{\alpha_{hn} U_n}{E_p I h_n^4 - m\omega^2} \sin(h_n(z_1 + \Delta H)) \quad (12)$$

The displacement of the soil layer at the pile is expressed as

$$U(z_1) = \sum_{n=1}^{\infty} U_n \sin(h_n(z_1 + \Delta H)) \quad (13)$$

The displacement compatibility between the pile and the soil layer is imposed. Then, the variable z_1 can be written as $z_1 = z - \Delta H$ and expanding $\sin(\lambda(z - \Delta H))$, $\cos(\lambda(z - \Delta H))$, $\sinh(\lambda(z - \Delta H))$ and $\cosh(\lambda(z - \Delta H))$ into a Fourier sine series of argument ($h_n z$), the following formula is obtained:

$$U_n = \frac{AF_{1n} + BF_{2n} + CF_{3n} + DF_{4n}}{1 + \left[\frac{\alpha_{hn}}{E_p I h_n^4 - m\omega^2} \right]} \quad (14)$$

where

$$\begin{cases} F_{1n} = \frac{2}{H_s} \int_0^{H_s} \sin(\lambda(z - \Delta H)) \sin(h_n z) dz \\ F_{2n} = \frac{2}{H_s} \int_0^{H_s} \cos(\lambda(z - \Delta H)) \sin(h_n z) dz \\ F_{3n} = \frac{2}{H_s} \int_0^{H_s} \sinh(\lambda(z - \Delta H)) \sin(h_n z) dz \\ F_{4n} = \frac{2}{H_s} \int_0^{H_s} \cosh(\lambda(z - \Delta H)) \sin(h_n z) dz \end{cases} \quad (15)$$

Substituting U_n into Eq. 12, the amplitude of the pile motion is

$$u(z) = A \sin(\lambda(z - \Delta H)) + B \cos(\lambda(z - \Delta H)) + C \sinh(\lambda(z - \Delta H)) + D \cosh(\lambda(z - \Delta H)) - \sum_{n=1}^{\infty} \frac{\alpha_{hn} (AF_{1n} + BF_{2n} + CF_{3n} + DF_{4n})}{E_p I h_n^4 - m\omega^2 + \alpha_{hn}} \sin h_n z \quad (16)$$

Using the displacement of the pile presented in Eq. 16, the amplitude of the angle of rotation θ , the bending moment M and the shear force S are obtained by the corresponding derivatives. The unknown coefficients A, B, C, D have been estimated by considering the boundary conditions and applying a unit horizontal translation and a unit rotation at the pile head as listed:

$$\left. \begin{aligned} u(H_s) = 1, \theta(H_s) = 0 \text{ for } \widetilde{K}_{Su} \text{ and } \widetilde{K}_{Mu} \\ u(H_s) = 0, \theta(H_s) = 1 \text{ for } \widetilde{K}_{S\theta} \text{ and } \widetilde{K}_{M\theta} \\ u(0) = 0, \theta(0) = 0 \end{aligned} \right\} \quad (17)$$

where \widetilde{K}_{Su} , \widetilde{K}_{Mu} , $\widetilde{K}_{S\theta}$ and $\widetilde{K}_{M\theta}$ are the complex valued impedances, which can be written in the following form:

$$\widetilde{K}_{**} = \text{Real}(\widetilde{K}_{**}) + i\text{Imag}(\widetilde{K}_{**}) = K_{**}(\omega)(1 + 2i\zeta_{**}) \quad (18)$$

The dynamic impedances \widetilde{K}_{Su} , \widetilde{K}_{Mu} , $\widetilde{K}_{S\theta}$ and $\widetilde{K}_{M\theta}$ at the level of the pile head are then calculated as reaction forces (S) and moments (M) for unit displacement (u) and rotation (θ). Therefore, the general expressions for dynamic displacement, rotation, bending moment and shear force of floating pile are given as follows:

$$\begin{pmatrix} u \\ \theta \\ M \\ \bar{e}_p \\ \bar{s} \\ \bar{e}_p \end{pmatrix} = \begin{pmatrix} \sin(\lambda(z - \Delta H)) - Y \sum_{n=1}^{\infty} F_{1n} \sin(h_n z) & \cos(\lambda(z - \Delta H)) - Y \sum_{n=1}^{\infty} F_{2n} \sin(h_n z) & \sinh(\lambda(z - \Delta H)) - Y \sum_{n=1}^{\infty} F_{3n} \sin(h_n z) & \cosh(\lambda(z - \Delta H)) - Y \sum_{n=1}^{\infty} F_{4n} \sin(h_n z) \\ \lambda \cos(\lambda(z - \Delta H)) - Y \sum_{n=1}^{\infty} h_n F_{1n} \cos(h_n z) & -\lambda \sin(\lambda(z - \Delta H)) - Y \sum_{n=1}^{\infty} h_n F_{2n} \cos(h_n z) & \lambda \cosh(\lambda(z - \Delta H)) - Y \sum_{n=1}^{\infty} h_n F_{3n} \cos(h_n z) & \lambda \sinh(\lambda(z - \Delta H)) - Y \sum_{n=1}^{\infty} h_n F_{4n} \cos(h_n z) \\ -\lambda^2 \sin(\lambda(z - \Delta H)) + Y \sum_{n=1}^{\infty} h_n^2 F_{1n} \sin(h_n z) & -\lambda^2 \cos(\lambda(z - \Delta H)) + Y \sum_{n=1}^{\infty} h_n^2 F_{2n} \sin(h_n z) & \lambda^2 \sinh(\lambda(z - \Delta H)) + Y \sum_{n=1}^{\infty} h_n^2 F_{3n} \sin(h_n z) & \lambda^2 \cosh(\lambda(z - \Delta H)) + Y \sum_{n=1}^{\infty} h_n^2 F_{4n} \sin(h_n z) \\ -\lambda^3 \cos(\lambda(z - \Delta H)) + Y \sum_{n=1}^{\infty} h_n^3 F_{1n} \cos(h_n z) & \lambda^3 \sin(\lambda(z - \Delta H)) + Y \sum_{n=1}^{\infty} h_n^3 F_{2n} \cos(h_n z) & \lambda^3 \cosh(\lambda(z - \Delta H)) + Y \sum_{n=1}^{\infty} h_n^3 F_{3n} \cos(h_n z) & \lambda^3 \sinh(\lambda(z - \Delta H)) + Y \sum_{n=1}^{\infty} h_n^3 F_{4n} \cos(h_n z) \end{pmatrix} \begin{pmatrix} A \\ B \\ C \\ D \end{pmatrix} \quad (19)$$

Where

$$Y = \alpha_{\text{in}} / (E_p I h_n^4 - m \omega^2 + \alpha_{\text{in}})$$

[9]

<http://mc.manuscriptcentral.com/nag>

VALIDATION WITH NUMERICAL MODEL

3D finite element models carried out in the commercial software ABAQUS [24] was established to validate the dynamic impedances of the floating pile obtained by the analytical formulation. Only half of the foundation and the surrounding soil were taken into account in the model, as a result of the symmetry of the problem. The foundation was modelled as a solid pile, discretized with 3D continuum elements (C3D8). The soil domain consisted of near-field soil ($L_{fin} = 180m$) surrounding the pile and the far-field soil ($L_{inf} = 180m$), modelled using infinite elements to avoid reflecting boundaries. A perfect bounded interface between the pile and soil was considered.

Steady state linearized response of the model subject to harmonic excitation in the frequency domain was performed. The dynamic impedances \widetilde{K}_{Su} , \widetilde{K}_{Mu} , $\widetilde{K}_{S\theta}$ and $\widetilde{K}_{M\theta}$ at the level of the pile head were then calculated as shear forces, S , and moments, M , when the head of the foundation is subjected to unit displacement, u , and rotation, θ . The mesh size was set small enough to capture the stress wave accurately. It was assumed a mesh size of at least 10 to 20 elements per wave length for the frequency range of interest, including up to the third eigenfrequency of the soil layer $\alpha_0 = 5/2\pi$. Note that α_0 is a dimensionless frequency related to the eigenfrequency of the soil layer, since it is given as the product of the wave number and the thickness of the soil layer.

$$\alpha_0 = \frac{\omega H_s}{V_s} \quad (25)$$

where ω (rad/sec), H_s (m) and V_s (m/s) are respectively the frequency, the height and the shear wave velocity of the soil layer.

It is worth mentioning that in the work of Latini and Zania [12] the present numerical methodology was also validated against the analytical solution of the dynamic response of end bearing piles suggested by Novak and Nogami [5]. It was found that the numerical results were consistent with those obtained by the analytical formulation.

The validation of the analytical solution was performed by considering a small diameter ($d = 2r_0 = 1m$) pile of height $H_p = 10m$ embedded in a homogeneous soil layer with thickness $H_s = 30m$ and constant profile of shear

1
2
3 wave velocity ($V_s = 250m/s$), hysteretic material damping ($\zeta = 5\%$) and Poisson's ratio ($\nu = 0.35$) over a wide
4 frequency range including at least the third eigenfrequency of the soil layer ($\alpha_0 = 5/2\pi$).
5

6
7 The static stiffness coefficients of the numerical model were calculated at low frequencies and presented in Table
8 1, along with the corresponding values obtained by applying the proposed analytical solution, the simplified
9 expressions of Syngros [25] for piles embedded in homogeneous halfspace and the analytical solution of
10 Randolph [26] for end bearing piles. A discrepancy of 2.5%, 32.5% and 9.7% between the results of the suggested
11 analytical formulation and the numerical model was obtained for the horizontal, coupling and rocking terms,
12 respectively. While the variation in percentage between the outcomes from the numerical model and the
13 simplified expressions of Syngros [25], was 2.7%, 7.7% and 21.5%. The sliding and coupling components of the
14 dynamic impedances are significantly overestimated by deploying the analytical solution of Randolph [26];
15 whereas the rocking component differs less than 5% with respect to the numerical outcomes.
16
17

18
19 In Figure 2 the real ($K_{Su}, K_{S\theta}$ and $K_{M\theta}$) and the imaginary ($2\zeta_{Su}, 2\zeta_{S\theta}$, and $2\zeta_{M\theta}$) parts of the dynamic
20 impedances are presented. It was observed a reduction of stiffness at the 1st and 2nd eigenfrequency of the soil
21 layer ($\alpha_0 = 1/2\pi$ and $3/2\pi$, accordingly). The numerical model exhibited an extra drop in stiffness attained
22 around the 1st vertical resonance $\alpha_0 = 1/2\pi\eta$, where $\eta = \sqrt{2(1-\nu)/(1-2\nu)}$ which was less evident for the
23 case of the cross coupling and rocking components. This can be motivated by the fact that the analytical solution
24 does not taken into account the vertical displacement in the estimation of the impedances of the soil-pile system.
25 Slightly scattered results were noticed comparing the analytical solution and the numerical model after the 2nd
26 horizontal eigenfrequency of the soil layer. The imaginary part of the dynamic component of the dynamic
27 impedances is associated to the generated damping, due to the soil-pile interaction. The radiation damping was
28 developed after the 1st eigenfrequency of the soil layer for all the components. Indeed, the step-linear increasing
29 values of the coefficients with frequency confirmed that viscous type damping was generated for this frequency
30 range. In Figure 3 the deformed shape of the pile is illustrated with respect the depth at the three first
31 eigenfrequencies of the soil layer. Results obtained from the proposed model were found to be in very good
32 agreement with the numerical outcomes. It is also worthwhile to illustrate the effect of the vertical displacements
33 on the dynamic response of floating piles. Figure 4 presents the vertical displacement of the pile obtained with
34 respect to the depth at the three first eigenfrequencies of the soil medium. Note that the abovementioned outcomes
35
36
37
38
39
40
41
42
43
44
45
46
47
48
49
50
51
52
53
54
55
56
57
58
59
60

1
2
3 were derived from the numerical models, since the analytical formulation only considers horizontal deformations.
4
5 It is evident that the vertical displacements along the depth of the soil layer increase considerably for higher
6
7 frequencies than the 1st resonance. Particularly, it was found that the vertical displacements at the pile tip recorded
8
9 at the 3rd eigenfrequency of the soil layer increase of 60% with respect to those at the 1st eigenfrequency. This
10
11 further explains the fact that the discrepancy between the dynamic impedances obtained by the numerical analysis
12
13 and the proposed analytical solution became more noticeable for frequencies higher than the 2nd resonance.
14
15
16
17

18 DYNAMIC IMPEDANCES

21 From the state of art it appears that theoretical approaches for predicting the dynamic behaviour of end bearing
22
23 pile foundations have been developed extensively. Particularly, the role of key dimensionless parameters such
24
25 as the stiffness ratio E_p/E_s , the slenderness ratio H_p/d and the pile flexibility factor K_r , on the response of end
26
27 bearing piles has been illustrated [26-27]. It must be highlighted that the effect of the dimensionless parameter
28
29 H_s/d , defined as the relative thickness of the soil layer, was studied only for the case of surface footings in the
30
31 work of Gazetas [14] and for suction caissons in the work of Latini and Zania [12]. There are few studies
32
33 investigating the influence of these major nondimensional parameters on the dynamic stiffness and damping of
34
35 the soil-pile system in the case of floating piles.
36
37

38 Hence, an overview of the applicability of the proposed analytical solution was provided along with an analysis
39
40 of the effect of the abovementioned dimensionless parameters affecting the dynamic soil-floating pile interaction.
41
42 The rationale behind their selection was to investigate piles with different slenderness ratio (H_p/d) embedded in
43
44 different site conditions (E_p/E_s , H_s/d). It is worth mentioning that the influence of the diameter on the dynamic
45
46 response of floating piles was not investigated, since previous studies [12,22] showed that the sensitivity of the
47
48 dynamic stiffness coefficients on the variation of the diameter was hardly noticeable for both end bearing piles
49
50 and suction caissons.
51
52

53 EFFECT OF THE SLENDERNESS RATIO

54
55 Figure 5 and 6 show the real (K_{Su} , $K_{S\theta}$ and $K_{M\theta}$) and the imaginary ($2\zeta_{Su}$, $2\zeta_{S\theta}$, and $2\zeta_{M\theta}$) parts of the dynamic
56
57 impedances by varying the slenderness ratio for different soil profiles $E_p/E_s = 60$ and 500, respectively. Results
58
59 definitely highlighted that the variation of the slenderness ratio H_p/d does not influence the dynamic impedances
60

of floating piles in the frequency range investigated. This was proved for both soft ($E_p/E_s = 500$) and medium stiff ($E_p/E_s = 60$) soil deposit. The definition of “active length” L_a given in the literature [13,26,28] for end bearing piles, namely no effect of the size $H_p - L_a$ on the dynamic impedances at the top of the pile when piles have length greater than L_a , doesn't have any implications in the design of floating piles. Indeed, any difference in the dynamic response was not observed for piles with length greater or smaller than L_a . In this study the dynamic active length is investigated by the bending moment distribution and it was found in agreement with the one suggested by Velez et al. [13], which is approximately $\frac{L_a}{d} = 11$ and 8.5 for floating piles embedded in a homogeneous soil profile with $E_p/E_s = 60$ and 500, respectively.

EFFECT OF THE RELATIVE THICKNESS OF THE SOIL LAYER

In Figure 7 the real (K_{Su} , $K_{S\theta}$ and $K_{M\theta}$) and the imaginary ($2\zeta_{Su}$, $2\zeta_{S\theta}$, and $2\zeta_{M\theta}$) parts of the dynamic impedances are presented varying the dimensionless parameter H_s/d . This was investigated by keeping all dimensionless parameters constant and changing only the thickness of the soil layer, while referring to the same slenderness ratio. The outcomes showed that the relative thickness of the soil layer H_s/d has a significant effect on the dynamic impedances in the frequency range considered. In the first place the reduction of stiffness attained at the 1st resonance ($\alpha_0 = \pi/2$) for all the components appeared to be more marked as the relative thickness of the soil layer H_s/d decreased. However, when the dynamic impedances of floating pile and end bearing pile ($H_s = H_p$) are compared, it was noticed that the highest decrease in stiffness at the 1st resonance was recorded for the case of the end bearing foundation. These findings proved to be consistent with the work of Nozoe et al. [19]. Additionally, this pattern is still evident for the sliding stiffness component of the floating pile at the 2nd and 3rd eigenfrequency of the soil layer. In light of the results it can be stated that the longer the path the propagating waves travel, the more the stress waves are attenuated with the distance and therefore the mismatch decay between the dynamic impedances is smaller. On the other hand for the coupling and rocking components at the anti-resonance frequencies ($\alpha_0 \cong 3$ and 7) the opposite effect is recorded namely increase of stiffness for lower values of H_s/d . This behaviour might be motivated by the fact that the resonance in rotation of the free-standing pile ($\lambda_0 = 3.141$) is attained closely to the anti-resonance, enhancing the stiffness for lower values of H_s/d . Additionally, the small reduction in stiffness attained at the anti-resonance frequencies can be also due to the less concurrent energy dissipation as shown hereafter.

1
2
3 Simultaneously, the imaginary component is characterized by a step-linear increasing pattern after the 1st
4 resonance with higher slope as the relative thickness of the soil layer decreases. The increase of damping ratio
5 depicted for smaller values of soil profile depth is due to the concurrent decrease of the dynamic component of
6 the stiffness coefficients. Differently to the trend of damping ratio, it was found that the increase of the viscous
7 damping coefficients in the frequency range investigated is related to the increase of H_s/d , in agreement with the
8 fact that more energy is dissipated as the propagating waves travel at longer distance. These findings are
9 consistent with previous studies reporting increase of damping ratio for suction caisson foundations, when H_s/d
10 decreases [12]. Moreover, the change in slope of the radiation damping recorded at each eigefrequency of the
11 soil layer was less pronounced for the rocking term.
12
13

14
15 On the basis of the bending moment distribution, in conjunction with the outcomes shown in Figure 8, dynamic
16 active lengths were estimated for floating piles with $H_s/d = 50$ and $H_s/d = 15$. Same values of the dynamic active
17 length ($L_a \approx 8.5m$) were obtained when the relative thickness of the soil layer is the only parameter varies. The
18 findings are in agreement with the active lengths proposed by Velez et al. [13] and they highlighted the fact that
19 the relative thickness of the soil layer has no effect on the dynamic active length of floating piles.
20
21
22

23 EFFECT OF THE SOIL STIFFNESS

24 In Figure 9 the real (K_{Su} , $K_{S\theta}$ and $K_{M\theta}$) and the imaginary ($2\zeta_{Su}$, $2\zeta_{S\theta}$, and $2\zeta_{M\theta}$) parts of the dynamic
25 impedances are illustrated varying the shear wave velocity of the soil layer for floating pile with slenderness
26 ratio $H_p/d = 10$. Note that the analytical solution is evaluated for pile-soil stiffness ratios which resemble soft,
27 medium and stiff soil profiles. The outcomes showed that the dynamic impedances slightly increase by increasing
28 of the shear wave velocity of the soil layer ($V_s > 250m/s$) for the frequency range investigated.
29
30
31

32 It was found that the highest gradient towards the 1st resonance was recorded for all the components of the
33 dynamic stiffness of pile embedded in soft soil profile; this observation is still valid for the outcomes of the
34 horizontal component recorded at the 2nd and 3rd eigenfrequency of the soil layer. Additionally, the difference in
35 the reduction of stiffness for all the components at the 1st resonance is approximately of 1% when the soil profile
36 varies from medium stiff to stiff. Moreover, the results highlighted that the effect of E_p/E_s reduces for the
37
38
39
40
41
42
43
44
45
46
47
48
49
50
51
52
53
54
55
56
57
58
59
60

1
2
3 coupling and rocking stiffness component, with the latter being practically equal to the static value for frequency
4
5 higher than the 1st resonance and for medium and stiff soil profiles.
6

7
8 Contrary to the behaviour of piles embedded in stiff and medium stiff soil layers, an increase of the coupling and
9
10 rocking components was clearly recorded for frequencies greater than $\alpha_0 \cong 5$ in the case of soft soil deposit.
11
12 After the 2nd resonance of the soil layer is reached the pile experiences higher rotation at the tip, which is further
13
14 enhanced when the foundation is embedded in a soft deposit. Indeed at high frequency ($\alpha_0 > 5$), the moment
15
16 reaction at the pile tip slightly decreases for higher values of the shear wave velocity of the soil layer, see Figure
17
18 10.
19

20
21 Simultaneously, the damping coefficients do not exhibit distinct differences for $E_p/E_s < 60$ over the frequency
22
23 range of interest. These discrepancies significantly increase with decreasing the shear wave velocity of the soil
24
25 layer ($E_p/E_s = 500$). Looking at the overall dynamic response, it seemed that the dynamic impedances were to
26
27 some extent affected by the variation of the soil stiffness in the frequency range considered, as previously
28
29 indicated by Latini and Zania [12] for suction caisson foundations.
30
31

32 33 34 DISCUSSION

35
36 A convenient way of describing the effect of the relative thickness of the soil layer on the dynamic response of
37
38 the pile is comparing the dynamic stiffness coefficients at the 1st resonance with respect to the relative thickness
39
40 of the soil layer H_s/d for different soil profiles ($E_p/E_s = 60$ and 500), see Figure 11. It was found that the
41
42 relative thickness of the soil layer influenced significantly all three dynamic stiffness coefficients for $H_s/d < 50$.
43
44 This means that there is no appreciable difference (less than 3%) between the static and the dynamic stiffness at
45
46 the 1st resonance for floating piles embedded in a soil layer with $H_s/d > 50$. Considering that after the 1st
47
48 resonance the frequency dependency of the stiffness components becomes less apparent, it can be concluded that
49
50 the dynamic component is negligible. This limit of the effect of the relative thickness of the soil layer is slightly
51
52 dependent on the stiffness of the soil medium. Indeed, the variation of dynamic stiffness components with H_s/d
53
54 became more apparent when the foundation is embedded in soft soil profiles. This suggests that in practical
55
56 structure-foundation interaction analyses one may ignore the dynamic component of the stiffness for floating
57
58 piles in deep soil deposit ($H_s/d > 50$). Hence, the pile foundation can be designed by applying the expressions
59
60 of the static stiffness coefficients available in the literature. Additionally, it is worth underlining that the

parametric graph shown in Figure 11 can be used in preliminary design calculations, giving an insight of the dynamic effects on the soil-floating pile system.

The independency of the dynamic active length on the slenderness ratio and the relative thickness of the soil layer previously observed, indicated that the dynamic active length can be only related to the stiffness contrast (E_p/E_s) as shown already for end bearing piles. In Figure 10 the dynamic active length is also illustrated for three different soil profiles ($E_p/E_s = 15, 60$ and 500). It is can be clearly seen that the dynamic active length increases for higher values of E_p/E_s and it coincides with the total pile length in the case of soft soil profile ($E_p/E_s = 500$). Furthermore, the values of the dynamic active length obtained for all the results presented in this study are in agreement with those calculated according to the formulation of Velez et al. [13].

CONCLUSIONS

In this study a continuum analytical solution for the estimation of the eigenfrequency and damping of floating piles is proposed. The analytical formulation was validated against finite element numerical models for floating piles. A parametric study was conducted to analyse the vibration characteristics and the effects of the main dimensionless parameters on the dynamic impedances of floating piles. The results presented herein are applicable to flexible floating piles; for short and rigid piles, the given formulation cannot reproduce correctly the dynamic response, since vertical displacements are not accounted for.

The dynamic soil-pile interaction analysis of flexible floating piles indicated that the slenderness ratio is not influential and consequently pointed out that the dynamic active length is not an appropriate design criterion for floating piles.

On the other hand the dynamic impedances were found to be strongly affected by the variation of the thickness of the soil layer. The variation of the dynamic stiffness with frequency becomes more apparent when the thickness of the soil layer is only marginally larger than the length of the pile, while the viscous damping increases with the increase of the thickness of the soil layer. However, it was shown that the dynamic stiffness coefficients for a floating pile can be disregarded when the foundation is embedded in deep soil deposit ($H_s/d > 50$).

Whereas the dimensionless parameter E_p/E_s affects slightly the stiffness and this was proven by slightly scattered outcomes particularly for soft soil deposits. Furthermore, the results highlighted that the stiffness ratio is the only

dimensionless parameter affecting the dynamic active length in agreement with previous studies for end bearing piles. The results of the current study support that the expression of dynamic active length by Velez et al. [13] can be applied also in the case of floating piles.

The presented analytical solution can be considered a very attractive tool that might be applied in the frame of the substructure approach, to perform complete dynamic soil-structure interaction analyses of structures on such kind of foundations. However, it must be mentioned that the suggested analytical formulation is limited to soil profiles with constant stiffness along the depth, nonlinear soil behaviour is not considered, and the sliding and the separation along the soil-pile interface is not taken into account.

ACKNOWLEDGMENTS

This work has been supported by the Danish Council for Strategic Research through the project “Advancing Beyond Shallow waterS (ABYSS) - Optimal design of offshore wind turbine support structures”. The author would like to acknowledge the support of the Technical University of Denmark for this study. The author would also like to thank the anonymous Reviewers whose comments and suggestions improved the manuscript.

REFERENCES

- [1]. Kausel E. Early history of soil–structure interaction. *Soil Dynamics and Earthquake Engineering* 2010; **30**(9): 822-832.
- [2]. Novak M. Dynamic stiffness and damping of piles. *Canadian Geotechnical Journal* 1974; **11**:574-598.
- [3]. Novak M, Aboul-Ella F. Impedance functions of piles in layered media. *Journal of Engineering Mechanics* 1978; **104**(6):643-661.
- [4]. Mylonakis G. Elastodynamic model for large diameter end-bearing shafts. *Soils Foundation* 2001; **41**(3):31-44.
- [5]. Nogami T, Novak M. Resistance of soil to a horizontally vibrating pile. *Earthquake Engineering and Structural Dynamics* 1977; **5**(3):249-261.
- [6]. Novak M, Nogami T. Soil-pile interaction in horizontal vibration. *Earthquake engineering and structural dynamics* 1977; **5**:263-281.
- [7]. Nogami T, Novak M. Coefficients of soil reaction to pile vibration. *Journal of Geotechnical Engineering, ASCE* 1980; **106**(6):565-70.
- [8]. Anoyatis G, Mylonakis G, Lemnitzer, A. Soil reaction to lateral harmonic pile motion. *Soil Dynamics and Earthquake Engineering* 2016; **87**:164-179.
- [9]. Liu H, Zheng C, Ding X, Kouretzis GP, Sloan SW. A revised solution for the horizontal vibration of an end-bearing pile in viscoelastic soil. *International Journal for Numerical and Analytical Methods in Geomechanics* 2016; **40**(13):1890-1900.

- 1
2
3 [10]. Blaney GW, Kausel E, Roesset J. Dynamic stiffness of piles. *Proceedings of 2nd International Conference*
4 *on Numerical Methods in Geomechanics* 1976; **2**:1001–1012.
- 5 [11]. Roesset JM, Angelides D. Dynamic stiffness of piles. *Proceedings of the International Conference on*
6 *Numerical Methods in Offshore Piling, Institution of Civil Engineers (ICE)* 1980.
- 7 [12]. Latini C, Zania V. Dynamic lateral response of suction caissons. *Soil Dynamics and Earthquake*
8 *Engineering* 2017; **100**:59-71.
- 9 [13]. Velez A, Gazetas G, Krishnan R. Lateral Dynamic Response of Constrained Head Piles. *Journal of*
10 *Geotechnical Engineering* 1983; **109**(8):1063–1081.
- 11 [14]. Gazetas G. Seismic response of end-bearing single piles. *Soil Dynamics and Earthquake Engineering*
12 1984; **3**(2):82–93.
- 13 [15]. Gazetas G, Dobry R. Horizontal response of piles in layered soils. *Journal of Geotechnical Engineering.*
14 *ASCE* 1984; **110**(1): 20-40.
- 15 [16]. Maeso O, Aznárez JJ, García F. Dynamic impedances of piles and groups of piles in saturated soils.
16 *Computers & structures* 2005; **83**(10):769-782.
- 17 [17]. Padrón LA, Aznárez JJ, Maeso O. BEM–FEM coupling model for the dynamic analysis of piles and pile
18 groups. *Engineering Analysis with Boundary Elements* 2007; **31**(6):473–84.
- 19 [18]. Ai ZY, Li ZX. Dynamic analysis of a laterally loaded pile in a transversely isotropic multilayered half-
20 space. *Engineering Analysis with Boundary Elements* 2015; **54**:68–75.
- 21 [19]. Nozoe H, Gyöten Y, Fukusumi T. Dynamic analysis of a soil-pile system by the finite Fourier-Henkel
22 transformation method – Case of a floating pile in horizontal vibration. *Theoretical and applied mechanics* 1985;
23 **33**:377-392.
- 24 [20]. Haldar SS, Bose SK. Dynamic soil stiffness in lateral vibrations of a floating pile. *Soil Dynamics and*
25 *Earthquake Engineering* 1990; **9**:51-56.
- 26 [21]. Latini C, Zania V, Johannesson B. Dynamic stiffness and damping of foundation for jacket structures.
27 *Proceedings of 6th International Conference on Earthquake Geotechnical Engineering.*
- 28 [22]. Zania V. Natural vibration frequency and damping of slender structures founded on monopiles. *Soil*
29 *Dynamics and Earthquake Engineering* 2014; **59**:8–20.
- 30 [23]. Hetényi M. Beams on Elastic Foundation - Theory with Applications in the Fields of Civil and
31 Mechanical Engineering. University of Michigan Press; 1971.
- 32 [24]. Simulia DS. Abaqus 6.13 User's Manual. Dassault Systems, 2013, Providence, RI.
- 33 [25]. Syngros C. Seismic Response of piles and pile-supported bridge piers evaluated through case histories
34 Ph.D. thesis, City University of New York; 2004.
- 35 [26]. Randolph MF. The response of flexible piles to lateral loading. *Géotechnique* 1981; **31**(2):247–59.
- 36 [27]. Poulos HG, Davis EH. Pile foundation analysis and design. New York, NY: John Wiley and Sons; 1980.
- 37 [28]. Kuhlemeyer RL. Static and dynamic laterally loaded floating piles. *Journal of Geotechnical and*
38 *Geoenvironmental Engineering* 1979; **105**
- 39
40
41
42
43
44
45
46
47
48
49
50
51
52
53
54
55
56
57
58
59
60

NOTATION

Latin upper case

A, B, C, D : integration constants

E_s : soil modulus of elasticity

E_p : Young modulus of pile

F_{in} : Fourier coefficients

G : soil shear modulus

H_s : thickness of soil layer

H_p : height of pile

I : moment of inertia of pile

K_r : pile flexibility factor

K_{Su} : dynamic stiffness coefficient -real part- force for unit displacement

K_{Mu} : dynamic stiffness coefficient -real part- moment for unit displacement

$K_{S\theta}$: dynamic stiffness coefficient -real part- force per unit rotation

$K_{M\theta}$: dynamic stiffness coefficient -real part- moment for unit rotation

K_{Su}^0 : static stiffness coefficient - force for unit displacement

K_{Su}^0 : static stiffness coefficient - moment for unit displacement

$K_{S\theta}^0$: static stiffness coefficient - force for unit rotation

$K_{M\theta}^0$: static stiffness coefficient - moment for unit rotation

M : reaction moment at the pile head

S : horizontal reaction force at the pile head

V_s : soil shear wave velocity

Latin lower case

a_n : complex constant of the soil layer in horizontal direction

d : diameter of pile

f_{in} : dimensionless coefficients

$h_n = (\pi/2H_s)(2n - 1)$, $n = 1, 2, \dots$, parameter

\bar{h}_n : dimensionless parameter

m : mass of pile

r_0 : radius of pile

u : translational degree of freedom at the pile head

z : vertical coordinate with respect to RS

z_1 : vertical coordinate with respect to RS1

Greek

α_0 : dimensionless eigenfrequency of soil layer

α_{hn} : horizontal resistance factor

ΔH : difference of soil thickness

ζ_{Su} : damping coefficient - force for unit displacement

ζ_{Mu} : damping coefficient - moment for unit displacement

$\zeta_{S\theta}$: damping coefficient - force for unit rotation

$\zeta_{M\theta}$: damping coefficient - moment for unit rotation

θ : rotational degree of freedom at the pile head

λ : dimensionless eigenfrequency of freestanding pile

ν : Poisson's ratio of soil layer

ζ : hysteretic soil damping ratio

ρ : density of soil

ω : circular frequency of harmonic applied displacement

TABLES10

Table 1. Static floating pile stiffness obtained from the numerical models and the analytical solution.

Reference	$K_{Su}/E_s d$	$K_{S\theta}/E_s d^2$	$K_{M\theta}/E_s d^3$
Proposed analytical solution	1.96	-0.93	1.17
Syngros [25]	1.96	-0.75	1.02
Randolph [26]	2.36	-1.03	1.23
Numerical model	1.91	-0.70	1.30

FIGURE LEGENDS

Figure 1: Analytical model of soil-pile system.

Figure 2: Variation of the three dynamic stiffness coefficients with respect to the dimensionless frequency. The real component and the imaginary component for the validation case.

Figure 3: Distribution of the pile displacement along the depth at the three first eigenfrequencies of the soil layer for the validation case.

Figure 4: Distribution of the vertical displacements along the pile depth at the three first eigenfrequencies of the soil layer for the validation case.

Figure 5: Variation of the three dynamic stiffness coefficients with respect to the non-dimensional frequency. Effect of the slenderness ratio on the real component (a) and the imaginary component (b). Results are presented for $H_s/d=30$ and $E_p/E_s=60$.

Figure 6: Variation of the three dynamic stiffness coefficients with respect to the non-dimensional frequency. Effect of the slenderness ratio on the real component (a) and the imaginary component (b). Results are presented for $H_s/d=30$ and $E_p/E_s=500$.

Figure 7: Variation of the three dynamic stiffness coefficients with respect to the non-dimensional frequency. Effect of the relative thickness of the soil layer on the real component (a) and the imaginary component (b). Results are presented for $H_p/d=10$ and $E_p/E_s=60$.

Figure 8: Distribution of the bending moment along the depth for $H_s/d=15$ and 50 at the 1st eigenfrequency of the soil layer.

Figure 9: Variation of the three dynamic stiffness coefficients with respect to the non-dimensional frequency. Effect of the soil stiffness on the real component (a) and the imaginary component (b). Results are presented for $H_s/d=30$ and $H_p/d=10$.

Figure 10: Distribution of the bending moment along the depth for $E_p/E_s=15$, 60 and 500 at the 3rd eigenfrequency of the soil layer. Results are presented for $H_s/d=30$ and $H_p/d=10$.

Figure 11: Variation of the dynamic stiffness with respect to the relative thickness of the soil layer H_s/d for $E_p/E_s=60$ and $E_p/E_s=500$ at the 1st eigenfrequency of the soil layer.

FIGURES

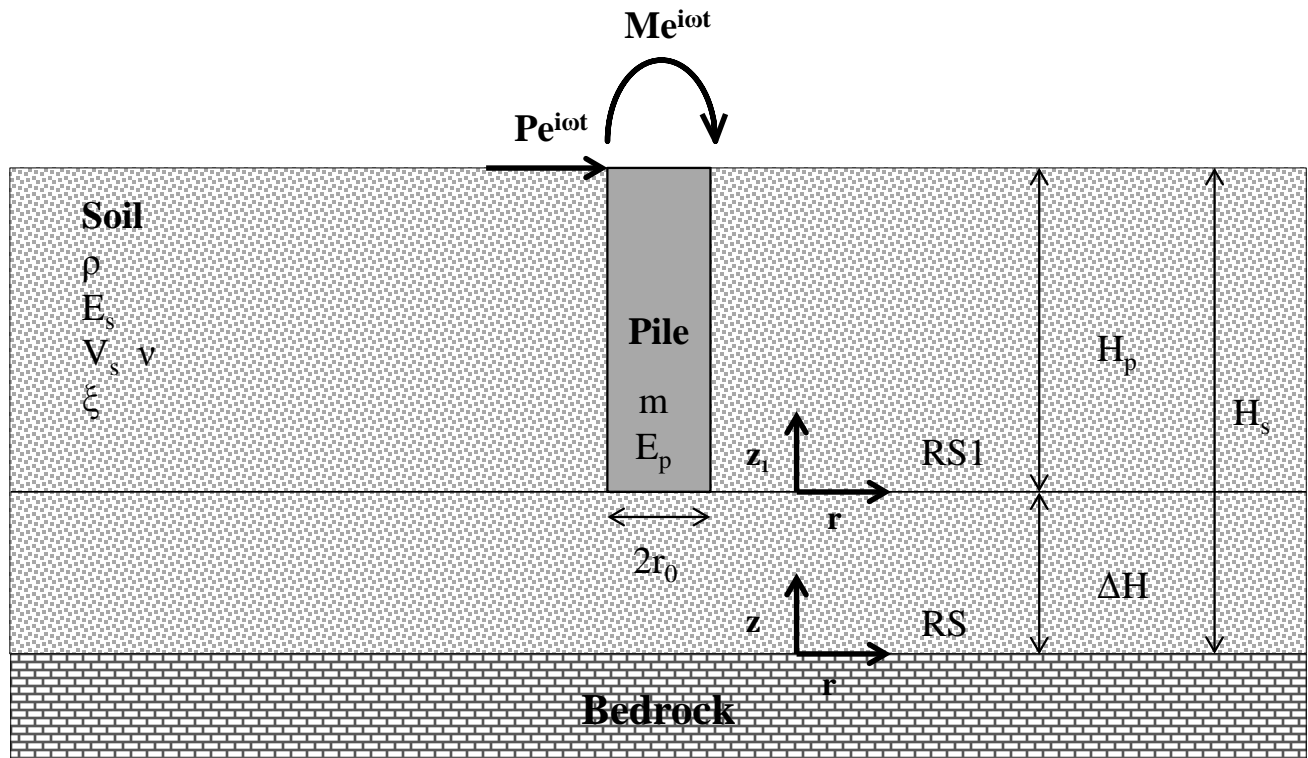


Figure 1: Analytical model of soil-pile system.

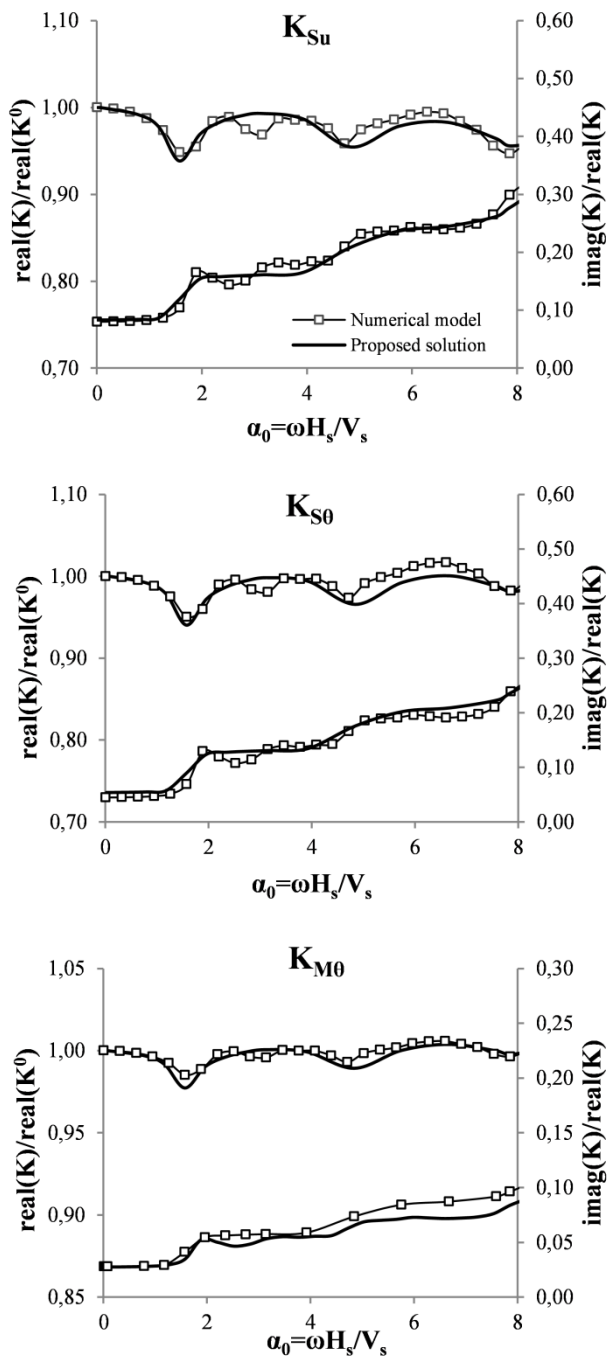


Figure 2: Variation of the three dynamic stiffness coefficients with respect to the dimensionless frequency. The real component and the imaginary component for the validation case.

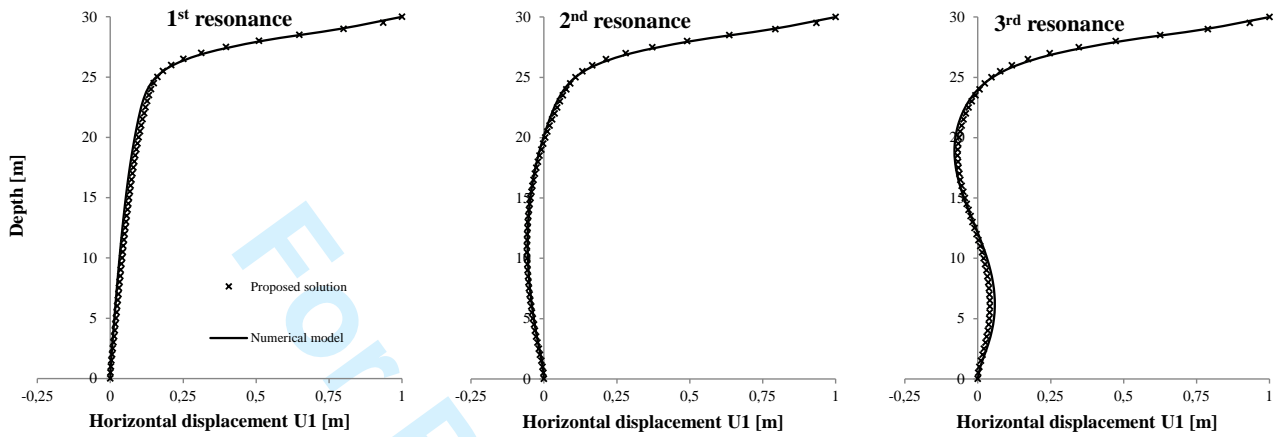


Figure 3: Distribution of the pile displacement along the depth at the three first eigenfrequencies of the soil layer for the validation case.

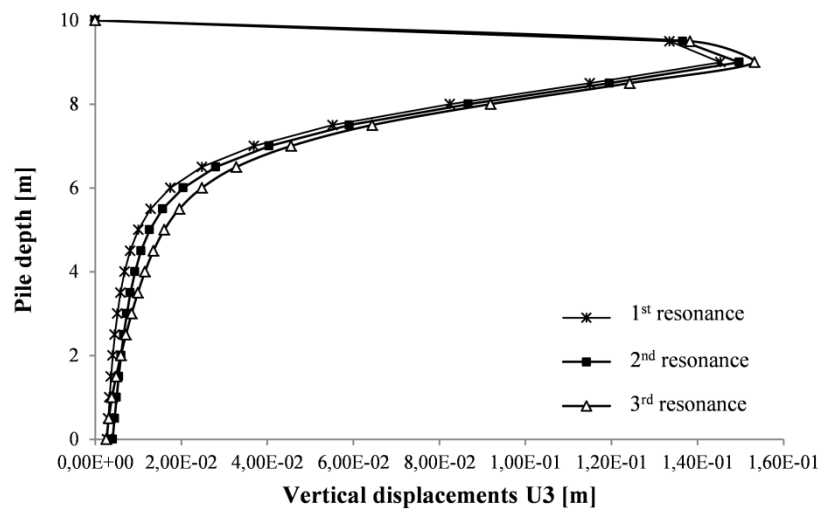


Figure 4: Distribution of the vertical displacements along the pile depth at the three first eigenfrequencies of the soil layer for the validation case.

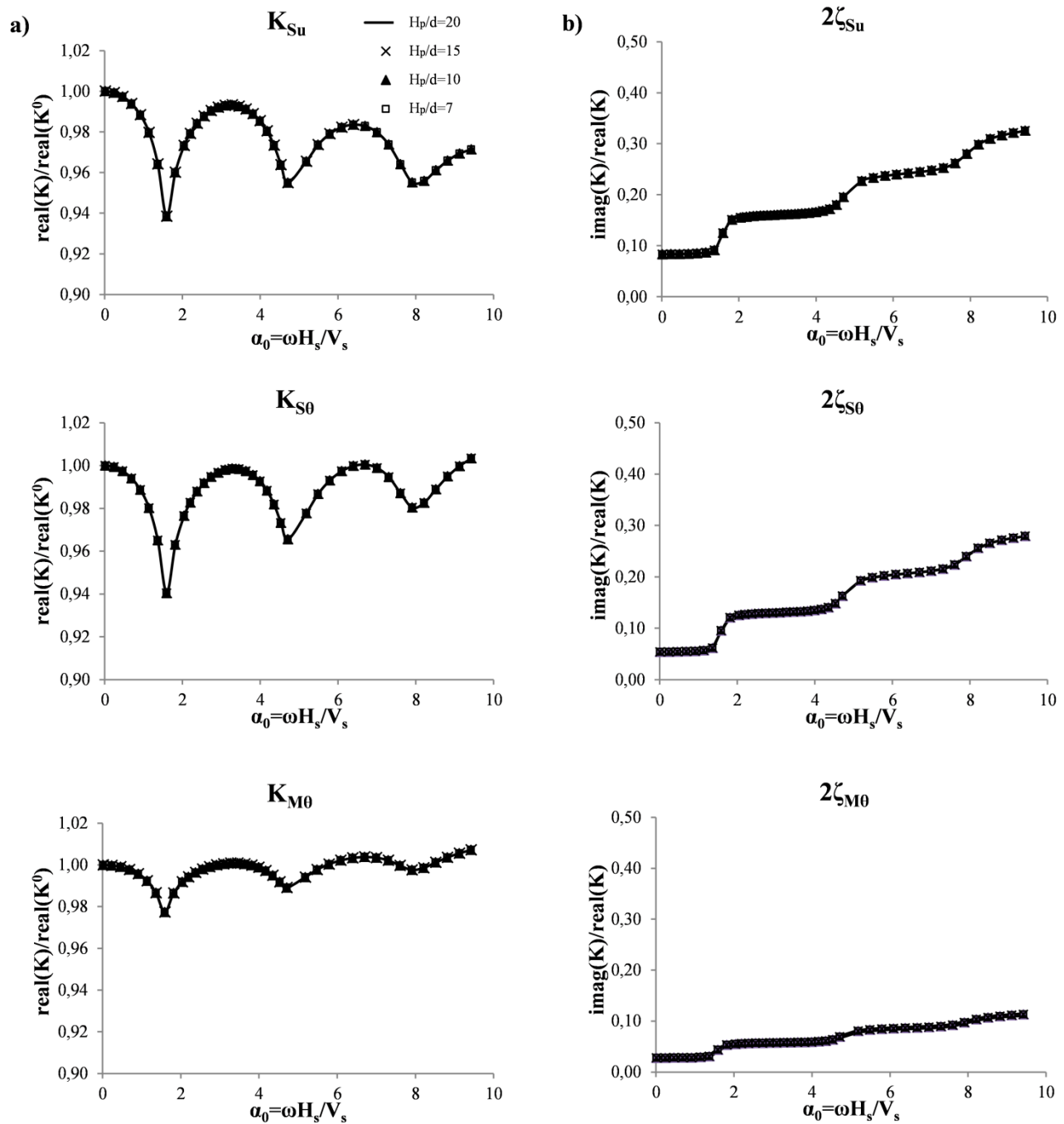


Figure 5: Variation of the three dynamic stiffness coefficients with respect to the non-dimensional frequency. Effect of the slenderness ratio on the real component (a) and the imaginary component (b). Results are presented for $H_s/d=30$ and $E_p/E_s=60$.

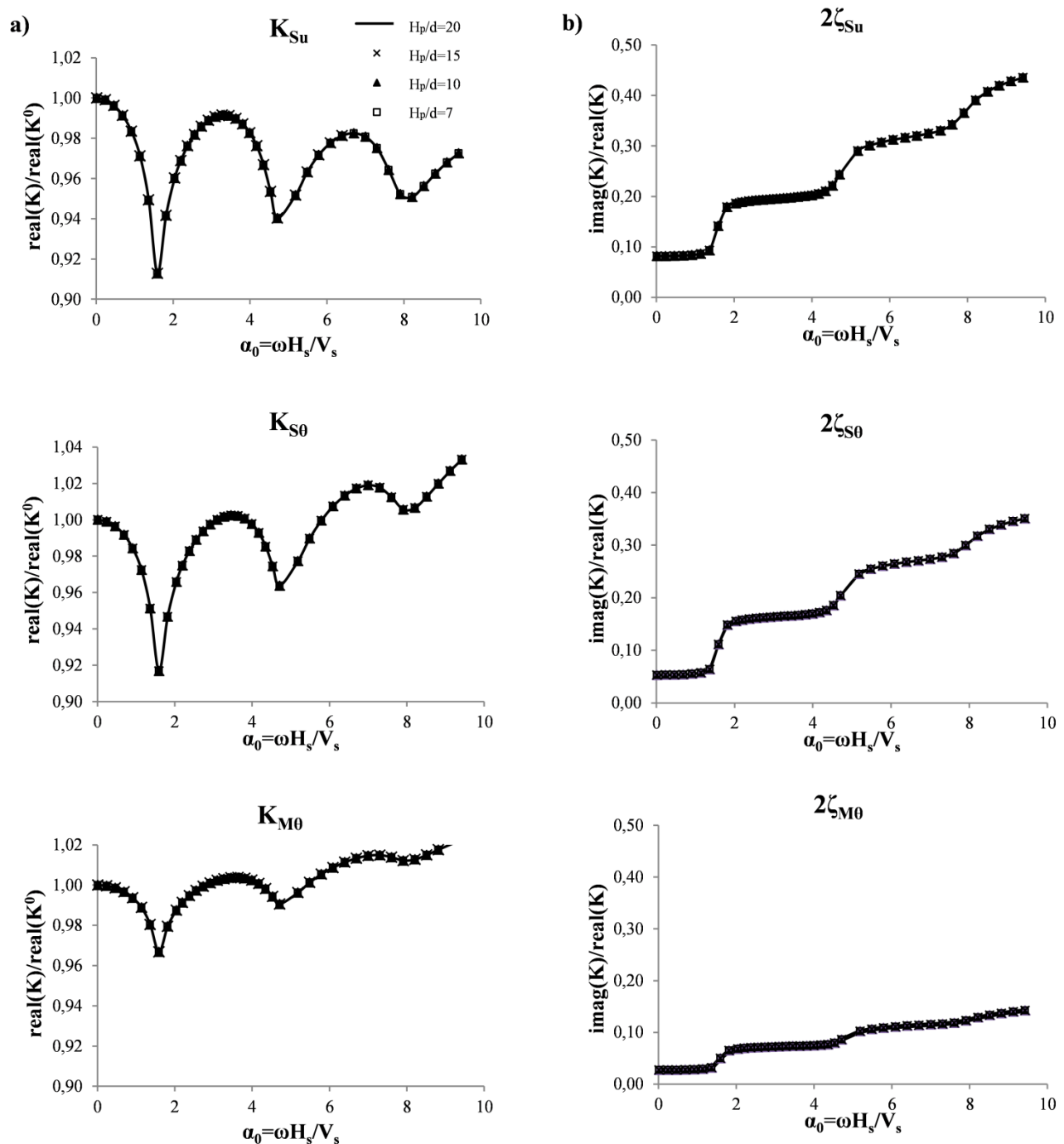


Figure 6: Variation of the three dynamic stiffness coefficients with respect to the non-dimensional frequency. Effect of the slenderness ratio on the real component (a) and the imaginary component (b). Results are presented for $H_s/d=30$ and $E_p/E_s=500$.

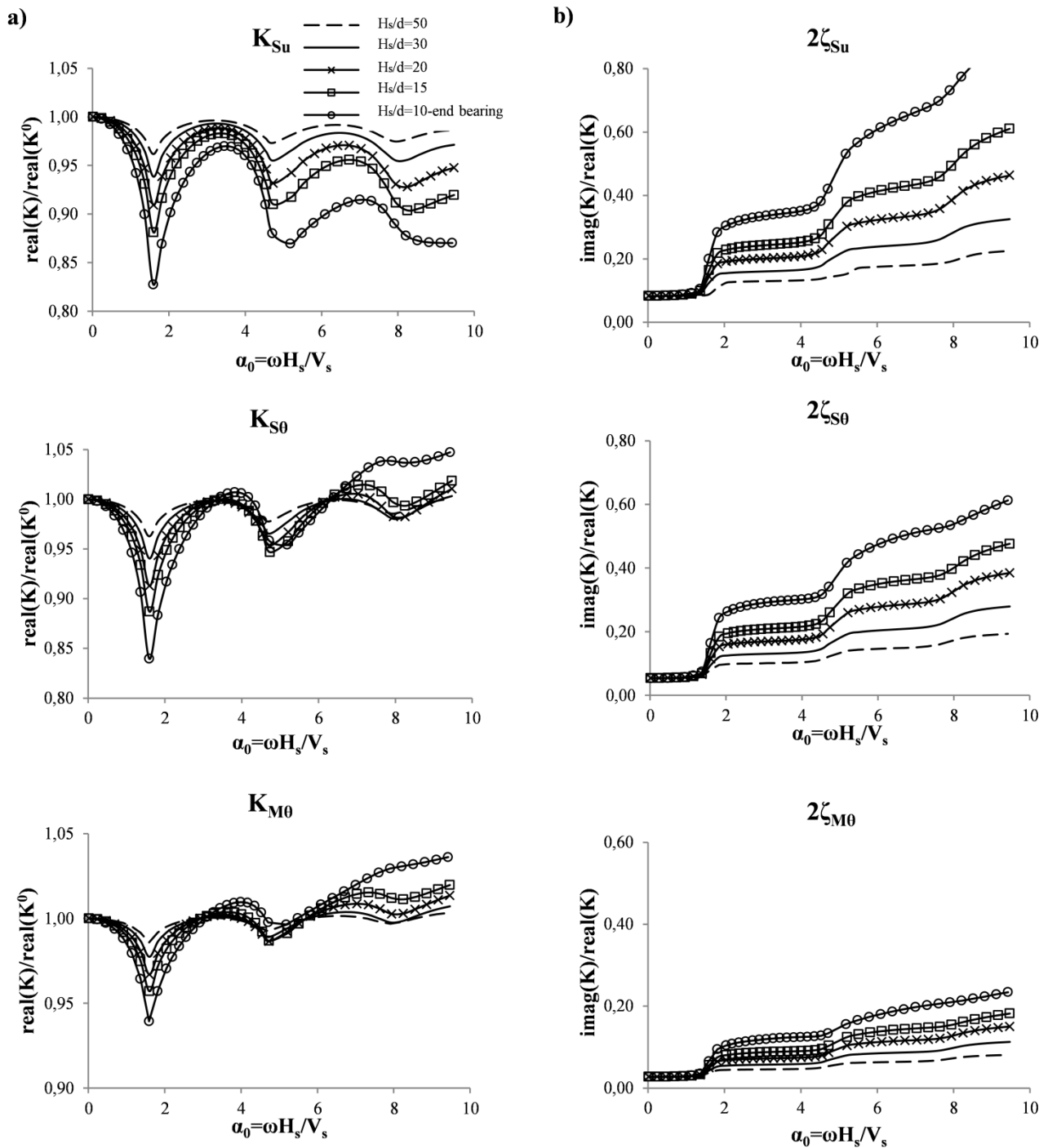


Figure 7: Variation of the three dynamic stiffness coefficients with respect to the non-dimensional frequency. Effect of the relative thickness of the soil layer on the real component (a) and the imaginary component (b). Results are presented for $H_p/d=10$ and $E_p/E_s=60$.

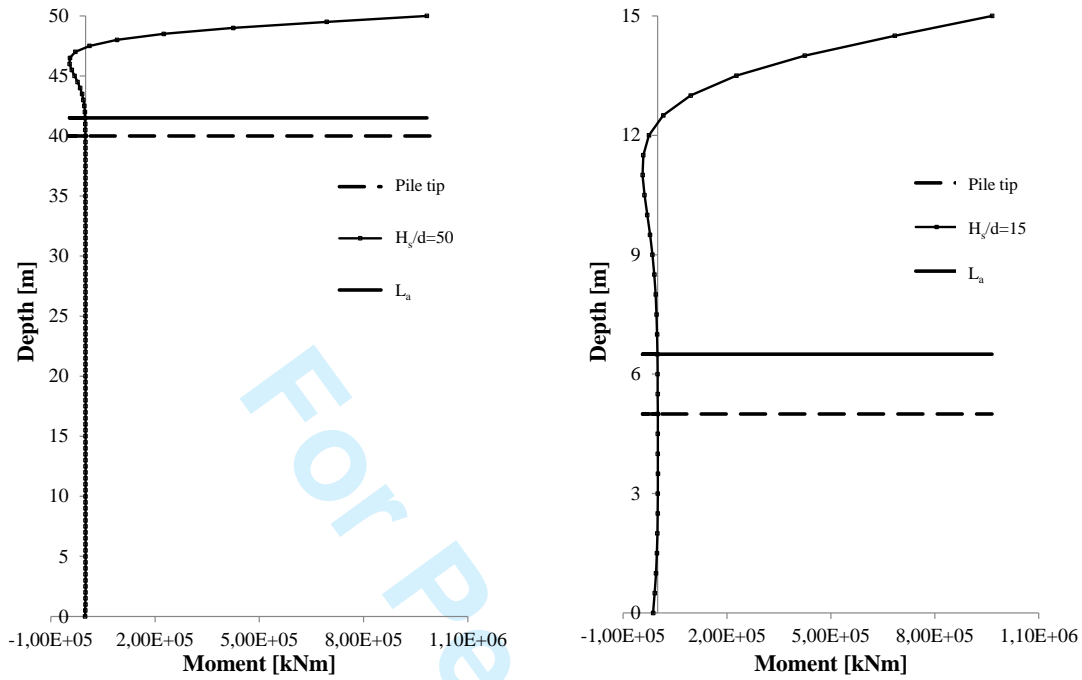


Figure 8: Distribution of the bending moment along the depth for $H_s/d=15$ and 50 at the 1st eigenfrequency of the soil layer.

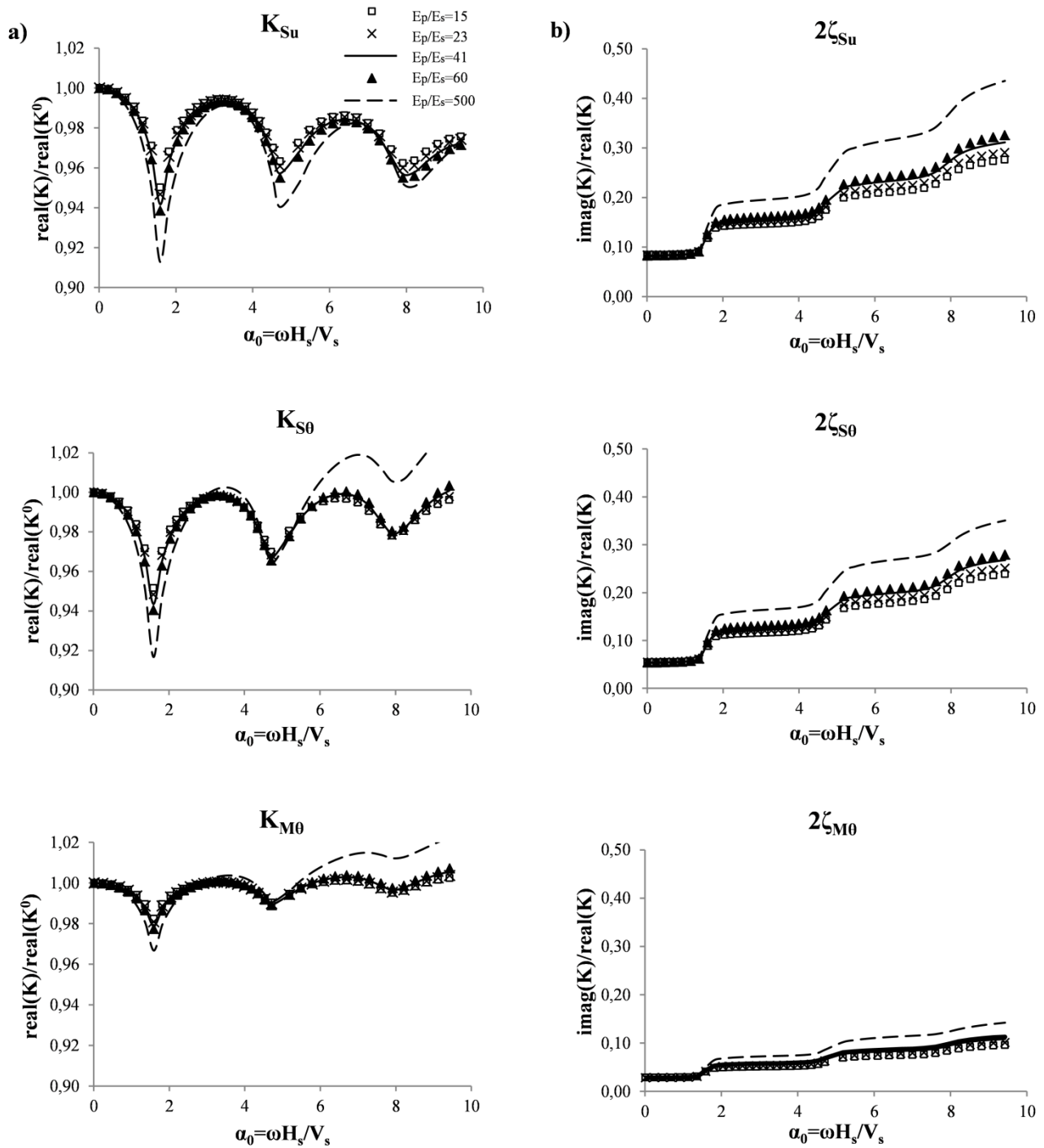


Figure 9: Variation of the three dynamic stiffness coefficients with respect to the non-dimensional frequency. Effect of the soil stiffness on the real component (a) and the imaginary component (b). Results are presented for $H_s/d=30$ and $H_p/d=10$.

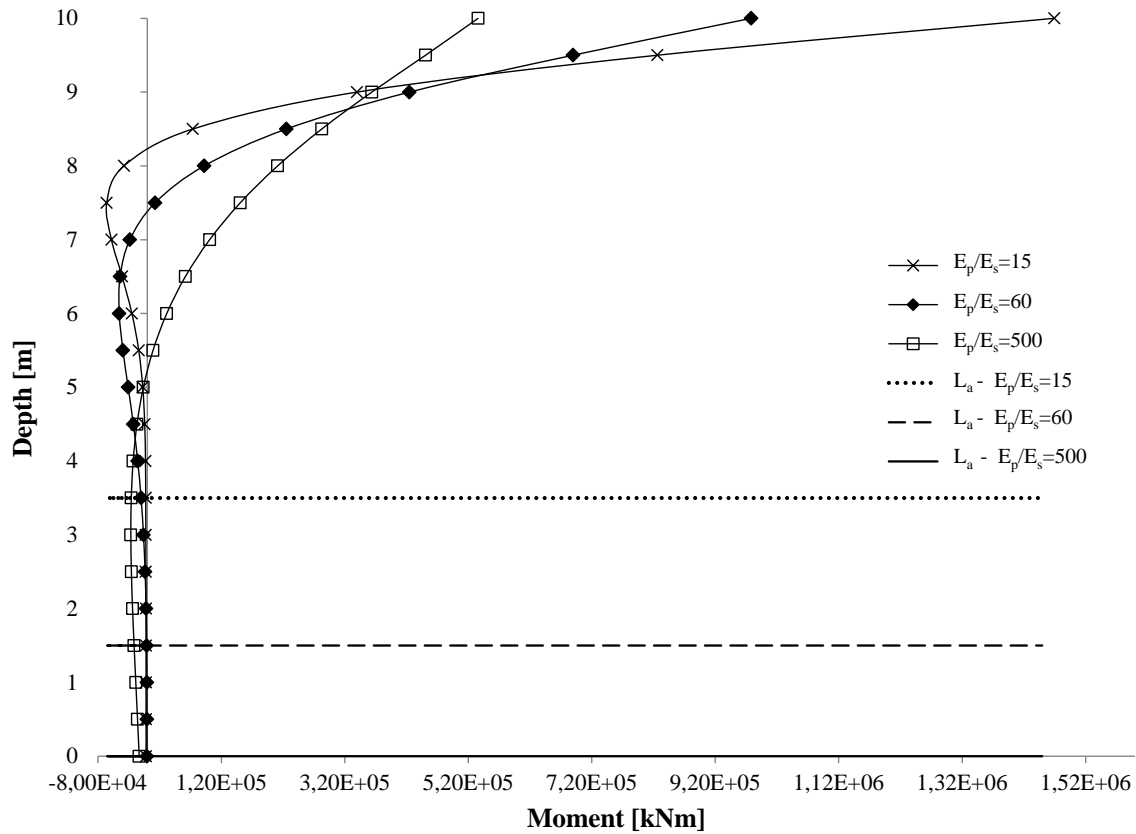


Figure 10: Distribution of the bending moment along the depth for $E_p/E_s=15$, 60 and 500 at the 3rd eigenfrequency of the soil layer. Results are presented for $H_s/d=30$ and $H_p/d=10$.

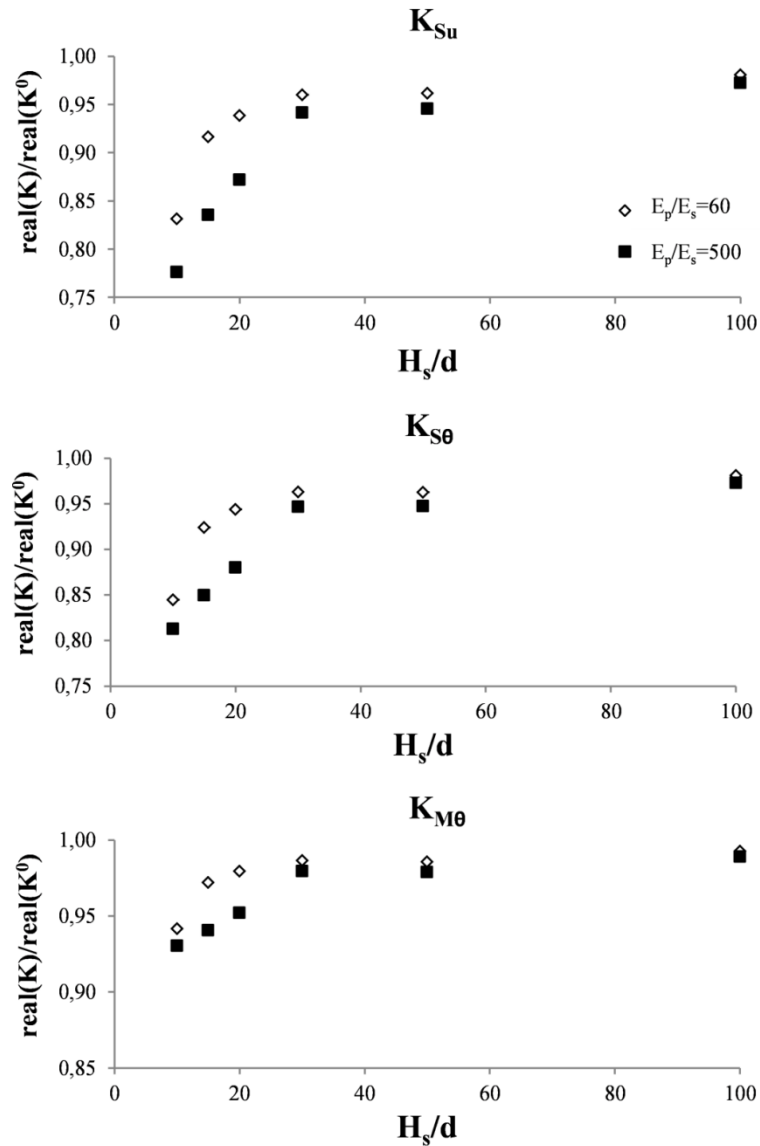


Figure 11: Variation of the dynamic stiffness with respect to the relative thickness of the soil layer H_s/d for $E_p/E_s=60$ and $E_p/E_s=500$ at the 1st eigenfrequency of the soil layer.

Paper II

Dynamic stiffness and damping of foundations for jacket structures

C. LATINI, V. ZANIA AND B. JOHANNESSON

Published in: Proceeding of the 6th International Conference on Earthquake Geotechnical Engineering, 2015



Dynamic stiffness and damping of foundations for jacket structures

C. Latini¹, V. Zania², B. Johannesson³

ABSTRACT

Foundation for offshore jacket structures may comprise of long floating piles. The dynamic response of floating piles to horizontal load is herein investigated. The analytical solution of horizontally vibrating end bearing piles by Novak & Nogami (1977) has been modified. At first the soil resistance as defined by Nogami & Novak (1977) is determined, considering 3D wave propagation within linear soil layer with hysteretic damping. Thereafter, the dynamic response of the pile is estimated assuming soil pressure equal to the soil resistance and imposing displacement compatibility. A parametric study clarifies the role of the parameters involved i.e. the depth of the soil layer, the pile diameter and the soil layer shear wave velocity. Results are presented in terms of dimensionless graphs which highlight the frequency dependency of the dynamic stiffness and damping.

Introduction

Nowadays, the offshore wind market is developing towards wind farms with higher capacity generators and in deeper waters, challenging the current offshore design procedures. So far the selection of the type of support structures for offshore wind turbines has been based on the water depth. In shallow waters, monopiles and monopod suction buckets are mostly utilized, while jacket structures with floating piles would be the design configuration for deeper waters following the traditional design of oil and gas industry (De Vries, 2007). In the design of offshore wind support structures fatigue derived from combined wind and wave loading is one of the critical issues. The potential of structural resonance with dynamic forces due to wind loading would result to large amplitude stresses and subsequent accelerated fatigue. For this reason the wind turbine support structure is practically designed by setting the tower fundamental resonance between the blade passing and the rotor frequency. In addition, the overall damping of the structure has an important impact on the fatigue damage, since the amplitude of vibrations at resonance is inversely proportional to the damping ratios (Devriendt et al., 2012).

Any structure subjected to dynamic load interacts with the foundation and the soil, altering thus the eigenfrequency and the damping (Kramer, 1996). Hence it is important to assess the dynamic stiffness and damping of the soil-foundation system. In order to rationally account for the dynamic interaction between the single pile foundation and the supporting soil deposit several analytical and numerical studies have been reported in the literature. Considering only those for

¹Phd Student, Civil Engineering Department, Technical University of Denmark, Lyngby, Denmark, chila@byg.dtu.dk

²Assistant Professor, Civil Engineering Department, Technical University of Denmark, Lyngby, Denmark, vaza@byg.dtu.dk

³Associate Professor, Civil Engineering Department, Technical University of Denmark, Lyngby, Denmark, bjojo@byg.dtu.dk

linear elastic soil layer they can be categorized according to the following: a) rigorous analytical continuum solutions for end bearing piles (Novak & Nogami, 1977, Nogami & Novak, 1977, Zheng et al., 2013), where the soil is modelled as homogeneous layer with hysteretic material damping; b) Winkler type analytical solutions (Novak, 1974, Novak & Aboul-Ella, 1978, Mylonakis, 2001), where the supporting soil is replaced by a bed of independent elastic springs resting on a rigid base. For dynamic problems the use of Winkler foundation coefficients based on Baranov's equation for in plane and out plane vibration of a disk has been proposed by Novak (1974). An improved model incorporating in the analysis the normal and shear stresses acting on the upper and lower faces of a horizontal soil element by integrating the governing equations over the thickness of the soil layer has been developed by Mylonakis (2001); c) numerical continuum finite element solutions (Blaney et al., 1976, Roesset & Angelides, 1980, Velez et al., 1983, Gazetas, 1984, Gazetas & Dobry, 1984), where the soil is treated as an elastic continuum and the pile is assumed to have rigid cross section and it is modelled as series of regular beam segments. Very limited studies have investigated the response of floating piles either numerically (Gazetas & Dobry, 1984) or analytically (Nozoe et al., 1983). Hence the aim of this paper is to formulate an analytical solution for the dynamic response of floating piles focusing on the estimation of the dynamic stiffness and damping coefficients with respect to the frequency. Hence an appropriately modified formulation based on the rigorous analytical solution of soil-pile vibration by Novak & Nogami (1977) has been developed. The comparison of the end bearing with the floating pile is further discussed. A parametric study has been performed accounting for the effect of the soil profile, the pile diameter and the stiffness of the soil on the soil-pile system response.

Methodology

The main assumptions of the solution presented here are: 1) the soil layer is linear, elastic, free at the surface; 2) the material damping is of the hysteretic type - frequency independent; 3) the pile is vertical, uniform, linearly elastic and of circular cross section. It is free at the tip and perfectly attached to the soil. In this formulation the reference system, RS1, is introduced to account the fact that the height of the viscoelastic layer undergoing harmonic motion is larger than the pile length as shown in Figure 1.

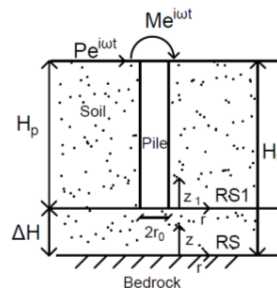


Figure 1. Analytical model of soil-pile system.

In the RS1 reference system the horizontal motion of the pile when subjected to harmonic excitation by end forces applied at the head of the pile is given as:

$$u(z_1, t) = u(z_1) e^{i\omega t} \quad (1)$$

where ω is the circular frequency and z_1 is the vertical coordinate of the pile. The governing equation of the pile motion follows the beam on elastic foundation by Hetényi (1971)

$$E_p I \frac{\partial^4}{\partial z_1^4} (ue^{i\omega t}) + m \frac{\partial^2}{\partial t^2} (ue^{i\omega t}) = -p(z_1)e^{i\omega t} \quad (2)$$

where $E_p I$ is the bending stiffness of the pile, m is the mass of the pile per unit length and $p(z_1)$ is the amplitude of the soil resistance to the motion of the pile. Whereas, the soil resistance expressed in the local pile's coordinate system is

$$p(z_1, t) = \sum_{n=1}^{\infty} \alpha_{hn} U_n \sin(h_n(z_1 + \Delta H)) \quad (3)$$

where α_{hn} is the horizontal resistance factor depending on the pile radius r_0 , shear modulus G and a number of dimensionless parameters such as the dimensionless frequency $a_0 = H_s \omega / V_s$, pile slenderness H_p / r_0 , material hysteretic damping ζ and Poisson's ratio ν ; U_n is the modal amplitude independent of z , $\sin(h_n(z_1 + \Delta H))$ is the n^{th} mode shape of the soil layer, $\Delta H = H_s - H_p$ and $h_n = (\pi/2H_s)(2n - 1)$ where H_s is the depth of the soil layer and n is the mode number. Substituting Equation 3 into Equation 2 and eliminating the time variable, t , the following expression for the pile amplitude is obtained as:

$$E_p I \frac{d^4 u}{dz_1^4} - m\omega^2 u = -\sum_{n=1}^{\infty} \alpha_{hn} U_n \sin(h_n(z_1 + \Delta H)) \quad (4)$$

The solution to Equation 4 is given as a sum of the complete solution of the homogeneous equation u_h , and a particular solution of the non-homogeneous equation u_p . The particular solution u_p can be expressed as

$$u_p = \sum_{n=1}^{\infty} a_n \sin(h_n(z_1 + \Delta H)) \quad (5)$$

where a_n is a complex constant. Substitution of Equation 5 into Equation 4 yields

$$E_p I \sum_{n=1}^{\infty} a_n h_n^4 \sin(h_n(z_1 + \Delta H)) - m\omega^2 \sum_{n=1}^{\infty} a_n \sin(h_n(z_1 + \Delta H)) = -\sum_{n=1}^{\infty} \alpha_{hn} U_n \sin(h_n(z_1 + \Delta H)) \quad (6)$$

Hence, the constant a_n can be determined as

$$a_n = \frac{-\alpha_{hn} U_n}{E_p I h_n^4 - m\omega^2} \quad (7)$$

The solution of the homogeneous equation can be written as

$$u_h = A \sin(\lambda z_1) + B \cos(\lambda z_1) + C \sinh(\lambda z_1) + D \cosh(\lambda z_1) \quad (8)$$

where A , B , C and D are the integration constants obtained by the boundary conditions at the tip of the pile and

$$\lambda = \sqrt[4]{\frac{m\omega^2}{E_p I}} \quad (9)$$

Then the pile displacement is given as:

$$u(z_1) = A \sin(\lambda z_1) + B \cos(\lambda z_1) + C \sinh(\lambda z_1) + D \cosh(\lambda z_1) - \sum_{n=1}^{\infty} \frac{\alpha_{hn} U_n}{E_p I h_n^4 - m\omega^2} \sin(h_n(z_1 + \Delta H)) \quad (10)$$

The displacement of the soil layer at the pile can be expressed as

$$U(z_1) = \sum_{n=1}^{\infty} U_n \sin(h_n(z_1 + \Delta H)) \quad (11)$$

The displacement compatibility between the pile and the soil layer is imposed. Then, the variable z_1 is written as $z_1 = z - \Delta H$ and expanding $\sin(\lambda(z - \Delta H))$, $\cos(\lambda(z - \Delta H))$, $\sinh(\lambda(z - \Delta H))$ and $\cosh(\lambda(z - \Delta H))$ into a Fourier sine series of argument $h_n z$, the following formula is obtained:

$$U_n = \frac{AF_{1n} + BF_{2n} + CF_{3n} + DF_{4n}}{1 + \left[\frac{\alpha_{hn}}{E_p I h_n^4 - m \omega^2} \right]} \quad (12)$$

where

$$\begin{cases} F_{1n} = \frac{2}{H_s} \int_0^{H_s} \sin(\lambda(z - \Delta H)) \sin(h_n z) dz \\ F_{2n} = \frac{2}{H_s} \int_0^{H_s} \cos(\lambda(z - \Delta H)) \sin(h_n z) dz \\ F_{3n} = \frac{2}{H_s} \int_0^{H_s} \sinh(\lambda(z - \Delta H)) \sin(h_n z) dz \\ F_{4n} = \frac{2}{H_s} \int_0^{H_s} \cosh(\lambda(z - \Delta H)) \sin(h_n z) dz \end{cases} \quad (13)$$

Substituting U_n into Equation 10, the amplitude of the pile motion is

$$u(z) = A \sin(\lambda(z - \Delta H)) + B \cos(\lambda(z - \Delta H)) + C \sinh(\lambda(z - \Delta H)) + D \cosh(\lambda(z - \Delta H)) - \sum_{n=1}^{\infty} \frac{\alpha_{hn}(AF_{1n} + BF_{2n} + CF_{3n} + DF_{4n})}{E_p I h_n^4 - m \omega^2 + \alpha_{hn}} \sin h_n z \quad (14)$$

Using the displacement of the pile presented in Equation 14, the amplitude of the angle of rotation, θ , the bending moment, M , and the shear force, S , are obtained from the corresponding derivatives. The unknown coefficients A , B , C , D are estimated by considering the boundary conditions and applying a unit horizontal translation and a unit rotation at the pile head. The dynamic impedances K_{su} , $K_{s\theta}$, K_{mu} and $K_{m\theta}$ at the level of the pile head are then calculated as shear forces, S , and moments, M , for unit displacement, u , and rotation, θ .

Parametric Study

The dynamic response of floating piles is analyzed by employing the method described in the previous section. In the current study the comparison of the end bearing with the floating pile is investigated and further, the effect of the pile diameter and the shear wave velocity of the soil layer on the soil-floating pile response are explored. This leads to some considerations of the role of popular dimensionless parameters such as the stiffness ratio E_p/E_s and the pile flexibility factor K_r (Poulos & Davis, 1980), on the dynamic components of the stiffness and the damping. The rationale for the selection of the dimensionless parameters was to examine small diameter ($d = 1 \div 3m$) – for offshore applications - hollow, flexible, steel piles embedded in a homogeneous soil layer with constant profile of shear wave velocities ($V_s = 100 \div 400m/s$), pile's thickness ($t = r_0/50$), hysteretic material damping ($\xi = 2.5\%$) and Poisson's ratio ($\nu = 0.35$) at quite wide frequency range including at least the third eigenfrequency of the soil layer ($\alpha_0 = 5/2\pi$). The reference case analyzed is $d = 1m$, $V_s = 250m/s$, $H_p = 20m$ and $H_s = 30m$. Note that all the investigated cases resemble flexible pile response according to the flexibility criterion suggested by Poulos and Davis (1980).

Comparison with end bearing piles

The comparison between horizontally vibrating end bearing piles and floating piles is presented. The reference case is analyzed by varying the boundary conditions at the pile tip, fixed and hinged for end bearing pile and, hinged and free for floating piles. In Figure 2a the dynamic component (real part of the complex valued stiffness terms divided by the corresponding static component K_{xx}^0) of the three stiffness terms is presented with respect to the non-dimensional frequency. It is recorded a drop of stiffness at the first eigenfrequency of the soil layer ($\alpha_0 = \pi/2$), which is more marked in the case of end bearing piles, while the drop of stiffness is observed at all three eigenfrequencies for the free tip floating pile. Sensitivity of the dynamic stiffness on the boundary conditions at the pile tip is observed only in the case of floating piles. In Figure 2b the dynamic component (imaginary part of the complex valued stiffness terms divided by the corresponding dynamic component K_{xx}) of the three stiffness terms is shown with respect to the non-dimensional frequency.

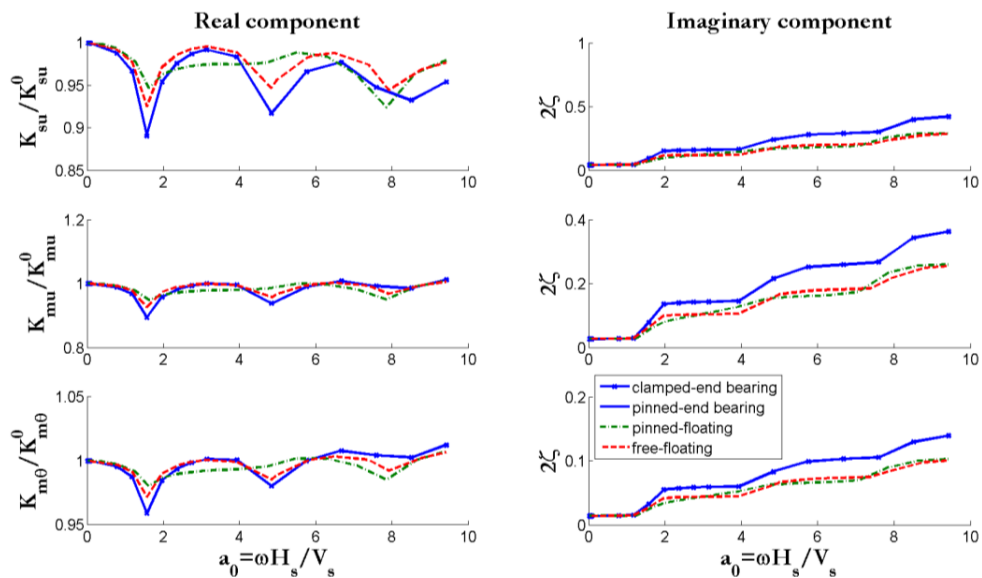


Figure 2. Variation of the three dynamic stiffness coefficients with respect to the dimensionless frequency. The real component (a) and the imaginary component (b) for the reference case and two soil profiles with various boundary conditions.

The radiation damping (viscous type) is generated for frequencies higher than the first eigenfrequency of the soil layer. After that, its trend increases almost monotonously over the frequency range for the case of the end bearing piles, while the pattern is less steep for floating piles. A slight change in the slope of the damping is also marked after each eigenfrequency of the soil layer. In Figure 3 the modal displacement of the pile and the soil layer at the eigenfrequencies of the soil layer (1st, 2nd and 3rd) are illustrated along the depth for both the floating (Figure 3a) and the end bearing pile (Figure 3b). It seems like that the floating pile allows for the development of the 3rd eigenfrequency. At the higher modes the modal response of the floating pile appears closer to the one of the soil layer alone.

Effect of the pile diameter

In Figure 4 the effect of the pile diameter is illustrated on the dynamic impedances by

considering all the other parameters identical to the reference case.

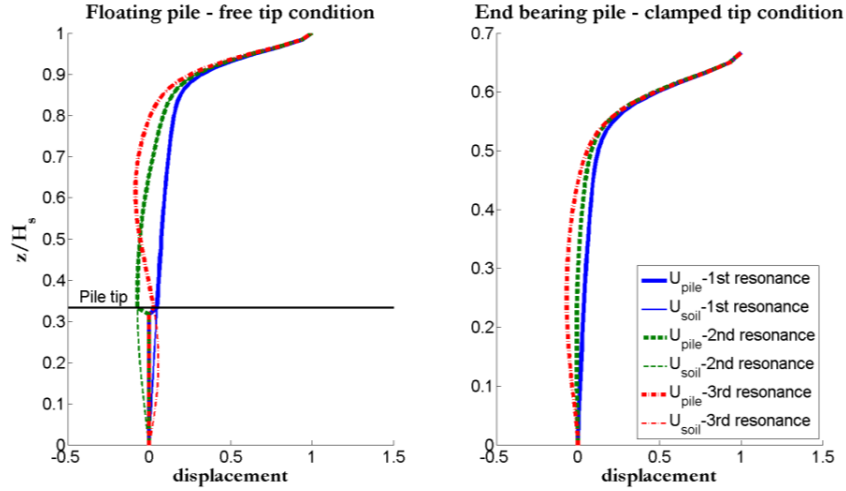


Figure 3. Distribution of the soil and pile displacement along the normalized depth z/H_s at the three first eigenfrequencies of the soil layer. The floating pile (a) and the end bearing pile (b) for the reference case are shown.

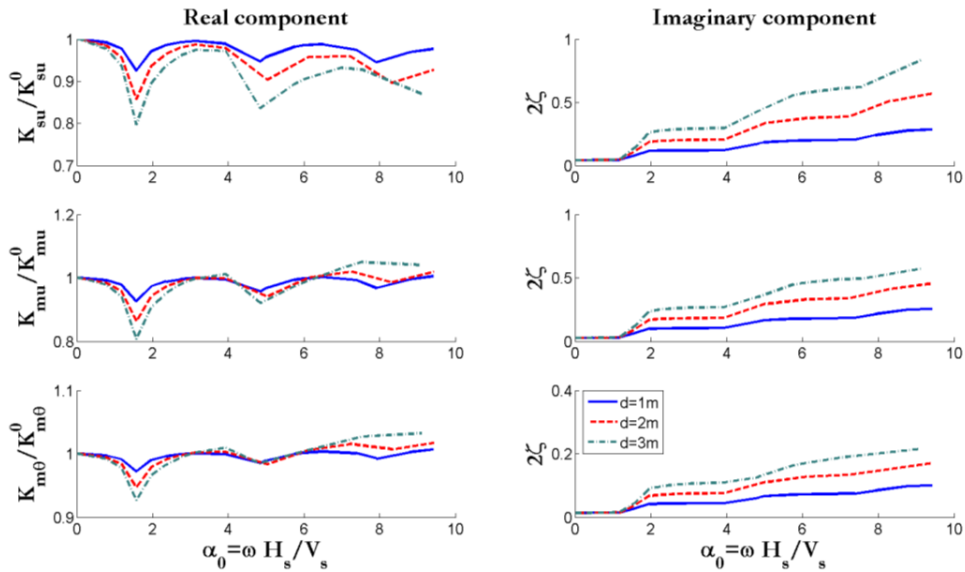


Figure 4. Variation of the three dynamic stiffness coefficients with respect to the dimensionless frequency. Effect of the diameter on the real component (a) and the imaginary component (b).

By keeping unchanged the height of the soil layer and the pile length the dimensionless parameters H_p/d and K_r varied. By decreasing the pile diameter the drop of stiffness at the resonance with the soil layer becomes less remarkable and a smoother pattern of the dynamic stiffness is obtained. The effect of the diameter is more prominent for the translational component of the dynamic stiffness, where the increase of the diameter enhances the dynamic stiffness reduction. The imaginary part of the dynamic component is shown in Figure 4b. The radiation damping exhibits almost constant variation in the intermediate frequency interval ($\alpha_0 = 2 - 4$) and therefore, it can be roughly approximated by linear function in the high frequency range. Moreover, it is observed that the radiation damping rises by increasing the pile

diameter. This suggests that an increase of the pile flexibility factor K_r and a decrease of the slenderness ratio H_p/d determine greater values of the imaginary and smaller value of the real component of the dynamic impedances.

Effect of the soil stiffness

In Figure 5a the real part of dynamic impedances is shown for different values of the shear wave velocity of the soil layer. By keeping the same values as in the reference case for the height of the pile and the soil layer the dimensionless parameters K_r and E_p/E_s varied.

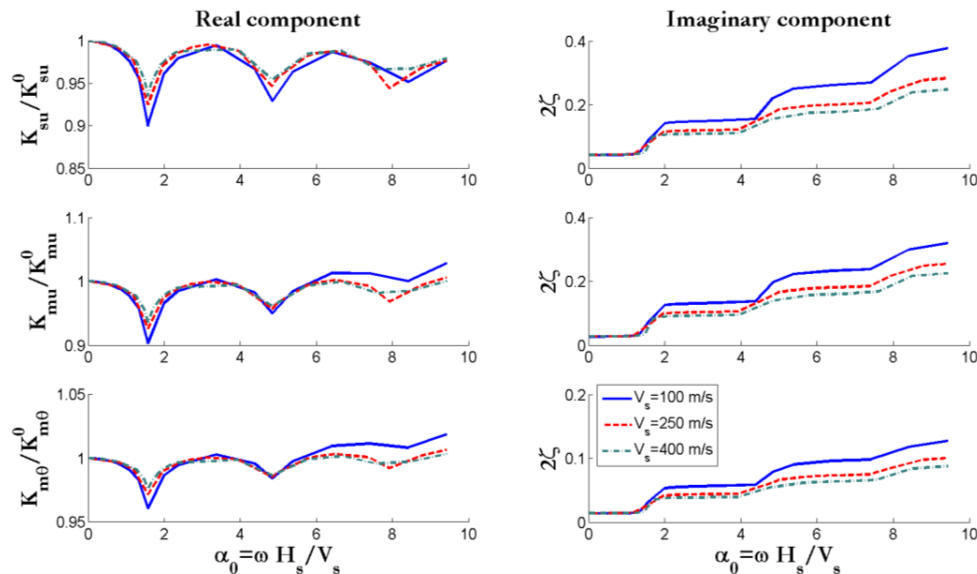


Figure 5. Variation of the three dynamic stiffness coefficients with respect to the dimensionless frequency. Effect of V_s on the real component (a) and the imaginary component (b).

Slightly scattered results are obtained by decreasing the shear wave velocity of the soil layer. This implies that the effect of the dimensionless parameters K_r and E_p/E_s is less prominent. In addition, the drop of stiffness recorded at the first eigenfrequency of the soil layer is slightly more marked for soft soil profiles ($V_s=100$ m/s). Moreover, it is noticed that the cross coupling and rocking stiffness coefficients exhibit higher values than the corresponding static component at higher frequencies. In Figure 5b the imaginary component is illustrated for different values of the shear wave velocity of the soil layer. A flat trend is observed at the intermediate frequencies ($\alpha_0 = 2 - 4$), while it increases monotonously in the high frequency range. By increasing E_p/E_s , the damping increases, an observation consistent to flexible end bearing pile's response.

Conclusions

The analytical solution for horizontally vibrating end bearing piles by Novak & Nogami (1977) has been modified for floating piles. The comparison between horizontally vibrating end bearing piles and floating piles has indicated that the drop of stiffness is stronger in the case of end bearing piles, while the radiation damping is suppressed for floating piles. The results of small diameter flexible floating piles have shown that the dynamic impedances are significantly affected by the variation of the pile diameter, whereas they are only slightly sensitive on the shear wave velocity.

Acknowledgments

This work has been supported by the Danish Council for Strategic Research through the project “Advancing Beyond Shallow waterS (ABYSS) - Optimal design of offshore wind turbine support structures”.

References

- Blaney GW, Kausel E, Roesset J. *Dynamic stiffness of piles, Proceedings of 2nd International Conference on Numerical Methods in Geomechanics, Blacksburg, USA, 2, 1001–1012, 1976.*
- De Vries WE. *Assessment of bottom-mounted support structure type with conventional design stiffness and installation techniques for typical deep water sites. Derivable report 2007.*
- Devriendt C, Jordaens PJ, De Sitter G, Guillaume P. *Estimating damping of an offshore wind turbine using n overspeed stop and ambient excitation. 15th International Conference on Experimental Mechanics 2012; 2897.*
- Gazetas G, Dobry R. *Horizontal response of piles in layered soils. Journal of Geotechnical Engineering 1984; 110(1): 20-40.*
- Gazetas G. *Seismic response of end-bearing single piles. Soil Dynamics and Earthquake Engineering 1984; 3(2): 82–93.*
- Hetényi M. *Beams on Elastic Foundation - Theory with Applications in the Fields of Civil and Mechanical Engineering. University of Michigan Press 1971.*
- Kramer SL. *Geotechnical Earthquake engineering, Prentice Hall, New Jersey, U.S.A, 1996.*
- Mylonakis G. *Elastodynamic model for large diameter end-bearing shafts. Soils and foundations 2001; 41(3): 31-44.*
- Nogami T, Novak M. *Resistance of soil to a horizontally vibrating pile. Earthquake Engineering and Structural Dynamics 1977; 5(3): 249-261.*
- Novak M, Aboul- Ella F. *Impedance functions of piles in layered media. Journal of Engineering Mechanics Division 1978; 104(6): 643-661.*
- Novak M, Nogami T. *Soil-pile interaction in horizontal vibration. Earthquake engineering and structural dynamics 1977; 5: 263-281.*
- Novak M. *Dynamic stiffness and damping of piles. Canadian Geotechnical Journal 1974; 11: 574-598.*
- Nozoe H, Gyōten Y, Fukusumi T. *Dynamic analysis of a soil-pile system by the finite Fourier-Henkel transformation method – Case of a floating pile in horizontal vibration. Theoretical and applied mechanics 1985, 33: 377-392.*
- Poulos HG, Davis EH. *Pile foundation analysis and design. New York, NY: John Wiley & Sons; 1980.*
- Roesset JM, Angelides D. *Dynamic stiffness of piles. Proceedings of the International Conference on Numerical Methods in Offshore Piling, Institution of Civil Engineers (ICE), London, 1980.*
- Velez A, Gazetas G, Krishnan R. *Lateral Dynamic Response of Constrained Head Piles. Journal of Geotechnical Engineering 1983; 109(8): 1063–1081.*
- Zheng C, Liu H, Ding X, Fu Q. *Horizontal Vibration of a Large-Diameter Pipe Pile in Viscoelastic Soil, Mathematical Problems in Engineering 2013.*

Paper III

Dynamic lateral response of suction caissons

C. LATINI AND V. ZANIA

Published in: Soil Dynamics and Earthquake Engineering



Contents lists available at ScienceDirect

Soil Dynamics and Earthquake Engineering

journal homepage: www.elsevier.com/locate/soildyn

Dynamic lateral response of suction caissons



C. Latini, V. Zania*

Civil Engineering Department, Technical University of Denmark, Denmark

ARTICLE INFO

Keywords:

Soil–structure–interaction
Dynamic stiffness
Damping
Floating foundations
Suction caissons
Numerical modelling
Site effects

ABSTRACT

Deeper water installations of offshore wind turbines may be supported by jacket structures. This study investigates the dynamic response of suction caissons for jackets by analysing 3D finite element models in the frequency domain. The numerical modelling was firstly validated by analytical solutions for pile foundations. Groups of crucial dimensionless parameters related to the soil profile and the foundation geometry are identified and their effects on the response of suction caissons are studied. Static stiffness coefficients are presented in a form of mathematical formulas obtained by fitting the numerical results, pertaining foundations with different slenderness ratios and embedded in different soil profiles.

Sensitivity of the dynamic impedances of suction caissons on the skirt length was showed in this study. Moreover, the results for the suction caissons indicated that the overall dynamic response is profoundly affected by the relative thickness of the soil layer and by the variation of soil stiffness with depth.

1. Introduction

The offshore wind market is developing towards wind farms with higher capacity generators and in deeper waters, which places new demands on current offshore design procedures. So far the selection of the type of support structures for offshore wind turbines are determined by the water depth. In shallow waters, monopiles and monopod suction buckets are mostly utilized, while jacket structures with piles or with suction caissons would be the design configuration for deeper waters following the designs traditionally used by the oil and gas industry [1]. In the work of Houlsby et al. [2] the applicability of suction caissons as offshore wind turbine foundations is suggested for suitable soil conditions and particularly for deeper waters, with a water depth of up to about 40 m. Suction caissons are skirted shallow foundations (with a slenderness ratio H_p/d lower than 4, where H_p and d are the foundation height and diameter, respectively) that are first installed using self-weight and then by pumping out the water trapped within the skirts [3]. In contrast to driven piles, heavy duty equipment is not required for suction caisson installation. Moreover the noise disturbance of the marine life is diminished, making this type of foundation an attractive alternative for deep water installations.

In the design of offshore wind support structures one of the critical issues is the fatigue that occurs due to the combination of wind, wave and earthquake loading. In addition, the potential of structural resonance with the dynamic forces of wind loading would result in large amplitude stresses and accelerated fatigue. Therefore, it is fundamental to accurately assess the resonance frequencies of the wind

turbine structure in order to ensure that the first resonance frequency of the wind turbines does not coincide with the excitation frequencies of the rotor system [4]. Furthermore, the overall damping of the structure reduces greatly fatigue damage, since the amplitude of vibrations at resonance is inversely proportional to the damping ratios [5]. Wolf [6] showed that both the eigenfrequency and the damping of any structure subjected to dynamic load are modified due to the soil–foundation interaction. Hence the dynamic stiffness and damping of the soil–foundation system should be included in the estimation of the natural vibration characteristics of any offshore wind turbine as indicated by several studies [7–9].

In the literature the problem of the dynamic soil–pile interaction has been extensively investigated. Indeed, there are several analytical and numerical studies on the estimation of the dynamic impedances of the horizontal vibration of single piles. Considering only those for a linear elastic soil layer they can be classified as follows:

- analytical continuum solutions for end bearing piles [10–12], where the soil was modelled as a homogeneous layer with hysteretic material damping;
- Winkler type analytical solutions [13–15], where the supporting soil was substituted by a bed of independent elastic springs overlying a rigid bedrock. For dynamic problems Novak [13] recommended the use of Winkler foundation coefficients based on Baranov's equation for the in-plane and out-plane vibration of a disk. An improved model incorporating in the analysis the normal and shear stresses acting on the upper and lower faces of a horizontal soil element by

* Corresponding author.

E-mail addresses: chila@byg.dtu.dk (C. Latini), vaza@byg.dtu.dk (V. Zania).

Nomenclature**Latin upper case**

E_s	soil modulus of elasticity
E_p	Young modulus of foundation
G	soil shear modulus
H_s	thickness of soil layer
H_p	height of foundation
I	moment of inertia of pile
L_{inf}	length of the infinite soil domain
L_{fin}	length of the finite soil domain
K_r	foundation flexibility factor
K_{su}	dynamic stiffness coefficient - force for unit displacement
K_{mu}	dynamic stiffness coefficient - moment for unit displacement
$K_{s\theta}$	dynamic stiffness coefficient - force per unit rotation
$K_{m\theta}$	dynamic stiffness coefficient - moment for unit rotation
K_{su}^0	static stiffness coefficient - force for unit displacement
K_{mu}^0	static stiffness coefficient - moment for unit displacement
$K_{s\theta}^0$	static stiffness coefficient - force for unit rotation
$K_{m\theta}^0$	static stiffness coefficient - moment for unit rotation
M	reaction moment at the foundation head
S	horizontal reaction force at the foundation head
V_s	soil shear wave velocity

V_0	surface soil shear wave velocity
V_H	reference base soil shear wave velocity

Latin lower case

d	diameter of foundation
n	dimensionless inhomogeneity factor
r_0	radius of foundation
t	thickness of foundation
t_{cap}	thickness of caisson cap
t_{skirt}	thickness of caisson skirt
u	translational degree of freedom at the foundation head

Greek

α_0	dimensionless eigenfrequency of soil layer
ζ_{su}	damping coefficient - force for unit displacement
ζ_{mu}	damping coefficient - moment for unit displacement
$\zeta_{s\theta}$	damping coefficient - force for unit rotation
$\zeta_{m\theta}$	damping coefficient - moment for unit rotation
θ	rotational degree of freedom at the foundation head
ν	soil's Poisson's ratio
ξ	hysteretic soil damping ratio
ρ	density of soil
η	wave velocity ratio

integrating the governing equations over the thickness of the soil layer was developed by Mylonakis [15];

- c) numerical continuum finite element solutions [16–20], where the pile was modelled as series of regular beam segments with a rigid cross section and the soil was considered as an elastic continuum.

Very few studies investigating the dynamic response of floating piles either numerically [20] or analytically [21–23] are available in the literature. It was shown that the stiffness and the thickness of the soil layer play a fundamental role in the estimation of the dynamic impedances of floating piles. In addition, there is a significant number of studies analysing the dynamic lateral response of single piles or pile groups embedded in a homogeneous half space, where numerical methods (e.g. finite element [24–26], and/or boundary element methods [27,28]) or analytical elastodynamic solutions [29–31] were employed.

In the case of suction caissons the vast majority of research studies has been focused on the analysis of the load capacity under the action of combined vertical, horizontal and moment loading [32–34]. Moreover, the seismic response of suction caisson foundations was also investigated [35]. However, the dynamic response of suction caissons has received less attention [36,37]. In the work of Liingaard [36] the dynamic stiffness coefficients were determined, considering linear viscoelastic soil and modelling the suction caisson using a coupled BE/FE model in homogeneous halfspace comparing the obtained results with analytical solutions for surface foundations. In that study it was shown that the dynamic impedances pattern suggested by the analytical solution for surface foundations did not resemble the one obtained from the numerical model for $H_p/d > 0.25$, while it was in good agreement with the outcomes of the BE/FE model for the case of surface footing. Moreover, Liingaard [36] highlighted the high dependency of the horizontal and rocking component of the stiffness on Poisson's ratio and examined the influence of the skirt flexibility on the dynamic response of caisson foundations embedded in a homogeneous soil layer. It was observed that the increase of the dynamic impedances of suction caisson in the frequency domain is more pronounced when the slenderness ratio increases ($H_p/d = 0.25-1$).

The current study aims at investigating the dynamic response characteristics of suction caissons, to formulate a basis for understanding

the natural vibrations characteristics of foundations for jacket structures. The literature study has shown that some aspects of the dynamic behaviour of this type of foundations has not been investigated so far (e.g. site effects). Therefore, a numerical study was performed and the dynamic impedances of suction caissons subjected to lateral loading were estimated. The vertical load response is not addressed in the present study due to space limitations, even though experimental studies [38] have shown that multi-caisson supported wind turbine structures are mainly influenced by this component. Due to the absence in the literature of analytical solutions on the dynamic response of suction caissons embedded in a soil layer on a rigid bedrock, the numerical modelling approach was validated with the analytical solution of dynamic vibration of soil-end bearing pile [10] and soil-floating pile [22]. The effect of the major parameters affecting the dynamic response of suction caissons embedded in a soil stratum on a rigid bedrock was investigated. The validated numerical methodology was adopted to perform the parametric study, while the rationale behind the selection of the parameters was to highlight the role of the nondimensional parameters of the problem such as the slenderness ratio H_p/d , the relative stiffness E_p/E_s and the relative thickness of the soil layer H_s/d . Furthermore, the dynamic response of suction caissons was analysed for different soil profiles, considering a stiffness distribution with depth.

2. Methodology

A series of 3D finite element models in the commercial software ABAQUS [39] were deployed to analyse the dynamic impedances of suction caissons. The numerical models accounted for the following hypotheses: 1) linear elastic isotropic behaviour of the foundation; 2) linear viscoelastic isotropic behaviour of soil with hysteretic type damping (frequency independent) and 3) perfect contact between the foundation and the soil during the analysis.

Only half of the foundation and the surrounding soil were taken into account in the model, as a result of the symmetry of the problem, see Fig. 1. Two different foundation modelling approaches were used: 1) shell cylinder, where the foundation was discretized by shell elements (S4) and 2) equivalent solid cylinder, for which equivalent material properties were applied to 3D continuum elements (C3D8) in order to

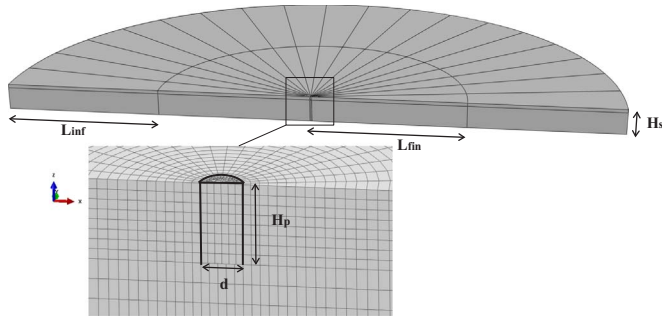


Fig. 1. Finite element model of the foundation and the surrounding soil.

match the bending stiffness of the hollow cylinder and the inner soil. The far field soil response ($L_{inf}=180$ m) was modelled using infinite elements to avoid spurious reflections. The near field soil domain ($L_{fin}=180$ m) was discretized by 8-node 3D continuum elements (C3D8). The soil and the foundation lateral surfaces were bonded together to satisfy displacement compatibility. The steady state linearized response of the model subjected to harmonic excitation in the frequency domain was obtained. The dynamic impedances K_{Su} , $K_{S\theta}$, K_{Mu} and $K_{M\theta}$ at the level of the foundation head were then calculated as shear forces, S , and moments, M , when the head of the foundation was subjected to unit displacement, u , and rotation, θ . The mesh size was set small enough to capture the stress wave accurately even at high frequency range. A mesh size of at least 10–20 elements per wave length for the frequency range of interest was used, including up to the third eigenfrequency of the soil layer $\alpha_0=5/2\pi$. Note that α_0 is a dimensionless frequency related to the eigenfrequency of the soil layer, since it is given as the product of the wave number and the thickness of the soil layer.

$$\alpha_0 = \frac{\omega H_s}{V_s} \quad (1)$$

where ω (rad/sec), H_s (m) and V_s (m/s) are respectively the frequency, the thickness and the shear wave velocity of the soil layer.

In addition, the aspect ratios of elements used in the mesh ranged from 1.6 near the foundation head to about 8 near the boundaries of the finite element mesh. A view of the model with the mesh refinement is shown in Fig. 1.

From the state of the art it is deduced that the dynamic behaviour of suction caissons embedded in a halfspace was already investigated, see [36]. Hence this study focused on the case of a soil layer overlying a rigid bedrock surface. 3D numerical models were first established to validate the numerical methodology against published analytical solutions of the dynamic response of end bearing (Fig. 2A) and floating piles (Fig. 2B). Consequently, the validation of the numerical methodology was performed by considering a small diameter ($d=2r_0=1$ m) hollow, flexible, steel pile of thickness $t=d/50$, height $H_p=10$ m embedded in a homogeneous soil layer with thickness $H_s=10$ m (Fig. 2A), 30 m (Fig. 2B) and constant profile of shear wave velocity ($V_s=250$ m/s), thickness ($t=r_0/50$), hysteretic material damping ($\zeta=5\%$, see [40]) and Poisson's ratio ($\nu=0.35$) over a wide frequency range including at least the third eigenfrequency of the soil layer ($\alpha_0=5/2\pi$).

The fact that the geometry of suction caissons differs from that of piles, due to the hollow section and the presence of the cap, could introduce different mechanisms of wave propagation, e.g. due to the contact of the cap with the soil. This was investigated in a former study by Latini et al. [37], which showed that the solid cylinder and the suction caisson does not exhibit different dynamic behaviour. Moreover the analytical solution for flexible floating piles [22] cannot capture the response of suction caissons, possibly due to the negligence of the vertical displacements and the effect of the smaller slenderness ratio in the generation of surface waves. Additionally, it was observed that the presence of the cap did not alter the dynamic response of the suction caissons. Hereafter, the geometry of the caisson comprising of a hollow cylinder (skirt) and a cap was modelled with shell elements (S4).

3. Validation with analytical solutions

First, the numerical model was validated with the analytical solution for horizontally vibrating end bearing piles proposed by

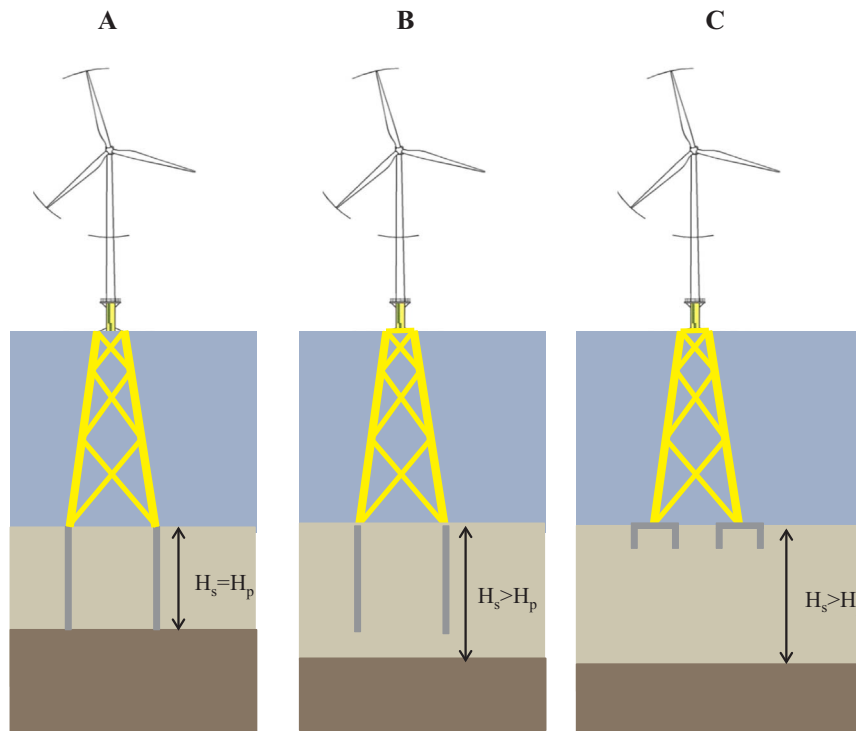


Fig. 2. Illustration of the two soil profiles and the foundation types investigated in this study. The soil profile and the foundation type in Fig. 2A and B are adopted in the validation; while those in Fig. 2C are deployed in the parametric study.

Table 1
Static end bearing and floating pile stiffness obtained from the numerical models and the analytical solutions [10,22].

Reference	$K_{Su}^0/E_s d$	$K_{S\theta}^0/E_s d^2$	$K_{M\theta}^0/E_s d^3$
Fig. 2A			
Novak and Nogami [10]	2.24	-1.02	1.23
Numerical model	1.96	-0.71	1.26
Fig. 2B			
Latini et al. [22]	1.96	-0.93	1.17
Numerical model	1.91	-0.70	1.30

Novak and Nogami [10] for the case of soil profile in Fig. 2A. The static stiffness coefficients of the numerical model were calculated at low frequencies and presented in Table 1, along with the corresponding values obtained by applying the analytical solution. A discrepancy of 12.5%, 30.5% and 2.3% was obtained for the horizontal, coupling and rocking terms, respectively. This difference can be motivated by the fact that the analytical solution does not taken into account the vertical displacements in the estimation of the impedances of the soil-pile system with the coupling component being mainly influenced. In Fig. 3a only the real (K_{Su}) and the imaginary ($2\zeta_{Su}$) part of the translational dynamic impedances are shown. However the conclusions drawn here are valid also for the other two components $K_{S\theta}$, and $K_{M\theta}$. A reduction of stiffness at the 1st and 2nd eigenfrequency of the soil layer ($\alpha_0 = 1/2\pi$ and $3/2\pi$, accordingly) is observed. The numerical model exhibited an extra drop in stiffness attained around the 1st vertical resonance $\alpha_0 = 1/2\pi\eta$, where $\eta = \sqrt{2(1-\nu)/(1-2\nu)}$, which was less marked for the case of the cross coupling and rocking components. This can be explained by the fact that in the analytical formulation vertical displacements are disregarded. The generated damping is associated to

the imaginary part of the dynamic coefficient of the dynamic impedances, due to the soil-pile interaction. Radiation damping was developed after the 1st eigenfrequency of the soil layer for all the components. Step increase of the damping ratio can be roughly approximated by linear function with the frequency, which is then modelled by viscous type damping. A slight increase in the slope of the damping ratio after each eigenfrequency of the soil layer is observed. In addition, the results of the shell pile and the equivalent solid pile model matched perfectly in the frequency interval investigated. The numerical results seemed to be in good agreement with those of the analytical solution, even if a slight discrepancy was recorded for frequencies higher than $\alpha_0 = 4$. In Fig. 3b the deformed shape of the pile is plotted as a function of the depth at the three first eigenfrequencies of the soil layer and the numerical trend resembled the one suggested by the analytical formulation.

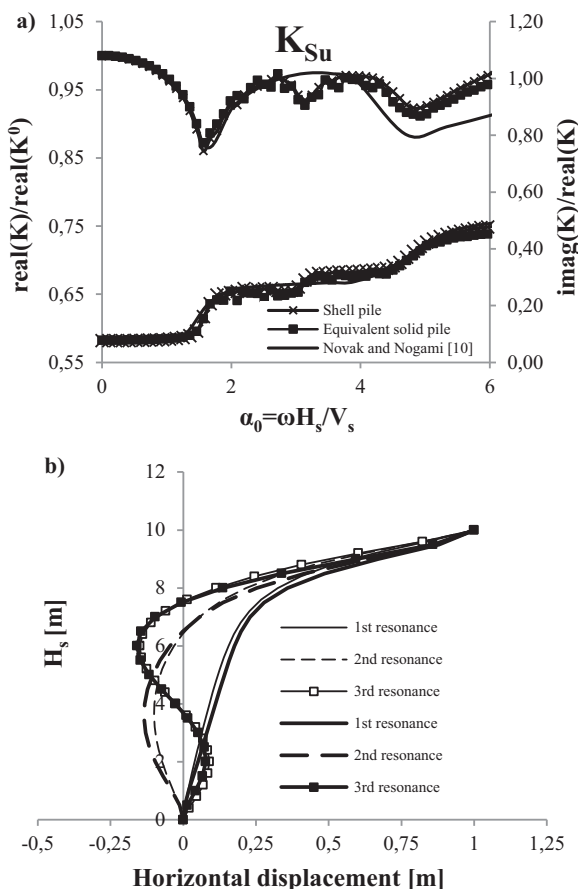


Fig. 3. End bearing pile. Variation of the translational stiffness and damping coefficients with respect to the dimensionless frequency (a) and distribution of the pile displacement along the depth at the three first eigenfrequencies of the soil layer (b) for profile in Fig. 2a.

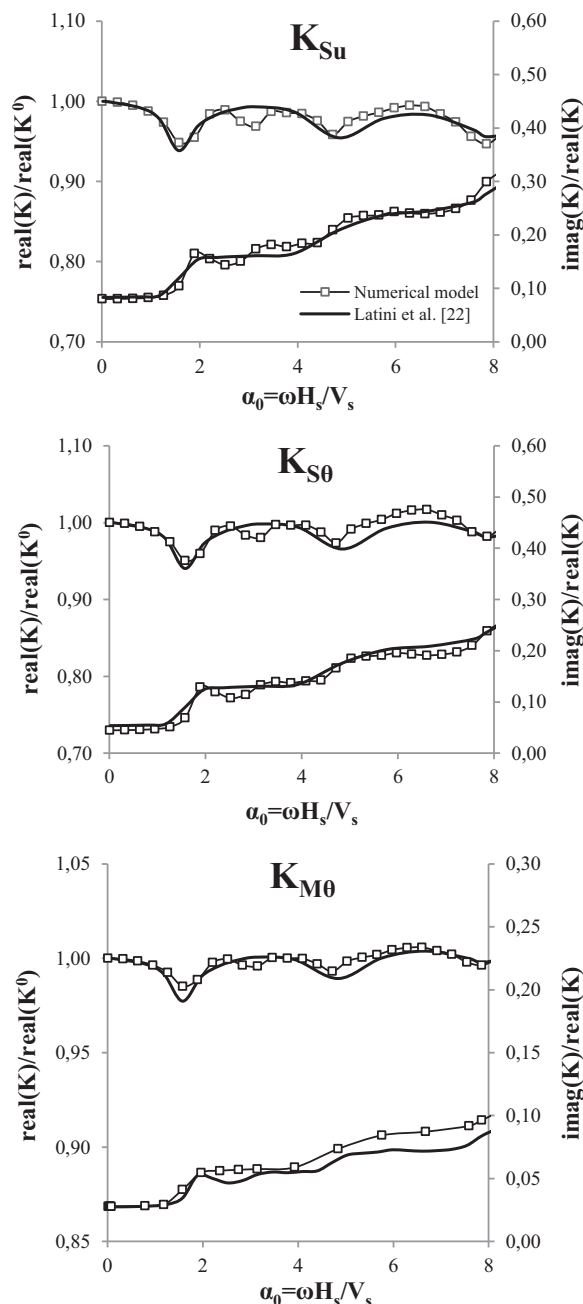


Fig. 4. Variation of the three dynamic stiffness coefficients with respect to the dimensionless frequency. The real component and the imaginary component for profile in Fig. 2b.

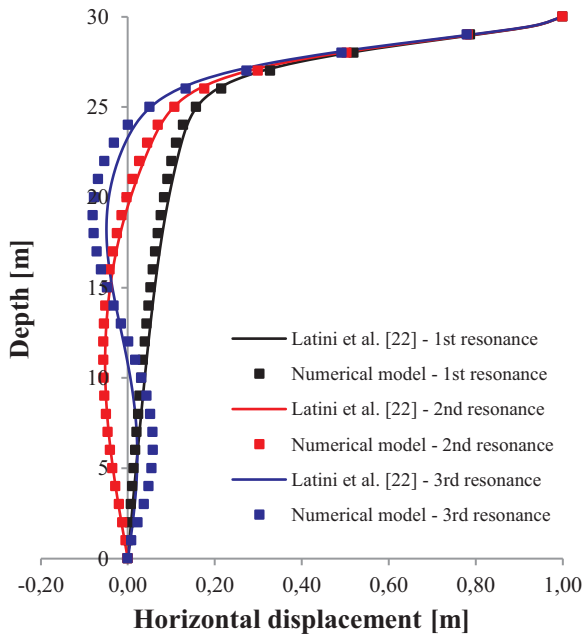


Fig. 5. Distribution of the pile displacement along the depth at the three first eigenfrequencies of the soil layer for profile in Fig. 2b.

For the floating pile, the numerical model was validated by deploying the analytical solution of Latini et al. [22]. The static stiffness coefficients were estimated and compared with those attained respectively by the analytical solution of Latini et al. [22]. The results are given in Table 1. The deviation in percentage between the results of the analytical formulation of Latini et al. [22] and the numerical model were 2.5%, 24.5% and 9.7%. It is evident that the numerical model



Fig. 6. Soil profiles considered for dynamic response of suction caissons.

achieved similar values to those obtained by using the analytical formulation, which slightly overestimated the lateral and coupling coefficients. In Fig. 4 the real (K_{Su} , $K_{S\theta}$, and $K_{M\theta}$) and the imaginary ($2\zeta_{Su}$, $2\zeta_{S\theta}$, and $2\zeta_{M\theta}$) parts of the dynamic impedances are presented. Note that the numerical model was established considering equivalent solid pile in order to be consistent with the assumption of solid pile cross section of the analytical formulation. Slightly scattered results were observed comparing the analytical solution of Latini et al. [22] and the numerical model after the 2nd horizontal eigenfrequency of the soil layer. The damping ratio obtained from the analytical solution was overestimated concerning the cross coupling stiffness term for frequencies smaller than the 1st horizontal eigenfrequency of the soil layer, while an increased variation of the damping coefficient was observed after the 1st horizontal resonance frequency of the soil layer for the rocking component.

In Fig. 5 the deformed shape of the pile is illustrated with respect the depth at the three first eigenfrequencies of the soil layer. The modal shapes obtained from the numerical model match almost perfectly those of the analytical solution, except only from the 3rd eigenfrequency where the analytical solution underestimates the deflection.

In this section the two numerical models were validated against analytical solutions and the comparison of Figs. 3 and 4 demonstrate that floating piles exert a different behaviour than end bearing piles.

Table 2
Dimensionless parameters and cases selected in the parametric analysis.

Case Nr.	H_s [m]	H_p [m]	d [m]	H_p/d	H_s/d	Soil Profile				E_p/E_s	K_r	Behaviour
						Type	n	V_H [m/s]	V_0/V_H			
1 (Ref.)	30	10	1	10	10	A	1	250	1	60	$2.88e-4$	Flexible
2	30	10	5	2	6	A	1	250	1	60	$1.80e-1$	Rigid
3	30	7.5	5	1.5	6	A	1	250	1	60	$5.68e-1$	Rigid
4	30	5	5	1	6	A	1	250	1	60	2.88	Rigid
5	30	2.5	5	0.5	6	A	1	250	1	60	46.08	Rigid
6	30	1.25	5	0.25	6	A	1	250	1	60	737.3	Rigid
7	30	1	4	0.25	7.5	A	1	250	1	60	737.3	Rigid
8	15	0.5	2	0.25	7.5	A	1	250	1	60	737.3	Rigid
9	30	8	4	2	7.5	A	1	250	1	60	$1.80e-1$	Rigid
10	15	4	2	2	7.5	A	1	250	1	60	$1.80e-1$	Rigid
11	30	0.5	2	0.25	15	A	1	250	1	60	737.3	Rigid
12	30	4	2	2	15	A	1	250	1	60	$1.80e-1$	Rigid
13	30	10	5	2	6	A	1	300	1	41	$1.28e-1$	Rigid
14	30	10	5	2	6	A	1	400	1	23	$7.20e-2$	Rigid
15	30	10	5	2	6	A	1	500	1	15	$4.71e-2$	Rigid
16	30	1.25	5	0.25	6	A	1	300	1	41	515.6	Rigid
17	30	1.25	5	0.25	6	A	1	400	1	23	295.1	Rigid
18	30	1.25	5	0.25	6	A	1	500	1	15	193.0	Rigid
19	30	7.5	5	1.5	6	A	1	500	1	15	$1.49e-1$	Rigid
20	30	5	5	1	6	A	1	500	1	15	$7.54e-1$	Rigid
21	30	2.5	5	0.5	6	A	1	500	1	15	12.1	Rigid
22	30	10	5	2	6	B	0.25	500	0.01	15	$4.71e-2$	Rigid
23	30	5	5	1	6	B	0.25	500	0.01	15	$7.54e-1$	Rigid
24	30	1.25	5	0.25	6	B	0.25	500	0.01	15	193.0	Rigid
25	30	10	5	2	6	C	0.5	500	0.1	15	$4.71e-2$	Rigid
26	30	5	5	1	6	C	0.5	500	0.1	15	$7.54e-1$	Rigid
27	30	1.25	5	0.25	6	C	0.5	500	0.1	15	193.0	Rigid

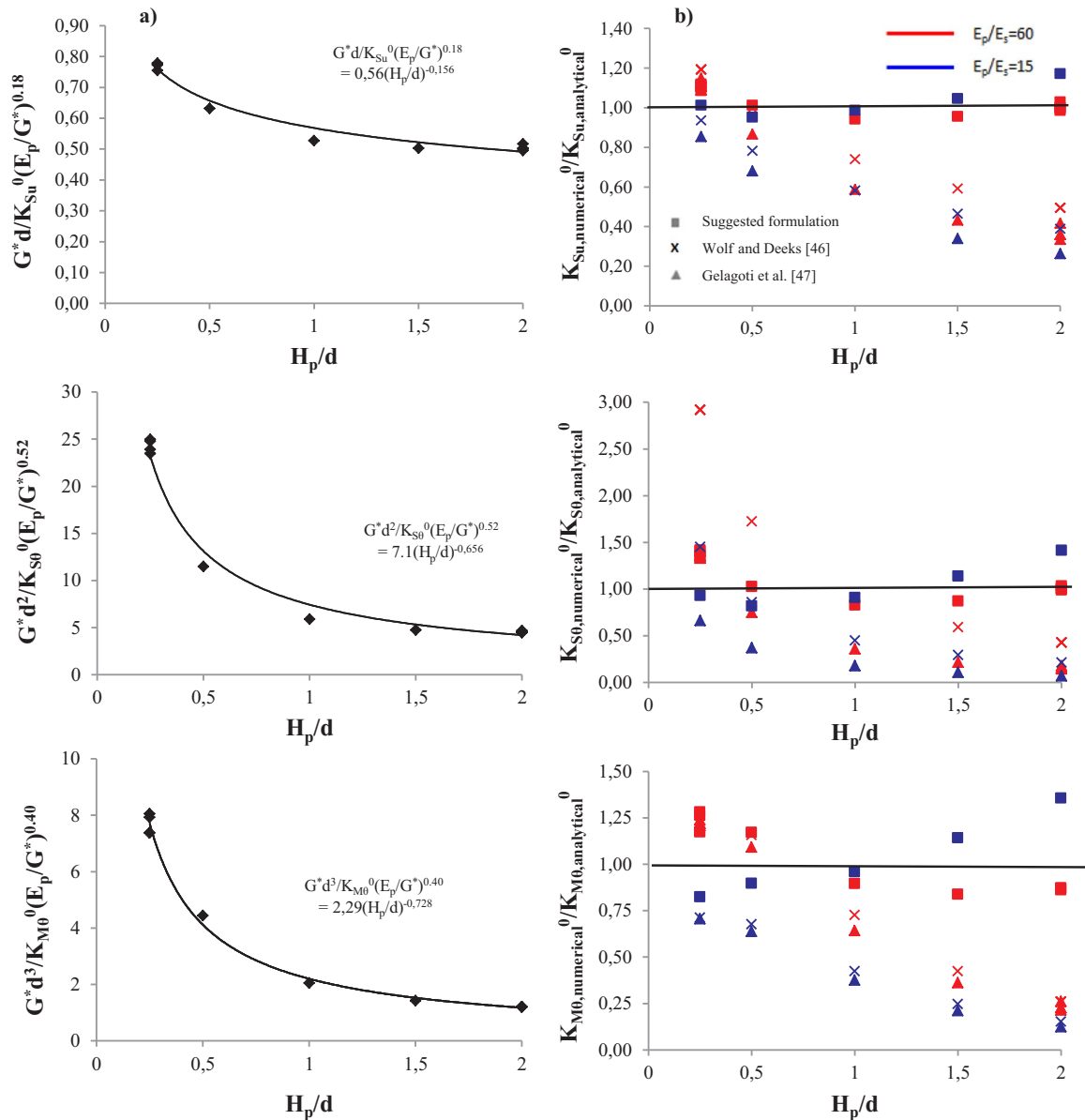


Fig. 7. Static stiffness components of suction caissons. Mathematical expressions for the static stiffness components (a). Comparison of the static stiffness components given by the numerical model and three analytical expressions (b).

4. Parametric study

The role of key dimensionless parameters such as the stiffness ratio E_p/E_s , the slenderness ratio H_p/d and the pile flexibility factor K_r on the response of end bearing piles has been illustrated previously ([41] and [42]). Moreover, studies on the dynamic response of floating piles ([21,22]) highlighted the influence of the thickness of the soil layer on the dynamic impedances of this type of foundations. The dependency of dynamic stiffness coefficients on the dimensionless parameter H_s/d , defined as the relative thickness of the soil layer, was pointed out only for the case of surface footings in the work of Gazetas [43]. Since these studies have been investigating piles with slenderness ratio more than 10 or surface footings, the relevance of these findings to suction caissons and the effects of the abovementioned dimensionless parameters to the dynamic soil suction caisson interaction is hereafter investigated. The cases selected in the current analysis and the dimensionless parameters are listed in Table 2, while the rationale behind their selection was to investigate foundations with different skirt length and diameter to study the dynamic response of suction caissons for different slenderness ratios (H_p/d) and site conditions (E_p/E_s , H_s/d).

E_s , H_s/d).

Three soil profiles were considered, each with a different distribution of $E_s(z)$ with depth as reported in Fig. 6. In the numerical analysis the shear wave velocity of the soil layer was assumed to increase with depth according to the following expression [44]:

$$V_s(z) = V_H \left[b + (1-b) \frac{z}{H_s} \right]^n \quad (2)$$

where b is given as a function of the shear wave velocity at the surface (V_0) and base (V_H) of the inhomogeneous soil layer ($b = (V_0/V_H)^{1/n}$), n is a dimensionless inhomogeneity factor ($n=0 \div 1$) and z represents the depth measured from the ground surface. Profile A has constant shear wave velocity ($V_s=250, 300, 400, 500$ m/s – cases 5–18), which is typical for overconsolidated clay deposits. The parameter n was set equal to 0.25 for profile B, representing uniform medium-dense sand deposits, see cases 19–21. In profile C, $E_s(z)$ is proportional to depth and $n=0.5$ was taken into account in order to investigate normally consolidated clay strata (cases 22–24).

Shear wave velocity ratio V_0/V_H (at the surface and the base of the

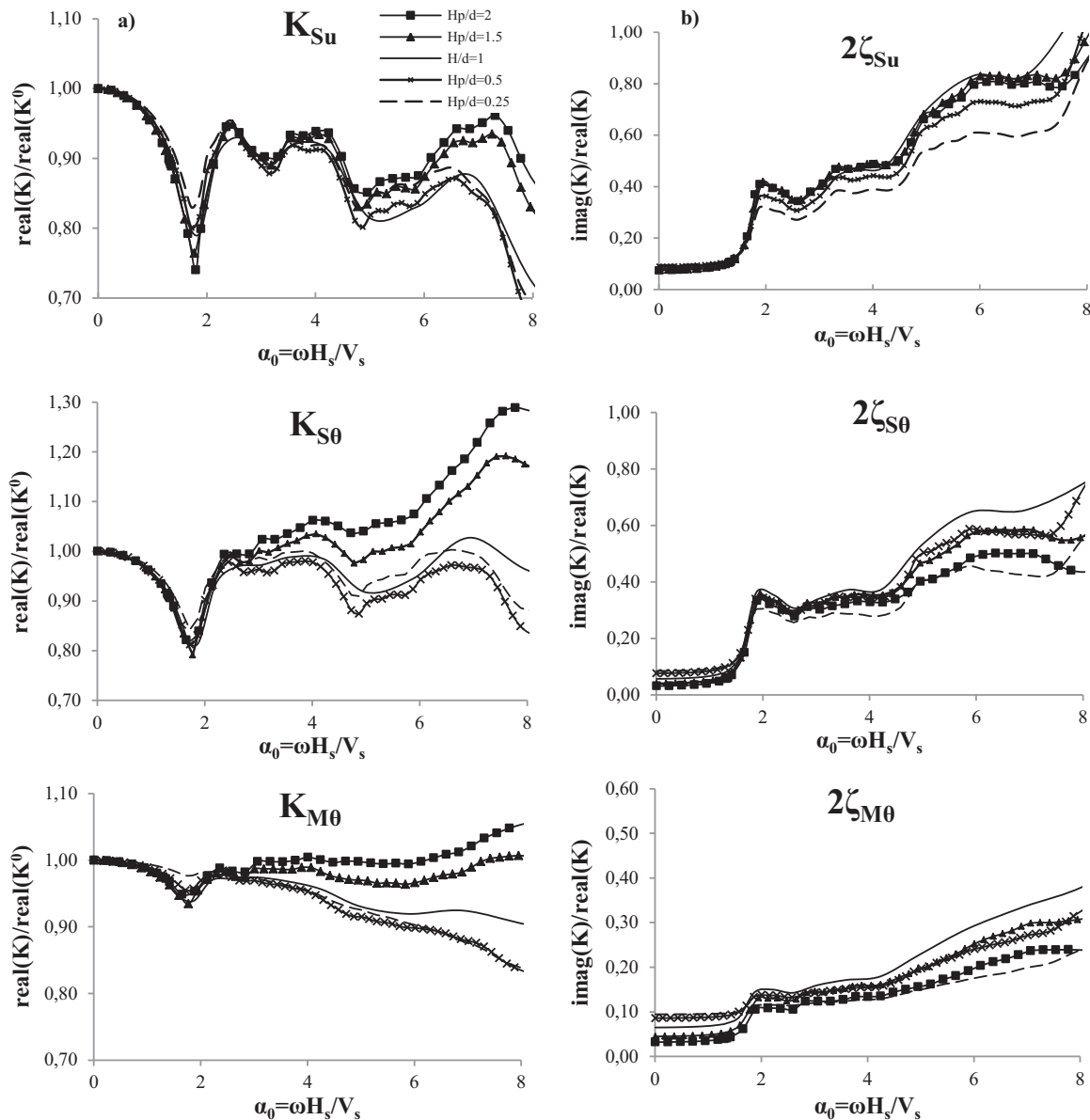


Fig. 8. Variation of the three dynamic stiffness and damping coefficients with respect to the non-dimensional frequency. Effect of the slenderness ratio on the real component (a) and the imaginary component (b).

inhomogeneous layer) was considered equal to 0.01 and 0.1 respectively for the soil models B and C to account for strong gradient in shear wave velocity. And the reference base shear wave velocity was 500 m/s in order to model a continuously inhomogeneous viscoelastic soil medium of thickness H_s over rigid bedrock. The hysteretic material damping ($\zeta = 5\%$) and Poisson's ratio ($\nu = 0.35$) were identical for all the examined cases. These three models may adequately represent the dynamic characteristics of a fairly wide range of real soil profiles.

4.1. Static stiffness

The effect of the slenderness ratio on the static stiffness components of suction caisson foundations was herein analysed. In the literature there are several approximate closed-form solutions expressions for the static stiffness terms of piles [19,41,42]. For large slenderness ratio ($H_p/d \geq 10$), Randolph [42] suggested a set of stiffness expressions depending on the stiffness ratio (E_p/G^*), where $G^* = G(1 + \frac{3}{4}\nu)$, in order to predict accurately the response of flexible foundations. Nevertheless, for smaller slenderness ratio – like in the case of suction caissons – the deformation mode changes and the H_p/d affects the static stiffness.

Carter and Kulhawy [45] accounted for this effect by suggesting expressions based on the slenderness ratio for rigid shafts. Another approach would be to consider the stiffness of surface foundations [46], while Gelagoti et al. [47] modified the previously suggested expressions for embedded foundations [43] by translating the load reference point at the top of the foundation.

In this work the closed-form expressions suggested by Randolph [42] for flexible piles were modified by accounting also the contribution of the slenderness ratio, in order to provide closer approximations of the static stiffness components of suction caissons. The results of the numerical analysis were fitted with the exponential functions shown in Fig. 7a. It was observed that the curve fitting is better for $H_p/d > 0.5$. In addition, the numerical results of the static stiffness components for the suction caisson case were compared respectively with previously published expressions [46–48]. The static stiffness components obtained by the mathematical expressions were divided by the corresponding numerical ones and they are presented with respect to the slenderness ratio in Fig. 7b. It may be observed that the expressions from Wolf and Deeks [46] slightly overestimate all the static components up to $H_p/d = 0.5$ for $E_p/E_s = 60$, while the opposite is observed for

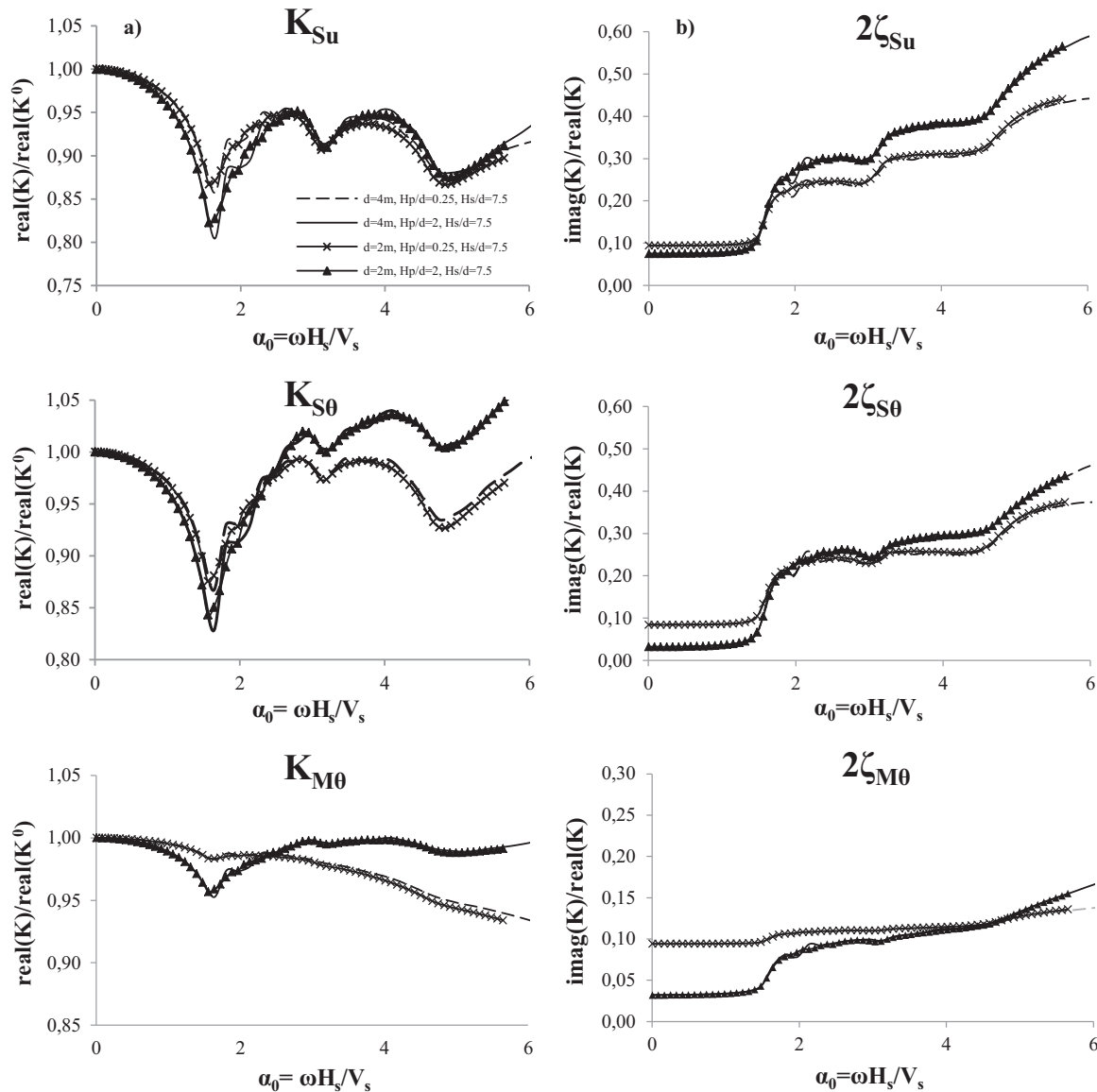


Fig. 9. Variation of the three dynamic stiffness and damping coefficients with respect to the non-dimensional frequency. Effect of the diameter of suction caisson on the real component (a) and the imaginary component (b).

the expressions of Gelagoti et al. [47] for the horizontal and coupling terms. In addition, the calculated stiffness coefficients using the expressions by Shadlou and Bhattacharya [48] which were developed for higher H_p/d values are very similar to the ones obtained by Gelagoti et al. [47]. The deviation of the previous studies [46–48] becomes more apparent for higher H_p/d values.

Thus, displacements of suction caissons can be expressed by these simple mathematical equations obtained by fitting the numerical data:

$$u = 0.56 \left(\frac{S}{G^*d} \right) \left(\frac{E_p}{G^*} \right)^{-0.18} \left(\frac{H_p}{d} \right)^{-0.156} + 7.10 \left(\frac{M}{G^*d^2} \right) \left(\frac{E_p}{G^*} \right)^{-0.52} \left(\frac{H_p}{d} \right)^{-0.656} \quad (3)$$

$$\theta = 7.10 \left(\frac{S}{G^*d^2} \right) \left(\frac{E_p}{G^*} \right)^{-0.52} \left(\frac{H_p}{d} \right)^{-0.656} + 2.29 \left(\frac{M}{G^*d^3} \right) \left(\frac{E_p}{G^*} \right)^{-0.40} \left(\frac{H_p}{d} \right)^{-0.728} \quad (4)$$

The new suggested expressions reduce substantially the scatter and provide a better approximation of static stiffness components of suction caissons.

4.2. Dynamic impedances

4.2.1. Effect of the slenderness ratio

Fig. 8 illustrates the real (K_{Su} , $K_{S\theta}$, and $K_{M\theta}$) and the imaginary ($2\zeta_{Su}$, $2\zeta_{S\theta}$, and $2\zeta_{M\theta}$) parts of the dynamic impedances for several values of the slenderness ratio H_p/d (cases 2–6, in Table 2) by varying the skirt length, while the same soil profile is considered. Note that all investigated cases resemble rigid foundation response according to the flexibility criterion suggested by Poulos and Davis [41]. Overall the pattern of the stiffness variation with frequency is influenced by the slenderness ratio after the 1st vertical eigenfrequency of the soil layer. It was observed that the reduction in stiffness attained at the 1st horizontal eigenfrequency ($\alpha_0 = \pi/2$) of the soil layer became less marked as the slenderness ratio decreased. The decrease of the dynamic stiffness components of suction caissons with decreasing slenderness ratio at higher frequency range, has been previously observed for the case of suction caisson in homogeneous halfspace [36]. Regarding the higher frequency range (larger than $\alpha_0 > 3$) a distinctively different behaviour is observed for $H_p/d > 1$, where the dynamic stiffness appears to increase attaining values even higher than the static ones especially for the coupling and rocking term. This can be explained by the effect of the coupling between the horizontal and the

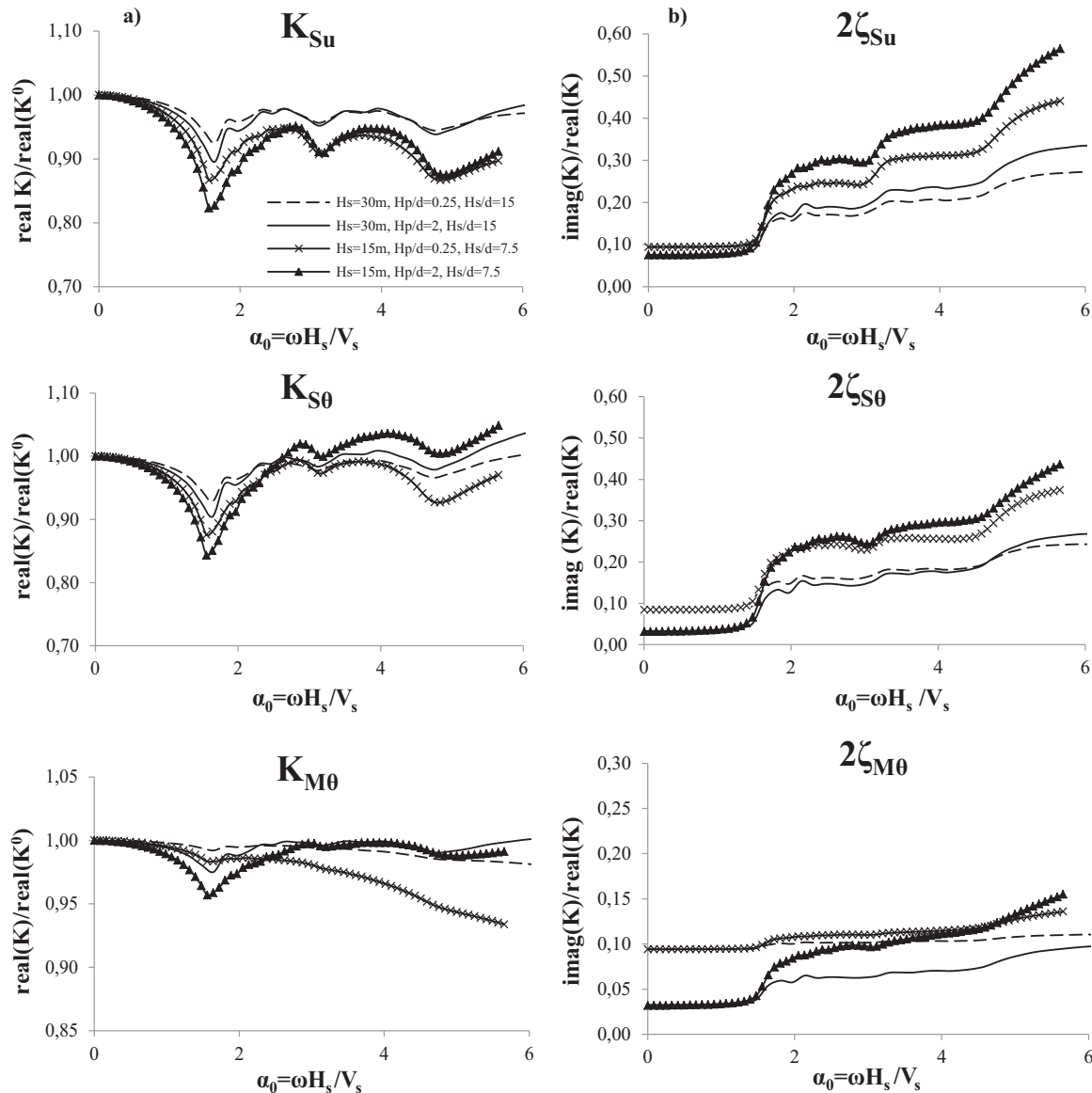


Fig. 10. Variation of the three dynamic stiffness and damping coefficients with respect to the non-dimensional frequency. Effect of the relative thickness of the soil layer on the real component (a) and the imaginary component (b).

rotational degrees of freedom, which appears more evident with increasing slenderness ratio ($H_p/d > 1$), as more rotation and less lateral governs the response. Results of the displacement vectors in the higher frequency range showed a kind of a scoop-slide mechanism, which resembled the failure mechanism of suction caissons embedded in clay as observed in the work of Randolph and House [33]. On the contrary, in the case of suction caissons with $H_p/d < 1$ horizontal vibrations due to the interaction between the foundation skirt and the soil layer are mainly transmitted to the surrounding soil at shallow depths, enhancing the lateral response of the foundation. Indeed, it was noticed that the contribution of the vertical displacement to the displacement resultant is negligible along the whole foundation skirt.

The effect of the skirt length on the damping is not consistent for all the damping components, while $H_p/d=0.25$ gives consistently the lowest damping ratios of all the examined cases. The pattern of the damping variation with respect to the normalised frequency is not affected by the slenderness ratio; it is still observed an increase of the slope after each eigenfrequency of the soil layer. There is indication that the increase of H_p/d would result to higher damping ratio, especially for the horizontal component and frequency range lower than the 2nd eigenfrequency of the soil layer.

4.2.2. Effect of the soil thickness

In order to address the effect of the thickness of the soil layer, first it is prudent to figure out the adequate corresponding dimensionless parameter. This was investigated by keeping all dimensionless parameters constant and changing only the diameter and the soil layer thickness, while referring to the same slenderness ratio and relative thickness of the soil layer (H_s/d) in the dynamic analysis of suction caissons. The results of the real (K_{Su} , K_{S0} , and K_{M0}) and the imaginary ($2\zeta_{Su}$, $2\zeta_{S0}$, and $2\zeta_{M0}$) parts of the dynamic impedances (cases 7–10, in Table 2) are reported in Fig. 9. It appears that the relative thickness of the soil layer H_s/d is an adequate nondimensional parameter in the estimation of the dynamic impedances of suction caissons, since the sensitivity of the dynamic stiffness coefficients on the variation of the diameter was found hardly noticeable for the frequency range investigated. Moreover, this conclusion is valid for both the minimum and maximum slenderness ratio in this study.

The effect of H_s/d ratio on the frequency variation of the dynamic stiffness and damping coefficients is depicted in Fig. 10 (cases 8, 10–12, in Table 2). The trend of the dynamic impedances appears to be influenced by the variation of the dimensionless parameter H_s/d in the frequency range considered. First the drop of stiffness exhibited at the

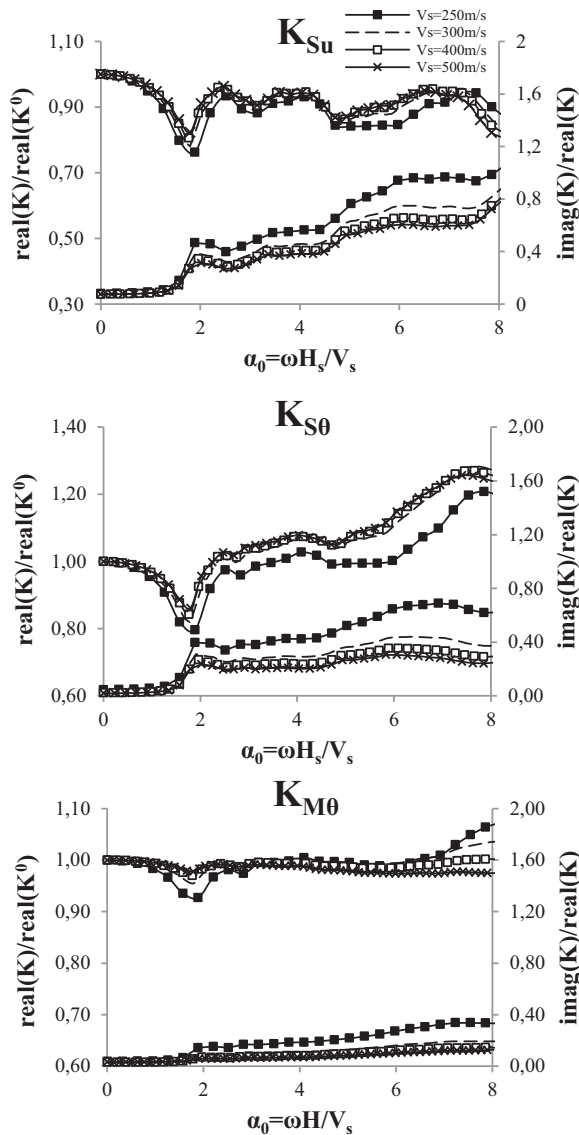


Fig. 11. Variation of the three dynamic stiffness and damping coefficients with respect to the non-dimensional frequency. Effect of the stiffness of homogeneous soil layer (profile A) on the real component and the imaginary component for $H_p/d=2$.

1st resonance, when referring to same slenderness ratio H_p/d , becomes more distinct as the relative thickness of the layer H_s/d decreased. This can be explained by the fact that the longer the path the propagating waves travel, the more the stress waves are attenuated with the distance and therefore the decay of the dynamic impedances is less appreciable. The decrease of the dynamic impedances with the smaller H_s/d has been previously observed for the dynamic response of surface footing [43].

A small influence of the relative thickness of the soil medium on the variation of the rocking component is recorded, while the translational and coupling coefficients seemed to be more affected by the dimensionless parameter H_s/d .

A possible explanation of this trend is that the coupling between the horizontal and the rotational degrees of freedom is enhanced by the nondimensional parameter H_s/d , since the suction caisson foundation experienced higher rotation at the tip for frequencies greater than the 1st vertical resonance when the relative thickness of the soil layer assumed lower values.

In regards to the imaginary components, it appears that the step-linear increasing pattern of the damping ratio at higher frequencies is characterized by higher slope as the relative thickness of the soil layer

decreases. This increase of the variation of the damping ratio observed for smaller values of soil profile thickness is related to the concurrent decrease of the dynamic component of the stiffness coefficients. On the other hand, the viscous damping coefficients in the frequency range studied increase by increasing H_s/d , in agreement with the fact that more energy is dissipated as the propagating waves travel at longer distance.

Concluding, the numerical outcomes show that the relative thickness of the soil layer H_s/d is a fundamental dimensionless parameter for understanding the dynamic response of floating foundations.

4.2.3. Effect of the soil stiffness

Fig. 11 shows the real (K_{Su} , K_{S0} , and K_{M0}) and the imaginary ($2\zeta_{Su}$, $2\zeta_{S0}$, and $2\zeta_{M0}$) part of the dynamic impedances varying the stiffness of the homogeneous soil layer (profile A) respectively for $H_p/d=2$ (cases 2, 13, 14 and 15). The increase of the shear wave velocity of the soil layer affects marginally the dynamic impedances, which are increased fairly constant with frequency particularly when it is higher than the 1st eigenfrequency of the soil medium, and when the factor K_r decreased. The damping ratios are slightly decreased for increased soil stiffness. The effect of the soil stiffness for profile A was also investigated for small slenderness ratio ($H_p/d=0.25$). The results, which are not presented here due to space limitations, indicated that at small skirt lengths the dynamic response of the caisson is insensitive to the soil stiffness at homogeneous soil layers. This can be motivated by the fact that the horizontal vibrations are transmitted to the surrounding soil at relatively larger depth than the tip of the caisson.

The effect of the stiffness variation with depth is presented in Figs. 12 and 13 respectively for profiles B and C. The outcomes are plotted with respect to the frequency normalised by the fundamental resonant frequency of the homogeneous soil layer, f_{1soil} (4.17 Hz). A common trend for all the stiffness components was the observed drop of stiffness at $f = 0.92 f_{1soil}$ (profile B) and $0.76 f_{1soil}$ (profile C), which is slightly shifted back from the 1st eigenfrequency of the homogeneous layer. The first resonance of the inhomogeneous soil profiles are in agreement with that calculated according to analytical solutions [44].

After the 1st resonance the lateral stiffness coefficient is characterized by a decreasing pattern, while the slope increased for lower value of the slenderness ratio H_p/d both for profiles B and C, with profile C attaining larger slope increase. Regarding the coupling and rocking stiffness term, the larger slenderness ratios are related with a fairly constant variation of stiffness with frequency for profile B. On the other hand, the same stiffness terms of the caisson with shorter skirt length showed a monotonous decrease trend after the 1st resonance for profile C.

The imaginary part of the dynamic impedances is associated with the generated damping due to soil-caisson interaction. The damping ratio for both profiles at the lower frequency range is decreasing for increasing slenderness ratio. In addition, it was found that the horizontal impedance obtained by considering profile C exhibited an exponential rather than a linear trend for frequencies higher than the first resonance and particularly for $H_p/d=0.25$. The sensitivity of the dynamic impedances on the variation of E_s in the high frequency range has been previously observed for end bearing piles [19].

Furthermore, looking at Fig. 13 it becomes apparent that the stronger the variation of E_s with respect to depth the higher is the reduction in dynamic stiffness after the 1st resonance. Additionally, this trend is even more emphasized by decreasing the slenderness ratio. Therefore, it can be stated that the type of variation of soil modulus with depth has a significant effect on the dynamic response of suction caissons, especially at high frequencies.

5. Conclusions

In this study numerical analyses were performed to investigate the

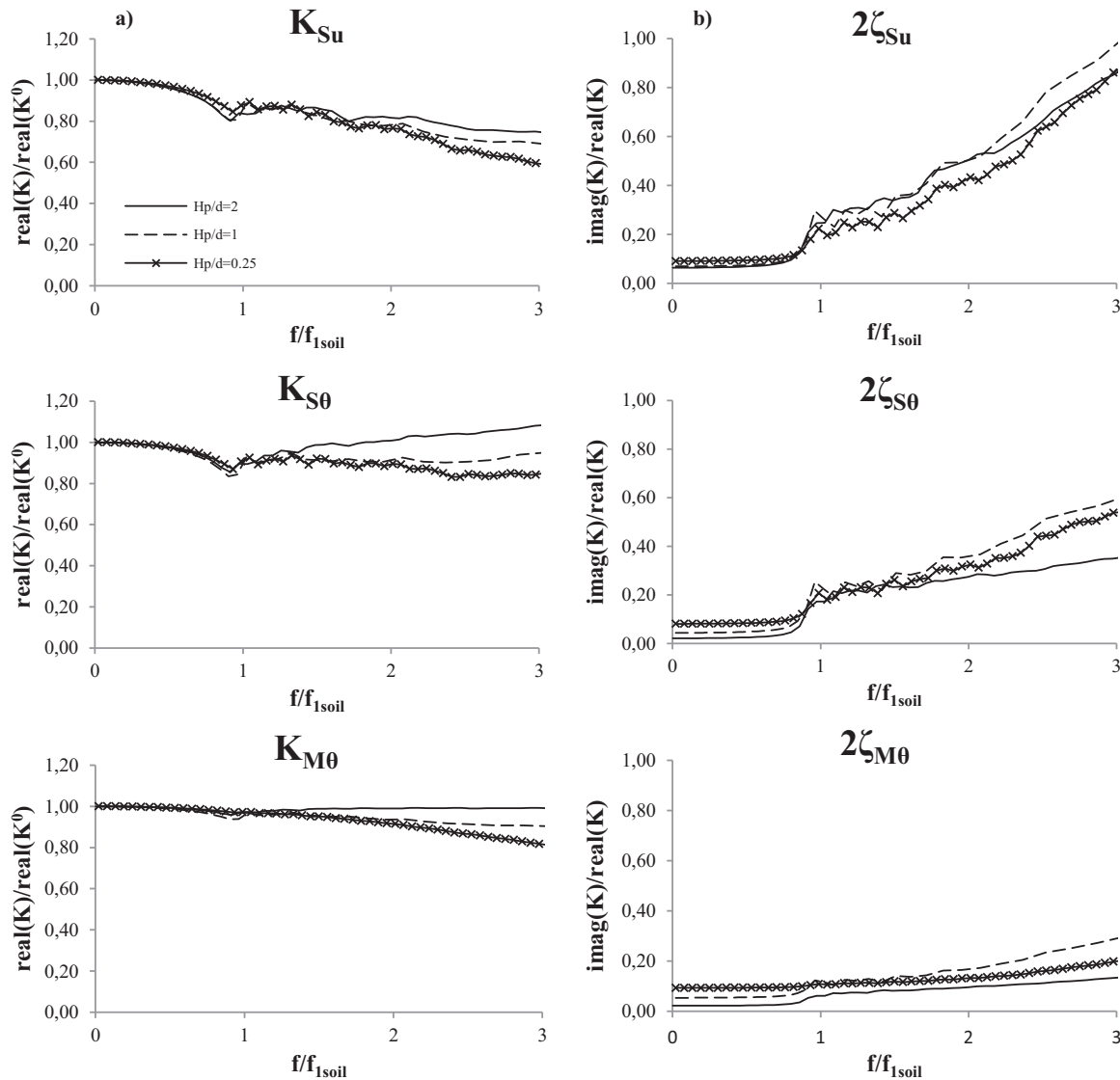


Fig. 12. Variation of the three dynamic stiffness and damping coefficients with respect to the non-dimensional frequency. Effect of slenderness ratio in the inhomogeneous soil layer (profile B) on the real component (a) and the imaginary component (b).

horizontal dynamic response of suction caissons embedded in viscoelastic soil. The numerical modelling procedure was validated against existing analytical solutions for end bearing and floating pile foundations. A parametric study was conducted to analyse the vibration characteristics and the effects of the main parameters on the dynamic impedances of suction caisson foundations. The numerical results provided the basis for the formulation of simple mathematical expressions for the static stiffness components of suction caissons. The proposed expressions accommodate a more accurate estimation of the stiffness components compared to previous analytical expressions.

The main nondimensional parameters investigated were the slenderness ratio, the relative soil layer thickness and the relative stiffness. The skirt length was found quite substantial parameter to determine the behaviour of the suction caissons. It can be stated that the dynamic stiffness coefficients of suction caissons increased by increasing the skirt length for frequencies higher than the 1st vertical resonance. In addition, the reduction in the dynamic stiffness due to the decrease of the soil stiffness with depth was more marked by decreasing the skirt length.

The influence of the stiffness ratio E_p/E_s for homogeneous profiles was proven to affect slightly the dynamic impedances of suction caissons in the frequency range investigated. On the other hand, the

type of variation of soil modulus with depth in inhomogeneous profiles had a significant effect on the dynamic response of suction caissons. The soil profile with linearly increasing stiffness with depth was shown to influence to a greater extent the dynamic stiffness and damping of the suction caisson in the examined frequency range, indicating that steep variations of stiffness with depth may lead to small dynamic stiffness and high damping ratios at high frequencies.

In addition, the study showed that the dynamic impedances of suction caissons are profoundly affected by the nondimensional parameter H_s/d and valuable insight on the physics of the problem is achieved by considering the relative thickness of the soil layer. The applied numerical methodology was shown to be a versatile practical tool that provides the soil-foundation dynamic impedances, which can be further applied to the dynamic response of the jacket. However, the suggested model is limited by the assumptions of linearity in the soil layer and foundation materials, and the perfect contact at the soil-foundation interface.

Acknowledgement

This work was funded by the Danish Council for Strategic Research through the project “Advancing BeYond Shallow waterS (ABYSS) –

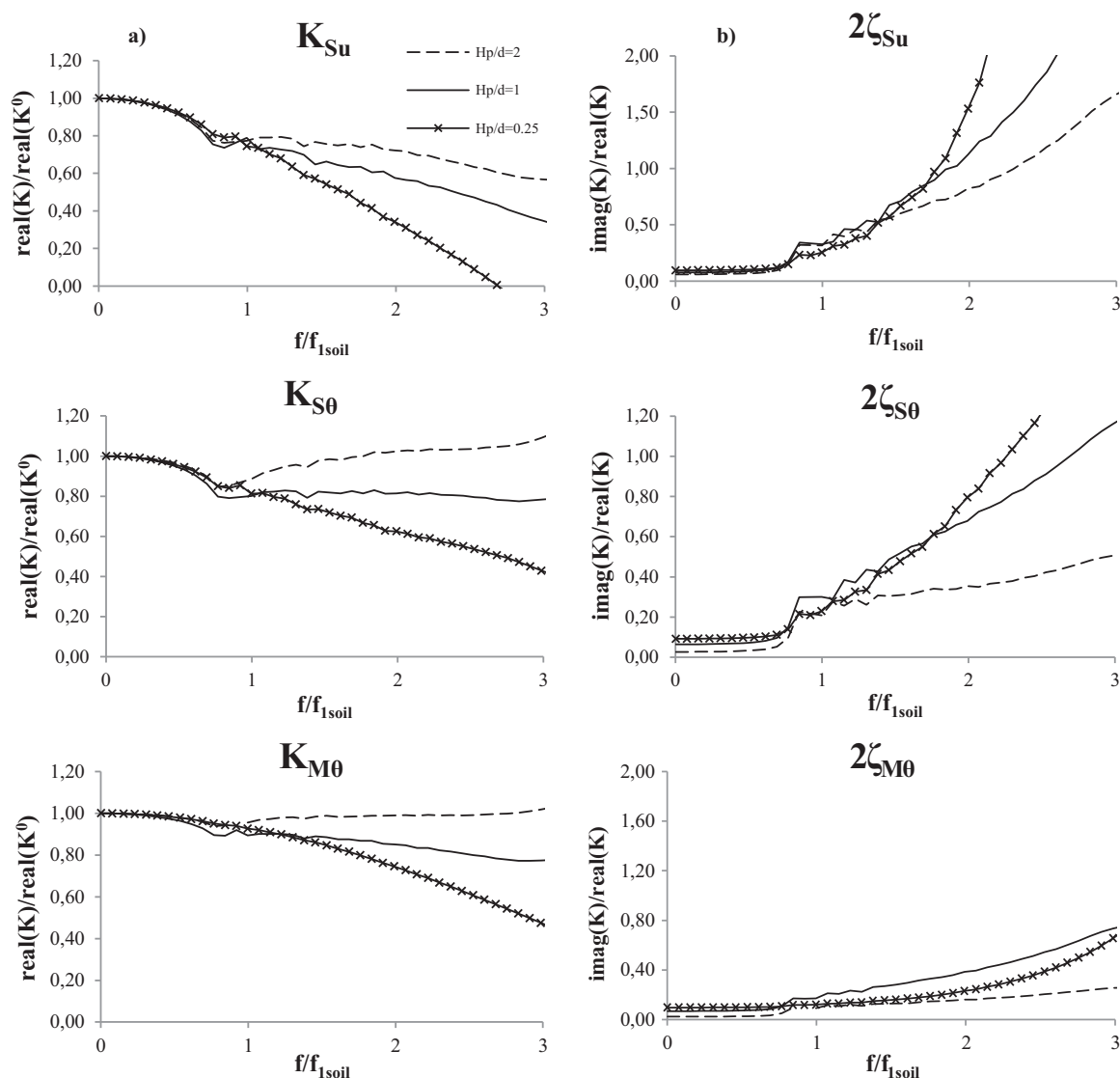


Fig. 13. Variation of the three dynamic stiffness and damping coefficients with respect to the non-dimensional frequency. Effect of the slenderness ratio in the inhomogeneous soil layer (profile C) on the real component (a) and the imaginary component (b).

Optimal design of offshore wind turbine support structures". The author would also like to acknowledge funding from the Technical University of Denmark for this study.

References

- [1] de Vries WE., Assessment of bottom-mounted support structure type with conventional design stiffness and installation techniques for typical deep water sites. Deliverable report; 2007.
- [2] Houslyb GT, Ibsen LB, Byrne BW. Suction caissons for wind turbines. Front Offshore Geotech ISFOG 2005 – Perth, Australia:75–94; 2005.
- [3] Byrne BW, Houslyb GT. Assessing novel foundation options for offshore wind turbines. World Mar Tech Conference, London, UK; 2006.
- [4] DNV-OS-J101. Design of Offshore Wind Turbines, Det Norske Veritas, Norway; 2004.
- [5] Devriendt C, Jordaens PJ, De Sitter G, Guillaume P. Estimating damping of an offshore wind turbine using an overspeed stop and ambient excitation. 15th Int Conf Exp Mech (ICEM15), Porto, Port 2012;2897.
- [6] Wolf JP. Dynamic soil-structure interaction. Prentice Hall int; 1985.
- [7] Adhikari S, Bhattacharya S. Dynamic analysis of wind turbine towers on flexible foundations. Shock Vib 2012;19. <http://dx.doi.org/10.3233/SAV-2012-0615>.
- [8] Alexander NA, Bhattacharya S. The dynamics of monopile supported wind turbines in nonlinear soil. In: Proceedings of the 8th International Conference Struct Dyn, Leuven, Belgium; 2011.
- [9] Zania V. Natural vibration frequency and damping of slender structures founded on monopiles. Soil Dyn Earthq Eng 2014;59:8–20. <http://dx.doi.org/10.1016/j.soildyn.2014.01.007>.
- [10] Novak M, Nogami T. Soil-pile interaction in horizontal vibration. Earthq Eng Struct Dyn 1977;5:263–81. <http://dx.doi.org/10.1002/eqe.4290050305>.
- [11] Nogami T, Novak M. Resistance of soil to a horizontally vibrating pile. Earthq Eng Struct Dyn 1977;5:249–61. <http://dx.doi.org/10.1002/eqe.4290050304>.
- [12] Nogami T. Coefficients of soil reaction to pile vibration. J Geotech Eng Div 1980:106.
- [13] Novak M. Dynamic Stiffness and Damping of Piles. Can Geotech J 1974;11(4):574–98. <http://dx.doi.org/10.1139/t74-059>.
- [14] Novak M, Aboul-Ella F. Impedance functions of piles in layered media. J Eng Mech Div 1978;104(3):643–61.
- [15] Mylonakis G. Elastodynamic model for large-diameter end-bearing shafts. Soils Found 2001;41(3):31–44.
- [16] Blaney GW, Kausel E, Roesset J. Dynamic stiffness of piles. Proc 2nd Int Conf Num Meth Geomech, Blacksbg, USA 1976;2:1001–12.
- [17] Roesset JM, Angelides D. Dynamic stiffness of piles. Proceedings International Conference Num Meth Offshore Piling, Institution of Civil Engineers, London; 1980.
- [18] Velez A, Gazetas G, Krishnan R. Lateral dynamic response of constrained head piles. J Geotech Eng 1983;109:1063–81. [http://dx.doi.org/10.1061/\(ASCE\)0733-9410\(1983\)109:8\(1063\)](http://dx.doi.org/10.1061/(ASCE)0733-9410(1983)109:8(1063)).
- [19] Gazetas G. Seismic response of end-bearing single piles. Int J Soil Dyn Earthq Eng 1984;3(2):82–93. [http://dx.doi.org/10.1016/0261-7277\(84\)90003-2](http://dx.doi.org/10.1016/0261-7277(84)90003-2).
- [20] Gazetas G, Dobry R. Horizontal response of piles in layered soils. J Geotech Eng 1984;110(1):20–40. [http://dx.doi.org/10.1061/\(ASCE\)0733-9410\(1984\)110:1\(20\)](http://dx.doi.org/10.1061/(ASCE)0733-9410(1984)110:1(20)).
- [21] Nozoe H, Gyöten Y, Fukusumi T. Dynamic analysis of a soil-pile system by the finite Fourier-Henkel transformation method – case of a floating pile in horizontal vibration. Theor Appl Mech 1985;33:377–92.
- [22] Latini C, Zania V, Johannesson B. Dynamic stiffness and damping of foundations for jacket structures. In: Proceedings of the 6th International Conference Earthq

- Geotech Eng; 2015.
- [23] Haldar SS, Bose SK. Dynamic soil stiffness in lateral vibrations of a floating pile. *Soil Dyn Earthq Eng* 1990;9(1):51–6.
- [24] El-Marsafawi H, Kaynia AM, Novak M. Interaction factors and the superposition method for pile group dynamic analysis [Report GEOT192, Geotechnical Research Center]. The University of Western Ontario; 1992.
- [25] Syngros C. Seismic Response of piles and pile-supported bridge piers evaluated through case histories [Ph.D. thesis]. City University of New York; 2004.
- [26] Kaynia AM, Kausel E. Dynamic stiffness and seismic response of pile groups [Research Report R82-03]. Cambridge, MA: Massachusetts Institute of Technology; 1982.
- [27] Maeso O, Aznárez JJ, García F. Dynamic impedances of piles and groups of piles in saturated soils. *Comput Struct* 2005;83(10):769–82.
- [28] Padrón LA, Aznárez JJ, Maeso O. Dynamic analysis of piled foundations in stratified soils by a BEM–FEM model. *Soil Dyn Earthq Eng* 2008;28(5):333–46.
- [29] Jin B, Zhou D, Zhong Z. Lateral dynamic compliance of pile embedded in poroelastic half space. *Int J Soil Dyn Earthq Eng* 2001;21(6):519–25.
- [30] Pak RYS, Jennings PC. Elastodynamic response of piles under transverse excitations. *J Eng Mech* 1987;113(7):1101–16.
- [31] Rajapakse RKND, Shah AH. On the lateral harmonic motion of an elastic bar embedded in an elastic half-space. *Int J Solids Struct* 1987;23(2):287–303.
- [32] Larsen KA, Ibsen LB, Barari A. Modified expression for the failure criterion of bucket foundations subjected to combined loading. *Can Geotech J* 2013;50(12):1250–9.
- [33] Randolph MF, House AR. Analysis of suction caisson capacity in clay. *Proceedings Annu Offshore Technol Conference*; 2002.
- [34] Aubeny C, Murff JD. Simplified limit solutions for undrained capacity of suction anchors. *Deep Mooring Syst: Concepts, Des, Anal Mater, Tex, USA 2003*:76–90.
- [35] Kourkoulis RS, Lekakakis PC, Gelagoti FM, Kaynia AM. Suction caisson foundations for offshore wind turbines subjected to wave and earthquake loading: effect of soil–foundation interface. *Géotechnique* 2014;64(3):171–85. <http://dx.doi.org/10.1680/geot.12.P.179>.
- [36] Liingaard M. Dynamic behavior of suction caissons [PhD Thesis]. Denmark: Aalborg University; 2006.
- [37] Latini C, Cisternino M, Zania V. Dynamic stiffness of horizontally vibrating suction caissons. *Proceedings 17th Nord Geotech Meet*; 2016.
- [38] Bhattacharya S, Nikitas N, Garnsey J, Alexander NA, Cox J, Lombardi D, Nash DF. Observed dynamic soil–structure interaction in scale testing of offshore wind turbine foundations. *Soil Dyn Earthq Eng* 2013;54:47–60.
- [39] Simulia DS. Abaqus 6.13 User's Manual. Dassault Systems, Providence, RI; 2003.
- [40] Darendeli MB. Development of a new family of normalized modulus reduction and material damping curves [PhD Thesis]. USA: The University of Texas at Austin; 2001.
- [41] Poulos HG, Davis EH. *Pile foundation analysis and design*. New York, NY: John Wiley & Sons; 1980.
- [42] Randolph MF. The response of flexible piles to lateral loading. *Géotechnique* 1981;31(2):247–59. <http://dx.doi.org/10.1680/geot.1981.31.2.247>.
- [43] Gazetas G. Analysis of machine foundation vibrations: state of the art. *Int J Soil Dyn Earthq Eng* 1983;2(1):2–42. [http://dx.doi.org/10.1016/0261-7277\(83\)90025-6](http://dx.doi.org/10.1016/0261-7277(83)90025-6).
- [44] Rovithis EN, Parashakis H, Mylonakis GE. 1D harmonic response of layered inhomogeneous soil: analytical investigation. *Soil Dyn Earthq Eng* 2011;31(7):879–90. <http://dx.doi.org/10.1016/j.soildyn.2011.01.007>.
- [45] Carter JP, Kulhawy FH. Analysis of laterally loaded shafts in rock. *J Geotech Eng* 1992;118(6):839–55. [http://dx.doi.org/10.1061/\(ASCE\)0733-9410\(1992\)118:6\(839\)](http://dx.doi.org/10.1061/(ASCE)0733-9410(1992)118:6(839)).
- [46] Wolf JP, Deeks AJ. Cones to model foundation vibrations: incompressible soil and axi-symmetric embedment of arbitrary shape. *Soil Dyn Earthq Eng* 2004;24(12):963–78. <http://dx.doi.org/10.1016/j.soildyn.2004.06.016>.
- [47] Gelagoti FM, Lekakakis PP, Kourkoulis RS, Gazetas G. Estimation of elastic and non-linear stiffness coefficients for suction caisson foundations. *Proceedings Xvi European Conference Soil Mech Geotech Eng, Edinburgh, UK*; 2015.
- [48] Shadlou M, Bhattacharya S. Dynamic stiffness of monopiles supporting offshore wind turbine generators. *Soil Dyn Earthq Eng* 2016;88:15–32.

Paper IV

Dynamic stiffness of horizontally vibrating suction caissons

C. LATINI, M. CISTERNINO AND V. ZANIA

Published in: Proceeding of the 17th Nordic Geotechnical Meeting, 2016

Dynamic stiffness of horizontally vibrating suction caissons

C. Latini

*Civil Engineering Department, Technical University of Denmark, Lyngby, Denmark,
 chila@byg.dtu.dk*

V. Zania

Civil Engineering Department, Technical University of Denmark, Lyngby, Denmark,

M. Cisternino

Civil Engineering Department, Technical University of Denmark, Lyngby, Denmark,

ABSTRACT

The promising potential for offshore wind market is on developing wind farms in deeper waters with bigger turbines. In deeper waters the design foundation configuration may consist of jacket structures supported by floating piles or by suction caissons. Taking the soil-structure interaction effects into consideration requires the prior estimation of the dynamic impedances of the foundation. Even though numerous studies exist for piles, only limited number of publications can be found for suction caissons subjected to dynamic loads. Therefore, the purpose of this study is to examine the dynamic response of this type of foundation using the finite element method (FEM) to account for the interaction with the soil. 3D numerical models for both the soil and the suction caisson are formulated in a frequency domain. The response of the soil surrounding the foundation is considered linear viscoelastic with hysteretic type damping. In addition, non-reflective boundaries are included in the model. Two different soil profiles are presented, one when the rigid bedrock is set close to the seabed and the other one when it is far away. The dynamic impedances at the top of the foundation are determined and compared to existing analytical solutions suggested for piles. Relatively good agreement has been achieved comparing the numerical results with the analytical solutions. Then, the effect of the soil layer shear wave velocity on the dynamic stiffness coefficients is analysed. The results have indicated that increasing the stiffness of the soil stratum the dynamic impedances grow, while the damping reduces in the frequency range investigated.

Keywords: soil-structure interaction, dynamic stiffness, damping, suction caissons, numerical modelling

1 INTRODUCTION

The offshore wind market is progressing by developing wind turbines with larger rotors and higher capacity generators, in order to deploy deep offshore designs. It is fundamental to assess the resonance frequencies of the wind turbine structure accurately in order to avoid the first resonance frequency of the wind turbines coinciding to the excitation frequencies of the

rotor system as delineated in DNV-OS-J101 (2004). In addition, the effect of the soil-foundation-structure interaction should be included in the estimation of the natural vibration characteristics of the OWTs as indicated by several studies (Adhikari and Bhattacharya, 2012; Alexander and Bhattacharya, 2011; Zania, 2014). The majority of installed or operating turbines are supported on fixed foundation system (Bhattacharya, 2014), while deep installations require jackets structures with

floating piles or with suction caissons. In the past, suction caissons have been deployed as anchors or as foundations for offshore platforms. According to Houlby et al. (2005), suction caissons can be adopted as offshore wind turbine foundations embedded in suitable soil conditions and especially for deeper waters installation, of water depth of approximately up to 40m.

Suction caissons differ from other foundation types such as piles, regarding the installation procedure applied offshore and the geometric properties including the rigid cap and the lateral flexibility (with slenderness ratio lower than 4). Contrary to offshore pile driving, heavy duty equipment is not required in the process of suction caisson installation, which is materialized by using self-weight and suction as the driving forces (Byrne and Houlby, 2006). This becomes a considerable advantage in the case of deep water installations.

In the literature the problem of the dynamic soil-pile interaction has been extensively investigated. Considering only the studies for linear elastic soil layer, they can be briefly categorized into analytical solutions (Novak and Nogami, 1977; Mylonakis, 2001; Nozoe et al., 1985; Latini et al., 2015) and numerical finite element solutions (Velez et al., 1983; Gazetas, 1984). On the other hand, the dynamic response of suction caissons received less attention (Liingaard, 2006). In the work of Liingaard (2006) the dynamic stiffness coefficients were determined, considering linear viscoelastic soil and modelling the suction caisson using a coupled BE/FE model in homogeneous halfspace comparing the obtained results with analytical solutions for surface foundations.

The purpose of the current study is to investigate the dynamic response of suction caissons for the estimation of the dynamic stiffness and damping coefficients with respect to the frequency. Therefore, 3D FE models were developed and the dynamic impedances to lateral loading were estimated. The results of the numerical models have been compared respectively with the rigorous analytical solution of soil-end bearing pile vibration by Novak et al. (1977) and the analytical solution proposed for floating piles

by Latini et al. (2015). The effect of the stiffness of the soil on the soil-caisson system response is further discussed.

2 METHODOLOGY

3D finite element models have been developed to investigate the dynamic impedances of the suction caisson in the commercial software ABAQUS (Simulia, 2013). The numerical models account for the following hypotheses: 1) linear elastic isotropic behaviour of the suction caisson; 2) linear viscoelastic isotropic behaviour of soil with hysteretic type damping and 3) perfect contact between the foundation and the soil during the analysis.

Due to the symmetry of the problem, only half of the foundation and the surrounding soil are taken into account. The suction caisson consists of steel with diameter $d=5\text{m}$, skirt length $H=10\text{m}$, Young's modulus $E_p = 210\text{ GPa}$ and Poisson's ratio $\nu=0.35$. The foundation skirt and the cap of the caisson have respectively thickness of $t_{\text{skirt}}=d/100$ and $t_{\text{cap}}=5t_{\text{skirt}}$.

Three different suction caisson modelling approaches are presented: 1) shell pile, where the foundation is modelled by shell; 2) caisson with cap; and 3) equivalent solid pile, for which equivalent material properties are applied to match the bending stiffness.

The soil surrounding the foundation has hysteretic type damping of $\zeta=5.0\%$ and constant profile of shear wave velocity $V_s=250\text{-}400\text{m/s}$. Hexahedral elements are used to discretize the soil domain of diameter $24d$ and height $H_s=6d=30\text{m}$. Infinite elements are placed at the boundaries in order to model the far field soil and avoid spurious reflection. The soil and the foundation skirt and the caisson cap are tied together in order to satisfy the displacement compatibility.

Steady state linearized response of the model subject to harmonic excitation in the frequency domain is performed. The dynamic impedances K_{su} , $K_{s\theta}$, K_{mu} and $K_{m\theta}$ at the level of the pile head are then calculated as shear forces, S , and moments, M , when the head of the suction caisson is subjected to unit displacement, u , and rotation, θ . The mesh size needs to be small enough to capture the

stress wave accurately. A mesh size of at least 10 to 20 elements per wave length is assumed a good approximation for the frequency range of interest, including up to the third eigenfrequency of the soil layer $\alpha_0 = 5/2\pi$. Note that α_0 is a dimensionless frequency related to the eigenfrequency of the soil layer, since it is given as the product of the wave number and the height of the soil layer:

$$\alpha_0 = \frac{\omega H_s}{V_s} \quad (1)$$

where ω (rad), H_s (m) and V_s (m/s) are respectively the circular frequency, the height and the shear wave velocity of the soil layer. A view of the model with the mesh refinement is shown in Figure 1.

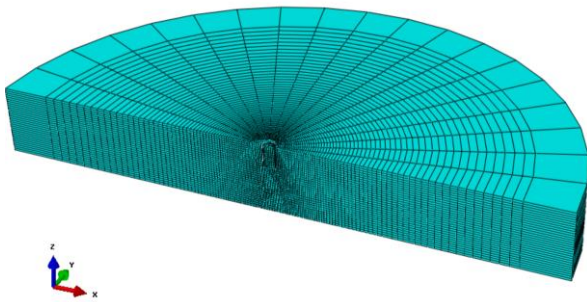


Figure 1 Finite element model of the suction caisson and the surrounding soil.

3 NUMERICAL RESULTS

Two layered soil profile characterized by high stiffness contrast is analyzed. Then, 3D numerical models are developed considering different depths of the surface soil layer with respect to the length of the skirt of the caisson, see Figure 2. In the study the soil profile with height equal to the caisson skirt length is defined as profile 1, while the one with increased height as profile 2.

The results for profile 1 and profile 2 are compared respectively with the rigorous continuum analytical solution formulated for end bearing piles by Novak et al. (1977) and that for floating piles by Latini et al. (2015). The different suction caisson modelling procedures with shell elements and continuum elements are implemented in order to achieve a direct comparison with the analytical solutions. The effect of the

stiffness of the soil on the soil-caisson system response is further discussed, by considering stiffer soil formation.

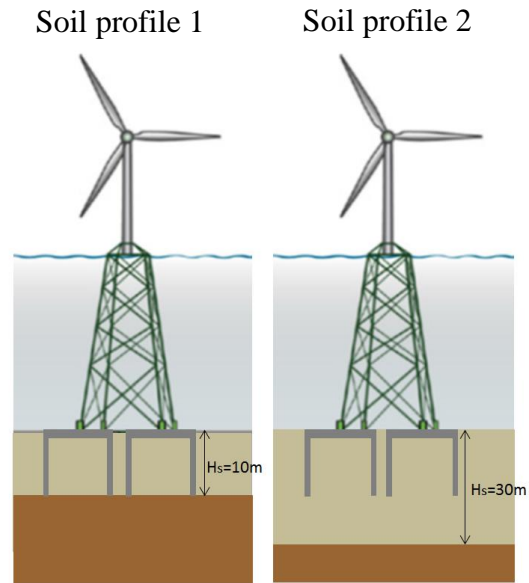


Figure 2 Illustration of the two soil profiles investigated in this study.

The dynamic component (real part of the complex valued stiffness terms divided by the corresponding static component K^0 and imaginary part of the complex valued stiffness terms divided by the corresponding dynamic component K_{xx}) of the three stiffness terms is presented with respect to the non-dimensional frequency α_0 .

First the static stiffness coefficients of the different modelling approaches are calculated and presented in Table 1 for the soil profile 1, along with the corresponding ones obtained from the analytical solution.

Table 1 Static suction caisson stiffness obtained from the numerical models and the analytical solution of Novak et al. (1977) for profile 1.

	Ksu [kN]	Ksθ [kN]	Kmθ [kNm]
Caisson	4.656E+6	-1.223E+7	1.120E+8
Shell pile	5.010E+6	-1.410E+7	1.325E+8
Solid eq. pile	7.109E+6	-2.384E+7	1.731E+8
Novak et al. (1977)	8.845E+6	-3.441E+7	2.148E+8

The stiffness components of the caisson model slightly differ from those of the shell pile, while the difference is more significant with the solid equivalent pile regarding all

the components. In addition, it is observed that the results obtained from the numerical models are overestimated by the analytical solution, particularly regarding the translational and the cross coupling terms.

In Figures 3, 4 and 5, the real (K_{su} , $K_{s\theta}$, and $K_{m\theta}$) and the imaginary ($2\zeta_{su}$, $2\zeta_{s\theta}$, and $2\zeta_{m\theta}$) part of the dynamic impedances are shown. A common trend for all the stiffness components is the observed drop of stiffness at the 1st eigenfrequency of the soil layer ($\alpha_0=1/2\pi$). A change in the pattern slope is attained around the first vertical resonance $\alpha_0=1/2\pi\eta$, where $\eta = \sqrt{\frac{2(1-\nu)}{1-2\nu}}$, which is mainly observed for the translational and rocking component; whereas the cross coupling coefficient is characterized by an increase of stiffness at the same normalized frequency.

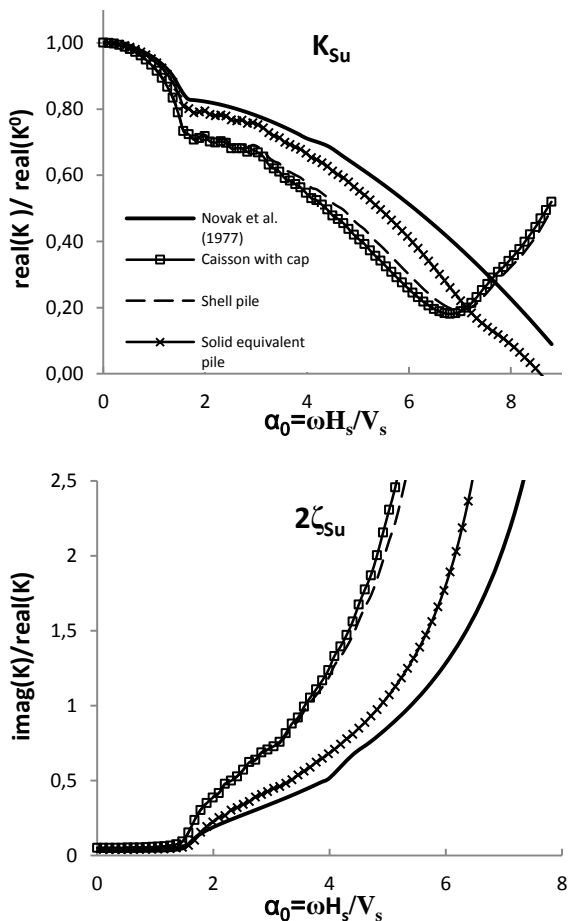


Figure 3 Variation of the translational stiffness and damping coefficients with respect to the dimensionless frequency for profile 1.

The intermediate frequency interval ($\alpha_0=1/2\pi\eta-6$) is characterized by a linearly

decrease of the dynamic stiffness consistent for all the components.

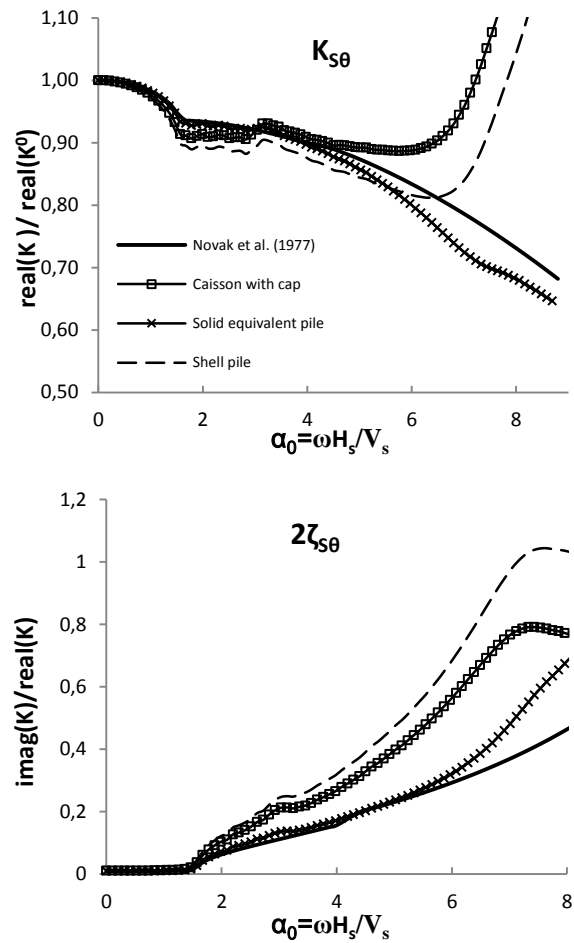


Figure 4 Variation of the coupling stiffness and damping coefficients with respect to the dimensionless frequency for profile 1.

On the contrary, in the high frequency range the solid equivalent pile shows a softer behavior with monotonically decreasing pattern with respect to the other two models for all the components. This trend resembles the one suggested by the analytical solution, although the latter is not able to capture the 1st vertical resonance.

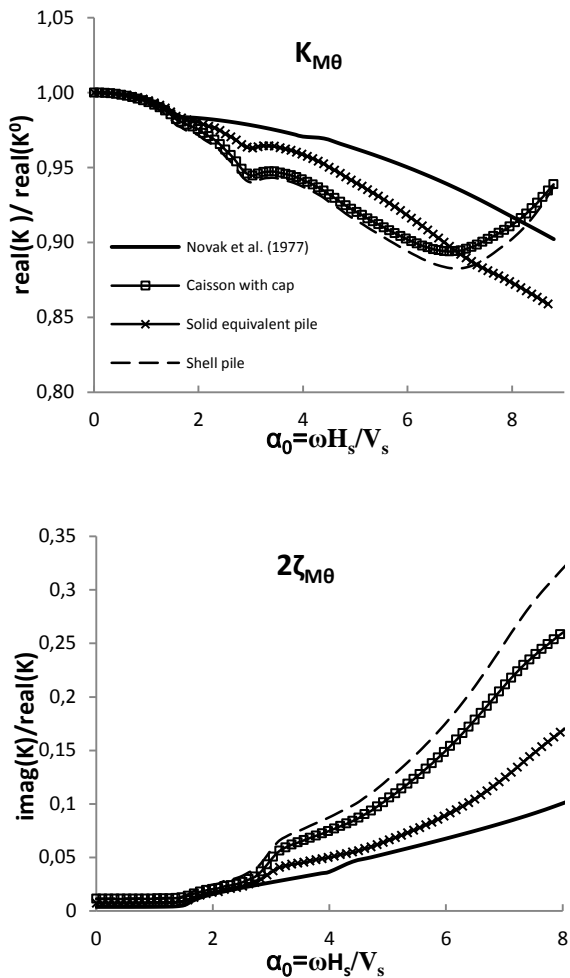


Figure 5 Variation of the rocking stiffness and damping coefficients with respect to the dimensionless frequency for profile 1

On the other hand the caisson and the shell pile model exhibit an exponential increase at the higher frequency range $\alpha_0=6.5-7$. This is possibly attributed to the presence of a surface wave (Rayleigh wave). Indeed, the displacement contour plot at this frequency (Figure 6) shows that the soil within the foundation and surrounding it experiences a surface wave with wave length almost equal to the diameter of the caisson and displays the occurrence of the Rayleigh wave through the s-pattern on the soil surface propagating radially from the caisson.

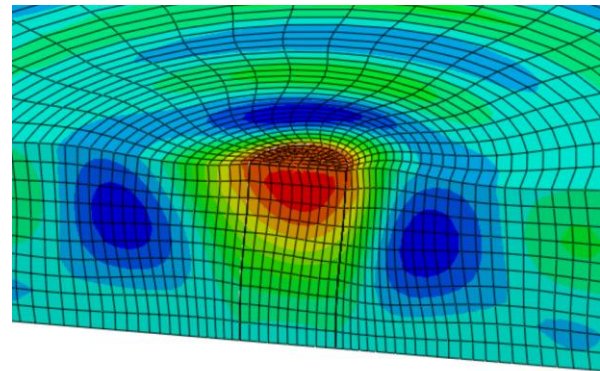


Figure 6 Displacement contour plot illustrating the presence of Rayleigh wave in the soil within the caisson.

The imaginary part of the dynamic impedances, is associated with the generated damping due to soil-caisson interaction. The radiation damping is generated for frequencies higher than the first eigenfrequency of the soil layer for all the components, and this is demonstrated by the increasing values of the coefficients with frequency (Figure 3,4, and 5). In the case of a linear increase viscous type damping is generated. This type of behavior is observed over the intermediate frequency range ($\alpha_0=2-4$). A slight change in the slope of the damping is also marked after each eigenfrequency of the soil layer. Moreover, it might be concluded that the presence of the cap does not affect the dynamic response of the soil-caisson system for the translation and rocking component, since the dynamic response of the shell pile and the caisson match almost perfectly. On the other hand a significant effect is noticed on the coupling stiffness term after the 1st vertical resonance for both stiffness and damping coefficients. The analytical solution is overestimating the dynamic stiffness and underestimating the damping for all the components, however it is in relatively good agreement with the equivalent solid pile. This indicates that the inner soil affects the dynamic response of the caisson, by allowing wave propagation of smaller wave lengths. The second soil profile describes a deep soil formation. For this case the response of the shell pile is not reported in the graphs, since it matches with the caisson case.

First the static stiffness coefficients were estimated and the results are presented in Table 2.

Table 2 Static suction caisson stiffness obtained from the numerical models and the analytical solution of Latini et al. (2015) for Profile 2.

	Ksu [kN]	Ksθ [kN]	Kmθ [kNm]
Caisson	3.220E+6	-9.237E+6	9.608E+7
Solid eq. pile	3.833E+6	-1.279E+7	1.191E+8
Latini et al. (2015)	4.288E+6	-1.529E+7	1.339E+8

The static stiffness coefficients of the solid equivalent pile are slight higher than those of the caisson model. The analytical solution suggests similar values to those obtained from the numerical models.

In Figures 7, 8 and 9, the real (K_{su} , $K_{s\theta}$, and $K_{m\theta}$) and the imaginary ($2\zeta_{su}$, $2\zeta_{s\theta}$, and $2\zeta_{m\theta}$) parts of the dynamic impedances are presented. A decrease of stiffness is marked after the 1st and 2nd horizontal eigenfrequencies ($\pi/2$ and $3\pi/2$ respectively) and the 1st vertical eigenfrequency of the soil layer for the translational stiffness component.

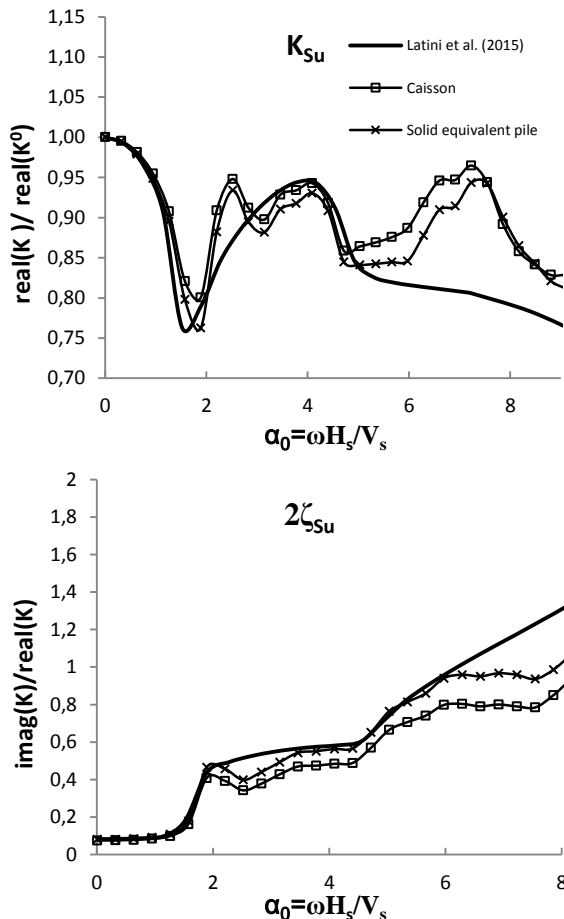


Figure 7 Variation of the translational stiffness and damping coefficients with respect to the dimensionless frequency for profile 2.

While, it seems that the coupling and the rocking stiffness terms are less sensitive to the 1st vertical resonance.

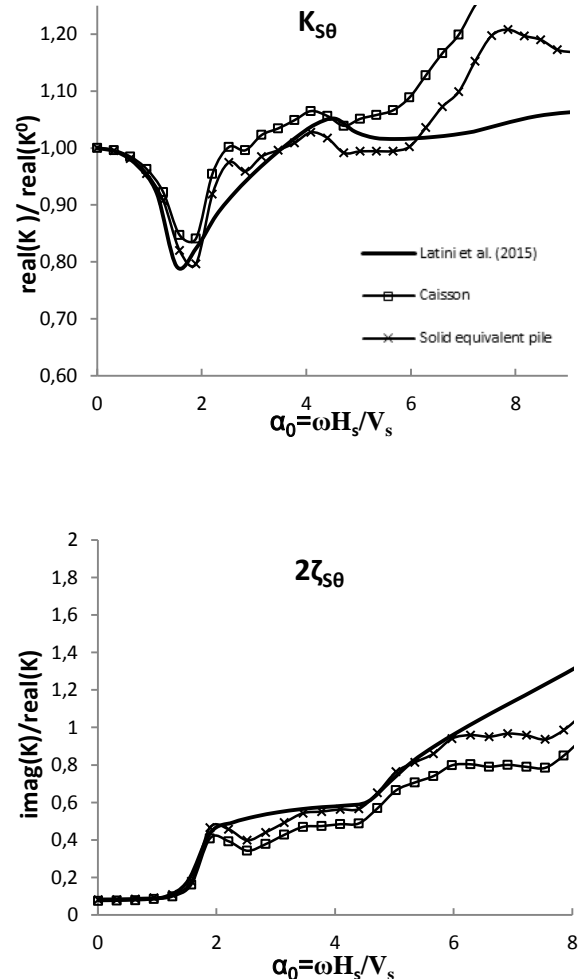


Figure 8 Variation of the coupling stiffness and damping coefficients with respect to the dimensionless frequency for profile 2.

In addition, they are characterized of an increase of stiffness approaching the 3rd eigenfrequency of the soil layer ($\alpha_0=5/2\pi$).

It is evident from the graphs that the dynamic response of the caisson is similar to the one of the solid equivalent pile, clearly for the translational and the rocking stiffness components. Furthermore, the analytical solution shows good agreement with the numerical results up to $\alpha_0 = 5$.

The imaginary part of the dynamic component is also shown in Figures 7, 8 and 9. The radiation damping exhibits a step variation in the frequency range, where the slope changes after each eigenfrequency of

the soil layer. This observation is consistent to previous studies on floating piles (Latini et al., 2015). Furthermore slightly higher damping is associated with the solid pile compared to the caisson.

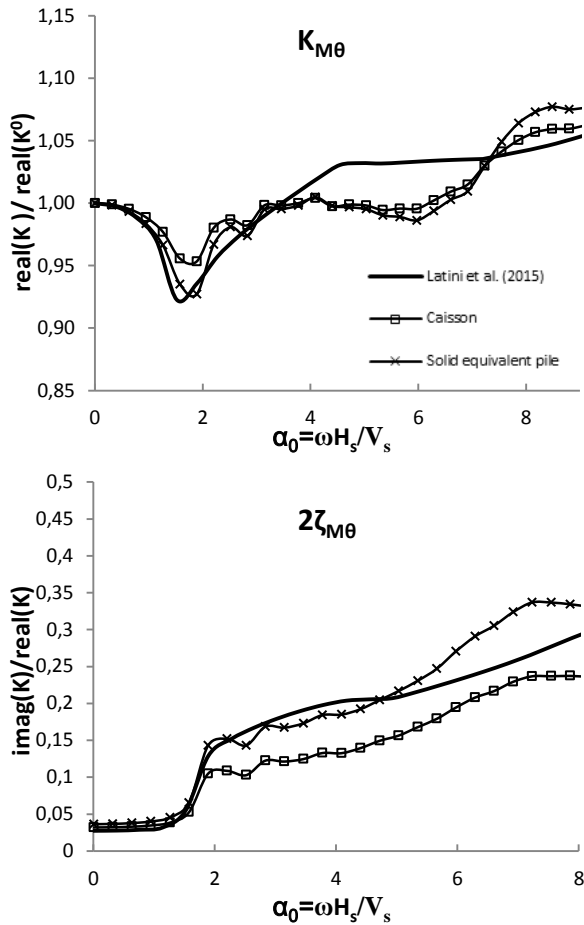


Figure 9 Variation of the rocking stiffness and damping coefficients with respect to the dimensionless frequency for profile 2.

In Figure 10, 11 and 12 the real (K_{su} , $K_{s\theta}$, and $K_{m\theta}$) and the imaginary ($2\zeta_{su}$, $2\zeta_{s\theta}$, and $2\zeta_{m\theta}$) parts of the dynamic impedances are presented for different values of the shear wave velocity of the soil layer ($V_s=250$ - 400 m/s).

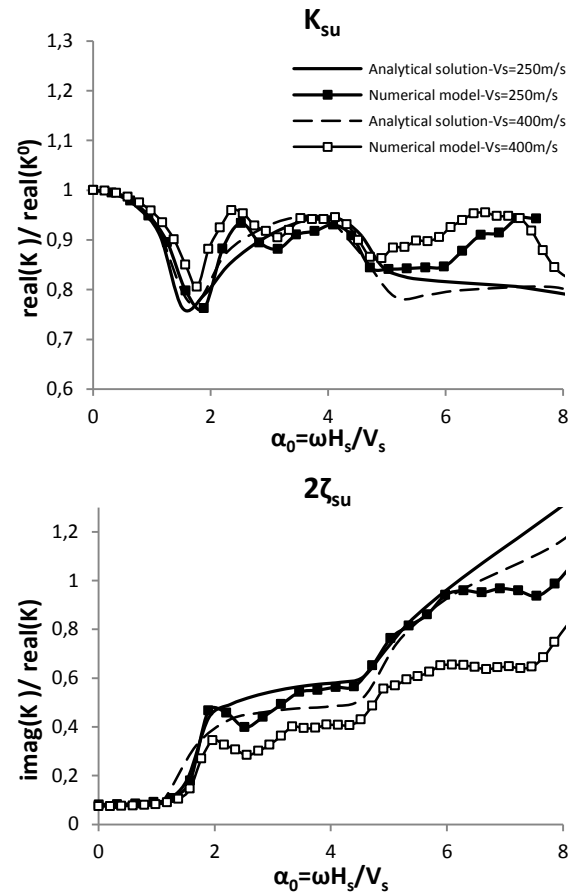


Figure 10 Variation of the translational stiffness and damping coefficients with respect to the dimensionless frequency. Effect of the soil stiffness on the real component and the imaginary component.

The same values as in the reference case are kept for the height of the foundation and the soil layer. Slightly scattered results are obtained by increasing the shear wave velocity of the soil layer. In addition, the drop of stiffness recorded at the first eigenfrequency of the soil layer is slightly more marked for medium soil profiles ($V_s=250$ m/s). Moreover, it is noticed that the cross coupling and rocking stiffness coefficients exhibit higher values than the corresponding static component at higher frequencies.

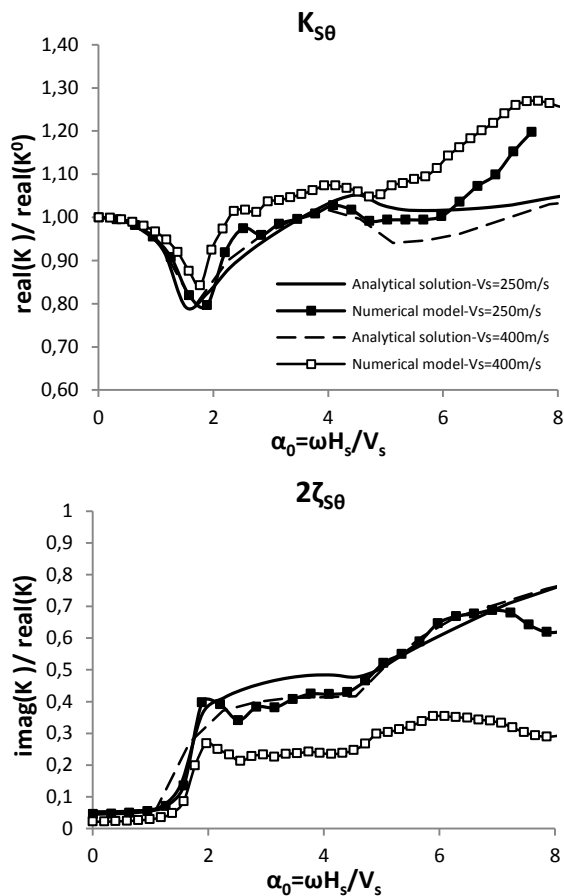


Figure 11 Variation of the coupling stiffness and damping coefficients with respect to the dimensionless frequency. Effect of the soil stiffness on the real component and the imaginary component.

In Figures 10, 11 and 12 the imaginary component is also illustrated for different values of the shear wave velocity of the soil layer. It is observed that increasing the stiffness of the soil or decreasing E_p/E_s the damping decreases. In addition, the radiation damping generated after the 1st eigenfrequency is almost zero for the rocking stiffness component. A significant offset is recorded comparing the numerical models with the analytical solution, when the stiffness of the soil layer is increased.

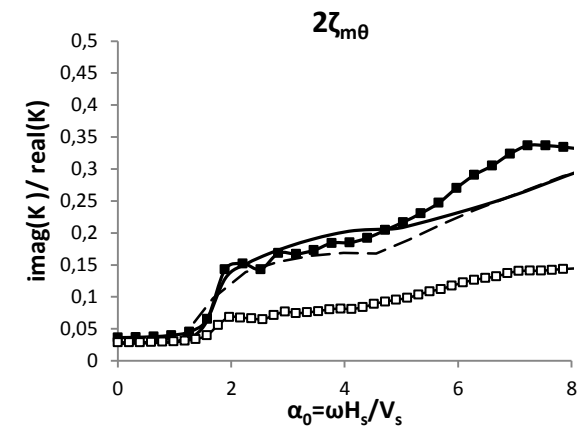
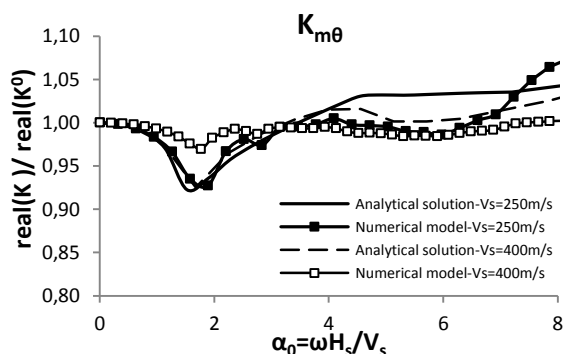


Figure 12 Variation of the rocking stiffness and damping coefficients with respect to the dimensionless frequency. Effect of the soil stiffness on the real component and the imaginary component.

4 CONCLUSIONS

Numerical analysis is undertaken to investigate the dynamic response of suction caissons. The study also provides comprehensive comparison of the numerical models with existing analytical solutions formulated for piles. From the results of this study it seems that the general behavior of the suction caissons follows the trend of the analytical solution suggested by Novak and Nogami (1977) for piles. However for the caisson a Rayleigh wave is experienced in the inner soil with wave-length $\lambda=D$ in the high frequency range. In addition, the presence of the cap in the caisson design does not affect significantly the dynamic response of the soil-foundation system. The analytical formulation of Latini et al. (1977) provides good agreement with the numerical model of a caisson on a deep soil layer for frequencies up to $\alpha_0 = 5$. Concerning the effect of the soil stiffness on the dynamic impedances, it is noticed that decreasing V_s the damping increases, which it is in agreement with what observed in the analytical formulation. However at larger shear wave velocities a larger discrepancy between the numerical model and the analytical solution was observed. The effect of the inner soil in the dynamic response of the caisson appears more important for shallow soil formations than for deeper ones.

ACKNOWLEDGMENTS

This work has been supported by the Danish Council for Strategic Research through the project “Advancing Beyond Shallow waters (ABYSS) - Optimal design of offshore wind turbine support structures”.

5 REFERENCES

- Adhikari, S., & Bhattacharya, S. (2012). Dynamic analysis of wind turbine towers on flexible foundations. *Shock and vibration* 19, 37-56.
- Alexander, N.A. & Bhattacharya, S. (2011). The dynamics of monopole supported wind turbines in nonlinear soil. Proceedings of the 8th International Conference on Structural Dynamics (EURODYN 2011), Leuven, Belgium.
- Bhattacharya, S. (2014). Challenges in design of foundations for offshore wind turbines. *Institution of Engineering and Technology* 10/2014.
- Byrne, B.W. & Houlby, G.T. (2006). Assessing novel foundation options for offshore wind turbines. World Maritime Technology Conference, London, UK.
- DNV (2010). Offshore standard DNV-OS-J101: Design of offshore wind turbine structures. Technical report DNV-OS-J101, Det Norske Veritas.
- Gazetas, G. (1984). Seismic response of end-bearing single piles. *Soil Dynamics and Earthquake Engineering* 3(2), 82-93.
- Latini, C., Zania, V. & Johannesson, B. (2015) Dynamic stiffness and damping of foundation for jacket structures. Proceedings of 6th International Conference on Earthquake Geotechnical Engineering (6ICEGE 2015), Christchurch, New Zealand.
- Liingard, M. (2006). Dynamic behavior of suction caissons. PhD Thesis. Aalborg University.
- Mylonakis, G. (2001) Elastodynamic model for large diameter end-bearing shafts. *Soils and foundations* 41(3), 31-44.
- Nogami, T. & Novak, M. (1977). Resistance of soil to a horizontally vibrating pile. *Earthquake Engineering and Structural Dynamic* 5(3), 249-261.
- Novak, M. & Nogami, T. (1977) Soil-pile interaction in horizontal vibration. *Earthquake engineering and structural dynamics* 5, 263-281.
- Nozoe H, Gyōten Y, & Fukusumi T. (1985) Dynamic analysis of a soil-pile system by the finite Fourier-Henkel transformation method – Case of a floating pile in horizontal vibration. *Theoretical and applied mechanics* 33, 377-392.
- Simulia, D. S. (2013) Abaqus 6.13 User's Manual. Dassault Systems, Providence, RI.
- Zania, V. (2014). Natural vibration frequency and damping of slender structures founded on monopiles. *Soil dynamics and Earthquake engineering*, 59, 8-20.

Paper V

Vertical dynamic impedance of suction caissons

C. LATINI AND V. ZANIA

Submitted for publication: -,2017

VERTICAL DYNAMIC IMPEDANCE OF SUCTION CAISSONS

C. Latini

PhD Student

Civil Engineering Department, Technical University of Denmark
e-mail: chila@byg.dtu.dk

V. Zania

Associate Professor

Civil Engineering Department, Technical University of Denmark
e-mail: vaza@byg.dtu.dk

ABSTRACT

Nowadays, suction caissons are being increasingly deployed as foundations to support offshore wind turbines (OWTs). Due to the overturning moment induced by waves and wind, vertical forces are the dominating ones acting on these foundations. The proposed study aims to investigate the dynamic stiffness and damping coefficients of suction caissons embedded in a viscoelastic soil layer over bedrock, subjected to vertical dynamic load. Numerical analyses of representative 3D finite element models were performed, while the numerical modelling was validated against existing analytical solutions for end bearing piles. The vertical dynamic response of suction caissons was evaluated by considering the effects of the foundation's geometry, i.e. the slenderness ratio, and the stiffness of the soil layer on the vertical dynamic impedance of suction caissons. Results showed that the overall dynamic response is profoundly affected by the skirt length and by the variation of soil stiffness with depth.

Mathematical expressions of the dynamic stiffness and damping coefficients were derived pertaining foundations with various slenderness ratios and embedded in different soil profiles. The proposed expressions can be implemented in structural models used for the dynamic analysis of the support structure of a wind turbine, taking thus into consideration the effects of soil-structure-interaction.

Keywords: soil-foundation interaction, dynamic stiffness, suction caisson, damping, impedance functions.

INTRODUCTION

Deep-water installations appear to be the future development in the offshore wind market. Although the majority of installed or operating turbines are supported on a fixed foundation system [1], jacket structures have been found more interesting for deep installations, since they are cost-effective to manufacture and install. Currently, the number of jackets installed in Europe has increased from 12 in 2015 to 67 in 2016 as reported in WindEurope survey [2]. Moreover, jackets with suction caissons are progressively becoming an economically viable alternative to driven piles in deep waters as suggested by Houlsby et al. [3]. This type of foundation has been widely deployed in the oil and gas industry; however relatively few offshore wind turbines are supported by suction caissons.

In regards with suction caissons, research effort has been primarily directed towards the evaluation of the limiting vertical capacity and of the kinematic mechanism accompanying failure, through empirical, analytical and numerical studies [4,5,6]. Nevertheless Ultimate Limit State (ULS) is rarely driving the design of offshore wind turbines, while Serviceability Limit State (SLS) and Fatigue Limit State (FLS) are usually the governing conditions, which require the accurate estimation of the foundation stiffness. In addition, since these types of structures are subjected to dynamic excitations, another aspect to consider in the design process is the dynamic soil-structure interaction, which considerably affects the eigenfrequency and the damping of the structure [7]. Solving the fully coupled problem, where the interrelation effects between wind turbine, foundation and soil are included in the dynamic analysis of the structure, requires advanced computational effort. Regarding the dynamic response of offshore wind turbine, a reduction approach, in order to decrease the number of degrees of freedom (DOFs) of the problem has been recently implemented in the estimation of the modified vibration response characteristics [8, 9]. In this approach the dynamic impedances of the foundation can be formulated into a lumped-parameter model (LPM) with frequency-independent coefficients that provide the generalized stiffness and damping matrix. The implementation of LPMs to account for dynamic soil structure interaction originates from early pioneering studies in earthquake engineering [10,11]. An advanced LPM formulation has been recently implemented to perform fully coupled aeroelastic simulations of a wind turbine in the nonlinear multi-body code HAWC2 and compare the response for different types of foundations [12,13]. The calibration of LPMs requires the estimation of the dynamic impedances, which can be evaluated by adopting analytical or numerical methodologies, with different degrees of accuracy and complexity, as proposed by several studies carried out in the literature. Due to their simplicity and versatility, the most adopted solutions are Winkler type analytical solutions [14-17], where the soil is modelled as a bed of independent elastic springs overlying rigid bedrock. Such formulations are usually defined as plane strain models, since zero strain is taken into account in the second horizontal direction. Winkler type analytical solutions are mostly deployed for slender piles ($H_p/d > 10$, where H_p and d are the foundation height and diameter, respectively), thus the assumption of

zero shear deformations along the pile length can be considered valid. Besides this the Winkler model neglects the soil-pile coupled vibration and the accuracy of the results is strongly influenced by the calibration of the model parameters. An improved model incorporating in the analysis the normal and shear stresses acting on the upper and lower faces of a horizontal soil element by integrating the governing equations over the thickness of the soil layer was developed by Mylonakis [17]. It is worth mentioning that a Winkler type analytical solution was also deployed to estimate the vertical dynamic impedance of floating piles (piles embedded in soil layers of depth greater than the pile length), as reported in the study of Novak [15]. A different formulation was proposed in the work of Nogami and Novak [18], Hu et al. [19], Anoyatis et al. [20] and Zheng et al. [21], where the soil surrounding the pile was modelled as a three-dimensional viscoelastic continuum. The three-dimensional continuum solutions are characterized by the advantage of treating the soil layer in more realistic manner than the plane strain models. Nevertheless, these formulations ignore the radial component of the soil displacements with the result that the effect of longitudinal waves is neglected. A more accurate elastodynamic solution, where both vertical and radial displacements are taken into account, was developed by Wu et al. [22]. Following the elastodynamic approach, Liu et al. [23] investigated the vertical dynamic behavior of a pipe pile installed in a saturated elastic layer, based on the dynamic consolidation theory of Biot [24]. This study showed that the influence of the porosity of the soil layer on the stiffness and damping of the pile can be considered negligible, since the oscillation amplitudes of the complex impedance decrease slightly by decreasing the permeability coefficient in the high frequency range. In addition to the aforementioned studies, analytical continuum formulations for investigating the vertical dynamic response of floating piles are proposed by Nozoe et al. [25] and Deng et al. [26].

In the literature other methodologies besides analytical solutions can be adopted to analyze the dynamic response of end bearing piles; an example is provided by numerical continuum finite element solutions. In these models the soil is treated as an elastic continuum and the pile is assumed to have rigid cross section and it is modelled as a series of regular beam segments, see the studies of Roesset and Angelides [27] and Kuhlemeyer [28]. Whereas the dynamic finite element formulation of Latini et al. [29] used shell elements to model both end bearing and floating steel hollow piles. It is common knowledge that numerical continuum finite element solutions provide accurate results with the disadvantage of being computationally intensive and time consuming.

The abovementioned works analyzed the vertical dynamic response of piles embedded in a homogeneous soil stratum over a rigid base. Nevertheless, a lot of studies in the literature investigated the dynamic vertical response of single piles and pile groups embedded in a halfspace domain by deploying analytical solutions [30-32], finite element methods [33-35] or boundary element methods [36,37].

The dynamic response of suction caissons has so far received less attention [29,38]. In the work of Liingaard [38] the dynamic vertical stiffness was estimated, considering linear viscoelastic soil and modelling the suction caisson using a coupled BE/FE model in homogeneous halfspace. The obtained results were compared with analytical solutions for surface foundations. The aforementioned study showed that the outcomes of the analytical solution for surface foundations resembled the one estimated from the numerical model only for $H_p/d \leq 0.25$. In addition, it was highlighted that the dynamic vertical impedance was relatively insensitive to the variation of Poisson's ratio; while the influence of the skirt flexibility on the dynamic behavior of suction caissons was proven significant.

Further results regarding the frequency dependent behavior of the soil-foundation system by applying LPMs [11] were also presented in the work of Liingaard [38].

The literature overview demonstrates that the dynamic response of suction caissons embedded in a halfspace is already analyzed [38]; thus the purpose of the current study is to examine the vertical dynamic response of suction caissons embedded in a soil layer overlying rigid bedrock with an emphasis on the stiffness and damping of the soil-suction caisson system. In addition, it was previously highlighted that some aspects of the dynamic response of suction caissons has not been analyzed so far (e.g. site effects). Hence, a numerical study was established in order to estimate the dynamic stiffness of suction caissons to vertical loading. It is worth highlighting that the dynamic response of the foundation group is mainly governed by the vertical stiffness component of the single foundation [39]; therefore the proposed study can be deployed for the dynamic analysis of multi-caisson supported wind turbine structures. Furthermore, this study is a continuation of previous work by the authors [40], conducted for estimating the lateral dynamic impedances of suction caissons.

In the absence of analytical formulations on the dynamic response of suction caissons in the literature, the numerical modelling approach is validated with the three different analytical solutions of dynamic vibration of soil-end bearing pile [18,21,22]. The validated numerical methodology was deployed to carry out a parametric study in order to analyze the influence of the skirt length of suction caissons on the soil-foundation system along with the site effects. For this purpose homogeneous and inhomogeneous soil profiles with different stiffness distributions have been analyzed and the effect on the dynamic impedance was estimated. The advantage of this approach is that it offers basic insight into the mechanism of the soil-suction caisson interaction. Moreover, the novelty of this study is also to present the vertical dynamic stiffness and damping coefficients in a form of mathematical formulas obtained after modifying the expressions of lumped-parameter models which had been suggested by Wolf [11]. These expressions can be used to predict dynamic suction caisson stiffness and damping, when the foundation is subjected to dynamic loading due to wind and waves; meanwhile they appear to be a good basis for obtaining an insight into vertical response of suction caissons due to earthquakes. From a wind turbine simulation point of view, an approach is to fit a parallel coupling of discrete masses, springs and dashpots to

the proposed mathematical expressions, in order to perform the aeroelastic analysis of offshore wind turbines, implemented in an integrated structural model considering dynamic soil-structure-interaction like in [41].

METHODOLOGY

NUMERICAL MODEL

The dynamic soil-caisson interaction was analyzed by 3D finite element models developed in the commercial software ABAQUS [42] and the vertical dynamic impedance of suction caissons was estimated. The main emphasis is placed upon the assumption on linear elasticity for the soil-foundation system and perfect bounding at the soil-foundation interface. In this study hysteretic type damping (frequency independent) for the soil layer was considered. The numerical methodology was validated against published analytical solutions of the dynamic response of end bearing piles subjected to axial loading [18,21,22].

Due to the symmetry of the problem, only half of the foundation and the surrounding soil were taken into account in the model. The far field soil response ($L_{inf}=180m$) was modelled using infinite elements to avoid spurious reflections. The near field soil domain ($L_{fin}=180m$) was discretized by 8-node 3D continuum elements (C3D8). Lateral surfaces of the soil and the foundation were tied together to satisfy displacement compatibility.

The mesh size was set small enough to capture the stress wave accurately even at high frequency range. A mesh size of at least 10 to 20 elements per wave length for the frequency range of interest was used, including up to the 2nd eigenfrequency of the soil layer $\alpha_0=3/2(\eta\pi)$, where $\eta = \sqrt{2(1-\nu)/(1-2\nu)} = 2.08$. Note that α_0 is a dimensionless frequency related to the eigenfrequency of the soil layer, since it is given as the product of the wave number and the depth of the soil layer.

$$\alpha_0 = \frac{\omega H_s}{V_s} \quad (1)$$

where ω (rad/sec), H_s (m) and V_s (m/s) are respectively the frequency, the thickness and the shear wave velocity of the soil layer.

The steady state linearized response of the model subjected to harmonic excitation in the frequency domain was obtained. The dynamic impedances K_v at the level of the foundation head was then calculated as axial force V , when the head of the foundation was subjected to unit displacement, U_3 . Hence the complex stiffness \tilde{K}_v can be expressed in any of the following ways:

$$\tilde{K}_v = K_v^0 (K_{v,dyn} + i\omega C_v) \quad (2)$$

$$\widetilde{K}_v = K_{v,dyn}(1 + i2\zeta_v) \quad (3)$$

Where $K_{v,dyn}$ represents the true stiffness, K_v^0 is the static stiffness, C_v is the coefficient of equivalent viscous damping, ω is circular frequency and $i = \sqrt{-1}$. In this study, the results are presented in terms of dimensionless coefficients $\left(\frac{K_{v,dyn}}{K_v^0}, 2\zeta_v\right)$ which highlight the frequency dependency of the dynamic stiffness and damping.

In the validation of the numerical methodology the pile was modelled as a solid cylinder (3D continuum elements), in order to be consistent with the assumption of solid pile cross section of the analytical formulations. In addition, three different modelling approaches for the suction caisson were implemented to investigate the effect of the inner soil: 1) equivalent solid pile, for which equivalent material properties are applied to match the axial stiffness; 2) shell pile, where the foundation is modelled by its shell and 3) caisson with cap, as illustrated in Figure 1. One of the two foundations adopted in the validation of the numerical methodology consists of a suction caisson with diameter $d=5\text{m}$ and height $H_p=10\text{m}$, embedded in a homogeneous soil layer with thickness $H_s=30\text{m}$ and constant profile of shear wave velocities ($V_s=250\text{m/s}$), hysteretic material damping ($\zeta=5\%$) and Poisson's ratio ($\nu=0.35$). For the parametric study the geometry of the caisson comprising of a hollow cylinder (skirt) and a cap was modelled with shell elements (S4). Note that the numerical analyses were conducted by considering that the foundation skirt and the cap had respectively thickness of $t_{skirt}=d/100$ and $t_{cap}=5t_{skirt}$.

VALIDATION WITH ANALYTICAL SOLUTIONS

The numerical results for the end bearing pile case were compared respectively with the different analytical solutions formulated by Nogami and Novak [18], Zheng et al. [21] and Wu et al. [22]. It is worth mentioning that first the validation of the numerical model was performed taking into account a solid concrete pile (case 1, Table 2), so that the assumptions are consistent with those of the analytical solutions.

The static stiffness coefficient of the numerical model was calculated at low frequencies and presented in Table 1, along with the corresponding analytical values. A discrepancy of less than 1% was achieved over the analytical solution of Nogami and Novak [18], Zheng et al. [21] and Wu et al. [22], while a greater variation (5.2%) was recorded with respect to the analytical formulation of Wu et al. [22]. Figure 2a shows the real (K_v) and the imaginary ($2\zeta_v$) part of the dynamic vertical impedance with respect to the non-dimensional frequency α_0 . Both the analytical solutions and the numerical model exhibited a drop of stiffness at the 1st eigenfrequency of the soil layer ($\alpha_0=1/2\eta\pi$). However, an additional cut-off frequency around $\alpha_0=2$ was recorded in the analytical formulation developed by Wu et al. [22] and Zheng et al. [21]. In the work of Zheng et al. [21] this extra drop of stiffness was assumed to represent the 1st horizontal resonance, since the radial

displacements were accounted for in the solution. The numerical results proved that this cannot be a possible explanation, since any limitations on the soil displacements were not considered in the finite element models and still this second decrease in stiffness was not observed. Nevertheless, the trend of the abovementioned analytical formulations resembled the numerical model pattern for frequencies higher than the 1st resonance. The imaginary part of the dynamic component of the vertical impedance showed that radiation damping was produced for frequencies higher than the 1st eigenfrequency of the soil medium. In addition, all the analytical studies converge to the same linear trend of the viscous type radiation damping for frequencies higher than $\alpha_0=1/2\eta\pi$. In Figure 2b the deformed shape of the pile is plotted as a function of the depth at the 1st vertical resonance of the soil layer and the numerical trend resembled the one suggested by the analytical formulation of Nogami and Novak [18].

The latter was adopted for the comparison with the numerical results of a foundation having smaller stiffness and slenderness ratio and larger diameter (case 2 in Table 2). It was found that the numerical results matched almost perfectly with the one proposed by the analytical solution regarding both the static and the dynamic term, see Figures 2c and 2d.

PARAMETRIC STUDY

The dynamic response of suction caissons is influenced by several parameters. Hereafter, the role of the slenderness ratio (H_p/d) and the soil profile (ν , E_p/E_s) on the dynamic response of the pile in the frequency domain was analyzed; all the cases investigated are shown in Table 2.

Three soil profiles were considered in order to address the effect of soil inhomogeneity, each with a different distribution of $E_s(z)$ with depth as reported in Figure 1. The distribution of $E_s(z)$ was calculated on the basis of the shear wave velocity of the soil layer, which was assumed to increase with depth according to the following expression (Rovithis et al. [43])

$$V_s(z) = V_H \left[b + (1 - b) \frac{z}{H_s} \right]^n \quad (4)$$

where b is given as a function of the shear wave velocity at the surface (V_0) and base (V_H) of the inhomogeneous soil layer ($b=(V_0/V_H)^{1/n}$), n is a dimensionless inhomogeneity factor and z represents the depth measured from the ground surface. Profile A has constant shear wave velocity ($V_s=250, 300, 400, 500\text{m/s}$ – cases 3, 12-14), which is typical for over-consolidated clay deposits. The parameter n was set equal to 0.25 for profile B, representing uniform medium-dense sand deposits, see cases 15-17. In profile C, $E_s(z)$ is proportional to depth and $n=0.5$ was taken into account in order to investigate normally consolidated clay strata (cases 18-20).

Shear wave velocity ratio V_0/V_H (at the surface and the base of the inhomogeneous layer) was considered equal to 0.01 and 0.1 respectively for the soil models B and C to account for strong gradient in shear wave velocity. And the reference base shear wave velocity was 500m/s in order to model a continuously inhomogeneous viscoelastic soil medium of thickness H_s ,

over rigid bedrock. The hysteretic material damping ($\zeta=5\%$) and Poisson's ratio ($\nu=0.35$) were identical for all the examined cases. These three models may adequately represent the dynamic characteristics of a fairly wide range of real soil profiles.

RESULTS

In this study the numerical outcomes of the static impedance were first compared respectively with Wolf [11] and Gelagoti et al. [44]. The comparison, which is not presented here due to space limitations, suggested that the numerical results and two sets of expressions were in good agreement.

Previous studies have investigated the effect of the inner soil on the vertical dynamic impedance of piles [21,23,29]. Particularly, the works of Zheng et al. [21] and Liu et al. [23] highlighted that the interaction of the inner soil with the pile under dynamic loading determined a considerably increase of the oscillation amplitudes at resonance frequencies in the high frequency range. While Latini et al. [29] showed that the influence of the inner soil on the vertical dynamic response became more apparent for frequencies higher than $\alpha_0=8$. Hence, the effect of the soil within the foundation is also analyzed for suction caissons by implementing the three modelling approaches (Figure 1) and the results of the vertical dynamic stiffness and damping are presented in Figure 3. The numerical outcomes of three modellings approaches match almost perfectly up to $\alpha_0=8$. It appears that the presence of the inner soil affects to some extent the vertical dynamic response of the foundation in the high frequency interval. This effect observed in the high frequency interval might also be due to the fact that hysteretic type damping is applied to the soil within the skirts of the caisson with cap and shell pile model.

In Figures 4a and 4b the real (K_v) and the imaginary ($2\zeta_v$) parts of the vertical dynamic impedance are displayed, while the effect of the skirt length is also demonstrated (cases 3-7).

The reduction in stiffness recorded at the 1st vertical eigenfrequency of the soil stratum is more evident by increasing the slenderness ratio H_p/d in agreement with the work of Liingaard [38]. The dynamic stiffness was characterized to some extent by linearly decreasing pattern for frequencies higher than $\alpha_0=4$. While the trend of the radiation damping exhibited an increased slope as the slenderness ratio increases. In Figures 4c and 4d the vertical displacement of the foundation normalized by the displacement at the top of the foundation is plotted as a function of the depth at the 1st and 2nd resonance. It appears that the dynamic response of suction caissons is controlled by the foundation rather than the soil and the behavior becomes stiffer by decreasing the slenderness ratio. This conclusion is supported by the vertical deformed shape of the foundation, which presented steeper slope with the decrease of caisson height (skirt length).

Figure 5 illustrates the real (K_v) and the imaginary ($2\zeta_v$) parts of the vertical dynamic impedance, varying the Poisson's ratio ν . It was observed that ν influenced significantly the frequency value, where the 1st vertical resonance was attained,

due to the dependency of η on Poisson's ratio. In the literature there are several studies [17,20] that investigated the high sensitivity of elastodynamic analytical solutions for piles to Poisson's ratio since, as ν approaches 0.5, the dilatational wave velocity tends to infinity. A detailed discussion on the use of the dimensionless parameter η for nearly incompressible soil medium was presented in the work of Mylonakis [17].

In the current study it was found that the value of the 1st vertical eigenfrequency of the soil layer obtained from the numerical models matched the one calculated by adopting $\eta = \sqrt{2(1 - \nu)/(1 - 2\nu)}$ when Poisson's ratio is less than 0.40. By increasing Poisson's ratio ν up to 0.35, the effect on the reduction in stiffness attained at the 1st vertical resonance is not influential, since less than 15% of difference was recorded over the frequency range investigated. Moreover, it was observed a change in the stiffness's slope, recorded at the 3rd horizontal resonance ($\alpha_0 \cong 7.85$), which became slightly more marked when the Poisson's ratio assumes small values ($\nu=0.1$ and $\nu=0.2$). This can be explained by the fact that the stiffer the soil is, the more the stress waves are attenuated and therefore the decay of the vertical dynamic impedance is less appreciable.

In regards with the imaginary component, the numerical models displayed similar results concerning the radiation damping associated to the vertical component of the stiffness. Indeed, the radiation damping was generated for frequencies higher than the 1st vertical resonance, which is shifted backwards as Poisson's ratio decreases. Furthermore, a steeper pattern of the radiation damping was recorded for frequencies greater than $\alpha_0 \cong 7.85$, when $\nu = 0.1 - 0.2$. Therefore, it may be concluded that the vertical dynamic stiffness is marginally sensitive to Poisson's ratio with values less than 0.4 in agreement to previous studies [38].

When Poisson's ratio approaches 0.5, the soil behaves as a nearly incompressible material and the numerically calculated impedances showed fluctuations around the 1st vertical resonance. To investigate these fluctuations two additional numerical models for suction caisson with $H_p/d=2$ were analyzed, where an assumption on the soil layer's displacements was enforced. In the first numerical model no horizontal displacements (U1) were considered, while the latter was characterized by zero displacements on both horizontal directions (U1 and U2). Figure 5c and 5d illustrate the effect of the horizontal displacements (U1 and U2) on the vertical dynamic stiffness for suction caisson with $\nu=0.4$ and $\nu=0.495$, respectively. Particularly, it was observed that the fluctuation of the vertical dynamic stiffness recorded for suction caisson with $\nu=0.4$ at $\alpha_0=3.0$ is mainly enhanced by the horizontal displacements (U1). Indeed, the elements at the edge of the foundation tip move horizontally and vertically, as a result of the bending response due to the axial force. As the Poisson's ratio approached 0.5, the numerical results showed that the drop of stiffness at the 1st vertical resonance is reduced by neglecting the horizontal displacements (U1), while it diminished when both horizontal displacements were restrained. This observation is attributed to volumetric locking. It has been previously reported in the literature as a well-known

problem that three-dimensional standard linear eight-node displacement element (C3D8) suffers of severe locking for nearly or fully incompressible material [45]. In the current study the occurrence of volumetric locking was demonstrated by the checkboard pattern of pressure values, changing significantly from one integration point to the next, as shown in Figure 6b. On the other hand this pattern is not seen when there are no constraints on the displacements (Figure 6a). The issue of volumetric locking can be overcome by adopting hybrid formulation, where hybrid elements are used (C3D8H) or by applying selectively reduced-integration (C3D8R) [42]. It is worth mentioning that the results presented for the incompressible soil medium ($\nu=0.495$) were obtained both adopting hybrid elements and elements with reduced integration formulation. However, it was showed that spurious pressure stresses developed at the integration points, resulting in an overly stiff response. Figure 7 shows the real (K_v) and the imaginary ($2\zeta_v$) part of the dynamic impedances varying the stiffness of the homogeneous soil layer (profile A) for $H_p/d=2$ (cases 3, 12-14). It is observed that increasing the shear wave velocity of the soil layer or decreasing E_p/E_s influence the dynamic stiffness amplitude but the frequency dependent behavior is similar. The drop in stiffness recorded at the 1st vertical eigenfrequency of the soil layer was to some extent less evident for stiff soil profiles ($V_s=500\text{m/s}$). In the intermediate frequency interval ($\alpha_0=4-7$) the vertical dynamic impedance was characterized by almost constant pattern with frequency, while the dynamic stiffness increases as the shear wave velocity increases. Particularly, when the soil is very stiff, the real component of the stiffness seemed even independent of the frequency after 1st vertical resonance. These findings are in agreement with the work of Nogami and Novak [18] for the case of end bearing piles. When it comes to the imaginary part, it was noticed that increasing the stiffness of the soil stratum the dimensionless coefficient $2\zeta_v$ exhibited lower values for frequencies smaller than the 1st resonance. Moreover, the radiation damping generated after $\alpha_0=4$ was characterized by a linear trend, which became steeper when the shear wave velocity of the soil layer decreased. The results highlighted overall that the stiffness of the soil profile influenced in a minor degree the vertical dynamic response of suction caissons and its effect is more prominent in the high frequency range as observed by Liingaard [38].

The effect of the stiffness variation with depth is illustrated in Figure 8 for profiles B and C. The outcomes are plotted with respect to the frequency normalized by the 1st vertical resonance of the homogeneous soil layer of shear wave velocity $V_s=500\text{m/s}$, f_{1st} . The drop of stiffness is slightly shifted backward from the 1st vertical eigenfrequency of the homogeneous layer as expected ($f/f_{1st}=0.81$ - profile B and 0.70 - profile C). In addition, it appeared that this reduction of stiffness is mainly influenced by the variation of the slenderness ratio than the type of soil profile. Indeed, the scatter between the vertical stiffness coefficients obtained for profile B and C at the 1st vertical eigenfrequency for a given value of H_p/d is relatively small (less than 1%). This is consistent with the normalized vertical displacements results at the 1st eigenfrequency of the soil layer for both $H_p/d=0.25$ and 2 . Indeed, it was found that the suction caisson foundation

embedded in profile B experienced similar vertical displacements as in the case of profile C, see Figure 9a and 9c. Additionally it is of interest to note that the vertical deformed shape of suction caissons embedded in profile B and C fairly resembled the one of the same foundation installed in homogeneous soil layer with shear wave velocity $V_s=250\text{m/s}$ (profile A) at the 1st resonance. The abovementioned observations highlighted the fact that the effect of the variation of stiffness with depth on the vertical dynamic impedance is not significant for frequencies lower than 1st vertical eigenfrequency.

After the 1st vertical resonance the effect of the stiffness variation with depth on the real component became more apparent. This is showed by the stiffness component of the vertical dynamic impedance, which followed a decreasing pattern, with profile C showing larger slope increase. Moreover, the numerical outcomes indicated that the vertical dynamic stiffness for suction caissons with low slenderness ratio ($H_p/d=0.25-1$) exhibited to some extent a similar trend, presenting a softer behavior than the foundation with $H_p/d=2$. The fact that the higher is the slenderness ratio the stiffer is the response of the foundation, diverges from the results achieved for the case of suction caissons embedded in a homogeneous soil layer. The outcomes showed that the foundation response is governed by the soil stiffness at the bottom of the suction caisson, which assumed higher values as the skirt length increased. Therefore it is expected that the suction caisson with smallest slenderness ratio ($H_p/d=0.25$) and embedded in soil profile C experienced significant variation of vertical displacements along the depth. The results in Figure 9b seem to confirm this trend, while similar pattern of the normalized vertical displacements along the depth was recorded for profile A and C, since the shear wave velocity at the foundation tip assumed comparable values.

In relation to the imaginary component, the trend of the dimensionless coefficient $2\zeta_v$ is consistent with the results of the stiffness component of the dynamic vertical impedance. It is evident that the type of variation of soil modulus with depth had a significant effect on the damping for frequencies higher than the 1st vertical resonance. Indeed, it was observed an exponential trend approaching $f/f_{1st} \cong 2$ for $H_p/d=0.25$ and 1, which became more apparent for foundations embedded in profile C. While the radiation damping for the case of suction caisson with $H_p/d=2$ outlined an exponential pattern, which increases less rapidly, for frequencies higher than $f/f_{1st} = 2$. In conclusion, it can be stated that the type of soil profile became the governing parameter for the estimation of the vertical dynamic impedance, when the soil stiffness varies significantly along the depth and for frequencies greater than the 1st vertical resonance.

SUGGESTED EXPRESSIONS

Soil-structure interaction in dynamic response has been introduced also as lumped-parameter models as proposed by Wolf [11]. The spring and damping coefficients $k(\alpha_0)$ and $c(\alpha_0)$ of the fundamental lumped-parameter model (monkey-tail version) are given as follows:

$$k(\alpha_0) = 1 - \frac{\mu_1 \alpha_0^2}{1 + \frac{\mu_1^2}{\gamma_1^2} \alpha_0^2} - \mu_0 \alpha_0^2 \quad (5)$$

$$c(\alpha_0) = \gamma_0 + \frac{\mu_1}{\gamma_1} \frac{\mu_1 \alpha_0^2}{1 + \frac{\mu_1^2}{\gamma_1^2} \alpha_0^2} \quad (6)$$

where

$$\gamma_0 = \frac{V_s C_0}{r_0 K} \quad (7)$$

$$\gamma_1 = \frac{V_s C_1}{r_0 K} \quad (8)$$

$$\mu_0 = \frac{M_0 V_s^2}{r_0^2 K} \quad (9)$$

$$\mu_1 = \frac{M_1 V_s^2}{r_0^2 K} \quad (10)$$

While the values of M_0 , M_1 , C_0 , C_1 and K refer to the components of the monkey tail model as presented by Wolf [11]. Inspired by the lumped-parameter model new expressions are developed in order to provide closer approximations of the numerical results:

$$K_V(\alpha_0) = 1 - \frac{c_{1,r} \alpha_0^2}{1 + c_{2,r} (\alpha_0 - c_{4,r} \alpha_{1st})^2} + c_{3,r} (\alpha_0 - c_{5,r} \alpha_{1st})^2 \quad (11)$$

$$2\zeta_V(\alpha_0) = c_{0,i} + \frac{c_{1,i} \alpha_0^2}{[1 + c_{2,i} (\alpha_0 - c_{4,i} \alpha_{1st})]^2} + \frac{c_{2,i} (\alpha_0 - c_{4,i} \alpha_{1st})^2}{[1 + c_{3,i} (\alpha_0 - c_{5,i} \alpha_{1st})]^2} \quad (12)$$

where $c_{j,r}$ and $c_{j,i}$ with $j=0, \dots, 5$ are the coefficients for the real and imaginary component, respectively. Note that the dimensionless frequency α_0 in the abovementioned formulas is calculated by adopting the base shear wave velocity (500m/s) for the case of inhomogeneous soil profiles.

In the proposed study the calibration of the coefficients was based on the selection of numerical cases that demonstrate characteristic behavior and they were representative for the parametric study.

Suction caisson foundations can be subjected to various types of dynamic loading arising from wind, wave and earthquake actions. Two different frequency ranges were established in order to evaluate the coefficients $c_{j,r}$ and $c_{j,i}$ under seismic and wind excitations, in order to establish the required accuracy and level of complexity in the proposed expressions (see respectively Table 3 and 4). It is noteworthy that these two sets of coefficients can be used accordingly depending on the governing excitation in the design of the foundation. In offshore applications the frequency range of interested can be

narrowed up to the 1st vertical resonance of the soil [12,39], and this allowed reducing the number of coefficients $c_{j,r}$ adopted in the suggested expressions for the estimation of the real component of the vertical dynamic impedance. The frequency range of earthquake loading ($0 \leq \alpha_0 \leq 3/2(\eta\pi)$) is much greater than a typical narrowband region considered in a design based on wind loads. In addition, the accuracy of the present formulas was showed by listing the percentage of the average relative error and the maximum relative error of the suggested expressions with respect to the numerical outcomes in the frequency intervals considered, as reported in Table 3 and Table 4.

In Figure 10 the comparison between the suggested expression and the numerical outcomes of the real and imaginary component of the vertical dynamic impedance for different cases is presented in the frequency range $[0; 3/2\eta\pi]$. It was observed good agreement between the real component of the dynamic vertical impedance (Figure 10a), obtained by modifying the expression of fundamental lumped-parameter model, and the numerical results for suction caissons with slenderness ratio $H_p/d=2$ and $H_p/d=0.25$, respectively. Indeed, an average discrepancy of 6% for suction caisson with $H_p/d=2$ and 5.1% for $H_p/d=0.25$ was recorded between the abovementioned solutions; whereas a maximum difference of 11.8% and 9.30% was obtained and only at $\alpha_0 \cong 3.5$. With reference to the damping coefficient (Figure 10b) the suggested expression provided slightly scattered results with respect to the numerical outcomes (average relative error of 10%) for suction caisson with slenderness ratio of $H_p/d=2$, while the difference doubled (average relative error of 20.5%) when the slenderness ratio decreases to $H_p/d=0.25$. Additionally, it was noticed that the maximum error of the real and the imaginary component is two times the average error.

Figure 10c and 10d show that the real and imaginary component of the vertical dynamic stiffness calculated by the suggested expression resembles the ones obtained by the numerical model for suction caissons embedded in a soil layer with Poisson's ratio $\nu=0.1$ and $\nu=0.495$. A difference of less than 3% was observed for the real part of the vertical dynamic stiffness; whereas the radiation damping exhibited values which differed less than 8% with respect to the numerical ones.

In the case of stiff soil layer ($V_s=500\text{m/s}$) the real component determined by the suggested formula approximates better the numerical outcomes than for the case of medium stiff soil profile as illustrated in Figure 8e. This was proved by the fact that the average and the maximum relative error reached small values (3.2% and 8.7%, respectively). On the contrary, a slightly increase of the average and the maximum relative error was recorded for the imaginary component.

The vertical dynamic impedance of suction caissons embedded in inhomogeneous soil profile B and C estimated by Equation (11) and (12) is presented in Figure 11. The real part of the vertical dynamic impedance for both profile B and C does not overcome the numerical results more than 5%. On the other hand, the inhomogeneity of the soil layer determined a more significant effect on the imaginary component, since the average relative error reached up to 30%. The maximum relative error recorded for the imaginary part is considerably high, even if it is attained for few values in the frequency

range ($\alpha_0 = 2 - 3$) where the numerical results are characterized by a peak, which cannot be captured by the suggested expression.

Looking at Table 4, it is evident that the average discrepancy between the real component calculated by the suggested expression considering a smaller frequency interval and those of the numerical model is less than 4%, while the maximum relative error does not overcome 9%. The average relative error corresponding to the imaginary component attained values lower than 10% for cases 3-14.

It can be concluded that the suggested expressions provide a fairly good approximation of dynamic vertical stiffness of suction caissons for both the frequency ranges considered.

CONCLUSIONS

In this study numerical analyses are performed to examine the vertical dynamic response of suction caissons embedded in viscoelastic soil. The numerical modelling procedure was validated against existing analytical solutions for end bearing foundations.

A parametric study was presented to analyze the vibration characteristics of suction caissons and illustrate the effects of major parameters on the stiffness and damping properties. The results highlighted that the variation of the skirt length influenced significantly the dynamic response of the soil-caisson system. An increase of the skirt length determined a more evident reduction of the stiffness term and increase of the damping term. However, the influence of Poisson's ratio with values less than 0.40 was proven to be negligible on the vertical response of suction caissons in the frequency range investigated. At higher values of Poisson's ratio the vertical eigenfrequency increases compared to the theoretical one, while the vertical dynamic stiffness is also affected by the horizontal displacements. The numerical outcomes at nearly incompressible soil medium ($\nu=0.495$) when the horizontal displacements are constrained can be considered unreliable.

In regards with the stiffness ratio E_p/E_s , it was found that the dynamic impedances are primarily influenced by E_p/E_s at the higher frequency range. On the other hand, it was shown that the type of variation of soil modulus with depth had a significant effect on the dynamic response of suction caissons for frequencies greater than the 1st vertical resonance.

The results of this study can provide useful insights and guidance when choosing design parameters for discretized models of suction caissons.

Additionally, the developed mathematical formulas for the estimation of the vertical dynamic impedances, take into consideration important aspects of the dynamic response of suction caissons such as the site effects and the skirt length. Two sets of coefficients for dynamic stiffness and damping were provided for two different frequency intervals, which

make it possible to simplify considerably the mathematical formulas in the case of the offshore wind applications where the frequency range of interest is narrower than in earthquake loading. A good agreement was achieved between the numerical results and the suggested expressions for both frequency ranges considered. The proposed mathematical expressions can provide the basis for the implementation of soil-structure-interaction effects in the dynamic analysis of a wind turbine and its support structure.

It is emphasized that the assumptions of linearity in the soil layer and foundation materials, and the perfect contact at the soil-foundation interface can limit the validity of the proposed numerical model.

ACKNOWLEDGMENTS

This work was funded by the Danish Council for Strategic Research through the project “Advancing Beyond Shallow waterS (ABYSS) - Optimal design of offshore wind turbine support structures”. The author would also like to acknowledge funding from the Technical University of Denmark for this study.

REFERENCES

- [1] Shadlou M, Bhattacharya S. Dynamic stiffness of monopiles supporting offshore wind turbine generators. *Soil Dynamics and Earthquake Engineering* 2016; **88**:15-32. doi: 10.1016/j.soildyn.2016.04.002
- [2] Ho A, Mbistrova A. The European offshore wind industry. 2016. WindEurope
- [3] Houlsby GT, Ibsen LB, Byrne BW. Suction caissons for wind turbines. Proceedings of Frontiers in Offshore Geotechnics (ISFOG2015), London,75-93.
- [4] Bransby F, Randolph M. The effect of embedment depth on the undrained response of skirted foundations to combined loading. *Soil and Foundations* 1999; **39**(4):19-33.
- [5] Kelly RB, Byrne BW, Houlsby GT, Martin CM. Pressure chamber testing of model caisson foundations in sand. *Proceedings of the international conference on foundations* 2003;421-431.
- [6] Gourvenec S. Effect of embedment on the undrained capacity of shallow foundations under general loading. *Géotechnique* 2008; **58**(3): 177-186. doi: 10.1680/geot.2008.58.3.177
- [7] Damgaard M, Andersen JKF, Ibsen LB, Andersen LV. Time-varying dynamic properties of offshore wind turbines evaluated by modal testing. *Proceedings of the 18th international conference on soil mechanics and geotechnical engineering* 2013;234.
- [8] Adhikari S, Bhattacharya S. Dynamic analysis of wind turbine towers on flexible foundations. *Shock and Vibration* 2012;**19**. doi:10.3233/SAV-2012-0615.
- [9] Zania V. Natural vibration frequency and damping of slender structures founded on monopiles. *Soil Dynamics and Earthquake Engineering* 2014; **59**:8–20. doi:10.1016/j.soildyn.2014.01.007.

- [10] Jennings PC, Bielak J. Dynamics of building-soil interaction. *Bulletin of the Seismological Society of America* 1973; **63**(1):9-48.
- [11] Wolf JP. Spring-dashpot-mass models for foundation vibrations. *Earthquake Engineering & Structural Dynamics* 1997; **26**(9):931-949.
- [12] Damgaard M, Bayat M, Andersen LV, Ibsen LB. Assessment of the dynamic behaviour of saturated soil subjected to cyclic loading from offshore monopile wind turbine foundations. *Computers and Geotechnics* 2014; **61**:116-126.
- [13] Damgaard M, Andersen LV, Ibsen, LB. Assessment of dynamic substructuring of a wind turbine foundation applicable for aeroelastic simulations. *Wind Energy* 2015; **18**(8):1387-1401.
- [14] Novak M. Dynamic stiffness and damping of piles. *Canadian Geotechnical Journal* 1974; **11**(4): 574-598.
- [15] Novak M. Vertical vibration of floating piles. *Journal of Engineering Mechanics Division* 1997; **103**(1): 153-168.
- [16] Novak M, Aboul-Ella F, Nogami T. Dynamic soil reactions for plane strain case. *Journal of the Engineering Mechanics Division* 1978; **104**(4): 953-959.
- [17] Mylonakis G. Elastodynamic model for large diameter end-bearing shafts. *Soils and Foundations* 2001; **41**(3): 31-44.
- [18] Nogami T, Novak M. Soil-pile interaction in vertical vibration. *Earthquake Engineering & Structural Dynamics* 1976; **4**(3):277-293.
- [19] Hu CB, Wang KH, Xie KH. Time domain analysis of vertical dynamic response of a pile considering the effect of soil-pile interaction. *Chinese Journal Computational Mechanics* 2004; **21**(8): 392-399.
- [20] Anoyatis G, Di Laora R, Mylonakis G. Axial kinematic response of end-bearing piles to P waves. *International Journal for Numerical and Analytical Methods in Geomechanics* 2013; **37**(17):2877-2896. doi: 10.1002/nag.2166
- [21] Zheng C, Ding XM, Li P, Qiang F. Vertical impedance of an end-bearing pile in viscoelastic soil. *International Journal for Numerical and Analytical Methods in Geomechanics* 2014; **39**(6): 676-684. doi: 10.1002/nag.2324
- [22] Wu WB, Wang KH, Zhang ZQ, Leo CJ. Soil-pile interaction in the pile vertical vibration considering true three-dimensional wave effect of the soil. *International Journal for Numerical and Analytical Methods in Geomechanics* 2013; **37**: 2860-2876.
- [23] Liu H, Zheng C, Ding X, Qin H. Vertical dynamic response of a pipe pile in saturated soil layer. *Computers and Geotechnics* 2014; **61**, 57-66.
- [24] Biot MA. Theory of propagation of elastic waves in a fluid-saturated porous solid. I. Low frequency range. *The Journal of the acoustical Society of america* 1956; **28**(2):168-178.
- [25] Nozoe H, Gyöten Y, Mizuhata K, Fukusumi T. Estimation of Impedance and Transfer Functions for End Bearing and Floating Piles. *Proceeding of 9th CEE*, Volli, 1988; 563-568.
- [26] Deng G, Zhang J, Wu, W, Shi, X, Meng F. Soil-pile interaction in the pile vertical vibration based on fictitious soil-pile model. *Journal of Applied Mathematics* 2014; **11**. doi:10.1155/2014/905194
- [27] Roesset JM, Angelides D. Dynamic stiffness of piles. *Proceedings of the International Conference on Numerical Methods in Offshore Piling* 1980, Institution of Civil Engineers (ICE), London.
- [28] Kuhlemeyer RL. Vertical vibration of piles. *Journal of Geotechnical Engineering Division* 1979; **105**(2): 273- 287.
- [29] Latini C, Cisternino M, Zania V. Vertical dynamic stiffness of offshore foundations. *26th International Ocean and Polar Engineering Conference (ISOPE 2016)*, Rhodes, Greece, 2016.
- [30] Kaynia AM. Dynamic stiffness and seismic response of pile groups. Research Report R83-03, Massachusetts Institute of Technology. Cambridge, MA; 1982.

-
- [31] Rajapakse RKND, Shah AH. On the longitudinal harmonic motion of an elastic bar embedded in an elastic half-space. *International Journal of solids and structures* 1987;**23**(2):267-285.
- [32] Zeng X, Rajapakse RKND. Dynamic axial load transfer from elastic bar to poroelastic medium. *Journal of Mechanical Engineering ASCE* 1999; **125**(9):1048–55.
- [33] El-Marsafawi H, Kaynia AM, Novak M. The superposition approach to pile group dynamics. *Piles Under Dynamic Loads* 1992.
- [34] Wang G, Chen L, Song C. Finite-infinite element for dynamic analysis of axisymmetrically saturated composite foundations. *International Journal for Numerical Methods in Engineering* 2006; **67**(7): 916–932. doi:10.1002/nme.1654
- [35] Zhou XL, Wang JH, Jiang LF, Xu B. Transient dynamic response of pile to vertical load in saturated soil. *Mechanics Research Communications* 2009; **36**(5): 618–624. doi:10.1016/j.mechrescom.2009.01.004
- [36] Maeso O, Aznárez JJ, García F. Dynamic impedances of piles and groups of piles in saturated soils. *Computers & structures* 2005; **83**(10): 769-782.
- [37] Padron LA, Aznárez JJ, Maeso O. BEM–FEM coupling model for the dynamic analysis of piles and pile groups. *Engineering Analysis with Boundary Elements* 2007; **31**(6): 473-484.
- [38] Liingaard M. Dynamic behavior of suction caissons. PhD Thesis. Aalborg University, Denmark, 2006.
- [39] Bhattacharya S, Nikitas N, Garnsey J, Alexander NA, Cox J, Lombardi D, Nash DF. Observed dynamic soil–structure interaction in scale testing of offshore wind turbine foundations. *Soil Dynamics and Earthquake Engineering* 2013; **54**:47-60.
- [40] Latini C and Zania V. Dynamic lateral response of suction caissons. *Soil Dynamics and Earthquake Engineering* 2017. doi: 10.1016/j.soildyn.2017.05.020
- [41] Carswell W, Johansson J, Løvholt F, Arwade SR, Madshus C, DeGroot DJ, Myers AT. Foundation damping and the dynamics of offshore wind turbine monopiles. *Renewable Energy* 2015; **80**: 724-736.
- [42] Simulia DS (2013) Abaqus 6.13 User’s Manual. Dassault Systems, Providence, RI.
- [43] Rovithis EN, Parashakis H, Mylonakis GE. 1D harmonic response of layered inhomogeneous soil: analytical investigation. *Soil Dynamics and Earthquake Engineering* 2011; **31**(7): 879-890.
- [44] Gelagoti FM, Lekkakis PP, Kourkoulis RS, Gazetas G. Estimation of elastic and non-linear stiffness coefficients for suction caisson foundations. *Proceedings of the Xvi European Conference on Soil Mechanics and Geotechnical Engineering* (ECSMGE 2015), Edinburgh, UK, 2015.
- [45] Doll S, Schweizerhof K, Hauptmann R, Freischläger C. On volumetric locking of low-order solid and solid-shell elements for finite elastoviscoplastic deformations and selective reduced integration. *Engineering Computations* 2000;**17**(7), 874-902.

NOTATION

Latin upper case

E_s : soil modulus of elasticity
 E_p : Young modulus of foundation
 G : soil shear modulus
 H_s : depth of soil layer
 H_p : height of foundation
 I : moment of inertia of foundation
 K_v : dynamic stiffness coefficient -real part- force for unit displacement
 K_v^0 : static stiffness coefficient - force for unit displacement
 V : vertical reaction force at the foundation head
 V_s : soil shear wave velocity
 V_0 : surface soil shear wave velocity
 V_H : reference base soil shear wave velocity
 K : spring constant Wolf [11]
 M_0 : lumped mass 0 Wolf [11]
 M_1 : lumped mass 1 Wolf [11]
 C_0 : dashpot 0 Wolf [11]
 C_1 : dashpot 1 Wolf [11]

Latin lower case

$c_{j,r}$: coefficients for the real component
 $c_{i,r}$: coefficients for the imaginary component
 d : diameter of foundation
 n : dimensionless inhomogeneity factor
 r_0 : radius of foundation
 t_{cap} : thickness of caisson cap
 t_{skirt} : thickness of caisson skirt
 w : translational degree of freedom at the foundation head

Greek

α_0 : dimensionless frequency of soil layer
 γ_0 : dimensionless damping factor Wolf [11]
 γ_1 : dimensionless damping factor Wolf [11]
 μ_0 : dimensionless mass factor Wolf [11]
 μ_1 : dimensionless mass factor Wolf [11]
 ζ_v : damping coefficient - force for unit displacement
 ν : soil's Poisson's ratio
 ζ : hysteretic soil damping ratio
 ρ : density of soil
 ω : circular frequency

TABLES

Table 1. Static end bearing pile and floating stiffness obtained from the numerical models and the analytical solutions Nogami and Novak [18], Hu et al. [19], Wu et al. [22] and Zheng et al. [21].

Reference	Nogami and Novak [18]	Hu et al. [19]	Wu et al. [22]	Zheng et al. [21]	Numerical model
$K_v/E_s d$	74.3	74.1	70.1	73.6	73.9

Table 2. Dimensionless parameters and cases selected in the parametric analysis.

Case Nr.	H_s [m]	H_p [m]	d [m]	ν	H_p/d	H_s/d	Soil Profile				E_p/E_s
							Type	n	V_H [m/s]	V_0/V_H	
1	10	10	1	0.40	10	10	A	1	67	1	893
2	10	10	5	0.35	2	2	A	1	250	1	30
3	30	10	5	0.35	2	6	A	1	250	1	30
4	30	7.5	5	0.35	1.5	6	A	1	250	1	30
5	30	5	5	0.35	1	6	A	1	250	1	30
6	30	2.5	5	0.35	0.5	6	A	1	250	1	30
7	30	1.25	5	0.35	0.25	6	A	1	250	1	30
8	30	10	5	0.10	2	6	A	1	250	1	37
9	30	10	5	0.20	2	6	A	1	250	1	34
10	30	10	5	0.40	2	6	A	1	250	1	29
11	30	10	5	0.495	2	6	A	1	250	1	27
12	30	10	5	0.35	2	6	A	1	300	1	21
13	30	10	5	0.35	2	6	A	1	400	1	12
14	30	10	5	0.35	2	6	A	1	500	1	8
15	30	10	5	0.35	2	6	B	0.25	500	0.01	8
16	30	5	5	0.35	1	6	B	0.25	500	0.01	8
17	30	1.25	5	0.35	0.25	6	B	0.25	500	0.01	8
18	30	10	5	0.35	2	6	C	0.5	500	0.1	8
19	30	5	5	0.35	1	6	C	0.5	500	0.1	8
20	30	1.25	5	0.35	0.25	6	C	0.5	500	0.1	8
21	30	10	5	0.40	2	6	A	1	250	1	29
22	30	10	5	No U1 0.40	2	6	A	1	250	1	29
23	30	10	5	No U1,U2 0.495	2	6	A	1	250	1	27
24	30	10	5	No U1 0.495 No U1,U2	2	6	A	1	250	1	27

Table 3. Constants of the suggested expression for the dynamic vertical stiffness and damping coefficient in the dimensionless frequency range $\alpha_0 \in [0; 3/2\eta\pi]$.

Case Nr.	Real component (K_v)							Imaginary component ($2\zeta_v$)							
	$c_{1,r}$	$c_{2,r}$	$c_{3,r}$	$c_{4,r}$	$c_{5,r}$	max error (%)	average error (%)	$c_{0,i}$	$c_{1,i}$	$c_{2,i}$	$c_{3,i}$	$c_{4,i}$	$c_{5,i}$	max error (%)	average error (%)
3	0.065	1.57	-0.0068	0.890	0.50	11.8 ($\alpha_0 = 3.5$)	6.0	-0.040	0.035	1.70	7.00	0.735	0.942	25.0 ($\alpha_0 = 3.0$)	9.9
7	0.042	3.00	-0.0068	0.890	0.64	9.3 ($\alpha_0 = 3.5$)	5.1	-0.020	0.020	1.30	9.00	0.750	0.942	38.1 ($\alpha_0 = 2.6$)	20.5
8	0.092	1.50	-0.0072	0.945	0.68	9.6 ($\alpha_0 = 7.0$)	2.2	-0.047	0.048	1.30	5.00	0.760	1.03	24.6 ($\alpha_0 = 1.5$)	7.5
11	0.045	0.83	-0.0085	0.935	0.50	6.9 ($\alpha_0 = 2.7$)	1.9	-0.091	0.040	1.10	4.00	0.840	1.02	24.7 ($\alpha_0 = 1.7$)	4.8
14	0.058	2.45	-0.0045	0.890	0.67	8.7 ($\alpha_0 = 1.8$)	3.2	-0.038	0.026	1.70	8.00	0.745	0.950	26.9 ($\alpha_0 = 2.6$)	11.3
15	0.062	3.00	-0.0130	0.790	0.0	8.9 ($\alpha_0 = 3.1$)	2.4	0.080	0.030	0.20	1.70	0.420	0.94	82.0 ($\alpha_0 = 2.2$)	29.0
17	0.040	11.00	-0.0120	0.790	0.0	9.8 ($\alpha_0 = 4.0$)	3.0	0.100	0.030	0.07	4.00	0.420	0.89	77.9 ($\alpha_0 = 2.2$)	28.9
18	0.080	6.20	-0.0270	0.680	0.0	11.7 ($\alpha_0 = 3.1$)	4.3	0.058	0.019	0.15	0.30	0.250	0.95	65.9 ($\alpha_0 = 1.9$)	15.6
20	0.035	5.00	-0.0400	0.680	0.0	8.6 ($\alpha_0 = 2.5$)	1.5	0.070	0.019	0.10	0.16	0.390	1.10	28.3 ($\alpha_0 = 2.4$)	9.4

Table 4. Constants of the suggested expression for the dynamic vertical stiffness and damping coefficient in the dimensionless frequency range $\alpha_0 \in [0; 4]$.

Case Nr.	Real component (K_v)							Imaginary component ($2\zeta_v$)							
	$c_{1,r}$	$c_{2,r}$	$c_{3,r}$	$c_{4,r}$	$c_{5,r}$	max error (%)	average error (%)	$c_{0,i}$	$c_{1,i}$	$c_{2,i}$	$c_{3,i}$	$c_{4,i}$	$c_{5,i}$	max error (%)	average error (%)
3	0.065	1.57	0.0	0.890	0.0	7.6 ($\alpha_0 = 2.9$)	3.9	-0.035	0.035	1.50	6.70	0.735	0.94	17.0 ($\alpha_0 = 1.7$)	8.7
7	0.042	3.00	0.0	0.890	0.0	8.1 ($\alpha_0 = 2.2$)	2.8	-0.020	0.019	1.30	7.80	0.760	0.93	37.0 ($\alpha_0 = 2.6$)	12.3
8	0.092	1.50	0.0	0.945	0.0	7.6 ($\alpha_0 = 2.9$)	2.2	-0.047	0.048	1.30	5.00	0.760	1.03	24.6 ($\alpha_0 = 1.54$)	10.3
11	0.045	0.83	0.0	0.950	0.0	6.1 ($\alpha_0 = 1.9$)	2.8	-0.091	0.040	1.10	4.00	0.840	1.02	24.7 ($\alpha_0 = 3.3$)	9.3
14	0.058	2.45	0.0	0.890	0.0	8.7 ($\alpha_0 = 2.1$)	3.4	-0.031	0.026	1.60	7.80	0.745	0.95	22.9 ($\alpha_0 = 2.6$)	9.8

FIGURE LEGENDS

Figure 1: Foundation geometries and soil profiles investigated for the case of caissons.

Figure 2: Variation of the vertical stiffness and damping coefficients with respect to the dimensionless frequency (a) and distribution of the pile normalized displacement along the depth at the 1st vertical eigenfrequency of the soil layer (b) for case 1. Variation of the vertical stiffness (c) and damping coefficients (d) with respect to the dimensionless frequency for case 2.

Fig. 3: Variation of the vertical dynamic stiffness and damping coefficients with respect to the non-dimensional frequency. Effect of the foundation geometry on the real component (a) and the imaginary component (b) for case 3.

Figure 4: Effect of the skirt length of the caisson on the real component (a) and the imaginary component (b) for cases 3-7. Distribution of the suction caisson normalized displacement along the skirt at the 1st vertical eigenfrequency (c) and 2nd vertical eigenfrequency (d) of the soil layer.

Figure 5: Variation of the vertical dynamic stiffness with respect to the non-dimensional frequency. Effect of Poisson's ratio on the real component (a) and the imaginary component (b) for $H_p/d=2$. Effect of the horizontal displacements on the real component for $\nu=0.4$ (c) and for $\nu=0.495$ (d).

Figure 6: Quilt-style contour plot of pressure in the soil medium for case 11 (a) and 24 (b) at the 1st vertical resonance.

Figure 7: Variation of the vertical dynamic stiffness with respect to the non-dimensional frequency. Effect of the stiffness of homogeneous soil layer (profile A) on the real component (a) and the imaginary component (b) for $H_p/d=2$.

Figure 8: Variation of the vertical dynamic stiffness with respect to the non-dimensional frequency. Effect of the inhomogeneous soil layer (profile B) on the real component (a) and the imaginary component (b). Effect of the inhomogeneous soil layer (profile C) on the real component (c) and the imaginary component (d).

Figure 9: Distribution of the suction caisson's vertical normalized displacements along the depth for $H_p/d=0.25$ at the 1st resonance (a) and $f=1.8f_{1st}$ (b) and for $H_p/d=2$ at the 1st resonance (c) and $f=1.8f_{1st}$ (d), considering homogeneous (profile A) and inhomogeneous (profile B and C) soil layer.

Figure 10: Comparison between the simplified expression and the numerical outcomes with respect to the non-dimensional frequency. Effect of the skirt length of the caisson on the real component (a) and the imaginary component (b) for cases 3 and 7. Effect of Poisson's ratio on the real component (c) and the imaginary component (d) for $H_p/d=2$. Effect of the shear wave velocity of the soil layer on the real component (e) and the imaginary component (f) for $H_p/d=2$.

Figure 11: Comparison between the simplified expression and the numerical outcomes with respect to the non-dimensional frequency. Effect of the stiffness of homogeneous soil layer (profile B) on the real component (a) and the imaginary component (b) for $H_p/d=2$ and 0.25. Effect of the stiffness of homogeneous soil layer (profile C) on the real component (c) and the imaginary component (d) for $H_p/d=2$ and 0.25.

FIGURES

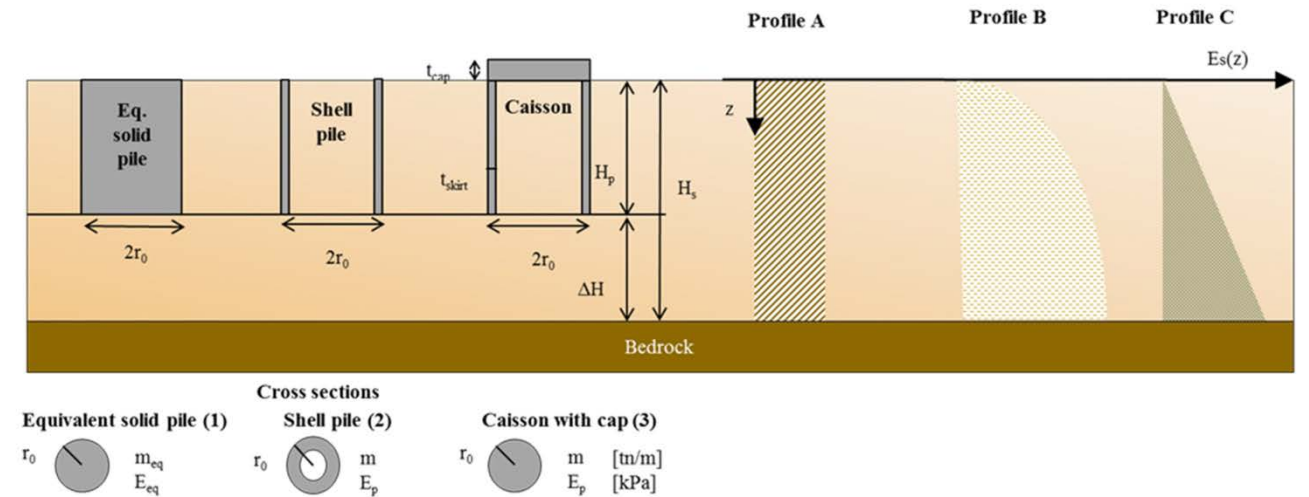


Figure 1: Foundation geometries and soil profiles investigated for the case of caissons.

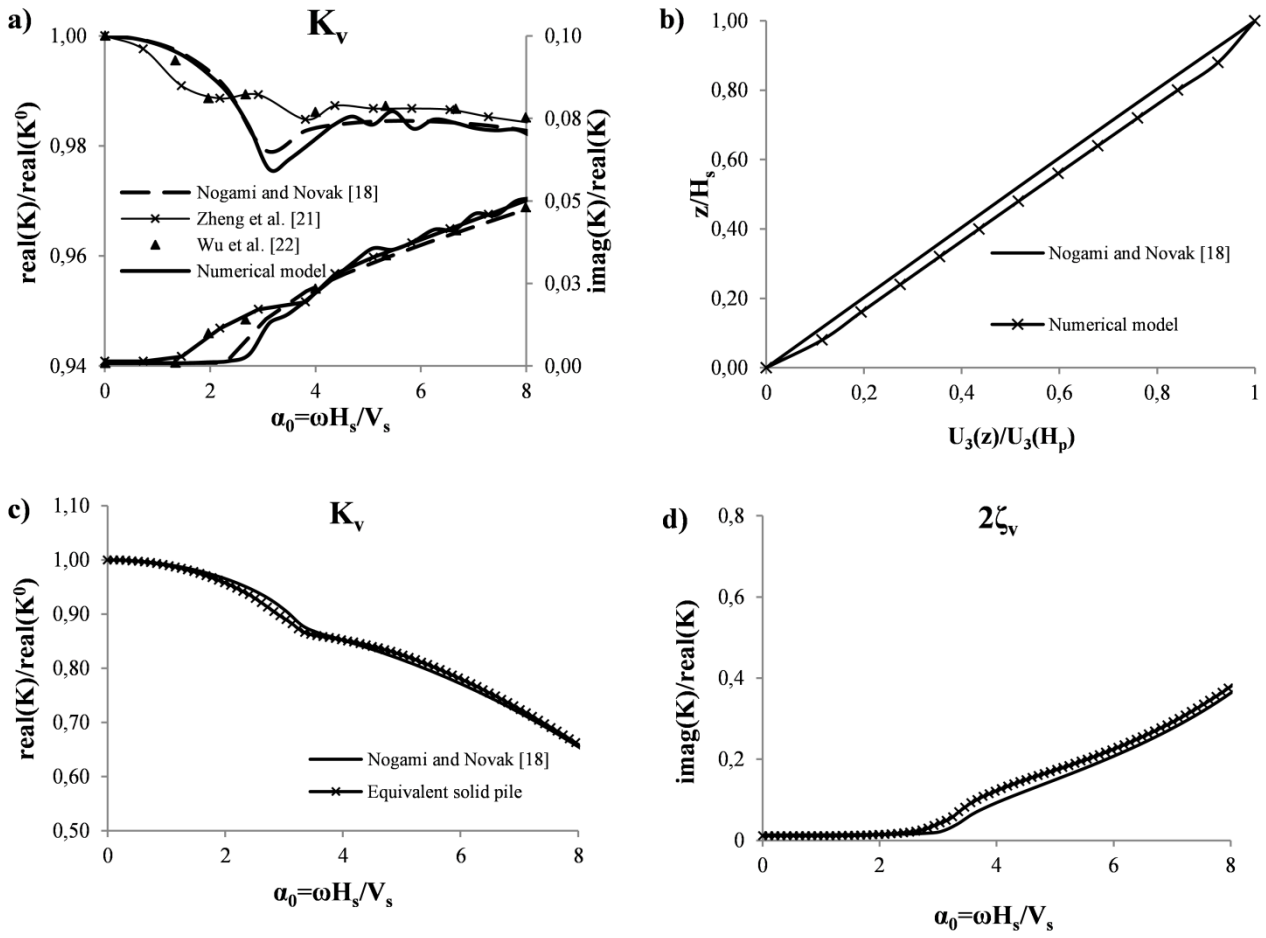


Figure 2: Variation of the vertical stiffness and damping coefficients with respect to the dimensionless frequency (a) and distribution of the pile normalized displacement along the depth at the 1st vertical eigenfrequency of the soil layer (b) for case 1. Variation of the vertical stiffness (c) and damping coefficients (d) with respect to the dimensionless frequency for case 2.

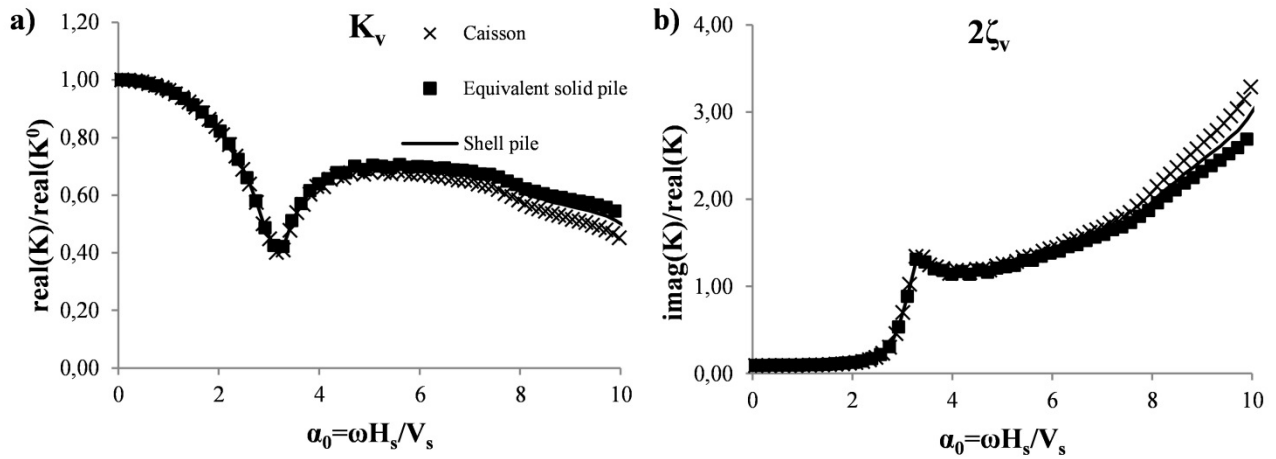


Figure 3: Variation of the vertical dynamic stiffness and damping coefficients with respect to the non-dimensional frequency. Effect of the foundation geometry on the real component (a) and the imaginary component (b) for case 3.

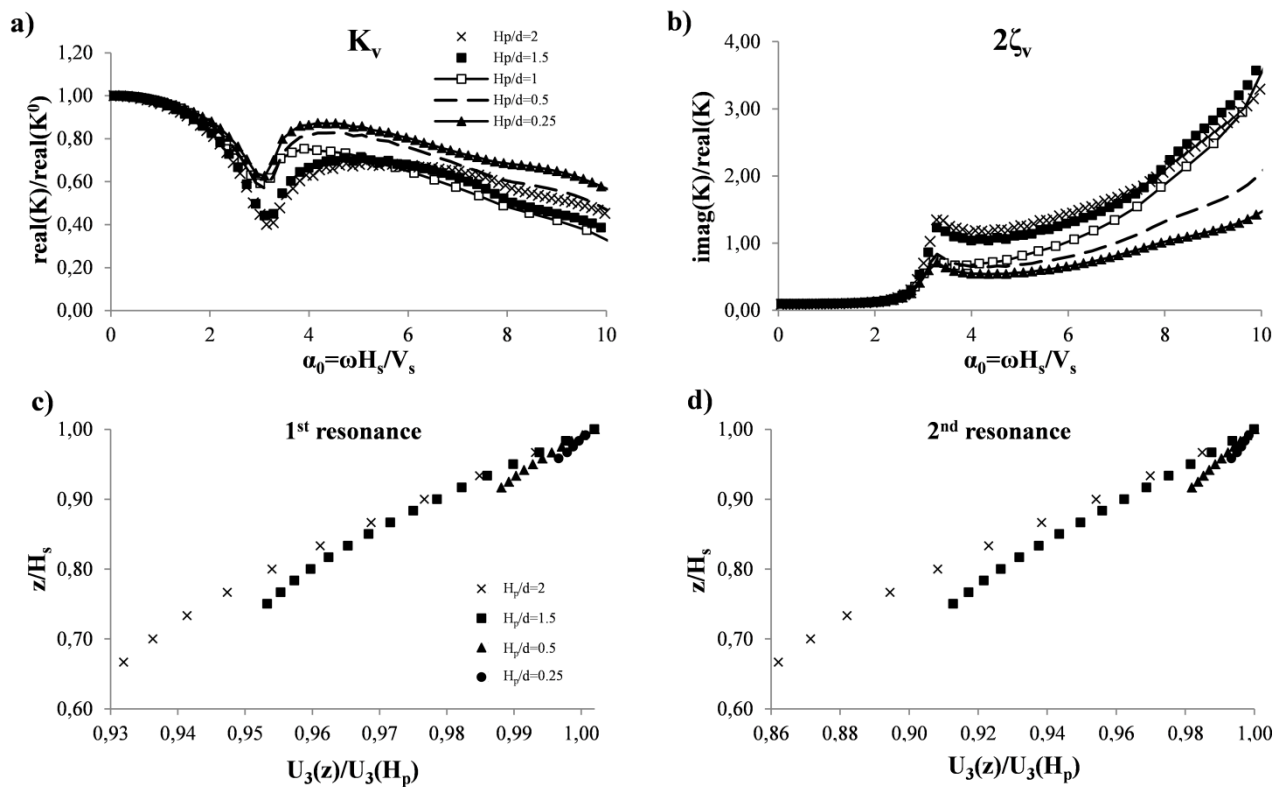


Figure 4: Effect of the skirt length of the caisson on the real component (a) and the imaginary component (b) for cases 3-7. Distribution of the suction caisson normalized displacement along the skirt at the 1st vertical eigenfrequency (c) and 2nd vertical eigenfrequency (d) of the soil layer.

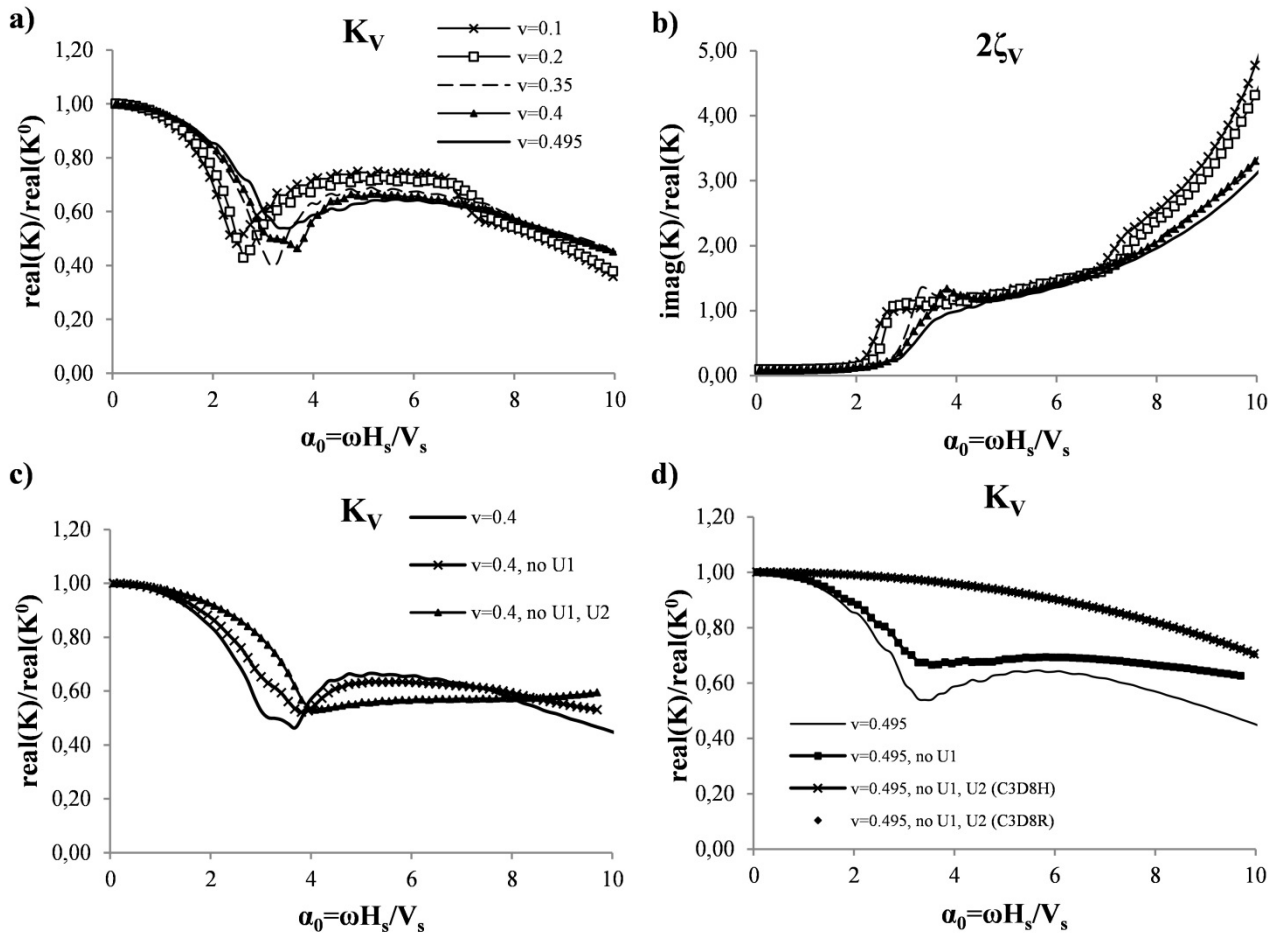


Figure 5: Variation of the vertical dynamic stiffness with respect to the non-dimensional frequency. Effect of Poisson's ratio on the real component (a) and the imaginary component (b) for $H_p/d=2$. Effect of the horizontal displacements on the real component for $\nu=0.4$ (c) and for $\nu=0.495$ (d).

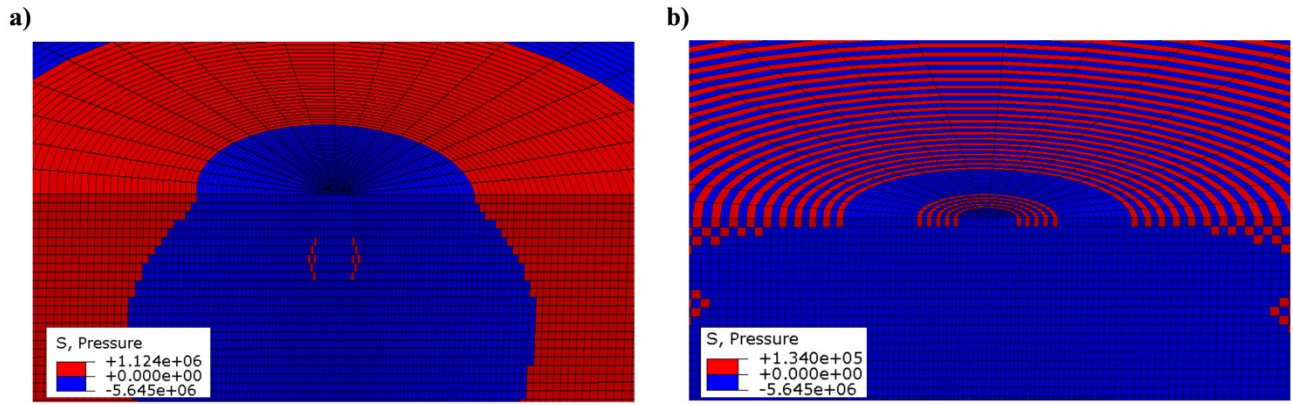


Figure 6: Quilt-style contour plot of pressure in the soil medium for case 11 (a) and 24 (b) at the 1st vertical resonance.

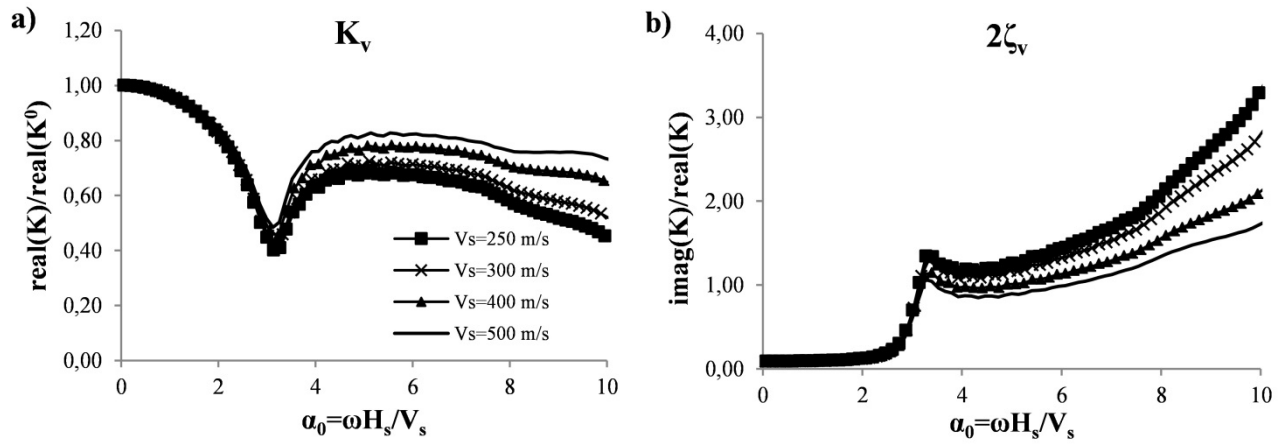


Figure 7: Variation of the vertical dynamic stiffness with respect to the non-dimensional frequency. Effect of the stiffness of homogeneous soil layer (profile A) on the real component (a) and the imaginary component (b) for $H_p/d=2$.

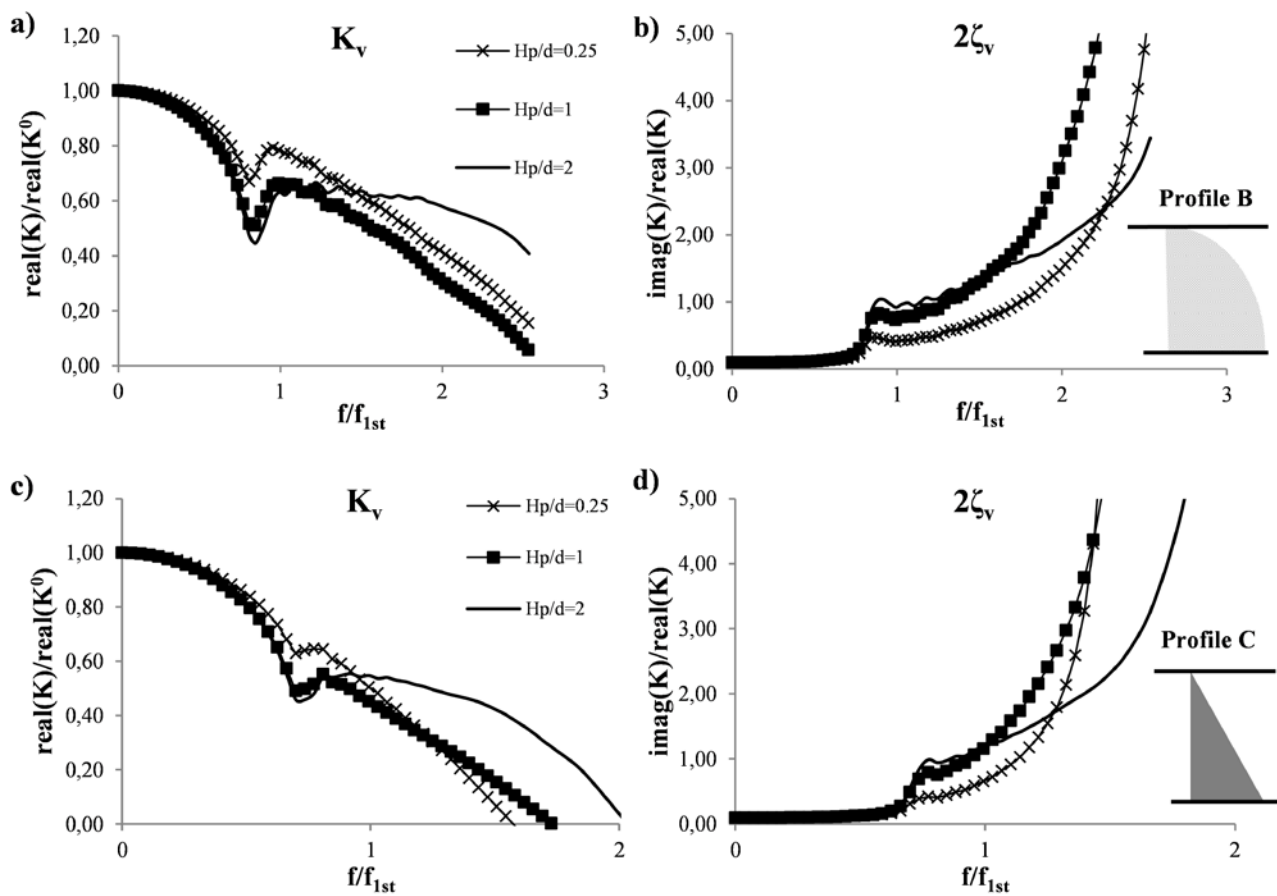


Figure 8: Variation of the vertical dynamic stiffness with respect to the non-dimensional frequency. Effect of the inhomogeneous soil layer (profile B) on the real component (a) and the imaginary component (b). Effect of the inhomogeneous soil layer (profile C) on the real component (c) and the imaginary component (d).

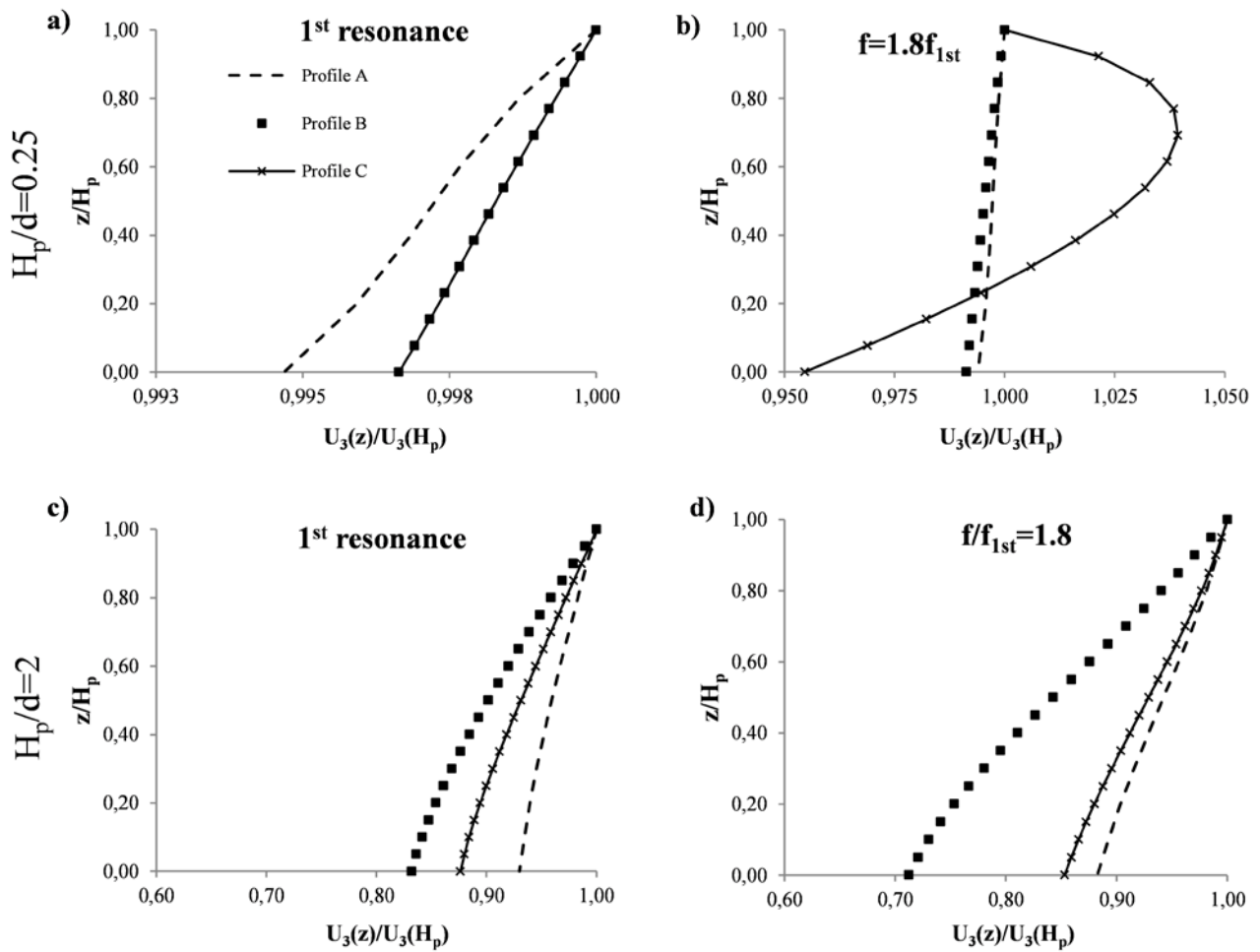


Figure 9: Distribution of the suction caisson's vertical normalized displacements along the depth for $H_p/d=0.25$ at the 1st resonance (a) and $f=1.8f_{1st}$ (b) and for $H_p/d=2$ at the 1st resonance (c) and $f=1.8f_{1st}$ (d), considering homogeneous (profile A) and inhomogeneous (profile B and C) soil layer.

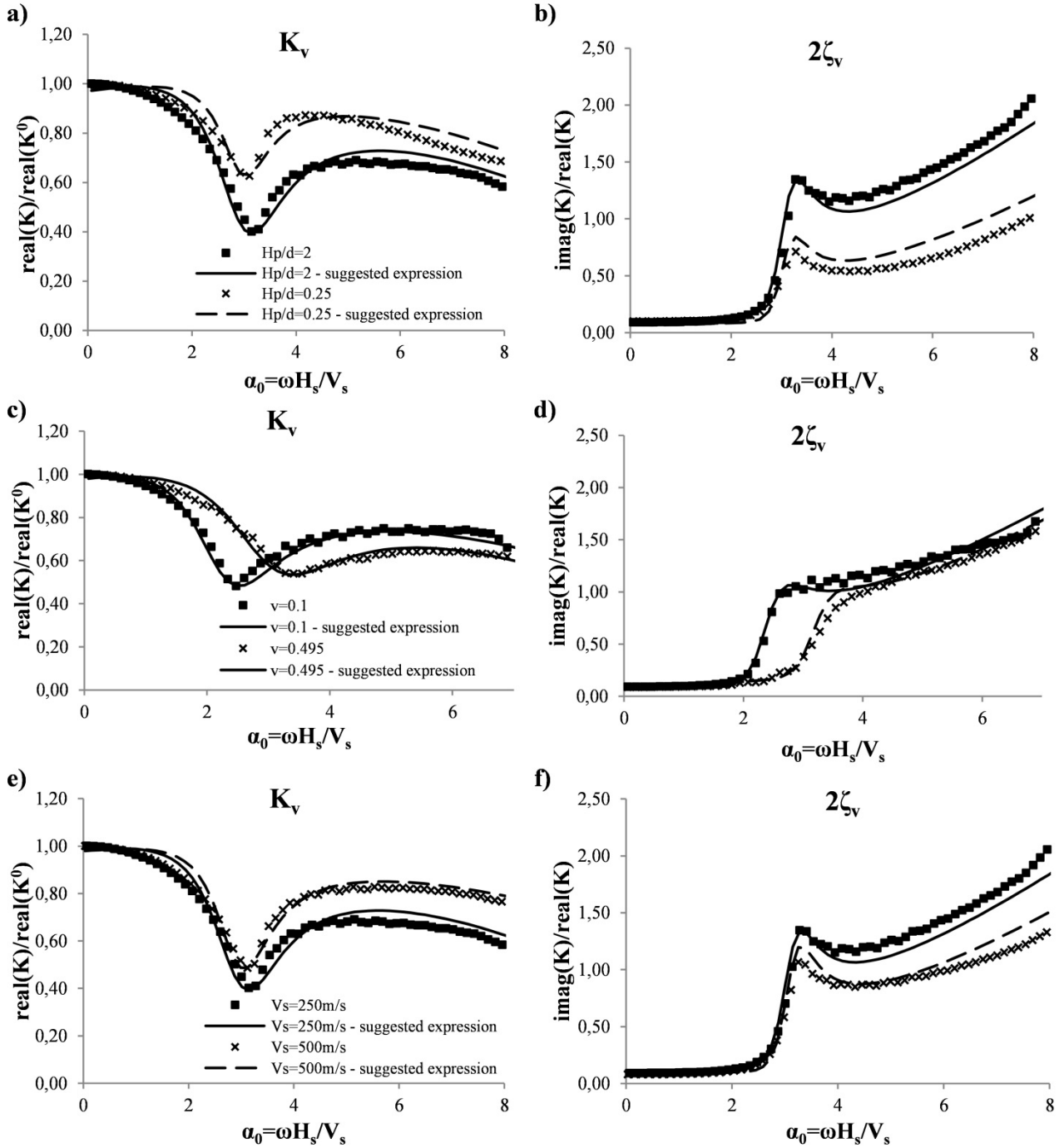


Figure 10: Comparison between the simplified expression and the numerical outcomes with respect to the non-dimensional frequency. Effect of the skirt length of the caisson on the real component (a) and the imaginary component (b) for cases 3 and 7. Effect of Poisson's ratio on the real component (c) and the imaginary component (d) for $H_p/d=2$. Effect of the shear wave velocity of the soil layer on the real component (e) and the imaginary component (f) for $H_p/d=2$.

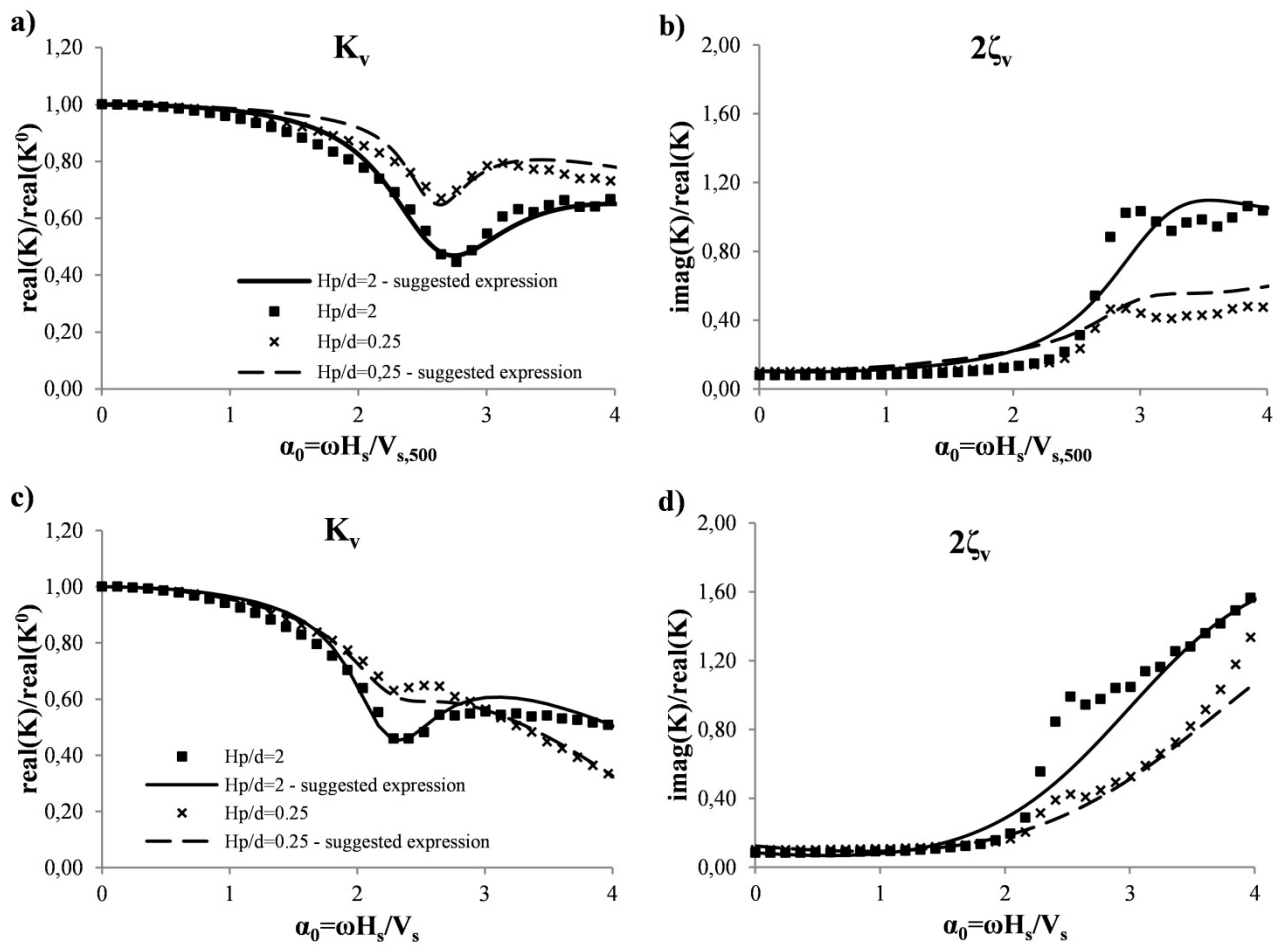


Figure 11: Comparison between the simplified expression and the numerical outcomes with respect to the non-dimensional frequency. Effect of the stiffness of homogeneous soil layer (profile B) on the real component (a) and the imaginary component (b) for $H_p/d=2$ and 0.25. Effect of the stiffness of homogeneous soil layer (profile C) on the real component (c) and the imaginary component (d) for $H_p/d=2$ and 0.25.



Paper VI

Vertical Dynamic Stiffness of Offshore Foundations

C. LATINI, M. CISTERNINO AND V. ZANIA

Published in: Proceeding of the 26th International Ocean and Polar Engineering Conference,
2016

Vertical Dynamic Stiffness of Offshore Foundations

Chiara Latini¹, Michele Cisternino¹, Varvara Zania¹

¹Civil Engineering Department, Technical University of Denmark
Lyngby, Denmark

ABSTRACT

Nowadays, pile and suction caisson foundations are widely used to support offshore structures which are subjected to vertical dynamic loads. The dynamic soil-structure interaction of floating foundations (foundations embedded in a soil layer whose height is greater than the foundation length) is investigated by numerical analyses of representative finite element models. The 3D numerical model is compared and validated with existing analytical solutions. A parametric study is carried out analyzing the effect of the slenderness ratio H_p/d and the height and the stiffness of the soil layer on the dynamic stiffness and damping.

KEY WORDS: soil-structure interaction; dynamic stiffness; damping; floating foundations; numerical modelling; elastodynamic analytical solution.

INTRODUCTION

Nowadays, the overall concept design for offshore wind farms is developing towards different foundation solutions. So far the support structures for offshore wind turbines have been classified into two main types: fixed (or grounded to the seabed) and floating. The majority of installed or operating turbines are supported on fixed foundation system (Bhattacharya, 2014), while deep installations require jackets structures with floating piles or with suction caissons. These types of foundations are subjected to dynamic load such as wind.

Houlsby et al. (2005) investigated the possibility of deploying suction caissons as offshore wind turbine foundations. In his work it was showed that suitable soil conditions are required and the functionality of suction caissons is limited up to water depth of approximately 40m. Suction caissons are skirted shallow foundations characterized by a slenderness ratio (foundation embedded length to foundation width) lower than 4 and they are put in place by creating negative pressure inside the caisson skirt by pumping out the water (Byrne and Houlsby, 2006). Consequently, suction caissons are preferred to driven piles, since their installation does not require heavy duty equipment. Due to its features this type of foundation is receiving more attention in the current research on deep water installations.

The way a foundation interacts during vibrations with the surrounding

soil influences considerably the dynamic characteristics of the foundation (Kramer, 1996). Hence it is fundamental to accurately evaluate the dynamic stiffness and damping of the soil-foundation system. Considering the estimation of the vertical dynamic soil-pile interaction many studies have been carried out by previous researchers by applying analytical solutions and numerical methods. Most of the past studies are based on the assumption that the soil around the foundation is a linear elastic single-phase medium. They can be categorized as follows:

- Rigorous analytical continuum solutions for end bearing piles (Nogami and Novak, 1976), where the soil was modelled as viscoelastic layer. In this formulation the displacement and the resistance factor of the soil layer were obtained neglecting the radial displacement of the soil medium.
- Winkler type analytical solution (Novak, 1974; Novak et al., 1978; Mylonakis, 2001; Hu et al., 2004; Wu et al., 2013; Zheng et al., 2014). For dynamic problems the use of Winkler foundation coefficients based on Baranov's equation for in plane and out plane vibration of a disk has been recommended by Novak (1974). An improved model incorporating in the analysis the normal and shear stresses acting on the upper and lower faces of a horizontal soil element by integrating the governing equations over the thickness of the soil layer has been developed by Mylonakis (2001). Wu et al. (2013) and Zheng et al. (2014) provided an extended model to study the vertical dynamic response of an end bearing pile by considering both the radial and the vertical displacement of the soil layer.
- Numerical continuum finite element solutions (Roesset & Angelides, 1980), where the soil is treated as an elastic continuum and the pile is assumed to have a rigid cross section and it is modelled as series of regular beam segments.

The abovementioned studies are founded on the assumption that the pile is embedded in a single-phase medium. However, the offshore environment is characterized by fully saturated soil and by water pressure acting on the foundation.

In literature there are a few works in which the dynamic response of pile foundations installed in a saturated elastic layer over a rigid bedrock was investigated, see Li et al. (2004) and Liu et al. (2014).

On the other hand the response of floating piles has been investigated either numerically (Kuhlemeyer, 1979) or analytically (Novak, 1977;

Nozoe et al., 1988; Deng et al., 2014; Zheng et al., 2015). However, the dynamic response of suction caissons has received less attention (Liingaard, 2006). In the work of Liingaard (2006) the dynamic stiffness coefficients were determined, considering linear viscoelastic soil and modelling the suction caisson using a coupled BE/FE model in homogeneous halfspace comparing the obtained results with analytical solutions for surface foundations.

The purpose of the current study is to examine the vertical dynamic response of floating piles and suction caissons in different soil conditions for the estimation of the dynamic stiffness and damping coefficients with respect to the frequency. Consequently, 3D FE models were established and the dynamic stiffness to vertical loading was determined. The results of the numerical models have been compared and validated respectively with the rigorous analytical solutions of soil-end bearing pile vibration by Nogami & Novak (1976), Hu et al. (2004), Wu et al. (2013), Zheng et al. (2014). Thereafter a parametric analysis investigated the effects of the stiffness and height of the soil layer on the soil-foundation system response. Moreover, the dynamic stiffness and damping are analyzed varying the slenderness ratio H_p/d . The frequency dependent stiffness and damping of suction caissons illustrates the effect of the cap on the vertical vibration.

METHODOLOGY

3D finite element models in the commercial software ABAQUS (Simulia, 2013) have been developed to investigate the dynamic impedances of the suction caisson.

The following assumptions are considered in the numerical models: 1) linear elastic isotropic behavior of the pile; 2) linear viscoelastic isotropic behavior of soil with hysteretic type damping and 3) perfect contact between the foundation and the soil during the analysis.

The symmetry of the problem has allowed taking into account only half of the foundation and the surrounding soil. The pile consists of steel with diameter $d=1\text{m}$, length $H_p=10\text{m}$, Young's modulus $E_p = 210\text{ GPa}$ and Poisson's ratio $\nu=0.35$. The pile foundation has thickness of $t=d/100$. Two different piles modelling approaches are used: 1) shell pile, where the foundation is modelled by its shell and 2) equivalent solid pile, for which equivalent material properties are applied to match the axial stiffness. The foundation is embedded in a soil layer with hysteretic type damping of $\zeta=5.0\%$ and constant profile of shear wave velocity $V_s=250\text{-}500\text{m/s}$.

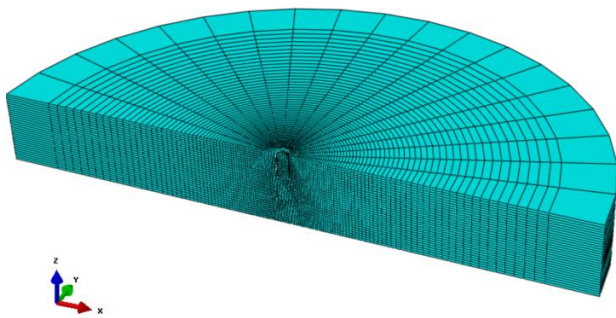


Fig. 1 Finite element model of the pile and the surrounding soil.

Hexahedral elements are deployed to discretize the soil domain of diameter $100d$ and height $H_s=30d=30\text{m}$. The boundaries are modelled by placing infinite elements in order to simulate the far field soil and avoid spurious reflection. Full contact among the pile lateral surface and the surrounding soil is ensured to prevent relative motion between them. Steady state linearized response of the model subject to harmonic excitation in the frequency domain is performed. The dynamic impedance K_v at the level of the pile head is then directly calculated as

axial force N , when the head of the pile is subjected to unit vertical displacement, v . The mesh size needs to be small enough to capture the stress wave accurately. A mesh size of at least 10 to 20 elements per wave length is used as good approximation for the frequency range of interest, including up to the 2nd eigenfrequency of the soil layer $\alpha_0=3/2\eta\pi$, where $\eta=\sqrt{2(1-\nu)/(1-2\nu)}$. Note that α_0 is a dimensionless frequency related to the eigenfrequency of the soil layer, since it is given as the product of the wave number and the height of the soil layer. The 3D model comprising the mesh refinement is shown in Fig. 1.

NUMERICAL STUDY

Two layered soil profile characterized by high stiffness contrast is analyzed. In Fig. 2 the two types of 3D numerical models developed to account for different depths of the surface soil layer with respect to the length of the foundation are shown. In the study the soil profile with height equal to the length of the pile is defined as Profile 1, while the one with increased height as Profile 2.

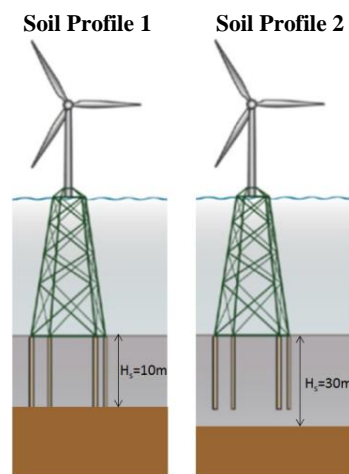


Fig. 2 Illustration of the two soil profiles investigated in this study.

First, the results only for the end bearing pile foundation (Profile 1) are compared with several analytical formulations available in the literature. The different pile modelling procedures with continuum elements and shell elements are implemented in order to achieve a direct comparison with the analytical solutions and consistency with the respective assumptions. As concerning floating piles (Profile 2), the effect of the height and stiffness of the soil stratum on the soil-foundation system response are further examined. A parametric study clarifies the role of the slenderness ratio and the foundation diameter on the vertical dynamic behavior of floating foundations.

VALIDATION OF THE NUMERICAL MODEL

The numerical results for the end bearing pile case are compared respectively with the different analytical solutions formulated by Nogami & Novak (1976), Hu et al. (2004), Wu et al. (2013) and Zheng et al. (2014). The reference case analyzed only for the validation of the numerical model consists of a solid concrete pile with diameter $d=1\text{m}$ and length $H_p=10\text{m}$, embedded in a soil layer with constant shear wave velocity $V_s=68\text{m/s}$, hysteretic material damping $\zeta=1.0\%$ and Poisson's ratio $\nu=0.40$. The two normalized dynamic components (real part of the complex valued stiffness term divided by the corresponding static component K^0 and imaginary part of the complex valued stiffness terms divided by the corresponding dynamic component K_v) of the vertical

stiffness is presented with respect to the non-dimensional frequency α_0 . In Fig. 3 the real (K_v) and the imaginary ($2\zeta_v$) part of the dynamic vertical impedance are shown. Both the analytical solutions and the numerical model exhibit a drop of stiffness at the 1st eigenfrequency of the soil layer ($\alpha_0=1/2\eta\pi$). However, the analytical formulation developed by Zheng et al. (2014) and Wu et al. (2013) results in an additional cut-off frequency around $\alpha_0=2$. Zheng et al. (2014) motivated it by the fact that the radial displacements were accounted for in the solution. Nevertheless, the trend of the abovementioned analytical formulations does not resemble the numerical model pattern, where there are not any limitations on the dynamic strains induced in the soil. In addition, the dynamic vertical stiffness is overestimated by the outcome of the implementation of the analytical solutions by Wu et al. (2013) and Zheng et al. (2014). After the 1st resonance of the soil layer, it is observed a linear decrease of the dynamic stiffness. The imaginary part of the dynamic component of the vertical impedance is combined with the generated damping due to soil-foundation interaction. The radiation damping is produced for frequencies higher than the 1st eigenfrequency of the soil layer. And after the 1st resonance of the soil medium all the analytical studies converge to the same linear trend of the viscous type radiation damping. The numerical model compares well with the analytical studies by Novak and Nogami (1976) and Hu et al. (2004). Hence this provides a validation of the numerical modelling methodology which is hereafter applied to a parametric study.

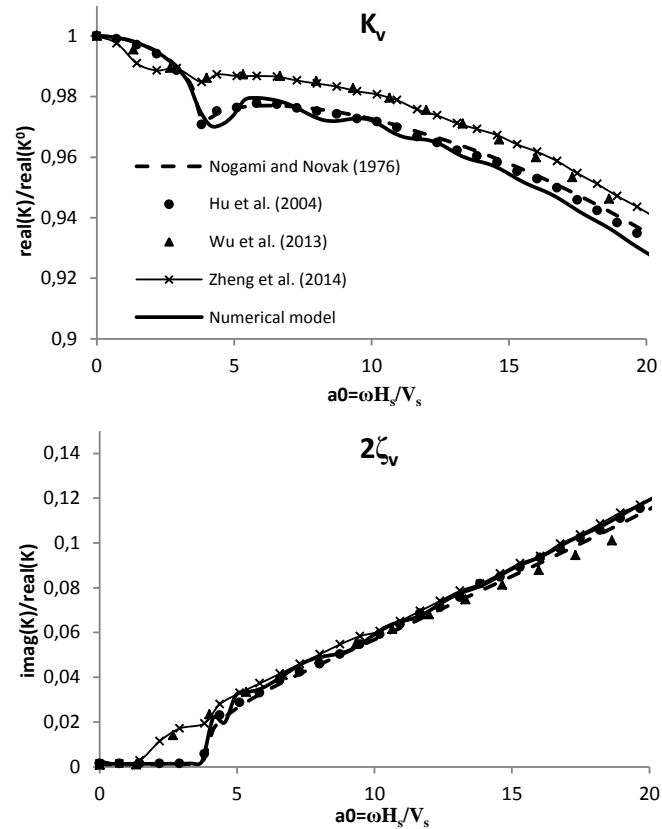


Fig. 3 Variation of the vertical stiffness and damping with respect to the dimensionless frequency for Profile 1.

PARAMETRIC STUDY

The dynamic response of floating piles (Profile 2) is analyzed by employing finite element analysis described in the previous section. In the current study the effects of the pile diameter, the height and the stiffness of the soil layer on the soil-floating pile response are

investigated. This makes it possible to discuss the role of some popular dimensionless parameters such as the stiffness ratio E_p/E_s and the slenderness ratio H_p/d on the dynamic behavior of the foundation.

The cases selected in this study including also the dimensionless parameters are listed in Table 1, while the rationale for their selection was to examine foundations (piles and suction caisson) with different slenderness ratio ($H_p/d=20, 10, 2$ and 1 –case 8, 1, 6 and 7, respectively) embedded in a homogenous soil layer with various constant profiles of shear wave velocity ($V_s=250,400$ and 500m/s – case 1, 4 and 5, respectively), thickness ($t=r_0/50$), hysteretic material damping ($\zeta=5.0\%$) and Poisson's ratio ($\nu=0.35$).

Table 1. Dimensionless parameters and cases selected in the parametric analysis.

Case Nr.	H_s [m]	H_p [m]	d [m]	V_s [m/s]	H_p/d	E_p/E_s
1 (Ref.)	30	10	1	250	10	60
2	15	10	1	250	10	60
3	20	10	1	250	10	60
4	30	10	1	400	10	23
5	30	10	1	500	10	15
6	30	10	5	250	2	60
7	30	5	5	250	1	60
8	30	20	1	250	20	60

The reference case analyzed is $d=1\text{m}$, $V_s=250\text{m/s}$, $H_p=10\text{m}$ and $H_s=30\text{m}$. Three different caisson modellings were deployed for case 6: 1) equivalent solid pile, for which equivalent material properties are applied to match the axial stiffness; 2) shell pile, where the foundation is modelled by its shell and 3) caisson with cap, as illustrated in Fig. 4. Concerning the caisson model with cap, the foundation skirt and the cap had respectively thickness of $t_{\text{skirt}}=d/100$ and $t_{\text{cap}}=5t_{\text{skirt}}$.

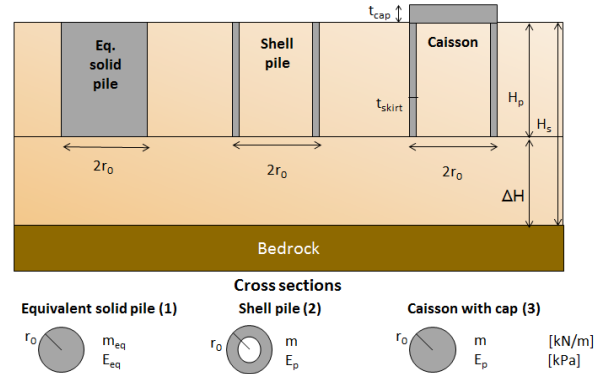


Fig. 4 Foundation geometries investigated for the case of caissons.

Effect of the height of the soil layer

In Fig. 5 the real (K_v) and the imaginary ($2\zeta_v$) components of the vertical stiffness are shown for different heights of the soil layer (case 1, 2 and 3). The drop of stiffness at the 1st eigenfrequency of the soil layer ($\alpha_0=1/2\eta\pi$) becomes more marked in the case of floating piles with $H_s/H_p=3$. In addition, it is observed a constant linear increase in the dynamic stiffness pattern for frequency higher than the 1st eigenfrequency of the soil layer. In the frequency range $\alpha_0=6-12$ it is

noticed that the vertical dynamic stiffness has higher values than the corresponding static component. The radiation damping (viscous type) is generated for frequencies higher than the 1st eigenfrequency of the soil layer. The three cases investigated exhibit identical slope, while the offset recorded approximately at the 1st resonance of the soil medium increases with H_s , implying higher radiation damping for deeper soil deposits.

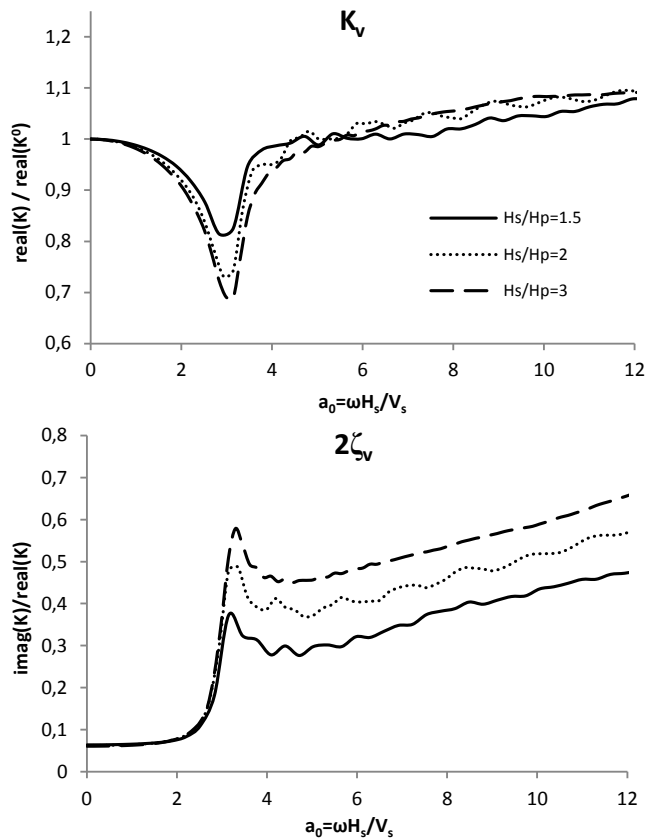


Fig. 5: Variation of the vertical dynamic stiffness and damping coefficients with respect to the non-dimensional frequency for Profile 2. Effect of the height of the soil layer on the real component and the imaginary component for cases 1, 2 and 3.

Effect of the stiffness of the soil layer

In Fig. 6 the real (K_v) and the imaginary ($2\zeta_v$) parts of the dynamic vertical impedance are presented for different values of the shear wave velocity of the soil layer ($V_s=250, 400$ and 500m/s - case 1, 4 and 5, respectively). The same values as in the reference case are used for the height of the foundation and the soil layer. Slightly scattered results are recorded by increasing the shear wave velocity of the soil layer.

The reduction of stiffness observed at the 1st eigenfrequency of the soil layer is to some extent less marked for stiff soil profiles ($V_s=500\text{m/s}$). The fact that the oscillation at the 1st resonance becomes more distinct when the soil stiffness decreases, is concurrent with the outcomes of Liingaard (2006). In the intermediate frequency interval ($\alpha_0=\eta\pi/2-7$) the vertical dynamic impedance does not seem to be substantially affected by the increase of the shear wave velocity of the soil medium. When the soil is very stiff, the real component of the stiffness tends to be considerably independent of the frequency after 1st resonance. These findings are in agreement with the work of Nogami et al. (1976) for the case of end bearing piles. In addition, a quite linear increase of the pattern is recorded in the high frequency range.

The analysis shows that increasing the shear wave velocity of the soil layer or decreasing E_p/E_s the damping decreases. In addition, the radiation damping generated after the 1st eigenfrequency is characterized by a linear trend which can be characterized as viscous.

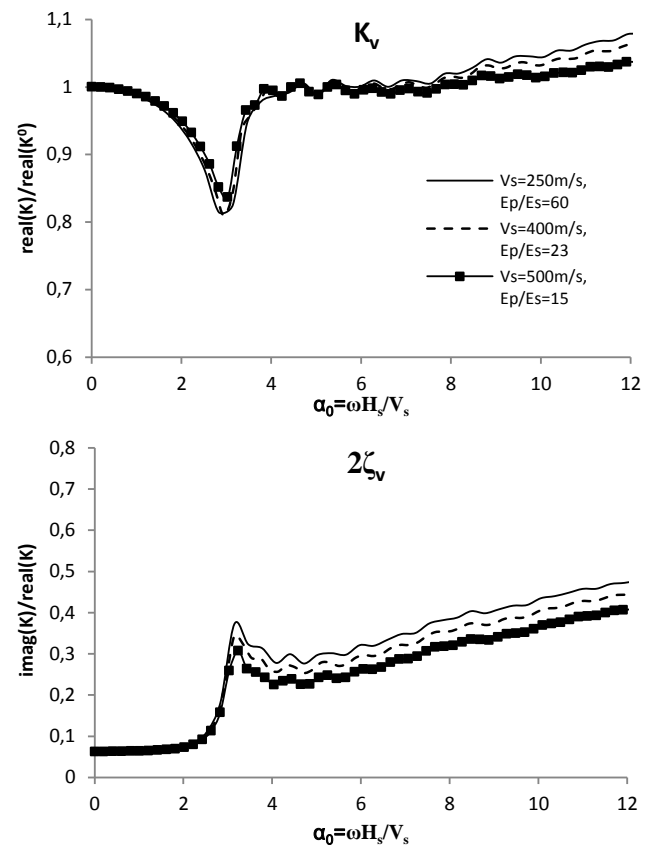


Fig. 6: Variation of the vertical dynamic stiffness and damping coefficients with respect to the non-dimensional frequency. Effect of the stiffness of the soil layer on the real component and the imaginary component for cases 1, 4 and 5.

Effect of the foundation geometry

Several numerical models were established to investigate the effect of the foundation geometry on the dynamic impedances particularly for suction caissons (case 6). In Fig. 7 the real (K_v) and the imaginary ($2\zeta_v$) part of the vertical dynamic impedances are shown for the case of the suction caisson modelled as 1) shell pile, 2) caisson with the cap and 3) equivalent solid pile. It was observed that all the three models attained the same reduction in stiffness at the 1st eigenfrequency of the soil medium. The numerical outcomes of the caisson with cap, solid equivalent pile and the shell pile modellings match almost perfectly up to $\alpha_0=8$. This indicates that the presence of the lid does affect slightly the vertical dynamic response of the foundation in the high frequency range. Moreover, the discrepancy in the numerical outcomes between the caisson with cap, equivalent solid and shell pile model observed in the high frequency interval might also be due to the fact that viscous damping is applied to the soil within the skirts of the caisson with cap and shell pile model. However, it might be concluded that the geometry of the foundation influenced slightly the vertical dynamic response for frequencies higher than $\alpha_0=8$. The numerical models displayed similar results concerning the radiation damping associated to the vertical component of the stiffness.

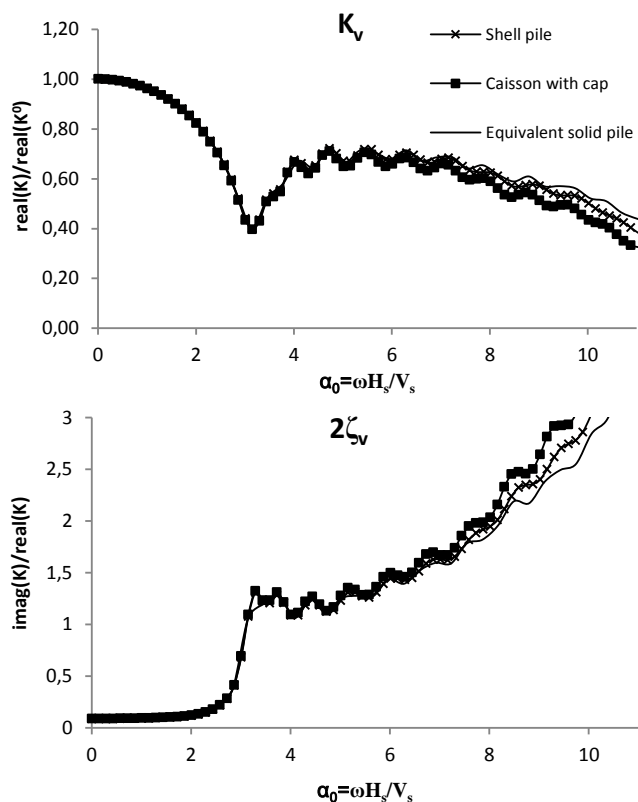


Fig. 7: Variation of the vertical dynamic stiffness and damping coefficients with respect to the non-dimensional frequency. Effect of the foundation geometry on the real component and the imaginary component for case 6.

Effect of the slenderness ratio

In Fig. 8 the real (K_v) and the imaginary ($2\zeta_v$) parts of the vertical dynamic impedance are displayed, varying the slenderness ratio H_p/d (cases 1, 6, 7 and 8). The parametric study is conducted keeping the same height and shear wave velocity of the soil layer as in the reference case. It is evident that two types of dynamic trend can be distinguished adopting the lateral rigidity criteria proposed by Randolph (1981). In the case of long piles ($H_p/d \geq 10$, case 1 and 8) the reduction in stiffness at the 1st eigenfrequency of the soil layer ($\eta\pi/2$) becomes more marked by decreasing the slenderness ratio. The dynamic impedance is moderately sensitive to the variation of H_p/d and it is characterized with some extent by an almost constant pattern for frequencies higher than the 1st resonance. Indeed, any drop of stiffness at the 2nd eigenfrequency of the soil medium is recorded. This might be attributed to the fact that response of the system is controlled to large extent by the dissipative soil medium as observed in Novak (1977) for end bearing piles. The corresponding results for shallow foundations ($H_p/d < 10$, case 6 and 7) are also plotted in Fig.8. The dynamic stiffness coefficient is substantially reduced in these cases. Note that the diameter of the caisson is larger hence this might be associated with the drop in the stiffness and increase of damping compared to the cases 1 and 8.

Furthermore, it is observed that the dynamic stiffness increases up to the 2nd horizontal eigenfrequency of the soil medium ($3\pi/2$), while just after $\alpha_0 = 3\pi/2$ this is reversed by a sudden decrease. This trend could be explained by recalling that the dynamic response is controlled by the caisson than the soil. In addition, the outcomes show that only a small change in the numerical results is detected from $H_p/d=1$ to $H_p/d=2$. It

can be noticed that the magnitude of the dynamic vertical impedance overall increases with the skirt length at higher frequencies ($\alpha_0 > 6$) as reported by Liingaard (2006).

Note that the difference between cases 1 and 8, and cases 6 and 7 can be also due to the effect of H_p/d derived by comparing impedances that refer to the same diameter.

The radiation damping presents an increased step variation on the frequency interval for $H_p/d < 10$. When referring to long piles (case 1 and 8) the imaginary part exhibits values lower than the damping ratio in the frequency range $\alpha_0 = 0 - \eta\pi/2$.

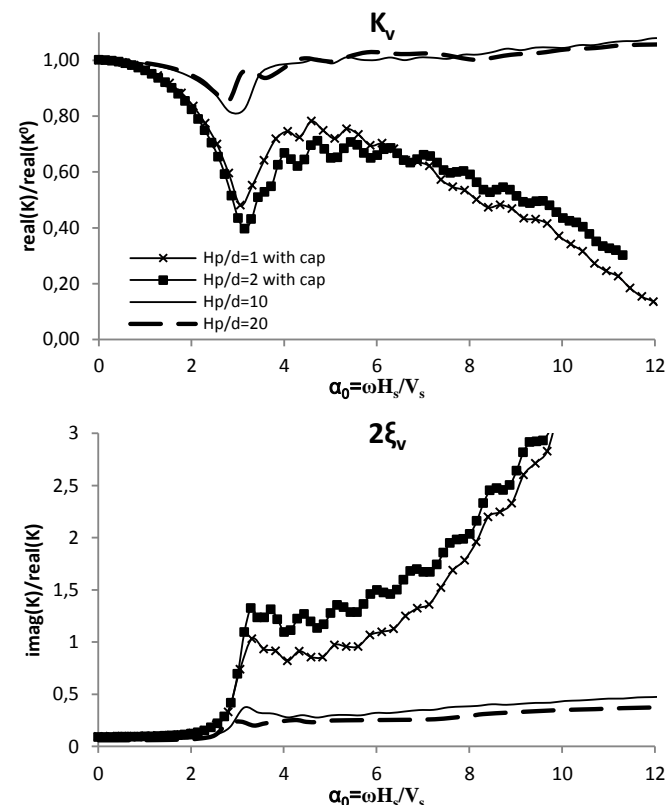


Fig. 8: Variation of the vertical dynamic stiffness with respect to the non-dimensional frequency. Effect of the slenderness ratio on the real component and the imaginary component for cases 1, 6, 7 and 8.

In Fig. 9 the vertical displacement of the foundation is plotted as a function of the depth at the 1st vertical resonance, highlighting the difference observed on the dynamic behavior between shallow foundations (case 6) and flexible piles (case 1).

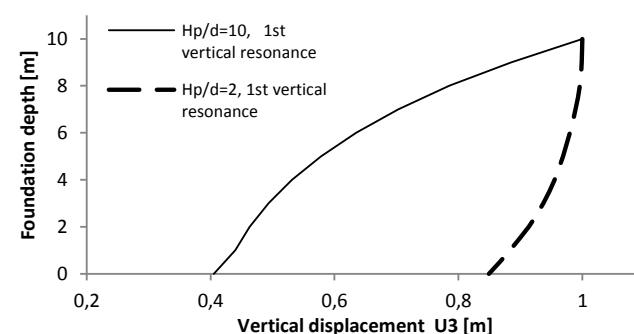


Fig. 9: Distribution of the foundation vertical displacement along the depth at the 1st vertical eigenfrequency of the soil layer for the case 1 and 6.

The deflected shape obtains a different curvature for the two cases, while the flexible pile seems to result in less displacement at the tip compared to the rigid caisson.

CONCLUSIONS

In this study numerical analysis is performed to investigate the vertical dynamic response of piles and suction caissons embedded in viscoelastic soil. Predictions from the numerical models have been found to be in good agreement with existing rigorous analytical solutions. A parametric study has been conducted to analyze the vibration characteristics and the effects of main parameters of floating foundations.

The dynamic soil-pile interaction analysis of floating piles has shown that the dynamic impedances are slightly affected by increasing E_p/E_s . On the other hand an increase of the height of the soil layer on the vertical dynamic impedance determines a more evident reduction of stiffness at the 1st resonance and consequently the damping generated is higher.

Moreover, the foundation diameter d has been found quite substantial parameter to determine the behavior of the foundation.

The proposed numerical model establishes a versatile practical tool that provides the soil-foundation vertical impedance coefficient. This might be applied in the frame of the substructure approach, to perform complete dynamic soil-structure interaction analyses of structures on such kind of foundations.

However, the suggested model is limited by the assumptions of linearity in the soil layer and foundation materials, and the perfect contact at the soil-foundation interface.

ACKNOWLEDGEMENTS

This work has been supported by the Danish Council for Strategic Research through the project "Advancing Beyond Shallow waterS (ABYSS) - Optimal design of offshore wind turbine support structures".

REFERENCES

- Bhattacharya, S (2014). *Challenges in design of foundations for offshore wind turbines*, Institution of Engineering and Technology 10/2014.
- Byrne, BW and Houlsby, GT (2006). "Assessing novel foundation options for offshore wind turbines," *Proc of the world maritime technology conference*, London.
- Deng, G, Zhang, J, Wu, W, Shi, X, and Meng, F (2014). "Soil-pile interaction in the pile vertical vibration based on fictitious soil-pile model," *J App Math*, 2014, 11.
- Houlsby, GT, Ibsen, LB, and Byrne, BW (2005). "Suction caissons for wind turbines," *Proc Frontiers in Offshore Geotechnics*, London, (ISFOG), 75-93.
- Hu, CB, Wang, KH, and Xie, KH (2004). "Time domain analysis of vertical dynamic response of a pile considering the effect of soil-pile interaction," *Chinese J Comp Mech*, 21(8), 392-399.
- Kramer, SL (1996). *Geotechnical Earthquake engineering*, Prentice Hall.
- Kuhlemeyer, RL (1979). "Vertical vibration of piles," *J Geotechnical Eng Div*, 105(2), 273- 287.
- Li, Q, Wang, KH and Xie, KH (2004). "Vertical vibration of an end bearing pile embedded in saturated soil," *Acta Mech Sin*, 36(4),435-442 [in Chinese].
- Liingaard, M (2006). *Dynamic behavior of suction caissons*, PhD Thesis, Aalborg University.

- Mylonakis, G (2001). "Elastodynamic model for large diameter end-bearing shafts," *Soils and foundations*, 41(3), 31-44.
- Nogami, T, and Novak, M (1976). "Soil-pile interaction in vertical vibration," *Earthquake Engineering & Structural Dynamics*, 4(3), 277-293.
- Novak, M (1974). "Dynamic stiffness and damping of piles," *Canadian Geotechnical J*, 11(4), 574-598.
- Novak, M (1977). "Vertical vibration of floating piles," *J Eng Mech Div*, 103(1), 153-168.
- Novak, M, and Aboul- Ella, F (1978). "Impedance functions of piles in layered media," *J Eng Mech Div*, 104(6), 643-661.
- Nozoe, H, Gyöten, Y, and Fukusumi, T (1985). "Dynamic analysis of a soil-pile system by the finite Fourier-Henkel transformation method – Case of a floating pile in horizontal vibration," *Theor App Mech*, 33, 377-392.
- Randolph, MF (1981). "The response of flexible piles to lateral loading," *Geotechnique*, 31(2), 247-59.
- Roesset, JM and Angelides, D (1980). "Dynamic stiffness of piles," *Proc of International Conference on Numerical Methods in Offshore Piling*, London.
- Simulia, DS (2013). *Abaqus 6.13 User's Manual*, Dassault Systems, Providence, RI.
- Wu, WB, Wang, KH, Zhang, ZQ and Leo CJ (2013). "Soil-pile interaction in the pile vertical vibration considering true three-dimensional wave effect of the soil," *Int J Numer Anal Meth Geomech*, 37, 2860-2876.
- Zeng, X and Rajapakse, RKND (1999). "Dynamic axial load transfer from elastic pile to poroelastic medium," *J Eng Mech*, 125(9),1048-1055.
- Zheng, C, Ding, XM, Li, P, and Qiang, F (2014). "Vertical impedance of an end-bearing pile in viscoelastic soil," *Int J Numer Anal Methods Geomech*, 39(6), 676-684.
- Zheng, C, Kouretzis, GP, Sloan, SW, Liu, H, and Ding, X (2015). "Vertical vibration of an elastic pile embedded in poroelastic soil," *Soil Dynamics and Earthquake Eng*, 77,177-181.

Paper VII

Modelling of constitutive behaviour of sand in the low stress regime: an implementation of SANISAND

C. LATINI, V. ZANIA AND C. TAMAGNINI

Published in: Proceeding of the 19th International Conference on Soil Mechanics and Geotechnical Engineering, 2017

Modelling of constitutive behavior of sand in the low stress regime: an implementation of SANISAND

Modélisation du comportement constitutif du sable dans un régime à faible contrainte: mise en œuvre sur SANISAND

Chiara Latini & Varvara Zania

Civil Engineering Department, Technical University of Denmark, Denmark, chila@byg.dtu.dk

Claudio Tamagnini

Civil Engineering Department, University of Perugia, Italy

ABSTRACT: The paper provides background information for the modification of SANISAND (2004) constitutive model in order to capture the mechanical behavior of sand in the low stress regime. In the implementation of this model in finite element programs, computational difficulties arise due to the gradient discontinuity which occurs at the apex of the yield surface when it deals with soil deposits subjected to low initial confining pressure. This singularity often causes the stress-point integration algorithm to perform inefficiently or even fail. In this study a hyperbolic yield surface was introduced to eliminate the singular tip from the original yield surface, by adjusting only one parameter. Undrained triaxial compression tests on Toyoura sand are performed to show the performance of the proposed formulation.

RÉSUMÉ: Cet article fournit des informations de base pour la modification du modèle constitutif de SANISAND (2004) afin de cerner le comportement mécanique du sable dans un régime à faible contrainte. Lors de l'utilisation de ce modèle dans des logiciels à éléments finis, des problèmes de calcul apparaissent à cause de la discontinuité du gradient qui se produit au sommet de la surface de limite élastique, pour des dépôts de sol soumis à une faible pression initiale de confinement. Cette singularité provoque souvent une mauvaise exécution de l'algorithme d'intégration des points de contrainte, voir son échec. Dans cette étude, une surface de limite élastique hyperbolique a été introduite pour éliminer le point singulier de la surface de limite élastique initiale, en ajustant uniquement un paramètre. Des essais de compression triaxiale non drainés sur du sable de Toyoura sont effectués pour montrer la performance de la formulation proposée.

KEYWORDS: anisotropy; sand; constitutive relations; plasticity; critical state, hyperbolic approximation

1 INTRODUCTION

Understanding the behavior of offshore marine sands subjected to cyclic loadings is essential for predicting the response of offshore foundations under monotonic and cyclic loading conditions. Therefore, it is necessary a constitutive material model that properly describes the characteristic behavior of water saturated soil under cyclic loading.

Constitutive models based on perfect plasticity are capable to reproduce nonlinearity and irreversible behavior of the soil when it is subjected to monotonic loadings. On the contrary, they are not sufficient to describe the highly non-linear stress path dependent shear stiffness, the accumulation of pore pressure, permanent shear strains and volumetric strains under repeated number of cycles. In the last two decades several advanced constitutive models (Cubrinovski and Ishihara 1998, Gajo and Wood 1999, Mroz and Pietruszczak 1983, Wang et al. 1990) have been carried out to investigate the cyclic/dynamic behavior of sands.

The three dimensional critical state two-surface plasticity models for sands proposed by Dafalias and Manzari (2004) is a conceptually simple constitutive model, which adequately describes induced anisotropy, history-dependent dilatancy and fabric evolution of sands. It is part of the SANISAND (Simple ANIso-tropic SAND) models developed by Dafalias and collaborators (Manzari and Dafalias 1997, Li and Dafalias 2000, Dafalias and Manzari 2004, Dafalias et al. 2004, Taiebat and Dafalias 2007).

Furthermore, this version of SANISAND has been implemented as a User defined Material (UMAT) code in Fortran for the Finite Element Code ABAQUS (Gudehus et al.

2008) and it can also be compiled together with IncrementalDriver (Niemunis 2008). Nonetheless, the implementation of SANISAND (2004) model in finite element programs involves computational difficulties due to the gradient discontinuities which occur at the tip of the yield surface. This implies that inefficient performance of the stress integration scheme might be experienced when the response of soil deposits in the low stress regime is investigated.

The objective of the present study is to propose a formulation which is able to model the mechanical behavior of sand subjected to low initial confining pressure. Therefore, the formulation aims at introducing a rounded hyperbolic yield surface to eliminate the singular apex from the original yield criterion. Due to this modification, the model is denoted the modified SANISAND (2004) model. The modification of the constitutive model is shown in details in multiaxial formulation. In addition, the performance of the modified SANISAND (2004) model is presented with respect to that of the original model (Dafalias and Manzari, 2004) to simulate undrained triaxial compression tests for loose sand subjected to low initial confining pressure.

1.1 Notation and assumptions

In this study the soil mechanics convention is considered, where compression is assumed positive and effective stresses are taken into account.

To represent vector and tensor quantities, the following standard notation is adopted. For any two vectors, $\mathbf{u}, \mathbf{v} \in \mathbb{R}^3$, the dot product is defined as: $\mathbf{u} \cdot \mathbf{v} = u_i v_i$ and the dyadic product as $[\mathbf{v} \otimes \mathbf{w}]_{ij} = v_i w_j$. For any two second-order tensors \mathbf{X}, \mathbf{Y}

$\in \mathcal{L}$, $\mathbf{X} \cdot \mathbf{Y} = X_{ij}Y_{ij}$ and $[\mathbf{X} \otimes \mathbf{Y}]_{ijkl} = X_{ij}Y_{kl}$. The quantity $\|\mathbf{X}\| = \sqrt{\mathbf{X} \cdot \mathbf{X}}$ represents the Euclidean norm of the second-order tensor \mathbf{X} .

Considering small deformations and rotations, the total strain rate can be divided into elastic ($\dot{\boldsymbol{\epsilon}}^e$) and plastic term ($\dot{\boldsymbol{\epsilon}}^p$):

$$\dot{\boldsymbol{\epsilon}} = \dot{\boldsymbol{\epsilon}}^e + \dot{\boldsymbol{\epsilon}}^p \quad (1)$$

where $\boldsymbol{\epsilon}$ is the strain tensor.

2 THE MODIFIED SANISAND (2004) MODEL IN TRIAXIAL SPACE

2.1 Yield surface

In the proposed formulation the elastic stress-strain relationship is defined as reported in the work of Dafalias and Manzari (2004). Regarding the yield surface, SANISAND (2004) constitutive model suggested the following expression:

$$f = \{(\mathbf{s} - p\boldsymbol{\alpha}) \cdot (\mathbf{s} - p\boldsymbol{\alpha})\}^{1/2} - \sqrt{\frac{2}{3}}mp = 0 \quad (2)$$

where \mathbf{s} is the deviatoric stress tensor and p is the pressure. While the stress-ratio quantity $\boldsymbol{\alpha}$ is called the back-stress ratio and it is the rotational hardening variable of the yield surface, which represents the slope in p - q space of the bisector of the yield surface. The coefficient m is the tangent of half the opening angle of the yield surface at the origin. However, the open conical yield surface is characterized by a singular point, which is the apex as shown in Figure 1.

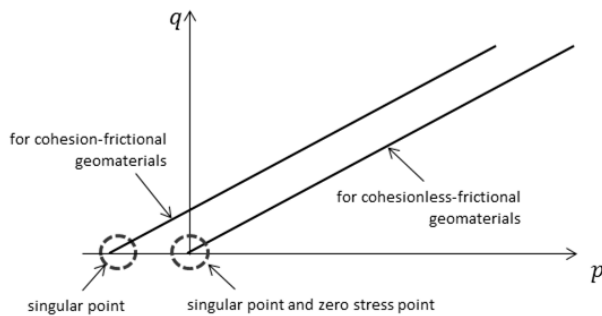


Figure 1: SANISAND (2004) yield surface in p - q plane.

In order to avoid the gradient discontinuity at the apex, a hyperbolic yield surface was introduced. Therefore, the yield surface was regularized by adopting the trigonometric rounding technique of Sloan and Booker (1986). The main features of this yield surface are: 1) continuous and differentiable at all stress states and 2) approximate SANISAND (2004) yield function as closely as required by adjusting one parameter. The model still maintains an open conical yield surface, which can rotate around the cone apex at the origin of the stress space, and three additional open wedge-type surfaces with apex at the origin of stress space: the critical state surface (CSS), the bounding surface (BS) and the dilatancy surface (DS).

In the present formulation the cohesion c was first introduced as $p_t = c \cot \phi$ and then, the hydrostatic pressure p^* is given as:

$$p^* = p + p_t \quad (3)$$

where ϕ is the friction angle. The distance between the vertex of the original yield surface and the hyperbolic yield

surface is defined by the constant parameter b , which is a fraction of p_t :

$$b = \eta p_t, \text{ with } \eta \in (0,1] \quad (4)$$

Therefore, the hyperbolic yield function can be written as follows:

$$f = \{(\mathbf{s} - p^*\boldsymbol{\alpha}) \cdot (\mathbf{s} - p^*\boldsymbol{\alpha}) + (mb)^2\}^{1/2} - \sqrt{\frac{2}{3}}mp = 0 \quad (5)$$

In the triaxial stress plane the equation of the yield surface is proposed in terms of the triaxial stress quantities $p = (\sigma_1 + 2\sigma_3)/3$ and $q = (\sigma_1 - \sigma_3)$, where σ_1 and σ_3 are respectively the maximum and the minimum principle stress:

$$f^* = \{(q - \alpha p^*)^2 + m^2 b^{*2}\}^{1/2} - mp^* = 0 \quad (6)$$

where $b^* = \sqrt{3/2}b$.

In Figure 2a and 2b the yield surface of the modified SANISAND (2004) model is illustrated in triaxial stress plane and in the multiaxial space, respectively along with the CSS (α^c), the BS (α^b) and the DS (α^d).

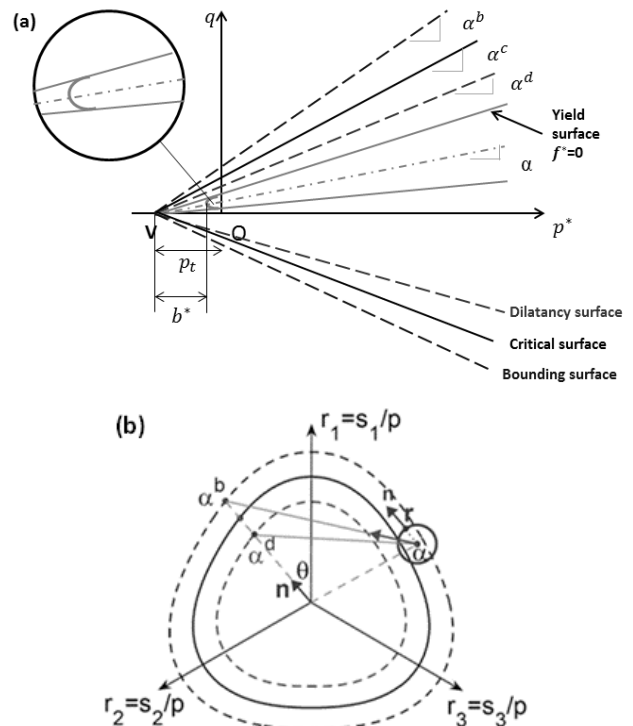


Figure 2: The yield surface of the modified SANISAND (2004) model in q - p^* plane (a) and in the multiaxial space (b).

Several meridional sections of the hyperbolic yield surface are plotted in Figure 3a, varying the parameter b^* and setting the hardening variable α equal to zero. Recall that the hyperbolic yield surface closely represents the original yield surface for $b^* \leq 0.25p_t$. While the effect of the back stress ratio is investigated by considering $b = p_t$, see Figure 3b.

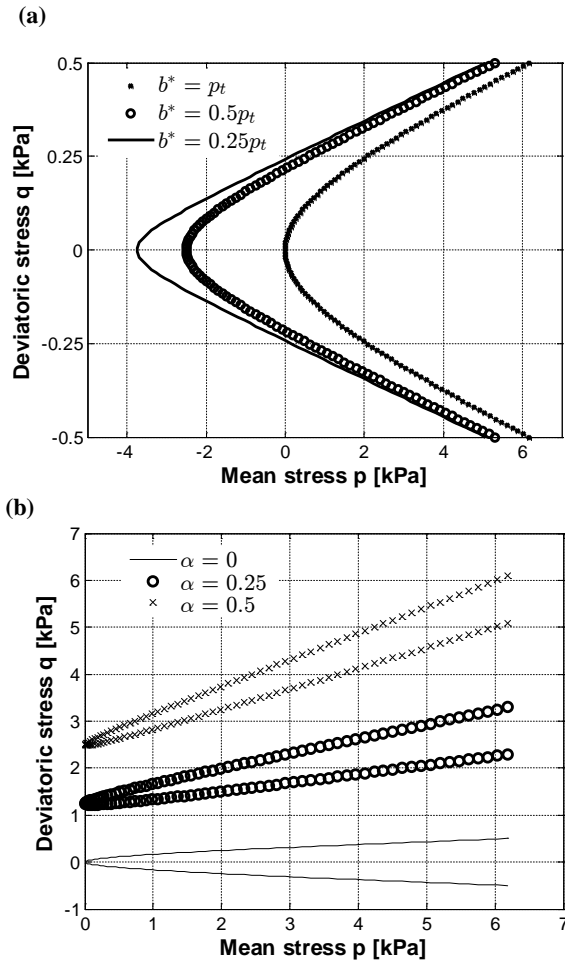


Figure 3: Effect of b^* parameter (a) and the back stress ratio α (b) on the hyperbolic yield surface in q - p plane.

The formulation of the critical state, bounding and dilatancy surfaces are considered depending on the back stress ratio α and they are defined as in the work of Dafalias and Manzari (2004). Note that in the original formulation the dependency of CSS, BS and DS in the q - p space on the Lode angle θ is given by the expression suggested by Argyris et al. (1974). Nevertheless, the implementation of the modified SANISAND (2004) takes into account the expression suggested by Van Eekelen (Van Eekelen, 1980), which is more accurate for high values of the critical state friction angle (Lin and Bazant, 1986).

2.2 Flow rule

The plastic flow direction is defined as:

$$\dot{\epsilon}^p = \dot{\gamma} \mathbf{R} \quad (7)$$

Where $\dot{\gamma} \geq 0$ and it represents the plastic multiplier. \mathbf{R} is the plastic potential, which is expressed as follows:

$$\mathbf{R} = \frac{\partial g}{\partial \boldsymbol{\sigma}} = \mathbf{n} + \frac{1}{3} \mathbf{D} \mathbf{I} \quad (8)$$

Where $\mathbf{n} = (\mathbf{s} - p^* \boldsymbol{\alpha}) / \|\mathbf{s} - p^* \boldsymbol{\alpha}\|$ and \mathbf{D} is the dilatancy coefficient. The flow rule is still considered non-associative as in SANISAND (2004) model and \mathbf{D} is given as:

$$\mathbf{D} = x \mathbf{D}_{DM} = \begin{cases} \mathbf{D} = \mathbf{D}_{DM}, & x = 1, \text{ if } p > p_t \\ \mathbf{D} = x \mathbf{D}_{DM}, & \text{if } p \in [0; p_t] \\ \mathbf{D} = 0, & \text{if } p < 0 \end{cases} \quad (9)$$

Where $x = \frac{p}{p_t}$ and \mathbf{D}_{DM} is the dilatancy coefficient defined by Dafalias and Manzari (2004). This implies that \mathbf{D} depends on the variation of the plastic volumetric strain, which was assumed zero for negative values of the mean pressure. The linear interpolation of the dilatancy coefficient in the interval $[0, p_t]$ was taken into account in order to have zero change in volume at the critical state and have a plastic potential function which varies in the proximity of the apex of the hyperbole. In addition, these assumptions may be considered valid, since the area subjected to regularization is small $[-p_t, p_t]$.

The loading index L is obtained by applying the consistency condition $\dot{f}^* = 0$ and yields to:

$$L = \frac{1}{K_p} \left(\frac{\partial f^*}{\partial p^*} \frac{\partial p^*}{\partial \boldsymbol{\sigma}} + \frac{\partial f^*}{\partial s} \frac{\partial s}{\partial \boldsymbol{\sigma}} \right) \quad (10)$$

$$K_p = - \left(\frac{\partial f^*}{\partial \boldsymbol{\alpha}} \right) \quad (11)$$

The partial derivatives of the yield surface with respect to the stress and the internal variables can be determined as follows:

$$\frac{\partial f^*}{\partial \boldsymbol{\sigma}} = \frac{\partial f^*}{\partial p^*} \frac{\partial p^*}{\partial \boldsymbol{\sigma}} + \frac{\partial f^*}{\partial s} \frac{\partial s}{\partial \boldsymbol{\sigma}} = \frac{1}{A_1} \left\{ (\mathbf{s} - p^* \boldsymbol{\alpha}) - \frac{1}{3} \mathbf{1} [\boldsymbol{\alpha} \cdot (\mathbf{s} - p^* \boldsymbol{\alpha})] \right\} - \frac{1}{3} \sqrt{\frac{2}{3}} m^2 \mathbf{1} \quad (12)$$

$$\frac{\partial f^*}{\partial \boldsymbol{\alpha}} = - \frac{1}{A_1} p^* (\mathbf{s} - p^* \boldsymbol{\alpha}) \quad (13)$$

Where

$$\frac{\partial f^*}{\partial s} = \frac{1}{A_1} (\mathbf{s} - p^* \boldsymbol{\alpha}) \quad (14)$$

$$\frac{\partial s}{\partial \boldsymbol{\sigma}} = \mathbf{I} - \frac{1}{3} \mathbf{1} \otimes \mathbf{1} \quad (15)$$

$$\frac{\partial f^*}{\partial p} = \frac{1}{A_1} (\mathbf{s} - p^* \boldsymbol{\alpha}) \cdot (-\boldsymbol{\alpha}) - \sqrt{\frac{2}{3}} m \quad (16)$$

$$\frac{\partial p}{\partial \boldsymbol{\sigma}} = \frac{1}{3} \mathbf{1} \quad (17)$$

$$\text{With } A_1 = \sqrt{(\mathbf{s} - p^* \boldsymbol{\alpha}) \cdot (\mathbf{s} - p^* \boldsymbol{\alpha}) + \frac{2}{3} m^2 b^*{}^2}.$$

3 THE MODIFIED SANISAND (2004) IN THE LOW STRESS REGIME

The implementation of the modified SANISAND (2004) model in finite element code was performed by modifying the subroutine freely available on the open-source database of constitutive models soilmodels.info (Gudehus et al., 2008). The modified SANISAND (2004) was implemented in the code by deploying an explicit, adaptive stress-point algorithm with error control, based on Runge-Kutta-Fehlberg scheme of third order (RKF-32) to integrate the constitutive equations at the Gauss point level.

In this section the performance of the stress integration scheme of the modified SANISAND (2004) model is compared with respect to that of the original constitutive soil model for the case of low stress regime, see Figure 4. The simulations of undrained triaxial tests for loose sandy sample ($e_0=0.996$) were carried out by deploying IncrementalDriver (Niemunis, 2008). In addition, the analyses were conducted setting $p_t = 5 \text{ kPa}$ and initial hydrostatic pressure $p_0 = 30 \text{ kPa}$. Note that the material constants considered are those referred to Toyoura sand, which are listed in the work of Dafalias and Manzari (2004).

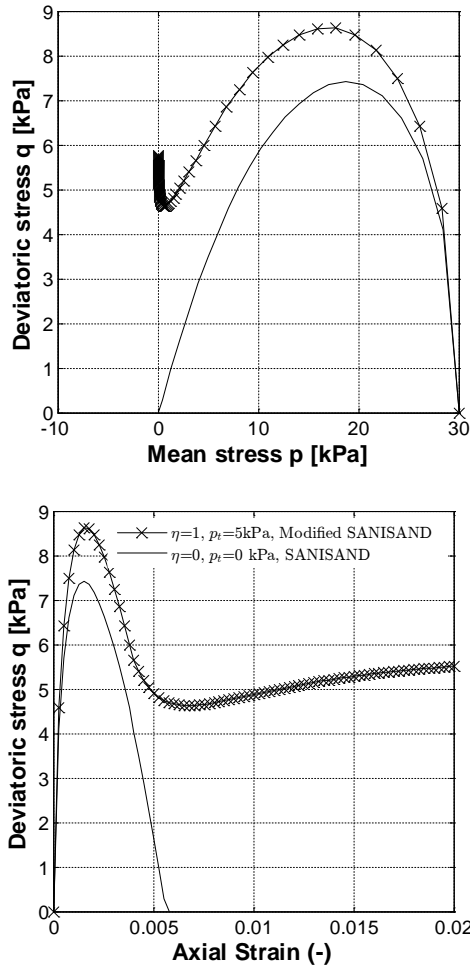


Figure 4: Monotonic undrained compression triaxial test on Toyoura sand. Comparison between the performance of SANISAND (2004) and the modified SANISAND (2004) model.

The outcomes highlighted that in the new formulation the stress integration does not fail as in the original formulation, when it deals with sandy soil deposits subjected to low initial confining pressure.

In addition, the algorithm was tested by decreasing the number of increments of the strain step applied ($N_{incr} = 500, 100$ and 50). First, it was observed that the outcomes of the simulations overlapped the results obtained by setting $N_{incr} = 1000$ for a given error tolerance of the explicit, adaptive stress-point algorithm ($TOL = 10^{-5}$). A relative error with respect the exact solutions of σ and α , obtained numerically by deploying the RKF23 for error tolerance of $TOL = 10^{-6}$, was calculated for each simulation. Results showed that a relative error of $ERR_{\sigma,\alpha} = 10^{-6}$ was achieved assuming $N_{incr} = 500$. While the accuracy of the algorithm was estimated for the following tolerance values: $TOL = 10^{-5}, 10^{-4}$ and 10^{-3} . It was noticed that the accuracy of the solution decreased by increasing the tolerance constant TOL . Furthermore, it was possible to obtain a relative error $ERR_{\sigma,\alpha} \leq 10^{-4}$, by setting the error tolerance not larger than 10^{-4} .

4 CONCLUSION

A smooth hyperbolic approximation to SANISAND (2004) yield function is derived. The rounded hyperbolic surface is

continuous and differentiable for all stress states, and it can approximate the original yield surface by adjusting one parameter. The present modification does not alter the features of the previous version of SANISAND (2004).

5 ACKNOWLEDGEMENTS

This work has been supported by the Danish Council for Strategic Research through the project “Advancing BeyondShallow waterS (ABYSS) - Optimal design of offshore wind turbine support structures”.

6 REFERENCES

- Argyris J.H., Faust G., Szimmat J., Warnke P. and William K. 1974. Recent developments in finite elements analyses of prestressed concrete reactor vessels. *Nuclear Engineering and Design* 28, 42–75.
- Cubrinovski M. and Ishihara K. 1998. State concept and modified elastoplasticity for sand modelling. *Soils Foundation* 38(4):213–225
- Dafalias Y.F. and Manzari M.T. 2004. Simple plasticity sand model accounting for fabric change effects. *Journal of Engineering Mechanics* 130(6):622–634.
- Dafalias Y.F., Papadimitriou A.G. and Li X.S. 2004. Sand plasticity model accounting for inherent fabric anisotropy. *Journal of Engineering Mechanics* 130(1): 1319-1333.
- Gajo A. and Wood D.M. 1999. A kinematic hardening constitutive model for sands: the multi-axial formulation. *International Journal for Numerical and Analytical Methods in Geomechanics* 23:925–965
- Gudehus G., Amorosi A., Gens A., Herle I., Kolymbas D., Masín D., Muir Wood D., Niemunis A., Nova R., Pastor M. et al. 2008. The soilmodels. info project. *International Journal for Numerical and Analytical Methods in Geomechanics* 32(12):1571–1572. <http://www.soilmodels.info>
- Li X.S. and Dafalias Y.F. 2000. Dilatancy for cohesionless soils. *Geotechnique* 54(4): 499-460.
- Lin F.B. and Bazant Z.P. 1986 Convexity of smooth yield surface of frictional material. *Journal of Engineering Mechanics* 112 1259–62.
- Manzari M.T. and Dafalias, Y.F. 1997. A critical state two-surface plasticity model for sands. *Geotechnique* 42(2): 255-272.
- Mroz Z. and Pietruszczak S. 1983. A constitutive model for sand and its application to cyclic loading. *International Journal for Numerical and Analytical Methods in Geomechanics* 7:305–320
- Niemunis A. 2008 IncrementalDriver users’s manual URL <http://www.rz.uni-karlsruhe.de/gn99>
- Sloan S.W. and Booker J.R. 1986 Removal singularities in Tresca and Mohr-Coloumb yield functions. *Communications in Applied Numerical Methods* 2:173-179.
- Taiebat M. and Dafalias Y.F. 2007. SANISAND: simple anisotropic sand plasticity model. *International Journal for Numerical and Analytical Methods in Geomechanics* 32(8): 915-948.
- Van Eekelen H.A.M. 1980. Isotropic yield surfaces in three dimensions for use in soil mechanics. *International Journal for Numerical and Analytical Methods in Geomechanics* 4, 89–101.
- Wang Z.L., Dafalias Y.F. and Shen C.K. 1990. Bounding surface hypoplasticity model for sand. *Journal of Engineering Mechanics* ASCE 116(5):983–1001

Paper VIII

Integrated optimal design of jackets and foundations

K. SANDAL, C. LATINI, V. ZANIA AND M. STOLPE

Submitted for publication:-, 2017

Integrated optimal design of jackets and foundations

Kasper Sandal ^{*} Chiara Latini [†] Varvara Zania [‡] Mathias Stolpe [§]

October 10, 2017

Abstract

The article proposes a method for integrated design of jackets and foundations using numerical structural optimization. Both piles and suction caissons are examined in both clayey and sandy soil, and several design procedures are taken into account. The optimal design problem enables an automatic design process which minimizes the primary steel mass of the jacket and the foundations. Both leg distance and soil stiffness are found to have a significant influence on the total mass as well as the first natural frequency of the full offshore wind turbine structure. The results indicate that an integrated design approach is valuable in the conceptual design phase. Firstly this is because the soil characteristics and foundation type have a significant influence on the optimal leg distance for the jacket. Secondly it is because the jacket mass have a significant influence on the optimal foundation type and foundation design.

Keywords: offshore wind energy, structural optimization, foundation design, suction caisson, pile, jacket structure, integrated design.

1 Introduction

The main objective for the offshore wind industry nowadays is to reduce the cost of energy, in order to be competitive with respect to fossil–fuel-based energy sources. Support structures comprise as much as 20% of capital expenditures, and have been identified as areas with high potential for cost reduction [37]. The cost-reduction targets set by industry can be met either by using new technologies or by optimization of design methods and existing technologies. In that regards, structural optimization appears as an attractive approach to investigate any potential cost benefits from the design optimization of the substructure and the foundation.

Optimization of wind turbine components has been well studied in the literature, and for example, a gradient based rotor optimization is presented in [17]. Integrated design of multiple

^{*}DTU Wind Energy, Technical University of Denmark, Frederiksborgvej 399, 4000 Roskilde, Denmark. E-mail: kasp@dtu.dk

[†]DTU Civil Engineering, Technical University of Denmark, Brovej Building 108, 2800 Kgs. Lyngby, Denmark. E-mail: chila@byg.dtu.dk

[‡]DTU Civil Engineering, Technical University of Denmark, Brovej Building 108, 2800 Kgs. Lyngby, Denmark. E-mail: vaza@byg.dtu.dk

[§]DTU Wind Energy, Technical University of Denmark, Frederiksborgvej 399, 4000 Roskilde, Denmark. E-mail: matst@dtu.dk

components of the offshore wind energy turbine, such as of tower and rotor, have been done in the work of e.g. Ashuri [2]. Here it was showed that an integrated approach towards optimization can considerably reduce the cost of energy, which often implicates a compromise between rotor and support structure design. However, the foundation was not optimized, since all degrees of freedom of the monopile at the seabed were constrained. Terminology of the main components of the support structures for offshore wind turbines are given in Figure 1. Detailed design of support structures according to rules and guidelines [21] implies that a large number of load cases must be assessed, which is a computationally expensive and time-consuming task. Many design approaches therefore use a reduced number of load cases [40].

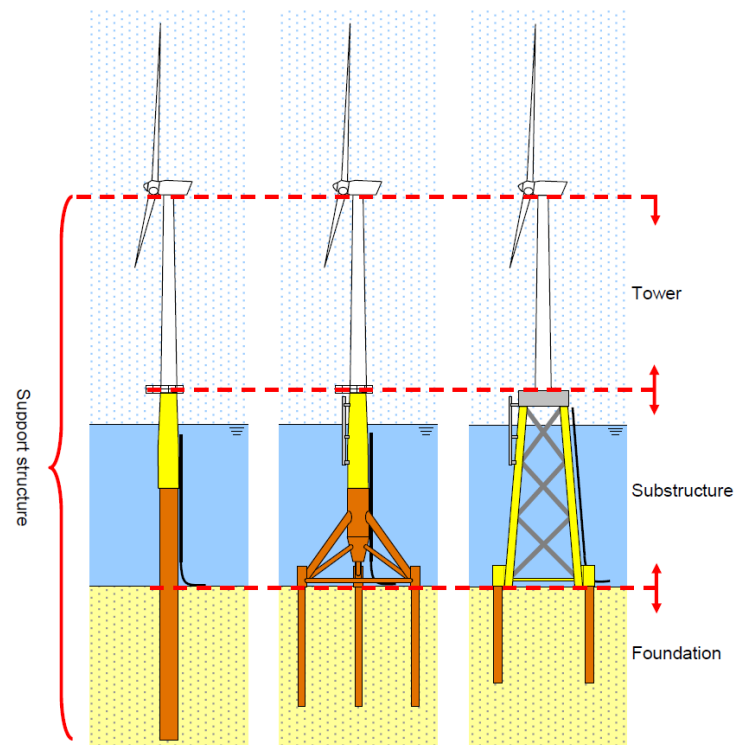


Figure 1: Definition of the main components of the support structure for offshore wind turbines. The jacket substructure can be further divided into the actual jacket, and the transition piece which connects it to the tower. [12].

Optimal design of support structures for offshore wind turbines has developed from gradient-free approaches where an aero-elastic software is used as a black-box for the function evaluations [41], towards the use of gradient-based methods [28]. The advantage of the black-box approach is that the analysis can be state-of-the-art. With gradient-based methods, one has so far been limited to elastic analysis, where the rotor loads are applied as time-series at the tower top. This is a simplification compared to the state-of-the-art aero-elastic analysis, where both the wind turbine generator and wind field are modelled. However, due to the nature of the industry, where turbine designers are unwilling to share models with the support structure designer, a

decoupled load model is actually industrially relevant. Gradient-based optimization of jacket substructures is presented in [29] and [9] with quasi-static and dynamic analysis, respectively. In these works, the fatigue and ultimate limit states were assessed during multiple 10-minute load cases. For conceptual design of jacket substructures, a load analysis with static damage equivalent loads, and static extreme loads can be sufficient [34].

Contrary to the mechanical engineering field, in the geotechnical sector numerical optimization methods have been only scarcely investigated in the literature. Few studies have been conducted on the dimension optimization of shallow foundations [23] and pile groups [8]; while the topology optimization of foundations in granular soils was addressed in the work of Pucker and Grabe [30] and Seitz and Grabe [35]. In the latter ones, a combined method of topology and shape optimization was implemented and linked up to a finite element program. The study [35] proved that the optimized foundation topologies are more efficient due to the significant improvement of the deformation behaviour when compared to quadratic surface foundations. It is worth mentioning the work of Barakat et al. [4], in which a general approach to the reliability-based analyses was performed to optimize designs of laterally loaded piles. For a monopile, Thiry et al [38] used a genetic algorithm to design a monopile in the frequency domain. Furthermore, a preliminary investigation of pile foundation design using structural optimization was performed in the work of Sandal and Zania [33]. The main conclusion derived from the above mentioned study was that the total mass of the piles was considerably influenced by the soil strength characteristics.

For an offshore wind turbine structure, the support structure design typically has some global requirements, e.g. on the first fundamental frequency [12] [5]. These global constraints are influenced by both the soil properties, the foundation design, as well as the substructure design. The foundation and substructure designs will in turn have their own design requirements. An integrated design approach would include all the design constraints for both the foundation, the substructure, and the full support structure in one design procedure. This can rapidly become too complex for it to be manually handled, but is well within the limits of computer-aided design approaches. One computer-aided design approach can be based on the principle of fully utilized design. The principle here is to establish limits for e.g. the maximum stress, and then adjust the structural dimensions iteratively until all design members are fully utilized with respect to this limit. However, a fully utilized design is generally not the same as an optimal design. A simple example which illustrates this is a thin-walled pipe subjected to bending loads. The pipe can be fully utilized and still have potential for lowering the mass by increasing the diameter and lower the wall thickness. An approach which is often better in dealing with such problems is numerical structural optimization, where the design problem is modelled as a mathematical program.

The advantage of the integrated design approach is that interaction effects between the foundation and support structure are properly accounted for. This way, one avoids a situation where new loads and designs are sent back and forth between the foundation designer and the support structure designer. The disadvantage of the integrated design approach is of course that it requires a more complex model, especially if variable soil conditions, foundation types and design procedures are included.

Integrated optimal design of foundation and jacket design has to the authors knowledge not

been performed yet. The aim of this paper is to investigate interaction effects between soil properties, foundation design, and support structure design for offshore wind turbines. This is achieved by automating six different design procedures for two different types of foundations and two different soil conditions with numerical structural optimization. The integration of the analysis models and sensitivity analyses with an existing framework for jacket design optimization allows for integrated design of foundations and jackets. The structural optimization problem is formulated in such a way to minimize the combined mass of jacket and foundation with requirements on fatigue, frequency, buckling, and foundation capacities. Additionally the design trends for varying jacket leg distance and soil stiffness are analysed. Moreover a comparison between the sequential and integrated optimization allows for estimation of the benefit from an integrated approach.

2 Modelling methodology

The structural design and analysis model is used to formulate an integrated optimal design problem for both the jacket and the foundation. The foundation models and capacities are explained, and the implementation details are given.

2.1 Model and design parametrization

The model is assembled by a design dependent foundation, a design dependent jacket, and a non-design dependent transition piece, tower, and rotor-nacelle-assembly (RNA). The non-design dependent part of the structure is necessary in the structural analysis because it is at the tower top the loads are applied, and it also influences the natural frequencies of the structure. The jacket design is described by

$$\mathbf{x} = (d_1^l \quad t_1^l \quad d_1^b \quad t_1^b \quad \dots \quad d_{n_s}^l \quad t_{n_s}^l \quad d_{n_s}^b \quad t_{n_s}^b)^T \in \mathbb{R}^{4n_s}$$

where d and t are the outer diameter and wall thickness of the members in the jacket. The superscript l and b refers to legs and braces, and the subscripts $1, \dots, n_s$ refers to the section number. Alas, there are four design variables per section of the jacket, as shown in Figure 2.

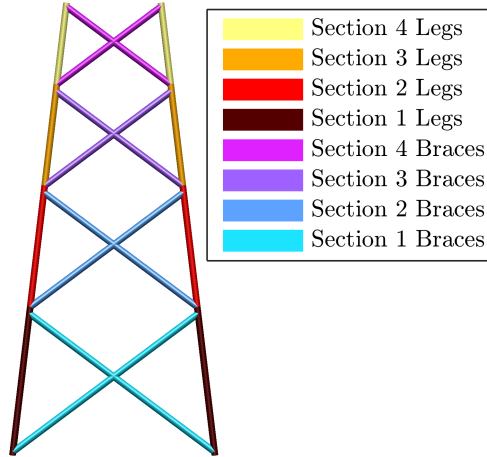


Figure 2: Overview of the jacket design parametrization.

The foundation design is described by

$$\mathbf{y} = (d, t, l)^T \in \mathbb{R}^3$$

where d , t , and l are the outer diameter, wall thickness, and length of the foundation. There is one foundation connected to each of the four jacket legs, and all the foundation designs are identical. The design parametrization is the same for both piles and suction caissons.

2.2 Structural analysis

The structural model is built from two types of two-noded finite elements. The jacket, transition piece and tower are modelled with 3D Timoshenko beam elements [11] for linear elasticity. The foundation is modelled with specialized foundation elements described in section 2.3.

The global stiffness matrix $\mathbf{K}(\mathbf{x}, \mathbf{y}) \in \mathbb{R}^{n \times n}$ is assembled as

$$\mathbf{K}(\mathbf{x}, \mathbf{y}) = \mathbf{K}_0 + \sum_{i=1}^{n_j} \mathbf{K}_i(\mathbf{x}) + \sum_{i=1}^{n_f} \mathbf{K}_i^f(\mathbf{y})$$

where n_j is the number of elements in the jacket, n_f is the number of foundations, and n is the number of unconstrained degrees of freedom. The stiffness matrices of elements in the non-design dependent part (tower, transition piece, and RNA) are collected in \mathbf{K}_0 , and the stiffness of the elements in the foundation and jacket are assembled as functions of the design variables. The assembly also distributes the element stiffness matrices to the appropriate degrees of freedom in the global stiffness matrix.

Static equilibrium is now given as

$$\mathbf{K}(\mathbf{x}, \mathbf{y})\mathbf{u}^\ell = \mathbf{f}^\ell(\mathbf{x}, \mathbf{y}).$$

where $\mathbf{f}^\ell(\mathbf{x}, \mathbf{y})$ is the ℓ th applied static load. The load is design dependent, because gravity forces on the jacket are included.

In the described structural model, the boundary conditions are applied on the foundation elements. Since the displacement field is a function of both foundation and jacket design, we refer to this model as the integrated model. A common assumption in analysis of jacket structures is that the bottom of the jacket is clamped, i.e., that there is no displacement or rotation in the foundation. This assumption can easily be applied to this model as well, by fixing the six degrees of freedom at the top node of the foundation. This model, from here referred to as the clamped model, will be used as a reference in the numerical simulations.

The global mass matrix $\mathbf{M}(\mathbf{x}) \in \mathbb{R}^{n \times n}$ is assembled as

$$\mathbf{M}(\mathbf{x}) = \mathbf{M}_0 + \sum_{i=1}^{n_j} \mathbf{M}_i(\mathbf{x})$$

where \mathbf{M}_0 contains the mass matrices of the elements in the transition piece, tower, and rotor-nacelle-assembly. Whereas the global stiffness matrix is a function of both the foundation and jacket design variables \mathbf{x} and \mathbf{y} , the mass matrix is here only a function of the jacket design variables \mathbf{x} . In this definition the contribution of the foundations to the mass matrix is neglected. This assumption disregards the frequency dependency of the foundation stiffness (impedance functions) due to the inertial response of the soil-foundation system which is commonly taken into consideration in dynamic soil-structure-interaction problems [5]. The abovementioned simplification is considered appropriate for the current study since the natural eigenfrequencies of the superstructure (wind turbine and jacket) are smaller than the eigenfrequencies corresponding to most of the considered soil conditions. The generalized eigenvalue problem is computed as

$$(\mathbf{K}(\mathbf{x}, \mathbf{y}) - \lambda_i \mathbf{M}(\mathbf{x})) \phi_i = 0, \quad i = 1, \dots, n$$

where λ_i and ϕ_i are the i th eigenvalue and eigenmode. We assume the eigenvalues to be distinct and sorted, $\lambda_1 < \dots < \lambda_n$, and compute the eigenfrequency in Hz as

$$\omega_i = \frac{\sqrt{\lambda_i}}{2\pi}.$$

The eigenvalues of a jacket structure is generally not distinct, as the structure is often symmetric. However, the model of the rotor-nacelle-assembly of the wind turbine breaks the structural symmetry, and this ensures distinct eigenvalues, at least for the first ones which are considered in this article.

2.3 Joint connection between jacket legs and foundations

We solve for the global displacement vector for a given load case as $\mathbf{u}(\mathbf{x}, \mathbf{y}) = \mathbf{K}(\mathbf{x}, \mathbf{y})^{-1} \mathbf{f}(\mathbf{x}, \mathbf{y})$, which illustrates that the displacement field is a function of both foundation and jacket design variables. The top node of the foundation is from here referred to as the *joint*, and it is the connection between the jacket legs and the foundations. From the global displacement vector $\mathbf{u}(\mathbf{x}, \mathbf{y}) \in \mathbb{R}^n$ we can extract the displacement vector for each joint, $\mathbf{u}_i^f(\mathbf{x}, \mathbf{y}) \in \mathbb{R}^6$, $i = 1, \dots, 4$. The reaction forces at the joints can now be computed as

$$\mathbf{f}_i^f(\mathbf{x}, \mathbf{y}) = \mathbf{K}_i^f(\mathbf{y}) \mathbf{u}_i^f(\mathbf{x}, \mathbf{y})$$

where $\mathbf{K}_i^f(\mathbf{y})$ is now only given for the joint degrees of freedom, so that

$$\mathbf{f}_i^f(\mathbf{x}, \mathbf{y}) = \begin{pmatrix} F_{x,i}(\mathbf{x}, \mathbf{y}) \\ F_{y,i}(\mathbf{x}, \mathbf{y}) \\ F_{z,i}(\mathbf{x}, \mathbf{y}) \\ M_{x,i}(\mathbf{x}, \mathbf{y}) \\ M_{y,i}(\mathbf{x}, \mathbf{y}) \\ M_{z,i}(\mathbf{x}, \mathbf{y}) \end{pmatrix}, \quad \mathbf{u}_i^f(\mathbf{x}, \mathbf{y}) = \begin{pmatrix} u_i(\mathbf{x}, \mathbf{y}) \\ v_i(\mathbf{x}, \mathbf{y}) \\ w_i(\mathbf{x}, \mathbf{y}) \\ \theta_{x,i}(\mathbf{x}, \mathbf{y}) \\ \theta_{y,i}(\mathbf{x}, \mathbf{y}) \\ \theta_{z,i}(\mathbf{x}, \mathbf{y}) \end{pmatrix},$$

$$\mathbf{K}_i^f(\mathbf{y}) = \begin{pmatrix} K_{su}(\mathbf{y}) & 0 & 0 & 0 & 0 & 0 \\ 0 & K_{su}(\mathbf{y}) & 0 & 0 & 0 & -K_{sc}(\mathbf{y}) \\ 0 & 0 & K_v(\mathbf{y}) & 0 & K_{sc}(\mathbf{y}) & 0 \\ 0 & 0 & 0 & K_{mc}(\mathbf{y}) & 0 & 0 \\ 0 & 0 & K_{sc}(\mathbf{y}) & 0 & K_{mc}(\mathbf{y}) & 0 \\ 0 & -K_{sc}(\mathbf{y}) & 0 & 0 & 0 & K_t(\mathbf{y}) \end{pmatrix},$$

and $\mathbf{K}_i^f(\mathbf{y})$ is the same for all four joints. The stiffness entries K_{su} , K_{sc} , and K_{mc} are different for piles and suction caissons, and are given in sections 2.6 and 2.7. The vertical and torsional stiffness coefficients K_t and K_v are evaluated according to the suggested expressions for piles by Randolph [31] and these expressions are also used for suction caissons:

$$K_t(d, l) = Gd^3 \left(\frac{2}{3} + \frac{\pi l}{d} \right)$$

$$K_v(d, l) = \frac{2Gd}{1-\nu} \left(1 + \frac{(1-\nu)\pi \tanh(\xi(d, l))l}{\zeta(d, l)d\xi(d, l)} \right)$$

where

$$\zeta(d, l) = \ln \left(\frac{5(1-\nu)l}{d} \right) \quad \text{and} \quad \xi(d, l) = \sqrt{\frac{2G}{\zeta E_p} \frac{2l}{d}},$$

and ν and G are the Poisson's ratio and shear stiffness of the soil.

2.4 Optimal design problem

We consider the optimal design problem, for now described in general terms,

$$\begin{aligned} & \underset{\mathbf{x} \in \mathbb{R}^{4n_s}, \mathbf{y} \in \mathbb{R}^3}{\text{minimize}} && f(\mathbf{x}, \mathbf{y}) \\ & \text{subject to} && \mathbf{A}_x \mathbf{x} + \mathbf{A}_y \mathbf{y} \leq \mathbf{b} \\ & && g_j(\mathbf{x}, \mathbf{y}) \leq 0, \quad j = 1, \dots, n_c \\ & && \underline{\mathbf{x}} \leq \mathbf{x} \leq \bar{\mathbf{x}} \\ & && \underline{\mathbf{y}} \leq \mathbf{y} \leq \bar{\mathbf{y}}, \end{aligned} \tag{P}$$

where $\underline{\mathbf{x}}$, $\bar{\mathbf{x}}$, $\underline{\mathbf{y}}$, and $\bar{\mathbf{y}}$ are lower and upper bounds on the design variables. The nonlinear constraint functions $g_j(\mathbf{x}, \mathbf{y})$ are used to model design requirements. This includes structural

frequencies, and local design requirements such as fatigue and buckling in the jacket, and load capacities for the foundation. The linear constraints model geometrical restrictions on the jacket and foundation designs (see below).

The optimal design problem (P) is a non-convex optimization problem in the variables \mathbf{x} and \mathbf{y} . The objective is to minimize the mass of the combined substructure

$$f(\mathbf{x}, \mathbf{y}) = \rho^j \sum_{i=1}^{n_j} V_i(\mathbf{x}) + \rho^f n_f V^f(\mathbf{y})$$

where V_i is the volume of element number i in the jacket, V^f is the volume of one foundation, and ρ^j and ρ^f is the material density in the jacket and the foundation, respectively. All elements are modelled as thin walled cylinders so that

$$V_i(d_i, t_i, l_i) = \frac{\pi}{4} (d_i^2 - (d_i - 2t_i)^2) l_i, \quad \text{and} \quad V^f(d, t, l) = \frac{\pi}{4} (d^2 - (d - 2t)^2) l,$$

where l_i is the length of the i th finite element in the jacket.

The mass of the structural connection between the foundation and the jacket leg is thus not modelled. For suction caissons there is a flat lid with stiffeners which can account for a significant part of the suction caisson mass. The objective function does not consider this part of the mass of the suction caisson, therefore the comparison between the mass of the suction caisson and the pile should be treated with caution.

Linear constraints, $\mathbf{A}_x \mathbf{x} + \mathbf{A}_y \mathbf{y} \leq \mathbf{b}$ are placed on both jacket and foundation design to ensure manufacturability and compliance with design requirements. For the pile foundation there is a wall thickness constraint $t^f \geq 6.3 + d^f/100$ which is assumed to avoid buckling during the pile driving procedure [1]. The same constraint is also applied to the suction caisson, although the installation procedure here is different there is still the risk of buckling due to the suction. Furthermore, in order to distinguish the capacity functions of piles and suction caissons the slenderness ratio (diameter over skirt length) is used as a criterion and this slenderness ratio is enforced in the linear constraints. For the jacket structure there is a validity range [14] which must be enforced when the design methodology for stress concentrations in welded joints are applied. For joints where braces b are welded onto legs l , the brace dimension should lie between 20 and 100% of the leg dimension. This results in the linear inequalities

$$\begin{aligned} \frac{d_i^l}{5} &\leq d_i^b \leq d_i^l, \quad i = 1, \dots, n_s \\ \frac{t_i^l}{5} &\leq t_i^b \leq t_i^l, \quad i = 1, \dots, n_s. \end{aligned}$$

The diameter to thickness ratio in all elements should satisfy

$$\begin{aligned} 16t_i^l &\leq d_i^l \leq 64t_i^l, \quad i = 1, \dots, n_s \\ 16t_i^b &\leq d_i^b \leq 64t_i^b, \quad i = 1, \dots, n_s. \end{aligned}$$

The constraints $g_j(\mathbf{x}, \mathbf{y})$ include design requirements on the jacket as well as the foundations. Since the displacements are functions of the both jacket and foundation design variables \mathbf{x} and

\mathbf{y} , most of the design requirements on the jacket and foundation are also functions of both \mathbf{x} and \mathbf{y} .

The nonlinear constraints on the jacket design include stress and buckling constraints. Stress constraints are computed in eight hot spots h in every finite element for all load cases. In the ultimate limit state load cases, local shell buckling and column buckling are considered according to the offshore standard [15] and the recommended practice [13]. Shell buckling is formulated as a design dependent stress constraint in compression,

$$\sigma_i^b(\mathbf{x}) - \sigma_{ih}(\mathbf{x}, \mathbf{y}) \leq 0, \quad i = 1, \dots, n_e, \quad h = 1, \dots, 8$$

for all finite elements i in the jacket. Here $\sigma_{ih}(\mathbf{x}, \mathbf{y})$ is the stress in element i at position h along the outer circumference of the element. The shell buckling capacity $\sigma_i^b(\mathbf{x})$ is defined as

$$\sigma_i^b(\mathbf{x}) = \frac{-\sigma_y}{\gamma_M \sqrt{1 + \left(\frac{\sigma_y}{f_i}\right)^2}}, \quad f_i = C_i \frac{\pi^2 E}{12(1 - \nu^2)} \left(\frac{t_i}{L_i}\right)^2, \quad C_i = \sqrt{1 + (\tilde{\rho}_i \tilde{\xi}_i)^2}$$

$$\tilde{\rho}_i = \frac{1}{2\sqrt{1 + \frac{d_i}{600t_i}}}, \quad \tilde{\xi}_i = 1.404 \frac{L_i^2}{d_i t_i} \sqrt{1 - \nu^2},$$

where σ_y is the material yield strength, ν is the Poisson's ratio, and $\gamma_M = 1.25$. L_i is the length of the member, from one joint to the next, to which the i th finite element belongs. Each member in the jacket is generally discretized with six finite elements.

Column buckling is a potential failure mode for slender members subjected to axial compression. According to [15], a buckling assessment must be performed for element i if

$$\frac{(kL_i)^2 A_i(d_i, t_i)}{I_i(d_i, t_i)} \geq \frac{2.5E}{\sigma_y} \quad (1)$$

where $k = 0.7$ is the effective column length. The inequality (1) is reformulated as a nonlinear constraint

$$\sqrt{\frac{3.2\sigma_y}{E} kL_i} - d_i^2 + 2d_i t_i - 2t_i^2 \leq 0, \quad i = 1, \dots, n_j \quad (2)$$

As long as this constraint is satisfied, column buckling is not a potential failure mode. Thus, we can refer to (2) as a conservative buckling constraint. Since the buckling constraint is load independent, it is only a function of the jacket design variables.

All the constraint functions are implemented as smooth, differentiable analytical functions. The nonlinear constraints on the foundation design are based on standard design procedures, and vary depending on the type of foundation and soil conditions. Details for the design requirements of these design cases are given in sections 2.6 and 2.7. Variable bounds are placed on both jacket and foundation variables, to avoid unrealistic designs.

2.5 Load cases

The static load cases applied in this study are listed in Table 1. The fatigue loads are damage equivalent 1 Hz loads based on aeroelastic simulations of a rotor, assuming a perfectly rigid

support structure. The ultimate loads are taken from the design report of the DTU 10 MW wind turbine [3]. No safety factors have been applied. The fatigue loads are applied as two different weighted combinations of damage equivalent loads in thrust, overturning moment, and torsion degrees of freedom. The two fatigue loads are then applied from two directions, 45 degrees apart, to increase the probability that the worst case is captured. The ultimate loads are also applied from two directions.

The fatigue loads are assumed to be design driving for the jacket, and the extreme loads are assumed to be design driving for the foundations. This means that in the optimal design problem, the constraints on the jacket are applied for the fatigue load cases, and the constraints on the foundations are applied in the extreme load cases. The use of damage equivalent loads for the fatigue constraints in the jacket is not perfectly accurate, but is a recommended approach for conceptual design [34]. The use of extreme static loads for the ultimate design of the piles is also a simplification.

Table 1: Static design loads applied at the tower top.

Load case	Limit state	Angle [deg]	Thrust force [MN]	Overturning moment [MNm]	Torsion [MNm]	Tower top mass [tons]
DEL00thrust	Fatigue	0	0.142	5.69	3.10	0
DEL45thrust	Fatigue	45	0.142	5.69	3.10	0
DEL00torsion	Fatigue	0	0.071	2.85	6.21	0
DEL45torsion	Fatigue	45	0.071	2.85	6.21	0
ULT00	Ultimate	0	4.61	17.9	0	677
ULT45	Ultimate	45	4.61	17.9	0	677

2.6 Pile stiffness and capacity formulations

This section outlines the joint stiffness expressions and capacity constraints used for piled foundations. The capacity constraints are given according to traditional design procedures, as well as a procedure based on cone-penetration-test (CPT) data.

2.6.1 Joint stiffness expression for piles

The stiffness coefficients of the soil-pile system have been estimated according to the expressions suggested by Randolph [31] for slender piles:

$$K_{su}(d, t) = 6.29G_s \left(\frac{E_c(d, t)}{G_s} \right)^{\frac{1}{7}} \left(\frac{d}{2} \right)$$

$$K_{sc}(d, t) = 2.21G_s \left(\frac{E_c(d, t)}{G_s} \right)^{\frac{3}{7}} \left(\frac{d}{2} \right)^2$$

$$K_{mc}(d, t) = 1.97G_s \left(\frac{E_c(d, t)}{G_s} \right)^{\frac{5}{7}} \left(\frac{d}{2} \right)^3$$

where E_c is the equivalent Young's modulus

$$E_c(d, t) = \frac{E_p I_p(d, t) + E_s I_s(d, t)}{I_p(d, t) + I_s(d, t)},$$

and E_s , I_s , E_p , and I_p are the Young's modulus and inertias of soil and pile. The coefficient $G_s = G(1 + 3/4\nu)$, where G and ν are the shear modulus and Poisson's ratio of the soil [31].

Design requirements on the axial and lateral ultimate capacities of the piles are computed according to the current state of practice for offshore foundations [1]. Axial pile resistance is given by two separate contributions: shaft resistance acting along the pile length and end bearing resistance at the pile tip. In this study both plugged and unplugged capacities have been estimated and the minimum of the two is taken as the final axial pile capacity.

2.6.2 Vertical capacity constraint for piles in sand and clay

The axial capacity constraints for piles in clay and sand are

$$-(Q_f(\mathbf{y}) + Q_b(\mathbf{y})) \leq F_{z,i}(\mathbf{x}, \mathbf{y}) \leq Q_f(\mathbf{y}), \quad i = 1, \dots, n_f, \quad (3)$$

where Q_f is the shaft friction capacity and Q_b is the end bearing capacity. Positive F_z equals tension force in the pile. Detailed expressions of the the friction capacity and the end bearing capacity adopted in the analyses are given in Appendix A for both sandy and clayey soil.

For clay profiles the shaft resistance can be formulated as a function of the effective overburden pressure at each given depth adopting the α -method formulated in [1], while the β -method [1] is used for the estimation of the shaft resistance in sands. The end bearing resistance of piles embedded in clay is governed by the maximum bearing strength of the soil, usually defined as $9s_u$, where s_u is the undrained shear strength of the soil. While in sands the end bearing behaviour of piles is defined by the effective vertical stress in the soil and a non-dimensional bearing factor N_q , which is dependent on the angle of friction ϕ in degrees.

2.6.3 Vertical capacity constraint for piles in sand based on CPT data

It is important mentioning that bearing capacity theory applied to estimate base resistance in cohesionless soils involves a rather approximate ϕ - N_q relationship which originates from Meyerhoff [27] coupled with the difficulty of determining a reliable and representative in-situ value of the ϕ angle and the assumption of a proper shear failure surface around the pile tip [10]. While CPT-based methods have shown statistically closer predictions of pile load test results and hence, their use is recommended by design codes [1]. In the proposed study the optimization of the pile foundation was also assessed by adopting the UWA [25] CPT-based method for the estimation of the friction and end bearing contribution to pile capacity in cohesionless soil (sand). The expression of the axial capacity according to the CPT-based method is given by:

$$-\left(\frac{3}{100}Q_f(\mathbf{y}) + Q_b(\mathbf{y})\right) \leq F_{z,i}(\mathbf{x}, \mathbf{y}) \leq \frac{11}{500}Q_f(\mathbf{y}), \quad i = 1, \dots, n_f, \quad (4)$$

where Q_f and Q_b also are function of the CPT-data set. The CPT-data are given as $q_c(z)$, which is the soil cone resistance at depth z below the seabed. The data are provided for every 2

centimeters from the seabed and down to approximately 50 meters, see Figure 4. The data set is interpolated in Matlab such that it is smooth and differentiable with respect to the depth. The friction capacity function Q_f is calculated as reported in Appendix A.

2.6.4 Lateral capacity constraint for piles in sand and clay

Finally, the lateral capacity of piles can be expressed as follows, considering Brom's theory [7] for flexible piles:

- in clay

$$-Q_l(\mathbf{y}) \leq \frac{F_{x,i}(\mathbf{x}, \mathbf{y})|F_{x,i}(\mathbf{x}, \mathbf{y})|}{9s_u d} + \frac{3F_{x,i}d}{2} + M_{y,i} \leq Q_l(\mathbf{y}), \quad i = 1, \dots, n_f$$

- in sand

$$-Q_l(\mathbf{y}) \leq \frac{0.544F_{x,i}(\mathbf{x}, \mathbf{y})|F_{x,i}(\mathbf{x}, \mathbf{y})|^{\frac{1}{2}}}{(dK_p\gamma)^{\frac{1}{2}}} + M_{y,i}(\mathbf{y}) \leq Q_l(\mathbf{y}), \quad i = 1, \dots, n_f,$$

where $K_p = \tan^2(45 + \frac{\phi}{2})$. Note that $Q_l(\mathbf{y})$ is computed as:

$$Q_l(\mathbf{y}) = \frac{2I(d, t)\sigma_y}{d},$$

which is only a function of the pile design, and not the soil properties. The sensitivity of the lateral capacity is the same for the pile in clay and sand. The absolute value is non-differential at zero, but since $F_{x,i}(\mathbf{x}, \mathbf{y})$ does not approach zero in the numerical experiments, this is not a problem.

2.7 Suction caisson stiffness and capacity formulation

Suction caisson is a novel foundation concept for jacket structures in offshore wind engineering. Detailed design guidelines are not well established for this type of foundation and hence, state-of-art formulations in the framework of API provisions [1] were adopted in the current work.

2.7.1 Joint stiffness expression for suction caissons

The stiffness components of the soil-suction caisson system have been defined according to the expressions proposed by Latini and Zania [24]:

$$\begin{aligned} K_{su}(d, l) &= \frac{G_s d}{0.560} \left(\frac{E_c(d, l)}{G_s} \right)^{0.18} \left(\frac{l}{d} \right)^{0.156} \\ K_{sc}(d, l) &= \frac{G_s d^2}{7.10} \left(\frac{E_c(d, l)}{G_s} \right)^{0.52} \left(\frac{l}{d} \right)^{0.656} \\ K_{mc}(d, l) &= \frac{G_s d^3}{2.29} \left(\frac{E_c(d, l)}{G_s} \right)^{0.40} \left(\frac{l}{d} \right)^{0.730} \end{aligned}$$

In regards with the optimization of the suction caisson, a fully encompassing yield surface in vertical load $F_{z,i}(\mathbf{x}, \mathbf{y})$, horizontal load $F_{x,i}(\mathbf{x}, \mathbf{y})$ and bending moment $M_{y,i}(\mathbf{x}, \mathbf{y})$ space is taken into account. The magnitude of the uniaxial capacity and the shape of the yield surface depend on the soil response to loading (undrained and drained), the soil strength profile, foundation shape, foundation embedment and inclusion of tension between the foundation and the soil. In the case of undrained soil conditions, the bearing capacity of suction caissons subjected to combined vertical, horizontal and moment loading is estimated by deploying the failure envelopes expressions suggested by [19] and [36]. Two different capacity functions were used for suction caissons in order to distinguish between slenderness ratios lower and larger than 1. In such ultimate limit states the soil medium was modelled as linear elastic – perfectly plastic material and Tresca criterion was used to define the failure conditions. For the tensile capacity, API provisions [1] suggest that uplift capacity should be analyzed as a reverse bearing capacity problem with a minimum recommended factor of safety factor equal to 2.0. Note that different formulations must be adopted based on the soil conditions.

2.7.2 Combined load capacity for non-slender ($l/d \geq 1$) suction caissons in clay

Particularly, the ultimate bearing capacity of suction caissons in clay with slenderness ratio $0 \leq l/d \leq 1$ is estimated according to Gouvernec [19] as follows:

$$\frac{F_{z,i}(\mathbf{x}, \mathbf{y})}{V_c(\mathbf{y})} - \left(1 - \frac{F_{x,i}(\mathbf{x}, \mathbf{y})}{H(\mathbf{y})}\right)^{p(\mathbf{y})} \leq 0, \quad i = 1, \dots, n_f,$$

where

$$V_c(\mathbf{y}) = \frac{6.05s_u\pi}{4}(d^2 + 0.86ld - 0.16l^2), \quad H(\mathbf{y}) = s_u \left(d + 4.46l - 1.52\frac{l^2}{d}\right), \quad (5)$$

$$\text{and } p(\mathbf{y}) = \begin{cases} 0.18 + 0.14\frac{l}{d}, & \text{for } \frac{l}{d} \leq \frac{1}{2} \\ \frac{1}{4}, & \text{for } \frac{l}{d} \geq \frac{1}{2} \end{cases}$$

There are two issues with this capacity function which can cause problems in the numerical examples. One is that $p(\mathbf{y})$ is non-differentiable at $l/d = 1/2$. The second is the case where $F_{x,i}(\mathbf{x}, \mathbf{y}) \geq H(\mathbf{y})$, as this produce a complex number. Firstly it was observed that all designs converged to solutions where $l/d > 1/2$, and secondly an additional constraint of $F_{x,i}(\mathbf{x}, \mathbf{y}) \leq H(\mathbf{y})$ was introduced. Neither issue influenced the numerical experiments.

In regards with suction caissons with slenderness ratio less than 1 and embedded in clayey soils, the maximum tensile design load must not exceed the design tensile capacity, given as the sum of the caisson weight, external shaft friction and reverse end bearing. Hence, the tensile capacity for suction foundation in clay can be estimated as

$$F_{z,i}(\mathbf{x}, \mathbf{y}) - \frac{1}{2}V_t(\mathbf{y}) \leq 0, \quad i = 1, \dots, n_f, \quad (6)$$

where

$$V_t(\mathbf{y}) = \frac{\pi\rho g}{200}d^3 + \pi\rho^f g(dt - t^2)l + \frac{9s_u\pi}{4}d^2 + \frac{s_u\pi}{5}dl \quad (7)$$

and ρ^f and g are the pile density and the gravitational constant, respectively. Here it is assumed that the thickness of the caisson lid is equal to $d/50$.

2.7.3 Combined load capacity for slender (1/d;1) suction caissons in clay

When the slenderness ratio is greater than 1, the expression of Supachawarote et al. [36] can be applied:

$$\left(\frac{F_{x,i}(\mathbf{x}, \mathbf{y})}{H(\mathbf{y})}\right)^{a(\mathbf{y})} + \left(\frac{F_{z,i}(\mathbf{x}, \mathbf{y})}{V_c(\mathbf{y})}\right)^{b(\mathbf{y})} - 1 \leq 0 \quad i = 1, \dots, n_f, \quad (8)$$

where

$$H(\mathbf{y}) = 4dls_u, \quad V_c(\mathbf{y}) = \frac{9s_u\pi}{4}d^2, \quad a(\mathbf{y}) = \frac{l}{2d} + 4.5, \quad \text{and} \quad b(\mathbf{y}) = -\frac{l}{4d} + 3.5.$$

When the suction caisson undergoes to tensile loads, a similar failure envelope as described in equation (8) is assumed with the difference that $V_c(\mathbf{y})$ is substituted by the tensile capacity given by equation (7).

2.7.4 Combined load capacity for suction caissons in sand

Due to the absence in the literature of mathematical formulations on the ultimate resistance of suction caissons embedded in sands, the closed-form expression suggested by Gottardi et al. [18] for circular footing on dense sand based on the concept of plasticity theory was adopted in this study:

$$\left(\frac{M_{y,i}(\mathbf{x}, \mathbf{y})}{Q_i(\mathbf{x}, \mathbf{y})}\right)^2 + \left(\frac{F_{x,i}(\mathbf{x}, \mathbf{y})}{H_i(\mathbf{x}, \mathbf{y})}\right)^2 + \frac{F_{x,i}(\mathbf{x}, \mathbf{y})M_{y,i}(\mathbf{x}, \mathbf{y})}{C_i(\mathbf{x}, \mathbf{y})} - 1 \leq 0, \quad i = 1, \dots, n_f,$$

where

$$Q_i(\mathbf{x}, \mathbf{y}) = 0.36F_{z,i}(\mathbf{x}, \mathbf{y}) \left(1 - \frac{F_{z,i}(\mathbf{x}, \mathbf{y})}{V_c(\mathbf{y})}\right) d, \quad H_i(\mathbf{x}, \mathbf{y}) = 0.48F_{z,i}(\mathbf{x}, \mathbf{y}) \left(1 - \frac{F_{z,i}(\mathbf{x}, \mathbf{y})}{V_c(\mathbf{x}, \mathbf{y})}\right),$$

$$C_i(\mathbf{x}, \mathbf{y}) = 0.39F_{z,i}(\mathbf{x}, \mathbf{y})^2 \left(1 - \frac{F_{z,i}(\mathbf{x}, \mathbf{y})}{V_c(\mathbf{y})}\right)^2 d, \quad V_c(\mathbf{y}) = c_{ult}d^3,$$

$$\text{and} \quad c_{ult} = 0.11\gamma\pi \tan \phi \left(e^{\pi \tan \phi} \tan \left(45 + \frac{\phi}{2} \right) - 1 \right)$$

On the other hand, the tensile capacity of suction caissons in sands is calculated according to the equation (6), where V_t is calculated as proposed by Houlsby et al. [20]:

$$V_t(\mathbf{y}) = \frac{\pi\rho g}{200}d^3 + \pi\rho g(dt - t^2)L + P_\gamma(d - t)L^2, \quad \text{and} \quad P_\gamma = \gamma\pi(1 - \sin \phi) \tan \frac{\phi}{3}$$

2.8 Design sensitivities of the joint reaction forces

The design sensitivities of the reaction forces $\mathbf{f}_i^f(\mathbf{x}, \mathbf{y})$ with respect to jacket variables \mathbf{x} and foundation variables \mathbf{y} can be computed as

$$\begin{aligned}\frac{d\mathbf{f}_i^f(\mathbf{x}, \mathbf{y})}{d\mathbf{x}} &= \mathbf{K}_i^f(\mathbf{y}) \frac{d\mathbf{u}_i^f(\mathbf{x}, \mathbf{y})}{d\mathbf{x}} \\ \frac{d\mathbf{f}_i^f(\mathbf{x}, \mathbf{y})}{d\mathbf{y}} &= \mathbf{K}_i^f(\mathbf{y}) \frac{d\mathbf{u}_i^f(\mathbf{x}, \mathbf{y})}{d\mathbf{x}} + \frac{d\mathbf{K}_i^f(\mathbf{y})}{d\mathbf{y}} \mathbf{u}_i^f(\mathbf{x}, \mathbf{y})\end{aligned}\tag{9}$$

where the sensitivities of the pile head displacements are found by solving the full system

$$\mathbf{K}(\mathbf{x}, \mathbf{y}) \frac{d\mathbf{u}(\mathbf{x}, \mathbf{y})}{dv_k} = \frac{d\mathbf{f}(\mathbf{x}, \mathbf{y})}{dv_k} - \frac{d\mathbf{K}(\mathbf{x}, \mathbf{y})}{dv_k} \mathbf{u}(\mathbf{x}, \mathbf{y})$$

for each variable v_k in \mathbf{x} and \mathbf{y} .

2.9 Implementation

The structural analysis model and sensitivity analysis are implemented in a Matlab package called JADOP (JACKET Design OPTimization), and interfaces the optimizer IPOPT [39]. JADOP is an analysis and optimization software developed for optimal design of jacket structures, and this paper documents the extension to foundation modelling and design. IPOPT is an open source software package for large-scale nonlinear optimization. It uses a primal-dual interior point method with filters to promote global convergence. The tolerance is set to 10^{-5} , and the parameter `nlp scaling` is turned off. Instead a user-defined scaling of 10^{-5} is applied to the stiffness and mass matrix, the load, the stresses, and the objective function.

3 Numerical study

The optimal design problem is solved to propose foundation and jacket designs for an offshore wind turbine at 50 m water depth. Piles and suction caissons are considered as foundation types, while different soil conditions are investigated as described in the following.

3.1 Definition of design parameters

A structural finite element model with piles, jacket, transition piece, and tower is built in JADOP, see Figure 3. All cross sections are assumed to be thin-walled pipes with constant cross section along the element length, and with a shear correction factor of 0.5 [11]. The material is steel, and the density and yield stress is set to 7800 kg/m^3 and 355 MPa for both jacket and foundation.

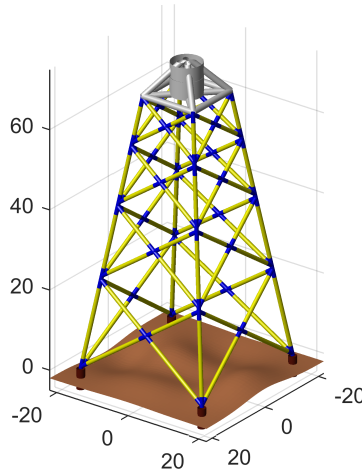


Figure 3: Describe the structure.

The jacket has four straight legs, and four levels of X-braces. The leg distance is 30 meters at the bottom, and 14 meters at the top. The structure is symmetric, and the footprint is square. The transition piece, tower, and RNA is modelled to be a close replica of the DTU 10 MW reference wind turbine, see [3] and [6].

In order to cover a broad spectrum of soil conditions, different sets of soil profiles have been taken into account, representing both cohesive (clay) and cohesionless (sand) soil. The definition of the soil profiles was based on the soil categorization scheme suggested in EC8 [16]. Five soil stiffnesses are considered, where A is very stiff, and E is very soft, as described in Table 2. For each soil profile, both sand and clay characteristics are given. For the softest soil profiles the problem was in some cases not feasible. The Young modulus of the soil was estimated based on the elastic shear wave velocity, thus it is representative of small strain stiffness. Unless otherwise specified, soil profile B is used in the numerical studies.

Table 2: Soil profiles considered in the optimal design problem.

Soil Profile	Shear wave velocity [m/s]	Youngs modulus [MPa]	Angle of friction [deg]	Undrained shear strength [kPa]	Unit weight [kN/m3]
A	600	2138	45	300	22
B	400	864	40	250	20
C	250	287	35	150	17
D	100	44.6	33	50	16.5
E	50	10.8	30	20	16

Moreover five different CPT records from offshore sites were analysed. The tip resistance is plotted in Figure 4 along with the results of the classification analysis which was carried out according to Robertson et al. [32]. The strength properties of the cohesionless layers were evaluated by first calculating the relative densities D_r [22] and then the angle of shearing resistance (friction) ϕ , while for the cohesive layers N_{kt} was assumed to be 15 [26]. As shown in Figure 4 the first CPT is characterized by a homogeneous sand layer of D_r equal to 80% and angle

of shearing resistance between 39° and 42° . Three different soil layers are found at the second CPT, starting from silt (from clayey to sandy), to alternating layers of sand and gravelly sand. The undrained shear strength was estimated for the silt layer to 200kPa, while the cohesionless layers had D_r between 77% and 87% with angles of friction 38.5° to 43.7° respectively. At the third CPT 4 layers were identified namely silty sand, sand, silty sand and gravelly sand. The relative density increases from the silty sand layers to the sand and the gravelly sand, and the same holds for the angle of friction as expected. The first 18m of the fourth CPT provided a very scattered trend in Robertson's classification chart [32] ranging from silty clay to silty sand without a clear pattern with increasing depth. The deeper layers are gravelly sand and sand with mean D_r 89% and 73% respectively. The last CPT is characterized by alternating sand and gravelly sand layers with very high D_r values ranging between 84% and 94%. Concluding it was found that most of the CPT profiles were characterized by cohesionless soil layers with relative densities D_r varying between 73% and 94% and angles of friction between 38° and 44° . Therefore the CPT data are appropriate for the implementation of the UWA method [25] for estimation of the axial pile capacity. Unless otherwise specified, the CPT–data named CPT4 is used in the numerical studies. The reason for including five different data sets is to observe how the soil properties influence the optimized design, e.g. comparing Figure 4 and Table 6.

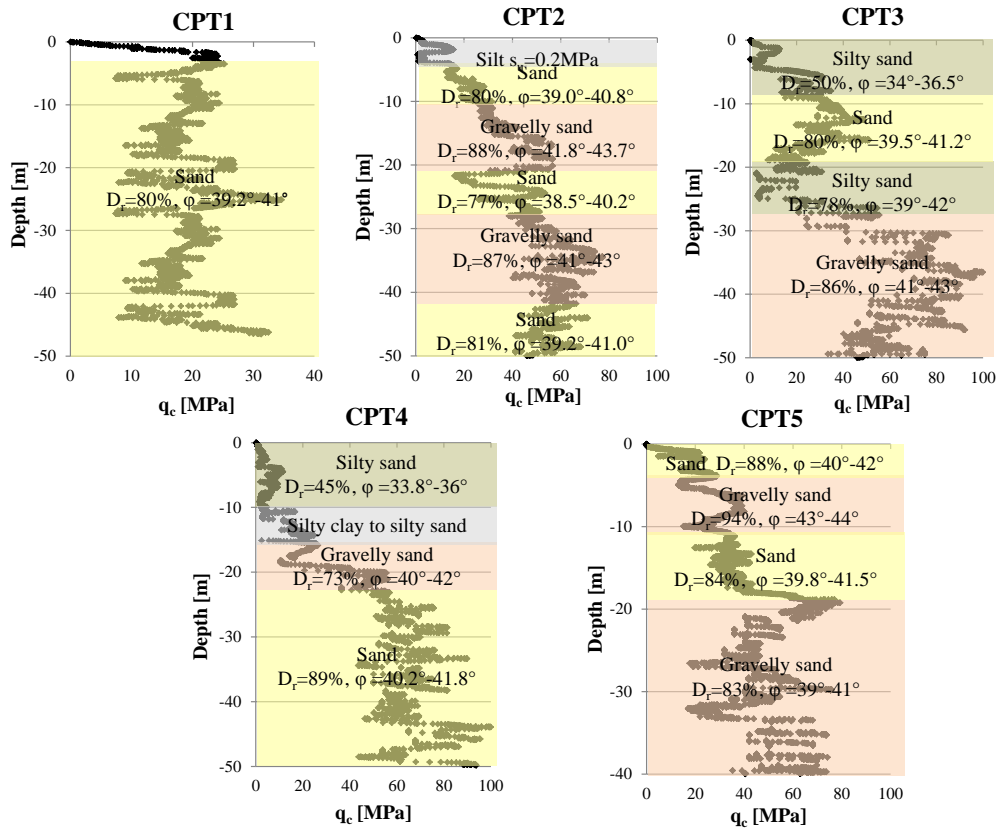


Figure 4: Five CPT data sets.

In the fatigue limit state load cases the stress constraints are bounded by an equivalent fatigue limit, which is the stress corresponding to 20 years of fatigue life when the 1 Hz damage equivalent load is applied. In addition, the stresses in the elements connected to a tubular joint are multiplied with stress concentration factors according to [14]. Bounds on the jacket and foundation design variables, natural frequency, as well as stress constraints in ultimate and fatigue load cases are given in Table 3. Note that the foundation capacity constraints and linear constraints are not included in Table 3.

Table 3: Bounds on the design variables and constraints.

Bounds	Jacket	Pile	Suction caisson	Full structure
Lower diameter	0.4 m	1 m	2 m	-
Upper diameter	1.4 m	6 m	11 m	-
Lower thickness	15 mm	15 mm	15 mm	-
Upper thickness	120 mm	120 mm	400 mm	-
Lower length	-	10 m	2 m	-
Upper length	-	60 m	20 m	-
Lower frequency	-	-	-	0.178 Hz
Upper frequency	-	-	-	0.270 Hz
Yield stress	355 MPa	355 MPa	355 MPa	-
Equivalent fatigue limit	11.5 MPa	-	-	-

3.2 Integrated optimal designs of jacket and foundations

The optimal design problem is solved for suction caissons and piles in both sand and clay (Profile B), and the results are shown in Table 4. All jacket designs converge to approximately the same mass and the same design. This indicates that jacket design is fairly decoupled from the design of the foundation for the soil conditions and jacket leg distance considered here.

The different foundation design cases lead to very different masses. It can be observed that the piles in clay are heavier than the ones designed for a sand site. Moreover for a clay site the best foundation solution, in terms of mass appears to be the suction caisson with slenderness ratio larger or equal to 1. Since the solution has a slenderness ratio very close to 1, it should be expected that the suction caisson with slenderness ratio less than 1 should converge to the same design. Since this is not the case, either the two design procedures do not produce the same result at slenderness ratio equal to 1, or that the optimization has found a local minimum. This illustrates the value of using more than one design procedure. An opposite trend is observed in sand, where the suction caisson is more than an order of magnitude heavier than the piles. As the pull-out force is design-driving for most of the foundation design cases, the suction caisson in sand becomes extremely heavy due to the poor tensile capacity. Additionally the CPT based method provides a more economic pile design in the sand site. Note that CPT4 can be grossly characterized as soil type B listed in Table 4, therefore the comparison of the pile designs is consistent. An alternative solution to make the use of suction caissons attractive would be to increase the mass of the structure, for example with a transition piece made by concrete. In the following numerical simulations the suction caisson in sand design case is excluded, as the design can be hardly comparable to the other design cases.

Table 4: Optimization results for integrated optimal design of jackets and foundations with two foundation types and two soil types.

Soil profile	Foundation design case	Jacket mass [tons]	Foundation mass [tons]	Foundation diameter [m]	Foundation wall thickness [mm]	Foundation length [m]
Clay	Pile	631	87.4	1.89	25.2	18.9
	Caisson	635	49.8	4.18	48.1	2.56
	Caisson ($l/d > 1$)	634	35.6	3.12	37.6	3.13
Sand	Pile	633	73.5	1.24	18.7	32.8
	Pile (CPT)	633	51.8	1.13	17.6	27.1
	Caisson	636	1727	9.13	97.6	20.0

3.3 Sequential optimal designs of jacket and foundations

In the previous example the design of foundation and jacket was done in an integrated optimization. A simpler approach is to do the designs sequentially. First the jacket design is optimized with clamped boundary conditions. Secondly, the jacket design is kept fixed, and the foundation design is optimized. The results are shown in Table 5.

Table 5: Optimization results for all two foundation types and two soil types, using pre-designed jacket.

Soil profile	Foundation design case	Jacket mass [tons]	Foundation mass [tons]	Foundation diameter [m]	Foundation wall thickness [mm]	Foundation length [m]
Clay	Pile	637	91.5	1.20	18.3	43.3
	Caisson	637	49.8	4.20	48.3	2.53
	Caisson ($l/d > 1$)	637	35.6	3.13	37.6	3.13
Sand	Pile	637	74.1	1.25	18.8	32.6
	Pile (CPT)	637	69.4	1.50	21.3	22.5
	Caisson	637	1726	9.12	97.5	20.0

The optimized jacket mass is of course the same for all foundation design cases, since it was designed without a foundation model. The jacket mass is heavier than in all of the integrated design cases, but the difference is less than 1%. This indicates that sequential design works well for the jacket, at least for the stiff soil profile considered here (Profile B).

The optimized suction caissons obtained from the sequential design procedure are practically identical with the designs obtained from the integrated design procedure. This might be either because the caissons are very stiff in rotation, and thus act similarly as a clamped boundary condition, or because the mass of the jacket is only marginally decreased in the integrated optimization with suction caissons.

The optimized piles obtained from the sequential design procedure are also comparable with the designs obtained from the integrated design procedure. Regarding the sand site, the pile design according to the CPT-based method, has 34% higher mass. However, it is still lighter than the traditional pile in sand design from the integrated design procedure. The CPT design

has also become less slender. The pile in clay becomes 5% heavier, and increases its slenderness ratio.

3.4 Influence of leg distance on foundation design

The loads on the foundation change when the leg distance of the jacket varies. Figures 5 and 6 show how the jacket and foundation change when the leg distance is varied between 18m and 38m.

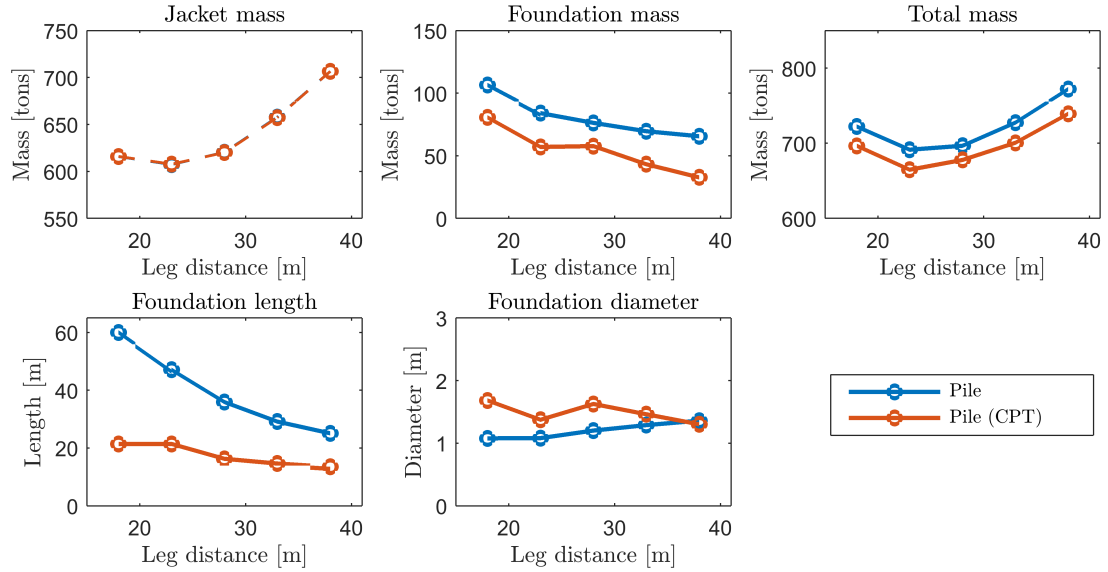


Figure 5: Variation of the jacket, foundation and total masses, foundation length and diameter with respect to the leg distance in sand soil profile.

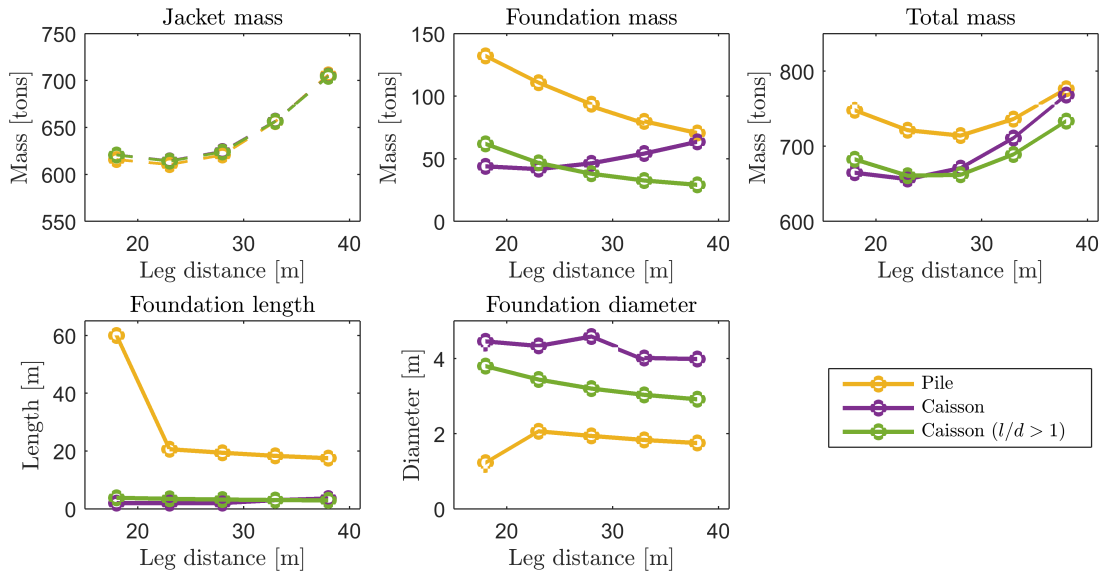


Figure 6: Variation of the jacket, foundation and total masses, foundation length and diameter with respect to the leg distance in clayey soil profile.

The integrated optimization for the jackets installed in sand profiles results in increased mass of the jacket as the leg distance increases. On the contrary the foundation (pile) mass decreases mainly due to the decrease of the pile length. The fact that the foundation mass reduces as the leg distance increases is determined by the redistribution of the axial forces among the single foundations. The total mass exhibits an increasing trend, as the foundation mass comprises a smaller portion with increasing leg distance. The pile design is influenced by the applied design method, and consistently the CPT based method provides shorter piles with larger diameters and smaller total mass. The jacket mass increases with increasing leg distance, and therefore the total substructure mass (left) is lowest at an intermediate leg distance between 23m and 28m, depending on foundation type.

The general trends in the jacket and foundation mass observed in the sand profile are also valid for the clay profile. Exception to this is the caisson with the slenderness ratio (L/d) smaller than 1, which appears to increase in mass with increasing leg distance of the jacket. This could be mean that the combined failure due to vertical and horizontal load becomes more critical as the pull out force decreases with increasing leg distance. It is also worth noticing that the suction caissons result always in lower foundation mass compared to the piles. Additionally the design of suction caisson in clayey soil with slenderness ratio $L/d > 1$ showed that the foundation diameter doubled as the leg distance reduces; while this increasing pattern is less apparent for the suction caisson with slenderness ratio $L/d \leq 1$.

3.5 Influence of soil properties on jacket and foundation design

Figures 7 and 8 show how the foundation design varies as a function of soil stiffness, where A and E represent the stiffest and the softest soil deposit, respectively. The CPT-pile design case is based on a medium to stiff soil profile, and is therefore only solved for soil types A, B and C.

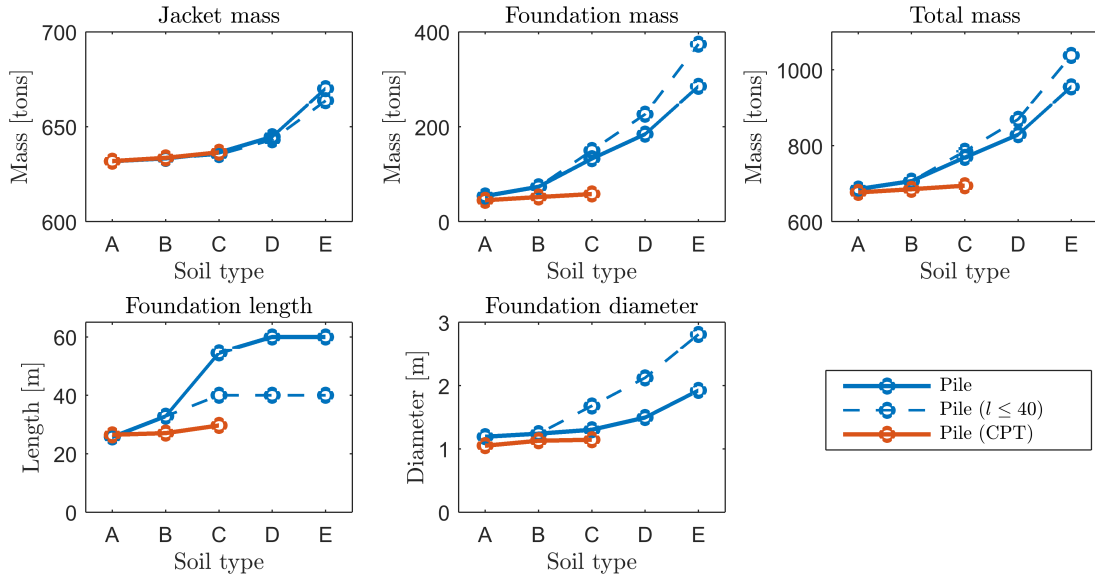


Figure 7: Effect of the soil type on the jacket, foundation and total masses, foundation length and diameter in sand soil profile.

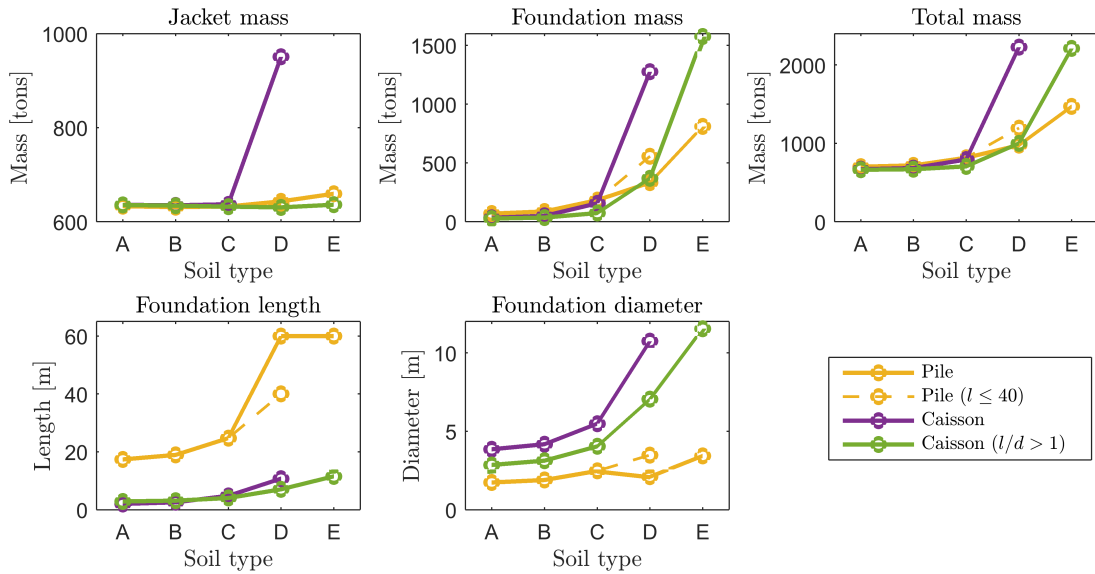


Figure 8: Effect of the soil type on the jacket, foundation and total masses, foundation length and diameter in clay soil profile.

The CPT based design was performed for the soil stiffness reported as soil type A, B and C, which is representative for the measured tip resistance of CPT 4. The investigation of the soil type effect on the optimization of the design in sand profiles demonstrates that the mass of the jacket is influenced by the foundation stiffness, especially for medium dense to loose sand

deposits (type D and E). As expected the foundation mass increases also as the stiffness and strength of the sand decreases. Note that the length is the preferred optimization parameter compared to the diameter. This is evident by comparing the results of the pile design with maximum length constraint set to 60m and 40m. It is shown that in the first case the length of the pile increases more rapidly compared to the diameter, while the opposite holds for the latter case. In regards with the CPT based method it is seen that the foundation mass is always smaller than the one provided by the traditional design approach, with the design diameter being always smaller and the pile length substantially reduced.

The jacket mass appears to increase with decreasing soil stiffness also for the foundation designs in clay, where particularly high mass is obtained for suction caissons with small slenderness ratio. On the contrary suction caissons with large slenderness ratio affect to a minor extent the design of the jacket, which could be attributed to their larger rotational and coupling stiffness components. When it comes to the foundation optimization the caisson with the larger slenderness ratio is the foundation type with the lower mass for soil types up to C, however for soil type D and E the long pile results in smaller mass.

3.6 Influence of CPT data on pile design

In the optimal design problem, the maximum pile length was set to 60m. To comply with such piles, the CPT data sets were linearly extrapolated. However, none of the CPT-piles in the numerical simulations exceeded 30m. The optimal design problem was solved for all five CPT data sets, and the results are shown in Table 6.

Table 6: Optimization results for all five CPT data sets.

Foundation design case	Pile mass [tons]	Diameter [m]	Wall thickness [mm]	Length [m]	Mean q_c [MPa]
Pile in sand (CPT1)	102	1.98	26.1	20.5	18.2
Pile in sand (CPT2)	44.7	1.22	18.5	20.5	26.7
Pile in sand (CPT3)	54.4	1.59	22.2	15.9	23.4
Pile in sand (CPT4)	51.8	1.13	17.6	27.1	21.4
Pile in sand (CPT5)	52.2	1.49	21.2	17.0	27.8

The foundation mass obtained after the optimization with the CPT records 2–5 is very similar, indicating that the sensitivity of the pile design to variations of the tip resistance is not significant. On the other hand the pile design according to the first CPT record resulted in a foundation mass double than the other records. This can be explained by the lower tip resistance values. As shown in Table 5, the mean tip resistance over the pile length for CPT1 is lower than the corresponding of CPTs 2–5. Comparing the CPT based design with the traditional approach the first record would be closer to soil type C, which resulted in mass slightly higher than 100tons according to Figure 7. It can be concluded that regardless of slight variations in the CPT data the CPT based method provides less conservative pile designs than the conventional design procedure.

3.7 Influence of leg distance and soil type on structural frequency

The first natural frequency of an offshore wind turbine structure should lie in the range between the 1P and 3P frequencies of the rotor to avoid resonance problems. For the DTU 10 MW reference wind turbine this range is from 0.16 to 0.30 Hz. A safety margin of 10% is often included, which means that the allowable frequency range is actually from 0.176 to 0.27 Hz, as shown in Table 3. While the frequency is dominated by the tower and turbine, the soil, foundation type, and jacket has some influence on the natural frequency.

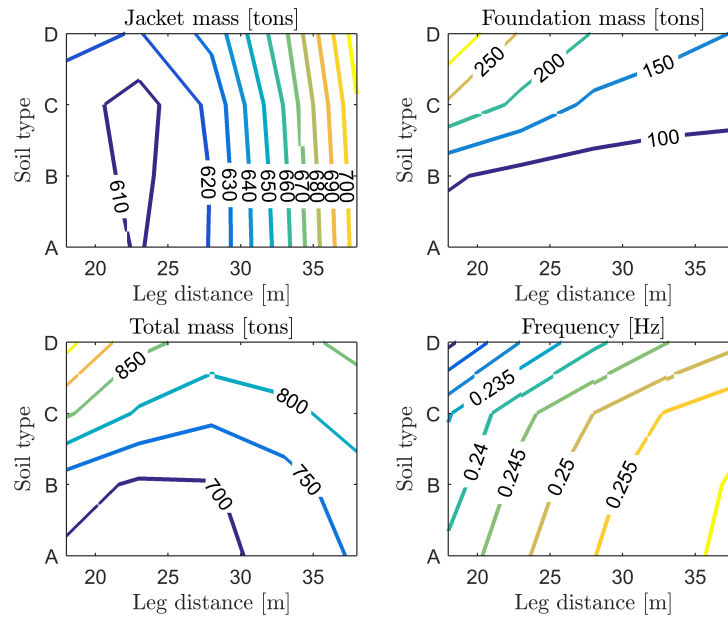


Figure 9: Variation of the frequency, jacket and foundation masses with respect to the leg distance and soil stiffness for pile foundation in sand.

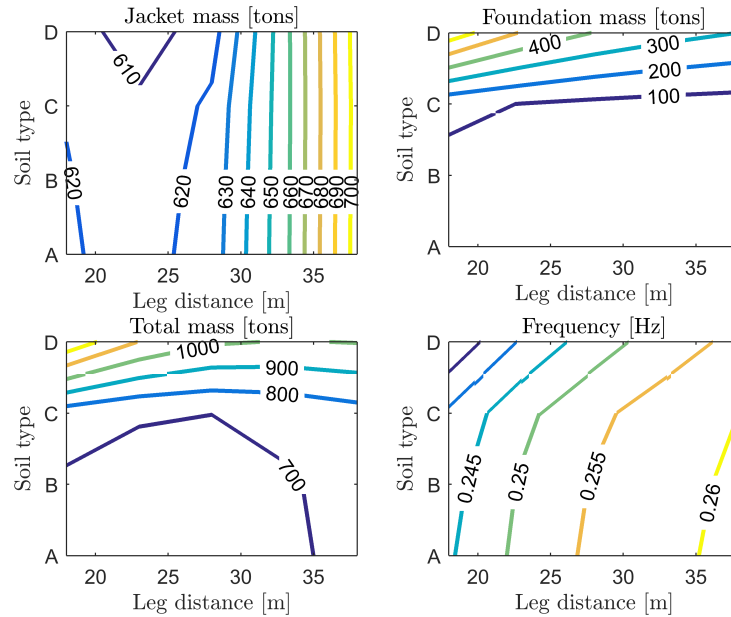


Figure 10: Variation of the frequency, jacket and foundation masses with respect to the leg distance and soil stiffness for suction caisson foundation ($l/d > 1$) in clay.

In Figures 9 and 10, the jacket mass, foundation mass, total mass, and the lowest natural frequency of the full structure is plotted as a function of both leg distance and soil type. All data points are the result of an integrated optimization as described previously. First of all, the jacket mass is mostly a function of the leg distance, though for leg distances below 30m the mass is also varying with soil type. The mass of the piles in sand increases with softer soil and smaller leg distance, as observed earlier. The mass of the suction caisson in clay, however, is almost exclusively dependent on the soil type. Finally, the frequency plots show how the frequency decreases with smaller leg distance and softer soil. Note that with softer soils, the foundation mass increases while the frequency drops. This means that even though the foundation mass increases, the stiffness of the foundation actually decreases.

Based on this numerical study, it seems that the foundation and jacket design are quite decoupled, especially for suction caissons, and at least for medium to stiff soils. However, with small leg distance, soft soils, and piled foundation, the interaction is too large to be ignored. Notice for example that the frequency of the pile in sand for a 20m leg distance decreases from 0.245 Hz to 0.225 Hz when the soil type is changed from A to D. This drop in frequency of 8% can have significant implications for the structural response, and should be considered throughout the design process.

4 Conclusion

In this paper we have demonstrated that numerical optimization can be applied to automate several of the standard procedures for foundation design. This is not only beneficial because new foundation designs can be generated quickly when the design conditions are changed. It also

allows for integrated design of the jacket and the foundation. Integrated design optimization of jacket and foundation for two different foundation types, a range of different leg distances, and ten soil profiles revealed some trends:

- The jacket design is not very dependent on foundation design. The exception is for very soft soils when jacket mass can increase by 10%.
- The jacket design depends mostly on leg distance, and a small leg distance is generally preferred.
- The foundation design is very dependent on the jacket mass. This is because the pull-out force is often design driving, and the pull-out force increases when the jacket mass decreases.
- The foundation design is very dependent on leg distance, and a large leg distance is generally preferred. This is because the pull-out force decreases with increased leg distance. The exception is suction bucket in clay, where increased leg distance actually increases foundation mass.
- The natural frequency of the overall structure is dependent on leg distance, and a larger leg distance gives a higher frequency.
- The natural frequency of the overall structure is partially dependent on soil stiffness. The first bending frequency is overestimated when the jacket is clamped at the seabed, but for stiff soils the error is smaller than 1%. For piled foundations in soft soil, the error can be up to 10%.
- Sequential design works better for design of suction caissons than it does for piles. This is because suction caissons are stiffer in rotation than piles.

These observations are based only on extreme static loads with linear elastic soil models. Dynamic loads and more complex soil models might give other insights. It should also be noted that the objective function was steel mass. Cost drivers such as manufacturing, transportation and installation were not taken into account. However it should be noted that the manufacturing costs are also dependent on the mass, and together with the material costs they comprise the largest part of the costs for construction of support structures. Also, the lid and stiffeners of the foundations were not included in the mass function. This leads to a non-conservative estimate of the mass, especially for the suction caissons.

Future work on design optimization of foundations should focus on more realistic load cases and more advanced soil models, ideally including the effects of cyclic loading and nonlinear response. Another interesting aspect is to include the foundation installation as a design variable, since pile driving costs depend on the sizing of the piles.

5 Acknowledgements

The research presented in this manuscript is part of the strategic research project ABYSS: Advancing BeYond Shallow waterS (www.abyss.dk) sponsored by the Danish Council for Strategic

Research. The funding is gratefully acknowledged. The authors would also like to thank Lone Krogh, Lead Geotechnical Specialist at DONG Energy Wind Power for providing the raw CPT data.

References

- [1] API. Geotechnical and foundation design considerations. ANSI/API RP 2GEO 1st edition Petroleum and natural gas industries: Specific requirements for offshore structures, Part 4. Technical report, API, 2011.
- [2] T. Ashuri. *Beyond Classical Upscaling : Integrated Aeroservoelastic Design and Optimization of Large Offshore Wind Turbines*. PhD thesis, Technische Universiteit Delft, 2012.
- [3] C. Bak, F. Zahle, R. Bitsche, T. Kim, A. Yde, L. C. Henriksen, A. Natarajan, and M. Hansen. The DTU 10 MW reference wind turbine. Technical report, DTU Wind Energy, 2013.
- [4] S. A. Barakat, A. I. Malkawi, and R. H. Tahat. Reliability-based optimization of laterally loaded piles. *Structural Safety*, 21(1):45 – 64, 1999.
- [5] S. Bhattacharya. Challenges in design of foundations for offshore wind turbines. *Engineering & Technology Reference*, 1(1), 2014.
- [6] T. Borstel. Design report - reference jacket. Technical Report D4.3.1, DTU Wind Energy, 2013.
- [7] B. Broms. Methods of calculation for laterally loaded piles. *Royal Swedish Geotechnical Institute – Reprints and Preliminary Reports*, (9), 1965.
- [8] C. M. Chan, L. M. Zhang, and J. T. Ng. Optimization of Pile Groups Using Hybrid Genetic Algorithms. *Journal of Geotechnical and Geoenvironmental Engineering*, 135(4):497–505, 2009.
- [9] K. H. Chew, K. Tai, E. Y. K. Ng, and M. Muskulus. Analytical gradient-based optimization of offshore wind turbine substructures under fatigue and extreme loads. *Marine Structures*, 47:23–41, 2016.
- [10] C. Clausen, P. Aas, and K. Karlsrud. Bearing capacity of driven piles in sand, the NGI approach. In *Proceedings of Proceedings of International Symposium. on Frontiers in Offshore Geotechnics, Perth*, pages 574–580, 2005.
- [11] R. D. Cook, D. S. Malkus, M. E. Plesha, and R. J. Witt. *Concepts and Applications of Finite Element Analysis*. John Wiley & Sons, fourth edition, 2007.
- [12] W. de Vries. Final report WP 4 . 2 Support Structure Concepts for Deep Water Sites. Technical report, Delft University of Technology, 2011.
- [13] DNV. RP-C202: Buckling Strength of Shells. Technical Report January, DNV, 2013.

-
- [14] DNVGL. RP-C203 Fatigue design of offshore steel structures. Technical report, DNVGL, 2014.
- [15] DNVGL. OS-C101 Design of Offshore Steel Structures, general - LRFD method. Technical Report July, DNVGL, 2015.
- [16] C. Eurocode. 8: Design of structures for earthquake resistance—part 1: General rules, seismic actions and rules for buildings (en 1998-1: 2004). *European Committee for Normalization, Brussels*, 2004.
- [17] P. Fuglsang and H. A. Madsen. Optimization method for wind turbine rotors. *Journal of Wind Engineering and Industrial Aerodynamics*, 80(1-2):191–206, 1999.
- [18] G. Gottardi, G. Houlsby, and R. Butterfield. Plastic response of circular footings on sand under general planar loading. *Géotechnique*, 49(4):453–470, 1999.
- [19] S. Gourvenec. Effect of embedment on the undrained capacity of shallow foundations under general loading. *Géotechnique*, 58(3):177–186, 2008.
- [20] G. T. Houlsby, R. B. Kelly, and B. W. Byrne. The tensile capacity of suction caissons in sand under rapid loading. In *Proceedings of the international symposium on frontiers in offshore geomechanics, Perth*, pages 405–410, 2005.
- [21] IEC. IEC 61400-3: Wind turbines - Part 3: Design requirements for offshore wind turbines. Technical Report 300 V, IEC, 2009.
- [22] M. Jamiolkowski, D. Lo Presti, and M. Manassero. Evaluation of relative density and shear strength of sands from cpt and dmt. In *Soil behavior and soft ground construction*, pages 201–238. 2003.
- [23] C. H. Juang and L. Wang. Reliability-based robust geotechnical design of spread foundations using multi-objective genetic algorithm. *Computers and Geotechnics*, 48:96 – 106, 2013.
- [24] C. Latini and V. Zania. Dynamic lateral response of suction caissons. *Soil Dynamics and Earthquake Engineering*, 100:59–71, 2017.
- [25] B. Lehane, J. Schneider, and X. Xu. The UWA-05 method for prediction of axial capacity of driven piles in sand. *Frontiers in Offshore Geotechnics: ISFOG*, pages 683–689, 2005.
- [26] T. Lunne, P. Robertson, and J. Powell. Cone penetration testing. *Geotechnical Practice*, 1997.
- [27] G. Meyerhof. Compaction of sands and bearing capacity of piles. *Transactions of the American Society of Civil Engineers*, 126(1):1292–1322, 1961.
- [28] M. Muskulus and S. Schafhirt. Design Optimization of Wind Turbine Support Structures — A Review. *Journal of Ocean and Wind Energy*, 1(1):12–22, 2014.

-
- [29] J. Oest, R. Sørensen, L. C. T. Overgaard, and E. Lund. Structural optimization with fatigue and ultimate limit constraints of jacket structures for large offshore wind turbines. *Structural and Multidisciplinary Optimization*, 55(3):779793, 2017.
- [30] T. Pucker and J. Grabe. Structural optimization in geotechnical engineering: Basics and application. *Acta Geotechnica*, 6(1):41–49, 2011.
- [31] M. F. Randolph. The response of flexible piles to lateral loading. *Geotechnique*, 31(2):247–259, 1981.
- [32] P. Robertson. Soil classification using the cone penetration test. *Canadian Geotechnical Journal*, 27(1):151–158, 1990.
- [33] K. Sandal and V. Zania. Optimization of pile design for offshore wind turbine jacket foundations. In *12th EAWC PhD seminar on Wind Energy in Europe*, 2016.
- [34] M. Seidel, S. Voormeeren, and J. van der Steen. State-of-the-art design processes for offshore wind turbine support structures. *Stahlbau*, 85(9):583–590, 2016.
- [35] K.-F. Seitz and J. Grabe. Three-dimensional topology optimization for geotechnical foundations in granular soil. *Computers and Geotechnics*, 80:41–48, 2016.
- [36] C. Supachawarote, M. Randolph, and S. Gourvenec. Inclined pull-out capacity of suction caissons. In *The Fourteenth International Offshore and Polar Engineering Conference*. International Society of Offshore and Polar Engineers, 2004.
- [37] The Crown Estate. Offshore wind cost reduction-Pathways study. Technical report, The Crown Estate, 2012.
- [38] A. Thiry, F. Bair, L. Buldgen, B. G. Raboni, and P. Rigo. Optimization of monopile offshore wind structures. *Advanced Marine Structures*, pages 633–642, 2011.
- [39] A. Waechter and L. T. Biegler. On the Implementation of a Primal-Dual Interior Point Filter Line Search Algorithm for Large-Scale Nonlinear Programming. *Mathematical Programming*, 106(1):25–57, 2006.
- [40] D. Zwick and M. Muskulus. The simulation error caused by input loading variability in offshore wind turbine structural analysis. *Wind Energy*, 18(8):1421–1432, 2014.
- [41] D. Zwick, M. Muskulus, and G. Moe. Iterative Optimization Approach for the Design of Full-Height Lattice Towers for Offshore Wind Turbines. *Energy Procedia*, 24:297–304, 2012.

A Appendix

This appendix describes the friction, end bearing, and lateral capacity functions for the piles in sand and clay, as well as for the pile design using the CPT approach. Note that the foundation variable is $\mathbf{y} = (d \ t \ l)^T$, where the superscript f is omitted for brevity.

A.1 Pile in clay

The friction capacity Q_f for piles in clay, as used in equation (3), is according to the α -method formulated in [1] computed as

$$Q_f(d, t, l) = \frac{2}{5}\pi ds_u^{\frac{3}{4}}\gamma^{\frac{1}{4}}z_{1c}^{\frac{5}{4}} + \frac{1}{3}\pi ds_u^{\frac{1}{2}}\gamma^{\frac{1}{2}}(l - z_{1c})^{\frac{3}{2}},$$

where

$$z_{1c}^c = \min\left(\frac{s_u}{\gamma}, l\right).$$

The non-differentiability of z_1 can potentially cause problems in the optimization, but this has not been observed in the numerical experiments. There are two alternatives for the end bearing capacities Q_b , and the lowest value shall be used. In practice that means that both alternatives can be applied as separate constraints, i.e.

$$-(Q_f(\mathbf{y}) + Q_{b_k}(\mathbf{y})) \leq F_{z,i}(\mathbf{x}, \mathbf{y}) \leq Q_f(\mathbf{y}), \quad i = 1, \dots, n_f, \quad k = 1, 2$$

where

$$Q_{b_1}(\mathbf{y}) = \frac{9s_u\pi d^2}{4}$$

$$Q_{b_2}(\mathbf{y}) = \frac{9s_u\pi}{4}(d^2 - (d - 2t)^2) + Q_{f_i}(\mathbf{y}),$$

and $Q_{f_i}(\mathbf{y})$ is the same as $Q_f(\mathbf{y})$, except with $d - 2t$ instead of d .

A.2 Pile in sand

The friction capacity Q_f for piles in sand, as used in equation (3), is according to the β -method formulated in [1] computed as

$$Q_f(d, t, l) = \frac{\pi}{2}d\beta\gamma z_{1s}^2 + \pi df_{max}(l - z_{1s}),$$

where

$$z_{1s} = \min\left(\frac{f_{max}}{\beta\gamma}, L\right).$$

There are four alternatives for the end bearing capacity Q_b , and the lowest value shall be used. In practice that means that all alternatives can be applied in separate constraints, i.e.

$$-(Q_f(\mathbf{y}) + Q_{b_k}(\mathbf{y})) \leq F_{z,i}(\mathbf{x}, \mathbf{y}) \leq Q_f(\mathbf{y}), \quad i = 1, \dots, n_f, \quad k = 1, \dots, 4 \quad (10)$$

where

$$\begin{aligned}
 Q_{b_1}(\mathbf{y}) &= \frac{N_q \gamma \pi d^2 l}{4} \\
 Q_{b_2}(\mathbf{y}) &= \frac{N_q \gamma \pi (d^2 - (d - 2t)^2) l}{4} + Q_{fi}(\mathbf{y}) \\
 Q_{b_3}(\mathbf{y}) &= \frac{q_{b,max} \pi d^2}{4} \\
 Q_{b_4}(\mathbf{y}) &= \frac{q_{b,max} \pi (d^2 - (d - 2t)^2)}{4} + Q_{fi}(\mathbf{y}).
 \end{aligned}$$

A.3 UWA-CPT based method

The friction capacity Q_f for piles in a soil described by CPT data, as used in equation (4), is according to the UWA-CPT method [25] computed as

$$Q_f(\mathbf{y}) = P_\phi d \left(\frac{4t(d-t)}{d^2} \right)^{0.3} \left(\sqrt{d} f(d, L) + 2g(d, L) \right)$$

where

$$P_\phi = \pi \tan(0, 75\phi), \quad f(d, L) = \int_0^{L-2d} \frac{q_c(z)}{\sqrt{L-z}} dz \quad \text{and} \quad g(d, L) = \int_{L-2d}^L q_c(z) dz.$$

The end bearing capacity is computed as

$$Q_b(d, t, L) = \frac{\pi}{40} \left(d + \frac{6t(d-t)}{d} \right) k(d, L)$$

where

$$k(d, L) = \int_{L-1.5d}^{L+1.5d} q_c(z) dz.$$

Internal report

Triaxial Tests in Fontainebleau Sand

C. LATINI AND V. ZANIA



TECHNICAL UNIVERSITY OF DENMARK

INTERNAL REPORT

Triaxial Tests in Fontainebleau Sand

Ph.D Student Chiara Latini

supervised by
Associate Professor Varvara Zania

January 22, 2018

Contents

1	Introduction	2
2	Data processing	3
2.1	Introduction	3
2.2	Measurement corrections	4
3	Results	6
3.1	Consolidation phase	6
3.2	Elasticity parameters	6
3.2.1	Unloading-reloading phase	7
3.2.2	Initial moduli	9
3.2.3	Secant moduli	9
3.3	Estimation of strength parameters of CID tests	11
3.4	Estimation of strength parameters of CUD tests	15
3.5	Estimation of dilation angle	19
3.6	Estimation of the critical state	19
4	Conclusions	21

Chapter 1

Introduction

The purpose of this internal report is to examine the influence of the relative density on the strength and deformation characteristics of Fontainebleau sand. Compression triaxial tests were performed on saturated sand samples with different densities and initial confining pressure σ'_r . Note that the testing procedure and the data processing were carried out according to the specifications of ETCS-F1.97. The internal report is divided into two chapters and four appendices associated with the results of chapter 2 are placed at the end of the report.

Chapter 2

Data processing

2.1 Introduction

Test setup

In Figure 2.1 the setup of a sample in the triaxial test can be seen. The sample, which has to be set dry, is packed in a cylindrical latex membrane with a flat, circular metal plate (pressure head) closing off the top and bottom ends. The cylinder (length $l=7\text{cm}$ and diameter $d=7\text{cm}$) is placed into a bath of a hydraulic fluid (water), to provide pressure along the sides of the cylinder. The top plate is mechanically driven up or down along the axis of the cylinder to apply pressure on the sample. The distance that the upper plate travels is measured as a function of the force required to move it, as the pressure of the surrounding water is carefully controlled. The net change in volume of the sample is also measured, by the amount of water flowing in or out of the sample's pores. Once the chamber is filled with water, the sample can be saturated. The water flows through the sample with the siphon-principle by connecting the lower pressure head with a de-aired water container and the upper pressure head with a drain hose, respectively.



Figure 2.1: Setup of a test.

Measured parameters

The parameters measured in the triaxial test are the axial displacement ΔH , the height of the sample using LVDT's, the change in volume ΔW_{water} by the amount of water flowing in or out the sample, the chamber pressure σ_r and the axial load applied by the piston on the upper pressure head $\sigma_a - \sigma_r$.

Sand type

The sand type deployed in the triaxial tests is a Fontainebleau sand. Fontainebleau sand is a well-sorted, clean sand with a particle size ranging from $0.063mm$ to $0.25mm$, and a uniformity index of $U < 2$. Further classification parameters are given in Table 2.1 and they have been determined according to Dansk geoteknisk forening (DGF)-Bulletin 15 (2001).

Relative grain density	d_s	2.655
Densest deposition	e_{min}	0.549
Loosest deposition	e_{max}	0.853

Table 2.1: Classification parameters for sand

Experimental series

Samples at various relative densities I_D were tested in drained and undrained triaxial compression conditions after having been isotropically consolidated (CID-CUD) to various cell pressures σ'_r . The shear phase is done under both drained and undrained conditions. The axial deformation rate is $\varepsilon'_a = 1\%/hour$. At approximately 50% of the expected peak deviatoric stress, q_{peak} , an unloading and reloading cycle was performed after which the sample was loaded in displacement control to full failure (approximately 15% axial strain ε_a). The test series is summarized in Table 2.2. Note that the relative density for the test series performed in undrained conditions cannot be determined, since the samples are looser than the loosest deposition, see Table 2.2.

2.2 Measurement corrections

Calculation of axial and volumetric strains requires accurate estimation of the initial height and area of the sample thus, corrections of the data have to be performed. According to the specifications of ETCS-F1.97 several corrections on the geometry of the samples have been applied for processing the data. The height and volume of sample after consolidation are given as:

$$H_c = H_0(1 - \varepsilon_a) \quad (2.1)$$

$$V_c = V_0 - \Delta V_c \quad (2.2)$$

where $\Delta V_c = \Delta W_{water}/\rho_{water}$. The axial and volumetric strain should be calculated, initializing the variations of height and volume at the beginning of the shearing phase. Thus, they are corrected according to:

$$\varepsilon_a = \frac{\Delta H}{H_c} \quad (2.3)$$

Nr. Test	σ'_r	Relative Density I_D	e_0
Test 1-CID	50kPa	0.53	0.699
Test 2-CID	100kPa	0.50	0.708
Test 3-CID	200kPa	0.57	0.684
Test 4-CID	50kPa	0.66	0.655
Test 5-CID	100kPa	0.65	0.660
Test 6-CID	200kPa	0.65	0.660
Test 7-CID	50kPa	0.80	0.612
Test 8-CID	100kPa	0.80	0.612
Test 9-CID	200kPa	0.80	0.612
Test 1-CUD	100kPa	*	0.856
Test 2-CUD	50kPa	*	0.844
Test 3-CUD	100kPa	*	0.921
Test 4-CUD	50kPa	*	0.908
Test 5-CUD	100kPa	*	0.901
Test 6-CUD	50kPa	*	0.920
Test 7-CUD	50kPa	*	0.877

Table 2.2: Experimental series in the triaxial apparatus

$$\varepsilon_v = \frac{\Delta V}{V_c} \quad (2.4)$$

Note that the area of the sample has to be corrected in order to calculate the axial stress for shearing phase:

$$A = \frac{1 - \varepsilon_v}{1 - \varepsilon_a} A_c \quad (2.5)$$

where $A_c = V_c/H_c$.

Chapter 3

Results

3.1 Consolidation phase

The bulk modulus K is a measure the compressibility of the sand. It is estimated during the consolidation phase as the slope of the axial stress p versus volumetric strain ε_v plot. Therefore it can be calculated according to:

$$\frac{\delta p}{\delta \varepsilon_v} = K \quad (3.1)$$

The bulk modulus for all drained triaxial tests is listed in Table 3.1.

Test	K
Test 1-CID	27.6MPa
Test 2-CID	38.0MPa
Test 3-CID	43.7MPa
Test 4-CID	30.9MPa
Test 5-CID	42.5MPa
Test 6-CID	43.0MPa
Test 7-CID	38.5MPa
Test 8-CID	43.9MPa
Test 9-CID	55.3MPa

Table 3.1: Bulk modulus K for all drained triaxial tests.

When the relative density of the sand is increased the sample becomes less compressible and hence a higher bulk modulus is expected. Also, for higher values of the confinement pressure it is expected that K will increase due to the increase in the radial pressure. The results seem to confirm this trend. The lowest bulk modulus was found for the Test 1, which has the lowest relative density and initial confining pressure. The highest bulk modulus was recorded for Test 9, which has the highest cell pressure and relative density, as it is expected.

3.2 Elasticity parameters

The elastic stiffness parameters of the soil are obtained from the shearing phase of the test. Depending on the plot the gradient in this phase will give Young's

Modulus, E , the shear Modulus, G , and Poisson's ratio, ν . The shear modulus is given as the slope of the deviatoric stress, δq versus the shear strain $\delta \varepsilon_q$ diagram describing the material's response to shear stress:

$$\frac{\delta q}{\delta \varepsilon_q} = 3G \quad (3.2)$$

Young's Modulus describes the resistance of the sand when it is deformed elastically. It is given as the slope of the deviatoric stress δq versus the axial strain $\delta \varepsilon_a$:

$$\frac{\delta q}{\delta \varepsilon_a} = E \quad (3.3)$$

Both E and G can be estimated theoretically from the initial shearing of the sample, E_i and G_i , when only elastic deformations occur. Hence E_i and G_i should be equal respectively to E and G , if the measurements of the triaxial setup are accurate in the low strains regime. The secant moduli E_{50} and G_{sec} are derived as the slope of

$$\frac{\delta q_{max,50}}{\delta \varepsilon_a} = E_{50} \quad (3.4)$$

$$\frac{\delta q_{max,50}}{\delta \varepsilon_q} = 3G_{sec} \quad (3.5)$$

where $q_{max,50}$ is 50% of the expected maximum stress value. Poisson's ratio ν , can be evaluated by plotting the ε_a and ε_r , where ε_r is the radial strain. For the estimation of ν the unloading and reloading phase is deployed and Poisson's ratio is given as follows:

$$\frac{\delta \varepsilon_r}{\delta \varepsilon_a} = \nu \quad (3.6)$$

The expected values for the Poisson's ratio is in the order of [0.20; 0.30].

3.2.1 Unloading-reloading phase

The unloading and reloading modulus is the average slope of the unloading and reloading curve and it can readily be determined using the data from triaxial tests. In Appendix A the Young modulus E_{ur} , shear modulus G_{ur} and Poisson's ratio ν_{ur} at the loading and reloading phase are shown with respect to strains for each test.

In Table 3.2 the unloading and reloading parameters for all tests are listed.

Test	E_{ur}	G_{ur}	ν_{ur}
Test 1-CID	160.2MPa	68.8MPa	0.41
Test 2-CID	127.3MPa	42.8MPa	0.43*
Test 3-CID	278.1MPa	105.4MPa	0.35
Test 4-CID	251.9MPa	151.3MPa	—
Test 5-CID	151.4MPa	56.6MPa	0.42
Test 6-CID	268.0MPa	105.9MPa	0.34
Test 7-CID	424.0MPa	264.0MPa	—
Test 8-CID	187.3MPa	73.9MPa	0.39
Test 9-CID	269.2MPa	110.6MPa	0.36

Table 3.2: Young modulus E_{ur} , shear modulus G_{ur} and Poisson's ratio ν_{ur} for all drained triaxial tests.

Duncan et al. (1970) showed that E_{ur} and G_{ur} increase with increases in the confining pressure, but they are independent of the stress level. This pattern is recorded for loose and dense sand samples, respectively Test 1,3, Test 4,6 and Test 8,9.

In addition, it is noticed that the moduli tends to be higher if the particle are closely packed (dense samples). This is evident by comparing the outcomes of Test 1,4 and Test 2,5,8. Consequently, it is expected that the highest value of E_{ur} and G_{ur} is reached in Test 9, where we have the highest initial confining pressure and relative density. However, Test 7 has showed the maximum value of E_{ur} and G_{ur} .

Poisson's ratio obtained from the unloading and reloading phase attains higher values than those expected for drained sandy samples. In Test 2, Poisson's ratio cannot be estimated graphically, hence it is obtained according to:

$$G = \frac{E}{2(1 + \nu)} \quad (3.7)$$

A graphical estimation of Poisson's ratio in Test 4 is not feasible. Due to the high shear modulus value, the numerical calculations resulted in a negative value and was not considered as a reliable result for Poisson's ratio, since that would be physically impossible. Furthermore, in Test 7 the estimation of Poisson's ratio cannot be considered reliable, due to the positive slope of the trendline of the unloading/reloading line in ε_r and ε_a .

No clear trend is seen for the Poisson's ratio in terms of confinement pressure or relative density. It is observed a small decrease in Poisson's ratio for samples with the same relative density, when the confining pressure increases. In terms of relative density it would be expected to see an increase in Poisson's ratio with increasing relative density; however the outcomes do not indicate this trend.

3.2.2 Initial moduli

The initial modulus is applicable only to very small deformations. Tatsuoka et al. (1997), Cuccovillo and Coop (1997) and Hoque and Tatsuoka (2004) showed that the deformation characteristics of sand samples are linear and elastic at strains of less than approximately 0.001%. In addition, the small-strain measurement requires relatively high accuracy. Therefore a significant small strain interval $\varepsilon_a = [0; 3e^{-4}]$ has been considered for the estimation of the initial moduli. The initial Young modulus E_i , shear modulus G_i and Poisson ratio ν_i are calculated and reported for each test in Appendix B. In Table 3.3 the initial elastic parameters for all drained triaxial tests are listed.

Test	E_i	G_i	ν_i
Test 1-CID	24.7MPa	8.13MPa	0.48
Test 2-CID	24.4MPa	8.13MPa	–
Test 3-CID	69.9MPa	59.5MPa	–
Test 4-CID	45.1MPa	19.8MPa	0.20
Test 5-CID	19.3MPa	3.9MPa	–
Test 6-CID	110.1MPa	30.6MPa	0.29
Test 7-CID	13.2MPa	5.1MPa	0.30
Test 8-CID	85.8MPa	29.6MPa	0.44
Test 9-CID	13.4MPa	9.0MPa	0.22

Table 3.3: Young modulus E_i , shear modulus G_i and Poisson's ratio ν_i for all drained triaxial tests.

Young's modulus E_i and shear modulus G_i are generally similar, see Test 1 and 2. This might be explained by the fact that the volumetric strains are near constant in the low strains range.

In addition, the value of Poisson's ratio is not feasible for Test 2,3 and 5, since Poisson's ratio cannot overcome 0.5 and then, it is not presented in Table 3.3. It can be stated that the outcomes in the low strain range are considerably scattered; therefore they are not reliable.

3.2.3 Secant moduli

The secant moduli are defined as the secant slope from the origin to a chosen point on the stress-strain curve. Note that the secant modulus does not respect the definition of elastic modulus in the classical elasticity theory, due to the fact that elastic deformation and plastic deformation develop simultaneously. In Table 3.4 the results of the secant moduli are listed for all drained triaxial tests. It is expected that the secant moduli increase by increasing the initial confining pressure σ'_r . Results show this pattern. Regarding dense sands, Test 7 and 8 are characterized by similar outcomes. The outcomes further indicate that relative density has a considerably influence in E_{50} and G_{sec} . Indeed, secant moduli increases by increasing the relative density. The maximum value of E_{50} and G_{sec} is attained in Test 6 and it is not in agreement with the prevision. Hence, it is expected that the test with the highest confining pressure and relative density provides the maximum value of elastic moduli. Furthermore, it has been noticed

that $3G_{sec}$ and E_{50} are almost identical. This can be explained by the fact the influence of the volumetric strains is considerably small for the range of strain investigated.

Test	E_{50}	G_{sec}
Test 1-CID	17.0MPa	5.7MPa
Test 2-CID	22.6MPa	7.8Pa
Test 3-CID	43.2MPa	14.8MPa
Test 4-CID	22.3MPa	7.5MPa
Test 5-CID	27.7MPa	8.9MPa
Test 6-CID	86.3MPa	27.7MPa
Test 7-CID	32.9MPa	11.3MPa
Test 8-CID	33.2MPa	11.5MPa
Test 9-CID	60.4MPa	20.8MPa

Table 3.4: Young modulus E_{sec} and shear modulus G_{sec} for all drained triaxial tests.

It is of interest to note that Young's modulus E_{ur} can be calculated according to Marcher and Vermeer (2001) as follows:

$$E_{ur} = 4E_{50} \quad (3.8)$$

Equation 3.8 underestimates significantly Young's modulus E_{ur} particularly for loose and medium dense sand.

3.3 Estimation of strength parameters of CID tests

The experimental data included plots of deviatoric stress versus deviatoric strain, as well as volumetric strain versus deviatoric strain, for a range of different confining pressures and void ratios, see Figure 3.1, 3.2 and 3.3.

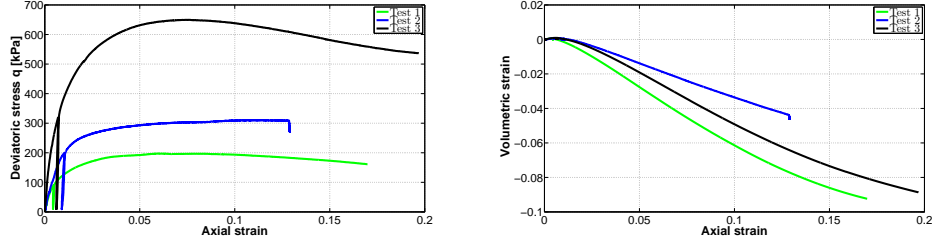


Figure 3.1: Variation of deviatoric stress versus axial strain and volumetric strain versus axial strain for Test 1, 2 and 3 (CID).

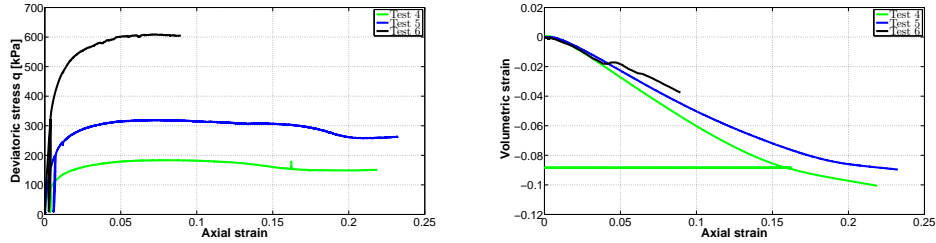


Figure 3.2: Variation of deviatoric stress versus axial strain and volumetric strain versus axial strain for Test 4,5 and 6 (CID).

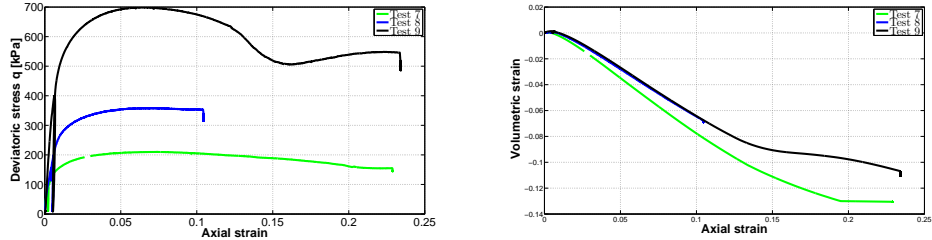


Figure 3.3: Variation of deviatoric stress versus axial strain and volumetric strain versus axial strain for Test 7,8 and 9 (CID).

The failure states in terms of p , q are used to determine the strength of the soil. The yield surface of Mohr-Coloumb criterion is presented in Equation 3.9.

$$q = Mp' + d \quad (3.9)$$

The strength characteristics of the soil are then the angle of friction φ and the cohesion c . The friction angle describes how well a soil sample can withstand shear stress. During shearing, the friction angle can be found as the angle between the normal force and the resultant force. While the cohesion c describes how a sample resists against a shearing deformation caused by a shear force. For $I_d = 0.5$ a friction angle between 30° and 35° is expected. For the sample of $I_d = 0.65$ the friction angle is expected to be higher and in the range of 35° and 40° . For

dense sand samples ($I_d > 0.80$) an angle of friction in the interval of $[40^\circ; 42^\circ]$ is usually considered. At failure the mobilized friction angle (φ) reaches to its final value.

$$M = \frac{(6 \sin \varphi_f)}{(3 - \sin \varphi_f)} \quad (3.10)$$

The strength characteristics of this model can be obtained by plotting the failure states in terms of (p,q) and finding the best regression line to them. Therefore, the friction angle and the cohesion can be obtained as following:

$$\varphi_f = \sin^{-1} \left(\frac{3M}{6 + M} \right) \quad (3.11)$$

$$c = \frac{d \tan(\varphi_f)}{M} \quad (3.12)$$

where d is the intercept of the failure line. No or very little cohesion in the order of $[0; 10]$ kPa is expected. In Table 3.5 the stresses (p, q_{peak}) and the strains ($\varepsilon_v, \varepsilon_q$) at the failure are reported.

Test	q_{peak}	p	ε_q	ε_v
Test 1-CID	197.3kPa	114.8kPa	7.12e-2	-3.46e-2
Test 2-CID	310.8kPa	204.6kPa	1.23e-1	-3.76e-2
Test 3-CID	649.7kPa	415.8kPa	8.75e-2	-3.50e-2
Test 4-CID	183.7kPa	113.7kPa	9.56e-2	-4.73e-2
Test 5-CID	319.8kPa	205.2kPa	8.77e-2	-3.72e-2
Test 6-CID	558.9kPa	387.6kPa	8.05e-2	-2.80e-2
Test 7-CID	210.2kPa	120.9kPa	9.34e-2	-5.64e-2
Test 8-CID	358.8kPa	220.6kPa	8.36e-2	-4.27e-2
Test 9-CID	698.9kPa	434.2kPa	7.56e-2	-3.70e-2

Table 3.5: Stress and strains at the failure for all drained triaxial tests.

The results in Table 3.5 show that the peak of deviatoric stress increases from loose to dense sample by keeping the same initial confining pressure σ'_r , as expected. Test 6 and Test 8 are characterized by an approximate value of the maximum deviatoric stress, since both triaxial tests did not reach 15% axial deformation. Table 3.6 shows the slope of the critical state line M and the angle of friction φ_f for each drained triaxial test.

Set	M	φ_f
Test 1-CID	1.72	41.0
Test 2-CID	1.52	37.3
Test 3-CID	1.56	38.2
Test 4-CID	1.61	39.8
Test 5-CID	1.56	38.0
Test 6-CID	1.50	37.0
Test 7-CID	1.74	42.4
Test 8-CID	1.62	39.8
Test 9-CID	1.61	39.4

Table 3.6: Failure line parameters for all drained triaxial tests.

In Table 3.7 the value of M coefficient (slope of the failure line), the angle of friction φ_f and the cohesion c at the failure are listed for all drained triaxial tests, gathered according to the same relative density. The failure line is shown in Figure 3.4, 3.5 and 3.6.

Set	I_D	M	φ_f	c
Test 1,2 and 3 (CID)	0.50	1.50	36.9	6.5kPa
Test 4,5 and 6 (CID)	0.66	1.50	36.9	9.5kPa
Test 7,8 and 9 (CID)	0.80	1.59	39.2	9.1kPa

Table 3.7: Failure line parameters for all drained triaxial tests.

The friction angle is larger for dense sand which is consistent, since the friction angle is greater if the sand is more compact. Indeed, the sand samples with high relative density are generally characterized by high friction angle, see both Table 3.6 and Table 3.7. It is evident that Test 1,2,3 and Test 4,5,6 are characterized by the same angle friction. It is expected that Test 1,2,3 provide lower friction angle, since they are loose sand samples.

In addition, the larger friction angle leads to a steeper slope in the Cambridge diagram, which results in a smaller intersection value, hence a smaller effective cohesion. This is not observed in the results achieved.

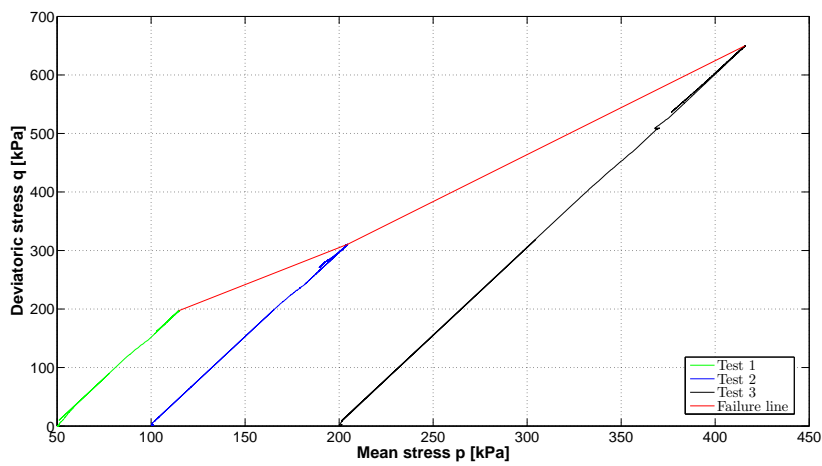


Figure 3.4: Failure line for Test 1,2 and 3 (CID)

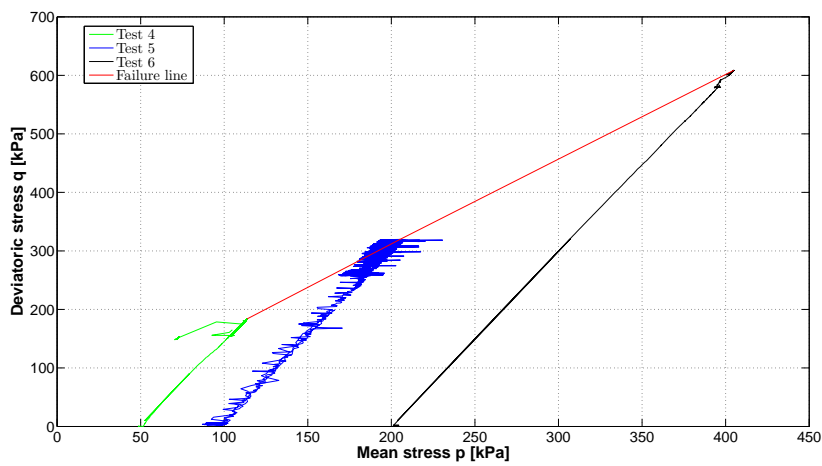


Figure 3.5: Failure line for Test 4,5 and 6 (CID)

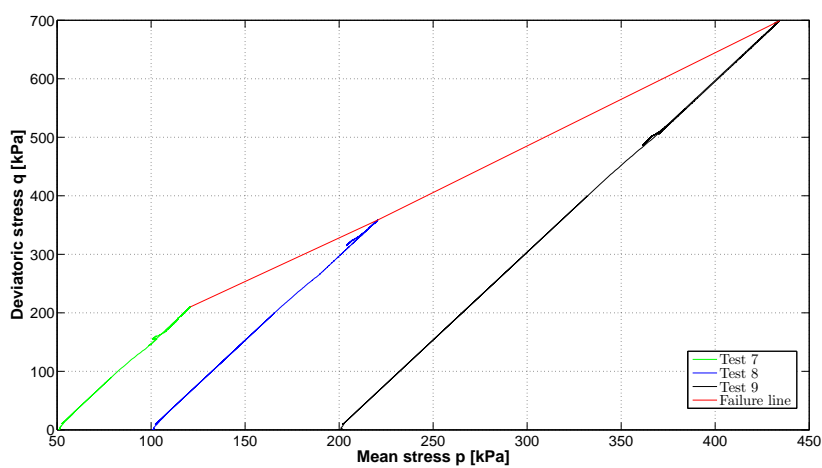


Figure 3.6: Failure line for Test 7,8 and 9 (CID)

3.4 Estimation of strength parameters of CUD tests

In Figure 3.7–3.12 pore pressure and deviator stress versus axial strain are shown for all the undrained tests. The pore pressure plotted with respect to axial strain shows a marked phase transformation from contraction (increase in pore pressure) to dilation (decrease in pore pressure) at about 2 – 2.5% axial strain.

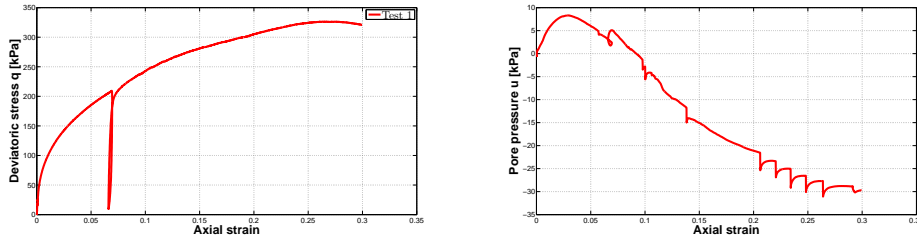


Figure 3.7: Variation of deviatoric stress versus axial strain and pore pressure versus axial strain for Test 1 (CUD).

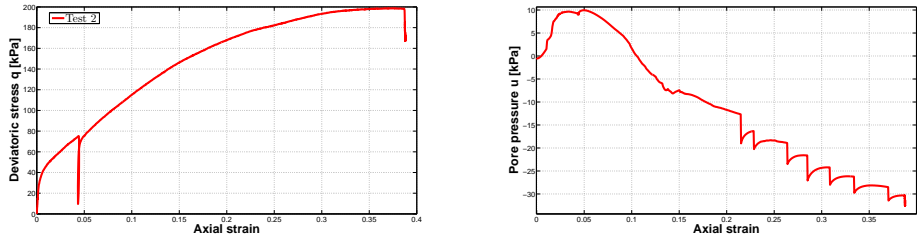


Figure 3.8: Variation of deviatoric stress versus axial strain and pore pressure versus axial strain for Test 2 (CUD).

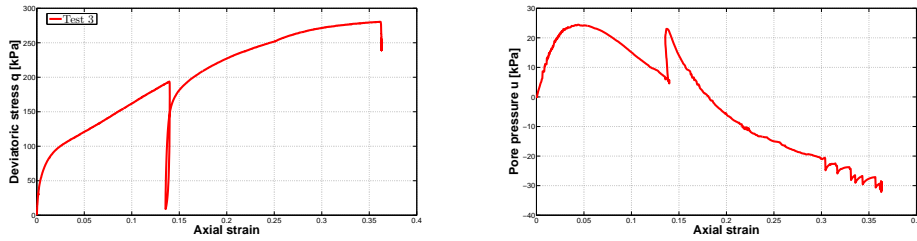


Figure 3.9: Variation of deviatoric stress versus axial strain and pore pressure versus axial strain for Test 3 (CUD).

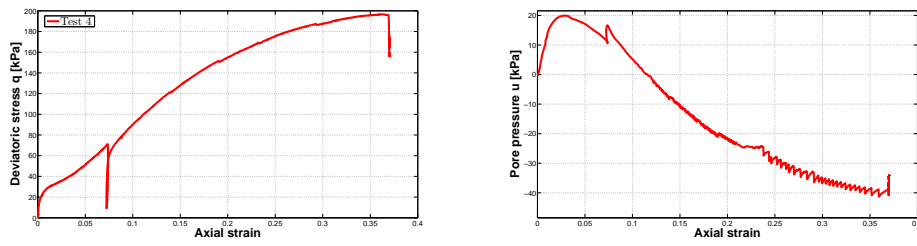


Figure 3.10: Variation of deviatoric stress versus axial strain and pore pressure versus axial strain for Test 4 (CUD).

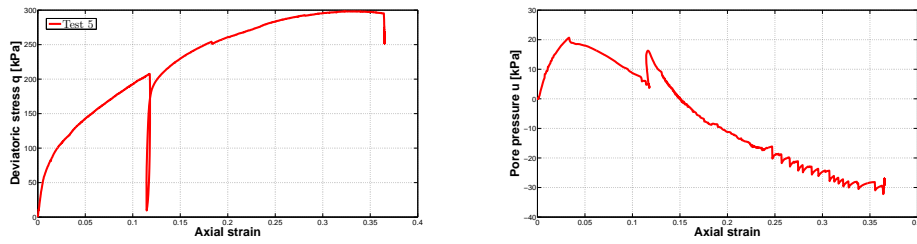


Figure 3.11: Variation of deviatoric stress versus axial strain and pore pressure versus axial strain for Test 5 (CUD).

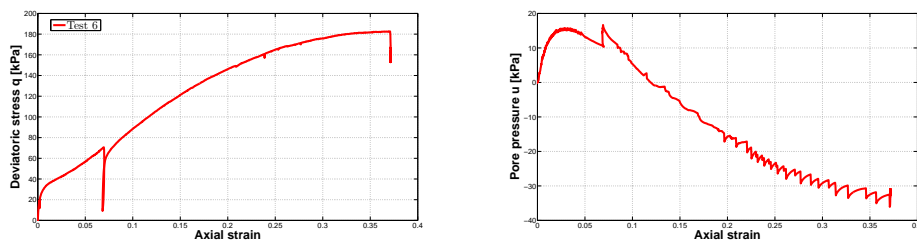


Figure 3.12: Variation of deviatoric stress versus axial strain and pore pressure versus axial strain for Test 6 (CUD).

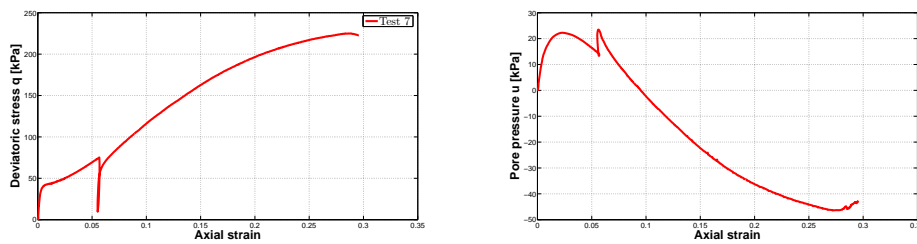


Figure 3.13: Variation of deviatoric stress versus axial strain and pore pressure versus axial strain for Test 7 (CUD).

While in Figure 3.14–3.17 the variation of the deviatoric stress q is illustrated with respect to the mean stress p for each undrained triaxial test.

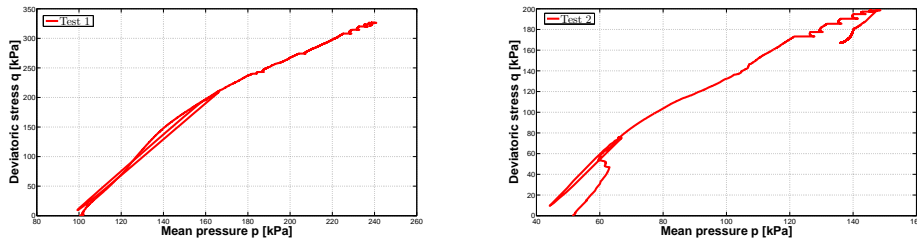


Figure 3.14: Variation of deviatoric stress versus mean stress for Test 1 and Test 2 (CUD).

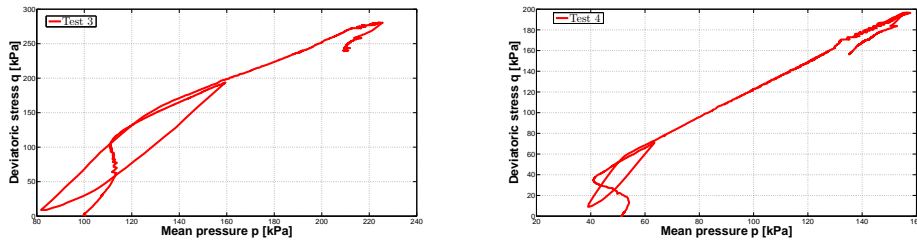


Figure 3.15: Variation of deviatoric stress versus mean stress for Test 3 and Test 4 (CUD).

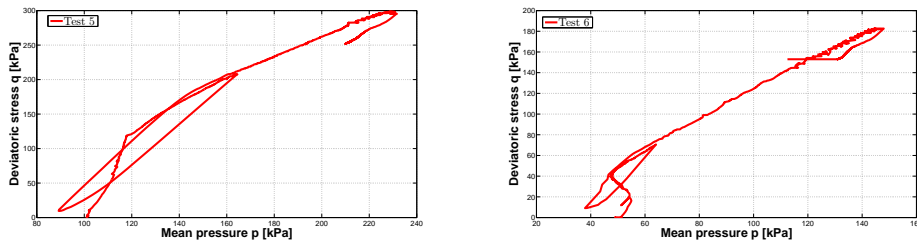


Figure 3.16: Variation of deviatoric stress versus mean stress for Test 5 and Test 6 (CUD).

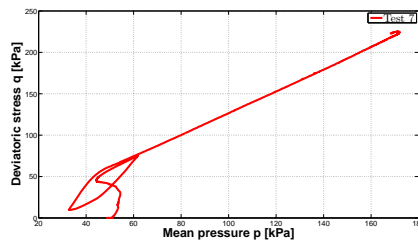


Figure 3.17: Variation of deviatoric stress versus mean stress for Test 7 (CUD).

The deviatoric and mean stress ($q_{failure}, p'$) at failure are listed in Table 3.8. The results show that the deviatoric stress at failure increases from very loose to loose sample by keeping the same initial confining pressure σ'_r , see Test 1,5,3 and Test 2,8,4,6. In Table 3.8 the value of M coefficient (slope of the failure line) and the angle of friction φ_f at the failure are also listed for all undrained triaxial tests.

Set	e_0	$q_{failure}$	p'	M	φ_f
Test 1-CUD	0.856	144.4kPa	138.9kPa	1.04	26.3
Test 2-CUD	0.844	59.2kPa	60.3kPa	0.98	24.9
Test 3-CUD	0.921	104.0kPa	110.9kPa	0.94	24.0
Test 4-CUD	0.908	40.1kPa	42.9kPa	0.93	23.7
Test 5-CUD	0.901	120.3kPa	119.5kPa	1.01	25.6
Test 6-CUD	0.920	40.1kPa	47.2kPa	0.85	21.9
Test 7-CUD	0.877	43.7kPa	44.5kPa	0.98	24.9

Table 3.8: Failure line parameters for all undrained triaxial tests.

It is expected that the friction angle increases by increasing the relative density for same initial confining pressure σ'_r . This trend is visible for Test 1,5,3 and Test 2,7,4,6. In addition, the angle of friction in all tests attains values lower than 30° , which is in agreement with the studies of Meyerhoff (1956) and Carter and Bentley (1991) for very loose sand samples. Furthermore, the maximum friction angle recorded is for the sand sample with higher relative density, see Test 2 for initial confining pressure $\sigma'_r = 50kPa$ and Test 1 for initial confining pressure $\sigma'_r = 100kPa$. Test 6 should be characterized by the minimum value of friction angle, since it has the highest void ratio for the smallest initial confining pressure in the tests' set. This is consistent with the outcome achieved for Test 6. In addition, the maximum value of the pore pressure and the relative stresses (u_{peak}, q, p') are reported in Table 3.9.

Set	e_0	σ'_r	q	p'	u_{peak}
Test 1-CUD	0.856	100kPa	133.0kPa	123.2kPa	8.1kPa
Test 2-CUD	0.844	50kPa	76.3kPa	66.5kPa	9.6kPa
Test 3-CUD	0.921	100kPa	112.0kPa	107.6kPa	24.4kPa
Test 4-CUD	0.908	50kPa	44.1kPa	41.9kPa	19.9kPa
Test 5-CUD	0.901	100kPa	131.1kPa	124.1kPa	20.7kPa
Test 6-CUD	0.920	50kPa	55.6kPa	52.7kPa	15.4kPa
Test 7-CUD	0.877	50kPa	51.7kPa	46.3kPa	22.3kPa

Table 3.9: Maximum pore pressure and relative stresses for all undrained triaxial tests.

3.5 Estimation of dilation angle

The dilation angle ψ is evaluated from the variation of volumetric strain versus the axial strain. Since the dilation angle is a measure of the volume change when the test is subjected to shear deformations, it should only be derived from the plastic strains:

$$\frac{\varepsilon_v}{\varepsilon_a} = -\frac{6 \sin \psi}{3 - \sin \psi} \quad (3.13)$$

The results are listed in Table 3.10 for all drained triaxial tests.

Test	I_D	σ_r	
Test 1-CID	0.50	50kPa	15.7
Test 2-CID	0.50	100kPa	10.8
Test 3-CID	0.50	200kPa	9.0
Test 4-CID	0.66	50kPa	16.7
Test 5-CID	0.66	100kPa	14.2
Test 6-CID	0.66	200kPa	13.9
Test 7-CID	0.80	50kPa	22.1
Test 8-CID	0.80	100kPa	18.9
Test 9-CID	0.80	200kPa	17.9

Table 3.10: Dilation angle for all drained triaxial tests.

It is expected that the dilation angle ψ reduces by increasing the initial confining pressure σ'_r . Looking at loose samples, the variation of dilation angle for Test 1, Test 2 and Test 3 with respect to the initial confining pressure is consistent. The same trend is observed for medium dense and dense samples, respectively Test 4,5,6 and Test 7,8,9.

In addition, the dilation angle should increase from loose to dense sands. For an initial confining pressure of $\sigma'_r = 50kPa$, this pattern has been noticed by comparing ψ of Test 3 with that of Test 4 and Test 7. The variation of dilation angle with the relative density is consistent for all the test; even though the dilation angle of Test 7 and Test 8 is quite high. As a rule of thumb, sand sample having a friction angle above 30° will be characterized by a dilation angle approximately equal to $\varphi - 30^\circ$, see Bolton (1984). This is seen not to be the case for the tests investigated.

3.6 Estimation of the critical state

The concept of the critical state is fundamental to understand the mechanical response of soil. The critical state has been defined as the state at which the soil "continues to deform at constant stress and constant void ratio" (Roscoe et al., 1958). The critical state is generally estimated from drained tests on dense sands. However the actual location of the line is difficult to assess. These difficulties are mainly due to experimental limitations and lack of accurate observations. Ultimate state generally takes place at large strains and these strains can sometimes exceed the limitations of a triaxial apparatus (Been et al., 1991). To solve the above-mentioned measurement problems, Castro (1969) performed undrained, stress-controlled triaxial tests on very loose sands to obtain a steady state line.

According to Poulos (1981), the steady state of deformation for any mass of particles is that state in which the mass is continuously deforming at constant volume, constant normal effective stress, constant shear stress, and constant velocity. Been et al. (1991) showed that the critical and steady state line are the same from a practical standpoint. Hence, the sample reaches the critical or steady state, when it will experience large strains under monotonic loading. Furthermore, it was proposed a unique critical state line (CSL) for each sand in an $e-\log p'_c$ plot which is independent of type of loading, sample preparation method and initial density. In this study it is possible to detect the critical state in Test 5,7 and 9 (CID), see Figure 3.1, 3.2 and 3.3, since shearing occurs with no volume change. In regards to undrained conditions the occurrence of the critical state becomes visible in Test 1,4,5,6 and 7(CUD) as shown in Figure 3.7, 3.10, 3.11, 3.12 and 3.13. Particularly, the critical state line can be obtained by plotting the results of triaxial compression tests at the critical state in $p-q$ space and fitting a best fit line through the data points as shown in Figure 3.18a. In addition, the void ratio at the critical state e_{cr} can be estimated by plotting undrained triaxial tests data in $e-\ln(p'_c)$ space and fit them to a line having expression as shown in Figure 3.18b. According to Been et al. (1991), this is a generally reasonable approximation for sub-angular or subrounded quartz sands in the stress range of 10 – 500kPa, which is the case of the triaxial tests performed in this study.

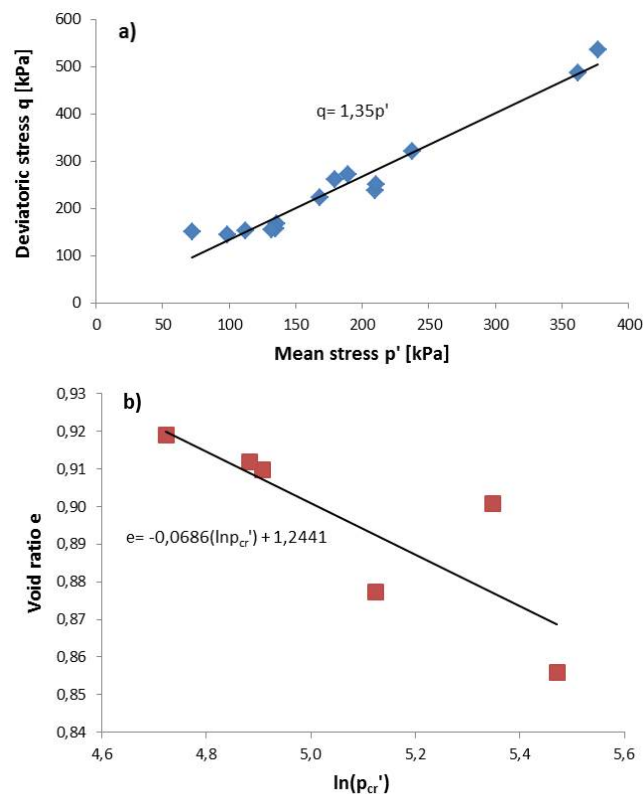


Figure 3.18: Critical state line in $q-p$ (a) and $e-\ln(p'_c)$ plane (b).

Chapter 4

Conclusions

The aim of this study was to present a series of triaxial tests carried out on Fontainebleau sand in order to investigate the influence of the relative density on the strength and deformation characteristics of this type of sand. In general the strength parameters found seemed sensible and within the range of what would be expected. For the elasticity parameters estimated in the unloading reloading phase no clear trend was seen for varying relative densities and confinement pressure.

References

- Been, K., Jefferies, M. G. and Hachey, J. 1991. Critical state of sands. *Geotechnique*, 41(3), 365-381.
- Bolton, M. D. 1984. *The strength and dilatancy of sands*. Cambridge University Engineering Department.
- Carter, M. and Bentley, S. 1991. *Correlations of soil properties*. Penetech Press Publishers, London.
- Castro, G. 1969. *Liquefaction of sands*. ph. D. Thesis, Harvard Soil Mech.
- Cuccovillo, T. and Coop, M. 1997. Yielding and prefailure deformation of structured sands. *Geotechnique*, 47(3), 491-508.
- Duncan, J.M. and Chang, C.Y. 1970. Nonlinear analysis of stress and strain in soils. *Journal of Soil Mechanics*, 96(5), 1629-1653.
- Hoque, E. and Tatsuoka, F. 2004. Effects of stress ratio on small strain stiffness during triaxial shearing. *Geotechnique*, 54(7), 429-439.
- Marcher, T. and P. A. Vermeer. *Macromodelling of softening in non-cohesive soils. Continuous and discontinuous modelling of cohesive-frictional materials*. Springer Berlin Heidelberg, 2001. 89-110.
- Meyerhof, G. 1956. Penetration tests and bearing capacity of cohesionless soils. *J Soils Mechanics and Foundation Division ASCE*, 82(SM1).
- Poulos, S. J. 1981. The steady state of deformation. *Journal of Geotechnical and Geoenvironmental Engineering*, 107(ASCE 16241 Proceeding).
- Roscoe, K. H., Schofield, A., and Wroth, C. P. 1958. On the yielding of soils. *Geotechnique*, 8(1), 22-53.
- Tatsuoka, F., Sato, T., Park, C., Kim, Y.S., Mukabi, J.N: and Kohata, Y. 1994a. Measurements of elastic properties of geomaterials in laboratory compression tests. *Geotechnical Testing Journal*, 17(1), 80-84.

Appendix A

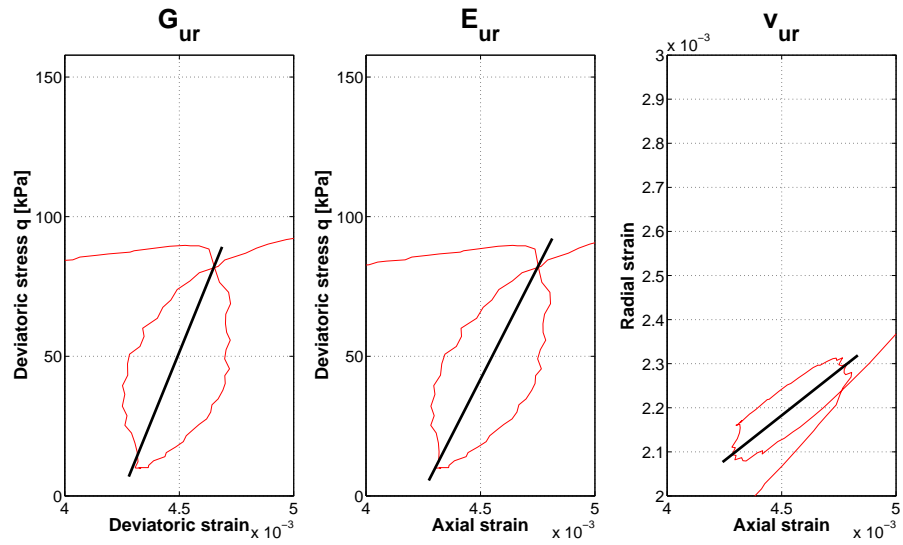


Figure 4.1: Young modulus E_{ur} , shear modulus G_{ur} and Poisson's ratio v_{ur} at unloading and reloading phase for test 1 (CID).

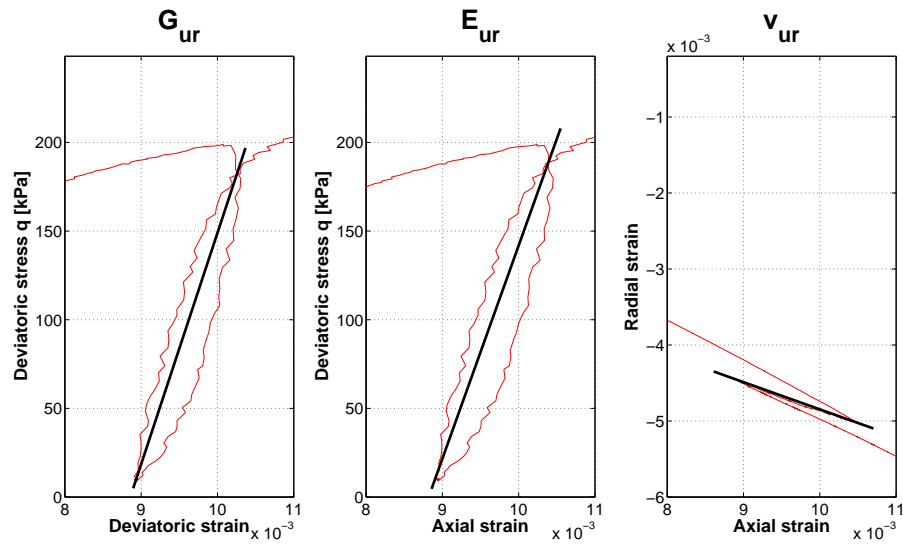


Figure 4.2: Young modulus E_{ur} , shear modulus G_{ur} and Poisson's ratio v_{ur} at unloading and reloading phase for test 2 (CID).

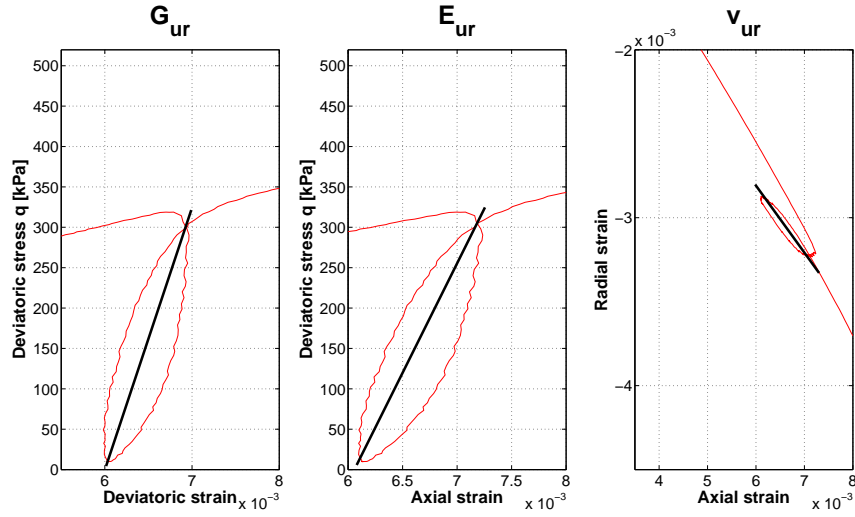


Figure 4.3: Young modulus E_{ur} , shear modulus G_{ur} and Poisson's ratio v_{ur} at unloading and reloading phase for test 3 (CID).

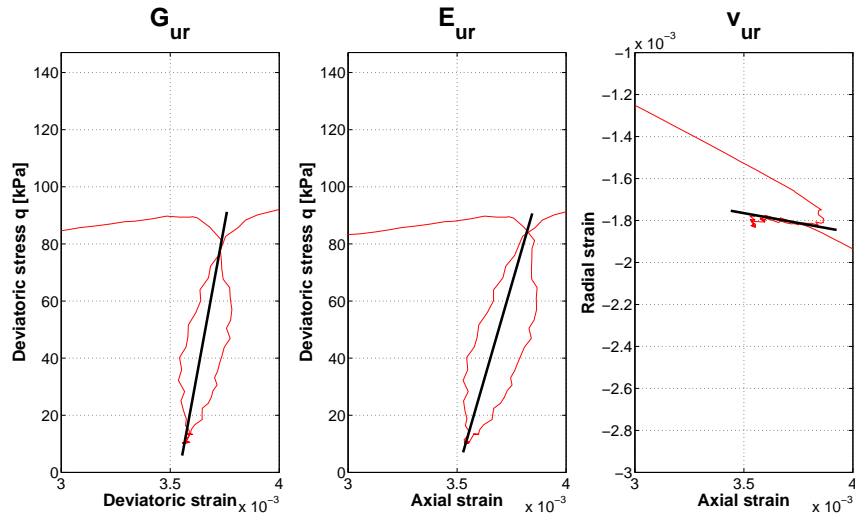


Figure 4.4: Young modulus E_{ur} , shear modulus G_{ur} and Poisson's ratio v_{ur} at unloading and reloading phase for test 4 (CID).

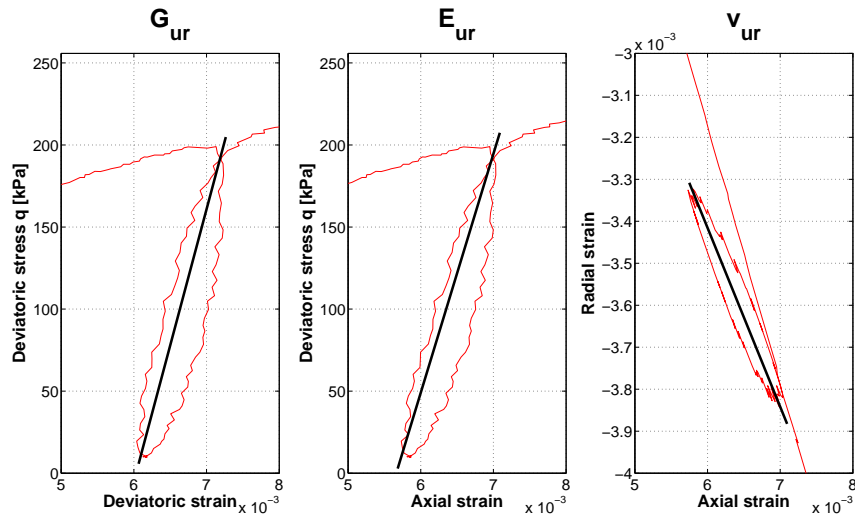


Figure 4.5: Young modulus E_{ur} , shear modulus G_{ur} and Poisson's ratio v_{ur} at unloading and reloading phase for test 5 (CID).

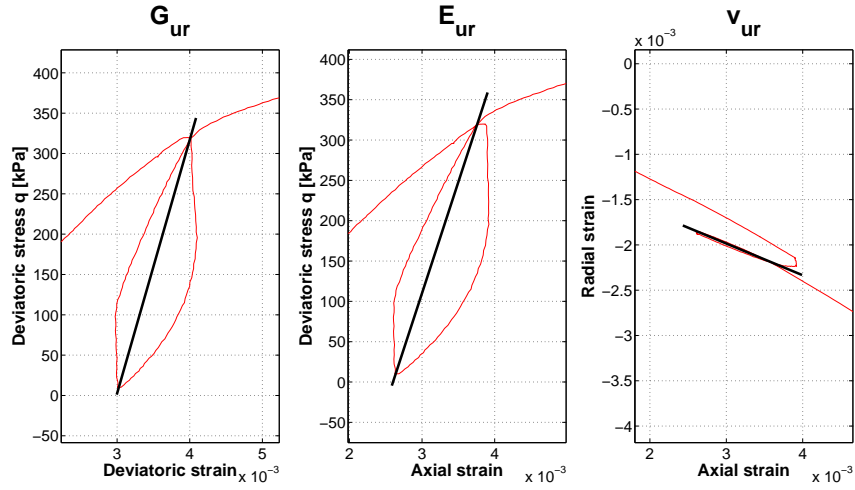


Figure 4.6: Young modulus E_{ur} , shear modulus G_{ur} and Poisson's ratio v_{ur} at unloading and reloading phase for test 6 (CID).

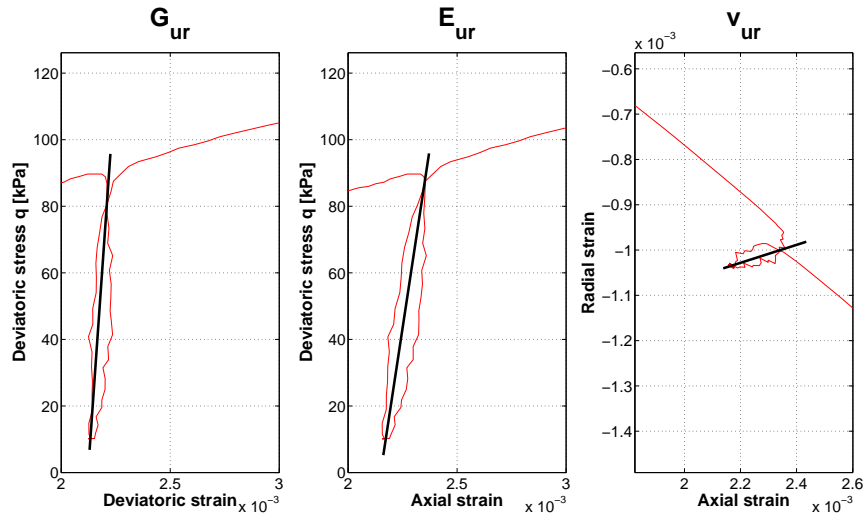


Figure 4.7: Young modulus E_{ur} , shear modulus G_{ur} and Poisson's ratio v_{ur} at unloading and reloading phase for test 7 (CID).

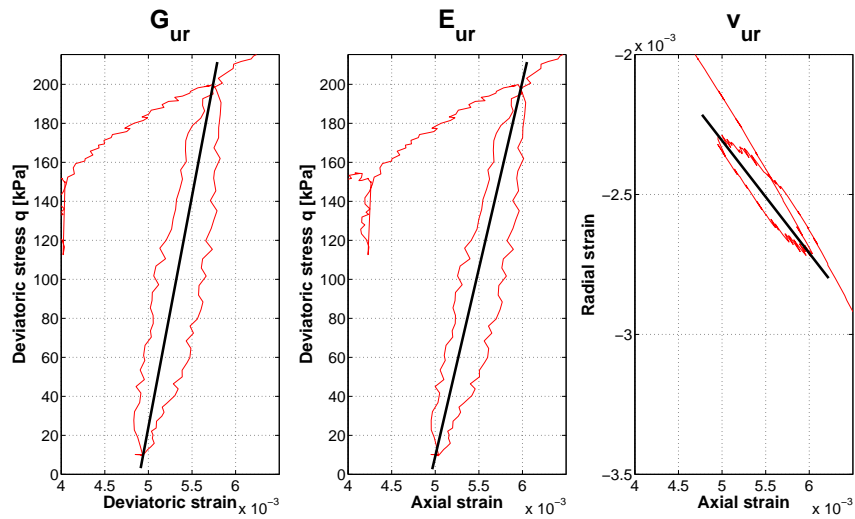


Figure 4.8: Young modulus E_{ur} , shear modulus G_{ur} and Poisson's ratio v_{ur} at unloading and reloading phase for test 8 (CID).

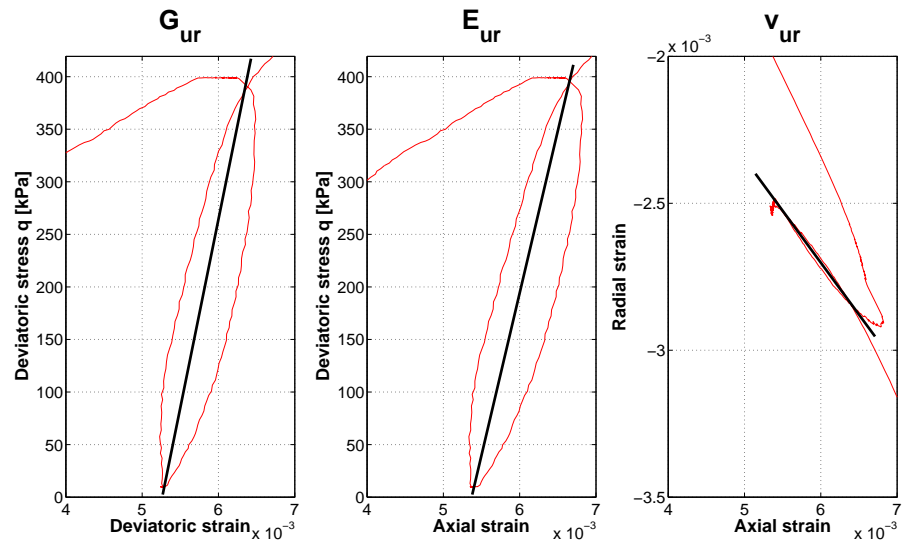


Figure 4.9: Young modulus E_{ur} , shear modulus G_{ur} and Poisson's ratio v_{ur} at unloading and reloading phase for test 9-CID.

Appendix B

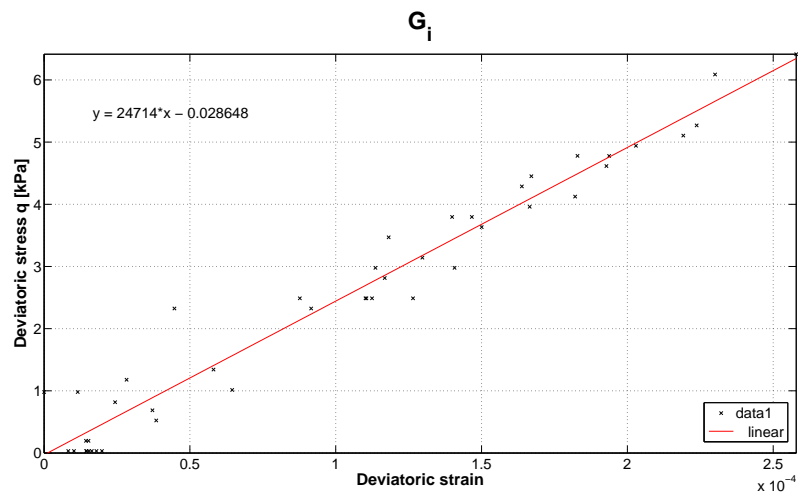


Figure 4.10: Initial Young modulus E_i for Test 1 (CID).

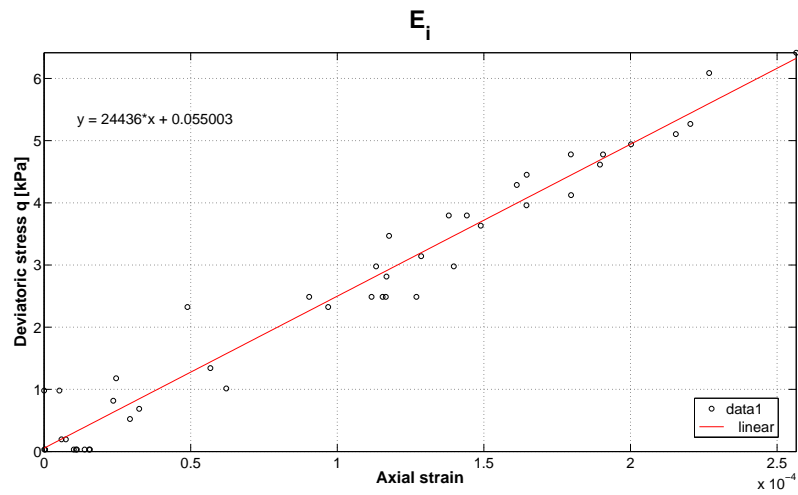
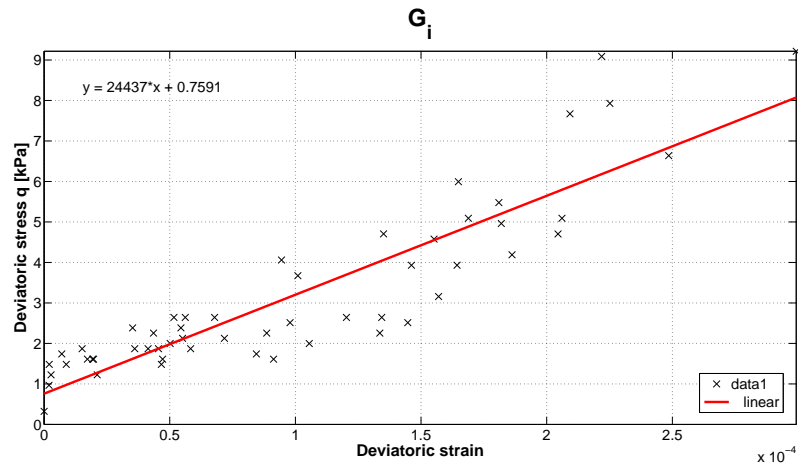
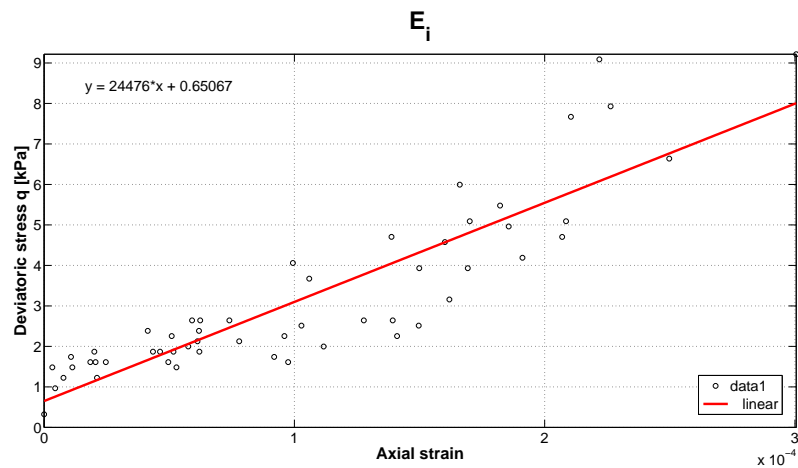
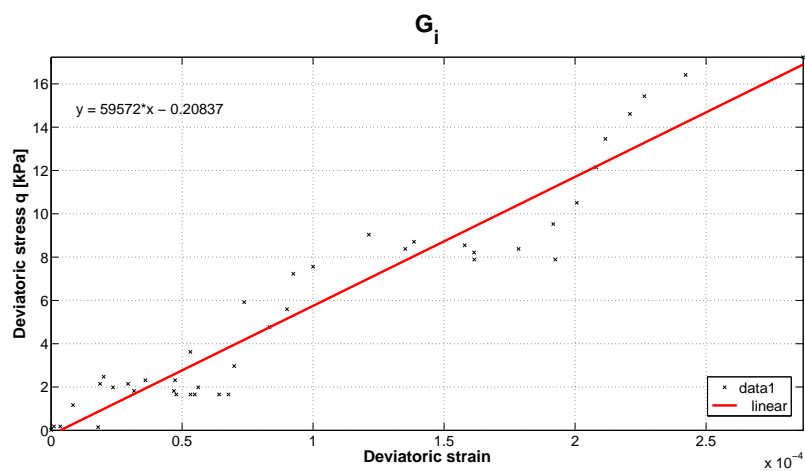


Figure 4.11: Initial shear modulus G_i for Test 1 (CID).

Figure 4.12: Initial Young modulus E_i for Test 2 (CID)..Figure 4.13: Initial shear modulus G_i for Test 2 (CID).Figure 4.14: Initial Young modulus E_i for Test 3 (CID).

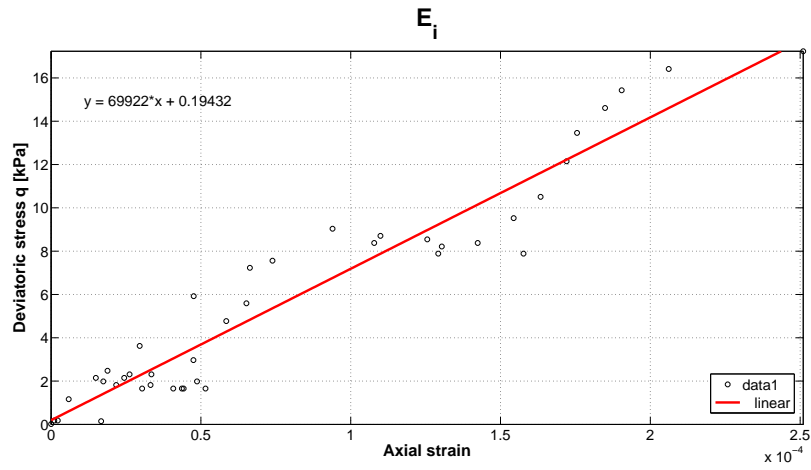


Figure 4.15: Initial shear modulus G_i for Test 3 (CID).

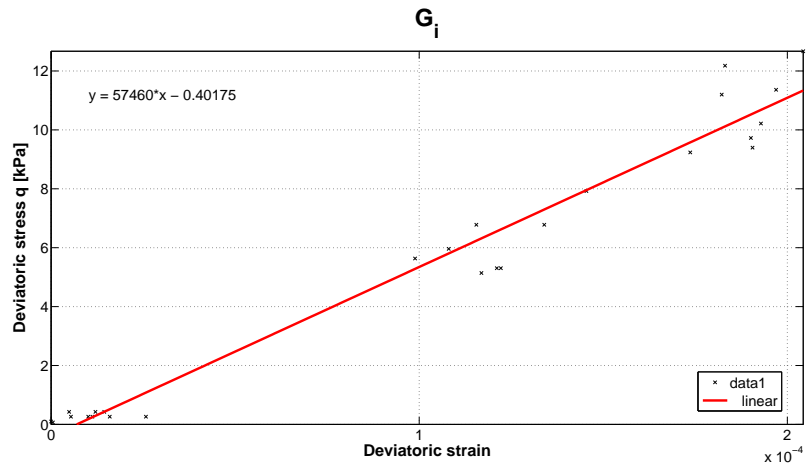


Figure 4.16: Initial Young modulus E_i for Test 4 (CID).

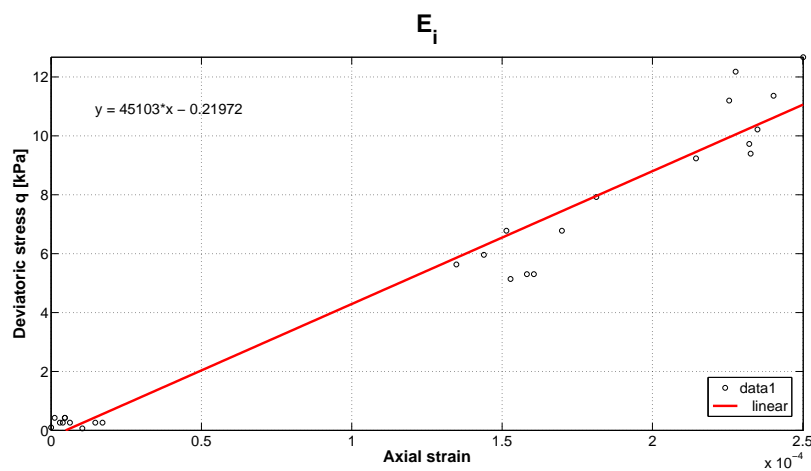


Figure 4.17: Initial shear modulus G_i for Test 4 (CID).

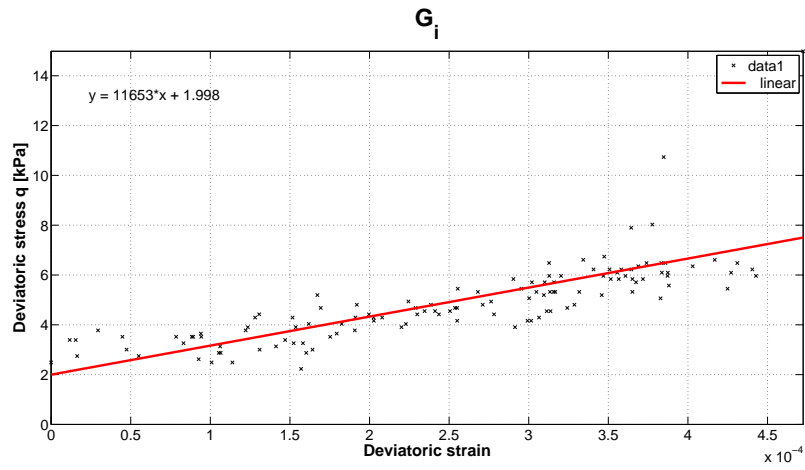


Figure 4.18: Initial Young modulus E_i for Test 5 (CID).

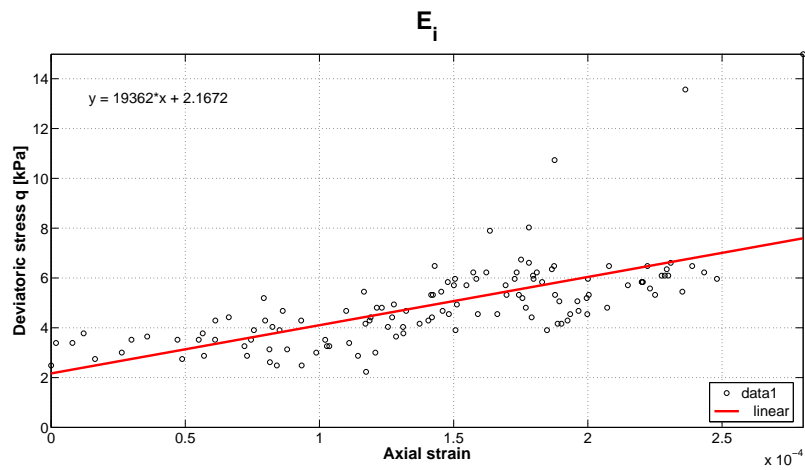


Figure 4.19: Initial shear modulus G_i for Test 5 (CID).

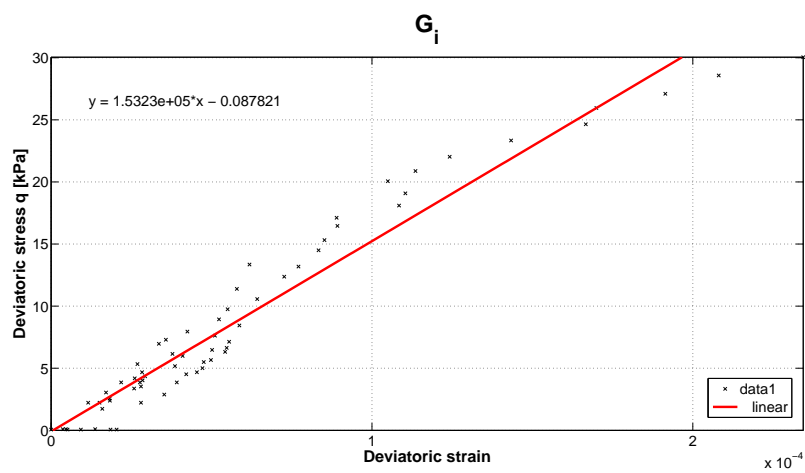


Figure 4.20: Initial Young modulus E_i for Test 7 (CID).

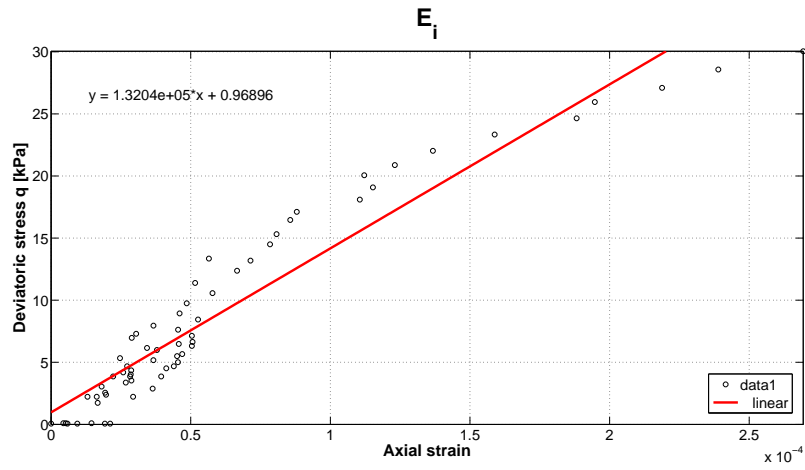


Figure 4.21: Initial shear modulus G_i for Test 7 (CID).

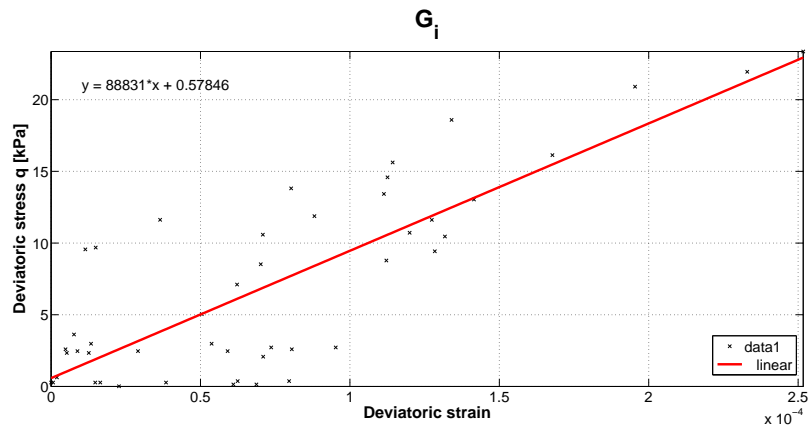


Figure 4.22: Initial Young modulus E_i for Test 8 (CID).

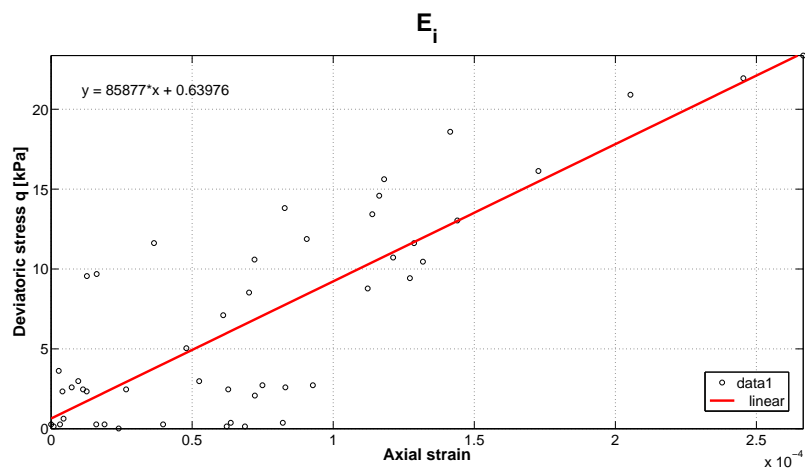


Figure 4.23: Initial shear modulus G_i for Test 8 (CID).

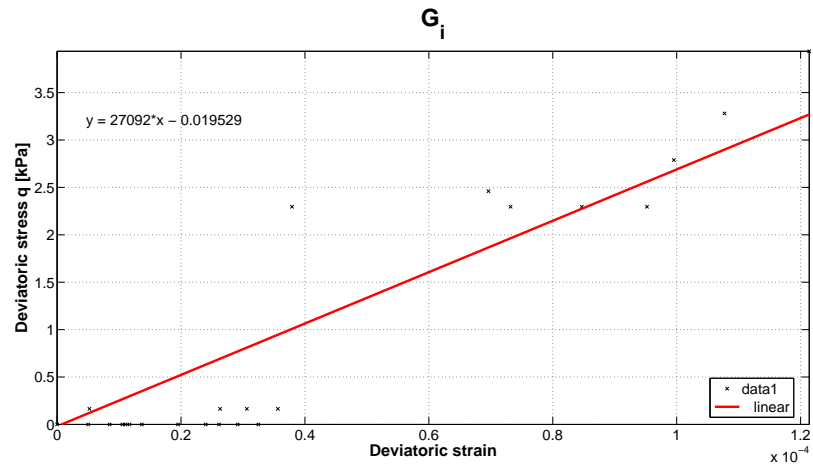


Figure 4.24: Initial Young modulus E_i for Test 9 (CID).

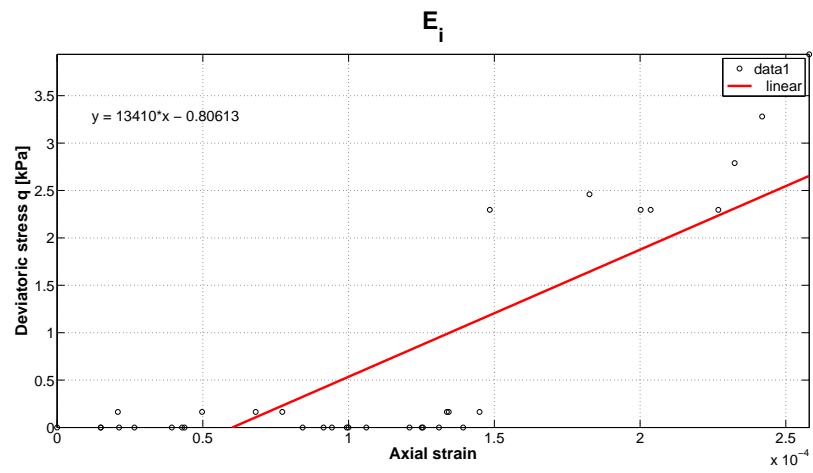


Figure 4.25: Initial shear modulus G_i for Test 9 (CID).

Appendix C

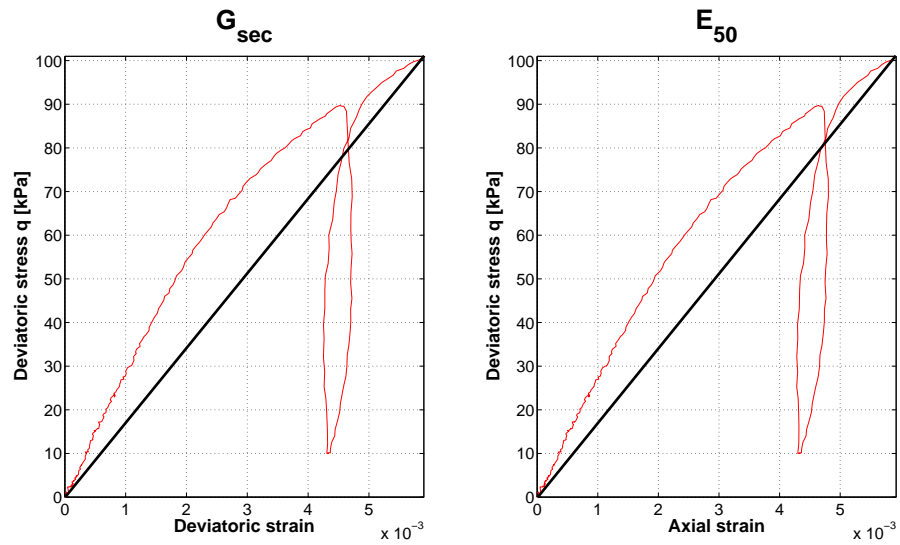


Figure 4.26: Young modulus E_{sec} and shear modulus G_{sec} for Test 1 (CID).

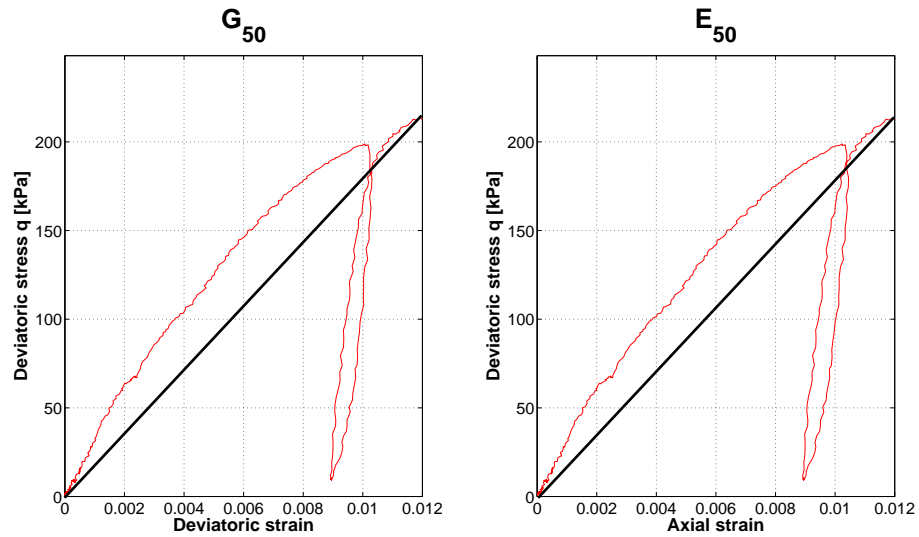


Figure 4.27: Young modulus E_{50} and shear modulus G_{sec} for Test 2 (CID).

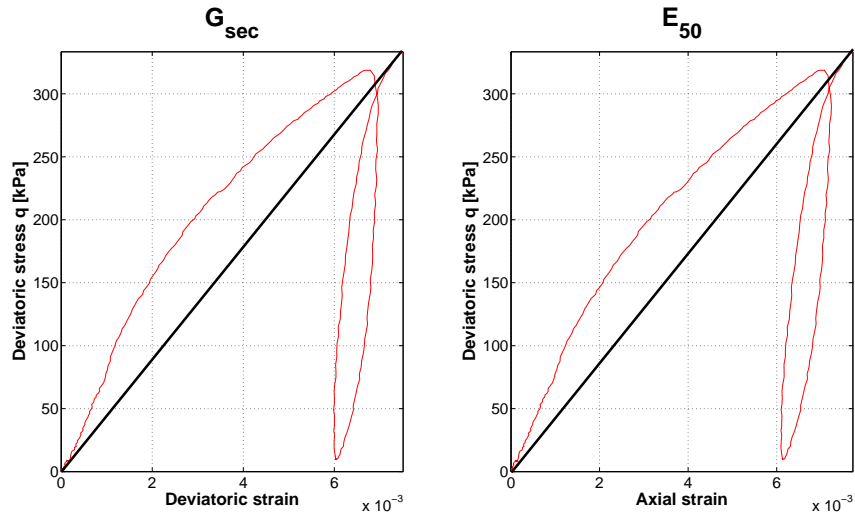


Figure 4.28: Young modulus E_{50} and shear modulus G_{sec} for Test 3 (CID).

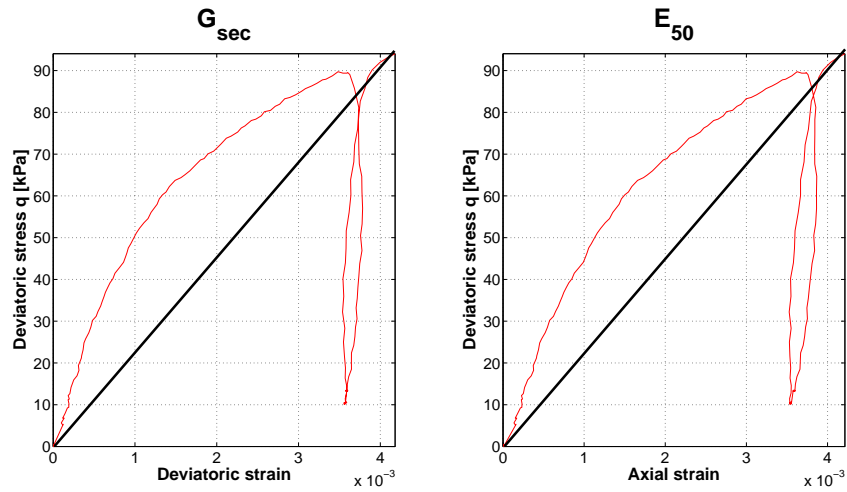


Figure 4.29: Young modulus E_{50} and shear modulus G_{sec} for Test 4 (CID).

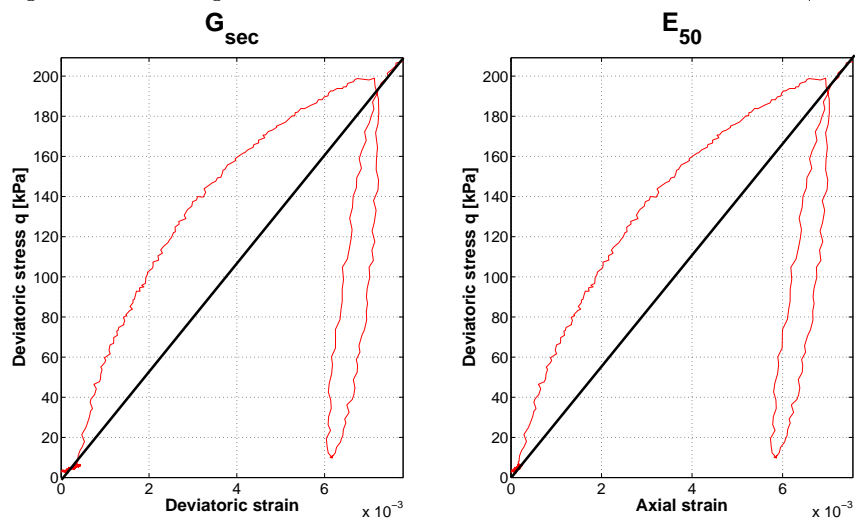


Figure 4.30: Young modulus E_{50} and shear modulus G_{sec} for Test 5 (CID).

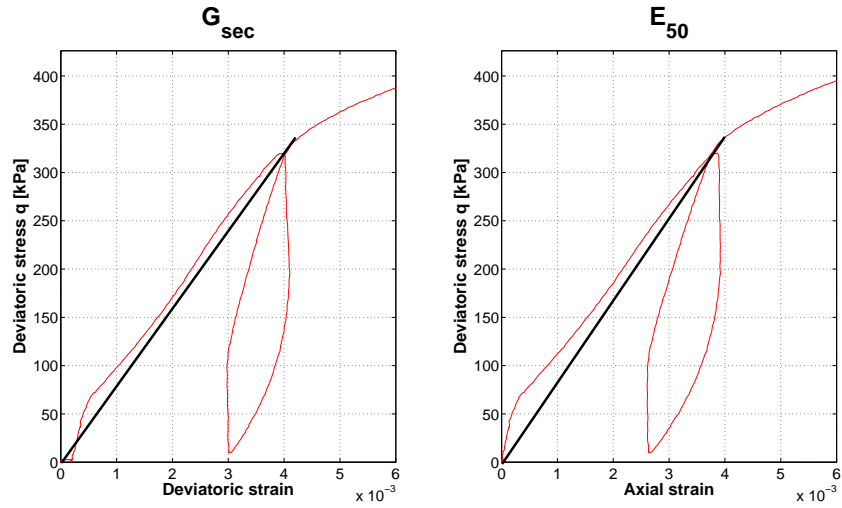


Figure 4.31: Young modulus E_{50} and shear modulus G_{sec} for Test 6 (CID).

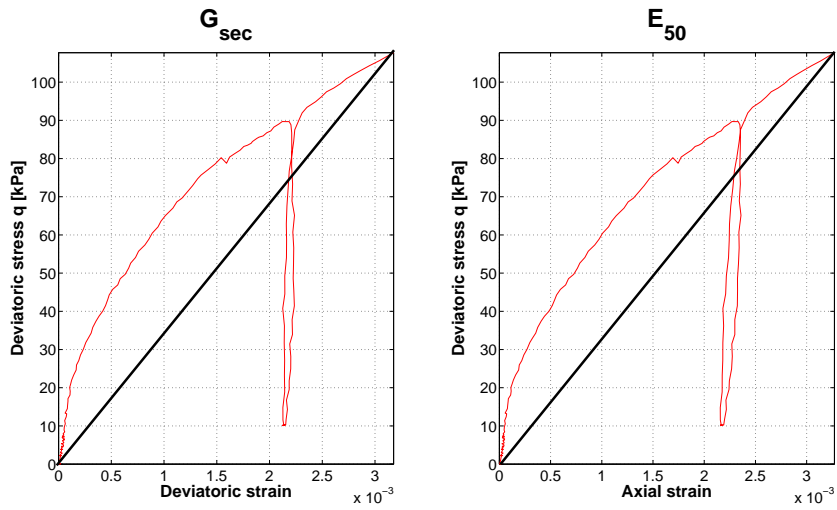


Figure 4.32: Young modulus E_{50} and shear modulus G_{sec} for Test 7 (CID).

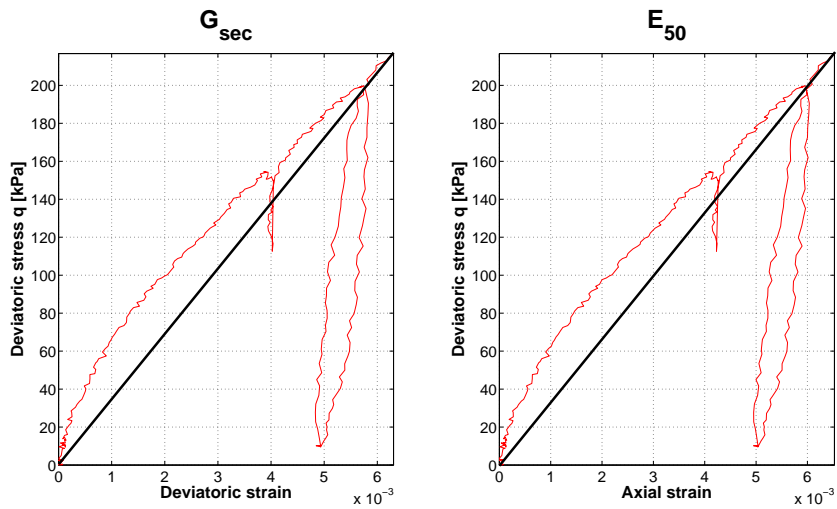


Figure 4.33: Young modulus E_{50} and shear modulus G_{sec} for Test 8 (CID).

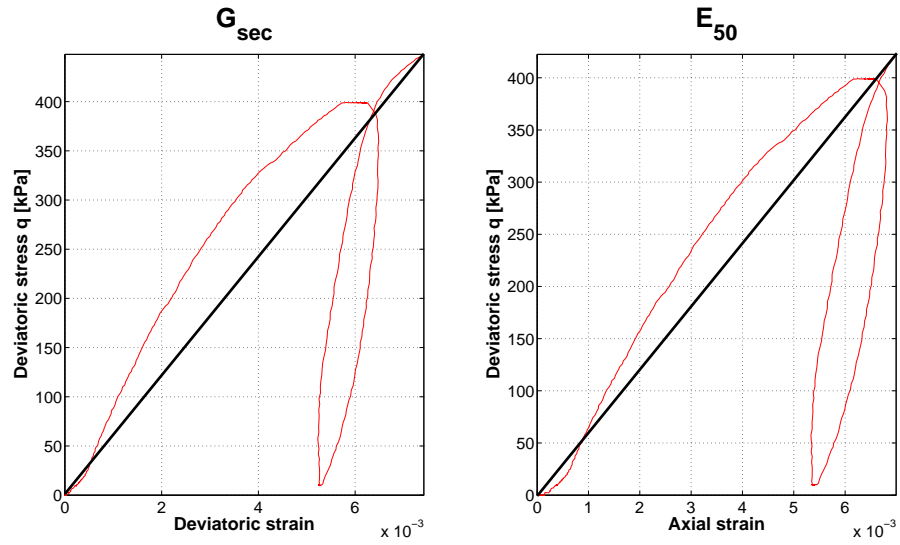


Figure 4.34: Young modulus E_{50} and shear modulus G_{sec} for Test 9 (CID).

Appendix D

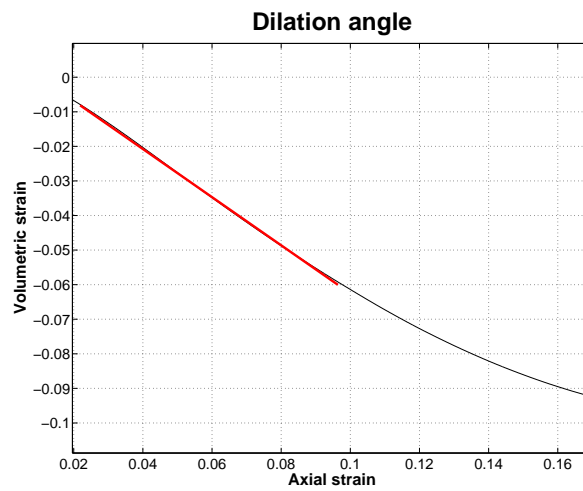


Figure 4.35: Dilation angle for Test 1 (CID).

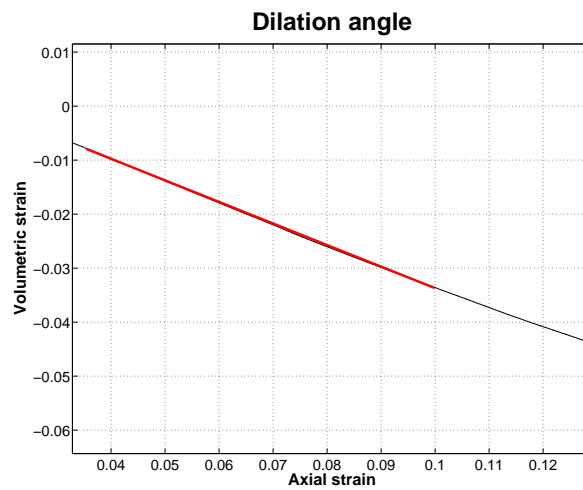


Figure 4.36: Dilation angle for Test 2 (CID).

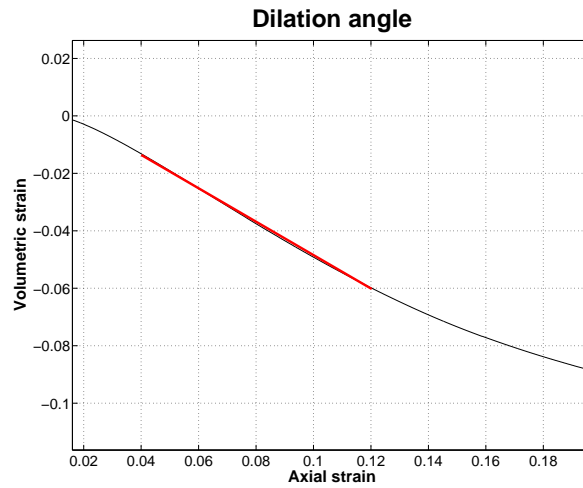


Figure 4.37: Dilation angle for Test 3 (CID).

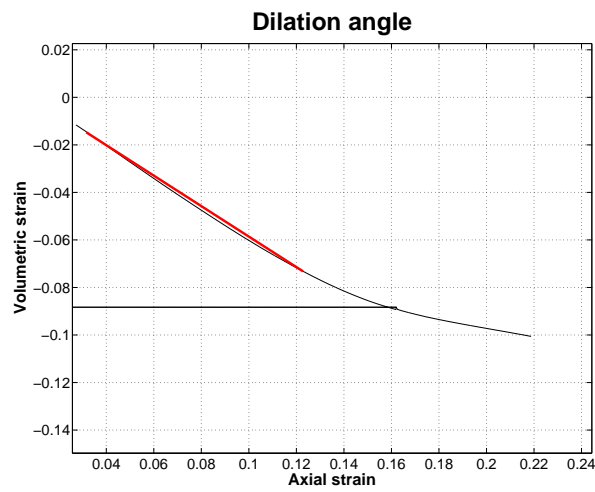


Figure 4.38: Dilation angle for Test 4 (CID).

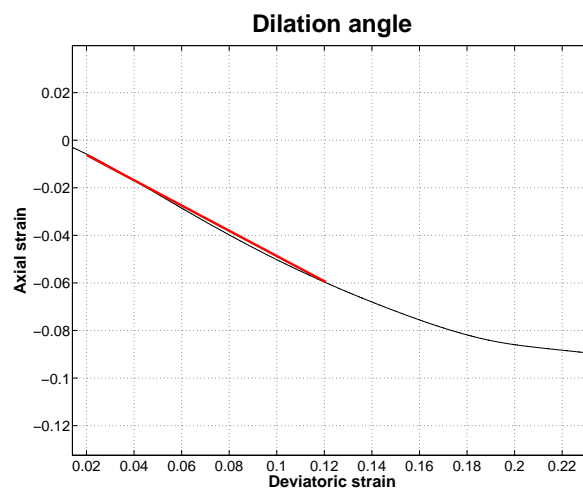


Figure 4.39: Dilation angle for Test 5 (CID).

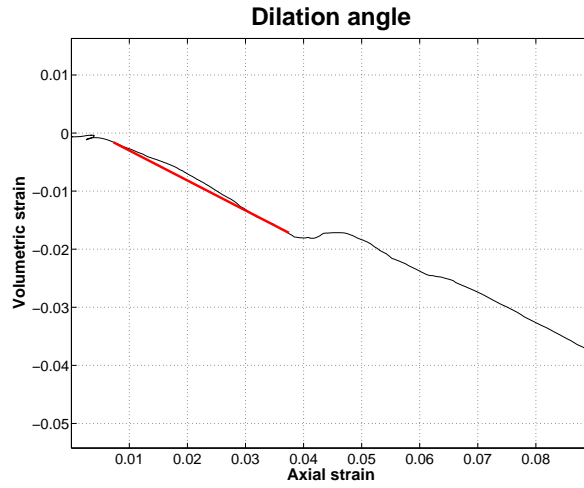


Figure 4.40: Dilation angle for Test 6 (CID).

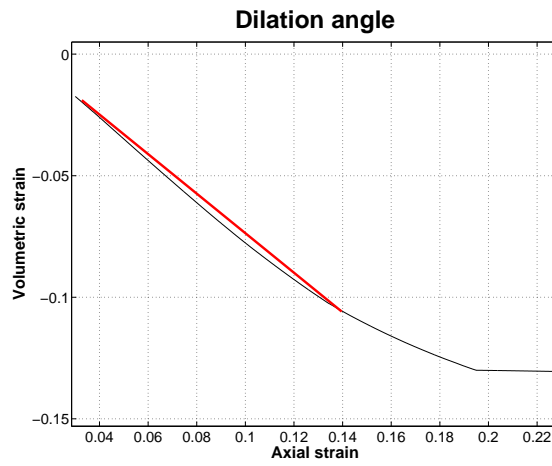


Figure 4.41: Dilation angle for Test 7 (CID).

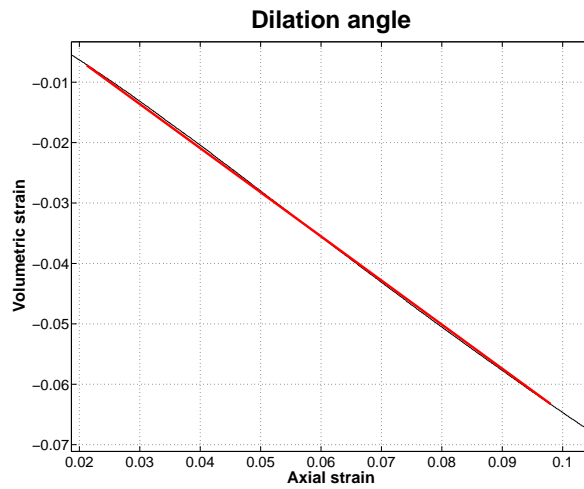


Figure 4.42: Dilation angle for Test 8 (CID).

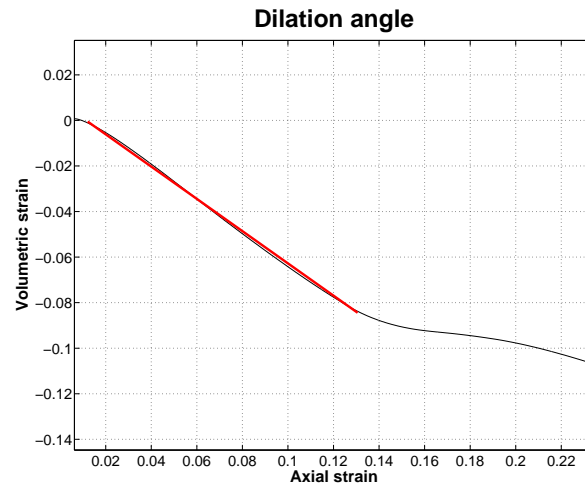


Figure 4.43: Dilation angle for Test 9 (CID).

Technical University
of Denmark



DTU Civil Engineering
Department of Civil Engineering
Technical University of Denmark

Brovej, Building 118
2800 Kgs. Lyngby
Telephone 45 25 17 00

www.byg.dtu.dk

Nowadays, the offshore wind market is moving towards wind farms with higher capacity generators and in deeper waters to increase energy production. In the future, the offshore wind market will require advanced models to reduce the cost of jacket foundations for offshore wind turbines. Therefore, it is necessary to improve the investigation of the dynamic response of jacket foundations. The purpose of this project is to develop a numerical model to capture the dynamic response of jacket foundations, accounting for the soil-foundation interaction, soil properties and foundation geometry.

DTU Civil Engineering
Technical University of Denmark

Brovej, building 118
28/00 Kongens Lyngby

www.byg.dtu.dk

ISBN 9788778774866
ISSN 1601-2917